Polarimetric properties of radar echoes from features on the ocean surface

James Thomas Stewart Morris

THE UNIVERSITY OF ADELAIDE
AUSTRALIA

Department of Electrical and Electronic Engineering
The University of Adelaide
South Australia 5005
Australia

A thesis submitted in fulfilment of the requirements for the degree of Doctor of Philosophy

September 2004

TABLE OF CONTENTS

Abstract

This thesis presents the results of an investigation of the polarimetric properties of radar echoes from features on the sea surface, including freely-propagating gravity and capillary waves, breaking waves and ship wakes. Analysis and interpretation of the data is based mainly on the Cloude-Pottier H/A/$\bar{\alpha}$ decomposition of the coherence / covariance matrix. Variations in the distribution of polarimetric entropy, scattering alpha and anisotropy of radar echoes are examined in the in the H–$\bar{\alpha}$, H–A and H–A–$\bar{\alpha}$ spaces to characterise the dominant scattering mechanisms.

First, a review of the concepts and theory of polarimetric scattering from point and distributed targets is given. A detailed examination of the theory and techniques developed to calibrate polarimetric radar systems follows, focussing on the need to calibrate in the field as opposed to the ideal laboratory environment. A new calibration scheme is described that employs a parabolic dish antenna with a dual linear feed horn with two delay lines to perform the radiometric calibration, while a rotating dihedral corner reflector is used to perform the phase calibration; this design achieves stable, accurate calibration to ±0.5 dB in magnitude and 4° in phase.

Radar scattering from the sea surface is then discussed in the context of the hydrodynamic problem of describing the sea surface and the electromagnetic problem of finding an approximate solution to Maxwell's equations. The X-Bragg model is applied to predict variations in the polarimetric parameters for progressive and breaking waves. The problem of validating polarimetric measurements of the sea surface is discussed and the possibility of exploiting a quasi-deterministic surface, in the form of a Kelvin wake generated by a moving ship, is proposed and assessed by experiment.

Investigations of the polarimetric characteristics of the near shore wave field are then reported and a comparison with the results predicted by the X-Bragg model given. Polarimetric wake measurements are analysed using (i) eigen-decomposition of the coherency matrix, and (ii) a novel method based on the distribution of the cross-polar nulls. These approaches are compared with the scattering predictions obtained using numerical wake prediction codes, combined with the Bragg scattering model. The application of wakes as a tool for studying highly nonlinear hydrodynamic processes is demonstrated using the interaction between the wake produced by a boat and ambient swell to initiate wave breaking events.

Statement of Originality

This work contains no material which has been accepted for the award of any other degree or diploma in any university or other tertiary institution and, to the best of my knowledge and belief, contains no material previously published or written by another person, except where due reference has been made in the text.

I consent to this copy of my thesis, when deposited in the University Library, being available for loan and photocopying.

James Morris

Date: 16th September 2004

LIST OF FIGURES

LIST OF TABLES

LIST OF SYMBOLS

Chapter 1

H	polarimetric entropy
A	polarimetric anisotropy
$\overline{\alpha}$	mean polarimetric scattering alpha

Chapter 2

$\vec{E}(\vec{r},t)$	instantaneous real electric field vector
$\vec{r}$	position vector
t	time
$\vec{k}$	propagation vector
ω	angular frequency of the wave
$\vec{E}$	constant complex amplitude vector of the electric field
E_h	complex horizontal component of the electric field
E_v	complex vertical component of the electric field
$\vec{h}$	unit vector in the horizontal plane
$\vec{v}$	unit vector in the vertical plane
a_h	magnitude of E_h
a_v	magnitude of E_v
δ_h	phase of E_h
δ_v	phase of E_v
τ	tilt angle of the polarisation ellipse
ε	ellipticity angle of the polarisation ellipse
α	auxiliary angle of the polarisation ellipse
a_η	minor semi axis of the polarisation ellipse
a_ξ	minor semi axis of the polarisation ellipse
A_0	wave amplitude of a plane monochromatic wave
ϕ_0	absolute phase reference
$\vec{q}$	Stokes vector
$\vec{E}_{mn}$	two dimensional complex Jones vector
$\vec{E}_+$	Jones vector for waves propagating in the $+\vec{k}$ direction
$\vec{E}_-$	Jones vector for waves propagating in the $-\vec{k}$ direction
ρ	complex polarisation ratio
$[U_n]$	n × n unitary complex transformation matrix
$\vec{E}^i$	incident electric field vector
$\vec{E}^s$	scattered electric field vector
$[S]$	2 × 2 complex coherent scattering matrix
$[T]$	2 × 2 complex Jones matrix

σ^{o}_{IJ}	radar cross section
$\vec{k}_4$	general four element complex scattering vector
$V([S])$	vectorisation operator
Ψ	complete set of 2×2 complex basis matrices
Ψ_L	Lexicographic basis set
$\vec{k}_{4L}$	4 element scattering vector (Lexicographic basis)
Ψ_P	Pauli basis set
$\vec{k}_{4P}$	4 element scattering vector (Pauli basis)
$[D_n]$	$n \times n$ transformation matrix from Pauli to Lexiographic basis
$[Q]$	4×3 transformation matrix (Lexicographic basis)
$\vec{k}_{3L}$	3 element backscattering scattering vector (Lexicographic basis)
$\vec{k}_{3P}$	3 element backscattering scattering vector (Pauli basis)
S_{XY}	symmetrised cross-polar component
$[C_n]$	$n \times n$ polarimetric covariance matrix
$[T_n]$	$n \times n$ polarimetric coherency matrix
λ_i	i^{th} eigenvalue
$\vec{e}_i$	i^{th} eigenvector
$[M]$	4×4 Mueller matrix (real)
$[A]$	4×4 Kronecker expansion matrix (real)
$[K]$	4×4 Kennaugh matrix (real)
$[R_n(\theta)]$	$n \times n$ LOS unitary rotation matrix (real)
$[\Lambda_n]$	$n \times n$ diagonal eigenvalues matrix (real)
$k_s, k_d^{\pm}, k_h^{\pm}$	Sphere, helix, diplane decomposition parameters
P_i	appearance probability of the i^{th} eigenvector
α	scattering alpha-angle
β	scattering beta-angle
$\bar{\alpha}$	mean scattering alpha-angle
$\bar{\beta}$	mean scattering beta-angle
$\vec{I}$	feature vector

Chapter 3

C_i	co-polar null
S_i	cross-polar maximum
X_i	cross-polar null
T_i	cross-polar saddle point
$[Z_{n\times m}]$	complex $n \times m$ system distortion matrix
$[R]$	complex 2×2 distortion matrix for the receive path

$[T]$	complex 2×2 distortion matrix for the transmit path
$[A_4]$	Kronecker distortion matrix
δ_i	phase distortion errors
r_i	amplitude distortion factor
$[R_{ZYL}]$	distortion matrix in the van Zyl algorithm

Chapter 4

F_{Start}	start frequency
$F_{Increment}$	frequency increment
F_{Local}	local oscillator frequency
N	number of frequency steps

Chapter 5

λ	dominant wavelength
f	frequency
d	water depth
k	wavenumber
ω	angular frequency
g	acceleration due to gravity
σ	surface tension
ρ	density
C	celerity
$S(\vec{k})$	directional wave spectrum
γ	peak shape parameter
l	characteristic length scale
$B_{\perp}$	Bragg coefficients perpendicular to the incidence plane
$B_{\parallel}$	Bragg coefficients parallel to the incidence plane
ε_0	complex permittivity
$\vec{e}_{3P}$	normalised Pauli scattering vector
α_B	Bragg model alpha parameter
θ	*local* angle of incidence
$\hat{Z}$	surface profile
B_{pq}	Bragg coefficients
$\vec{n}$	local surface normal
γ	range slope
ω	azimuth slope
$\vec{t}$	local surface tangent
ϕ	angle of incidence
β	effective rotation angle
$P(\beta)$	distribution of surface slopes
β_1	width of the distribution of surface slopes

ν_e	water eddy viscosity
γ_{LLRR}	left-right circular coherence
a_k^+	creation operator
a_k	annihilation operator
ψ_k	normal modes
$\Psi(t)$	state vector

Chapter 6

u	ship speed perpendicular to the wave crests
d	water depth
g	gravitational acceleration
L	swell wavelength
t_{wb}	time between induced wave breaking events
k	wave number

LIST OF ABBREVIATIONS

AGC	Automatric Gain Control
AIC	Akaike Information Criteria
BCD	Binary Coded Decimal
BSA	Backscatter Alignment
CAD	Computer Aided Design
CTD	Coherent Target Decomposition
CW	Continuous Wave
DRA	Defence Research Agency
DSTO	Defence Science And Technology Organisation
EKA	Extended Kirchhoff Approximation
FLTK	Fast Light Toolkit
FSA	Forward Scattering Alignment
GBVP	Global Boundary Value Problem
GTD	Geometrical Theory of Diffraction
GUI	Graphical User Interface
IACT	Isolated Antenna Calibration Technique
IEEE	Institute of Electrical and Electronic Engineers
IF	Intermediate Frequency
IPU	International Physical Union
JONSWAP	Joint North Sea Wave Project
JPL	Jet Propulsion Laboratory
KA	Kirchhoff Approximation
LCM	Landing Craft (Mechanized)
LGA	Low Grazing Angles
LOS	Line Of Sight
NFSFS	Nonlinear Free-Surface Flow Solver
NRL	Naval Research Laboratory
OEL	Ocean Engineering Laboratory
ONERA	Office National d'Etudes et de Recherches Aérospatiales
PARCS	Polarimetric Active Radar Calibrators
PCTD	Partially Coherent Target Decomposition
PPM	Phase Perturbation Method
RAM	Radar Absorbing Material
RCS	Radar Cross Section
SAR	Synthetic Aperture Radar
SNR	Signal To Noise Ratio
SPM	Small Perturbation Method
SPST	Single Pole Single Throw
SSA	Small Slope Approximation
SSCM	Symmetric Scattering Characterisation Method
STCT	Single Target Calibration Technique
SWPE	Sea Wave Pattern Evaluation
TSM	Two-Scale Model
TWTA	Travelling Wave Tube Amplifier
UCSB	University Of California, Santa Barbara
UPM	Unified Perturbation Method
VTK	Visualisation Toolkit
X-Bragg	Extended Bragg

ACKNOWLEDGMENTS

The work presented in this thesis would not be possible without the support and encouragement of many people. First and foremost, I would like to acknowledge and thank my principal supervisor Professor Stuart Anderson for his encouragement and guidance, for teaching me how to recognise the cardinal properties of complex data sets and interpret these in terms of physical processes, for inspiring me with the intrinsic value of scientific inquiry and for the many improvements and suggestions that he has made to the content of this work. I would also like to thank my supervisor at DSTO, Dr Cheng Anderson who encouraged me to undertake a PhD, supported my application for candidature and ensured that the necessary resources were available to complete this work. Both Cheng and Stuart have been extremely generous with their time, even at the busiest of periods, and have always provided honest, constructive feedback and for this I am extremely grateful.

I would also like to express my gratitude to my employer, the Defence Science and Technology Organisation, in particular the Executive of the Electronic Warfare and Radar Division, for the opportunity to pursue this work as part of its research programme. I am grateful to Dr Andrew Shaw for his suggestions and improvements he contributed to this work.

Thanks are also due to the Department of Electrical and Electronic Engineering at The University of Adelaide for endorsing and supporting my candidature. In particular Dr Andrew Parfitt for his role as my academic supervisor while he was at the University.

Mr Paul Dansie, Mr Mark Ingham and Mr John Senior deserve a large amount of credit for building, maintaining and upgrading the DSTO radar system. Their assistance during the experimental measurements and willingness to adapt both the radar hardware and software to accommodate my requirements has been greatly appreciated. Mr Layton Catford and Mr Peter Drake provided great assistance with the field calibration and anechoic chamber measurements and thanks are also due to the EWRD workshop for their excellent work in producing the calibration targets that were used in this study.

I am grateful to the members of the Scientific & Engineering Services, in particular Mr Colin Pratt and Mr Tony Campman, for creating the CAD models used in the SWPE simulations and for their assistance with the printing of conference posters.

Professor Wolfgang-Martin Boerner from the University of Illinois, Chicago has been a continual source of encouragement since our meeting prior to IGARSS'01 and provided me with many important references and contacts that were invaluable during this work and I am particularly appreciative of his input. My thanks also go to Professor Shane Cloude for his assistance with the calibration procedure, guidance through the extended Bragg model and for the many discussions on the entropy-alpha decomposition and its interpretation and for the Matlab code for performing the eigenvalue decomposition. Our trip to Evans Head and search for the ideal measurement location remains one of the highlights of my experiences in the field.

Finally, I am completely indebted to my family for the love and support they have given me over the years. Particularly my parents and sister Ali who have always been a great source of inspiration and encouragement and my wife Tania who has provided assistance in so many ways and helped me to achieve my dreams. I will always be grateful to you.

Chapter 1 Introduction

The polarisation dependence of the radar scattering behaviour of targets of interest, natural and man-made, has been studied extensively for many years, but radar technology capable of exploiting this dependence effectively is a relatively recent development. The development of operational systems in the 1980's and the subsequent refinement and improvement of modern sensors has ensured that radar polarimetry has become an indispensable tool in modern radar and imaging technology. Experimental polarimetric radar systems have been built by groups in Europe, the USA, Russia, Japan and elsewhere, and used in both SAR and real aperture configurations, but many questions remain unanswered, particularly in the areas of enhanced detection, target classification and polarisation-adaptive signal design, and in the exploitation of polarimetric analysis to study the geometry and dynamics of the ocean surface.

This chapter provides a perspective on the historical development of radar polarimetry and reviews the polarimetric studies of the sea surface that have been reported in the literature. Particular attention is given to low grazing angle measurements performed with high resolution polarimetric radar systems. The problems addressed in this thesis are then outlined, the contributions made as a result of this study are highlighted and the structural format of this thesis is laid out.

1.1 Historical development of radar polarimetry

In the eleventh century, whilst navigating in the Baltic Sea and Arctic waters, the Vikings used the "*findlings stone*", made from some form of dichroic mineral like cordierite, to navigate in the absence of direct sunlight. In so doing they were possibly the first humans to exploit polarimetric effects as a tool [1].

The Vikings did not understand the phenomenon that they were using and it was not until the early seventeenth century that the first scientific experiments related to polarised electromagnetic energy were performed, led by Bartolinus (1625-1695), Huygen (1629-1695) and Malus (1755-1821). Malus first used the term *polarisation* in 1808 to explain the refraction of light through calcite crystals. In 1815, Brewster

(1781-1868) discovered the relationship between the polarising angle and the relative refractive power of the dielectric material. In 1832 Faraday (1791-1867) published his postulations of the physical laws of electromagnetism. This was followed by his discovery in 1845 of the rotation of the polarisation plane in magnetic fields. In 1852 Stokes (1819-1903) published a method for representing polarised, unpolarised and partially polarised streams of light and in 1873 Maxwell (1831-1879) succeeded in providing a rigorous formulation of Faraday's postulates. This led to the formulation of diffraction theories by Helmholtz (1881) and Kirchhoff (1883). In 1892 Henri Poincaré (1854-1912) contributed to the understanding of polarised light by showing that points on the Riemann sphere could represent all possible states of polarisation. During 1886-1888 Hertz (1857-1894) demonstrated the application (including the polarisation state dependence) of electromagnetic theory as it applies to lower frequencies such as radio waves.

A more detailed history of these events is presented in [1] and additional information can be found in a variety of sources including [2, 3]. The work of Hertz marks the advent of modern applications of electromagnetic waves. From it evolved radio wave communication, object detection and ranging. Hülsmeyer first implemented these techniques between 1896 and 1904 and is now acknowledged as the true father of radar [4].

Radar was re-explored during the 1920's and 1930's and further advances were made during the Second World War by both competing factions. These advances are described by Guerlac [5], Burns [6], Pritchard [4] and Skolnik [7]. The radars developed during this period used only the amplitude information in the backscattered wave and failed to exploit the polarimetric information contained in the signal.

A detailed review of the historical events that led to the development of polarimetric radar has been prepared by Boerner [1]. This paper describes the fundamental studies by Sinclair [8], Rumsey and Kennaugh [9], Deschamps [10] and Gent [11]. These studies identified that radar targets act as polarisation transformers, which subsequently led to the concept of optimal target polarisations. Based on Kennaugh's original pioneering work on discovering the properties of the "*Spinorial Polarisation*

Fork" concept [9, 12], Huynen [13] developed a *"Phenomenological Approach to Radar Polarimetry"*. He developed the "*orthogonal (group theoretic) target scattering matrix decomposition*" [14-16] and extended the characteristic optimal polarisation state concept of Kennaugh [9, 12, 17], which lead to the renaming of the spinorial polarisation fork concept to the so called '*Huynen Polarisation Fork*' [17]. Copeland's [18] work, which culminated in the first practical scheme for classification and identification of radar targets, is also noted in Boerner's review along with the work of Eaves [19], who developed the concept of intra-pulse polarisation agile radar, and Poelman [20], who worked on pulse switching and polarimetric multi-notch filtering.

Boerner's review concentrates on the developments made in the West and only briefly discusses the work performed in Russia in the late sixties and early seventies. A more detailed account of this latter work can be found in [21], which highlights the fact that the Russians quickly recognised the potential improvements that radar polarimetry could offer. Consequently, they vigorously pursued polarimetric radar investigations following the publication of Huynen's dissertation.

The earlier phase of radar polarimetry might be considered to end with the publication of Huynen's dissertation. No real progress was made in advancing the fundamentals of radar polarimetry until a renewed effort was initiated by Boerner [22] at the University of Chicago in 1978. The aim of this study was to reassess the work of Kennaugh and Huynen. This resulted in new methods for calculating the characteristic polarisation states, new target decomposition algorithms, new imaging radar systems (including polarimetric SAR systems) and several other theoretical and experimental techniques. Boerner and his collaborators [23-25] successfully extended Kennaugh's and Huynen's work to the general bistatic case. Further advances in this area have more recently been made by Czyz [26, 27], Germond, Pottier and Saillard [28-30] and Lüneburg and Cloude [31]. Significant improvements in radar detection, recognition, discrimination and identification have resulted from the introduction of the covariance matrix optimisation procedures of Tragl [32], Novak *et al.* [33], Lüneburg [34] and Cloude and Pottier [35]. In particular the '*Cloude-Pottier Polarimetric Entropy H, Anisotropy A, Feature Angle* $\bar{\alpha}$ *parametric decomposition*'

[36] has had a great impact since it allows unsupervised target feature interpretation. Significant progress in interpreting and analysing POL-SAR image features has been made using the various fully polarimetric target feature syntheses [37], polarisation contrast optimisation [38] and polarimetric entropy/anisotropy classifiers [39-41]. In all of these techniques, well calibrated scattering matrix data is an essential pre-requisite [42]. The development of polarimetric calibration techniques is discussed in detail in Chapter 3.

In the past 20 years, radar polarimetry has been applied to remote sensing and other fields with great success, particularly in the area of classification schemes of earth terrain. Examples include techniques developed by van Zyl [43], Pottier [44], Cloude and Pottier [36, 40], Krogager *et al.* [37], Lee [45] and Freeman [46]. The interpretation of polarimetric SAR imagery has been helped by the implementation of the 'Lee Filter' [47-49] for speckle reduction, while the 'Polarimetric Lee-Wishart distribution' [50] has been used by many to improve image feature characterisation.

Another initiative has been the extension of polarimetric concepts to radar systems at low frequencies, VHF and even HF. For VHF radars operating through the ionosphere, Anderson *et al.* [51] showed that spatial diversity should enable S-matrix determination even though Faraday rotation during propagation through the ionospheric magneto-plasma introduces *a priori* unknown transformation of the signal polarisation. At HF, the polarimetric aspects of skywave propagation and scattering from targets have been explored both theoretically [52] and experimentally [53-55] in the context of over-the-horizon radar.

During the past decade several diverse multiple-baseline SAR techniques have also been developed for space and airborne platforms. Recently powerful techniques such as polarimetric SAR interferometry [56-59] and polarimetric SAR tomography have been demonstrated [60, 61]. An excellent review of these recent advances and many others in extra-wide band polarimetry, interferometry and polarimetric interferometry has been prepared by Boerner [62].

1.2 Polarimetric measurements of the sea surface

Observations of the sea surface performed using microwave radars located on ships or land based platforms generally view the ocean surface at low grazing angles while observations from airborne or spaceborne sensors view the sea surface from much higher grazing angles, typically between 20° – 70°. Consequently, the behaviour of electromagnetic waves scattered from the ocean surface over a wide range of measurement geometries is of interest.

At high grazing angles, ocean backscattering is reasonably well understood in terms of the two-scale or composite surface scattering models. Polarimetric observations of the ocean surface at mid grazing angles (40° – 70°) have been performed using airborne SAR systems. The majority of the initial data was collected by the JPL AIRSAR and focused on the influence of long waves and ocean features on the polarimetric signatures. Schuler *et al.* [63] made comparisons of AIRSAR data collected at P-band with modelled results derived from a tilted Bragg model and the composite-surface model developed by Valenzuela [64] and demonstrated that the models correctly predicted the scattering effects observed. Particular attention was paid to the P-band results due to the high coherence values [63] that enabled the polarimetric effects of long wave tilts to be studied separately without the influence of the small scale structure. This research demonstrated that modelling of surface tilts was essential for predicting the polarimetric signatures and other properties, along with the realisation that long wave tilts in the azimuthal direction could be measured directly from their influence on the polarimetric signature. Schuler *et al.* [63] demonstrated that the location of the co-polarised maximum moved parallel to the orientation axis in response to the surface tilt. Schuler and Lee [65] applied this result to improve the visibility of azimuthally travelling waves and to measure terrain slopes on land [66]. These studies also highlighted the fact that the measured polarisation signatures are strongly influenced by the incident angle.

At low grazing angle the composite surface theory models cannot explain the observed large cross section for horizontal polarisation in low grazing angle measurements. High-contrast scattering events known as sea spikes are often observed in high resolution horizontally polarised backscatter with amplitudes that are

10 – 20 dB higher than the predictions obtained from Bragg models [67]. Kalmykov *et al.* [68] performed some of the first polarimetric investigations of sea spikes in the Caspian Sea. Measurements were performed at X band from a 12 m high platform at grazing angles below 8°. A range resolution of 6 m was used enabling different parts of the ocean wave profile to be resolved. High amplitude clutter events were observed on the HH and cross-polar channels (HV and VH) with values 10 to 15 dB higher than the neighbouring backscatter levels. Similar events were not seen in the VV data. The absence was explained with a two-scale model and proposed wedge shaped scatterers representing the steep wave crests as the source of the sea spikes. The opposite experimental result (low HH/VV ratios) was also explained using the wedge shaped scatterers (pointing upwards) by Lewis and Olin [69] and detailed discussions of wedge scattering models is given in [70, 71].

Polarimetric measurements [72, 73] in the Black Sea also showed that there was a substantial difference in the polarisation signatures of sea clutter when sea spikes were present. The co-polar signatures obtained when sea spikes were absent exhibited low coefficients of variation [74] suggesting that the scattered return is highly polarised. The VV and HH polarised radar echoes were shown to be strongly correlated, while the VV:HH polarisation ratio was much less than unity, suggesting that a single mechanism dominates the radar return. In contrast, the co-polar signatures for sea spikes exhibit large pedestals and large coefficients of variation [74] suggesting that the echoes are weakly polarised. The VV and HH polarised signals associated with the sea spike events were also shown to be weakly correlated. Such scattering behaviour cannot be explained in terms of a single mechanism and lead to the conclusion that the sea spikes are caused by multiple, independent scattering mechanisms.

A possible explanation for the different signatures was proposed by Olin [75] and Trizna [76] and Hansen and Cavaleri [77] who found that the distribution functions of the VV scatter could be fitted to a single Weibull distribution, while the HH polarisation required two independent distributions. They suggested that distributed Bragg scattering [67] dominates in the absence of sea spikes whereas a combination of Bragg resonant waves and non-Bragg scatterers contribute to the sea spike events.

Similar arguments were used by Eckert *et al.* [78] and Lee *et al.* [79] to explain the polarised Doppler spectra for these events.

The importance of multipath interference and Brewster angle attenuation for sea spike images has also been recognised for many years [80, 81]. These effects were thoroughly investigated at the Naval Research Laboratory (NRL) in the 1990's, using wideband polarimetric radar [82] in the field [74, 83, 84], in wave tank measurements [85] and using numerical simulations [86-88]. These studies focussed mainly on the RCS statistics, frequency responses and the Doppler spectra characteristics at low grazing angles.

Detailed investigations [89-92] of both the cause and structure of sea spikes were initiated in 1994 at the Ocean Engineering Laboratory, University of California, Santa Barbara (UCSB). A high resolution, polarimetric FMCW radar was used to study breaking waves in the controlled environment of the large wind-wave tank at the Ocean Engineering Laboratory. The specific purpose of these investigations was to correlate the polarised backscatter with detailed observations of the wave processes as they occur, in order to gain a better understanding of the hydrodynamic sources and temporal structure of sea spikes.

While it is generally accepted that multiple scattering has a major role at low grazing angles, the underlying physics is not yet fully understood [84]. Sletten and Wu [85], Ebuchi *et al.* [93] and Trizna *et al.* [76] found in laboratory studies that the strongest returns could be associated with fast moving crests of sharp-crested or breaking waves. Measurements and simulations of ultrawide-band radar scattering from spilling breakers in wavetanks performed by Sletten and Wu [85] and West and Sletten [94] suggest that the scattering mechanism is dominated by multipath effects. Fuchs *et al.* [90] gave a physical explanation for the high HH/VV ratios observed using ray diagram calculations combined with a LONGTANK [95] simulation of the time variation in breaking wave shape which illustrated the phenomenon of ray focusing from the falling jet.

Recently, Plant [96] showed that there was no evidence for non-Bragg scattering for incidence angles up to about 50° and that the discrepancies in the RCS values were caused by fading, with the standard two-scale model scattering theory yielding probabilities of finding $\sigma^0_{HH} > \sigma^0_{VV}$ that were only slightly smaller than those found experimentally. Discrepancies still occur at very high angles of incidence (LGA) and Plant's theory does not account for the differences in the RCS values, but the addition of a non-Bragg component that is independent of the incidence angle and polarisation, brings the simulated cross sections and probability distributions into good agreement with the experimental data. Plant proposed that the physical interpretation of the non-Bragg component is return from the sea spray just above the air/sea surface.

Apart from the discrepancies in the σ_{HH} values at low grazing angles, the difference in the mean Doppler shift for horizontally and vertically polarised sea returns has been known for more than 30 years [97-99]. In the VV polarisation case, the observed behaviour can be explained using the Bragg model [68, 100] with the peak of the Doppler spectrum being related to the motion of the sea surface. Trizna [101] exploited this property in the measurement of ocean currents. In the HH case, the Doppler spectrum has been found to be a sensitive indicator of wave breaking [102] and Allan [103, 104] demonstrated that it can be used to estimate the degree of wave breaking at different locations relative to the fronts. According to composite surface theory, the return for both polarisations is due to scattering from Bragg-resonant surface waves of a few centimetres in length. The HH and VV Doppler shifts should be identical if the resonant waves are freely propagating at their intrinsic phase speed and are simply advected by currents due to the orbital velocities of longer waves, aside from a small difference due to power-frequency correlation noted many years ago by Hasselmann and Schieler [105]. Numerous wave-tank and field measurements [79, 102, 106, 107] have been performed to try to explain the observations at very high incidence angles, although they generally only considered the HH and VV cases and did not investigate the cross-polar spectra. Fuchs *et al.* [90] studied the variations in the Doppler spectra in low grazing angle measurements of breaking waves at UCSB and identified four phases in the wave breaking process that can be distinguished by variations in the hydrodynamic phenomena within them, corresponding to differing wave morphology. Other studies [89, 90, 106-111] have

led investigators to postulate that the difference in Doppler shifts is due to scattering from *fast scatterers*, which are more prominent in HH returns than in VV. Plant [112] also showed that for higher incident angles, Bragg scattering from bound, tilted waves could be used to account for anomalies in the Doppler spectra and for part of the under-prediction of the σ^0_{HH} values.

1.3 Problems and contributions

The work presented in this thesis focuses on three main areas. First, the problem of polarimetric calibration of high resolution polarimetric radar systems is addressed focussing on the need to be able to calibrate in the field as opposed to the ideal laboratory environment. Accurate phase calibration is a critical step if one is to obtain meaningful information from the polarimetric decomposition of the coherency matrix or infer information about the scattering characteristics of targets based on the distribution or location of the optimal polarisation states on the Poincaré sphere. The contributions in this area include

(i) a detailed review of calibration targets, their polarimetric properties and the techniques and theory developed to calibrate a variety of polarimetric systems.

(ii) an experimental comparison and assessment of several calibration techniques

(iii) a new calibration that employs a parabolic dish antenna with a dual linear feed horn with two delay lines to perform the radiometric calibration, while a rotating dihedral corner reflector is used to perform the phase calibration; this design achieves stable, accurate calibration to ±0.5 dB in magnitude and 4° in phase.

The second area that is examined embraces the polarimetric properties of the sea surface at X band for low grazing angle measurements. While numerous radar studies have been performed in this regime, few investigations have been performed with polarimetric radar. Almost all of the previous analysis of low grazing angle polarimetric measurements has focused on the dependence of clutter power on co- versus cross- polarisation and the form of the Doppler spectra for events such as sea spikes. Analysis of the coherence/covariance matrices using techniques like the Cloude-Pottier H/A/$\bar{\alpha}$ decomposition [36] have not previously been fully exploited in these types of measurements. The H–$\bar{\alpha}$, H–A and H–A–$\bar{\alpha}$ spaces have great

potential for examining scattering features in this regime. Accordingly, the majority of the analysis performed in this dissertation focuses on the variations in the polarimetric entropy, scattering alpha and anisotropy while using the H–$\overline{\alpha}$, H–A and H–A–$\overline{\alpha}$ spaces to examine and characterise the scattering mechanisms present. Analysis of measurements of progressive and breaking waves is presented resulting in the following contributions

(i) the measurements of breaking waves at low grazing angles demonstrate that there are characteristic changes in the polarimetric entropy, anisotropy and scattering alpha values as the waves form and break

(ii) the entropy values of the breaking waves are observed to remain fairly constant while both the anisotropy and scattering alpha values exhibit drop. These observations are shown to be consistent with the predictions obtained using the extended Bragg scattering model

(iii) the image products formed between the entropy and anisotropy images and their complementary images confirm that multiple scattering mechanisms are present during wave breaking events and are consistent with wave tank results.

The third area addressed in this work investigates the polarimetric properties of ship wakes observed at low grazing angles. While studies [113, 114] have been reported that have shown the potential for using polarimetry for detecting ship wakes in polarimetric SAR imagery at high elevation angles, few polarimetric studies of wakes have been performed at low grazing angles. This work highlights the potential for using wakes as a tool for validating ocean surface measurements and studying nonlinear events such as wave breaking. A key difficulty of validation of ocean surface polarimetric analysis is the presence of two unknowns – the scattering model being assessed and the stochastic surface geometry that provides the test environment. To overcome this ambiguity, the possibility of replacing the stochastic surface with a quasi-deterministic one is proposed - in the form of the Kelvin wake generated by a moving ship. The contributions in this area include

(i) the demonstration of the capability to measure the polarimetric properties of ship wakes at low grazing angles

(ii) an experimental comparison of ship wakes produced by a pilot boat and the surface elevations predicted by a numerical model using the Michell-Kelvin "thin ship" approximation

(iii) the development of a technique for classifying wake regions based on the distribution of the cross polar null states.

(iv) the demonstration of a technique of initiating wave breaking events with some control over where and when the events take place through the interactions of the ship wake with the ambient sea swell.

1.4 Organisation of the thesis

This thesis is organised into seven chapters. Chapter one introduces the problems to be considered, reviews the development of radar polarimetry and low angle polarimetric studies of the sea surface and highlights the contributions arising from this work.

Chapter 2 reviews the concepts and theory of scattering from discrete and distributed targets. It discusses methods for representing the polarisation state of electromagnetic waves and the process of converting between arbitrary polarisation bases using unitary transformation matrices. The concepts of optimal polarisation states and target decomposition theorems are then described. Particular attention is given to the eigen-decomposition of the coherency matrix and the associated methods for identifying and classifying scattering mechanisms.

Chapter 3 provides a detailed examination of polarimetric calibration techniques, concentrating on the problem of the polarimetric calibration in field conditions, with particular reference to the DSTO high resolution polarimetric radar system. It begins with a review of common calibration targets and their polarimetric properties. Particular attention is placed on the suitability of these targets for field calibrations. The evolution of polarimetric calibration techniques using the matrix representation of system distortions and the vectorised form of the $[S]$ matrix is then presented. The distortion model proposed by Barnes, which is the basis of most calibration techniques, is discussed in detail. An alternative formulation using the Kronecker distortion matrix model is also discussed. Methods for solving this system are then

reviewed using active and passive point targets, symmetrisation and exploitation of the statistical properties of distributed clutter targets. An examination of the published field calibration methodologies is given, followed by a description of several calibration techniques tested during the formulation of a strategy for calibrating the DSTO radar facility. A new technique is then presented, using a dual delay line calibrator in concert with a rotating dihedral corner reflector. This formulation, based on a least squares matrix technique, permits the adoption of average calibration and symmetrisation procedures for polarimetric single-look complex data sets. Results from field measurements are examined and demonstrate the quality of the calibration procedure. These tests show that phase errors of less than 4° are achieved and demonstrate that the channel isolation of the DSTO radar is ≥ 27 dB at X band.

Chapter 4 discusses the technical characteristics of the DSTO radar system, emphasizing the changes introduced to provide a full polarimetric capability, together with the software tools that were developed to process and analyse the data collected in this study. The XPOL_VIS software package that was developed for visualising the power distributions and optimal polarisation states on the Poincaré sphere is described and a number of example outputs are shown.

Chapter 5 examines the models adopted to describe radar scattering from the ocean surface that provide a basis for the prediction and interpretation of polarimetric signatures. It discusses the hydrodynamic problem of describing the sea surface, using linear models based on parametric wave models and nonlinear models that provide a description of weakly interacting wind waves. It outlines the modelling of quasi-deterministic features arising from ship wakes using linear and nonlinear numerical codes and discusses the accuracy requirements of the hydrodynamic models and the needs for wave-resolving radar measurements.

The electromagnetic aspects of scattering from features on the ocean surface are then discussed. An overview of the scattering techniques from rough surfaces is given and the justification for adopting the two-scale model based on the extended Bragg models is presented. The Bragg and extended Bragg model are formulated using a

covariance matrix approach, illustrating the manner in which depolarisation can be introduced.

The hydrodynamic and electromagnetic models are combined to illustrate the modelling of the polarimetric variations of breaking waves. The validation of scattering models using the surface elevations, slope and velocity fields predicted by the computational model SWPE combined with a two-scale model is presented and the potential for using this technique to validate the Doppler measurements performed with the DSTO radar system is discussed. Finally an example illustrating the differences arising from the linear and nonlinear wake models is given which highlights the importance of modeling the nonlinear components of gravity waves.

Chapter 6 contains the results of experimental polarimetric measurements performed at low grazing angles. Measurements of breaking waves in the littoral zone performed at Evans Head, NSW are described and the variations in the polarimetric parameters derived from the eigen-decomposition are compared with the results predicted by the extended Bragg model discussed in Chapter 5. A simpler scattering scenario is then considered, involving an almost monochromatic swell at a location near Yallingup, WA. Much lower entropy values were observed with a much smaller spread in the $H-\bar{\alpha}$ space. The extended Bragg model again explained the observed variations in the polarimetric parameters. Measurements of a wave-piercing catamaran, conducted in Darwin Harbour, are then shown that demonstrate the ability to image wakes at low grazing angles. Additional measurements, performed at Queenscliff, Victoria of a pilot boat wake, are examined using an entropy-based approach and a scalar parameter derived from the cross-polar null distribution. Finally a technique is described for initiating wave breaking events using the wake produced by a ship.

Chapter 7 summarises the results obtained and highlights areas where additional work could be performed, including a summary of some future investigations and hardware upgraded that are planned with the DSTO high resolution polarimetric radar system.

Chapter 2 Polarimetric theory

2.1 Introduction

This chapter describes the polarimetric concepts and theory of scattering from point and distributed targets. Two conceptual formalisms are introduced that are the basis of all polarimetric analysis. The first, based on the Stokes vector, provides a real space description of the polarimetric properties of electromagnetic waves. The second is a complex space formalism based on the Jones vector. The Stokes representation leads to the Mueller matrix for the description of the polarimetric properties of the scatterer while the Jones vector representation utilises the covariance or coherency matrix. Both description are complete and hence can be interchanged unambiguously by a suitable linear transformation. The concept of distributed scatterers is also introduced along with target decomposition theorems for identifying the dominant scattering mechanisms. Classification techniques in the $H-\bar{\alpha}$ and $H-A-\bar{\alpha}$ spaces are described and examples of these techniques applied to measurements of a pilot boat wake observed at a low grazing angle are presented.

2.2 Polarisation description of plane EM waves

For linear source-free homogeneous media, the solution of the wave equation, derived from Maxwell's equations, yields plane waves [115]. These are the simplest form of the electromagnetic waves with constant amplitude in the plane perpendicular to the direction of propagation. The instantaneous real electric field vector $\vec{E}(\vec{r},t)$, defined by the position vector $\vec{r}$ at time t propagating in the direction $\vec{k}$, is given by

$$\vec{E}(\vec{r},t)=\vec{E}(\vec{r})\cos\omega t \tag{2.1}$$

$\vec{E}(\vec{r})$ is the real amplitude of the electric field and ω is the angular frequency of the wave. If the electric field vector varies in time with a single angular frequency, then the wave is called monochromatic. The corresponding complex representation of the electric field according to the IPU (International Physical Union) convention is given by

$$\vec{E}(\vec{r}) = \vec{E} \cdot e^{(i\vec{k}\vec{r})} \tag{2.2}$$

$\vec{E}$ is the constant complex amplitude vector of the electric field which is independent of time. Introducing a right-handed orthogonal coordinate system $(\vec{h},\vec{v},\vec{k})$, the complex amplitude vector $\vec{E}$ can be decomposed into two orthogonal complex components E_h and E_v defined as

$$\vec{E} = (\vec{h} \cdot \vec{E})\vec{h} + (\vec{v} \cdot \vec{E})\vec{v} = E_h\vec{h} + E_v\vec{v} \tag{2.3}$$

The projections of $\vec{E}$ onto the basis vectors can be written in terms of a real amplitude and phase difference

$$E_j = \vec{j} \cdot \vec{E} = \left|E_j\right| e^{i\delta_j} = a_j e^{i\delta_j} \tag{2.4}$$

where j denotes h or v. The real time dependent expressions are then given by

$$\begin{aligned} E_j(\vec{r},t) &= \Re\{E_j \exp i(\vec{k} \cdot \vec{r} - \omega t)\} = \Re\{a_j \exp i(\vec{k} \cdot \vec{r} - \omega t + \delta_j)\} \\ &= a_j \cos(\vec{k} \cdot \vec{r} - \omega t + \delta_j) = a_j \cos(\tau + \delta_j) \end{aligned} \tag{2.5}$$

where

$$\tau = \vec{k} \cdot \vec{r} - \omega t \tag{2.6}$$

If we define an angle $\delta = \delta_v - \delta_h$ representing the phase difference between the two components, then

$$\begin{aligned} \frac{E_v(\vec{r},t)}{a_v} &= \cos(\tau + \delta + \delta_h) \\ &= \cos(\tau + \delta_h)\cos\delta - \sin(\tau + \delta_h)\sin\delta \\ &= \cos(\tau + \delta_h)\cos\delta - \sqrt{1 - \cos^2(\tau + \delta_h)}\sin\delta \end{aligned} \tag{2.7}$$

Substituting for $\cos(\tau + \delta_h)$ using Equation (2.5) yields

$$\frac{E_v(\vec{r},t)}{a_v} = \frac{E_h(\vec{r},t)}{a_h}\cos\delta - \sqrt{1 - \frac{E_h^2(\vec{r},t)}{a_h^2}}\sin\delta \tag{2.8}$$

Rearranging gives

$$\frac{E_v^2(\vec{r},t)}{a_v^2}+\frac{E_h^2(\vec{r},t)}{a_h^2}-2\cos\delta\frac{E_v(\vec{r},t)E_h(\vec{r},t)}{a_v a_h}=\sin^2\delta \tag{2.9}$$

Equation (2.9) is the general representation of a conic section and in most cases represents a rotated ellipse since the associated determinant is non-negative, as shown in Equation (2.10) [59].

$$\det\begin{vmatrix}\frac{1}{a_h^2} & \frac{-\cos\delta}{a_h a_v}\\ \frac{-\cos\delta}{a_h a_v} & \frac{1}{a_v^2}\end{vmatrix}=\frac{1}{a_v a_h}(1-\cos^2\delta)=\frac{\sin^2\delta}{a_v a_h}\geq 0 \tag{2.10}$$

2.3 The polarisation ellipse

By definition, the polarisation state of a plane wave is the locus and sense of rotation of the extremity of the electric field vector $\vec{E}$ in the plane perpendicular to the direction of propagation $\vec{k}$, as a function of time. From Equation (2.9) it follows that, in general, the tip of the electric field vector defines an ellipse, which is commonly known as the polarisation ellipse [3 , 42] as shown in Figure 2-1.

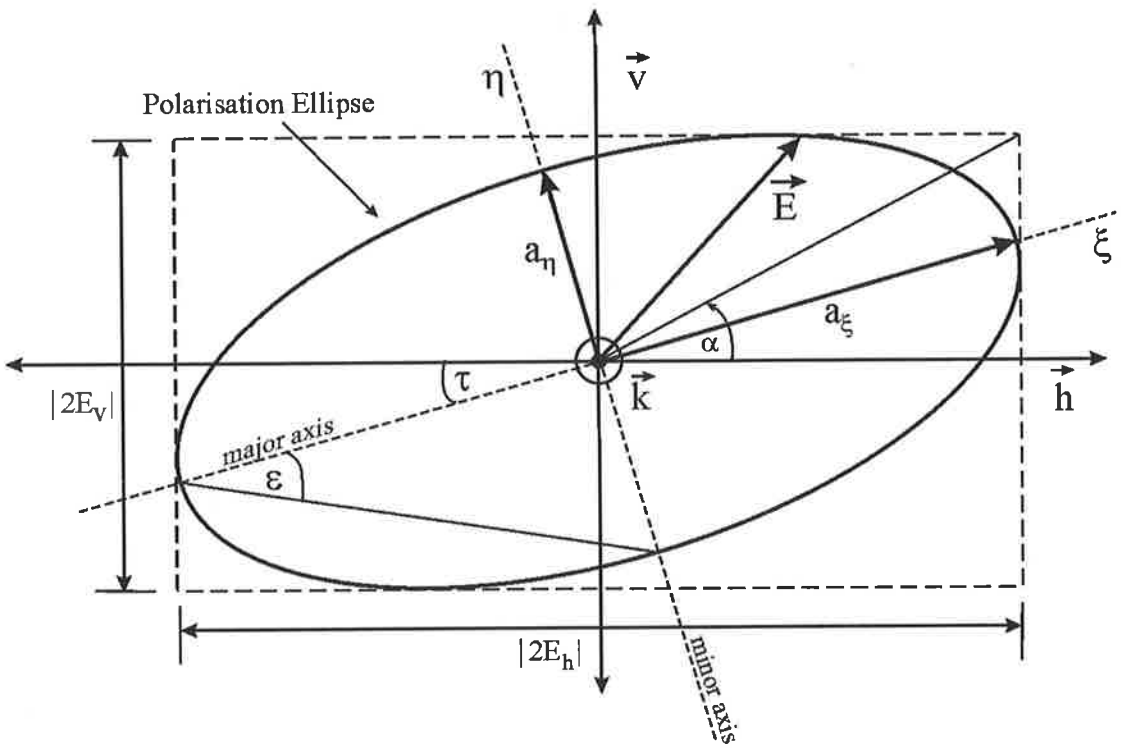

Figure 2-1 Polarisation ellipse

An area of much confusion relates to the definition of the direction of rotation of the polarisation ellipse. According to the IEEE Standard Definition of Terms for Antennas [116] the polarisation is said to be left-handed (right-handed) if the endpoint of the electric vector $\vec{E}$ appears to describe an ellipse in the counterclockwise (clockwise) direction when observed, looking into the direction of wave propagation. For an observer looking in the direction from which the wave is coming left and right-handed conventions must be interchanged.

The shape of the polarisation ellipse is defined by the three real parameters a_v, a_h and δ. However, it is often more convenient to express the polarisation state of the plane wave by defining two angles, the tilt angle τ and the ellipticity angle ε, based on the geometrical properties of the ellipse. These angles are shown in Figure 2-1, with the tilt angle τ defined as the major axis orientation angle. If the auxiliary angle α is defined as [117]

$$\tan\alpha = \frac{|E_v|}{|E_h|} = \frac{a_v}{a_h} \qquad 0 \le \alpha \le \frac{\pi}{2} \tag{2.11}$$

then the tilt angle can be related to the wave parameters by [117]

$$\tan 2\tau = \tan 2\alpha \cos\delta \tag{2.12}$$

The ellipticity angle ε is defined as the ratio of the minor semi axis a_η to its major semi axis a_ξ and in terms of the wave parameters can be written as [117]

$$\sin 2\varepsilon = \frac{2a_v a_h}{a_v^2 + a_h^2}\sin\delta = \sin 2\alpha \sin\delta \qquad -\frac{\pi}{4} \le \varepsilon \le \frac{\pi}{4} \tag{2.13}$$

If the ellipticity angle $\varepsilon = 0°$, the ellipse degenerates to a straight line with an inclination given by the tilt angle τ. In this case, $\tau = 0°$ defines horizontally polarised waves, while $\tau = 90°$ defines vertically polarised waves. Ellipticity angles between 0° and 45° describe elliptically polarised waves and when $\tau = 45°$, the ellipse becomes a circle, describing circular polarisation. Table 2-1 summarises the polarisation angles for some commonly used polarisation states.

In general, a plane monochromatic wave has potentially four degrees of freedom. Thus, in addition to the two polarisation angles τ and ε, the wave amplitude A_0 and an initial phase reference ϕ_0 are required to completely define a plane monochromatic wave. Both the wave amplitude and initial phase reference are wave characteristics and are not essential for the definition of the polarimetric state of the wave. Consequently they will be ignored in the following treatment.

Table 2-1 Polarisation descriptors for characteristic polarisation states

Polarisation	Tilt angle (τ)	Ellipticity (ε)
Horizontal	0°	0°
Vertical	90°	0°
Linear +45°	45°	0°
Linear +135°	135°	0°
Left Circular	0° to 180°	45°
Right Circular	0° to 180°	–45°

2.4 Stokes vector representation

The previous section defined two real parameter representations of the polarisation state of a monochromatic plane wave. A quantitative approach using four parameters q_0, q_1, q_2 and q_3 was introduced by Sir George Stokes in 1852 [118]. The Stokes parameters can be used to describe the amplitude and polarisation of both monochromatic and partially polarised waves and can be written in a single vector form as [3, 119]

$$\vec{q} = \begin{bmatrix} q_0 \\ q_1 \\ q_2 \\ q_3 \end{bmatrix} = \begin{bmatrix} |E_h|^2 + |E_v|^2 \\ |E_h|^2 - |E_v|^2 \\ 2\Re\{E_h^* E_v\} \\ 2\Im\{E_h^* E_v\} \end{bmatrix} = \begin{bmatrix} a_h^2 + a_v^2 \\ a_h^2 - a_v^2 \\ 2a_h a_v \cos\delta \\ 2a_h a_v \sin\delta \end{bmatrix} = \begin{bmatrix} a^2 \\ a^2 \sin 2\tau \cos 2\varepsilon \\ a^2 \cos 2\tau \cos 2\varepsilon \\ a^2 \sin 2\varepsilon \end{bmatrix} \tag{2.14}$$

The Stokes vector is an element in the four-dimensional Minkowski space with a metric (1, –1, –1, –1) [120]. Only three of the four parameters are independent since they are related (in the case of a completely monochromatic wave) by the following identity

$$q_0^2 = q_1^2 + q_2^2 + q_3^2 \tag{2.15}$$

Thus only three of the four parameters are required to represent the polarisation state of a monochromatic wave. In the case of partially polarised waves, the identity in Equation (2.15) is no longer valid. In these situations, the appropriate relationship between the Stokes parameters is given by [3]

$$q_0^2 \geq q_1^2 + q_2^2 + q_3^2 \tag{2.16}$$

In practice it is often convenient to normalise the Stokes vector so that the polarisation state is independent of the amplitude value. This is achieved by setting

$$q_0 = a_h^2 + a_v^2 = 1 \tag{2.17}$$

Partially polarised waves can be described through the time average of the Stokes vector. Using the Stokes vector treatment, a partially polarised wave can be uniquely decomposed into completely polarised wave components (polarisation does not change with time) and completely unpolarised wave components (where the polarisation changes randomly). This leads to the definition of the degree of polarisation. This is defined as the ratio of the power densities of the polarised part and the total wave [117]. The degree of polarisation for completely polarised waves is equal to one while partially polarised waves have values that are less than unity. A detailed treatment that illustrates the mathematical formulation of partially polarised waves using Stokes parameters is given in [117, 121].

There are distinct advantages in distinguishing the direction of propagation of waves by using directional Stokes vectors, as it removes the ambiguity in converting from one polarisation basis to another. Oppositely directed waves are related by the complex conjugate operations and these and other properties are discussed in detail in [122].

One of the main advantages of the Stokes parameter representation is that all four parameters have the same physical dimension, namely intensity. This property is crucial in optical polarimetry as it enables the experimental determination of the polarimetric properties of the wave using intensity measurements only.

2.5 Poincaré sphere

Three of the Stokes parameters q_1, q_2 and q_3 define the Cartesian coordinates of a point on a sphere in the three dimensional real space where the radius of the sphere is given by q_0. This representation is known as the Poincaré sphere [3 , 9, 123]. Poincaré was led to this particular representation because the effects of polarisation transformations can be represented as rotations of the sphere.

From Equation (2.14) it is clear that the polarisation states can be plotted on the sphere using 2ε for the latitude and 2τ for the longitude. In this representation, the equator of the Poincaré sphere represents all linear polarisation states. Elliptical polarisation states are points off the equator, being right-hand-sensed in the southern hemisphere and left-hand-sensed in the northern hemisphere. There is a one-to-one correspondence between polarisation states and points on the sphere with diametrically opposite points representing orthogonal polarisations. This is illustrated in Figure 2-2.

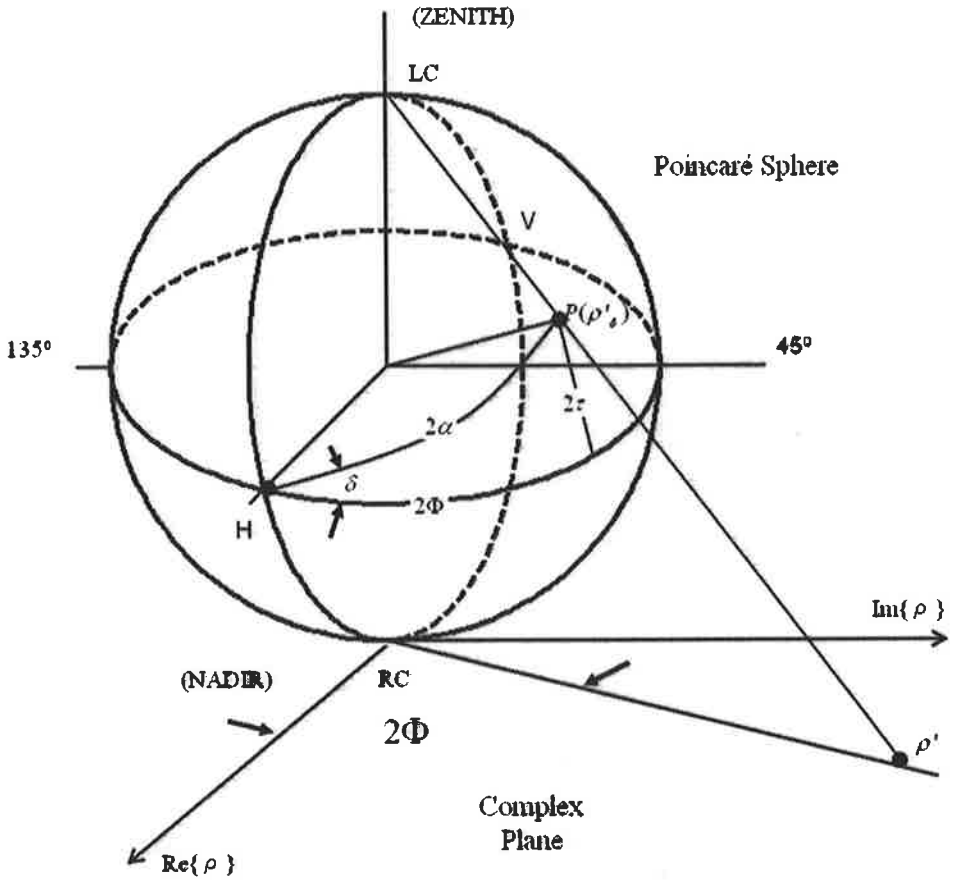

Figure 2-2 The Poincaré sphere

Deschamps [10] recognised that the Poincaré sphere could be used to solve problems involving radio waves and antennas. He demonstrated that the Poincaré sphere could be used to determine the polarisation state of an unknown wave. This method used geometrical constructions on the Poincaré sphere based on measurements with antennas of known polarisation.

In an extension [123] to his earlier work, he introduced a technique for representing partially polarised waves using points defined inside the Poincaré sphere and demonstrated that this representation was useful in the analysis and measurement of partially polarised waves.

2.6 Jones vectors

In Equation (2.3) the complex amplitude of the electric field vector $\vec{E}$ is expressed in terms of a linear combination of two orthogonal linear polarisations $\vec{h}$ and $\vec{v}$ weighted by the complex amplitudes E_h and E_v. This can be considered as a component representation of the electric field vector in a two-dimensional complex space with respect to the $\{\vec{e}_h, \vec{e}_v\}$ basis. Similarly the electric field vector $\vec{E}$ can be represented in an arbitrary polarisation reference basis $\{\vec{\varepsilon}_m, \vec{\varepsilon}_n\}$ by defining two orthonormal polarisation states $\vec{\varepsilon}_m$ and $\vec{\varepsilon}_n$ and projecting $\vec{E}$ onto the basis polarisations as

$$\vec{E} = E_m \vec{\varepsilon}_m + E_n \vec{\varepsilon}_n \tag{2.18}$$

Using the complex amplitudes E_m and E_n, the electric field strength of a monochromatic plane wave can be expressed in terms of a two dimensional complex electric field vector $\vec{E}_{mn}$ called the Jones vector [124-126].

$$\vec{E}_{mn} = \begin{bmatrix} E_m \\ E_n \end{bmatrix} = \begin{bmatrix} a_m e^{i\delta_m} \\ a_n e^{i\delta_n} \end{bmatrix} \tag{2.19}$$

The Jones vector fully describes the characteristic properties of the polarisation state of a monochromatic wave once a polarisation basis has been selected [127]. The only quantity that cannot be constructed from the Jones vector is the handedness due to the suppression of the phase factor ϕ_0. The handedness is related to the relative phase

difference between the components of the Jones vector. A change of the handedness infers a change of sign of the relative phase difference or the transition to the complex conjugate of the Jones vector.

Thus it is not only expedient, but absolutely necessary to distinguish Jones vectors corresponding to opposite directions of propagation [122]. The Jones vectors defined by Equation (2.19), representing two plane waves propagating in opposite directions, will be the same. To overcome this limitation the subscripts "+" and "–" are used to distinguish between the two propagation directions where $\vec{E}_+$ represents waves propagating in the $+\vec{k}$ direction, $\vec{E}_-$ denotes waves propagating in the $-\vec{k}$ direction.

$$E_+(\vec{r},t) = \Re\{\vec{E}_+ \exp i(\vec{k}\cdot\vec{r} - \omega t)\} \text{ and } E_-(\vec{r},t) = \Re\{\vec{E}_- \exp i(-\vec{k}\cdot\vec{r} - \omega t)\} \tag{2.20}$$

Directional Jones vectors were first introduced by Graves in 1956 [124] but initially had limited use. A number of more recent papers [122, 128, 129] have been published using this convention, since it removes the ambiguity in converting from one polarisation basis to another. In this convention, oppositely directed waves with the same polarisation are related by the complex conjugate operation that results from the time reversal operation associated with the Backscatter Alignment (BSA) convention [130]. This property is described in more detail by Gottfried [131] and by Bebbington [132] using a spinorial approach.

The Jones vector can be expressed in terms of the tilt angle τ, the ellipticity angle ε, the wave amplitude A_0 and the initial absolute phase reference ϕ_0 as [117]

$$\vec{E}_{mn} = A_o e^{i\phi_0} \begin{bmatrix} \cos\tau & -\sin\tau \\ \sin\tau & \cos\tau \end{bmatrix} \begin{bmatrix} \cos\varepsilon \\ i\sin\varepsilon \end{bmatrix} \tag{2.21}$$

Equation (2.21) demonstrates the equivalence between the real and complex space representations of the polarimetric properties of electromagnetic waves.

2.7 Complex polarisation ratio

Polarisation states can also be characterised in the complex space by defining the complex polarisation ratio ρ, defined as the ratio of the orthonormal complex electric field components [24, 117, 133].

$$\rho = \frac{E_n}{E_m} = \frac{a_n}{a_m} e^{i(\delta_n - \delta_m)} = \tan\alpha \cdot e^{i\delta} \tag{2.22}$$

The two angles α and δ are known as the Deschamps parameters and are defined as

$$\tan\alpha = \frac{a_n}{a_m} \qquad \delta = \delta_n - \delta_m \tag{2.23}$$

Both α and δ range from 0 to 2π and are an alternative two parameter real set description of the polarisation state of the wave in terms of an amplitude ratio and phase difference.

The complex polarisation ratio can also be expressed in terms of the polarisation angles as [117]

$$\rho = \frac{\cos 2\varepsilon \sin 2\tau + i \sin 2\varepsilon}{1 + \cos 2\varepsilon \cos 2\tau} \tag{2.24}$$

Similarly, given the complex polarisation ratio ρ, the corresponding polarisation angles of the polarisation ellipse are uniquely given by [117]

$$\tau = \frac{1}{2}\arctan\left(\frac{2\Re(\rho)}{1+|\rho|^2}\right) \quad \text{and} \quad \varepsilon = \frac{1}{2}\arcsin\left(\frac{2\Im(\rho)}{1+|\rho|^2}\right) \tag{2.25}$$

As a complex scalar, the complex polarisation ratio has two degrees of freedom, expressed by the two Deschamps angles. There is a one to one correspondence between all possible polarisation states and all points in the two dimensional complex plane. The mapping of the Poincaré sphere into the complex plane is illustrated in Figure 2-2. Linear polarisations are represented by real ρ (δ= 0 or ε= 0), while elliptical polarisations are represented by a complex ρ. Care should be taken when using this representation as the polarisation ratio varies with changes of polarisation basis. This is illustrated in Table 2-2, which lists the polarisation ratios and normalised Jones vectors $\vec{E}_{mn}$ for some common polarisation states.

Table 2-2 Common polarisation states in terms of ρ_{mn} and $\vec{E}_{mn}$

Polarisation	{H,V} basis		{45°,135°} basis		{L,R} basis	
	ρ_{HV}	$\vec{E}_{HV}$	$\rho_{45°135°}$	$\vec{E}_{45°135°}$	ρ_{LR}	$\vec{E}_{LR}$
Linear Horizontal	0	$\begin{bmatrix}1\\0\end{bmatrix}$	-1	$\frac{1}{\sqrt{2}}\begin{bmatrix}1\\-1\end{bmatrix}$	1	$\frac{1}{\sqrt{2}}\begin{bmatrix}1\\1\end{bmatrix}$
Linear Vertical	∞	$\begin{bmatrix}0\\1\end{bmatrix}$	1	$\frac{1}{\sqrt{2}}\begin{bmatrix}1\\1\end{bmatrix}$	-1	$\frac{1}{\sqrt{2}}\begin{bmatrix}-i\\i\end{bmatrix}$
45° Linear	1	$\frac{1}{\sqrt{2}}\begin{bmatrix}1\\1\end{bmatrix}$	0	$\begin{bmatrix}1\\0\end{bmatrix}$	i	$\frac{1}{2}\begin{bmatrix}1 & -i\\1 & i\end{bmatrix}$
135° Linear	-1	$\frac{1}{\sqrt{2}}\begin{bmatrix}-1\\1\end{bmatrix}$	∞	$\begin{bmatrix}0\\1\end{bmatrix}$	$-i$	$\frac{1}{2}\begin{bmatrix}-1 & -i\\-1 & i\end{bmatrix}$
Left-handed Circular	i	$\frac{1}{\sqrt{2}}\begin{bmatrix}1\\i\end{bmatrix}$	i	$\frac{1}{2}\begin{bmatrix}1 & i\\-1 & i\end{bmatrix}$	0	$\begin{bmatrix}1\\0\end{bmatrix}$
Right-handed Circular	$-i$	$\frac{1}{\sqrt{2}}\begin{bmatrix}1\\-i\end{bmatrix}$	$-i$	$\frac{1}{2}\begin{bmatrix}1 & -i\\-1 & -i\end{bmatrix}$	∞	$\begin{bmatrix}0\\1\end{bmatrix}$

2.8 Polarisation signature

A useful technique for visualising the variations in the received power as a function of the incident polarisation is the polarisation signature. This display was first introduced by van Zyl [134]. The polarisation signature consists of a three dimensional plot of the received power as a function of the ellipticity and tilt angles. This representation is particularly useful for identifying scattering mechanisms and scattering features. For example, some signatures appear to sit on a *pedestal*, indicating that part of the return cannot be completely nulled out. This property often results from diffuse scattering or the presence of noise. The polarisation signatures of a dihedral corner reflector are shown in Figure 2-3 for the backscattering case. Additional examples for a variety of common elementary targets are given in [135-137] and in Section 3.2.

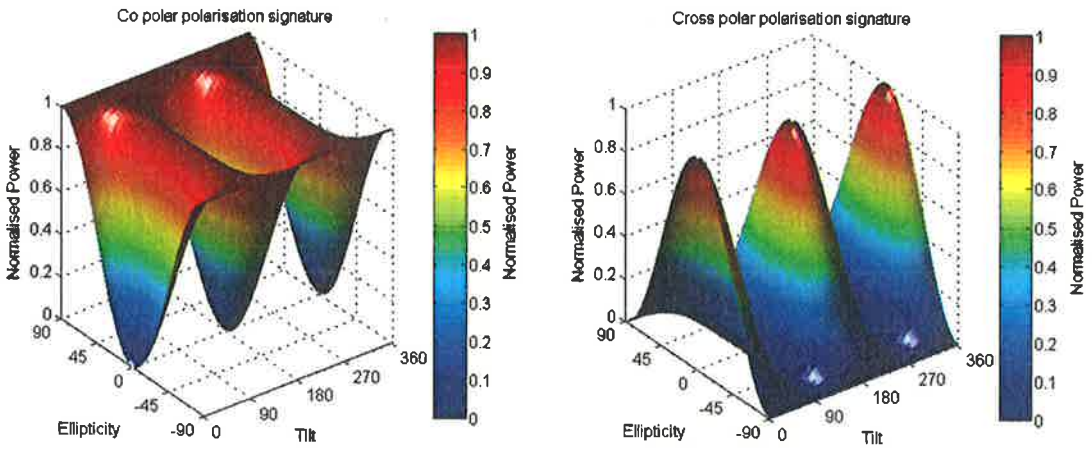

Figure 2-3 Example polarisation signatures for a dihedral corner reflector

2.9 Change of polarisation basis

An infinite number of polarisation bases exist since the only requirement is that the basis vectors $\vec{e}_m$ and $\vec{e}_n$ must be orthogonal. The polarisation of the wave is independent of the reference basis but its representation does depend on the chosen reference frame. The effect of changing between two orthonormal polarisation bases $\{\vec{\varepsilon}_m, \vec{\varepsilon}_n\}$ and $\{\vec{\varepsilon}_i, \vec{\varepsilon}_j\}$ is illustrated below. First the plane wave $\vec{E}$ can be decomposed into its projections onto the basis polarisations as

$$\vec{E} = \vec{\varepsilon}_m E_m + \vec{\varepsilon}_n E_n = \vec{\varepsilon}_i E_i + \vec{\varepsilon}_j E_j \tag{2.26}$$

The corresponding Jones vectors are

$$\vec{E}_{mn} = \begin{bmatrix} E_m \\ E_n \end{bmatrix} \text{ and } \vec{E}_{ij} = \begin{bmatrix} E_i \\ E_j \end{bmatrix} \tag{2.27}$$

The 2×2 complex transformation $[U_2]$ defines the relationship between the two Jones vectors as follows

$$\vec{E}_{ij} = [U_2]\vec{E}_{mn} \rightarrow \vec{E}_{mn} = [U_2]^{-1}\vec{E}_{ij} \tag{2.28}$$

The transformation matrix $[U_2]$ is a special unitary 2×2 complex matrix with a unit determinant. Both constraints are required to ensure that the amplitude of the wave remains the same (unitarity) and that the phase of the wave is consistently defined in the new polarisation basis. In terms of the tilt angle τ, ellipticity angle ε and the initial phase ϕ_0 the transformation matrix is defined as [138]

$$[U_2]=\begin{bmatrix}\cos\tau & -\sin\tau\\ \sin\tau & \cos\tau\end{bmatrix}\begin{bmatrix}\cos\varepsilon & i\sin\varepsilon\\ i\sin\varepsilon & \cos\varepsilon\end{bmatrix}\begin{bmatrix}e^{-i\phi_0} & 0\\ 0 & e^{i\phi_0}\end{bmatrix} \tag{2.29}$$

This expression can also be written in terms of the complex polarisation ratio ρ of the Jones vector of the new basis [42]

$$[U_2]=\frac{1}{\sqrt{1+\rho\rho^*}}\begin{bmatrix}1 & -\rho^*\\ \rho & 1\end{bmatrix}\begin{bmatrix}e^{-i\delta} & 0\\ 0 & e^{i\delta}\end{bmatrix} \text{ with } [U_2]^{-1}=[U_2]^{\dagger} \tag{2.30}$$

where

$$\delta=\arctan(\tan\tau\tan\varepsilon)-\phi_0 \tag{2.31}$$

In order to determine the initial phase of the Jones vector in the new reference basis a phase reference for the new basis states is required. The angle δ is used as this reference.

2.10 The polarimetric scattering problem

The previous sections have described methods for representing the polarisation state of plane waves. The next step is to consider the polarimetric properties of the interaction of waves with scattering objects. The general formulation of the scattering problem can be described as follows. Consider a fully polarised monochromatic wave $\vec{E}^i$ travelling towards a scatterer in the incident direction $\vec{k}_i$. By defining a right-handed orthogonal coordinate system $(\vec{h}_i,\vec{v}_i,\vec{k}_i)$ located at the transmitting antenna, the incident wave can be written as

$$\vec{E}^i=E_h^i\vec{h}_i+E_v^i\vec{v}_i \tag{2.32}$$

When the wave interacts with the scatterer a change in the polarisation and the degree of polarisation may occur. The incident wave gives rise to a scattered field with directional characteristics depending on the scatterer. A receiving antenna located in a direction $\vec{k}_s$ in the far field region of the scatterer (where the scattered wave is considered to be a plane wave) receives the scattered wave $\vec{E}^s$. In a right-handed

orthogonal coordinate system $(\vec{h}_s, \vec{v}_s, \vec{k}_s)$ located at the receiving antenna, the received wave can be written as

$$\vec{E}^s = E_h^s \vec{h}_s + E_v^s \vec{v}_s \tag{2.33}$$

There are two conventions in the literature that define the scattered wave coordinate system $(\vec{h}_s, \vec{v}_s, \vec{k}_s)$ with respect to the incident wave coordinate system $(\vec{h}_i, \vec{v}_i, \vec{k}_i)$ [130]. The first is known as the Forward Scattering Alignment (FSA). In this representation the local right-handed coordinate system is defined with respect to the direction of wave propagation. Thus the FSA is a wave oriented reference frame and is mainly used in forward and bistatic electromagnetic wave scattering problems. The second is known as the Backscatter Alignment (BSA) convention, shown in Figure 2-4, which defines the local coordinate system with respect to the polarisation of the radar antennas.

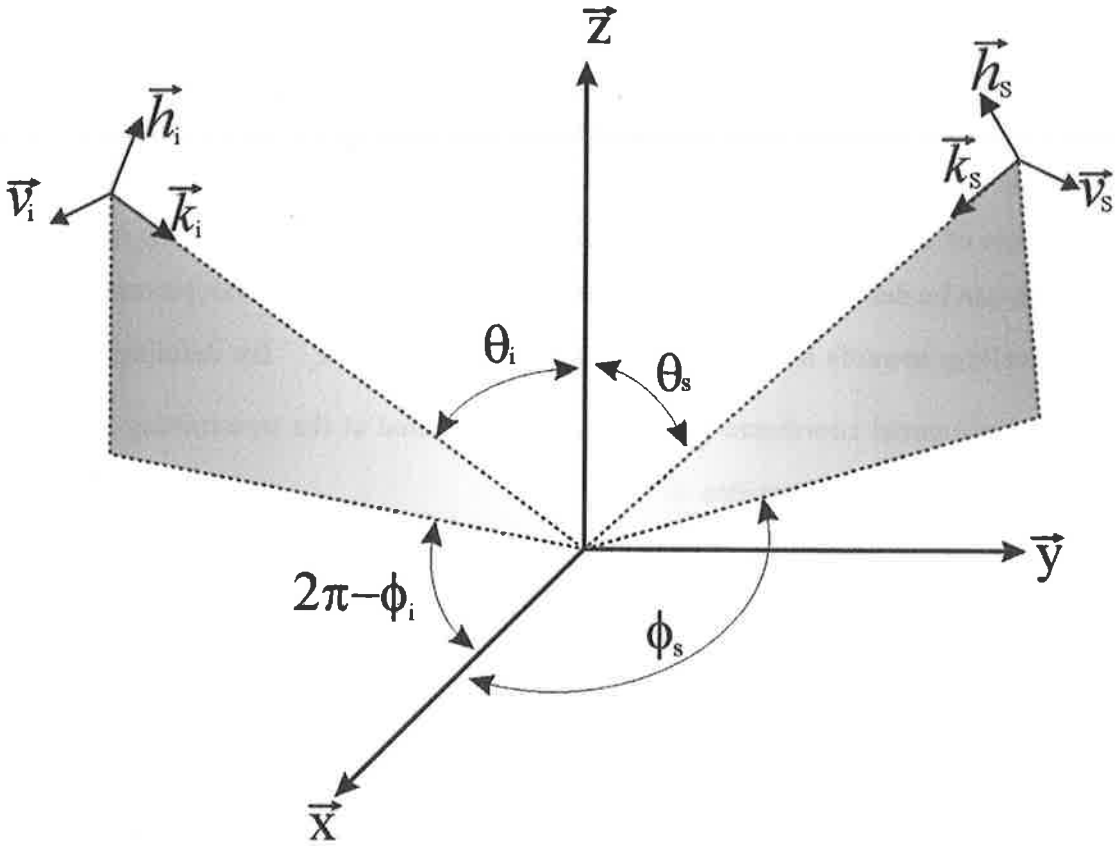

Figure 2-4 Backscatter Alignment Convention

The BSA is an antenna oriented reference frame in which the polarisation of an antenna is defined to be the polarisation of the wave radiated by the antenna, referred to as a right-handed coordinate system with the axis of radiation pointing away from the antenna, even when the antenna is used as the receiver. Adopting this convention ensures that when the receiving and transmitting antennas are co-located, the two local coordinate systems coincide. This is the preferred reference frame in radar backscattering problems and is the convention that is adopted in this study. Both conventions are more than just an arrangement of coordinate systems as they define the local coordinate system with respect to the direction of propagation. Consequently, they involve a convention concerning the representation of polarisation states for different propagation directions for transmission and reception.

Now, consider the Jones vectors representing the incident and scattered waves

$$\vec{E}^i = \begin{bmatrix} E_h^i \\ E_v^i \end{bmatrix} \quad \text{and} \quad \vec{E}^s = \begin{bmatrix} E_h^s \\ E_v^s \end{bmatrix} \tag{2.34}$$

The two Jones vectors are related by a 2×2 complex matrix known as the coherent scattering matrix $[S]$ which is conveniently described as the matrix part (antimatrix) of an antilinear backscatter operator S_a connecting the conjugate propagation spaces for the incoming and backscattered waves travelling in opposite directions [139]. If the BSA convention is adopted, then the polarisation space of the incident waves represents the domain of S_a and the polarisation space of the scattered waves represents the range of S_a. In the backscattering case this matrix is commonly referred to as the Sinclair matrix or the radar scattering matrix, while its representation under the FSA convention is referred to as the Jones matrix $[T]$.

The relationship between the two Jones vectors and the 2×2 complex matrix $[S]$ can be written as [12, 117, 128, 140]

$$\vec{E}^s = [S]\vec{E}^i \rightarrow \begin{bmatrix} E_h^s \\ E_v^s \end{bmatrix} = \frac{e^{ikr}}{r} \begin{bmatrix} S_{HH} & S_{HV} \\ S_{VH} & S_{VV} \end{bmatrix} \begin{bmatrix} E_h^i \\ E_v^i \end{bmatrix} \tag{2.35}$$

Similarly the relationship for the Jones matrix $[T]$ and the two Jones vectors defined using the FSA convention is [34, 128, 141]

$$\vec{E}^s = [T]\vec{E}^i \rightarrow \begin{bmatrix} E_h^s \\ E_v^s \end{bmatrix} = \frac{e^{ikr}}{r} \begin{bmatrix} T_{HH} & T_{HV} \\ T_{VH} & T_{VV} \end{bmatrix} \begin{bmatrix} E_h^i \\ E_v^i \end{bmatrix} \tag{2.36}$$

The exponential factor accounts for the spherical wave propagation between the transmitting antenna and scattering object. The absolute phase factor, which is a function of distance between the scattering object and the transmitting antenna, is not a scatterer related parameter and is generally ignored in conventional polarimetric applications. However, in polarimetric interferometry the absolute phase of [S] is important and provides an estimate for the three-dimensional location of the scatterer [59, 142].

If the target's time scale of temporal fluctuations is much larger than the measurement time of the observing radar device, then the target may be treated as deterministic [32]. For plane electromagnetic waves, coherent backscattering from deterministic targets can be expressed in terms of a complex 2×2 Sinclair scattering matrix [S]. The elements of the scattering matrix [S] are known as the complex scattering amplitudes and are not related to each other except through the physics of the scatterer. They are independent of the polarisation of the incident wave and, for fixed scattering geometry and frequency, depend only on the physical and geometrical characteristics of the scatterer. Changing the polarisation of the incident wave results in a change to the scattered wave while [S] remains invariant. This property of the scattering matrix establishes the great advantage of radar polarimetry.

Most polarimetric radars operate in the $\{\vec{e}_h, \vec{e}_v\}$ polarisation basis. The scattering matrix is obtained by varying the transmitted pulse polarisation on a pulse to pulse basis and receiving the scattered waves in two orthogonal polarised channels. For example, if in the first cycle the transmitted wave is horizontally polarised, then the receiver will measure the S_{HH} and S_{VH} coefficients. During the second cycle the transmitted pulse will be changed to vertical polarisation enabling the S_{VV} and S_{HV} coefficients to be measured. As a result the elements of the [S] matrix are not measured at precisely the same time instant but are separated by the pulse repetition interval.

The elements of the scattering matrix S_{IJ} are related to the corresponding radar cross section σ^0_{IJ} and in the $\{\vec{e}_h, \vec{e}_v\}$ polarisation basis values with calibration factor c via the following relationships [12]

$$\begin{aligned} S_{HH} &= c \cdot e^{-i\phi_{HH}} \sqrt{\sigma^0_{HH}} \\ S_{HV} &= c \cdot e^{-i\phi_{HV}} \sqrt{\sigma^0_{HV}} \\ S_{VH} &= c \cdot e^{-i\phi_{VH}} \sqrt{\sigma^0_{VH}} \\ S_{VV} &= c \cdot e^{-i\phi_{VV}} \sqrt{\sigma^0_{VV}} \end{aligned} \tag{2.37}$$

The total power scattered is given by the span of $[S]$, defined as the sum of the squares of the absolute values of the complex scattering amplitudes. This property was shown to be invariant by Boerner *et al.* in [143].

$$Total\ power = |S_{HH}|^2 + |S_{HV}|^2 + |S_{VH}|^2 + |S_{VV}|^2 \tag{2.38}$$

In the general bistatic case the scattering matrix consists of seven independent parameters described by four amplitudes and three relative phases. In the case of monostatic measurements in a reciprocal scattering medium the $[S]$ matrix becomes symmetric. Consequently $S_{HV} = S_{VH}$ and only five independent parameters consisting of three amplitudes and two relative phases are required to describe $[S]$. In the monostatic case the $[S]$ matrix is commonly referred to as the symmetric Sinclair matrix [117, 144].

2.11 The scattering vector

In some instances it is more convenient to use a vectorised form of the scattering matrix. The scattering matrix can be rewritten as a four element complex scattering vector $\vec{k}_4$ defined as

$$[S] = \begin{bmatrix} S_{HH} & S_{HV} \\ S_{VH} & S_{VV} \end{bmatrix} \rightarrow \vec{k}_4 = V([S]) = \left(\Psi^i, [S]\right) = \left[k_0, k_1, k_2, k_3\right]^T \tag{2.39}$$

where $V([S])$ is the vectorisation operator. Here Ψ is a basis for the space of 2×2 complex matrices and $(\Psi^i, [S])$ denotes an Hermitian inner product [145]. In principle, any complete orthonormal basis set of four 2×2 matrices can be used, as long as the Euclidean norm of the vector $\vec{k}_4$ is invariant. Two basis sets are widely

used in the literature. The first, known as the lexicographic basis is the simple lexicographic expansion of [S] defined as [13, 146]

$$\Psi_L = \left\{ 2\begin{bmatrix} 1 & 0 \\ 0 & 0 \end{bmatrix}, 2\begin{bmatrix} 0 & 1 \\ 0 & 0 \end{bmatrix}, 2\begin{bmatrix} 0 & 0 \\ 1 & 0 \end{bmatrix}, 2\begin{bmatrix} 0 & 0 \\ 0 & 1 \end{bmatrix} \right\} \tag{2.40}$$

The corresponding vector $\vec{k}_{4L}$ is directly related to the system measurables and contains the complex elements of $[S]_{HV}$

$$\vec{k}_{4L} = [S_{HH}, S_{HV}, S_{VH}, S_{VV}]^T \tag{2.41}$$

The vectorisation process can also be performed using the basis formed by the Pauli spin matrices [145]

$$\Psi_P = \left\{ \sqrt{2}\begin{bmatrix} 1 & 0 \\ 0 & 1 \end{bmatrix}, \sqrt{2}\begin{bmatrix} 1 & 0 \\ 0 & -1 \end{bmatrix}, \sqrt{2}\begin{bmatrix} 0 & 1 \\ 1 & 0 \end{bmatrix}, \sqrt{2}\begin{bmatrix} 0 & -i \\ i & 0 \end{bmatrix} \right\} \tag{2.42}$$

The Pauli basis is closely linked with the physics of wave scattering and hence enables straightforward physical interpretations in terms of elementary scattering mechanisms while ensuring relative polarisation plane preservation.

The vectorisation of [S] carried out using the Pauli matrices basis set, leads to the Pauli scattering vector for the bistatic case with the explicit form

$$\vec{k}_{4P} = \frac{1}{\sqrt{2}}[S_{HH} + S_{VV}, S_{HH} - S_{VV}, S_{HV} + S_{VH}, i(S_{HV} - S_{VH})]^T \tag{2.43}$$

Each of the Pauli basis matrices represent isotropic scattering mechanisms. Note in this context isotropic means that $|HH| = |VV|$. The first Pauli matrix can be interpreted as the scattering matrix of an isotropic "odd bounce" scatterer. Such scatterers are characterised by $S_{HH} = S_{VV}$ and $S_{VH} = S_{HV} = 0$. Spheres, flat plates or trihedral corner reflectors are examples of scatterers with these scattering characteristics. The second Pauli matrix is also diagonal but generates a 2π phase difference between the diagonal elements. It indicates isotropic "even bounce" scattering which is characterised by $S_{HH} = -S_{VV}$ and $S_{VH} = S_{HV} = 0$. Such scattering behaviour is observed from dihedral corner reflectors. The third Pauli spin matrix can

be interpreted as the scattering matrix from an isotropic even bounce scatterer with a relative orientation of $\pi/4$ with respect to the horizontal, as it may be obtained from the second Pauli matrix by rotation of the reference axes by $\pi/4$. The last Pauli matrix represents a scatterer that transforms all incident polarisation states into their orthogonal states. It signifies leakage of the symmetry of $[S]$ and consequently disappears for reciprocal backscattering problems.

The relationship between the Pauli and the lexicographic scattering vectors can be expressed in terms of a 4×4 unitary transformation matrix $[D_4]$

$$\vec{k}_{4P} = [D_4]\vec{k}_{4L} \quad \text{and} \quad \vec{k}_{4L} = [D_4]^{-1}\vec{k}_{4P} \tag{2.44}$$

with $[D_4]$ defined as [42]

$$[D_4] = \frac{1}{\sqrt{2}}\begin{bmatrix} 1 & 0 & 0 & 1 \\ 1 & 0 & 0 & -1 \\ 0 & 1 & 1 & 0 \\ 0 & i & -i & 0 \end{bmatrix} \quad \text{and} \quad [D_4]^{-1} = [D_4]^{\dagger} = \frac{1}{\sqrt{2}}\begin{bmatrix} 1 & 1 & 0 & 1 \\ 0 & 0 & 0 & -i \\ 0 & 0 & 1 & i \\ 1 & -1 & 0 & 0 \end{bmatrix} \tag{2.45}$$

The electromagnetic reciprocity theorem constrains the scattering matrix to be complex symmetric in the case of backscattering in reciprocal medium, thus instead of a four dimensional scattering vector, a reduced three dimensional version can be used. The relationship between the two representations in the lexicographic basis is given by

$$\vec{k}_{3L} = [Q]\ \vec{k}_{4L} = \left[S_{HH}, \sqrt{2}S_{HV}, S_{VV}\right] \tag{2.46}$$

where

$$[Q] = \begin{bmatrix} 1 & 0 & 0 & 0 \\ 0 & 1/\sqrt{2} & 1/\sqrt{2} & 0 \\ 0 & 0 & 0 & 1 \end{bmatrix} \tag{2.47}$$

The factor of $\sqrt{2}$ is required to ensure that the vector norm (total power) is consistent with the four dimensional representation of the scattering vector. In the Pauli spin basis the relationship is given by

$$\vec{k}_{3P} = [Q]\ \vec{k}_{4P} = \frac{1}{\sqrt{2}}[S_{HH} + S_{VV}, S_{HH} - S_{VV}, 2S_{HV}] \tag{2.48}$$

The reduced three-dimensional scattering vectors in the Pauli and lexicographic bases are related via a 3×3 special unitary matrix $[D_3]$ of the following form

$$\vec{k}_{3P} = [D_3]\vec{k}_{3L} \quad \text{and} \quad \vec{k}_{3L} = [D_3]^{-1}\vec{k}_{3P} \tag{2.49}$$

with $[D_3]$ given by [42]

$$[D_3] = \frac{1}{\sqrt{2}}\begin{bmatrix} 1 & 0 & 1 \\ 1 & 0 & -1 \\ 0 & \sqrt{2} & 0 \end{bmatrix} \quad \text{and} \quad [D_3]^{-1} = [D_3]^{\dagger} = \frac{1}{\sqrt{2}}\begin{bmatrix} 1 & 1 & 0 \\ 0 & 0 & \sqrt{2} \\ 1 & -1 & 0 \end{bmatrix} \tag{2.50}$$

2.12 Basis transformations of the scattering matrix

The following section investigates the effect of changing the reference frame used to describe the polarisation state of the incident and scattered waves. From Equation (2.35) we know that the relationship between the Jones vectors of the incident and scattered waves referred to the linear $\{\vec{e}_h, \vec{e}_v\}$ basis, using the BSA convention for backscattering and ignoring the spherical wave factor, can be written as

$$\vec{E}^s_{HV} = [S]_{HV}\vec{E}^{i*}_{HV} \tag{2.51}$$

In Section 2.9 the transformation of the Jones vector from one orthonormal polarisation basis was shown to be related by a special unitary matrix $[U_2]$ defined in Equation (2.30). Thus the relationship between the Jones vectors of incident and scattered waves in the $\{\vec{\varepsilon}_i, \vec{\varepsilon}_j\}$ basis is given by

$$\vec{E}^i_{ij} = [U_2]\vec{E}^i_{HV} \rightarrow \vec{E}^i_{HV} = [U_2]^{-1}\vec{E}^i_{ij} \text{ and } \vec{E}^s_{ij} = [U_2]\vec{E}^s_{HV} \rightarrow \vec{E}^s_{HV} = [U_2]^{-1}\vec{E}^s_{ij} \tag{2.52}$$

Substituting (2.52) into (2.51) gives

$$\vec{E}^s_{HV} = [U_2]^{-1}\vec{E}^s_{ij} = [S]_{HV}([U_2]^{-1}\vec{E}^i_{ij})^* \rightarrow \vec{E}^s_{ij} = [U_2][S]_{HV}[U_2]^T\vec{E}^{i*}_{ij} \tag{2.53}$$

Hence the scattering matrix $[S]_{IJ}$ in the new polarisation basis is a unity congruence transformation of the original scattering matrix $[S]_{HV}$ given by

$$[S]_{IJ} = [U_2][S]_{HV}[U_2]^T \tag{2.54}$$

This result illustrates the power of the scattering matrix concept since the knowledge of the scattering matrix in one polarisation basis allows us to derive the scattering matrix in any other orthonormal polarisation basis using the change of basis transformation. The scattering matrix components of the transformed scattering matrix are simply complex linear combinations of the elements of the scattering matrix in the original matrix. Substituting Equation (2.30) into Equation (2.54) gives

$$\begin{bmatrix} S_{II} & S_{IJ} \\ S_{JI} & S_{JJ} \end{bmatrix} = \frac{1}{1+\rho\rho^*} \begin{bmatrix} e^{-i\delta} & -\rho^* \\ \rho & e^{i\delta} \end{bmatrix} \begin{bmatrix} S_{HH} & S_{HV} \\ S_{VH} & S_{VV} \end{bmatrix} \begin{bmatrix} e^{-i\delta} & -\rho \\ -\rho^* & e^{i\delta} \end{bmatrix} \tag{2.55}$$

Expanding the expression above gives

$$\begin{aligned}
S_{II} &= \frac{1}{1+\rho\rho^*}\left[S_{HH}\cdot e^{-i2\delta} - \rho^* S_{HV} - \rho^* S_{VH} + \rho^{*2} S_{VV}\cdot e^{i2\delta}\right] \\
S_{IJ} &= \frac{1}{1+\rho\rho^*}\left[\rho\, S_{HH}\cdot e^{-i2\delta} + S_{HV} - \rho\rho^* S_{VH} - \rho^* S_{VV}\cdot e^{i2\delta}\right] \\
S_{JI} &= \frac{1}{1+\rho\rho^*}\left[\rho\, S_{HH}\cdot e^{-i2\delta} - \rho\rho^* S_{HV} + S_{VH} - \rho^* S_{VV}\cdot e^{i2\delta}\right] \\
S_{JJ} &= \frac{1}{1+\rho\rho^*}\left[\rho^2 S_{HH}\cdot e^{-i2\delta} + \rho\, S_{HV} + \rho\, S_{VH} + S_{VV}\cdot e^{i2\delta}\right]
\end{aligned} \tag{2.56}$$

In the case of backscattering from reciprocal media, $S_{HV} = S_{VH} = S_{XY}$ and $S_{IJ} = S_{JI}$ thus Equation (2.56) reduces to

$$\begin{aligned}
S_{II} &= \frac{1}{1+\rho\rho^*}\left[S_{HH}\cdot e^{-i2\delta} - 2\rho^* S_{XY} + \rho^{*2} S_{VV}\cdot e^{i2\delta}\right] \\
S_{IJ} &= \frac{1}{1+\rho\rho^*}\left[\rho\, S_{HH}\cdot e^{-i2\delta} + (1-\rho\rho^*) S_{XY} - \rho^* S_{VV}\cdot e^{i2\delta}\right] \\
S_{JJ} &= \frac{1}{1+\rho\rho^*}\left[\rho^2 S_{HH}\cdot e^{-i2\delta} + 2\rho\, S_{XY} + S_{VV}\cdot e^{i2\delta}\right]
\end{aligned} \tag{2.57}$$

For completeness it should be noted that there is one additional case that could eventuate when the incident and scattered waves are not referred to the same polarisation basis. In this scenario the unitary matrices are no longer identical.

Additional discussion of this scenario can be found in [59], however in the following sections the same polarisation reference frame will be assumed for the incident and scattered waves.

2.13 Characteristic polarisation states

The theory of characteristic polarisation states was first introduced by Kennaugh [9] for deterministic targets using the scattering matrix concept. Kennaugh's theory was later studied and redeveloped by Huynen [13], Boerner *et al.* [17, 23, 24, 121, 137, 143, 147], van Zyl [148], Mott [117], Lüneburg and Cloude [31] and Yamaguchi *et al.* [149].

A variety of techniques have been developed from Kennaugh's and Huynen's work that partially solved the problem of determining the characteristic polarisation states from deterministic targets. These methods included the voltage equation [9], the eigenvalue problem of the power scattering matrix [23], unitary transformation techniques [137, 150] and the three step procedure [24]. These early techniques were concerned with the optimisation of the received voltage or power transfer (its squared absolute value). This led to the controversial opinions concerning the correct form of transformation of the scattering matrix under orthogonal changes of polarisation bases and to the incorrect belief that radar polarimetry was a mixture of field theory and radar network performance. This highlighted the importance of the consimilarity transformation [151] in the context of the antilinear nature of the backscatter operator. This property has been stressed in papers by Kostinski and Boerner [24], Hubbert [152] and Lüneburg [128].

The analysis of similarity versus consimilarity eigenvalue/vector problems led to more rigorous formulations of the characteristic polarisation state optimisation problems for both the propagation (similarity) and backscattering (consimilarity) cases [31]. In these formulations the subtle differences in the coherent radar transformation phase can be resolved and correct transformation matrices can be uniquely determined through the inclusion of energy conservation principles. Two distinct matrix sets and the associated similarity/consimilarity problems can be defined, from which the optimal polarisation states can be determined together with the complementing set of two Huynen polarisation forks. In the radar community the

equation for the backscattering case is known as the Kennaugh pseudo eigenvector equation and, according to the Takagi theorem [153], has two orthogonal solutions which match the solutions obtained via the Graves power matrix equation.

A complete solution for the coherent case was finally found by Boerner and Xi [17] using a unitary transformation approach expressed in terms of the polarisation transformation ratio ρ. This solution was in complete agreement with Huynen's polarisation fork concept and demonstrated that five unique pairs of characteristic polarisation states exist for the monostatic (back-scattering) reciprocal case.

Two pairs, the cross-polarisation (x-pol) nulls and co-polarisation (co-pol) maxima, were shown to be identical in this case, while the x-pol maxima and x-pol saddle point pairs were shown to be distinct. When plotted on the Poincaré sphere, these three pairs of characteristic states can be shown to be mutually at right angles to one another. In general the fifth pair, the non-orthogonal co-pol null pair, lies in the plane spanned by the co-pol max and the x-pol max pairs. The co-pol max, co-pol null and x-pol max pairs define the target characteristic plane (circle) of Kennaugh [154]. The angle between the co-pol nulls is bisected by a line joining the two co-pol maxima and with the orthogonal x-pol saddlepoint pair they re-establish Huynen's polarisation fork concept. These properties are illustrated in Figure 2-5 which shows the position of the characteristic polarisation states for a general target with [S] matrix of the form

$$[S]=\begin{bmatrix} 2i & 0.5 \\ 0.5 & -i \end{bmatrix} \tag{2.58}$$

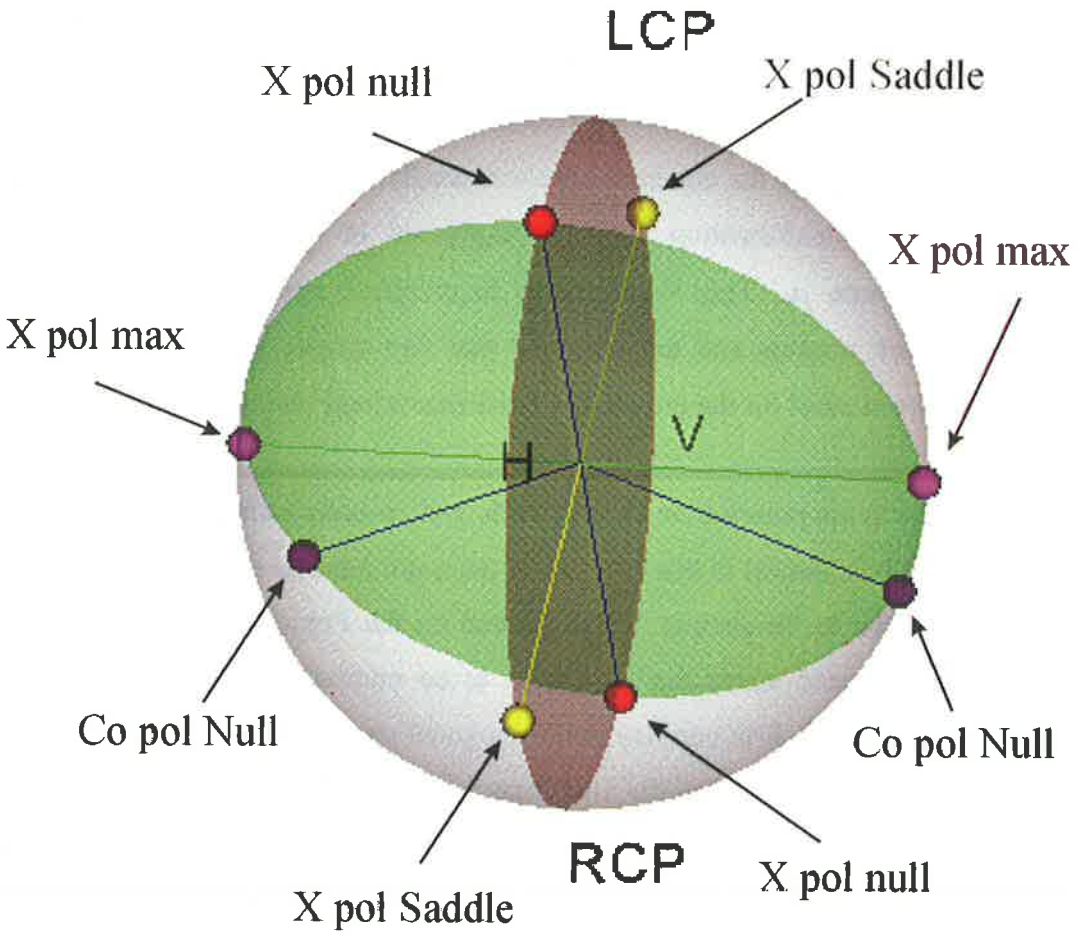

Figure 2-5 Characteristic polarisation states for the [*S*] matrix shown in Equation (2.58)

Recently a new approach has been developed by Yang *et al.* [155] using the geometrical relations of the characteristic states on the Poincaré sphere to obtain simple expressions for all the characteristic polarisation states. This approach was used to calculate the characteristic polarisation states in this study since it can be readily vectorised allowing for efficient calculation of the characteristic polarisation states for large data sets. Examples of the location of the characteristic polarisation states for a number of elementary scatterers are given in Section 3.2. These examples illustrate a number of special cases that result in multiple solutions for the characteristic states, leading to numerical problems in the previously developed techniques.

Other techniques using the covariance matrix approach have been developed which led to an eigenvector solution. The first techniques were seriously flawed and Cloude

[156] demonstrated that the solutions were biased as they failed to impose unitary constraints on the transmit and receive antenna states. Consequently, these solutions violated fundamental energy and minimum phase conservation principles.

A corrected formulation of the covariance matrix approach was developed by Tragl [32]. The optimal polarisation states were determined by decomposing the unitary transformation matrix into normalised, two-parameter, complex column vectors. Expressions for the mean power can then be obtained in the co-polar and cross-polar channels. These are continuous functions of the transmitter polarisation characterised by the complex polarisation ratio ρ. The existence of maximum and minimum points in the power signatures is guaranteed by the Weierstrass theorem [151] due to the compactness of the set of all possible optimal polarisation states on the Poincaré polarisation sphere. The maximum and minimum values of the power functions can be determined by equating the first derivatives simultaneously to zero. This formulation is given in [154] and [32]. The resulting expressions can be solved by numerical techniques, either directly in the complex plane, or by reducing the problem to that of the numerical solution of two coupled non linear equations. This involves separating the expressions into real and imaginary parts and leads to a long and tedious solution process.

A more elegant method [157] has been developed using unconstrained real vectors, but separate optimisation procedures need to be used for the co-polar and cross-polar channels. These techniques are summarised in [154].

Alternative techniques have also been conceived using the Mueller matrix approach. The first Mueller matrix optimisation procedures using the Lagrange multiplier method in radar polarimetry were initiated at The University of Chicago [121, 158]. Other methods were also developed independently by van Zyl [148].

The Mueller matrix methods can be used to determine the characteristic polarisation state for the "degenerate coherent Stokes vector case". Using the method derived in [121], the characteristic polarisation states can be found for the symmetric (reciprocal), asymmetric (nonreciprocal), monostatic and bistatic cases. These

methods use the Lagrange multiplier techniques applied to the received power expressed in terms of the Kennaugh matrices and Stokes vectors. The power expressions are maximised subject to the constraint that the transmitted wave must be completely polarised. The characteristic polarisation states for the co-polar, cross-polar and matched two antenna cases need to be considered separately but the solutions obtained can be shown to be identical to the results obtained via the unitary transformation technique [159].

Alternatively, the characteristic polarisation states in the cross-polarised channel can be determined for the monostatic reciprocal case using a technique that leads to an eigenvalue equation. This technique is described in [149] and gives results that are consistent with [159]. An explicit formula [160] for determining the characteristic polarisation states of the co-polar channel has also been developed for symmetric and asymmetric scattering matrices. This technique has also been successfully used to find solutions to contrast enhancement problems.

2.14 Distributed scatterers

The previous sections describe scattering from deterministic targets that are completely described by a single scattering matrix or scattering vector. When a target consists of multiple scatterers (distributed) it is not sufficient to describe the target by a single fixed scattering matrix. Instead it is necessary to use another descriptor to describe the scattering process as the elements of the scattering matrix are now stochastic variables. The average of the time-dependent scattering matrix cannot be used as it does not provide any information about the correlation properties of the scattering matrix elements. If a statistically time-varying scatterer is illuminated by a monochromatic wave, the backscattered wave will be partially polarised with incoherent scattering contributions [133]. Alternative descriptors such as the target coherency, covariance and Mueller or Kennaugh matrices must be used in these situations. These representations are described in the following sections.

2.14.1 The target coherency and covariance matrices

To analyse distributed scatterers in the complex domain, the concept of a scatterer covariance or coherency matrix can be introduced. The 4×4 polarimetric covariance matrix $[C_4]$ is defined using the outer product of the lexicographic scattering vector

$\vec{k}_{4L}$ with its conjugate transpose, where $\langle \ldots \rangle$ indicates spatial ensemble averaging [157, 161, 162].

$$[C_4] = \left\langle \vec{k}_{4L} \cdot \vec{k}_{4L}^{\dagger} \right\rangle = \begin{bmatrix} \left\langle |S_{HH}|^2 \right\rangle & \left\langle S_{HH} S_{HV}^* \right\rangle & \left\langle S_{HH} S_{VH}^* \right\rangle & \left\langle S_{HH} S_{VV}^* \right\rangle \\ \left\langle S_{HV} S_{HV}^* \right\rangle & \left\langle |S_{HV}|^2 \right\rangle & \left\langle S_{HV} S_{VH}^* \right\rangle & \left\langle S_{HV} S_{VV}^* \right\rangle \\ \left\langle S_{VH} S_{HH}^* \right\rangle & \left\langle S_{VH} S_{HV}^* \right\rangle & \left\langle |S_{VH}|^2 \right\rangle & \left\langle S_{VH} S_{VV}^* \right\rangle \\ \left\langle S_{VV} S_{HH}^* \right\rangle & \left\langle S_{VV} S_{HV}^* \right\rangle & \left\langle S_{VV} S_{VH}^* \right\rangle & \left\langle |S_{VV}|^2 \right\rangle \end{bmatrix} \tag{2.59}$$

Similarly the 4×4 polarimetric coherency matrix $[T_4]$ is defined as the averaged outer product of the Pauli scattering vector with its complex conjugate. Using Equation (2.44) the relationship between the coherency and covariance matrices is given by

$$[T_4] = \left\langle \vec{k}_{4P} \cdot \vec{k}_{4P}^{\dagger} \right\rangle = \left\langle [D_4] \vec{k}_{4L} \cdot \vec{k}_{4L}^{\dagger} [D_4]^{\dagger} \right\rangle = [D_4] \left\langle \vec{k}_{4L} \cdot \vec{k}_{4L}^{\dagger} \right\rangle [D_4]^{\dagger} = [D_4][C_4][D_4]^{\dagger} \tag{2.60}$$

The information content of the coherency and covariance matrices can be compactly assessed from their eigenvalue spectrum. Both $[T_4]$ and $[C_4]$ are positive semi-definite and hence have eigenvalues that are real and non-negative, $\lambda_1 \geq \lambda_2 \geq \lambda_3 \geq \lambda_4 \geq 0$. In the general bistatic case both the coherency and covariance matrices will generally be of full rank four. This implies the existence of four linearly independent non-zero eigenvectors. The smaller eigenvalues λ_2, λ_3 and λ_4 are often non-zero due to statistical fluctuations and the averaging inherent in Equations (2.59) and (2.60). Although the absolute values of the eigenvalues are important to assess the total scattered power by the target, it is the distribution of this power across the eigenvalue spectrum that is important in assessing the processing gains to be had in polarimetric processing.

In the monostatic backscatter case where the reciprocity theorem forces a symmetric underlying scattering matrix, the $[T_3]$ and $[C_3]$ matrices will in general be of rank three. A reciprocal partial scatterer is completely described either by the 3×3 polarimetric covariance matrix $[C_3]$

$$[C_3]=\left\langle \vec{k}_{3L}\cdot\vec{k}_{3L}^{\dagger}\right\rangle=\begin{bmatrix} \left\langle |S_{HH}|^2\right\rangle & \sqrt{2}\left\langle S_{HH}S_{HV}^{*}\right\rangle & \left\langle S_{HH}S_{VV}^{*}\right\rangle \\ \sqrt{2}\left\langle S_{HV}S_{HH}^{*}\right\rangle & 2\left\langle |S_{HV}|^2\right\rangle & \sqrt{2}\left\langle S_{HV}S_{VV}^{*}\right\rangle \\ \left\langle S_{VV}S_{HH}^{*}\right\rangle & \sqrt{2}\left\langle S_{VV}S_{HV}^{*}\right\rangle & \left\langle |S_{VV}|^2\right\rangle \end{bmatrix} \tag{2.61}$$

or by the 3×3 polarimetric coherency matrix $[T_3]$ defined as

$$[T_3]=\left\langle \vec{k}_{3P}\cdot\vec{k}_{3P}^{\dagger}\right\rangle=\begin{bmatrix} \left\langle |S_{HH}+S_{VV}|^2\right\rangle & \left\langle (S_{HH}+S_{VV})(S_{HH}-S_{VV})^{*}\right\rangle & 2\left\langle (S_{HH}+S_{VV})S_{HV}^{*}\right\rangle \\ \left\langle (S_{HH}-S_{VV})(S_{HH}+S_{VV})^{*}\right\rangle & \left\langle |S_{HH}-S_{VV}|^2\right\rangle & 2\left\langle (S_{HH}-S_{VV})S_{HV}^{*}\right\rangle \\ 2\left\langle S_{HV}(S_{HH}+S_{VV})^{*}\right\rangle & 2\left\langle S_{HV}(S_{HH}-S_{VV})^{*}\right\rangle & 4\left\langle |S_{HV}|^2\right\rangle \end{bmatrix} \tag{2.62}$$

It should be noted that both the coherency and covariance matrix data have a reduced resolution due to the spatial (or temporal) averaging needed to form the $[C]$ and $[T]$ matrices. The loss in resolution is compensated by the fact that the speckle noise is reduced in the averaging process. Using an adaptive polarimetric speckle filter, such as the one first proposed by Lee [47, 48], instead of the box filter enables a trade off to be achieved between high resolution for point scatterers and lower speckle noise for distributed scatterers.

The rank of the covariance and coherency matrices for point scatterers is always one, and the ensemble averaging becomes irrelevant. In these situations the $[S]$ matrix fully describes the scattering processes. However, for distributed scatters the single scattering matrix representation is inadequate. This can be clearly seen by considering the degrees of freedom of each representation. In the general case, $[T_4]$ and $[C_4]$ contain 16 independent variables, namely four real power values in the main diagonal and six complex off–diagonal cross correlations, containing information about the correlation between the complex elements of $[S]$ over the spatial averaging. In the monostatic backscattering case the number of independent variables is reduced to nine (three power terms and three complex cross correlations). Comparing this with the general bistatic $[S]$ matrix representation that has seven independent parameters, (reducing to five in the case of reciprocal backscatter) it is clear that the single scattering matrix is unable to completely represent a partial scatterer due to the lack of degrees of freedom.

2.14.2 Mueller matrix

The Mueller matrix describes the linear relationship between the two Stokes vectors corresponding to the transmitted and reflected waves. It was first introduced by Mueller [163] in the field of optics and is represented as a 4×4 matrix. For deterministic targets there exists a one-to-one correspondence between the Jones matrix $[T]$ and the Mueller matrix, which can be written as [133]

$$[M] = 2\, diag[\,1\ 1\ 1\ -1][A]^{T^{-1}}\left([T]\otimes[T]^*\right)[A]^{-1} = [A]\left([T]\otimes[T]^*\right)[A]^{-1} \tag{2.63}$$

where $\otimes$ symbolises the standard Kronecker matrix product [164] and $[A]$ is the Kronecker expansion matrix given by

$$[A] = \begin{bmatrix} 1 & 0 & 0 & 1 \\ 1 & 0 & 0 & -1 \\ 0 & 1 & 1 & 0 \\ 0 & i & -i & 0 \end{bmatrix} \tag{2.64}$$

An explicit expansion for the elements of $[M]$ is given in [42].

In the past, various denominations have been used for the Mueller matrix. Van de Hulst [165] called it the *transformation matrix* $[F]$, Deirmendjian [166] called it the *Stokes matrix* and Chandrasekhar [167] refers to it as the *phase matrix* $[P]$.

The Mueller matrix describes the scattering phenomenon in terms of power quantities. This has the advantage that it eliminates the absolute phase from the target. Therefore the elements of the Mueller matrix are incoherently additive. This aids in the interpretation of different electromagnetic phenomena as they are seen as being independent.

The classical representation using the scattering matrix describes a single physical event. The power representation allows the same physical event to be evaluated in different ways by considering the results as independent measurements. Thus it is possible to measure the Mueller matrix independently by combining different transmitting and receiving polarisation states corresponding to the six canonical polarisation states [168].

Huynen demonstrated that the Mueller matrix could be written so that it is independent of roll angle [13]. Thus rotation of the target along the line of sight of the radar does not affect the matrix values. He also showed that the Mueller matrix could be expressed in terms of nine parameters, now known as the *Huynen parameters*. These parameters are useful for general target analysis as each of them contains real physical target information. With this information a complete structure diagram can be assembled that displays the symmetry between the target parameters.

Consequently, the diagonal elements of the Mueller matrices are called the *generators* of the off-diagonal Huynen parameters. Huynen identified the three structure generators corresponding to generators of symmetry, target non-symmetry and target irregularity. These properties are discussed in more detail in [13] and [168].

2.14.3 Kennaugh matrix

In radar applications the scattered wave is usually of less interest than the power available at the radar receiver. The evaluation of the received power requires the knowledge of another 4 × 4 matrix that is similar to, but not identical to, the Mueller matrix. Kennaugh introduced this matrix for evaluating the received power in a radar with an impedance matched receiver. In recent texts [42, 130] this matrix is referred to as the Kennaugh matrix and denoted by the symbol $[K]$. For a target with a Sinclair matrix $[S]$, the Kennaugh matrix is defined as [129]

$$[K] = 2[A]^{T-1}\left([S]\otimes[S]^{*}\right)[A]^{-1} \tag{2.65}$$

where $[A]$ is the Kronecker expansion matrix defined in Equation (2.64). Explicit expansions for evaluating the elements of $[K]$ in terms of the Sinclair matrix elements S_{IJ} are given in [42].

In the past there has been much confusion as to the difference between the Kennaugh and Mueller matrices. Often there is no distinction made between the two matrices [169] while other papers refer to the Kennaugh matrix by names such as the *Stokes reflection matrix* [13] or the *Stokes scattering operator* [130]. The group of van Zyl at the Jet Propulsion Laboratory used the name *Stokes scattering matrix* [136] with the notation $[M]$, but elsewhere [43] used the same notation for the Mueller matrix. Further confusion was generated by Pottier and Saillard [170] who asserted that the

Mueller matrix was symmetric for the backscattering case. This can be shown to be only true for the Kennaugh matrix [171]. Additional discussion on the problems with nomenclature are given in [172].

Simple matrix relations can be derived that illustrate the link between the Kennaugh and Mueller matrices using directional Stokes vectors. The Kennaugh matrix connects Stokes vectors defined in the same polarisation space and uses the BSA coordinate system where the origin is taken on the radar [117]. The Mueller matrix, on the other hand, connects directional Stokes vectors pertaining to different propagation spaces with the origin of the coordinate system of the scattered wave taken on the target, as defined in the FSA convention. This is discussed further in [173].

2.15 Line of sight rotation

When a scattering object or the antenna used for transmission of reception is rotated about the Line of Sight (LOS), defined as the line connecting the antenna phase centre with the scatterer, a polarisation transformation occurs. Rotation of a scatterer by an angle θ about the LOS is equivalent to rotating the antenna by an angle of $-\theta$ which results in a rotated reference basis for transmission and reception. Consequently the LOS transformation can be considered as a special subspace of the change of basis transformation described by a unitary transformation matrix with a single degree of freedom, namely the rotation angle θ [44]. The following sections illustrate this, showing the effect that the LOS rotation has on the scattering matrix $[S]$, the scattering vector $\vec{k}_{4P}$ and coherency matrix components.

2.15.1 LOS rotation of the scattering matrix

Consider the scattering matrix $[S]$ defined as

$$[S] = \begin{bmatrix} S_{HH} & S_{HV} \\ S_{VH} & S_{VV} \end{bmatrix} \tag{2.66}$$

Huynen [13] observed that a rotation of a scatterer about the LOS by an angle θ results in a transformation of the scattering matrix into $[S(\theta)]$ via the following unitary transformation

$$[S(\theta)] = [R_2(\theta)][S][R_2(\theta)]^{-1} \tag{2.67}$$

where the matrix $[R_2(\theta)]$ is a real 2×2 unitrary rotation matrix, given by

$$[R_2(\theta)] = \begin{bmatrix} \cos\theta & \sin\theta \\ -\sin\theta & \cos\theta \end{bmatrix} \quad \text{where } [R_2(\theta)]^{-1} = [R_2(\theta)]^T = [R_2(-\theta)] \tag{2.68}$$

Substituting Equation (2.68) into Equation (2.67) yields

$$[S(\theta)] = \begin{bmatrix} S_{HH}(\theta)\ S_{HV}(\theta) \\ S_{VH}(\theta)\ S_{VV}(\theta) \end{bmatrix} = \begin{bmatrix} \cos\theta & \sin\theta \\ -\sin\theta & \cos\theta \end{bmatrix} \begin{bmatrix} S_{HH} & S_{HV} \\ S_{VH} & S_{VV} \end{bmatrix} \begin{bmatrix} \cos\theta & -\sin\theta \\ \sin\theta & \cos\theta \end{bmatrix} \tag{2.69}$$

This expression gives the relationships for the individual elements

$$\begin{aligned} S_{HH}(\theta) &= S_{HH}\cos^2\theta + S_{HV}\cos\theta\sin\theta + S_{VH}\cos\theta\sin\theta + S_{VV}\sin^2\theta \\ S_{HV}(\theta) &= -S_{HH}\cos\theta\sin\theta + S_{HV}\cos^2\theta - S_{VH}\sin^2\theta + S_{VV}\cos\theta\sin\theta \\ S_{VH}(\theta) &= -S_{HH}\cos\theta\sin\theta - S_{HV}\sin^2\theta + S_{VH}\cos^2\theta + S_{VV}\cos\theta\sin\theta \\ S_{VV}(\theta) &= S_{HH}\sin^2\theta - S_{HV}\cos\theta\sin\theta - S_{VH}\cos\theta\sin\theta + S_{VV}\cos^2\theta \end{aligned} \tag{2.70}$$

For reciprocal media $S_{HV} = S_{VH} = S_{XY}$ and $S_{HV}(\theta) = S_{VH}(\theta) = S_{XY}(\theta)$, thus Equation (2.70) reduces to

$$\begin{aligned} S_{HH}(\theta) &= S_{HH}\cos^2\theta + 2S_{XY}\cos\theta\sin\theta + S_{VV}\sin^2\theta \\ S_{XY}(\theta) &= (S_{VV} - S_{HH})\cos\theta\sin\theta + S_{XY}(\cos^2\theta - \sin^2\theta) \\ S_{VV}(\theta) &= S_{HH}\sin^2\theta - 2S_{XY}\cos\theta\sin\theta + S_{VV}\cos^2\theta \end{aligned} \tag{2.71}$$

In the special case where the cross-polarised S_{XY} return is zero, Equation (2.71) reduces to

$$\begin{aligned} S_{HH}(\theta) &= S_{HH}\cos^2\theta + S_{VV}\sin^2\theta \\ S_{XY}(\theta) &= (S_{VV} - S_{HH})\cos\theta\sin\theta \\ S_{VV}(\theta) &= S_{HH}\sin^2\theta + S_{VV}\cos^2\theta \end{aligned} \tag{2.72}$$

From Equation (2.72) it is clear that the rotated scattering matrix $[S(\theta)]$ now has a non zero cross-polarised component $S_{XY}(\theta)$ induced by the rotation about the LOS. The

induced cross-polarised returns will be completely correlated with the co-polarised components, whereas the returns generated by the scattering process will be uncorrelated. This property is extremely useful and has been used in the determination of azimuthal slopes by Schuler *et al.* [174] and Lee *et al.* [175].

2.15.2 LOS rotation of the scattering vector and coherency matrix

The LOS rotation on the general Pauli scattering vector $\vec{k}_{4P}$ yields the rotated scattering vector $\vec{k}_{4P}(\theta)$ defined as

$$\vec{k}_{4P}(\theta)=\frac{1}{\sqrt{2}}[S_{HH}(\theta)+S_{VV}(\theta),S_{HH}(\theta)-S_{VV}(\theta),S_{HV}(\theta)+S_{VH}(\theta),i(S_{HV}(\theta)-S_{VH}(\theta))]^{T} \quad (2.73)$$

Substituting the values in Equation (2.70) into Equation (2.73) gives

$$\vec{k}_{4P}(\theta)=\begin{bmatrix} S_{HH}(\theta)+S_{VV}(\theta) \\ S_{HH}(\theta)-S_{VV}(\theta) \\ S_{HV}(\theta)+S_{VH}(\theta) \\ i(S_{HV}(\theta)-S_{VH}(\theta)) \end{bmatrix}=\begin{bmatrix} S_{HH}+S_{VV} \\ (S_{HH}-S_{VV})\cos 2\theta+(S_{HV}+S_{VH})\sin 2\theta \\ -(S_{HH}-S_{VV})\sin 2\theta+(S_{HV}+S_{VH})\cos 2\theta \\ i(S_{HV}-S_{VH})\cos 2\theta \end{bmatrix} \quad (2.74)$$

This can be rewritten in matrix form as

$$\vec{k}_{4P}(\theta)=[R_{4P}(\theta)]\vec{k}_{4P} \quad (2.75)$$

where

$$[R_{4P}(\theta)]=\begin{bmatrix} 1 & 0 & 0 & 0 \\ 0 & \cos 2\theta & \sin 2\theta & 0 \\ 0 & \sin 2\theta & \cos 2\theta & 0 \\ 0 & 0 & 0 & \cos 2\theta \end{bmatrix} \quad (2.76)$$

Equation (2.74) demonstrates that the (S_{HH} + S_{VV}) component of the Pauli scattering vector is invariant to LOS rotation [9, 13]. The rotated scattering vector $\vec{k}_{4P}(\theta)$ can be used to generate the rotated coherency matrix $[T_4(\theta)]$ using Equation (2.60)

$$[T_4(\theta)]=\left\langle \vec{k}_{4P}(\theta)\cdot\vec{k}_{4P}^{\dagger}(\theta)\right\rangle=[R_{4P}(\theta)]\left\langle \vec{k}_{4P}\cdot\vec{k}_{4P}^{\dagger}\right\rangle[R_{4P}(\theta)]^{T} \quad (2.77)$$

which leads to

$$[T_4(\theta)]=[R_{4P}(\theta)][T_4][R_{4P}(\theta)]^{-1} \quad (2.78)$$

Similar analysis can be performed for the rotated covariance matrix $[C_4(\theta)]$ using the rotated scattering vector $\vec{k}_{4L}(\theta)$ defined in the lexicographic basis, leading to

$$[C_4(\theta)] = [R_{4P}(\theta)][D_4][C_4][D_4]^{\dagger}[R_{4P}(\theta)]^{-1} \tag{2.79}$$

For the backscattering case, the rotated scattering vector $\vec{k}_{3P}(\theta)$ vector can be written as

$$\vec{k}_{3P}(\theta) = [R_{3P}(\theta)]\vec{k}_{3P} \qquad \text{where } [R_{3P}(\theta)] = \begin{bmatrix} 1 & 0 & 0 \\ 0 & \cos 2\theta & \sin 2\theta \\ 0 & -\sin 2\theta & \cos 2\theta \end{bmatrix} \tag{2.80}$$

while the rotated 3 × 3 coherency matrix $[T_3(\theta)]$ is given by

$$[T_3(\theta)] = \left\langle \vec{k}_{3P} \cdot \vec{k}_{3P}^{\dagger} \right\rangle = [R_{3P}(\theta)][T_3][R_{3P}(\theta)]^{-1} \tag{2.81}$$

The LOS rotations can be used to demonstrate the roll invariance of polarimetric parameters. In particular it can be shown that the mean scattering alpha, the polarimetric entropy and anisotropy are all roll invariant [39]. This is a very important result in polarimetry and is discussed in more detail in Section 2.18.

2.16 Symmetry properties of distributed scatterers

Distributed scatterers are characterised by the superposition of elementary scattering centres and are completely described by their coherency matrix $[T_4]$. In the most general case, the $[T_4]$ matrix contains four real elements on the diagonal and six complex off-diagonal elements. Thus the matrix can be described by sixteen parameters. If one is to make assumptions about the distribution of scatterers, then simplifications can be made and this allows for quantitative conclusions about their scattering behaviour. For example, if the scattering matrix is known for a given position and direction, then the $[S]$ matrix of its mirrored or rotated image in certain symmetrical positions is also known. This concept was first introduced by Van de Hulst using the Mueller matrix formulation [165]. He considered three special cases of reflection, rotation and azimuthal symmetry that are illustrated in Figure 2-6. The following sections illustrate how these cases can also be formulated in terms of the coherency matrix, which enables the scattering to be described with fewer parameters.

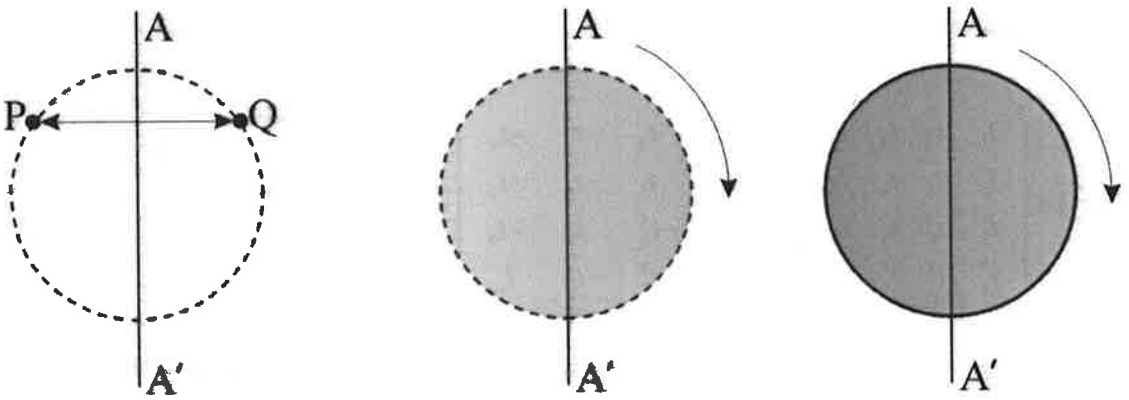

Figure 2-6 (a) Reflection, (b) rotation and (c) azimuthal symmetry cases

2.16.1 Reflection symmetry

Figure 2-6 (a) shows the case of reflection symmetry, which is characterised by a symmetry plane that contains the radar LOS. A typical example of a scattering situation that exhibits this type of behaviour is scattering from smooth surfaces. Consider a scatterer P, located on one side of the symmetry plane with scattering vector $\vec{k}_{4P}^{P}$ defined as

$$[S_P]=\begin{bmatrix} S_{HH} & S_{HV} \\ S_{VH} & S_{VV} \end{bmatrix} \text{ and } \vec{k}_{4P}^{P}=\frac{1}{\sqrt{2}}[S_{HH}+S_{VV}, S_{HH}-S_{VV}, S_{HV}+S_{VH}, i(S_{HV}-S_{VH})]^T \quad (2.82)$$

Reflection symmetry implies that for each P there is a mirrored scatterer Q on the other side of the symmetry plane with scattering vector $\vec{k}_{4P}^{Q}$ defined as [165]

$$[S_Q]=\begin{bmatrix} S_{HH} & S_{HV} \\ S_{VH} & S_{VV} \end{bmatrix} \text{ and } \vec{k}_{4P}^{Q}=\frac{1}{\sqrt{2}}[S_{HH}+S_{VV}, S_{HH}-S_{VV}, S_{HV}+S_{VH}, i(S_{HV}-S_{VH})]^T \quad (2.83)$$

The coherency matrix $[T_4]$ of a medium which exhibits reflection symmetry can be written as the superposition of the coherency matrices for both symmetrical components.

$$[T_4]=[T_{4P}]+[T_{4Q}]=\left\langle \vec{k}_{4P}^{P}\cdot\vec{k}_{4P}^{P\dagger}\right\rangle+\left\langle \vec{k}_{4P}^{Q}\cdot\vec{k}_{4P}^{Q\dagger}\right\rangle \quad (2.84)$$

In this case the averaging for $[T_{4P}]$ is performed over the scatterers located on one side of the symmetry plane while the averaging of $[T_{4Q}]$ is performed over scatterers

located on the mirrored side. Substituting Equations (2.82) and (2.83) into (2.84) gives a coherency matrix of the form

$$[T_4]=\begin{bmatrix} t_1 & t_2 & t_3 & t_4 \\ t_2^* & t_5 & t_6 & t_7 \\ t_3^* & t_6^* & t_8 & t_9 \\ t_4^* & t_7^* & t_9^* & t_{10} \end{bmatrix}+\begin{bmatrix} t_1 & t_2 & -t_3 & -t_4 \\ t_2^* & t_5 & -t_6 & -t_7 \\ -t_3^* & -t_6^* & t_8 & -t_9 \\ -t_4^* & -t_7^* & -t_9^* & t_{10} \end{bmatrix}=\begin{bmatrix} t_1 & t_2 & 0 & 0 \\ t_2^* & t_5 & 0 & 0 \\ 0 & 0 & t_8 & 0 \\ 0 & 0 & 0 & t_{10} \end{bmatrix} \tag{2.85}$$

Equation (2.85) illustrates that certain elements of $[T_{4P}]$ and $[T_{4Q}]$ will be the same, while other components will be oppositely signed, which means that the coherence matrix $[T_4]$ for the reflection symmetry case has only six non zero elements. Consequently the $[T_4]$ matrix can be completely characterised by six parameters consisting of the four real elements on the diagonal (t_1, t_5, t_8 and t_{10}) and the two remaining complex cross-correlations (t_2 and t_2^*) between the co-polarised channels. In the backscattering case, further simplifications can be made. The coherency matrix in this case can be written as

$$[T_3]=\begin{bmatrix} t_1 & t_2 & t_3 \\ t_2^* & t_4 & t_5 \\ t_3^* & t_5^* & t_6 \end{bmatrix}+\begin{bmatrix} t_1 & t_2 & -t_3 \\ t_2^* & t_4 & -t_5 \\ -t_3^* & -t_5^* & t_6 \end{bmatrix}=\begin{bmatrix} t_1 & t_2 & 0 \\ t_2^* & t_4 & 0 \\ 0 & 0 & t_6 \end{bmatrix} \tag{2.86}$$

and can be described by only five parameters. Note that in the backscattering case the correlation between the co-polarised terms ($S_{HH}+S_{VV}$) and ($S_{HH}-S_{VV}$) and the cross-polarised terms S_{XY} is zero. Thus all reflection symmetric media are characterised by the following relationship

$$\left\langle (S_{HH}+S_{VV})S_{XY}^* \right\rangle = \left\langle (S_{HH}-S_{VV})S_{XY}^* \right\rangle = 0 \tag{2.87}$$

2.16.2 Rotation symmetry

Rotation symmetry refers to situations that are invariant under LOS rotations. In such situations the coherency matrix remains constant when the scatterers are rotated about the LOS by an angle θ. From Equation (2.78), we know that the general expression for the rotated coherence matrix $[T_4(\theta)]$ is given by

$$[T_4(\theta)]=[R_{4P}(\theta)][T_4][R_{4P}(\theta)]^{-1} \tag{2.88}$$

where $[R_{4P}(\theta)]$ is the unitary 4 × 4 LOS rotation matrix given by

$$[R_{4P}(\theta)] = \begin{bmatrix} 1 & 0 & 0 & 0 \\ 0 & \cos 2\theta & \sin 2\theta & 0 \\ 0 & \sin 2\theta & \cos 2\theta & 0 \\ 0 & 0 & 0 & \cos 2\theta \end{bmatrix} \quad \text{with } [R_{4P}(\theta)]^{-1} = [R_{4P}(\theta)]^{T} \tag{2.89}$$

The four complex eigenvectors of $[R_{4P}(\theta)]$ are

$$\vec{e}_1 = \begin{bmatrix} 1 \\ 0 \\ 0 \end{bmatrix} \quad \vec{e}_2 = \frac{1}{\sqrt{2}} \begin{bmatrix} 0 \\ 1 \\ i \end{bmatrix} \quad \vec{e}_3 = \frac{1}{\sqrt{2}} \begin{bmatrix} 0 \\ 1 \\ -i \end{bmatrix} \quad \vec{e}_4 = \begin{bmatrix} 0 \\ 0 \\ 1 \end{bmatrix} \tag{2.90}$$

and by definition the eigenvectors are invariant under rotations about the LOS since

$$[R_{4P}(\theta)]\vec{e}_i = \lambda_i \vec{e}_i \tag{2.91}$$

Thus a rotation invariant coherency matrix must be constructable from a linear combination of the outer products of the eigenvectors [35] which can be expressed as

$$[T_4] = f_1\left(\vec{e}_1 \cdot \vec{e}_1^{\dagger}\right) + f_2\left(\vec{e}_2 \cdot \vec{e}_2^{\dagger}\right) + f_3\left(\vec{e}_3 \cdot \vec{e}_3^{\dagger}\right) + f_4\left(\vec{e}_4 \cdot \vec{e}_4^{\dagger}\right) \tag{2.92}$$

Substituting Equation (2.90) into (2.92) and simplifying the resulting expressions gives

$$[T_4] = \begin{bmatrix} f_1 & 0 & 0 & 0 \\ 0 & \frac{f_2 + f_3}{2} & \frac{i(f_2 + f_3)}{2} & 0 \\ 0 & \frac{-i(f_2 + f_3)}{2} & \frac{f_2 + f_3}{2} & 0 \\ 0 & 0 & 0 & f_4 \end{bmatrix} \tag{2.93}$$

Note that two of the terms on the diagonal are equal hence the coherency matrix can be completely described by five parameters. In the backscattering case the form of the coherency matrix is

$$[T_3]=\begin{bmatrix} f_1 & 0 & 0 \\ 0 & \frac{f_2+f_3}{2} & \frac{i(f_2+f_3)}{2} \\ 0 & \frac{-i(f_2+f_3)}{2} & \frac{f_2+f_3}{2} \end{bmatrix} \tag{2.94}$$

Unlike the reflection symmetric case, the correlation between the $(S_{HH}+S_{VV})$ and the S_{XY} does not vanish but the correlation between the $(S_{HH}+S_{VV})$ and $(S_{HH}-S_{VV})$ and $(S_{HH}+S_{VV})$ and S_{XY} becomes zero. From Equation (2.94) it is clear that the general properties of reflection symmetric media can be summarised as

$$\begin{gathered} \left\langle (S_{HH}+S_{VV})(S_{HH}-S_{VV})^* \right\rangle = \left\langle (S_{HH}+S_{VV})S_{XY}^* \right\rangle = 0 \\ \left\langle (S_{HH}-S_{VV})S_{XY}^* \right\rangle \neq 0 \\ \left| \left\langle (S_{HH}-S_{VV})^2 \right\rangle \right| = 4\left| \left\langle S_{XY}^2 \right\rangle \right| \end{gathered} \tag{2.95}$$

2.16.3 Azimuthal symmetry

Azimuthal symmetry arises when both reflection and rotation symmetry are present. In this case all planes including the LOS direction are reflection symmetry planes. The coherency matrix describing this type of scattering is regarded as being composed of two reflection symmetric terms where each of them is rotation symmetric. This can be expressed as

$$[T_4]=\begin{bmatrix} f_1 & 0 & 0 & 0 \\ 0 & \frac{f_2+f_3}{2} & \frac{i(f_2+f_3)}{2} & 0 \\ 0 & \frac{-i(f_2+f_3)}{2} & \frac{f_2+f_3}{2} & 0 \\ 0 & 0 & 0 & f_4 \end{bmatrix} + \begin{bmatrix} f_1 & 0 & 0 & 0 \\ 0 & \frac{f_2+f_3}{2} & \frac{-i(f_2+f_3)}{2} & 0 \\ 0 & \frac{i(f_2+f_3)}{2} & \frac{f_2+f_3}{2} & 0 \\ 0 & 0 & 0 & f_4 \end{bmatrix} \tag{2.96}$$

Adding the two matrices gives

$$[T_4]=\begin{bmatrix} f_1 & 0 & 0 & 0 \\ 0 & f_2+f_3 & 0 & 0 \\ 0 & 0 & f_2+f_3 & 0 \\ 0 & 0 & 0 & f_4 \end{bmatrix} \tag{2.97}$$

From Equation (2.97) it can be seen that azimuthal symmetry can be described by three parameters. In the case of backscattering, the expression for the coherency matrix $[T_3]$ is

$$[T_3] = \begin{bmatrix} f_1 & 0 & 0 \\ 0 & f_2 + f_3 & 0 \\ 0 & 0 & f_2 + f_3 \end{bmatrix} \tag{2.98}$$

From Equation (2.98) it is clear that media with azimuthal symmetry can be described by two parameters and can be characterised by the following properties:

$$\begin{gathered} \left\langle (S_{HH} + S_{VV})(S_{HH} - S_{VV})^* \right\rangle = \left\langle (S_{HH} + S_{VV}) S_{XY}^* \right\rangle = \left\langle (S_{HH} - S_{VV}) S_{XY}^* \right\rangle = 0 \\ \left| \left\langle (S_{HH} + S_{VV})^2 \right\rangle \right| = 4 \left| \left\langle S_{XY}^2 \right\rangle \right| \end{gathered} \tag{2.99}$$

2.16.4 Summary of symmetry properties

Symmetry is a powerful property that can help reduce the number of parameters required to describe the coherency matrix. In the most general case, sixteen parameters are needed to describe the coherency matrix $[T_4]$, however if rotation symmetry can be assumed, the number can be reduced to six. If reflection symmetry applies only five parameters are required to fully describe $[T_4]$ while in the most restrictive case of azimuthal symmetry, which leads to a diagonal matrix, only three parameters are needed. In the case of backscattering, similar reduction occur with the general case requiring nine parameters, reflection symmetry requiring five, rotation symmetry needing four and azimuthal symmetry requiring only two.

2.17 Target decomposition theorems

Many targets exhibit the effects of coherent speckle noise and random vector scattering effects. These targets require multivariate statistical descriptors such as averaged Kennaugh and covariance matrices to describe the scattering process. For such targets the concept of an average or dominant scattering mechanism is of interest for the classification or inversion of scattering data. One of the main advantages of polarimetric data is the possibility of separating and associating scattering contributions into elementary scattering mechanisms using target decomposition techniques.

Chandrasekhar [167] provided the first example of a target decomposition technique in his investigations of lateral scattering of light by small anisotropic particles. He decomposed the total average phase matrix into the sum of a phase matrix representing the scattering from a dipole and a phase matrix representing pure random scattering or noise. He followed the principle used to represent the Stokes vector of partially polarised waves as the sum of two Stokes vectors representing fully polarised and completely unpolarised waves.

The first matrix decomposition approaches in radar polarimetry were performed by Kennaugh [12] and were based on group theory concepts from quantum mechanics. Huynen [13] later published a technique that decomposed the Mueller/Kennaugh matrix into a sum of a deterministic single target component and a distributed residue component matrix (*N-target*) related to the non symmetric scattering contributions. Questions were raised in relation to the uniqueness of this decomposition as this approach was shown to be incapable of uniquely yielding the dominant scattering process in different polarisations. Cloude [176] showed that the *N-target* is just one of an infinite set of residue matrices. Huynen claimed this to be false and suggested a scenario in which Cloude's decomposition was not unique. These arguments are discussed in [177] and [14].

Two main classes of decomposition techniques may be distinguished: coherent target decomposition (CTD) and partially coherent target decomposition (PCTD). CTD deals with the coherent decomposition of the scattering matrix describing completely polarised scattered waves. The best known techniques are the Huynen [178], Krogager [179] and Cameron *et al.* [180] methods. The PCTD methods, such as the Cloude [35] and Huynen [178] techniques, decompose the power reflection matrices that represent partially polarised scattered waves. In optics, the decomposition of the Mueller/Kennaugh matrices is preferred while the covariance/coherency matrices are generally analysed in remote sensing applications. As a result, approaches based on the more compact coherence and covariance matrices have been preferred in recent years. A detailed discussion of target decomposition algorithms is given in a review paper by Cloude and Pottier [35]. This paper concluded that there is no decisive decomposition technique. The following sections give more detailed discussions of the decomposition techniques used in Chapter 6.

2.17.1 Coherent target decomposition techniques

Coherent decomposition techniques decompose the [S] matrix into scattering matrices corresponding to elementary scattering matrices that can be associated with certain deterministic scattering mechanisms. The vectorisation of the scattering matrix described in Section 2.11 using the Pauli or lexicographic basis is an example of such a decomposition. The decomposition of the [S] matrix using the Pauli basis can be written as

$$[S]=\begin{bmatrix} a+b & c-id \\ c+id & a-b \end{bmatrix}=a\begin{bmatrix} 1 & 0 \\ 0 & 1 \end{bmatrix}+b\begin{bmatrix} 1 & 0 \\ 0 & -1 \end{bmatrix}+c\begin{bmatrix} 0 & 1 \\ 1 & 0 \end{bmatrix}+d\begin{bmatrix} 0 & -i \\ i & 0 \end{bmatrix} \qquad (2.100)$$

where the complex coefficients a, b, c and d are proportional to the elements of the scattering vector $\vec{k}_{4P}$. The advantage of the Pauli decomposition is that the scattering mechanisms are orthogonal and so their separation is possible, even in the case where noise and depolarisation effects are present.

Cameron [181] developed a method that maximised the symmetrical component of coherent scattering and then decomposed the scattering matrix using the Pauli basis set. The target matrix is then grouped into three general classes: non-reciprocal scatter, asymmetric scatter and symmetric scatter. In this approach a symmetric scatterer is defined in [178] as a target having an axis of symmetry in the plane orthogonal to the radar line of sight. Such targets can be diagonalised by a rotation about the LOS in a basis of linear eigenpolarisations. Cameron introduced a classification method using his decomposition technique which has been used for identification and characterisation of point targets such as ships [182] and small planes [183]. Misleading results can occur due to the significant radiometric dispersion that is tolerated in each of the elemental scatterer classes, as well as the implicit assumption on the coherent nature of target scattering. Touzi [184] proposed a new method called the symmetric scattering characterisation method (SSCM) to better exploit the information provided by the largest target symmetric scattering component, under coherent conditions. This approach expresses the symmetric scattering in terms of the Poincaré sphere angles and permits a better characterisation of target symmetric scattering and permits the generation of coherent scattering segmentation of much higher resolution in comparison with Cameron's segmentation.

Another approach was proposed by Krogager [179, 185] and involves decomposing the scattering matrix into a combination of fundamental elements such as a sphere, a helix and a diplane (corner reflector). The decomposition of the [*S*] matrix in the (*H,V*) polarisation basis can be written as

$$[S] = k_s S_s + e^{i\varphi}\left\{k_d S_{d(\theta)} + k_h S_{h(\theta)}\right\} \tag{2.101}$$

where S_s represents the scattering matrix for a sphere defined as

$$S_s(H,V) = \begin{bmatrix} 1 & 0 \\ 0 & 1 \end{bmatrix} \tag{2.102}$$

$S_{d(\theta)}$ represents the scattering from a diplane at angle θ defined as

$$S_{d(\theta)}(H,V) = \begin{bmatrix} \cos^2\theta & \sin^2\theta \\ \sin^2\theta & -\cos^2\theta \end{bmatrix} \tag{2.103}$$

And $S_{h\pm}$ represents the left (+) and right (–) sensed helices defined as

$$S_{h\pm}(H,V) = \frac{1}{2}\begin{bmatrix} 1 & \pm i \\ \pm i & 1 \end{bmatrix} \tag{2.104}$$

While the helical targets are somewhat artificial, helical type returns are frequently encountered in both urban and rural scattering scenarios from the interaction of two diplanes with a relative orientation angle of 45° and a displacement angle of ⅛ of a wavelength. Helical returns can also be used to determine left versus right sensed feature torsion in nature using Huynen's concept of polarimetric phyllotaxis [186]. Krogager's decomposition is often re-expressed in the circular polarisation basis (*R,L*) leading to the following orientation invariant representation for the left-wound helix

$$[S] = e^{i\xi}\left\{e^{i\psi_s}k_s\begin{bmatrix} 0 & i \\ i & 0 \end{bmatrix} + k_d\begin{bmatrix} e^{i2\theta} & 0 \\ 0 & -e^{-i2\theta} \end{bmatrix} + k_h\begin{bmatrix} e^{i2\theta} & 0 \\ 0 & 0 \end{bmatrix}\right\} \tag{2.105}$$

The decomposition parameters can be written as

$$\xi = \frac{1}{2}(\varphi_{RR} + \varphi_{LL} - \pi) \qquad k_s = |S_{RL}|$$

$$\theta = \frac{1}{4}(\varphi_{RR} + \varphi_{LL} + \pi) \qquad k_d^+ = |S_{LL}| \;\; k_d^- = |S_{RR}| \tag{2.106}$$

$$\psi_s = \varphi_{RL} - \frac{1}{2}(\varphi_{RR} + \varphi_{LL}) \qquad k_h^+ = |S_{RR}| - |S_{LL}| = -k_h^-$$

Krogager's technique yields a roll invariant decomposition but the fundamental elements are not mutually orthogonal. Nevertheless, there are some distinct advantages in this approach. The practical disadvantage of Pauli decomposition is that a double bounce reflector appears in both the unrotated and 45° tilted diplane components. In the Krogager decomposition, each of the three different elementary scatterers appear in only one of the three components, although the diplane and helix components are not independent. This means that in the presence of both a helix and a diplane, the decomposition will in general not extract the actual strengths of the respective reflectors. The main problem encountered with the coherent decomposition techniques is the lack of invariance under the change of basis transformations [35].

2.17.2 Partially coherent decomposition techniques (PCTD)

The second class of decomposition theorems, based on the eigenvalue analysis of the coherence matrix [T], was first proposed by Cloude [14, 176] and is capable of covering the whole range of scattering mechanisms. This approach is automatically basis invariant due to the invariance of the eigenvalue problem under unitary transformations. Since the coherency matrix [T_4] is a Hermitian positive semi-definite matrix, it can always be diagonalised by a unitary similarity transformation [15, 187] of the form

$$[T_4] = [U_4][\Lambda_4][U_4]^\dagger \quad \text{where } [\Lambda_4] = \begin{bmatrix} \lambda_1 & 0 & 0 & 0 \\ 0 & \lambda_2 & 0 & 0 \\ 0 & 0 & \lambda_3 & 0 \\ 0 & 0 & 0 & \lambda_4 \end{bmatrix} \text{ and } [U_4] = [\vec{e}_1 \;\; \vec{e}_2 \;\; \vec{e}_3 \;\; \vec{e}_4]^T \tag{2.107}$$

where [Λ_4] is a diagonal eigenvalue matrix with elements corresponding to the eigenvalues of the [T_4] matrix, which are real and non-negative with $\lambda_1 \geq \lambda_2 \geq \lambda_3 \geq \lambda_4 \geq 0$. [$U_4$] is the unitary eigenvector matrix with columns corresponding to the orthonormal eigenvectors of [T_4]. By performing the eigenvalue

decomposition of $[T_4]$, it is then possible to rewrite the matrix as the incoherent sum of four independent coherency matrices $[T_i]$ such that

$$[T_4] = \lambda_1(\vec{e}_1 \cdot \vec{e}_1^{\dagger}) + \lambda_2(\vec{e}_2 \cdot \vec{e}_2^{\dagger}) + \lambda_3(\vec{e}_3 \cdot \vec{e}_3^{\dagger}) + \lambda_4(\vec{e}_4 \cdot \vec{e}_4^{\dagger}) = [T_a] + [T_b] + [T_c] + [T_d] \quad (2.108)$$

This essentially represents a decomposition of $[T_4]$ into four single scattering matrices of rank one described by $[T_a]$, $[T_b]$, $[T_c]$ and $[T_d]$, each representing a deterministic scattering contribution. The strength of each contribution, in power terms, is given by the appropriate eigenvalue, while the type of scattering is determined by the form of the eigenvectors. In addition, the total scattered power is given by the sum of the eigenvalues:

$$Total\ Power = \lambda_1 + \lambda_2 + \lambda_3 + \lambda_4 \quad (2.109)$$

The physical basis of the eigenvector decomposition is provided by the orthogonal nature of the eigenvectors, which guarantees the existence of a set of basis matrices in which the expansion of $[T_4]$ leads to a diagonal coherency matrix. The statistical significance of this is equally important, as the absence of off-diagonal terms establishes the statistical independence between the component vectors.

In the case of reciprocal backscatter, $\lambda_4 = 0$ and Equation (2.107) can be rewritten as

$$\langle [T_3] \rangle = [U_3][\Lambda_3][U_3]^{\dagger} = [U_3] \begin{bmatrix} \lambda_1 & 0 & 0 \\ 0 & \lambda_2 & 0 \\ 0 & 0 & \lambda_3 \end{bmatrix} [U_3]^{\dagger} \quad (2.110)$$

In this case the unitary matrix $[U_3]$ can be written in the form

$$[U_3] = \begin{bmatrix} \cos\alpha_1 & \cos\alpha_2 & \cos\alpha_3 \\ \sin\alpha_1 \cos\beta_1 e^{i\delta_1} & \sin\alpha_2 \cos\beta_2 e^{i\delta_2} & \sin\alpha_3 \cos\beta_3 e^{i\delta_3} \\ \sin\alpha_1 \cos\beta_1 e^{i\gamma_1} & \sin\alpha_2 \cos\beta_2 e^{i\gamma_2} & \sin\alpha_3 \cos\beta_3 e^{i\gamma_3} \end{bmatrix} \quad (2.111)$$

and the corresponding eigenvector expansion of $[T_3]$ can be written as

$$[T_3] = \sum_{n=1}^{3} \lambda_n [T_n] = \lambda_1(\vec{e}_1 \cdot \vec{e}_1^{\dagger}) + \lambda_2(\vec{e}_2 \cdot \vec{e}_2^{\dagger}) + \lambda_3(\vec{e}_3 \cdot \vec{e}_3^{\dagger}) \quad (2.112)$$

2.18 Polarimetric entropy and anisotropy

Two secondary functions can also be defined from the eigenvalues of the coherency matrix. The first is the polarimetric scattering entropy H, defined in the Von Neumann sense as the logarithmic sum of the eigenvalues of $[T_3]$ [35, 188].

$$H = \sum_{i=1}^{3} -P_i \log_3 P_i \qquad \text{where } P_i = \frac{\lambda_i}{\lambda_1 + \lambda_2 + \lambda_3} \tag{2.113}$$

P_i represents the appearance probability of each scattering type defined by the associated eigenvector and ranges from zero to one. Similarly, by definition, the polarimetric scattering entropy also ranges from zero to one and can be interpreted as the degree of randomness of the scatter. Entropy is generally defined as the measure of the disorder within a system. Systems tend to go from a state of order (low entropy) to a state of maximum disorder (high entropy). In the case of radar scattering, an entropy value of zero describes a non depolarising scattering process which can be completely described by a single scattering matrix. In this scenario, the $[T_3]$ matrix degenerates to a matrix of rank one with only one non zero eigenvalue (λ_2 and λ_3 both equal zero). Conversely, an entropy of one represents the situation in which the incident electromagnetic wave is completely depolarised regardless of the polarisation. In effect this represents the state of maximum disorder and the target scattering is truly a random noise process. In most cases, scatterers will lie between these two extremes having intermediate entropy values. As the entropy increases the number of distinguishable classes identifiable from polarimetric observations is reduced, thus in order to exploit the polarisation domain, one hopes to encounter situations with low to intermediate entropy values.

While the entropy is a useful scalar descriptor of the randomness of the scattering process, it is not a unique function of the eigenvalue ratios and gives no direct information about the relationship between λ_2 and λ_3. A secondary function, known as the polarimetric anisotropy can be introduced, defined as the normalised difference between the appearance probabilities of the second and third scattering components [36]

$$A_{23} = \frac{P_2 - P_3}{P_2 + P_3} = \frac{\lambda_2 - \lambda_3}{\lambda_2 + \lambda_3} \tag{2.114}$$

The anisotropy also ranges in value from zero to one and provides the relationship between the secondary scattering processes. For high or very low entropy situations, the anisotropy yields no additional information. In the high entropy case all the eigenvalues are nearly equal thus the anisotropy value tends to zero while in the very low entropy case both λ_2 and λ_3 are close to zero. Medium entropy situations imply that more than one scattering mechanism contributes to the signal, however the entropy value does not indicate if one or two additional scattering mechanisms are present. In these cases the anisotropy provides complementary information since a high value suggests that only the second scattering mechanism is important while a low anisotropy value indicates that the third scattering mechanism also plays a role.

The great advantage of the entropy and anisotropy parameters comes from the invariance of the eigenvalue problem under unitary transformations, which ensures that the values are independent of the polarisation basis used.

2.19 The entropy/anisotropy plane

The feasible regions of values in the entropy/anisotropy plane can be determined by considering the range of possible values for the appearance probabilities P_1, P_2 and P_3. These values are constrained by the following expressions

$$P_1 + P_2 + P_3 = 1 \quad \text{and} \quad P_1 \geq P_2 \geq P_3 \geq 0 \tag{2.115}$$

This defines a plane bounded by three lines defined as

$$\begin{aligned} &\textit{Line } 1: (P_1, P_2, P_3) = (1,0,0) + t(-2/3, 1/3, 1/3) \\ &\textit{Line } 2: (P_1, P_2, P_3) = (1,0,0) + t(-1/2, 1/2, 0) \qquad 0 \leq t \leq 1 \\ &\textit{Line } 3: (P_1, P_2, P_3) = (1/2, 1/2, 0) + t(-1/6, -1/6, 1/3) \end{aligned} \tag{2.116}$$

These lines define a triangular region as shown in Figure 2-7.

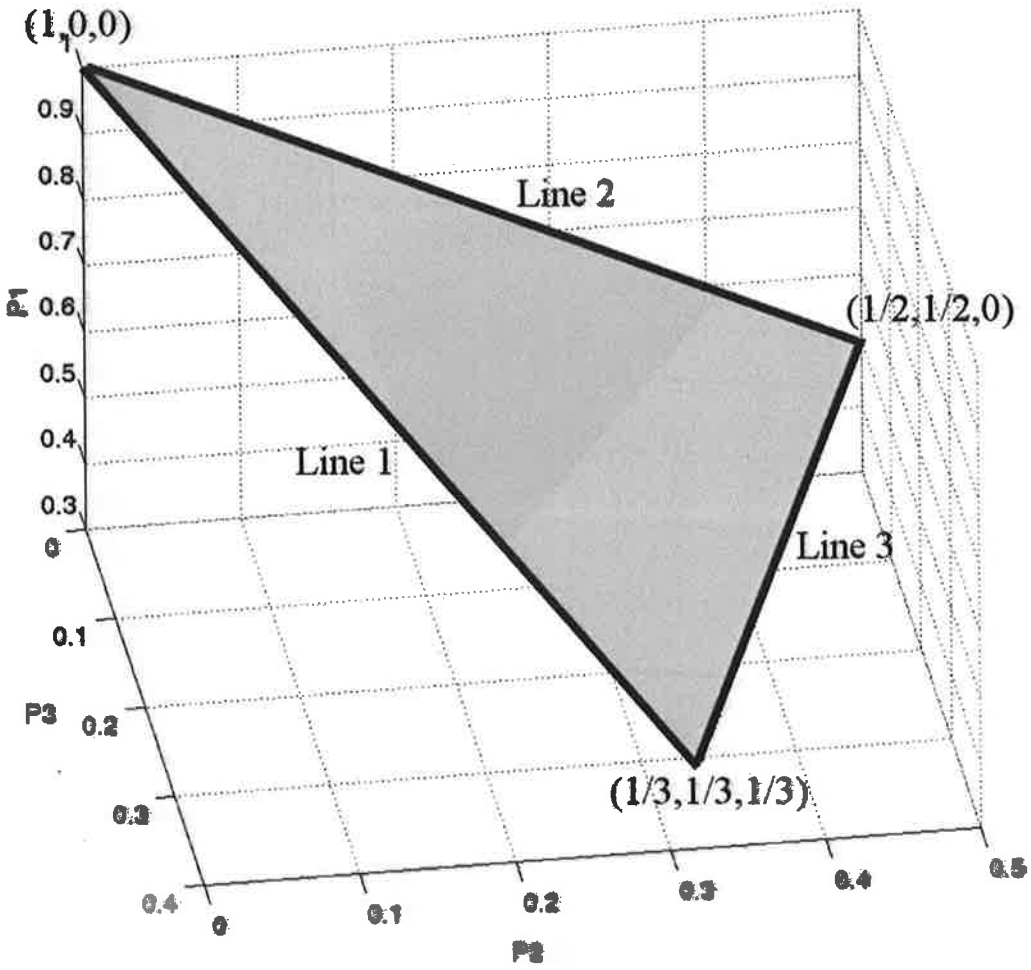

Figure 2-7 Feasible region of appearance probability values

The entropy values within the feasible range can be determined by evaluating Equation (2.113). A colour coded plot illustrating the variation in entropy values within this region is shown in Figure 2-8. This plot indicates that in most of the domain the entropy is high. In fact, the median entropy value within the feasible region was determined to be 0.79. Plots of the distribution of entropy values and the probability distribution function are shown in Figure 2-9 and indicate that less than ten percent of the points in the feasible region lie in the low entropy range ($H < 0.5$). Similar analysis can be performed on the polarimetric anisotropy. The anisotropy values within the feasible region, found by evaluating Equation (2.114), are shown in Figure 2-10.

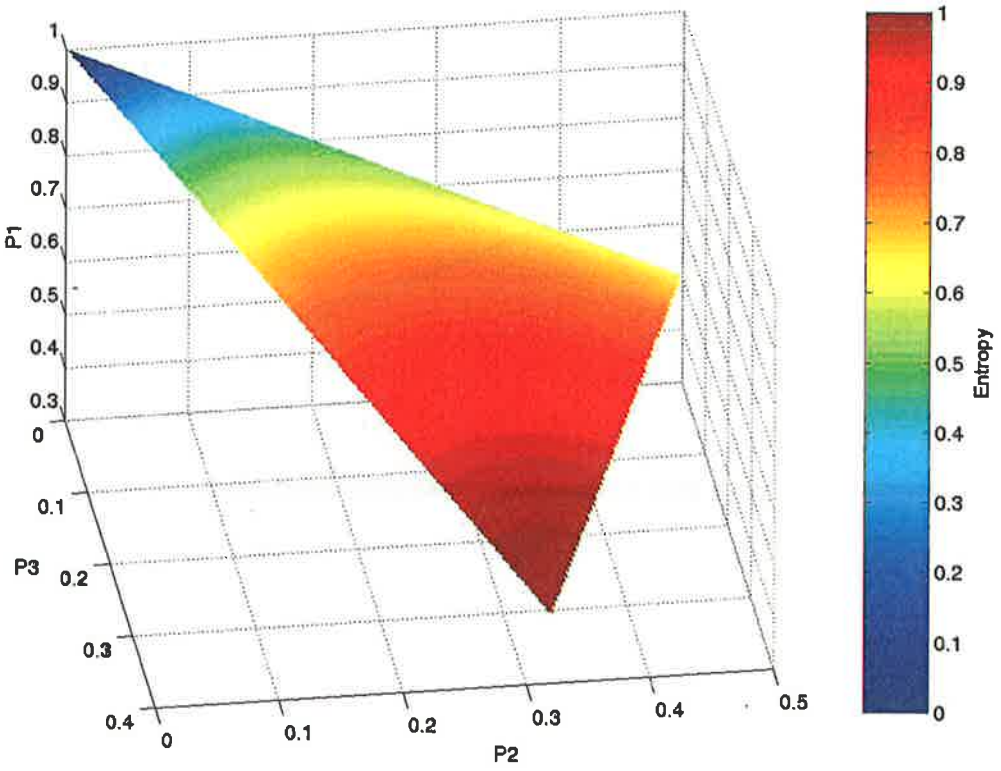

Figure 2-8 Entropy values within the feasible region of appearance probabilities

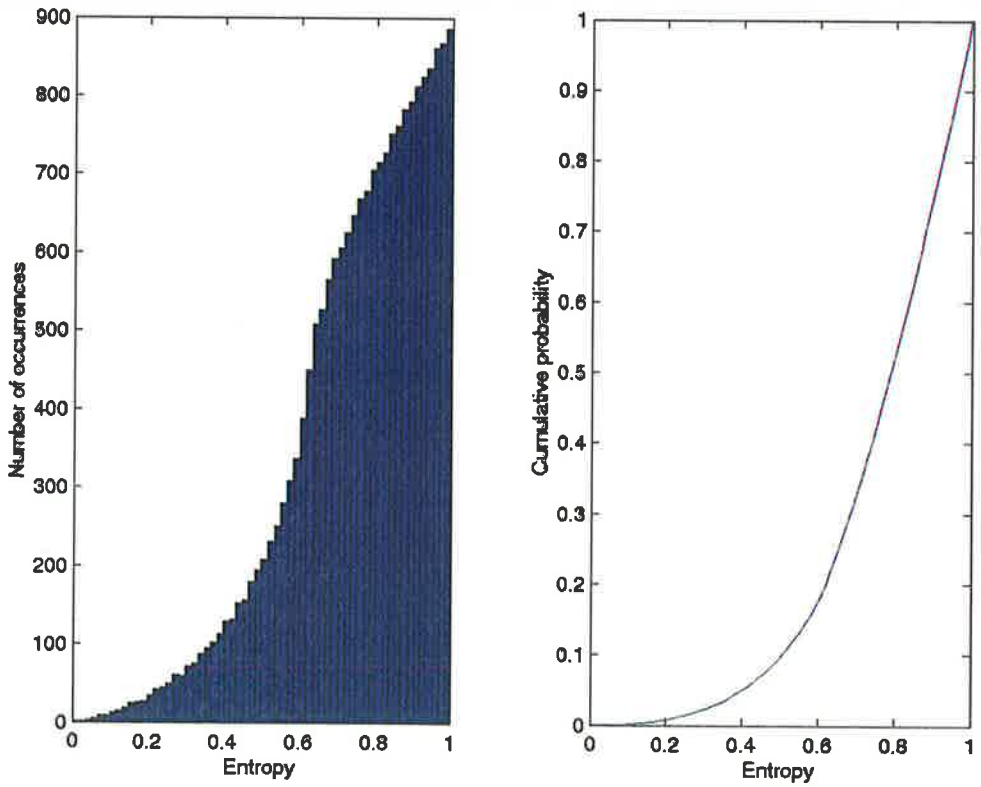

Figure 2-9 The distribution of entropy values within the feasible region defined in Figure 2-7

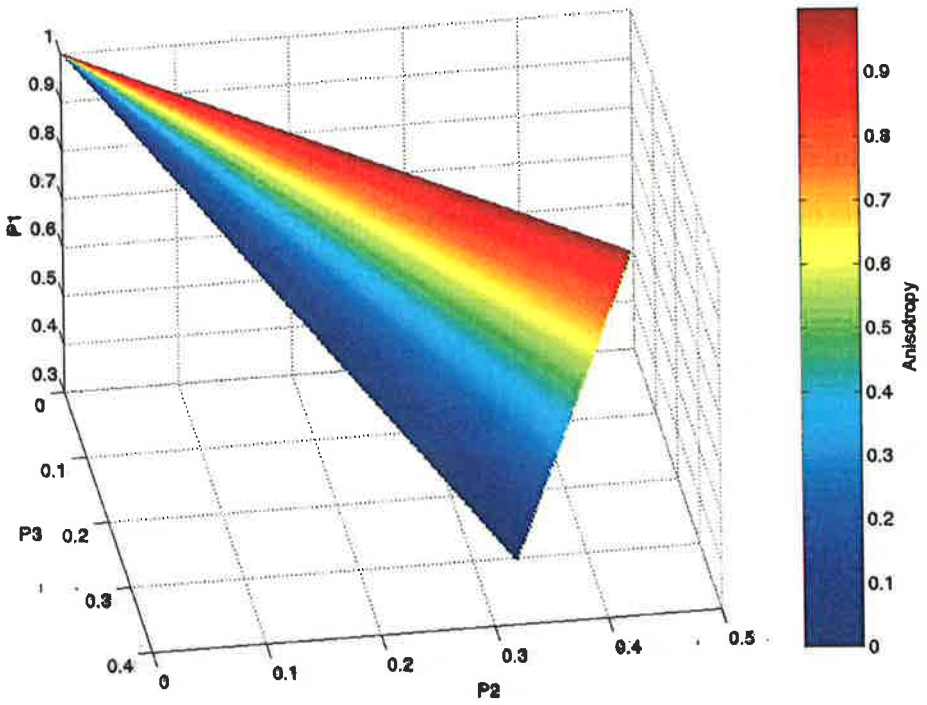

Figure 2-10 Anisotropy values within the feasible region of appearance probabilities

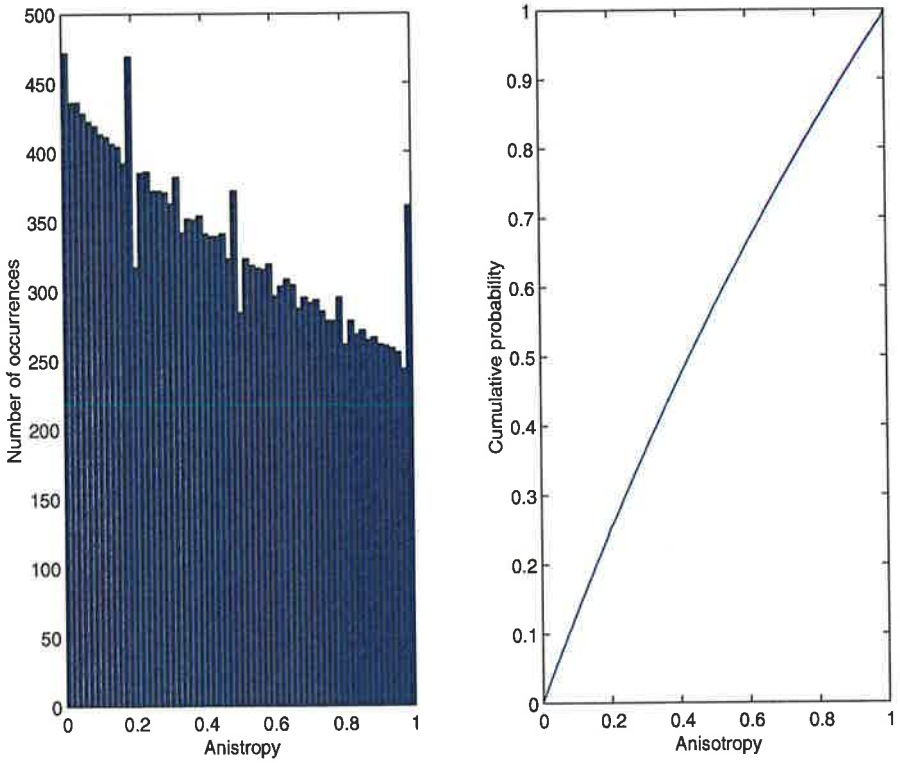

Figure 2-11 The distribution of anisotropy values within the feasible region defined in Figure 2-7

The distribution of the sampled anisotropy values and cumulative probability distribution functions for the anisotropy are shown in Figure 2-11. The distribution of the anisotropy values is quite different from the entropy values, with values being more evenly distributed resulting in a median value of 0.43.

The results in Figure 2-8 and Figure 2-10 can be combined to give a plot of the feasible region in the entropy/anisotropy space as shown in Figure 2-12.

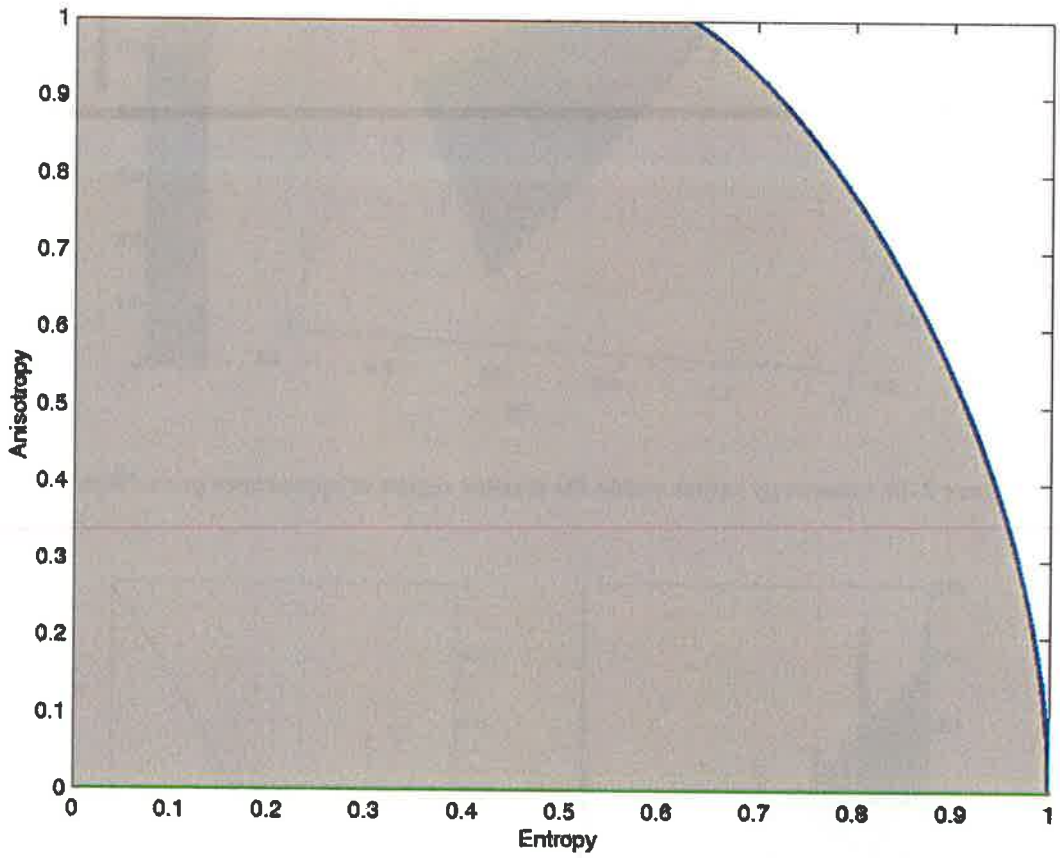

Figure 2-12 Feasible region of values in entropy / anisotropy space

The results in Figure 2-12 illustrate that for low to moderate entropy values, the anisotropy can span the full range of values between zero and one. When the entropy exceeds 0.63 (corresponding to the situation where $\lambda_1 = 0.5$, $\lambda_2 = 0.5$ and $\lambda_3 = 0$) the range of possible anisotropy values begins to decrease as the role of the third scattering component λ_3 becomes more significant. When the entropy is equal to one, the anisotropy can only be equal to zero and yields no additional information. However, for medium entropy situations, where more than one scattering mechanism is present, the anisotropy value contains valuable information regarding the number of

scattering mechanisms that play an important role. This property is used for classification purposes by Pottier [41]. An example plot showing the distribution of values within the entropy/anisotropy space obtained from a measurement of the wake produced by a pilot boat is shown in Figure 2-13.

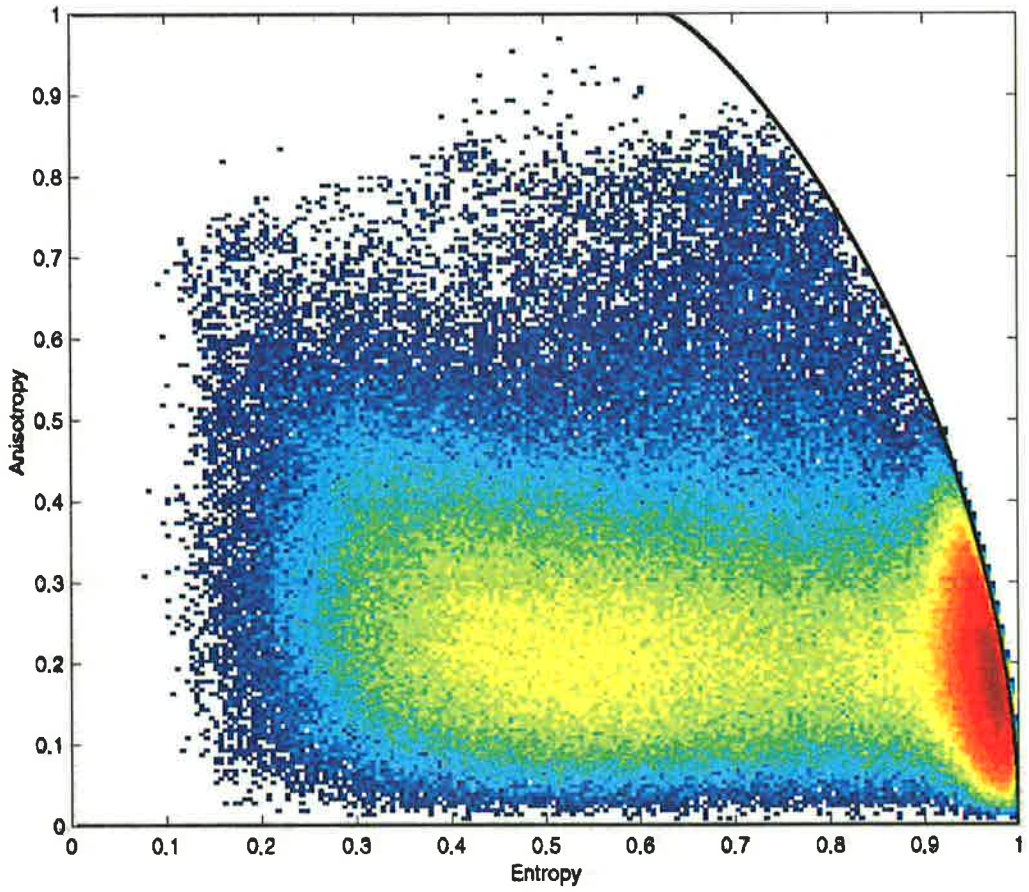

Figure 2-13 Distribution of values in the H - A space for a pilot boat wake

2.20 Scattering mechanisms

The essential advantage of polarimetric data is the possibility of extracting information about the scattering mechanisms. In order to classify the scattering mechanisms, not only is it necessary to extract and separate the scattering processes but one must also identify scattering mechanisms present. While the diagonalisation of the coherency matrix [T] produces a representation in terms of three orthogonal components, the physical significance of these components and the corresponding eigenvectors is not immediately apparent. In order to understand this, it is necessary to investigate the important role that general unitary matrix transformations have on the scattering vector $\vec{k}_{4L}$.

Unitary matrix transformations preserve both the norm and the definition of phase of a vector. Consider the transformation of the lexicographic scattering vector $\vec{k}_{4L}$ from the linear $\{\vec{e}_h, \vec{e}_v\}$ basis to any other elliptical polarisation basis $\{\vec{e}_i, \vec{e}_j\}$ characterised by a complex polarisation ratio ρ which can be written as [145]

$$\vec{k}_{4L_{IJ}} = [U_{4L}]\vec{k}_{4L_{HV}} \tag{2.117}$$

where $[U_{4L}]$ is the transformation matrix derived from the Kronecker product of the 2 × 2 matrix $[U_2]$ (see Equation (2.30)). The expression for the $[U_{4L}]$ in terms of the polarisation ratio ρ can be written as [162]

$$[U_{4L}] = [U_2] \otimes [U_2]^T = \frac{1}{1+\rho\rho^*} \begin{bmatrix} 1 & -\rho^* & -\rho^* & \rho^{*2} \\ \rho & 1 & -\rho\rho^* & -\rho^* \\ \rho & -\rho\rho^* & 1 & -\rho^* \\ \rho^2 & \rho & \rho & 1 \end{bmatrix} \tag{2.118}$$

Similar expressions can be derived for the change of basis transformations for the backscattering case and lead to the following relationships [145]

$$\vec{k}_{3L_{IJ}} = [U_{3L}]\vec{k}_{3L_{HV}} \tag{2.119}$$

where

$$[U_{3L}] = \frac{1}{1+\rho\rho^*} \begin{bmatrix} 1 & \sqrt{2}\rho & \rho^2 \\ -\sqrt{2}\rho^* & 1-\rho\rho^* & \sqrt{2}\rho \\ \rho^{*2} & -\sqrt{2}\rho^* & 1 \end{bmatrix} \tag{2.120}$$

Since $[U_2]$ has only two degrees of freedom (α and δ), both $[U_{4L}]$ and $[U_{3L}]$ also have only two degrees of freedom. However, a general n × n unitary matrix has n^2-1 degrees of freedom [145] thus the unitary matrix $[U_3]$ in Equation (2.111) contains eight degrees of freedom, six more than the two provided by the change of polarisation basis. Thus Equation (2.110) not only describes the polarimetric basis transformations, but also the linear combinations of three orthogonal coherent scattering mechanisms, which correspond to changes in the selected scattering mechanism [35]. In order to proceed with the physical interpretation of the

eigenvector decomposition, a link between unitary complex vectors and polarimetric scattering mechanisms is required. This link is formed by the Scattering Vector Reduction Theorem [187].

Consider the vectorised form of the [S] matrix for the backscattering case represented as a scattering vector $\vec{k}_{3P}$ using the Pauli basis

$$[S]=\begin{bmatrix} S_{HH} & S_{HV} \\ S_{VH} & S_{VV} \end{bmatrix} \Rightarrow \vec{k}_{3P}=\frac{1}{\sqrt{2}}\begin{bmatrix} S_{HH}+S_{VV} \\ S_{HH}-S_{VV} \\ 2S_{XY} \end{bmatrix} \tag{2.121}$$

Any three dimensional unitary complex vector has five degrees of freedom, thus it can be parameterised in terms of a set of five angles as [187]

$$\vec{k}_{3P}=\left|\vec{k}_{3P}\right|\begin{bmatrix} \cos\alpha e^{i\phi} \\ \sin\alpha\cos\beta e^{i\delta} \\ \sin\alpha\sin\beta e^{i\gamma} \end{bmatrix} \tag{2.122}$$

Often the scattering vector $\vec{k}_{3P}$ is normalised in order to obtain an associated unitary vector $\vec{e}$ defined as

$$\vec{e}=\frac{1}{\left|\vec{k}_{3P}\right|}\vec{k}_{3P}=\frac{1}{\left|\vec{k}_{3P}\right|}\begin{bmatrix} \cos\alpha e^{i\phi} \\ \sin\alpha\cos\beta e^{i\delta} \\ \sin\alpha\sin\beta e^{i\gamma} \end{bmatrix}=\frac{1}{\sqrt{2}\left|\vec{k}_{3P}\right|}\begin{bmatrix} S_{HH}+S_{VV} \\ S_{HH}-S_{VV} \\ 2S_{XY} \end{bmatrix} \tag{2.123}$$

Small changes in the angles α and β correspond to differential changes from one scattering mechanism $\vec{e}$ to $\vec{e}'$

$$\begin{aligned} \vec{e}'=[R_1]\vec{e}&=\begin{bmatrix} 1 & 0 & 0 \\ 0 & \cos\Delta\beta & -\sin\Delta\beta \\ 0 & \sin\Delta\beta & \cos\Delta\beta \end{bmatrix}\vec{e} \\ \vec{e}'=[R_2]\vec{e}&=\begin{bmatrix} \cos\Delta\alpha & -\sin\Delta\alpha & 0 \\ \sin\Delta\alpha & \cos\Delta\alpha & 0 \\ 0 & 0 & 1 \end{bmatrix}\vec{e} \end{aligned} \tag{2.124}$$

From the above expressions it is clear that the transformation matrices [R_1] and [R_2] correspond to simple plane rotations. This observation leads to the *Scattering Vector*

Reduction Theorem [187] which states that any polarimetric backscattering mechanism, represented by a complex unitary vector $\vec{e}$ obeying reciprocity, can be reduced to the identity $[1,0,0]^T$ by a series of three matrix transformations.

$$\begin{bmatrix}1\\0\\0\end{bmatrix}=\begin{bmatrix}\cos\alpha & \sin\alpha & 0\\ -\sin\alpha & \cos\alpha & 0\\ 0 & 0 & 1\end{bmatrix}\begin{bmatrix}1 & 0 & 0\\ 0 & \cos\beta & \sin\beta\\ 0 & -\sin\beta & \cos\beta\end{bmatrix}\begin{bmatrix}e^{-i\phi} & 0 & 0\\ 0 & e^{-i\delta} & 0\\ 0 & 0 & e^{-i\gamma}\end{bmatrix}\vec{e} \qquad (2.125)$$

The third matrix represents a set of scattering phase angles while the first two are mathematically canonical forms of plane rotations. Physically, only the second matrix involving the β parameters corresponds to a physical rotation of the sensor coordinates. The β parameter physically represents the orientation of the scatterer about the radar line of sight, provided that the Pauli basis is used for the vectorisation of the scattering matrix. This correspondence follows directly from the nature of the Pauli spin matrices, which relate rotations to matrix transformations as first shown in [15, 145]. This calculation is much simpler than using the polarimetric signature or Stokes reflection matrix to determine the orientation.

The α angle is not related to the orientation, although it appears in the mathematical form as a plane rotation. It represents an internal degree of freedom and can be used to describe the type of scattering mechanism. It is a continuous parameter that ranges from 0° to 90° and covers a range of different scattering mechanisms as illustrated in Figure 2-14 where isotropic implies that $|S_{HH}|=|S_{VV}|$.

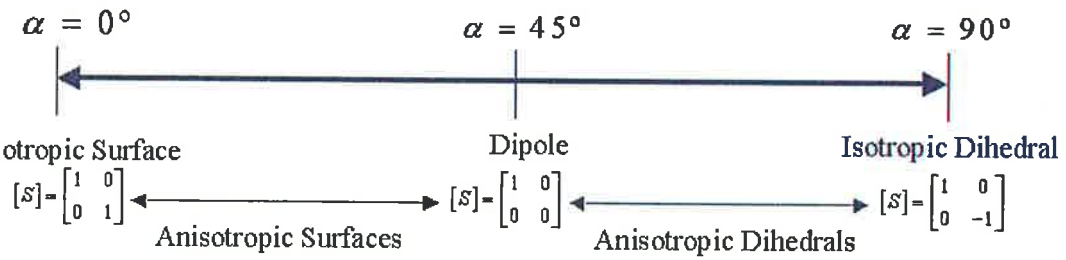

Figure 2-14 Interpretation of the α parameter

Note that α is decoupled from β so is rotation invariant. Thus we can identify the scattering mechanisms independently of their physical orientation in space. It should be noted that while the eigenvalues (and hence the entropy H) are independent of the

basis used to construct the scattering vector $\vec{k}$, the α and β angles, which are determined from the eigenvectors, are not independent of the basis choice.

2.21 Parameter estimation

The alpha parameter provides a powerful extension of the Pauli scattering decomposition as it enables scattering other than isotropic scattering mechanisms to be considered. The eigenvector decomposition of the coherency matrix $[T_3]$ produces three eigenvalues and eigenvectors and estimates of the entropy H and anisotropy A can be found by evaluating Equations (2.113) and (2.114) respectively. An alpha angle α_i can be extracted from arc cosine of the absolute value of the first element of each of the eigenvectors $\vec{e}_1$, $\vec{e}_2$ and $\vec{e}_3$ defined as

$$\alpha_1 = \arccos\left(\left|e_{1_1}\right|\right) \qquad \alpha_2 = \arccos\left(\left|e_{2_1}\right|\right) \qquad \alpha_1 = \arccos\left(\left|e_{2_1}\right|\right) \tag{2.126}$$

The β value can also be extracted from the eigenvectors and is defined as the arc tangent of the ratio of the absolute values of the second and third eigenvector elements

$$\beta_1 = \arctan\left(\frac{\left|e_{1_3}\right|}{\left|e_{1_2}\right|}\right) \qquad \beta_2 = \arctan\left(\frac{\left|e_{2_3}\right|}{\left|e_{2_2}\right|}\right) \qquad \beta_3 = \arctan\left(\frac{\left|e_{3_3}\right|}{\left|e_{3_2}\right|}\right) \tag{2.127}$$

Expressions for the scattering angles ϕ, δ, γ can also be determined in terms of the eigenvector elements defined as

$$\begin{aligned}
\phi_1 &= \arctan\left(\frac{\Im\left(e_{1_1}\right)}{\Re\left(e_{1_1}\right)}\right) \qquad \delta_1 = \arctan\left(\frac{\Im\left(e_{2_1}\right)}{\Re\left(e_{2_1}\right)}\right) \qquad \gamma_1 = \arctan\left(\frac{\Im\left(e_{3_1}\right)}{\Re\left(e_{3_1}\right)}\right) \\
\phi_2 &= \arctan\left(\frac{\Im\left(e_{1_2}\right)}{\Re\left(e_{1_2}\right)}\right) \qquad \delta_2 = \arctan\left(\frac{\Im\left(e_{2_2}\right)}{\Re\left(e_{2_2}\right)}\right) \qquad \gamma_2 = \arctan\left(\frac{\Im\left(e_{3_2}\right)}{\Re\left(e_{3_2}\right)}\right) \\
\phi_3 &= \arctan\left(\frac{\Im\left(e_{1_3}\right)}{\Re\left(e_{1_3}\right)}\right) \qquad \delta_3 = \arctan\left(\frac{\Im\left(e_{2_3}\right)}{\Re\left(e_{2_3}\right)}\right) \qquad \gamma_3 = \arctan\left(\frac{\Im\left(e_{3_3}\right)}{\Re\left(e_{3_3}\right)}\right)
\end{aligned} \tag{2.128}$$

In total there are fifteen angles that can be extracted from the three eigenvectors. The general $[U_3]$ transformation contains only eight degrees of freedom, hence the fifteen extracted angles are not independent. This complicates the interpretation of

individual α_i and β_i and instead the concept of a dominant scattering mechanism is introduced. A three symbol Bernoulli model is used which gives the best estimate, in a maximum likelihood sense, of the average scattering mechanisms $\bar{\alpha}$ and $\bar{\beta}$

$$\begin{aligned}\bar{\alpha} &= P_1\alpha_1 + P_2\alpha_2 + P_3\alpha_3 \\ \bar{\beta} &= P_1\beta_1 + P_2\beta_2 + P_3\beta_3\end{aligned} \tag{2.129}$$

P_i represents the appearance probability of each scattering mechanism as defined in Equation (2.113). Identification of the dominant scattering mechanisms enables a range of classification schemes to proceed.

2.22 Classification in the $H-\bar{\alpha}$ space

The entropy H and $\bar{\alpha}$ values form a subset of the plane that can be used for classification purposes. The averaging inherent in the definitions of $\bar{\alpha}$ and $\bar{\beta}$ requires that as the entropy values increase, the range of possible values decreases. As a result the regions within the $H-\bar{\alpha}$ space are not all equally populated. This reflects the increasing inability to distinguish between scattering mechanisms as the underlying entropy increases. The bounds of these values can be determined using symmetry arguments. Within the $H-\bar{\alpha}$ plane, the feasible range of values is bounded by two curves, defining azimuthal symmetry matrices. These bounding curves are shown in Figure 2-15. From Section 2.16.3 we know that the canonical form of the coherency matrix representing the first curve is given by

$$[T]_I = \begin{bmatrix} 1 & 0 & 0 \\ 0 & m & 0 \\ 0 & 0 & m \end{bmatrix} \quad \text{for } 0 \le m \le 1 \tag{2.130}$$

The appearance probabilities P_i for a matrix of this form are given by

$$P_1 = \frac{1}{1+2m} \quad P_2 = \frac{m}{1+2m} \quad P_3 = \frac{m}{1+2m} \tag{2.131}$$

Substituting into Equation (2.113) and (2.129) yields

$$H = \frac{-1}{1+2m}\left(\log_3\left(\frac{m^{2m}}{(1+2m)^{2m+1}}\right)\right) \qquad \bar{\alpha} = \frac{m\pi}{1+2m} \tag{2.132}$$

The coherency matrices for the second curve are defined as

$$[T]_{II}=\begin{bmatrix}0&0&0\\0&2m&0\\0&0&1\end{bmatrix}\quad \text{for } 0\le m\le 0.5 \qquad [T]_{II}=\begin{bmatrix}2m-1&0&0\\0&1&0\\0&0&1\end{bmatrix}\quad \text{for } 0.5\le m\le 1 \tag{2.133}$$

For the case of $0\le m\le 0.5$ the expressions for the entropy H and $\bar{\alpha}$ will be given by

$$H=\frac{-1}{1+2m}\log_3\left(\frac{(2m)^{2m}}{(1+2m)^{1+2m}}\right)\qquad \bar{\alpha}=\frac{\pi}{2}\quad 0\le m\le 0.5 \tag{2.134}$$

For $0.5\le m\le 1$ the corresponding entropy and $\bar{\alpha}$ values will be given by

$$H=\frac{-1}{1+2m}\log_3\left(\frac{(2m-1)^{2m-1}}{(1+2m)^{1+2m}}\right)\qquad \bar{\alpha}=\frac{\pi}{1+2m}\quad 0.5\le m\le 1 \tag{2.135}$$

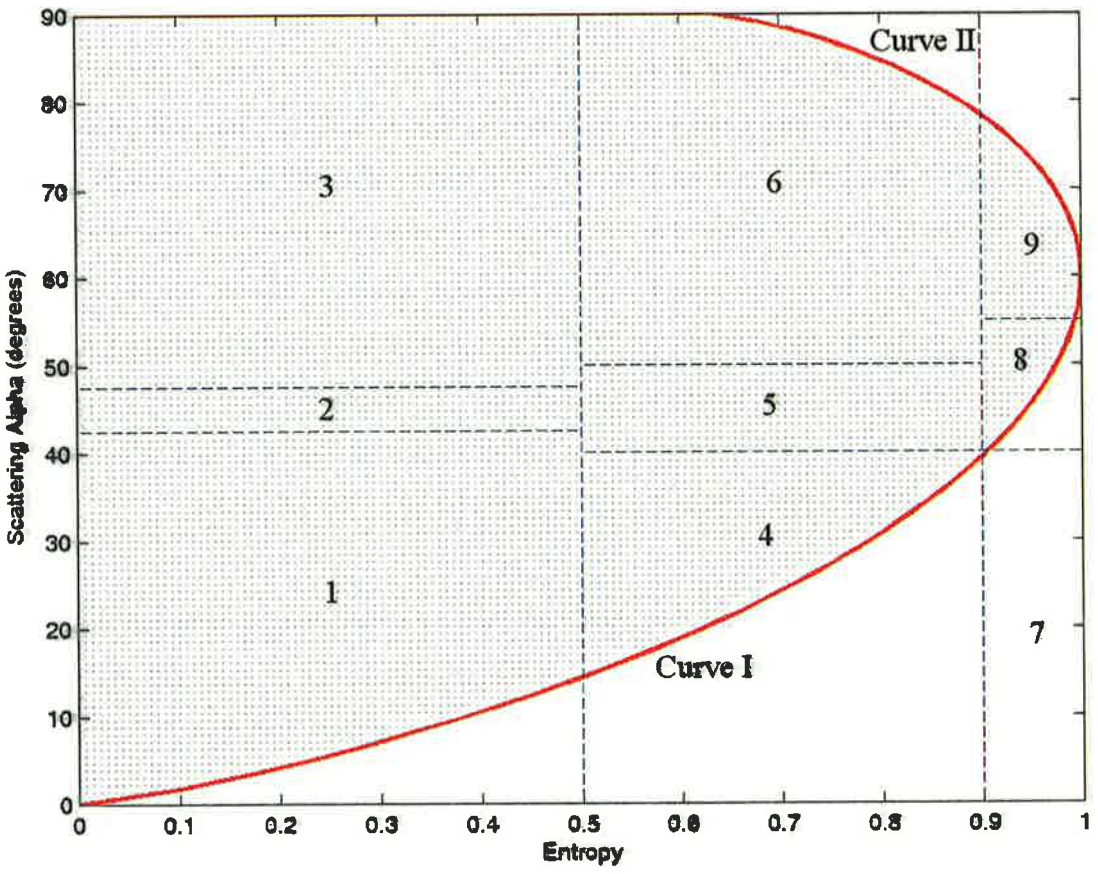

Figure 2-15 $H-\bar{\alpha}$ classification space

The $H-\bar{\alpha}$ classification space can be divided into zones that represent different scattering mechanisms. The subdivision shown in Figure 2-15, corresponds with the subdivision proposed by Cloude and Pottier [36] in their entropy-based classification scheme for land applications. There is some degree of arbitrariness as to how to subdivide the $H-\bar{\alpha}$ space. The zone boundaries are usually chosen based on the knowledge of the quality of the calibration, the noise floor level and the variance of the parameter estimates.

In the subdivision shown in Figure 2-15, region 1 corresponds to the low entropy surface scatter region with $\bar{\alpha}$ values of less that 42.5°. The region incorporates Bragg surface scattering and geometrical and physical optical surface scattering along with specular scattering that does not involve a 180° phase inversion between the HH and VV components. Scattering from calm seas, spheres and flat plates all fall into this category. Region 2 represents low entropy dipole scattering. This corresponds to scattering situations with strongly correlated mechanisms that have a large imbalance between the HH and VV components in amplitude. An isolated dipole or a Bragg surface viewed at low grazing angles are both scatterers that would appear in this region. The width of this zone is determined by the quality of the calibration as it relates to the radar's ability to measure HH/VV ratio. Region 3 corresponds to low entropy multiple (even) bounce scattering such as scattering from metallic dihedrals. The upper entropy bound chosen for the first three zones is chosen as the basis of tolerance to perturbations of first order scattering theories. Such theories generally predict zero entropy for all scattering processes. By estimating the level of entropy change due to second order and higher events, tolerance can be built into the classifier so that the important first order processes can still be correctly identified.

Regions 4, 5 and 6 correspond to medium entropy scattering situations with the dominant scattering mechanism being surface, dipole and multiple scattering respectively. These zones represent situations with higher entropy values due to increased surface roughness or due to the physics of secondary wave propagation and scattering mechanisms. The upper bound for these cases is set at an entropy of H = 0.9. For higher entropy values one cannot distinguish surface scattering as a direct consequence of our decreasing ability to classify scattering types with increasing

entropy. To reinforce this fact, Cloude and Pottier included region 7, representing high entropy surface scatter, which does not lie within the feasible region defined in the $H-\bar{\alpha}$ space, to highlight the fact that radar polarimetry will be most successfully applied in low entropy problems.

Regions 8 and 9 represent high entropy scattering scenarios. For H > 0.9 it may still be possible to distinguish double bounce mechanisms such as from a cloud of anisotropic needle-like particles. In the extreme case in region 8 where the entropy goes to one, we have random noise with no polarisation dependence.

An example plot showing the distribution of values in the $H-\bar{\alpha}$ space for a measurement of a pilot boat wake is shown in Figure 2-16.

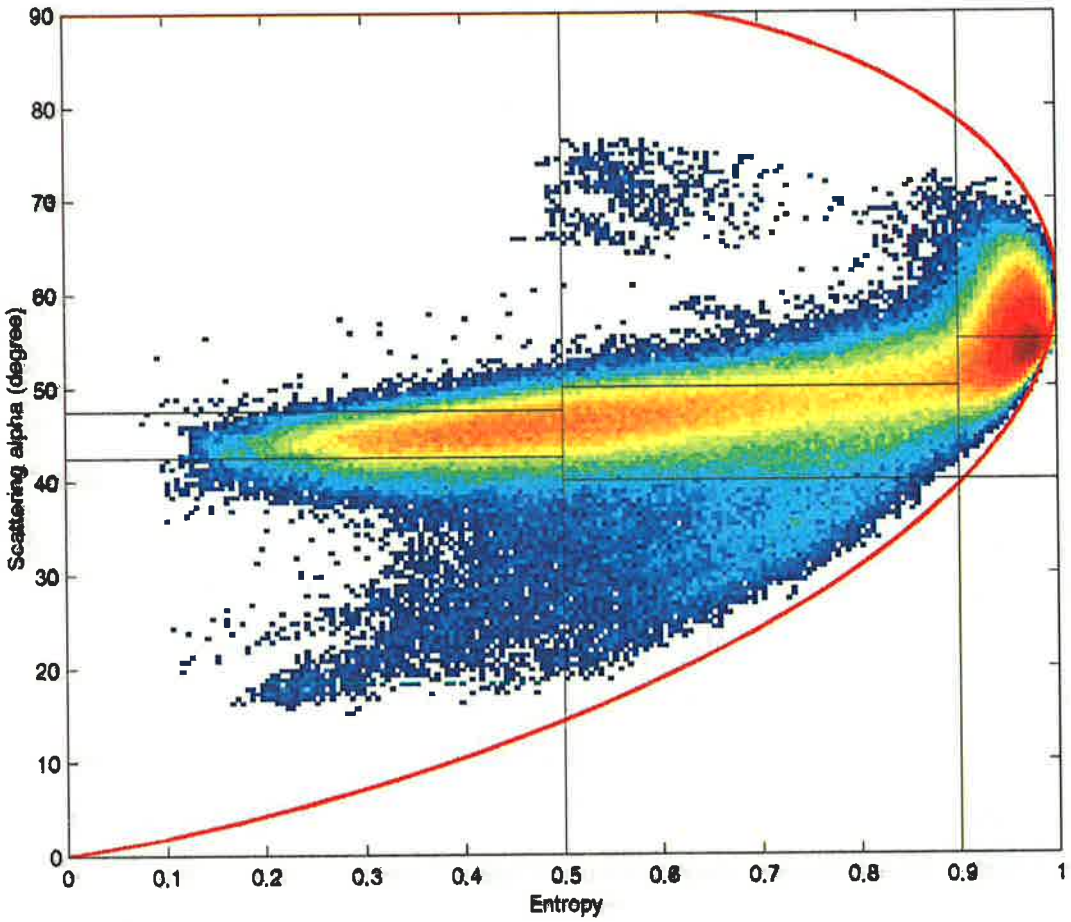

Figure 2-16 Distribution of values in the $H-\bar{\alpha}$ space for a pilot boat wake

2.23 Classification in the H - A - $\bar{\alpha}$ space

By including the anisotropy information, it is possible to extend and improve the classification schemes. For example, consider the case where the entropy H is equal to 0.9. The two limits bounded by the curves shown in Figure 2-15 have associated eigenvalue spectra given by $\lambda_1 = 1$, $\lambda_2 = 0.4$, $\lambda_3 = 0.4$ and $\lambda_1 = 1$, $\lambda_2 = 1$, $\lambda_3 = 0.3$ and anisotropy values of 0 and 0.54 respectively. Incorporating the anisotropy information provides a means of distinguishing between these two different scattering processes. This approach has been used by Pottier and Lee [39] to develop an unsupervised combined Wishart classifier for polarimetric SAR data. They proposed the use of a feature vector $\vec{I}$ defined as

$$\vec{I} = \begin{bmatrix} \alpha \\ [H][A] \\ [H][1-A] \\ [1-H][A] \\ [1-H][1-A] \end{bmatrix} \tag{2.136}$$

In this technique combinations of the $[H]$, $[1-H]$, $[A]$ and $[1-A]$ matrices are formed using element by element multiplication. Using the results shown in Figure 2-8 and Figure 2-10, a colour coded plot of $[H][A]$ within the region defined in Figure 2-7 can be produced and is shown in Figure 2-17. The values range from 0 to 0.6521 with high values indicating the presence of two scattering mechanisms with the same probability (high entropy and high anisotropy with $\lambda_3 \approx 0$). The maximum of the $[H][A]$ product was found numerically by evaluating the function on a very fine grid. The maximum value was found to occur at (P_1, P_2, P_3) = (0.490, 0.490, 0.019) which lies on the boundary line (Line 3) defined in Equation (2.116). Generally the matrix products are displayed on a colour scale that ranges from zero to one, thus it would seem appropriate to scale the $[H][A]$ product by 1.53. The unscaled version of the $[H][A]$ product is also shown in Figure 2-17. The colour coded plot of the $[H][1-A]$ product was also produced and is shown in Figure 2-18.

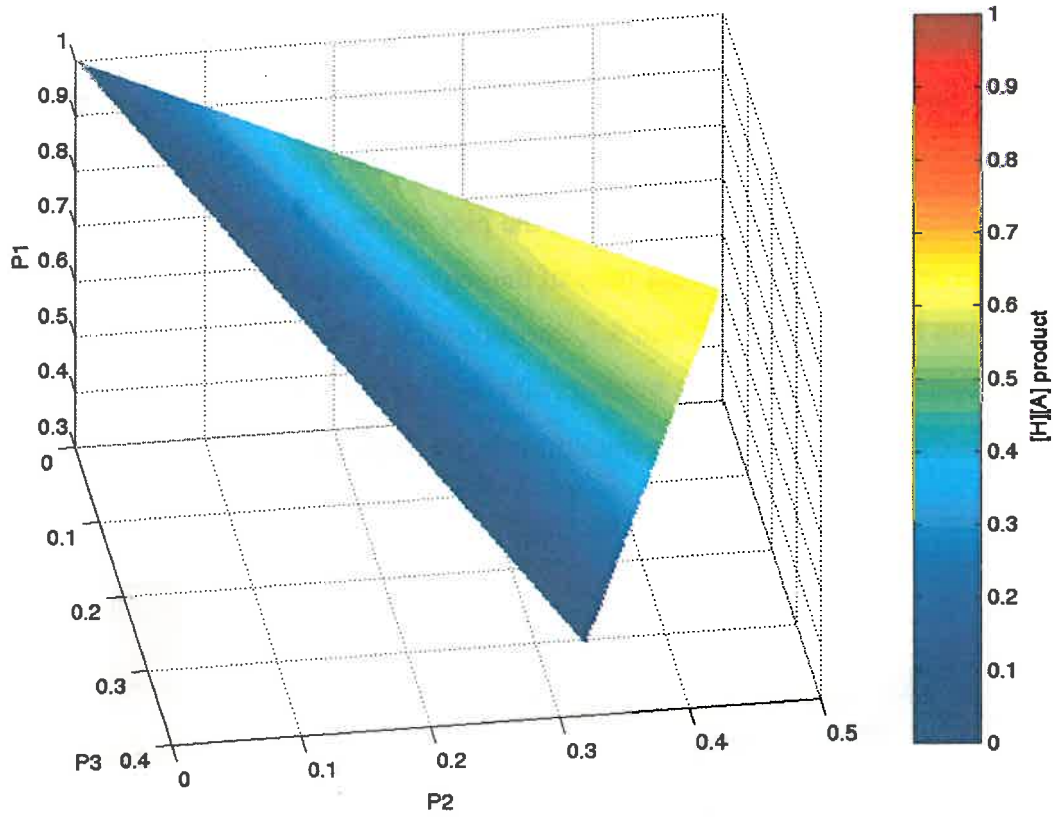

Figure 2-17 [*H*][*A*] product values within the feasible region of appearance probabilities

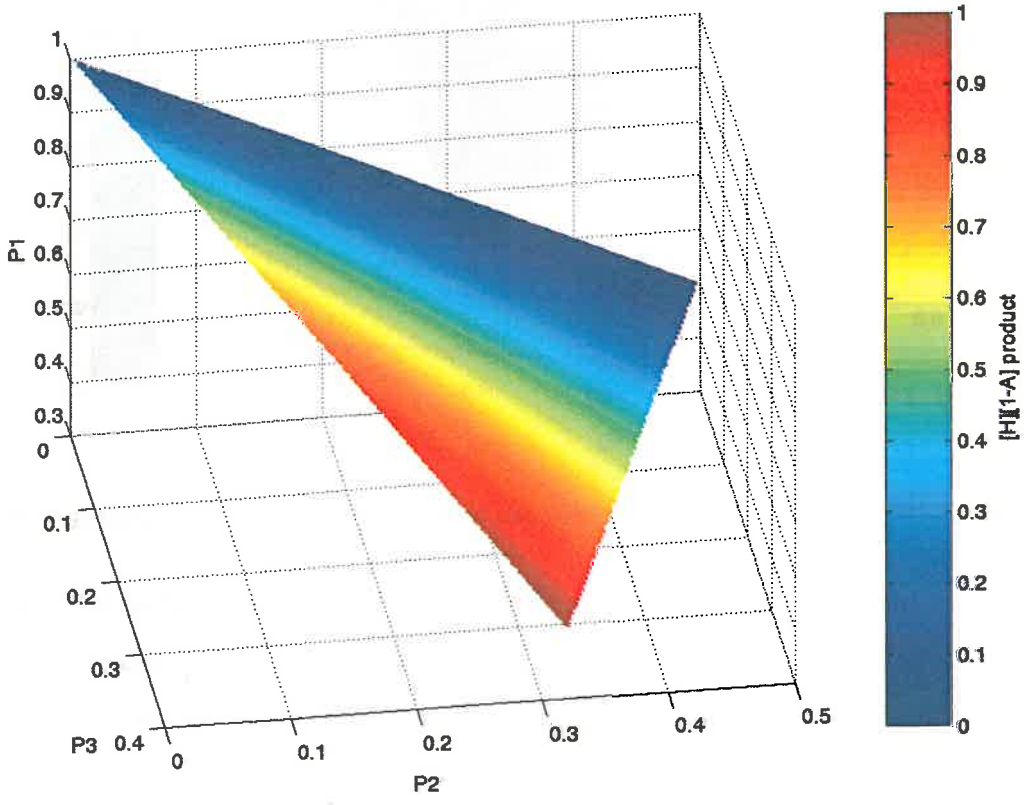

Figure 2-18 [*H*][1−*A*] product values within the feasible region of appearance probabilities

The values of the $[H][1-A]$ matrix product range from zero to one with high values indicating the presence of random scattering processes (high entropy and low anisotropy with $\lambda_1 \approx \lambda_2 \approx \lambda_3$). The $[1-H][A]$ image was also evaluated in the feasible region defined in Figure 2-7 and produces the plot shown in Figure 2-19. The values range from zero to one with the majority of the region having low values. Only a very small region has values higher than 0.7, corresponding to the situation in which there are two scattering mechanisms present with a dominant process (low to medium entropy) and a second one with medium probability (high anisotropy with $\lambda_3 \approx 0$).

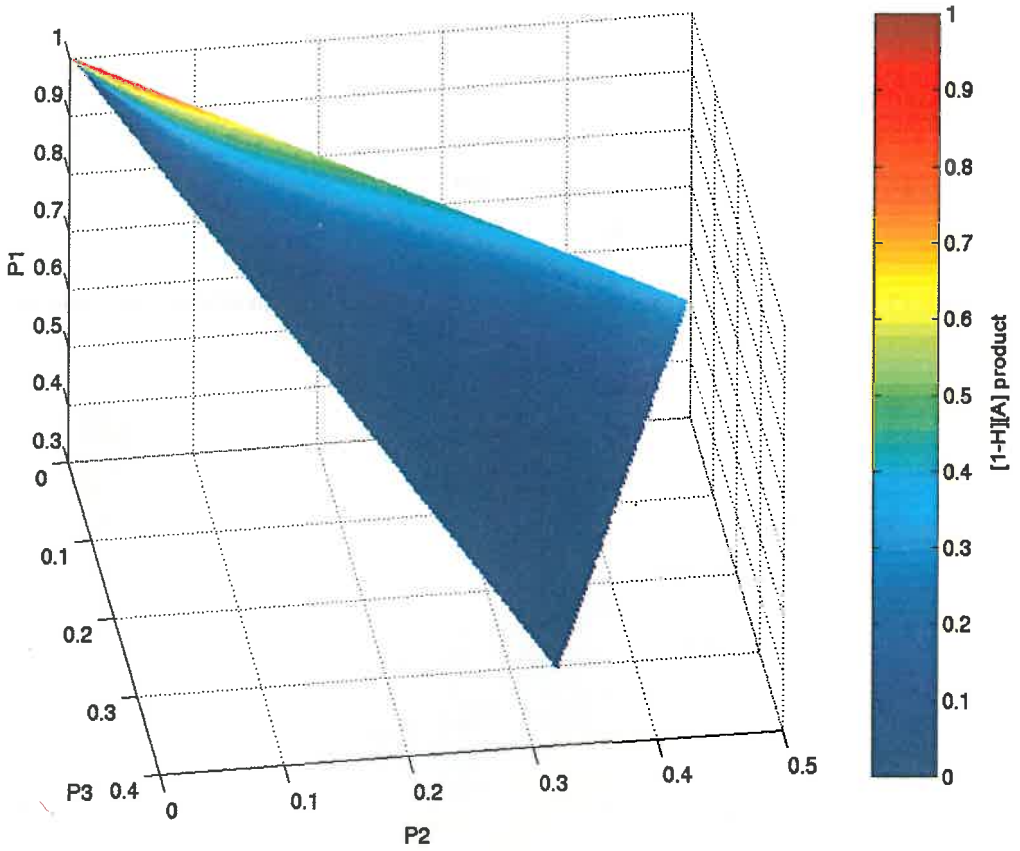

Figure 2-19 $[1-H][A]$ product values within the feasible region of appearance probabilities

The plot of the final product, $[1-H][1-A]$ in the feasible region of values is shown in Figure 2-20. The values range from zero to one and once again there is only a small region of values for which the $[1-H][1-A]$ product is greater than 0.7. In this case the high values indicate the presence of a single dominant scattering process (low entropy and low anisotropy with $\lambda_2 \approx \lambda_3 \approx 0$).

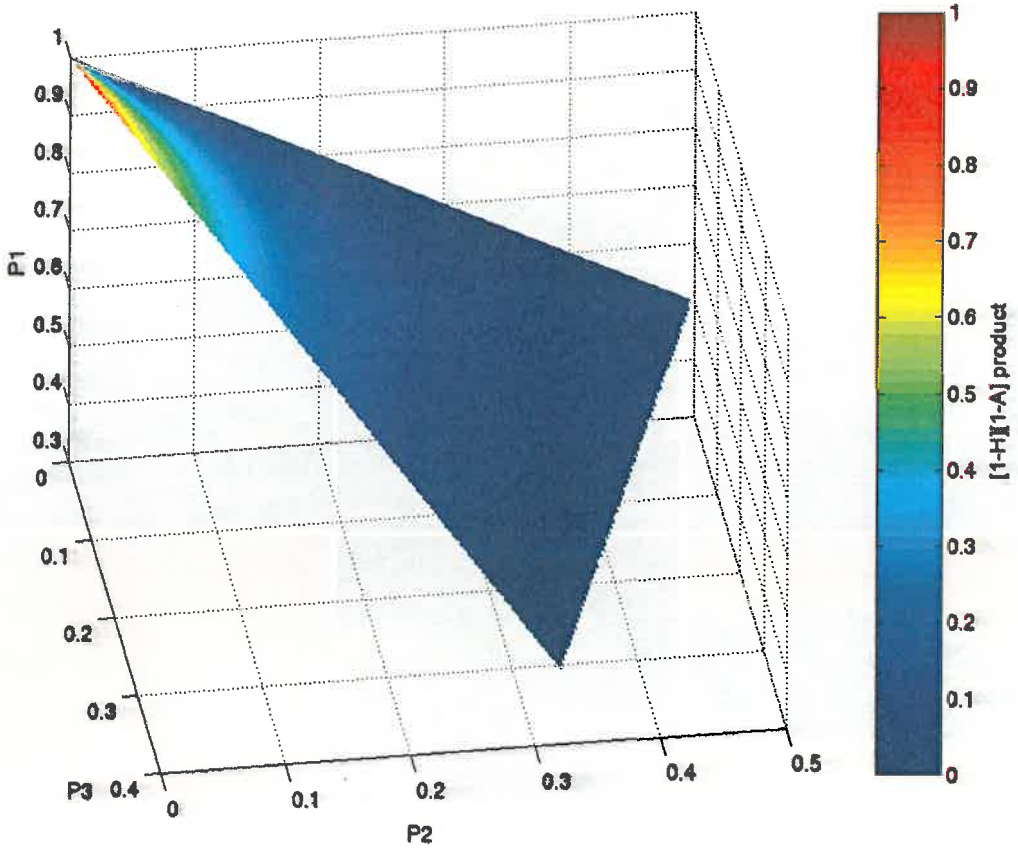

Figure 2-20 [1–*H*][1–*A*] product values within the feasible region of appearance probabilities

Figure 2-21 illustrates the result of performing the matrix products between the entropy and anisotropy images obtained from a polarimetric measurement of a ship wake produced by a pilot boat. Very little additional information can be gained from the [*H*][*A*] image suggesting that there are very few situations in which there are two dominant scattering processes with similar probability values. The scaled version of the [*H*][*A*] product is shown in Figure 2-21 and ensures that all of the images have the same dynamic range. The [*H*][1–*A*] image highlights the clutter regions while the [1–*H*][1–*A*] image demonstrates that the majority of the scattering in the wake region results from the presence of a single dominant scattering process. The most interesting image appears to be the image formed between [1–*H*][*A*]. This highlights regions in which there are two scattering mechanisms present with the secondary process having a medium probability. There are a number of regions on the diverging wake arms that are highlighted in the [1–*H*][*A*] image which are not immediately apparent in the individual [*H*] and [*A*] images. In Chapter 6 it is shown that these regions indicate the presence of wave breaking events.

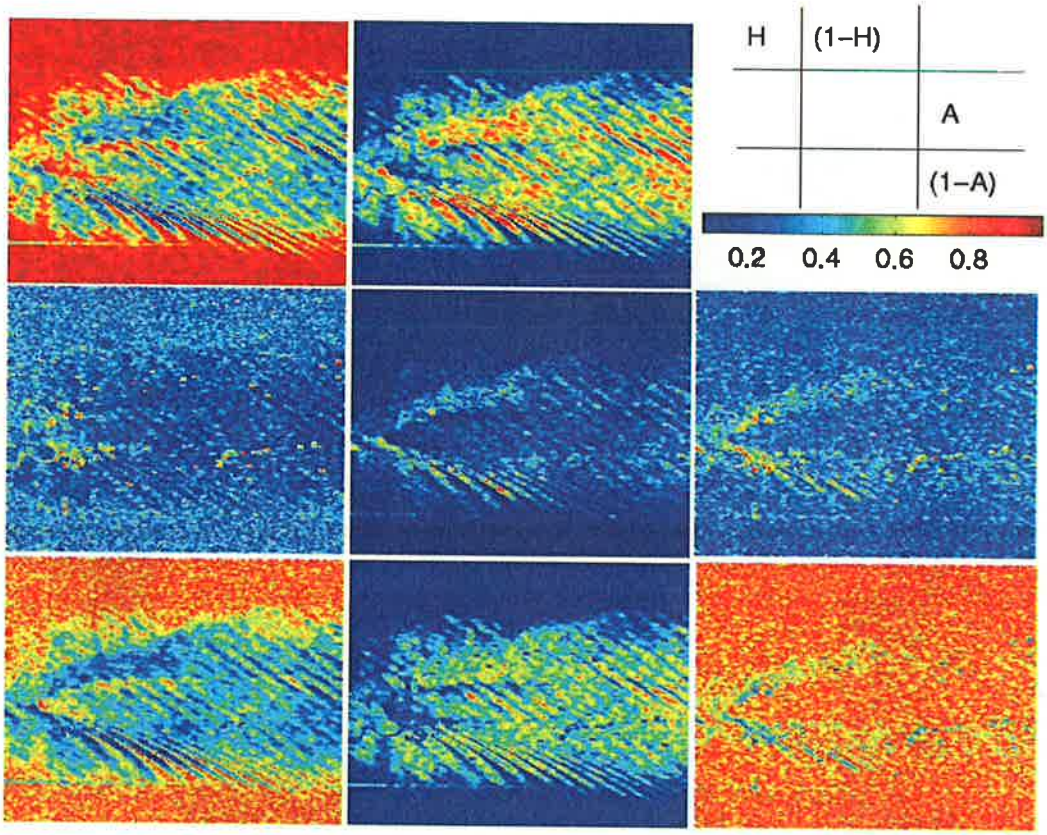

Figure 2-21 Combinations between the entropy [H] and anisotropy [A] images

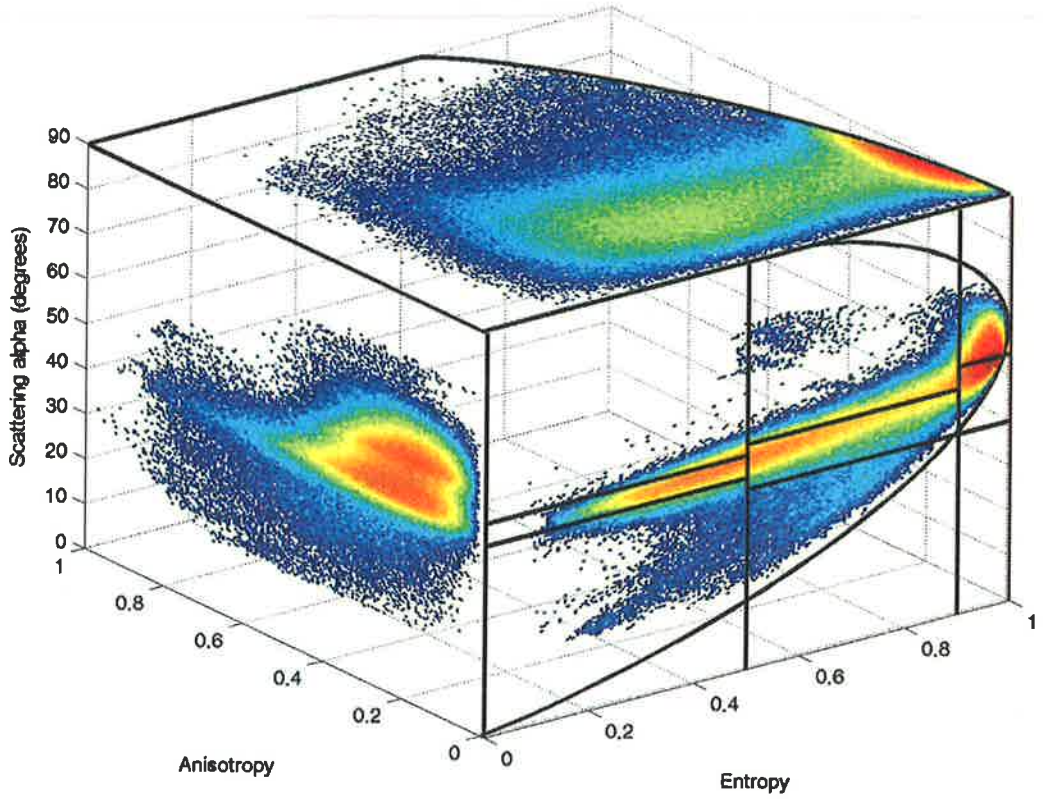

Figure 2-22 The distribution of values in the three-dimensional $H-A-\overline{\alpha}$ classification space

It is also possible to create an extended and complemented three-dimensional $H-A-\bar{\alpha}$ classification space as shown in Figure 2-22. This representation was used by Pottier [39] to illustrate that it is possible to discriminate new classes using the anisotropy value and highlights the importance of the anisotropy parameter in the analysis and inversion of polarimetric data. Additional examples using the $H-\bar{\alpha}$ and $H-A-\bar{\alpha}$ space techniques are presented in Chapter 6.

2.24 Synopsis

In this chapter the polarimetric concepts and theory of scattering from point and distributed targets have been illustrated using both the real space description based on the Stokes vector and the complex space formalism based on the Jones vector. The description of the polarimetric properties of scatterers using the Mueller matrix derived from the Stokes representation has been presented in conjunction with the equivalent description based on the Jones vector, which results in the covariance or coherency matrix. These concepts are the basis of all polarimetric analysis and are essential for the understanding of the work presented in the following chapters.

The representation of the polarisation state using the real space description based on the orientation and tilt angles and the complex space formalism based on the complex polarisation ratio has been discussed. The importance of the change of polarisation basis using the unitary transformation matrix $[U_2]$ has been highlighted. The relationships between this transformation and its role in the change of basis of the scattering matrix, scattering vector and the coherency matrix has been demonstrated for the general bistatic and backscattering cases.

The concept of optimal polarisation states and their geometrical relationships on the Poincaré sphere has been discussed along with the methods developed for calculating the locations of these states. These results are used in the following chapter in the analysis of the polarimetric properties of common calibration targets.

The concept of distributed scatterers has been introduced along with a discussion of the symmetry properties that are commonly assumed in target models. Reflection symmetry is used in Chapter 5 to simplify the description of the scattering from the

sea surface, while the role of azimuthal symmetry in clutter calibration techniques is discussed in Chapter 3.

A review of the commonly used target decomposition theorems, which are particularly useful for identifying the dominant scattering mechanisms, has been presented. Classification techniques in the $H-\bar{\alpha}$ and $H-A-\bar{\alpha}$ spaces have been described in detail; these techniques are used extensively in Chapters 3 and 6.

While it is impossible to cover every topic relevant to radar polarimetry, the main concepts and theory relevant to the work covered in the following chapters have been presented. There are numerous other excellent descriptions of various aspects of the theory of radar polarimetry that complement and extend the work covered here. In particular the works by Huynen [13], Boerner [42, 143, 189], Cloude [15, 35, 36, 145], Pottier [190], Mott [117], Papathanassiou [59], Hajnsek [142], Krogager [191] and Yang [192] provide authoritative accounts of both theoretical and practical concepts.

Chapter 3 Calibration

3.1 Introduction

Calibration and error correction of radar data is essential for reliable interpretations of radar measurements. Over the past twenty years there have been several different schemes proposed for the calibration of polarimetric radars. For conventional radar systems, standard calibration techniques [193] exist for obtaining calibrated power measurements. The evolution of polarimetric systems has complicated the problem of system calibration and new methods are needed to ensure that accurate phase information is obtained. Calibration of the phase terms is a critical stage in such measurements as it determines the validity of the polarimetric parameters derived. This chapter describes the evolution of polarimetric calibration techniques using a matrix representation of the system distortions and the vectorised form of the $[S]$ matrix. It begins by describing a number of common calibration targets and their polarimetric properties. Next, a review of the commonly used calibration techniques is presented, noting their deficiencies in the context of practical application for calibration in the field, as opposed to the laboratory. Several of these calibration methods were tested, using specially constructed scatterers, so that an independent judgement of their suitability could be made. Drawing on the experience gained from these experiments, a new hybrid technique was proposed, together with a least-squares data processing algorithms that estimates averaged calibration parameters from properly symmetrised quad-pol single-look complex data measurements. This calibration procedure was validated on reference scatterers and is now used routinely with the DSTO radar.

3.2 Calibration targets

Before discussing calibration techniques, a review of the commonly used calibration targets will be presented. The choice of calibration targets is strongly influenced by the measurement environment. In a laboratory the emphasis is placed on the accuracy of the theoretical scattering matrices of the calibration targets. The sensitivity to positioning is a secondary concern, as there is the fine control over the target orientation and placement. For field measurements, target alignment is difficult to control and targets that are insensitive to positioning errors are generally used. The

errors in the theoretical scattering matrices for these targets are usually determined from laboratory measurements using a set of very accurate calibration targets. The following section discusses the properties of the commonly used calibration targets and highlights their suitability for field and laboratory measurements.

3.2.1 Metallic sphere

A commonly used calibration target is the metallic sphere. Its physical symmetry yields scattering matrix elements that are insensitive to orientation, thus eliminating alignment and orientation errors. Spheres are the only three-dimensional structures for which an exact theoretical scattering matrix is known. In principle the scattering matrix elements can be computed exactly using the Mie scattering expressions and many computational algorithms [166, 193, 194] have been published for evaluating these expressions efficiently for spheres with arbitrary size and constitutive parameters. Metallic spheres can be produced with very high precision ($\Delta R < 5\mu m$) over a wide range of diameters [195] and gold plated spheres are often used in precision calibrations in order to obtain more repeatable results.

Spheres do have some intrinsic limitations. They can only be used to calibrate the co-polar channels, as the cross-polar responses for linear polarisations are zero. They also have small radar cross sections and large spheres are required for field calibrations in order that the return is sufficiently larger than the background noise. Examples of calibration spheres are shown in Figure 3-1.

Figure 3-1 Calibration spheres

The polarimetric properties of a sphere are shown in Figure 3-2. This illustrates the general form of the [S] matrix, the polarisation signatures and phase-correlation plots for the co- and cross-polar channels and the location of the characteristic polarisation states on the Poincaré sphere. The sphere represents a special degenerate case for the solution of the characteristic polarisation states since multiple solutions for cross-polar nulls exist. These states lie on a circle defined in the plane orthogonal to the characteristic plane shown in Figure 3-2 (d). The equation of this plane is derived by Yang *et al.* in [155]. The co-polar nulls and cross-polar maxima pairs (C_1,S_1) and (C_2,S_2) coincide and lie on the normal to the plane containing the cross-polar null circle.

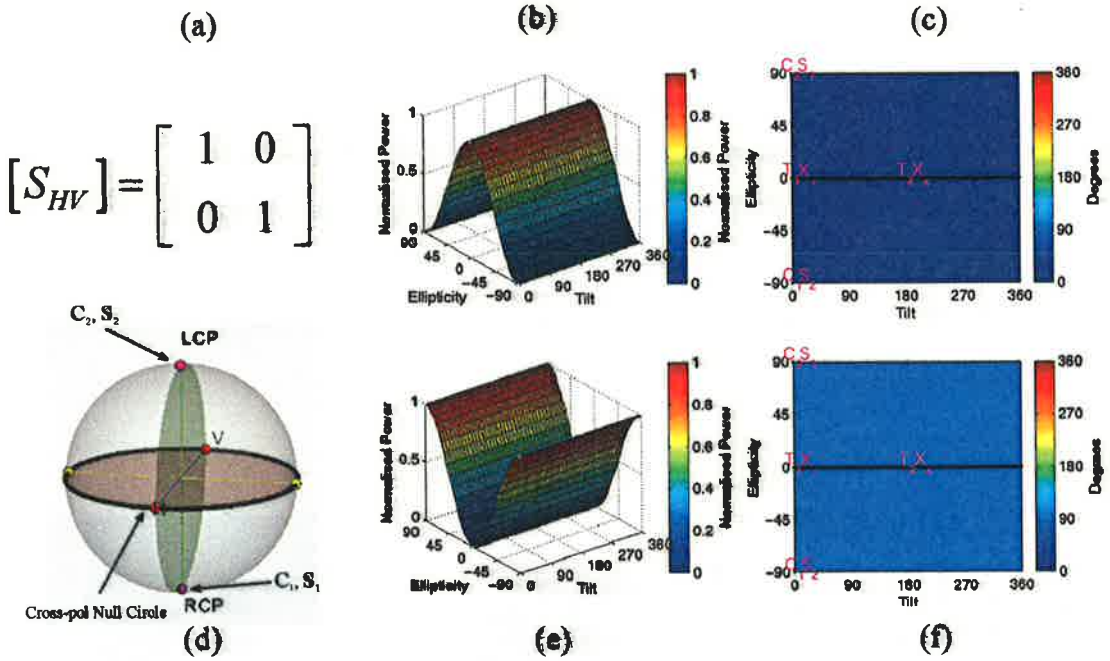

Figure 3-2 Summary of the polarimetric properties of sphere targets

(a) S matrix (b) Co-pol power spectrum (c) Co-pol relative phase-correlation plot
(d) Polarisation fork (e) Cross-pol power spectrum (f) Cross-pol relative phase-correlation plot

3.2.2 Trihedral corner reflector

Trihedral corner reflectors are often used in polarimetric calibrations and can be designed to provide a large radar cross section over a wide range of aspect angles. They are relatively inexpensive to manufacture and have a wide beamwidth (typically ~30°) in both azimuth and elevation dimensions and can be used to calibrate across frequencies. They are often used to calibrate airborne and spaceborne synthetic aperture radars; Figure 3-3 shows examples of triangular trihedral corner reflectors.

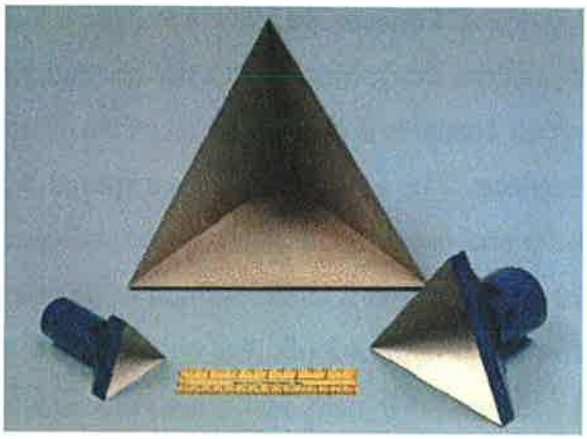

Figure 3-3 Triangular trihedral corner reflectors

On axis, the reflected fields undergo three reflections each introducing a 180° phase shift and expressions of the peak RCS values and scattering matrices are given in [193]. A conventional trihedral corner reflector returns linearly polarised incident waves without modification but reverses the sense of elliptically or circularly polarised waves. The scattering matrices of these targets illuminated along boresight are identical to that of a large sphere except for a multiplicative constant. As a result, they are insensitive to LOS rotations. The polarimetric properties of the trihedral are summarised in Figure 3-3.

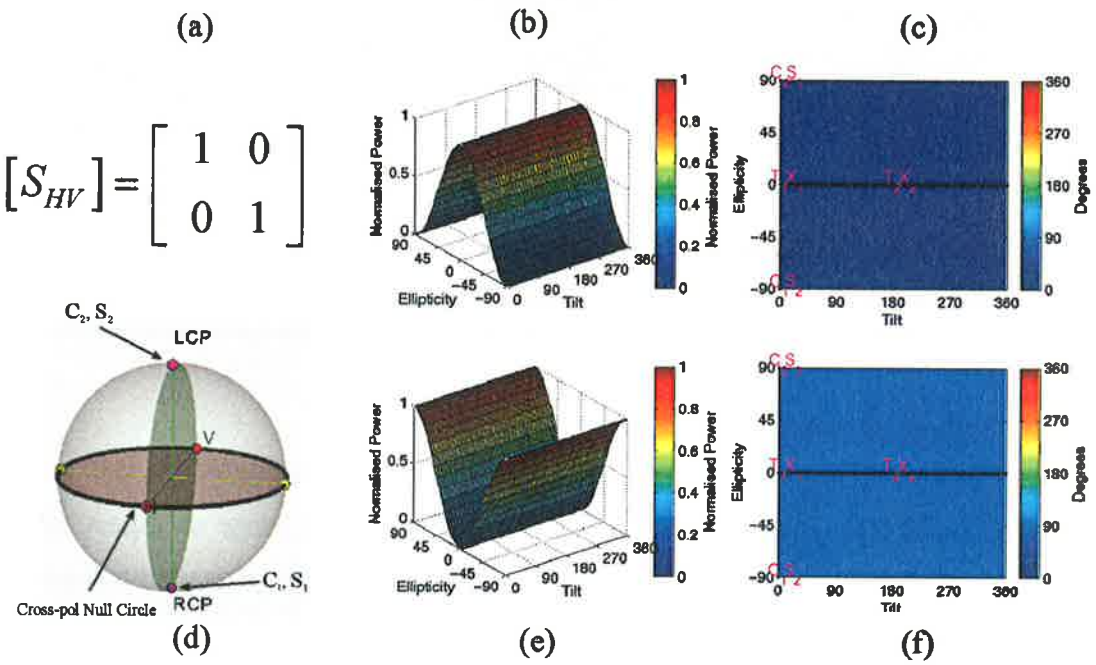

Figure 3-4 Summary of the polarimetric properties of a trihedral

(a) S matrix (b) Co-pol power spectrum (c) Co-pol relative phase-correlation plot
(d) Polarisation fork (e) Cross-pol power spectrum (f) Cross-pol relative phase-correlation plot

Although trihedrals are commonly used to calibrate polarimetric radar systems, their usefulness is limited by their inability to generate a strongly cross-polarised return. A variety of patents have been issued to designs that yield the desired cross-polarised response using wire grids and dielectric materials, but such reflectors are expensive to manufacture and are susceptible to mechanical and environmental damage. Michelson *et al.* [196] developed a depolarising reflector that overcomes many of these limitations by combining a conventional corner reflector with a reflection polariser formed from a corrugated or finned metal surface. The reflection polariser is mounted on one panel of the trihedral such that the axis of the fins is aligned parallel to one of the principal axes of the trihedral. Thus the axes of the original fins and those in the images that are projected onto each of the other two faces of the trihedral are oriented identically for all angles of incidence. This yields a target that provides both the large radar cross section and wide angular response of a trihedral corner reflector and the unique polarisation response of a twist reflector in a compact structure.

3.2.3 Dihedral corner reflector

A dihedral corner reflector is a passive reflector that consists of two, usually rectangular, flat metallic plates that are joined at right angles along an edge. Example dihedrals are shown in Figure 3-5.

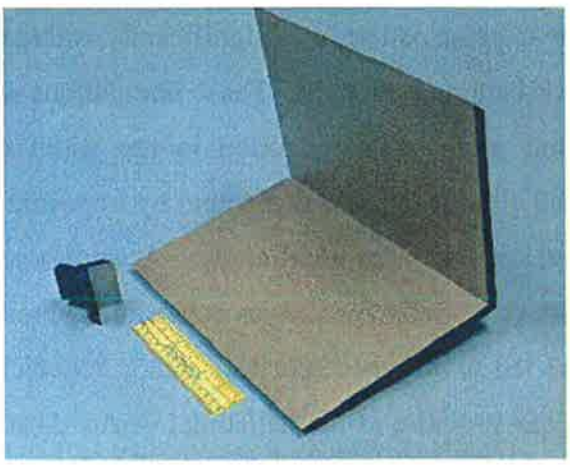

Figure 3-5 Dihedral corner reflectors

In polarimetric measurements the dihedral plays an important role due to its high RCS and double bounce scattering mechanism. On axis, the reflected fields undergo two reflections each introducing a 180° phase shift as illustrated in Figure 3-6.

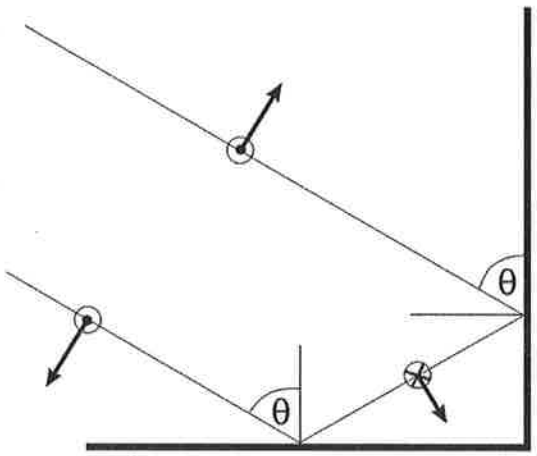

Figure 3-6 Reflection of two orthogonal components from a dihedral

Dihedrals are extremely sensitive to the orientation of the target relative to the polarisation coordinate system [197]; in addition, effects such as edge scattering can lead to significant errors between the calculated and measured values of the scattering amplitudes. The orientation problems can be reduced to an acceptable level when operating in an anechoic chamber under controlled laboratory conditions but pose difficulties in field calibrations. Modification of the dihedral vertex can be used to reduce the sensitivity to orientation. In a study by Souyris *et al.* [198] the co-polar and cross-polar backscattering characteristics for a number of shaped dihedrals were studied. The cross-polar backscattering diagram for the regular dihedral was shown to be very narrow due to the rectilinear vertex. By changing the rectilinear vertex to a circular vertex, the cross-polar pattern was significantly enlarged but exhibited large undulations in the backscattering diagram. These undulations were reduced by using an elliptical vertex but produced a reduction in the width of the backscattering diagram. An optimised elliptical vertex was found by imposing a low oscillation rate and low co-polar level over a given solid angle. A similar procedure was used to design a calibrator with cross-polar features as constant as possible over a given solid angle. This procedure led to a shaped dihedral with a helicoidal vertex. Unlike the elliptical vertex case, the structure of the helicoidal vertex dihedral produces a cross-polar response with both a reduced undulation rate and wide cross-polar backscattering characteristics. The principal disadvantage of all shaped dihedrals is that physically large structures are required in order to provide adequate returns, while shaping the vertex substantially increases the manufacturing costs.

The polarimetric properties of a dihedral including the general form of the [S] matrix for normal incident waves, the polarisation fork, the co-polar and cross-polar polarisation signatures and phase correlation plots are illustrated in Figure 3-7. The dihedral is another example of a special case in the solution of the characteristic polarisation states. In this case there are multiple solutions for the cross-polar nulls, which define a circle on the Poincaré sphere. Detailed analysis is presented in [155] including a derivation of the expression for the equation of the circle. Once again the co-polar nulls and cross-polar maxima pairs (C_1,S_1) and (C_2,S_2) coincide and lie on the normal to the plane containing the cross-polar null circle.

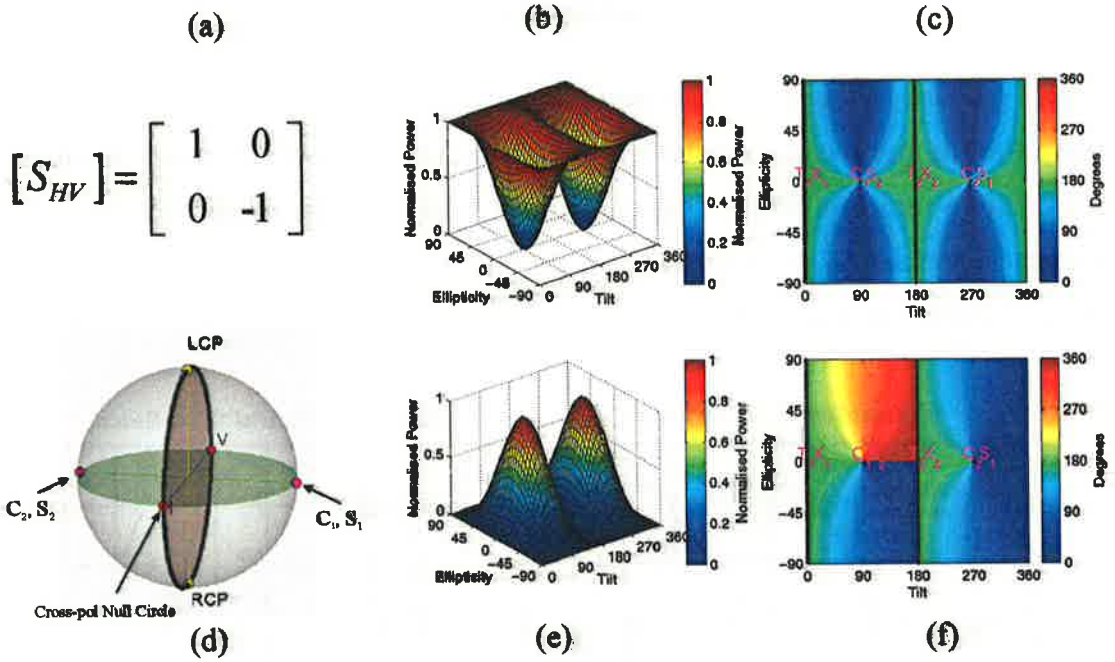

Figure 3-7 Summary of the polarimetric properties of dihedrals

(a) S matrix (b) Co-pol power spectrum (c) Co-pol relative phase-correlation plot
(d) Polarisation fork (e) Cross-pol power spectrum (f) Cross-pol relative phase-correlation plot

3.2.4 Bruderhedral

The bruderhedral is a passive radar target with unique scattering characteristics and is ideally suited for use with polarimetric radar systems. The bruderhedral is an even bounce reflector formed from a dihedral in which one face is a flat plate and the other is a section of a cylinder. It produces strongly co-polarised returns but can be oriented to calibrate both co-polar and cross-polar radar receiver channels. An example bruderhedral is shown below in Figure 3-8.

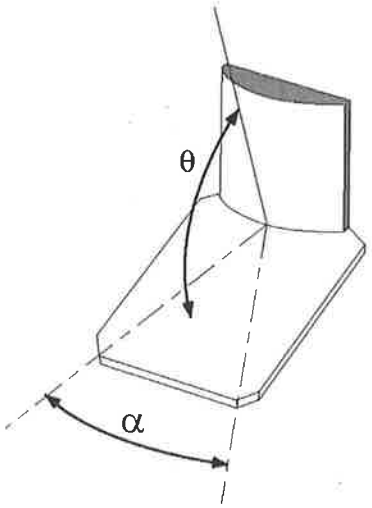

Figure 3-8 Bruderhedral

It has a relatively large radar cross section and exhibits a much wider lobe in the plane parallel to the seam than a standard dihedral reflector. The net effect is to produce a dihedral-like response, while decreasing the directivity in the plane along the seam without significantly affecting its other properties. The performance of a typical bruderhedral is illustrated below in Figure 3-9.

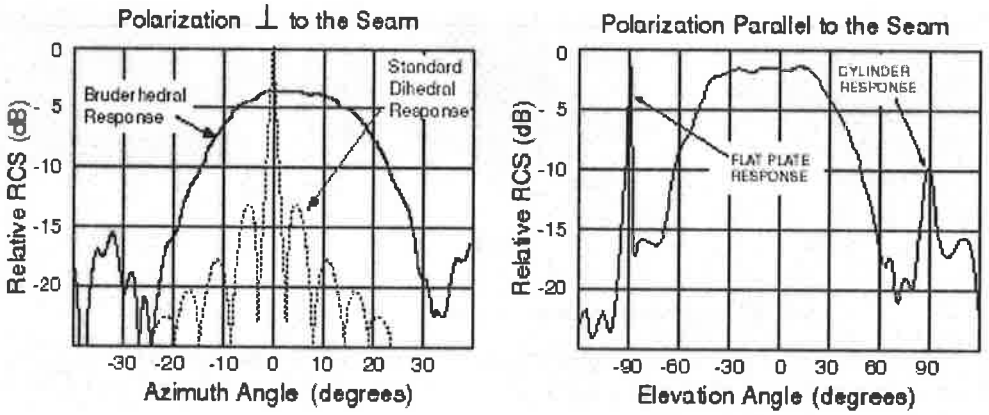

Figure 3-9 Comparison of bruderhedral and dihedral responses [199]

3.2.5 Finite length cylinders

An exact theoretical solution of the scattering from a finite length conducting cylinder does not exist but the solution based on the assumption that the current along the axis of the cylinder is constant provides accurate results in the specular direction if the length of the cylinder is much larger than the wavelength. The effect of edge scattering from the ends of the cylinder can be minimised by ensuring that the diameter of the cylinder is much smaller than the wavelength. Numerical solutions to

the problem of scattering from metallic and dielectric cylinders are presented in [193]. In general the complex dielectric constant is not known accurately and metallic cylinders are preferred. They have low RCS values and like dihedrals are extremely sensitive to the orientation of the target relative to the polarisation coordinate system. Consequently they are not suitable targets for use in field calibrations

3.2.6 Dipoles

Dipoles have a strong polarising effect, which acts on and re-radiates the electric field components parallel to their orientation. Linearly polarised waves are always returned, regardless of the incident polarisation. In calibration measurements, dipoles are generally not implemented with wires due to their low RCS value and instead the dipole return is obtained using screened trihedrals [200], either screened across the front face or screened along one sides. The scattering characteristics are extremely dependent on the target orientation relative to the polarisation coordinate system. First we consider the case of the horizontal dipole. A summary of the polarimetric properties is shown in Figure 3-10 and illustrates that there are multiple solutions for the location of the cross-polar maxima and that the co-polar nulls C_1 and C_2 and one of the cross-polar nulls X_1 coincide and lie on the normal to the plane containing the cross-polar max circle.

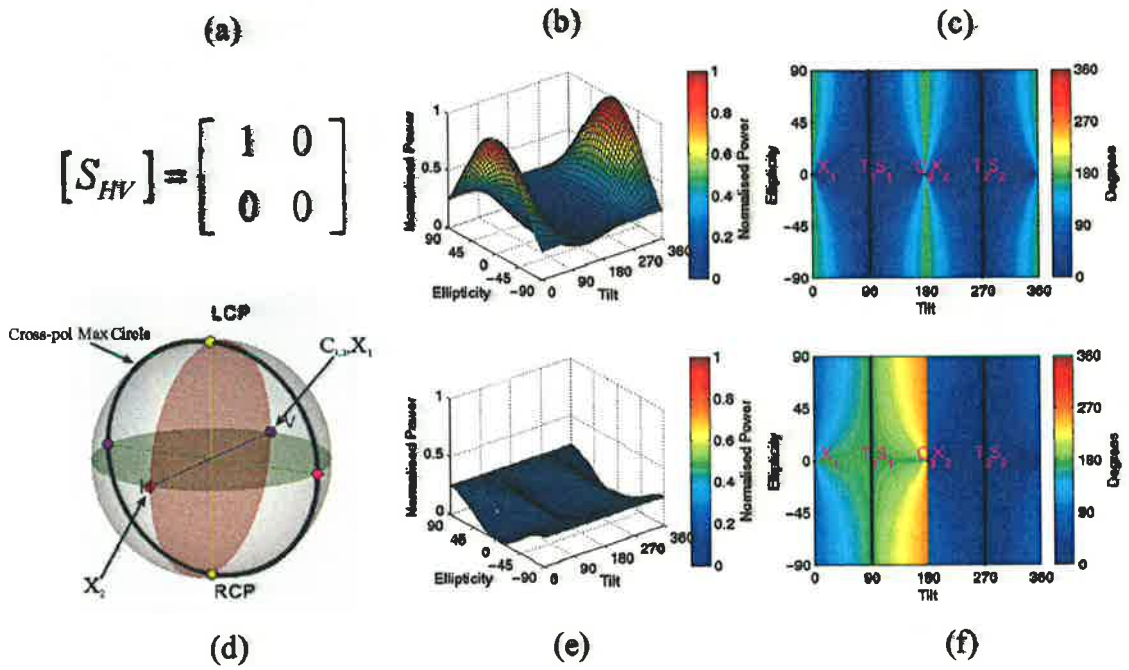

Figure 3-10 Summary of the polarimetric properties of a horizontal dipole

(a) S matrix (b) Co-pol power spectrum (c) Co-pol relative phase-correlation plot
(d) Polarisation fork (e) Cross-pol power spectrum (f) Cross-pol relative phase-correlation plot

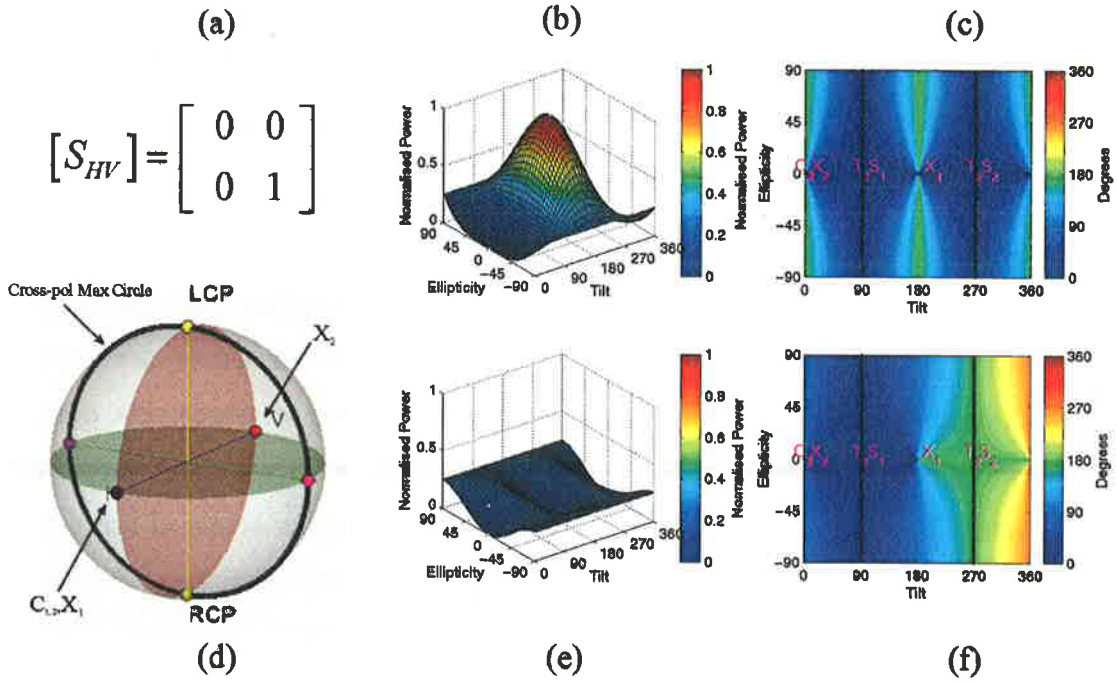

Figure 3-11 Summary of the polarimetric properties of a vertical dipole

(a) S matrix (b) Co-pol power spectrum (c) Co-pol relative phase-correlation plot
(d) Polarisation fork (e) Cross-pol power spectrum (f) Cross-pol relative phase-correlation plot

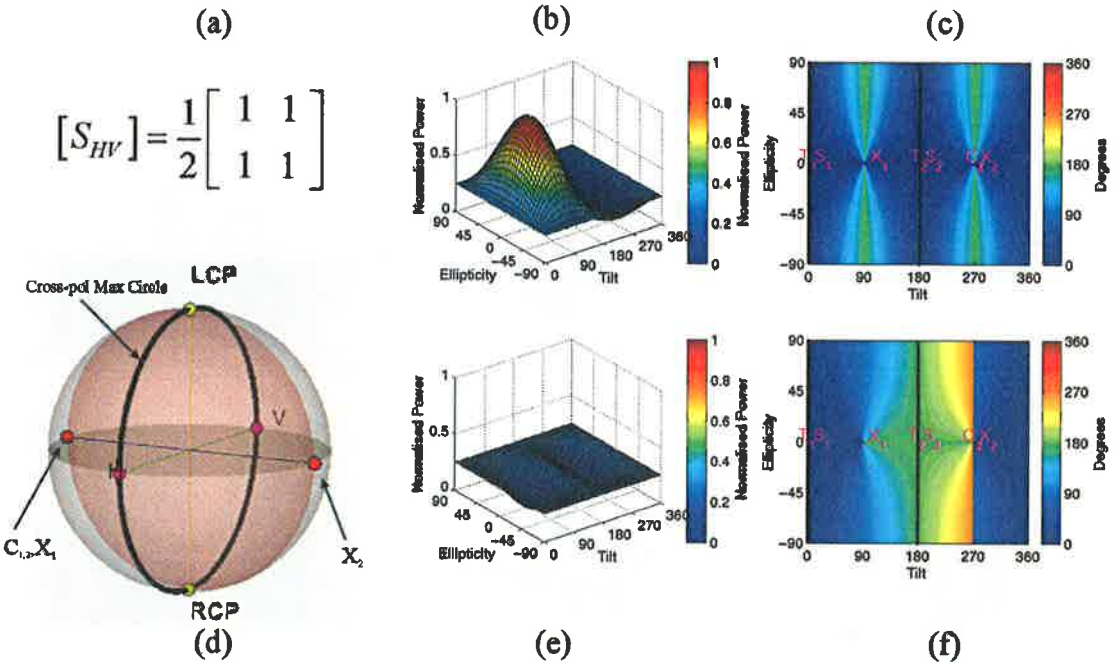

Figure 3-12 Summary of the polarimetric properties of a 45° dipole

(a) S matrix (b) Co-pol power spectrum (c) Co-pol relative phase-correlation plot
(d) Polarisation fork (e) Cross-pol power spectrum (f) Cross-pol relative phase-correlation plot

Corresponding results are obtained for the vertical dipole and for a 45° dipole. Once again the general form of the [*S*] matrix, the polarisation fork, the co-polar and cross-polar polarisation signatures and phase correlation plots are displayed in Figure 3-11 for the vertical case and Figure 3-12 for the 45° case. As with the horizontal case, there are multiple solutions for the locations of the cross-polar maxima in both situations.

3.2.7 Helix

The helix represents the circular counterpart to the linear dipole, in that it has the property that it will always generate circular polarisation regardless of the incident polarisation. A helix can be regarded as being composed of two dihedrals with a 45° difference between their orientation angles and a (two-way) 90° phase difference (corresponding to a $\lambda/8$ displacement) between them [191]. This gives the helix a more important role in practical situations than might immediately be expected, since this type of scattering behaviour is frequently encountered in both urban and rural situations [42]. The polarimetric properties of left- and right-handed helixes are presented in Figure 3-13 and Figure 3-14.

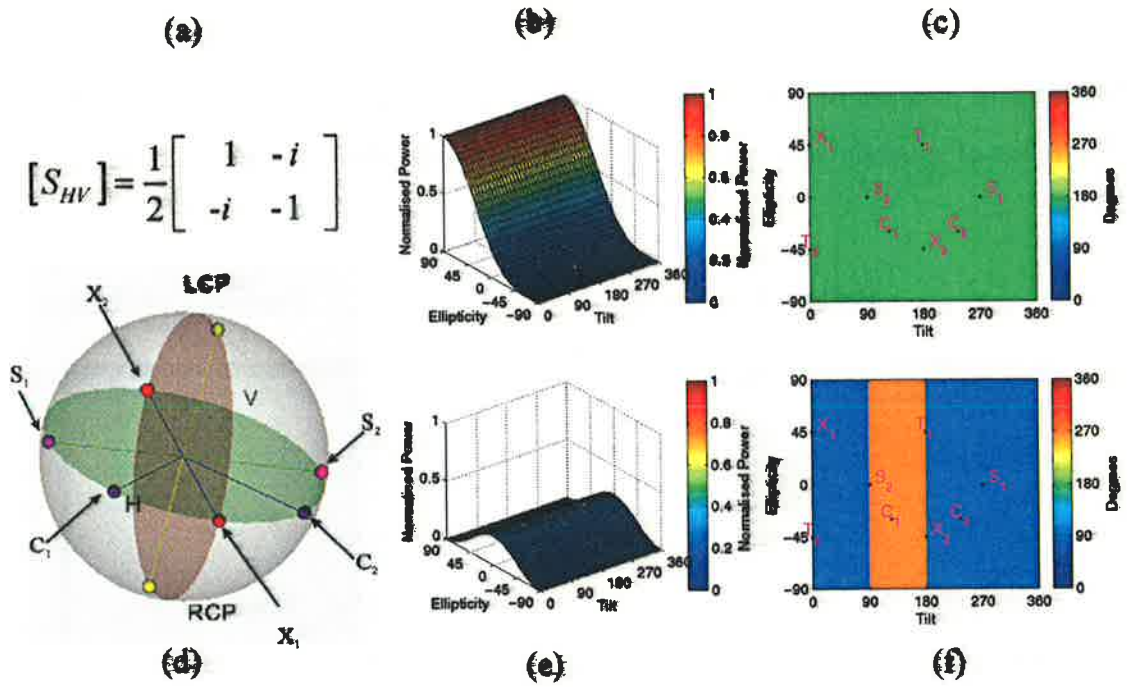

Figure 3-13 Summary of the polarimetric properties of right helix

(a) S matrix (b) Co-pol power spectrum (c) Co-pol relative phase-correlation plot
(d) Polarisation fork (e) Cross-pol power spectrum (f) Cross-pol relative phase-correlation plot

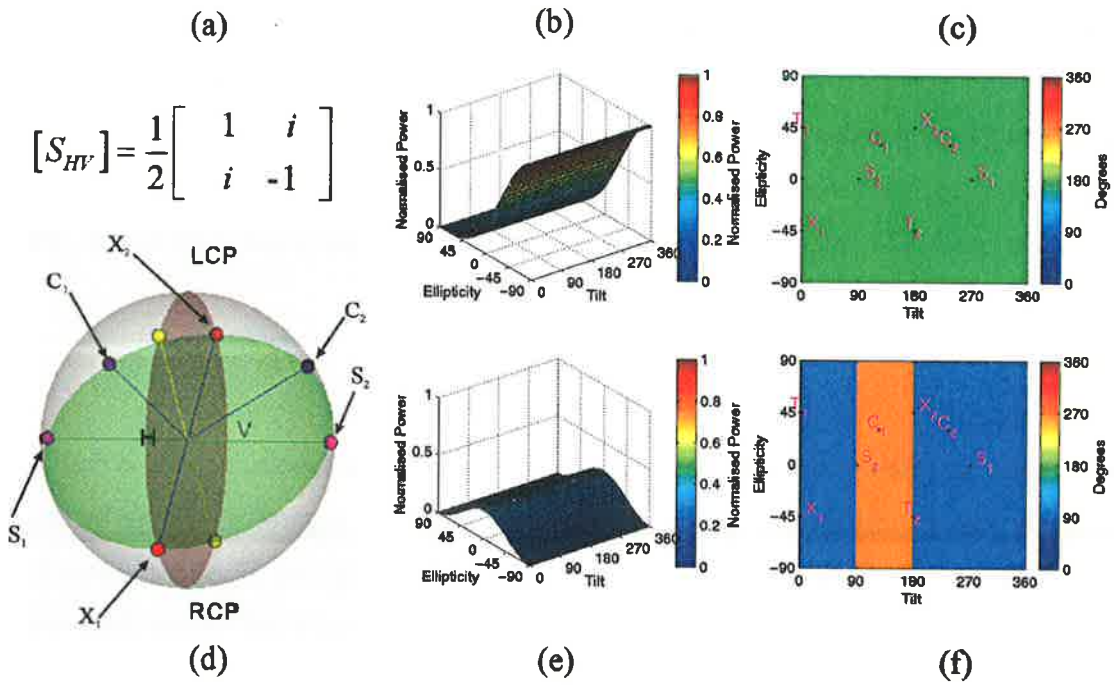

Figure 3-14 Summary of the polarimetric properties of left helix

(a) S matrix (b) Co-pol power spectrum (c) Co-pol relative phase-correlation plot
(d) Polarisation fork (e) Cross-pol power spectrum (f) Cross-pol relative phase-correlation plot

3.2.8 Quarter wave reflector

A quarter wave plate can be obtained by combining the scattering matrix of an odd bounce reflector with that of an even bounce reflector offset by an eight of a wavelength or with a perfectly conducting surface covered with a uniaxially linearly birefringent material of varying thickness (depending on the phase change required). Examples of quarter wave plates with +90° and –90° phase changes are shown in Figure 3-15.

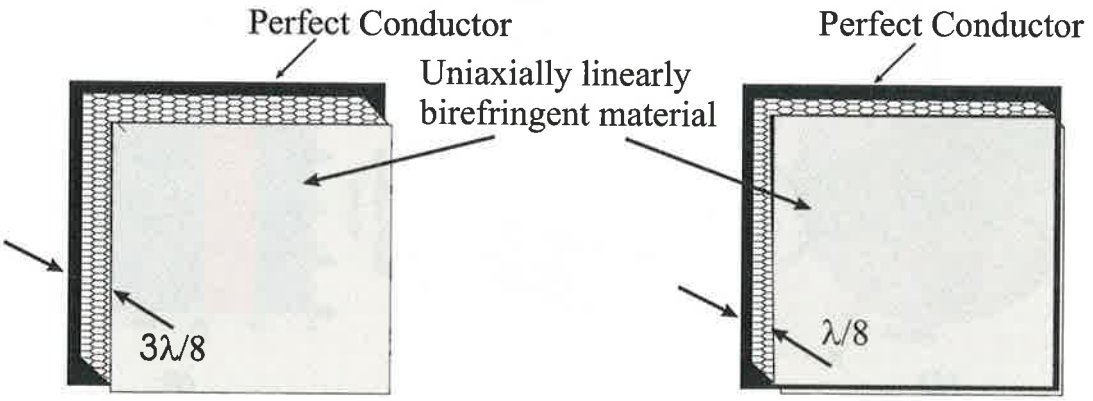

Figure 3-15 Examples of quarter wave plate reflectors

Figure 3-16 and Figure 3-17 show the properties of the two quarter plate reflectors. Once again the solution of the characteristic polarisation states results in multiple solutions of the location of the cross-polar maxima. The analysis of this special case is described in detail in [155]

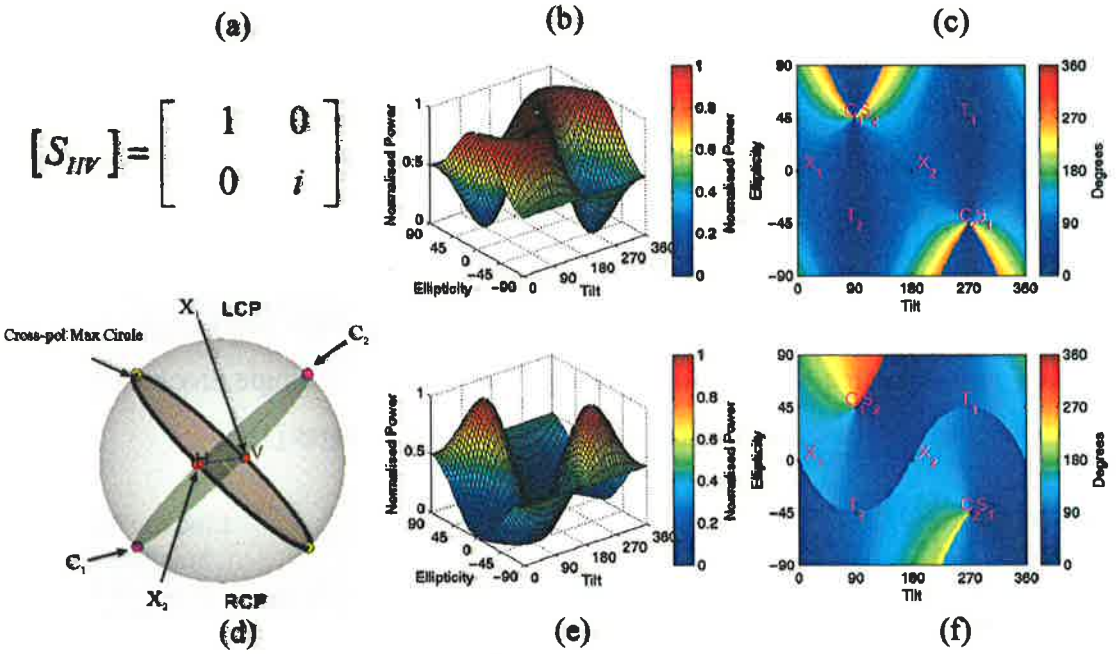

Figure 3-16 Summary of the polarimetric properties of a quarter wave plate with +90° phase

(a) S matrix (b) Co-pol power spectrum (c) Co-pol relative phase-correlation plot
(d) Polarisation fork (e) Cross-pol power spectrum (f) Cross-pol relative phase-correlation plot

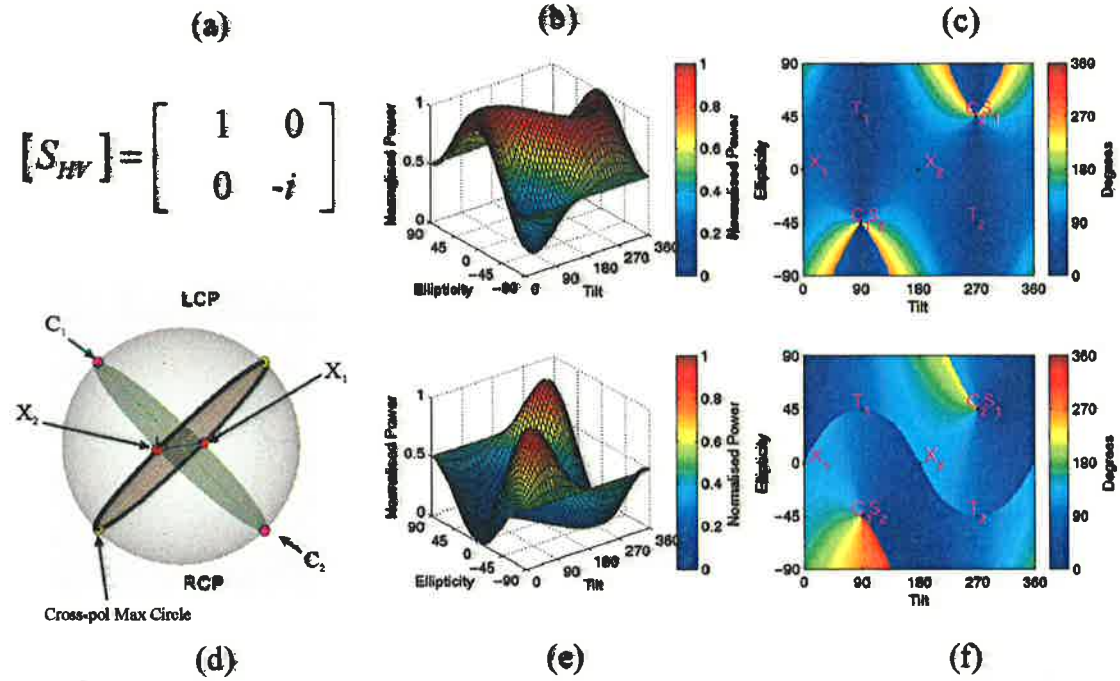

Figure 3-17 Summary of the polarimetric properties of a quarter wave plate with -90° phase

(a) S matrix (b) Co-pol power spectrum (c) Co-pol relative phase-correlation plot
(d) Polarisation fork (e) Cross-pol power spectrum (f) Cross-pol relative phase-correlation plot

3.2.9 Polarimetric Active Radar Calibrator (PARCS)

Reflectors with specific scattering matrices can be realised by active devices called Polarimetric Active Radar Calibrators (PARCS). They usually consist of a high-gain amplifier connected between two orthogonal linearly polarised horn antennas. Their advantages include wide beamwidths in both azimuth and elevation and the ability to generate a high signal-to-background clutter ratio. They are designed to have good polarisation isolation and use orthogonal horns to ensure low cross-coupling. They are usually small in size, portable and can be powered by a battery making them well suited to field calibrations. A schematic diagram of a typical PARC is shown in Figure 3-18. Their disadvantages include a relatively high production cost, an external power source requirement and the limitation to a single frequency band. Their characteristics are also sensitive to environmental changes [198].

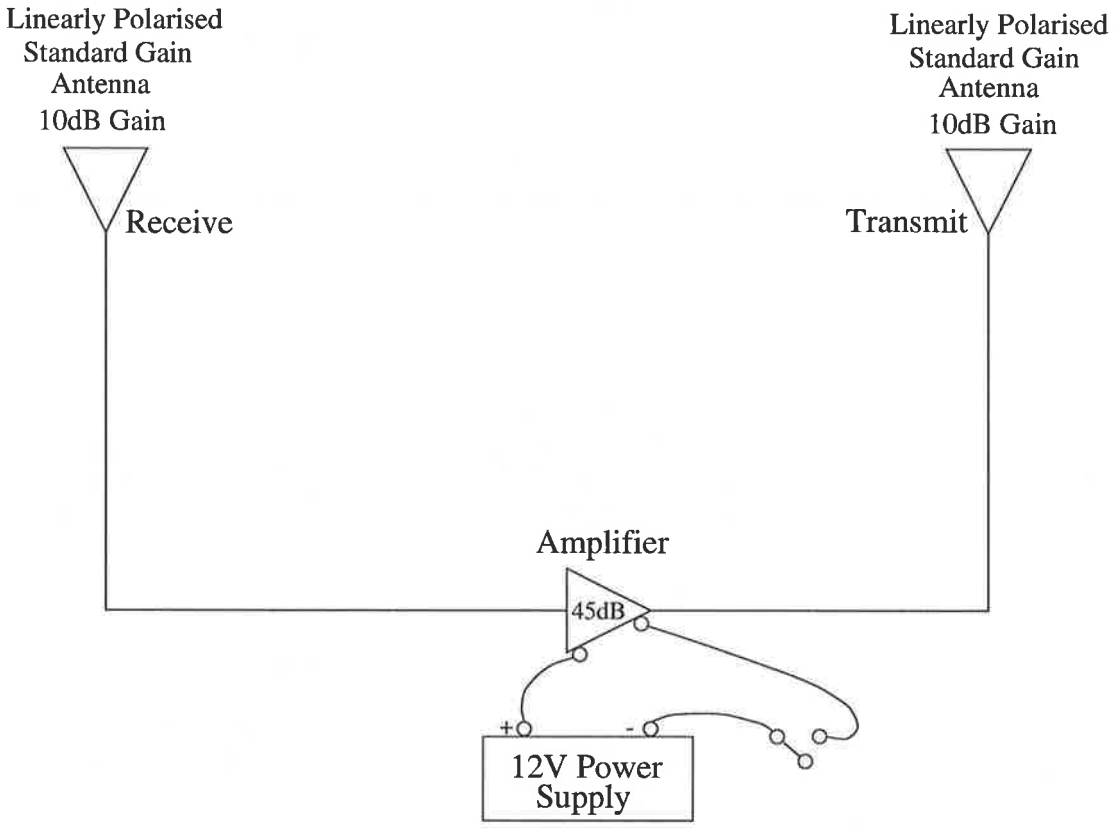

Figure 3-18 Schematic diagram of a typical PARC

3.2.10 Polarimetric delay calibrator

Delay line calibrators have the advantage that they separate the target return in range from the structure on which they are mounted. McLaughlin *et al.* [74] used a

polarimetric delay calibrator made from a pair of standard-gain horn antennas, interconnected through isolators and a 30 metre length of coaxial cable. The isolators prevent RF energy from flowing clockwise through the structure while the delay line separates the calibration signal from the clutter background. The antennas are orientated so that they are perpendicular to each other and the axis of the entire structure is orientated 45° with respect to the horizontal plane. A schematic diagram of this device is shown in Figure 3-19.

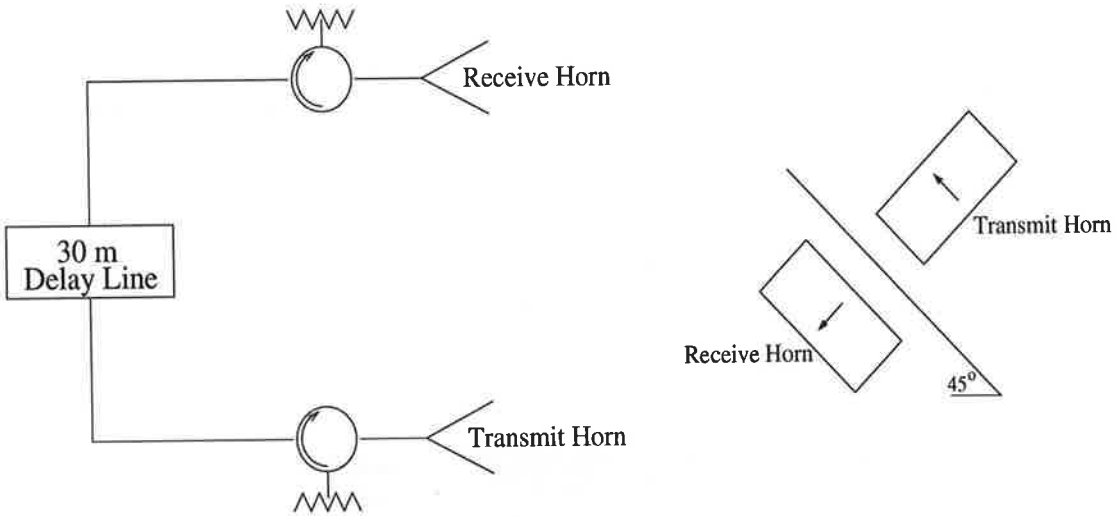

Figure 3-19 Polarimetric delay line calibrator

The theoretical polarisation scattering matrix of the delay line calibrator is given as [74]:

$$[S] = \sigma_t \begin{bmatrix} 1 & 1 \\ -1 & -1 \end{bmatrix} \tag{3.1}$$

The σ_t constant depends on the gain of the two antennas and on the propagation loss through the delay line used in the target but is not required to calibrate the system.

3.2.11 Polarimetric dual delay calibrator

A device, similar the delay line calibrator used by McLaughlin *et al.* [74], was designed and constructed during this study. Instead of a pair of standard gain antennas, a parabolic dish antenna with a dual linear feed horn with two delay lines was used. The calibrator was constructed using an 8 – 18 GHz, 18 inch TECOM parabolic dish antenna and is shown in Figure 3-20. This antenna has frequency independent, dual polarised primary feeds that are capable of receiving simultaneous

vertical and horizontal polarisations. The gain and beamwidth of the antenna varies from 26 dB and 6° at 8 GHz to 33 dB and 2.6° at 18 GHz. The delay lines were constructed using flexible storm cable assemblies that were 0.29 inches in diameter and were fitted with SMA straight plugs on each end. Two circulators and isolators were also required in the design. These components have a maximum insertion loss of 0.6 dB and a minimum isolation of 16 dB. The delay lines were deliberately made from different length cables so that the return from each path is separated in range to minimise any cross-talk effects. The calibrator has been tested in the DSTO anechoic chamber in a variety of configurations. Tests were performed with the delay line configured to produce a strong cross-polarised return by connecting the lines such that the received signal is retransmitted on the orthogonal channel, although normally the delay lines are connected so that the received and retransmitted signal have the same polarisation. In normal use the calibrator is configured so that the return from the horizontal channel will appear closer in range than the vertical signal, however, rotating the device through 90° reverses this behaviour.

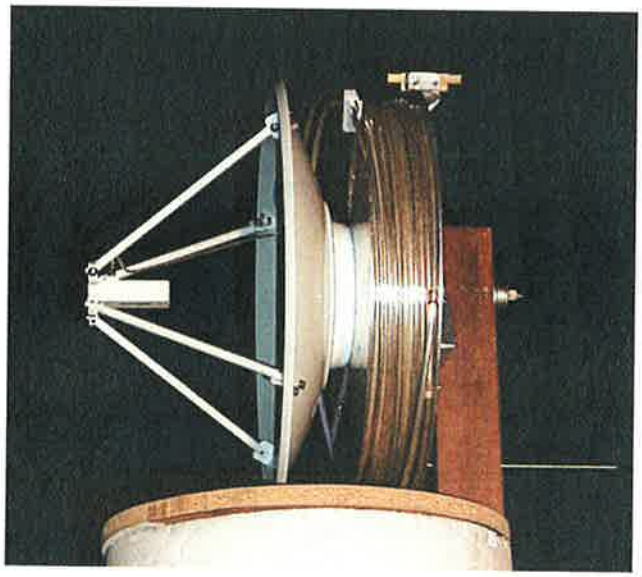

Figure 3-20 Dual delay line calibrator

3.3 Polarimetric calibration techniques

The aim of a polarimetric calibration technique is to compensate for the distortions of waves propagating in the transmitter and receiver channels. These distortions arise from polarisation coupling between channels and from gain and phase imbalances that occur in the transmitter, receiver and antenna systems. Considerable effort has been devoted to the development of techniques for calibrating polarimetric radar systems.

In the most general case, to calibrate polarimetric radar it is necessary to measure the response of four calibration targets, with target vectors that form an orthonormal set. The number of targets can only be reduced if simplifying assumptions are made concerning the form of the distortion matrices that characterise the radar system.

The most commonly used calibration approach involves simplifying the system model to yield a matrix calibration procedure in which a set of unknown system parameters is determined by external calibration and then removed from target measurements via an inverse matrix product. In the monostatic backscattering case, we assume that reciprocity holds and hence that the cross-polar terms are equal. This reduces the number of targets that need to be measured and ensures that the transmission and reception matrices can be completely characterised by measuring the responses of a single odd bounce reflector and a pair of even bounce reflectors that have been rotated about the radar line of sight with respect to each other. In the case of imaging radars, the scattering properties of the clutter are often used to simplify the calibration process. Examples include the methods developed by van Zyl [201] and Klein [202]. These estimate the cross-talk contamination of the radar by assuming that the co- and cross-polarised responses of natural targets with azimuthal symmetry are uncorrelated.

The calibration technique used is strongly influenced by operating conditions and often a strategy must be designed to find a trade-off between the accuracy and reliability of results [203]. The key elements of interest when deciding on the suitability of a calibration scheme include the complexity of the calibration process, the target deployment requirements, the accuracy of the symmetrisation procedure (for monostatic systems) and the validity of assumptions about the quality of the antenna/RF polarimetric isolation.

The overall objective of all such schemes is to provide calibrated radar data, so that the receiver channel powers can be related to the chosen representation of target scattering behaviour, such as the normalised radar cross section. However, the case for polarimetric radars is complicated by the fact that such systems provide a multi-dimensional complex description of the object. Thus there are many different parameters that can be used to describe the scatterer, many of which are formed as

complex ratios and are insensitive to specific types of system error. Consequently, some parameters are more sensitive to the quality of calibration than others. For example, the complex co-polar correlation coefficient is insensitive to system cross-talk but failure to correctly account for the cross-talk will affect other parameters like the location of the optimal polarisation states and can lead to incorrect classification of scattering behaviour.

All of this makes it difficult to decouple questions about the required accuracy of calibration from the more general question of signal processing. Typically, calibration aims at achieving ≤ 0.1 dB amplitude measurement accuracy, $\leq 3°$ phase accuracy and ≥ 30 dB cross-polar isolation. These levels enable the application of a range of target classification and identification methods.

Nonetheless, some care is required when choosing a calibration procedure, as all such schemes make important assumptions about the radar system. It should be an important feature of all useful schemes that they not only permit simple and effective calibration but also permit the identification of situations where the validity of the assumed models deteriorates. It is the objective of the following sections to outline how such a choice can be made.

3.4 Matrix formulation of the calibration problem

The conversion of the 2×2 complex scattering matrix $[S]$ into a target vector is an important step in the development of matrix formulations of the calibration process. The vectorisation process can be performed using any orthogonal basis. The two commonly used bases are the Pauli or lexicographic expansion described in Section 2.11 yielding the scattering vector $\vec{k}_{4P}$ or $\vec{k}_{4L}$ respectively. The $\vec{k}_{4P}$ vector, based on the Pauli expansion, ensures that all of the asymmetric components of $[S]$ are contained in one component. This property is important when considering symmetrisation routines. The vector $\vec{k}_{4L}$ obtained using the lexicographic expansion is also widely used for calibration studies as it relates the elements of $[S]$ to a target vector in a very simple manner but spreads the asymmetric components of $[S]$ over two terms.

The matrix approach to calibration begins with the following linear system model defined as

$$\vec{k}_{4L}^{obs} = [Z_4]\,\vec{k}_{4L} \tag{3.2}$$

where $\vec{k}_{4L}^{obs}$ is the observed scattering vector and $[Z_4]$ is a 4×4 complex matrix accounting for distortions caused by the system. In general, $[Z_4]$ has sixteen complex elements and hence requires a minimum of sixteen equations in sixteen unknowns to solve the linear system represented in Equation (3.2). With $[Z_4]$ so established we can then estimate the true scattering vector as

$$\vec{k}_{4L} = [Z_4]^{-1}\,\vec{k}_{4L}^{obs} \tag{3.3}$$

Clearly, a minimum of four special calibration targets is required to obtain an estimate of $[Z_4]$. To solve the linear system in Equation (3.2), the four targets chosen must have a set of target vectors that form an orthonormal set. Targets with properties corresponding to the Pauli basis matrices are one possible solution, requiring measurements of a sphere, a dihedral corner reflector aligned at 0° or 90° to radar co-ordinates, a dihedral corner reflector at 45° to radar co-ordinates, and a target that generates in reflection the orthogonal polarisation to any incident wave.

The linear distortion model can then be applied, but it offers little physical insight into the various system mechanisms responsible for the distortion of $\vec{k}_{4L}$. It also involves a relatively large number of complicated calibration targets. For field calibration, there is great interest in reducing the number and complexity of calibration targets required. The following section illustrates how the distortion model developed by Barnes [204] reduces the calibration problem to a twelve parameter calibration procedure. Such a model is at the heart of most approaches to polarimetric calibration.

3.5 Distortion matrix models

The first polarimetric calibration techniques considered antenna polarisation radiation patterns [205] and the isolation of RF system elements separately. Such internal calibration techniques were not suited to complicated operational systems, so there

was a need to develop external methods[1]. Two of the first publications to outline radar calibration as a general multi-port network problem were published in 1986 by Barnes [204] in the USA and Woods [206] at DRA Malvern. These two publications (particularly that by Barnes) have formed the basis for most subsequent developments, and although there have been several publications which point out the limitations of this approach [207] , they still offer the key elements of relative simplicity which is required for implementation in operational radar systems.

Barnes [204] modelled the distortions that occur in a radar system by accounting for system frequency response, mismatch effects and cross-polarisation coupling of antennas by defining transfer matrices for the transmitting and receiving antennas. This approach is referred to by Whitt *et al.* [208] as the constrained calibration technique (CCT). The relationship between the measured target scattering matrix $[S^m]$ and the true target scattering matrix $[S]$ can be expressed as

$$\left[S^m\right]=[R]\ [S]\ [T] \tag{3.4}$$

where $[R]$ is a 2×2 symmetric complex distortion matrix describing the receive path and $[T]$ is the transmit path. This model is usually referred to as the *RST* model and in its expanded form is written as:

$$\begin{bmatrix} S^m_{HH} & S^m_{HV} \\ S^m_{VH} & S^m_{VV} \end{bmatrix} = \begin{bmatrix} R_{HH} & R_{HV} \\ R_{VH} & R_{VV} \end{bmatrix} \begin{bmatrix} S_{HH} & S_{HV} \\ S_{VH} & S_{VV} \end{bmatrix} \begin{bmatrix} T_{HH} & T_{HV} \\ T_{VH} & T_{VV} \end{bmatrix} \tag{3.5}$$

A derivation of this relationship is given in [209]. The subscripts H and V represent horizontal and vertical polarisation and the order indicates the polarisation state of the receiver followed by the transmitter.

One of the problems with a model such as Equation (3.5) is that it assumes the transmit and receive paths are independent. Consequently, the distortion model for the receive path would be independent of the transmit polarisation, which may not always be valid [207] and depends on the RF switching technology used. This assumption

[1] The Danish EMISAR system is one counter-example of a current radar system that adopts an internal calibration scheme

may be invalid in high power radar systems where switches using ferrite devices must be used. Lower power systems, such as the DSTO high resolution radar system use PIN or FET switches and have better isolation properties, so the assumption that the transmit and receive paths are independent is usually acceptable.

The elements of the transfer matrices model different distortion effects. T_{VH} and T_{HV} account for the coupling that occurs between the H and V channels of the transmitter while T_{HH} and T_{VV} account for amplitude and phase errors present in the transmitted signal. Similarly, R_{HH} and R_{VV} represent the amplitude and phase errors introduced by the receiver and R_{HV} and R_{VH} represent the cross-polarisation coupling terms for the receiver. These relationships are shown in Figure 3-21.

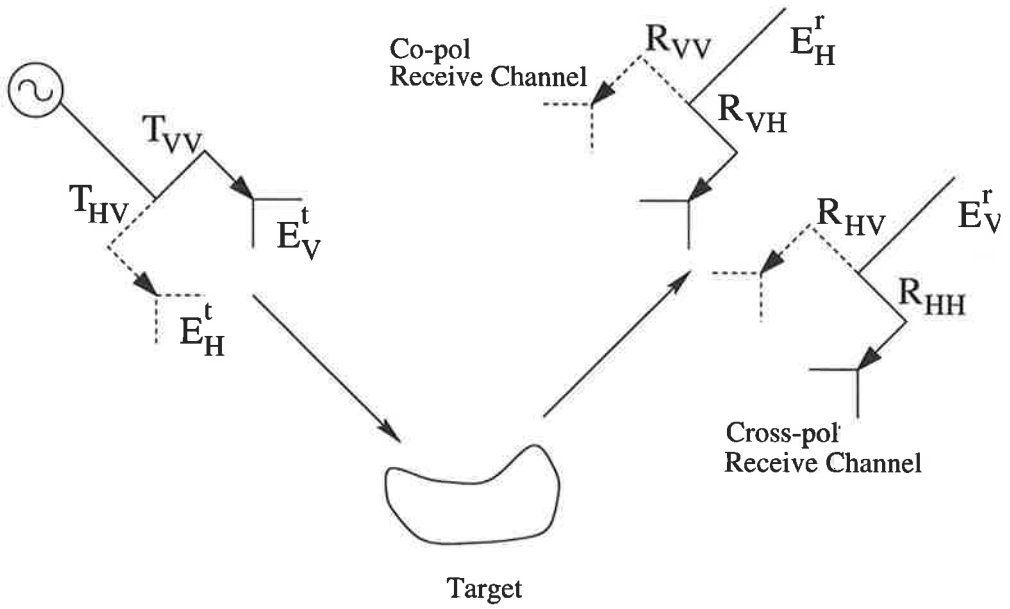

Figure 3-21 Relationship between the distortion matrix elements

Freeman *et al.* [210] developed a similar approach to Barnes but used PARCS to realise the known target scattering matrices. The method introduced by Riegger *et al.* [211] characterised the system errors in terms of coupling coefficients between elements of the theoretical scattering matrix and elements of the measured scattering matrix. This approach is essentially the same as Barnes except that Riegger expanded the matrix product resulting in twice as many unknowns. The main drawback of this procedure is that it requires the measurements of targets with a particular form of scattering matrix that are often difficult to realise.

Wiesbeck *et al.* [212] published a complete twelve term error model for the systematic errors in polarimetric free space measurements called the radiation transfer matrix. In addition to the multiplicative [T] and [R] matrices, an additive isolation matrix [I] is included to account for residual reflections from the surrounding environment and errors induced by direct coupling between the transmit and receive paths. The isolation matrix [I] is usually associated with a zero mean Gaussian random process with unit covariance matrix. The relationship between the measured target scattering matrix [S^m] and the true target scattering matrix [S] in this model is given by

$$\begin{bmatrix} S^m_{HH} & S^m_{HV} \\ S^m_{VH} & S^m_{VV} \end{bmatrix} = \begin{bmatrix} I_{HH} & I_{HV} \\ I_{VH} & I_{VV} \end{bmatrix} + \begin{bmatrix} R_{HH} & R_{HV} \\ R_{VH} & R_{VV} \end{bmatrix} \begin{bmatrix} S_{HH} & S_{HV} \\ S_{VH} & S_{VV} \end{bmatrix} \begin{bmatrix} T_{HH} & T_{HV} \\ T_{VH} & T_{VV} \end{bmatrix} \tag{3.6}$$

This error model can be represented as a signal flow graph that illustrates the signal flow in the system and highlights the points of influence for errors like spurious signals, reflections and coupling. The properties and advantages of using this type of representation are discussed further in [212].

The RST model reduces the number of unknowns from sixteen to twelve, which also reduces the number of calibration targets required from four to three (again, they must be a set with independent target vectors). Barnes originally suggested the following set of calibration matrices

$$F_1 = \begin{bmatrix} 1 & 0 \\ 0 & 0 \end{bmatrix} \quad F_2 = \begin{bmatrix} 0 & 0 \\ 0 & 1 \end{bmatrix} \quad F_3 = \begin{bmatrix} 1 & 1 \\ 1 & 1 \end{bmatrix} \tag{3.7}$$

Barnes proposed that such a calibration triplet could be realised using gridded trihedral reflectors. In the case of the calibration of the DSTO radar system, the calibration matrices have been realised using a dual delay line calibrator (described in Section 3.2.11), mounted in a helicopter. The delay permits range separation of the calibrator from the helicopter direct return and the delay lines separate F_1 and F_2 in range. By rotating the device through 45°, F_3 can also be realised. Typically, trihedral

reflectors and two dihedrals with relative orientations of 45° are used as calibration targets.

Having determined estimates for the [R] and [T] distortion matrices, the true scattering matrix [S] can be obtained by inverting the matrix expressions. This relies on the distortion matrices being invertible which is generally true for actual radar systems [130]. If a matrix is ill-conditioned, standard regularisation techniques can be applied. Methods have been developed that reduce the number of targets that need to be measured by making further assumptions about the form of the distortion matrices.

It is common to extract a complex number factor from the general expression shown in Equation (3.4). The magnitude of this factor is determined by absolute radiometric calibration and the phase is the absolute phase of the scattering matrix. This phase angle is a function of the distance from the radar to the target and can generally be ignored for polarimetric calibration. However, there is some difficulty over how to uniquely define the absolute phase. In the review by [213] for example, the phase of the HH term of [S] is arbitrarily chosen as reference. There are problems associated with such a general definition (for example HH might be zero for some targets) and there has been debate in the literature over a suitable invariant definition of absolute phase [132, 214].

Despite these problems, it is standard to extract these two parameters (one complex number) before performing polarimetric calibration. It is also common to assume that [R] and [T] have at least one complex element in common. This leaves only eight calibration parameters from Equation (3.4) (plus one noise parameter) to be determined.

A key advantage of the Barnes model is that sensible physical models for system behaviour can be built into [R] and [T] to reduce the number of unknowns. For example, the small coupling hypothesis is often employed which assumes that the cross-polarisation coupling terms for the transmit and receiver paths are small.

$$|R_{ij}|,|T_{ij}| \ll |R_{ii}|,|T_{ii}| \quad i,j = H,V \tag{3.8}$$

In one calibration scheme proposed by Ulaby [208, 215, 216], the antennas are assumed to have perfect isolation and so $[R]$ and $[T]$ are diagonal. This then reduces the number of unknowns to four, which can be solved using only two calibration targets. If we assume that the $[S]$ matrix is symmetric, then the scattering vector of only one of the two targets needs to be known accurately to solve the system of equations. In general, the assumption of zero cross-talk is seldom valid, so the small coupling hypothesis is more commonly used.

3.6 Kronecker distortion matrix model

In the previous section a physically based distortion model was described. Another model can be obtained by reformulating the distortion model in terms of target vectors using the Kronecker or direct matrix product using the following relationship

$$[A]\ [S]\ [B] \equiv [A] \otimes [B]^T \vec{k}_{4L} \tag{3.9}$$

The disadvantage of such a formulation is that the model becomes a non-linear function of the system parameters as a result of the direct product. Nevertheless, incorporating the small coupling hypothesis means that a simple, tractable calibration procedure can be developed

If noise matrix contribution is initially ignored, Equation (3.6) can be re-written using Equation (3.9) giving

$$\vec{k}_{4L}^{obs} = [R] \otimes [T]^T \vec{k}_{4L} = [A_4]\ \vec{k}_{4L} = \begin{bmatrix} r_{11}t_{11} & r_{11}t_{21} & r_{12}t_{11} & r_{12}t_{21} \\ r_{11}t_{12} & r_{11}t_{22} & r_{12}t_{12} & r_{12}t_{22} \\ r_{21}t_{11} & r_{21}t_{21} & r_{22}t_{11} & r_{22}t_{21} \\ r_{21}t_{12} & r_{21}t_{22} & r_{22}t_{12} & r_{22}t_{22} \end{bmatrix} \vec{k}_{4L} \tag{3.10}$$

It is clear that the resulting matrix is composed of quadratic products of the elements of $[R]$ and $[T]$. Using the small coupling hypothesis, some of the elements of $[A_4]$ can be ignored because they are second order terms that are small compared with other terms. This reduces the number of unknowns in $[A_4]$ and simplifies the calibration procedure. Clearly, once $[A_4]$ has been determined, an estimate of the true target vector can be obtained via

$$\vec{k}_{4L} = [A_4]^{-1} \; \vec{k}_{4L}^{obs} \tag{3.11}$$

The target vector formulation of Equation (3.10) naturally defines a covariance matrix for the statistical variation of the scattering matrix. From Section 2.14.1 we know that the relationship between the coherency matrix $[T_4]$ and the covariance matrix $[C_4]$ can be written as

$$[T_4] = \left\langle \vec{k}_{4P} \cdot \vec{k}_{4P}^{\dagger} \right\rangle = [D_4] \; \left\langle \vec{k}_{4L} \cdot \vec{k}_{4L}^{\dagger} \right\rangle \; [D_4]^{\dagger} = [D_4] \; [C_4] \; [D_4]^{\dagger} \tag{3.12}$$

where $[D_4]$ is the unitary transformation matrix defined in Equation (2.45). The system distortion model defined in Equation (3.9) leads to the observed covariance matrix has the general form

$$[C_{obs}] = [A] \; [C] \; [A]^{\dagger} + [C_N] \tag{3.13}$$

where $[C_N]$ is the noise covariance matrix. This relation is very important since it can be used to obtain calibration data (i.e. information about the matrix $[A]$) from the eigenvectors of $[C_{obs}]$, which itself can be numerically approximated from the observed scattering matrix data. The components of $[A]$ can be determined in a variety of ways using external radar measurements but the primary techniques involve measurements of active/passive point targets, symmetrisation using the vector reciprocity theorem and exploitation of the statistical properties of distributed clutter targets. In general a combination of these techniques is used. These approaches are discussed in the following subsections.

3.6.1 Passive/active reflectors

Techniques exploiting passive reflectors such as dihedrals and trihedrals to determine the elements of $[A]$ were used in the earliest calibration studies. Typically three large passive reflectors were deployed, usually consisting of a trihedral and two dihedrals (at 0° and 45°). Other reflector combinations are also possible such as a 45° dihedral and a pair of dipoles. The dipoles are not generally realised as thin wires as their RCS values are too small and instead the dipole return is obtained using screened trihedrals

[200], either screened across the front face or screened along one side. In theory, only two calibration targets are required to solve for all the elements of $[A]$ although no suitable combination has been found. Consequently, most systems require measurements of three calibration targets, although it is possible to reduce this number by making further assumptions about the elements of $[A]$.

Ulaby [216] published a general procedure for obtaining a suitable set of three such targets and made no assumptions about the form or content of $[R]$ and $[T]$. A similar approach was proposed by Yueh [217] which makes use of the small coupling hypothesis. These procedures are useful for evaluating sets of calibration targets, but in most instances dihedral and trihedral reflectors are preferred due to their ease of manufacture and deployment (although the dihedrals are difficult to align, having a narrow beam width in one plane).

More recently the use of active transponders (PARCS) has become more common. Several groups around the world are currently developing and using PARCS to calibrate their radar systems [218-220]. PARCS are preferred since their stability and calibration ensures that good point target measurements of the matrix $[A]$ can be achieved. Their primary disadvantage is their cost and complexity when compared with passive reflectors. A technique for finding the elements of $[A]$ has been developed by Freeman [221] using the small coupling hypothesis. This approach demonstrates that the scattering matrices of the PARCS must have the following form.

$$[S_1] = a\begin{bmatrix} 0 & 0 \\ 1 & 0 \end{bmatrix} \qquad [S_2] = b\begin{bmatrix} 0 & 1 \\ 0 & 0 \end{bmatrix} \qquad [S_3] = c\begin{bmatrix} -1 & -1 \\ 1 & 1 \end{bmatrix} \tag{3.14}$$

Sensitivity analysis of all these methods to small errors in orientation have been discussed in the literature [213, 222].

3.6.2 Symmetrisation

The reciprocity theorem states that in network terms the quadratic form of the received voltage at the terminals of an antenna is invariant under exchange of transmitter and receiver [117]. This theorem is strong in the sense that it applies to all radar signals in the absence of non-reciprocal propagation media such as magnetised

ferrites. In the case of backscatter in the BSA co-ordinate system, the reciprocity theorem ensures that the [S] matrix is complex symmetric. Thus S_{HV} and S_{VH} are equal in both amplitude and phase. This property can be used to reduce the number of unknowns in the solution of the elements of [A]. This symmetry property does not mean that the observed scattering matrix will be symmetric, and in general the system distortions and imbalances will generally cause the observed matrix to be non symmetric. As a result it is critical that good estimates of the true symmetric cross-polar values are obtained if target classification is to be performed.

The process of estimating a symmetric matrix from the observed data is termed symmetrisation and several different strategies have appeared in the literature [201, 223, 224]. In some systems like the NASA JPL system, symmetrisation is performed before calibration and so the symmetrisation scheme employed is very important. The simplest and most widely used approach was proposed by van Zyl [201].

Consider the expression for the measured [S] matrix

$$[S]_{Measured} = \begin{bmatrix} 1 & 0 \\ 0 & r_1 e^{i\delta_1} \end{bmatrix} \begin{bmatrix} S_{11} & S_{12} \\ S_{21} & S_{22} \end{bmatrix} \begin{bmatrix} 1 & 0 \\ 0 & r_2 e^{i\delta_2} \end{bmatrix} = \begin{bmatrix} S_{11} & S_{12} r_2 e^{i\delta_2} \\ S_{21} r_1 e^{i\delta_1} & S_{22} r_1 r_2 e^{i(\delta_1+\delta_2)} \end{bmatrix} \tag{3.15}$$

Equation (3.15) illustrates that the presence of transmit/receive phase errors can lead to non symmetry in the observed complex matrix. The distortion factors $r_1 e^{i\delta_1}$ and $r_2 e^{i\delta_2}$ are generally different and this mechanism enables the difference of phase calibration errors ($\delta_1 - \delta_2$) to be found using a calibrator with large cross-polar RCS such as a dihedral rotated at 45°. An estimate of the sum of the phase errors ($\delta_1 + \delta_2$) can be obtained using a calibrator with a large co-polar RCS such as a trihedral. This approach is exploited in calibrating the DSTO high resolution radar system.

In the van Zyl approach the symmetric matrix is formed as a straight average of the cross-polar terms

$$S_{HV} = S_{VH} = \frac{1}{2}(S_{12} + \frac{r_2}{r_1} S_{21} e^{i(\delta_1-\delta_2)}) e^{-i\frac{(\delta_1-\delta_2)+(\delta_1+\delta_2)}{2}} \tag{3.16}$$

The amplitude and phase calibration of the VV channel is performed using

$$S_{VV} = \frac{1}{r_1 r_2} S_{VV} e^{-i(\delta_1+\delta_2)} \tag{3.17}$$

Other symmetrisation strategies have also been developed by Yueh [223] and Quegan [224]. There is no difference between these methods for systems with low cross-talk (smaller than –25 dB) but if the cross-talk increases there can be problems using the simple van Zyl scheme.

The symmetrisation employed in Equation (3.16) is a straightforward solution of the calibration equations, ignoring any SNR problems in parameter estimation. In more general schemes, a weighted average of the cross-polar terms is employed for symmetrisation, accounting also for the effects of noise and cross-talk, the latter of which influences estimation of the cross-polar scattering amplitudes much more than the co-polar.

If we assume reciprocity, the observed scattering vector is related to the underlying matrix by a new relation of the form

$$\vec{k}_{4L}^{obs} = [Z_{4\times3}]\vec{k}_{3L} \tag{3.18}$$

where $[Z_{4\times3}]$ is a 4 × 3 matrix with twelve unknowns in place of the sixteen in Equation (3.2). For this general model only three standard targets are required to determine the elements of $[Z_{4\times3}]$. Further, if we adopt the system model of [R] and [T] in Equation (3.9) we can write $[Z_{4\times3}]$ in the form

$$\vec{k}_{4L}^{obs} = \begin{bmatrix} S_{HH} \\ S_{HV} \\ S_{VH} \\ S_{VV} \end{bmatrix} = [Z_{4\times3}]\vec{k}_{4L} = \begin{bmatrix} r_{11}t_{11} & r_{11}t_{21}+r_{12}t_{11} & r_{12}t_{21} \\ r_{11}t_{12} & r_{11}t_{22}+r_{12}t_{12} & r_{12}t_{22} \\ r_{21}t_{11} & r_{21}t_{21}+r_{22}t_{11} & r_{22}t_{21} \\ r_{21}t_{12} & r_{21}t_{22}+r_{22}t_{12} & r_{22}t_{22} \end{bmatrix} \cdot \begin{bmatrix} S_{HH} \\ S_{HV} \\ S_{VV} \end{bmatrix} \Rightarrow \vec{k}_{4L} = \left(Z_{4\times3}^{\dagger} Z_{4\times3}\right)^{-1} Z_{4\times3}^{\dagger} \vec{k}_{3L} \tag{3.19}$$

which can be further simplified if we adopt the small coupling hypothesis as

$$[Z_{4\times3}]=\begin{bmatrix} r_{11}t_{11} & r_{11}t_{21}+r_{12}t_{11} & 0 \\ r_{11}t_{12} & r_{11}t_{22} & r_{12}t_{22} \\ r_{21}t_{11} & r_{22}t_{11} & r_{22}t_{21} \\ 0 & r_{21}t_{22}+r_{22}t_{12} & r_{22}t_{22} \end{bmatrix} \tag{3.20}$$

Quegan [224] outlines a least squares solution to Equation (3.20) which implicitly involves a symmetrisation step involving a weighted average of cross-polar terms such that an estimate of the true scattering vector can be obtained as shown in Equation (3.19). Note that the observed covariance matrix is of the form

$$\left[C_4^{obs}\right]=[Z_{4\times3}][C_3][Z_{4\times3}]^{\dagger} \tag{3.21}$$

where $\left[C_4^{obs}\right]$ is 4×4 but has rank 3. This means that the observed covariance matrix should have one zero eigenvalue. This can be used as an experimental check of the validity of the system distortion model. The observed covariance matrix can be of rank 4 in the presence of system noise in which case the smallest eigenvalue gives an estimate of the noise floor.

Klein [202] showed that the eigenvector associated with the zero eigenvalue contains valuable information about the calibration matrices [*R*] and [*T*]. This lead Yueh [223] to constructed a symmetrisation operator from this eigenvector with the following form

$$\vec{e}=[e_1 \quad e_2 \quad e_3 \quad e_4] \tag{3.22}$$

If the matrix [*Q*] is defined as

$$[Q]=\begin{bmatrix} e_3^* & -e_1^* \\ e_4^* & -e_2^* \end{bmatrix} \tag{3.23}$$

the observed scattering matrix $[S_{obs}]$ can then be symmetrised in one of two ways as

$$\left[\hat{S}\right]_1=[S_{obs}][Q] \quad \text{or} \quad \left[\hat{S}\right]_2=\left([Q]^{\mathrm{T}}\right)^{-1}[S_{obs}] \tag{3.24}$$

This procedure uses the eigenvector to eliminate either $[R]$ or $[T]$ from Equation (3.4) but assumes that the underlying true covariance matrix has rank 3. In Yueh's method the covariance matrix is formed through azimuth integration of the SAR image, however, there is an implicit assumption that the eigenvector can be extracted from an average over many pixels, which may not always be valid.

3.7 Clutter calibration

For a wide class of clutter target types, the assumption of reflection symmetry is often made. In these cases it has been demonstrated [225] that the co- and cross-polarised backscatter terms are uncorrelated which in mathematical terms can be expressed as

$$\langle S_{HH} S_{HV}^{*} \rangle = \langle S_{VH} S_{VV}^{*} \rangle = 0 \tag{3.25}$$

In Section 2.16.1 it was shown that the general form of the covariance and coherency matrices for reflection symmetry are

$$\langle C \rangle = \begin{bmatrix} x & 0 & x \\ 0 & x & 0 \\ x & 0 & x \end{bmatrix} \text{ and } \langle T \rangle = \begin{bmatrix} x & x & 0 \\ x & x & 0 \\ 0 & 0 & x \end{bmatrix} \tag{3.26}$$

The clutter calibration approach was originally demonstrated for specific random media scattering problems using the second Born approximation [146]. However, this result has now been established as a robust phenomenon for a wide range of distributed target types. As a result, Equation (3.25) has been included in many calibration routines and provides two complex equations for the unknown elements of $[A]$ or $[Z]$. In many cases only an additional trihedral calibration step is required.

3.8 Field calibration methodologies

The following section reviews the variety of calibration routines that have been used with polarimetric radar systems. A good introductory review is provided by Freeman [213] but this does not include some of the more recent work A good review of laboratory based bistatic calibration routines can be found in [226].

3.8.1 Van Zyl Algorithm

The van Zyl algorithm [201] is widely used and referenced due to its computational simplicity and the fact that it requires only one corner reflector. However, it makes assumptions about the distortion model, many of which may not be valid. In this approach the measured scattering matrix is first symmetrised and then modelled as

$$[S_{obs}] = Ae^{i\phi}\begin{bmatrix} 1 & \delta_2 \\ \delta_1 & f \end{bmatrix}\begin{bmatrix} S_{HH} & S_{HV} \\ S_{VH} & S_{VV} \end{bmatrix}\begin{bmatrix} 1 & \delta_1 \\ \delta_2 & 1 \end{bmatrix} = Ae^{i\phi}\left[R_{zyl}\right][S]\left[R_{zyl}\right]^T \qquad (3.27)$$

The matrices representing the receiver and transmitter channels are assumed to be identical although the matrix $[R_{zyl}]$ is not in general equal to either $[R]$ or $[T]$ but is instead a mixture of the two. In this calibration technique three parameters need to be determined, namely

- δ_1 - cross-talk when V polarisation is transmitted or received
- δ_2 - cross-talk when H polarisation is transmitted or received
- f - co-polarised channel imbalance in amplitude and phase

The cross-talk terms are calibrated using the zero correlations for clutter scenes in the image and the channel imbalance is determined by using a reference trihedral corner reflector. The assumptions made about the clutter make this technique inappropriate for calibrating the DSTO high resolution radar system.

3.8.2 Klein method

The Klein method [202] is based on the eigenvector extraction for rank 3 observed covariance matrices of the form shown in Equation (3.23). It requires measurements from a single trihedral but unlike the van Zyl technique makes no assumptions about the matrices $[R]$ and $[T]$. This means it is expensive in terms of data storage and computation and assumes that there is access to a scene with known rank 3 underlying covariance matrix. It uses azimuth symmetry plus a trihedral point reflector to solve for the elements of $[R]$ and $[T]$. It is more suited to calibration of polarimetric SAR systems rather than systems like the DSTO high resolution radar system as the assumptions about the clutter statistics are too restrictive.

3.8.3 Freeman method

Freeman proposed a method [221, 222, 227] using a set of 3 PARCS to solve for the elements of system distortion matrices [R] and [T]. It makes no assumptions, other than the validity of the Barnes model, but it suffers in terms of cost and complexity. The lack of a suitable PARC meant that this calibration approach was not attempted.

3.8.4 Wiesbeck method

Wiesbeck [195] developed a calibration routine based on the Kronecker product model discussed in Section 3.6 using a three target calibration procedure where only one of the targets needs to be known accurately. This technique has been extended [228] to include the calibration of bistatic polarimetric radar systems. This particular method is more suited to laboratory or chamber based calibration rather than field operations and consequently was not pursued with the DSTO radar system.

3.8.5 Nesti approach

Nesti *et al.* [197] developed a technique using a metallic sphere as the reference object and a dihedral reflector in two different orientations as an auxiliary calibrator. The scattering response of the dihedral is not required. Initially the co-polar channels of the system are calibrated by measuring a metallic sphere. This enables the calibrated co-polar response of the vertically orientated dihedral reflector to be determined. The cross-polar response of the tilted dihedral is then used to calibrate the cross-polar channels. Accurate range positioning of the dihedral is not essential, provided that it remains strictly constant for the two angular positions. However, this method does assume that the scattering matrix of the dihedral corner reflector in the vertical position is diagonal.

Alignment of the dihedral reflector is critical to the validity of this technique. In an anechoic chamber an angular accuracy of 0.2° can be achieved using positioning lasers. The effect of dihedral alignment errors has been measured [197] and the results indicated that small rotations about the vertical axis of the dihedral had only a minor effect (<0.1 dB/degree). More significant effects (about 1 dB/degree) were observed due to alignment errors with the horizontal axis perpendicular to the antenna bore-sight. This strong requirement for the accurate alignment of the dihedral makes this technique difficult to implement in field calibrations.

3.8.6 Gau algorithm

Gau *et al.* [229] proposed a calibration scheme that uses a single dihedral corner reflector. This technique is only valid for monostatic or quasi-monostatic radar systems and requires measurements to be made at two target orientations. The calibration model used in this method separates the antenna polarisation effects from the possibly nonreciprocal channel behaviour. This leads to four independent channel parameters and only six instead of eight parameters are need to model the general radar system. Since all the desired calibration measurements are taken using a single dihedral that is simply rotated about the line of sight axis, propagation phase errors associated with inaccurate positioning of multiple targets can also be avoided. But, like the method proposed by Nesti *et al.* [197] this technique assumes that the scattering matrix of the dihedral corner reflector in the vertical position is diagonal. Thus the validity of this approach is determined by the alignment accuracy of the dihedral in the vertical position. This strong requirement for accurate alignment meant that this approach was not feasible in field conditions and this approach was not attempted.

3.8.7 Muth technique

Muth [230] proposed a calibration technique using a continually rotating dihedral which claims to offer many improvements in calibration data diagnostics and analysis by making the uncertainty analysis tractable. The calibration procedure involves collecting a complete polarimetric data set as the dihedral rotates through the full 360°. Independent Fourier analysis on each of the polarimetric components of the data is used to examine the lack of symmetries in the data and perform the error analysis. Nonlinear constraints are incorporated into the Fourier analysis to ensure data and model consistency and the residuals are used to assess random uncertainties. Triangular dihedrals have been shown to produce good results [231] with this technique and repeated measurements of different sized dihedrals can be used as a convenient consistency check. The insensitivity of this technique to knowledge of instantaneous orientation suggested that it might form one part of a suitable calibration scheme for the DSTO radar.

3.8.8 Quegan method

Quegan [224] proposed a non-iterative technique using a single corner reflector calibration, based on the assumptions of azimuthal symmetry and the small coupling

hypothesis. The solution to the calibration problem is found using a least squares approach. This method is particularly good at identifying when the underlying assumptions fail and to see how such a scheme relates to the more widely used but more restrictive van Zyl method.

3.8.9 Ulaby and Sarabandi algorithms

Sarabandi *et al.* [215] proposed another single reference calibration technique called the isolated antenna calibration technique (IACT). This technique provides a fast and efficient method for which only two calibration targets are required. Its primary advantage is that there is no need for accurate alignment of the reflectors so it is well suited for field calibration studies.

This method uses a sphere and any other depolarising calibration target to determine the distortion matrices. The advantage of this technique is that the scattering matrix of the depolarising target need not be known. This gives the technique immunity to errors caused by target orientation and lack of precise knowledge of the theoretical scattering matrix elements.

The restriction of this approach is that it assumes that there is perfect isolation between the receiver channels. The cross coupling terms in the distortion matrices, T_{HV}, T_{VH}, R_{HV} and R_{VH} are assumed to be zero and this assumption leads to simple expressions for the scattering matrix elements [215].

The validity and accuracy of the IACT has been shown to be in good agreement with theoretical results in both anechoic chamber and field calibration measurements. McLaughlin *et al.* [74] used this approach to calibrate a polarimetric radar operating at X band in their study of the polarimetric properties of sea clutter at low grazing angles. A modified version [203] has been used to calibrate data collected using MERIC [232], an experimental polarimetric radar at ONERA.

The main disadvantage of the IACT is that it does not account for the cross-polar contamination that takes place in the orthogonal mode transducer and in the antenna structure itself. In general it is impossible to achieve perfect isolation between the receiver channels and cross-talk contamination can lead to significant errors in the

cross-polarised terms when the ratio of cross- to co-polarised terms is small and/or the cross-talk contamination is large. The polarisation isolation between channels needs to be at least 25 dB for this technique to be valid [215] and since the IACT ignores the effects of cross-polar contamination there is no improvement to the effective polarisation isolation of the system after the data has been calibrated. Other techniques can improve the effective polarisation isolation by as much as 25 dB.

To overcome the limitations of the IACT, Sarabandi *et al.* [209] published a method for calibrating single-antenna systems called the single target calibration technique (STCT). The antenna system and two orthogonal directions in free space are modelled as a four port network and channel imbalances and cross-talk contamination are determined by measuring the backscatter from a single calibration target. This technique uses the reciprocity relations for the passive network and assumes that the cross-coupling terms of the antenna are equal. The cross-talk factors of the antenna system and the transmitter and receiver channel imbalances can then be determined using measurements from a single calibration target. The scattering matrix of this target is assumed to be diagonal with equal diagonal entries. This scattering matrix can be realised with either a metallic sphere or trihedral corner reflector. This technique makes use of the radar's range-gating capability to remove short-range reflections from the antenna system and multiple bounces between the antenna and target. Like the IACT, the STCT is insensitive to target orientation, but accounts for antenna cross-talk contamination. If the antenna cross-talk contamination is small then the STCT is not appropriate and the IACT should be used instead. The validity and accuracy of the STCT has been demonstrated using X band scatterometers in an anechoic chamber and under field conditions [209]. An ambiguity in the sign of the cross-talk parameter is incurred but this can be resolved by measuring a target that has a known phase relationship between the elements of its scattering matrix such as a tilted cylinder.

3.8.10 Brock procedure

Brock [233] also published a calibration method using a single calibration target that provides a good response for all polarisation combinations. This approach has no phase ambiguity associated with the cross-polarised terms but requires the transmitter and receiver distortion matrices to be symmetric and identical. Since most system

include nonreciprocal devices such as switches and circulators, the distortion matrices are usually non-symmetric but symmetry can be restored and the effective transmit and receive matrices can be made identical through the use of a reference target.

3.8.11 Chen method

Chen *et al.* [234] also proposed a single reference calibration technique using three perfect polarisation isolated calibrators. The technique uses a flat plate, a dihedral corner reflector and an arbitrarily rotated corner reflector. The magnitudes of the co-polarisation terms in the polarisation scattering matrices of each calibrator are assumed to be equal but a generalised approach has also been published [235] that removes this requirement. In the generalised technique only the co-polarised terms in the polarisation scattering matrix of the first calibrator are required. The range and co-polarised RCS of the other two calibrators and the rotation of the third calibrator can be derived and used to verify the calibration process.

3.9 Calibration of the DSTO high resolution radar system

The following section examines the techniques investigated for calibrating the DSTO high resolution radar system. Many of the calibration techniques described in the previous section are unsuitable due to a variety of reasons such as restrictive alignment or positioning requirements, invalid assumptions such as the isolation between channels or properties of the clutter. Consequently a hybrid method was developed using the delay line calibrator, described in Section 3.2.11, to perform the radiometric calibration while calibration of the relative phases of the scattering matrix elements was performed using a rotating dihedral positioned on the ground. The least squares solution developed by Quegan [224] can then be applied to further reduce the cross-talk if required.

3.9.1 Corrugated parallel plate target

The first attempt at polarimetric calibration was performed using a corrugated parallel plate target proposed by Kitayama *et al.* [236]. This target consists of parallel vertical metallic plates arranged in a toothshaped electromagnetic absorber as shown in Figure 3-22. This type of target has properties that are similar to that of a linear wire target but with a larger radar cross section.

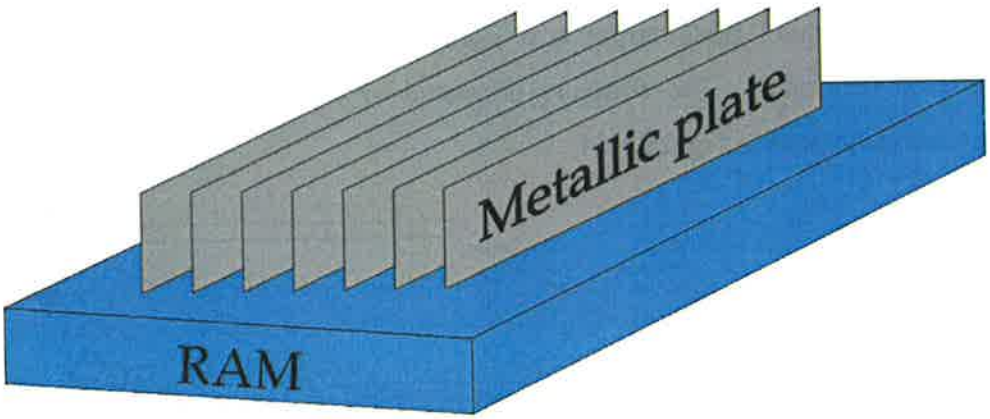

Figure 3-22 Corrugated parallel plate

Assuming that the polarisation parallel to the edge of the metal plate is horizontal and orthogonal to the edge is vertical, then the conceptual scattering mechanism can be explained (somewhat simplistically) as follows. Figure 3-23 illustrates the scattering mechanisms that occur when horizontally and vertically polarised waves encounter the corrugated parallel plate target.

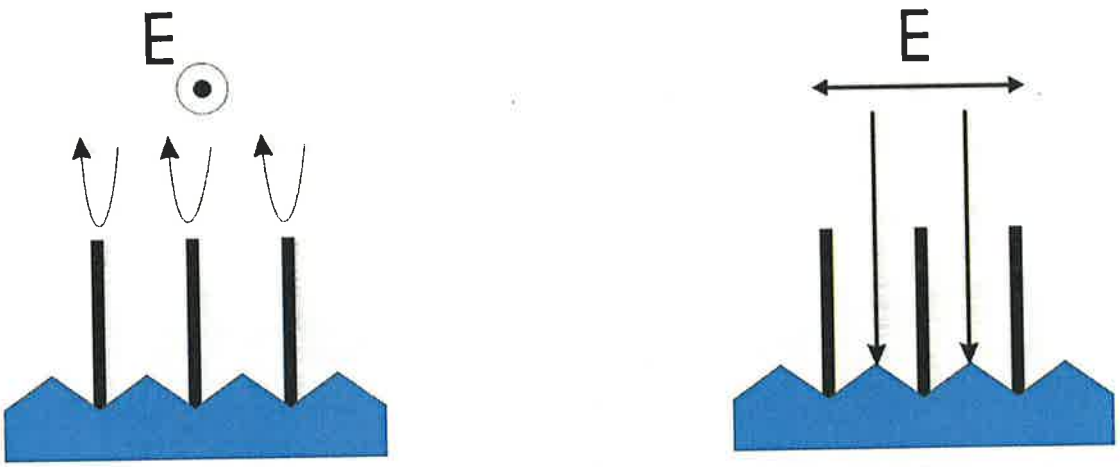

Figure 3-23 Scattering mechanisms from the corrugated parallel plate

When a vertically polarised wave encounters the target, the parallel plates have no effect and the wave passes through the structure to the RAM material where it is attenuated. A horizontally polarised wave, however, cannot penetrate the structure due to the cut off condition of the parallel plate waveguides and thus is totally reflected by the edge plates yielding a large RCS. This behaviour occurs for all frequencies below cut off ensuring that the structure is extremely broadband.

A corrugated parallel plate target was constructed to assess its suitability as a polarimetric calibrator. The structure consisted of twenty aluminium plates with dimensions illustrated in Figure 3-24.

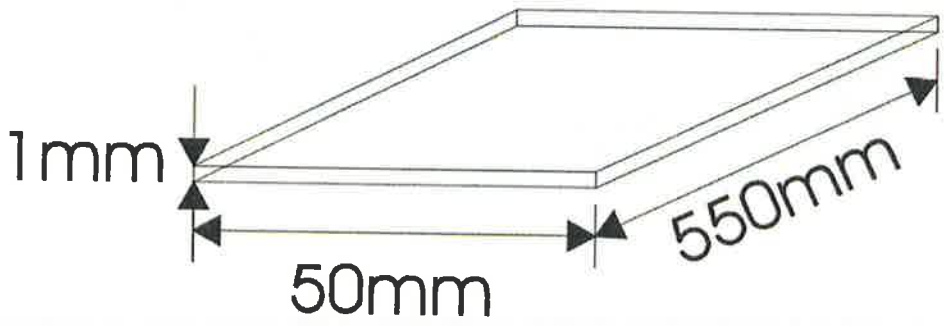

Figure 3-24 Plate dimensions

The plates were arranged such that the spacing between the parallel plates was 8 mm. In this configuration the theoretical cut off frequency of the parallel plate waveguides is approximately 18.75 GHz [236]. The plates were joined together using polystyrene strips positioned at the ends and at the centre of the plates. This ensured that the plate remained parallel and gave the structure sufficient strength and stability to be mounted on a foam column in an anechoic chamber. The plates were then attached to a 600 × 230 mm section of RAM, which provided 50 dB of attenuation for the frequencies of interest as shown in Figure 3-25.

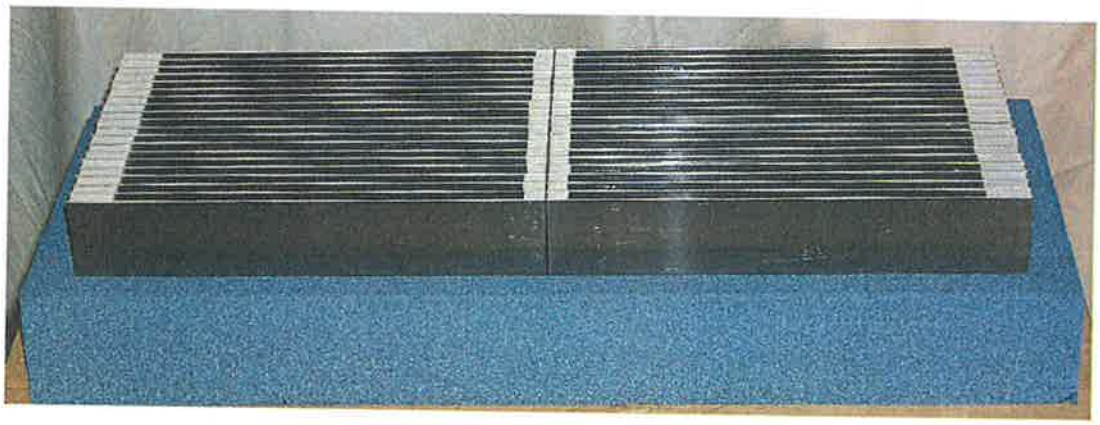

Figure 3-25 Parallel plate target

The calibrator was found to be unsuitable for field calibrations due to the difficulties in mounting and aligning the device accurately and low RCS values compared with a similarly sized trihedral or dihedral. Consequently, other calibration devices were investigated.

3.9.2 Trihedral calibration

While calibration using only a trihedral corner reflector only provides an estimate for the sum of the phase errors, field tests were performed to assess the consequences of ignoring the cross-talk and helicity phase errors on both the eigenvalue decompositions and polarisation signatures.

A number of trihedral targets were measured during the field trials. The first consisted of an array of four small trihedral corner reflectors arranged on a wooden structure shown in Figure 3-26. Each reflector consisted of a $89 \times 89 \times 89$ mm square trihedral with an RCS of 2.1 dBm^2 at 9.5 GHz, arranged such that each reflector is separated in height and range by a distance of 0.75 m.

Figure 3-26 Trihedral corner reflector array

This trihedral array is normally used in ground based RCS field trials to assist in the determination of the optimal antenna height. This process involves varying the antenna height so that the target return is maximised from the trihedral reflector that

best represents the scattering centre of the object to be measured. In the calibration studies described here, the antenna height was adjusted so that the return from the second reflector on the array was maximised, corresponding to a height of 1.5 m above the ground.

A typical range profile obtained from the array of corner reflectors is shown below in Figure 3-27. The profile was obtained using a stepped frequency waveform consisting of 256 frequencies, separated by 3.75 MHz, with a centre frequency of 9.5 GHz. This produces a 40 m range window with a range resolution of 0.15 m and ensures that the returns from the individual trihedrals in the array can be resolved.

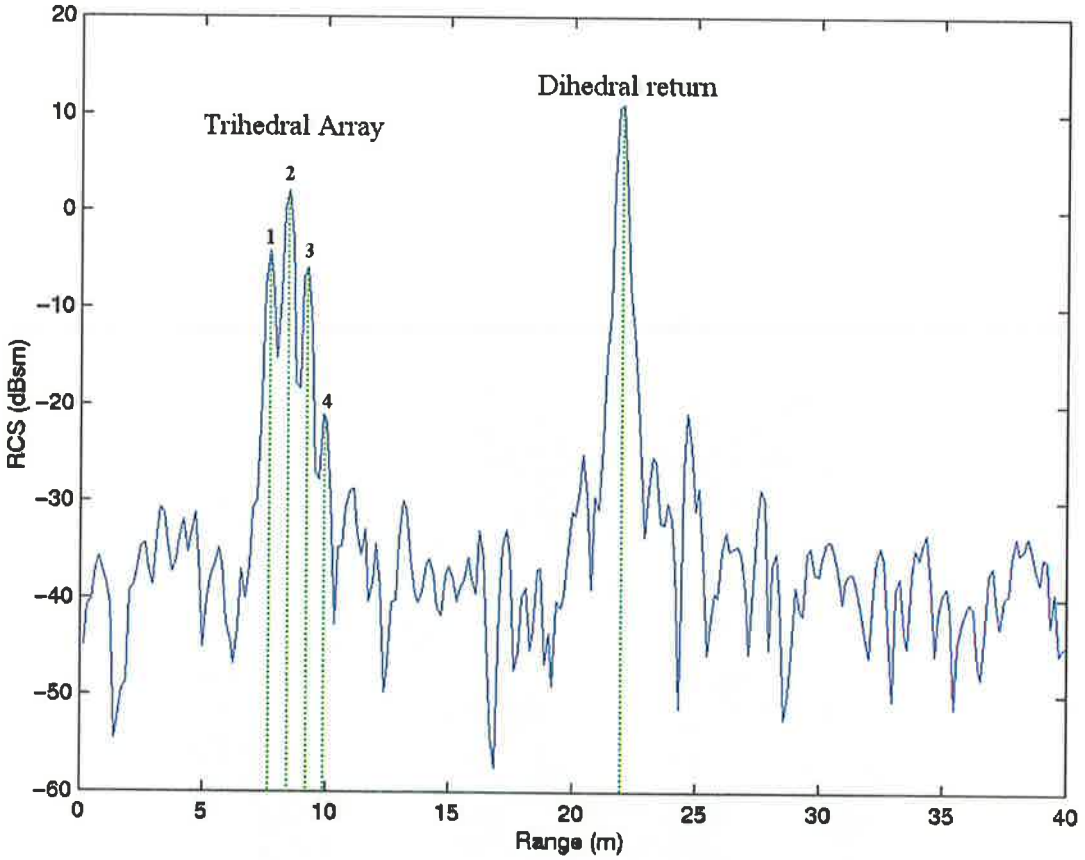

Figure 3-27 Range profile of the trihedral corner reflector array

The polarisation of the transmitted signal was varied on a pulse-to-pulse basis enabling the full scattering matrix to be obtained. The trihedral alone gives a good estimate for HH/VV phase estimation ($\delta_1 + \delta_2$) and enables radiometric calibration of HH/VV channels. The estimated HH/VV phase using the return from the second reflector in the array was found to be 166.5°.

The trihedrals used in the array were not precision made. To evaluate the influence that the manufacturing deficiencies might have on the estimate of the HH/VV phase, measurements were also performed on a precision made 305 × 305 × 430 mm triangular corner reflector shown in Figure 3-28. This reflector has an RCS of approximately 15.5 dBm^2 at 9.5 GHz and was mounted on a 1 m high foam pedestal support and was measured at a range of 450 m.

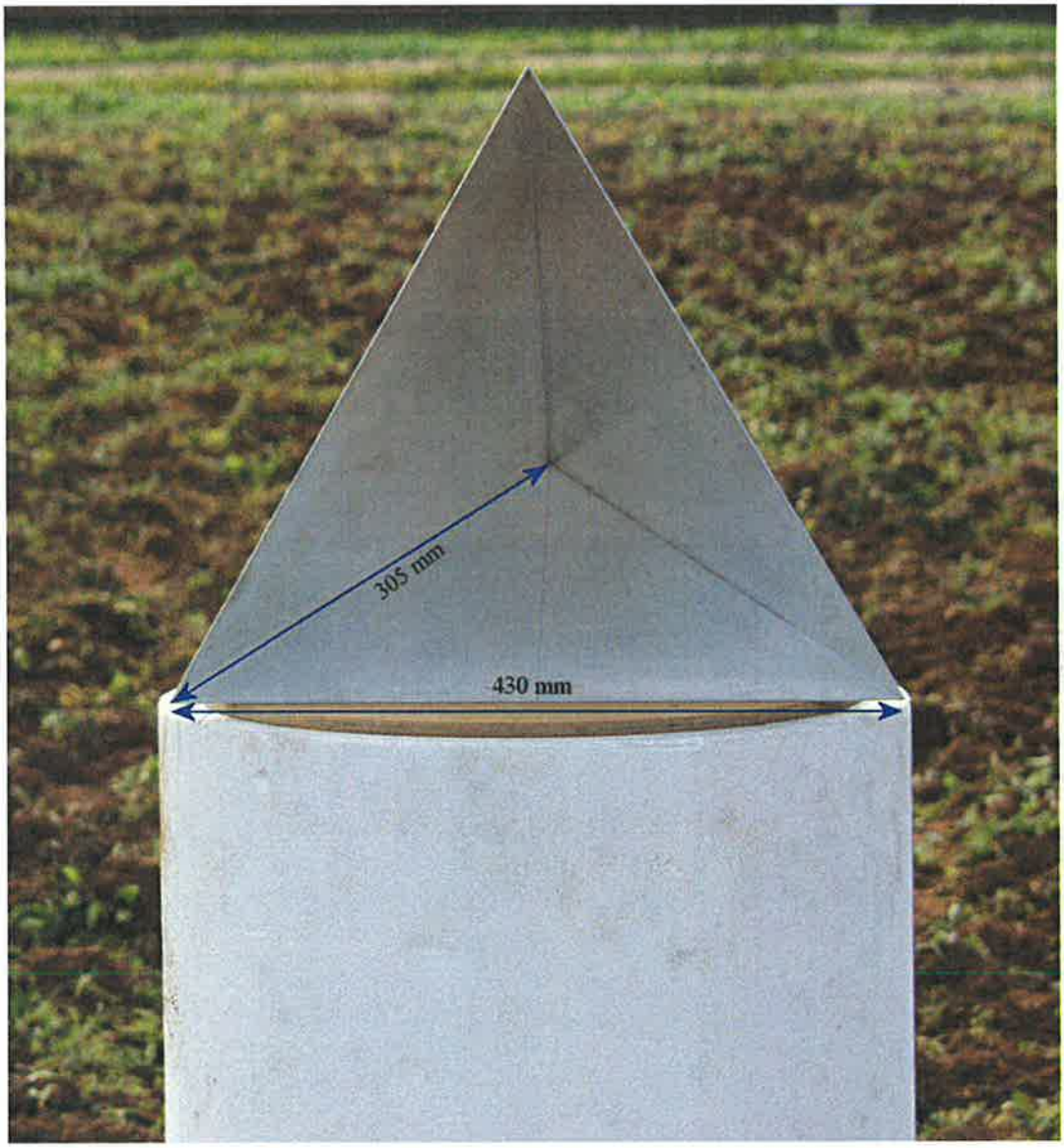

Figure 3-28 Triangular trihedral corner reflector

The reflector was carefully aligned with the radar antenna and positioned with a look-down angle of 35° to ensure that the maximum RCS was achieved. The estimated

HH/VV phase was determined again using the same technique that was used with the trihedral array and found to be 168°.

The previous two measurements were both ground-based measurements, performed on the outdoor antenna test range and hence are subject to multipath interference. To study the effect that this might have on the HH/VV estimates, further tests were performed with a trihedral corner reflector deployed in a small helicopter at a range of 2000 m and a height of 300 m to ensure that the multipath effect would be negligible. In this test a 400 × 400 × 400 mm square corner reflector was used, as shown in Figure 3-29. The reflector has a sighting scope attached that enables the holder to point the calibration device accurately towards the radar antenna. This reflector has been measured at the DSTO outdoor antenna test range and is known to have an RCS of 28.7 dBm^2 at 9.5 GHz.

Figure 3-29 400 × 400 × 400 mm Trihedral corner reflector

The range profile obtained when the corner reflector was deployed in the helicopter is shown in Figure 3-30. A single dominant return is observed which is 25 dB greater than the helicopter return. The phase difference between the HH and VV signals from

the range cell corresponding to the corner reflector was again determined and found to be on average around 168°. This is in good agreement with the trihedral array results.

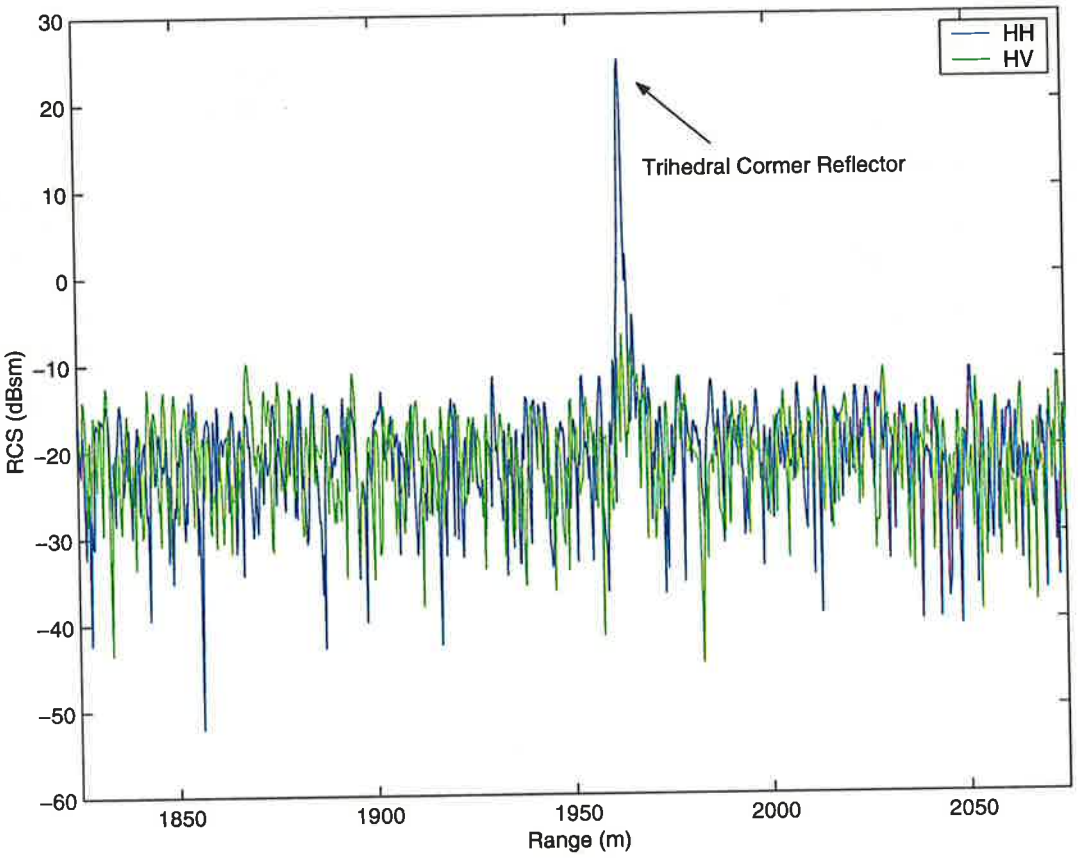

Figure 3-30 Trihedral corner reflector return deployed in helicopter

To illustrate the deficiencies of the trihedral (only) calibration technique, measurements of a rotating dihedral corner reflector were made and then calibrated using only the HH/VV phase correction terms. A dihedral corner reflector was chosen since the ideal behaviour is easy to model when rotated about the line of sight. A dihedral corner reflector (300 mm × 300 mm) was constructed and rotated using an electrical stepper motor shown in Figure 3-31. The rotating device is capable of varying the speed of rotation of the dihedral by varying the supply voltage. Measurements were performed with the dihedral rotating at a rate of 1° per second.

Figure 3-31 300 × 300 mm dihedral and stepper motor

The scattering matrix of an ideal dihedral, tilted an angle θ in the x-y plane can be modelled using an [S] matrix of the form [191]

$$S_{Dihedral(\theta)} = 2\sqrt{2\pi}\frac{ab}{\lambda}\begin{bmatrix}\cos 2\theta & \sin 2\theta \\ \sin 2\theta & -\cos 2\theta\end{bmatrix} \tag{3.28}$$

It is clear, from Equation (3.28) that the HH and VV phases will always be 180° out of phase while the cross-polar terms are in phase with the HH signal for angles ranging from 0° to 90° and 180° to 270°, and 180° out of phase with the HH return for angles between 90° to 180° and 270° to 360° as illustrated in Figure 3-32. Measurements of the rotating dihedral were made using the same waveform used in the trihedral measurements. The trihedral array was placed 10 m in front of the dihedral. The range cell containing the return from the dihedral was identified and then the observed [S] matrices were extracted from the measurements as the dihedral rotated through 360°. The uncalibrated phase relationships observed between the [S] matrix elements as the dihedral rotated are shown in Figure 3-33. The distortion in both the co- and cross-polar channels is clearly evident. The HH and VV signals are almost in phase, rather than being 180° out of phase, while the two cross-polar phases differ by about 70°.

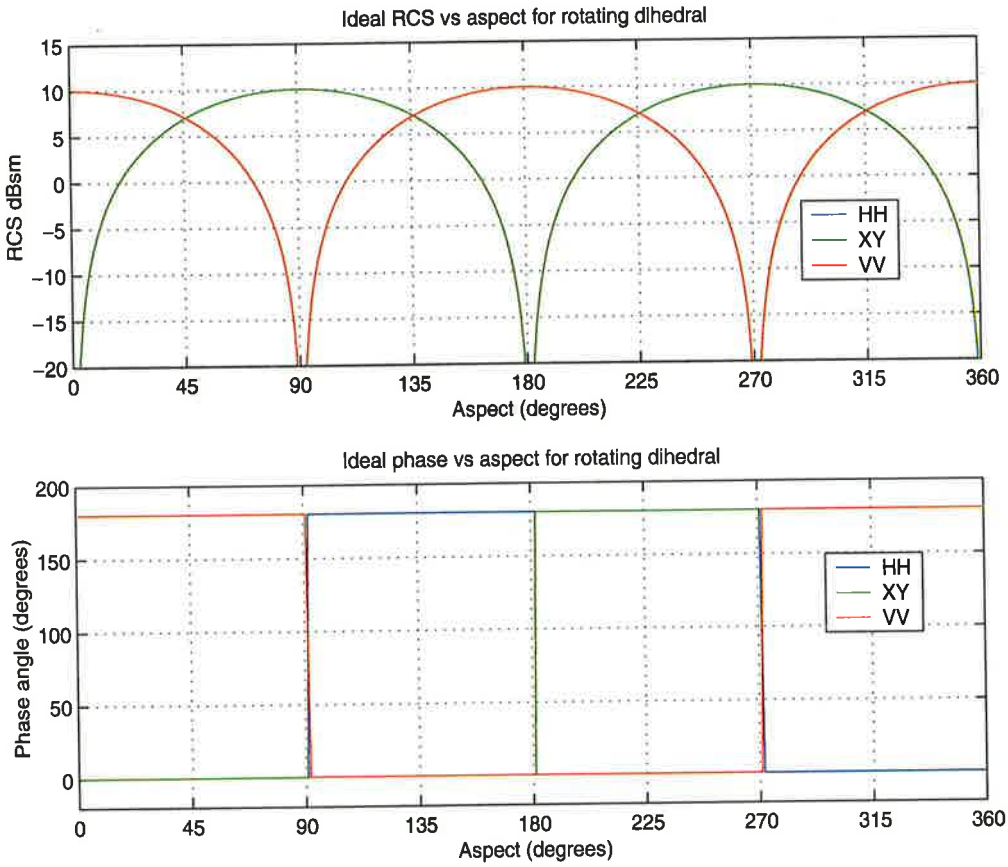

Figure 3-32 Phase and amplitude variations of an ideal rotating dihedral

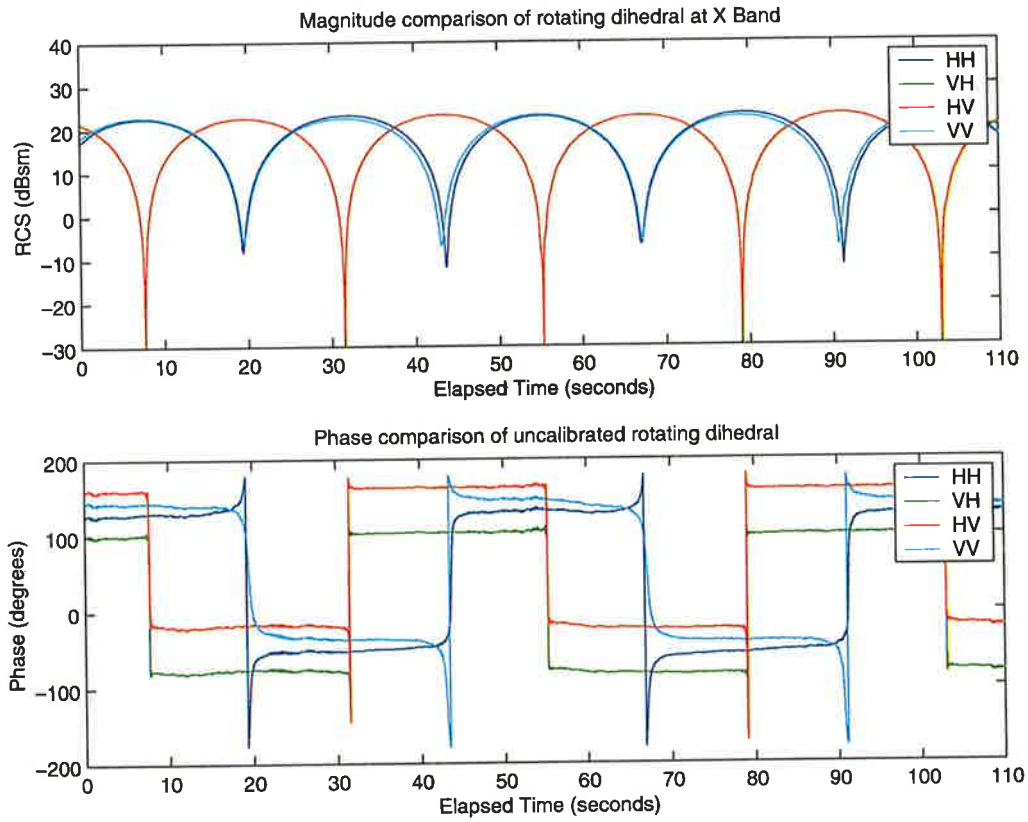

Figure 3-33 Uncalibrated phase returns from rotating dihedral

Applying the phase correction factor determined in the trihedral measurements yields the results shown in Figure 3-34. The HH and VV phases curves are now 180° out of phase but the relationship between cross-polar phase and the co-polar phases is still distorted. It is clear that if the trihedral (only) calibration was used that a phase error of approximately 35° would exist between the HH and HV channels. If uncorrected this error would manifest itself as helicity, and hence incorrectly suggest that the target is capable of producing elliptical polarisation from incident linear polarisation.

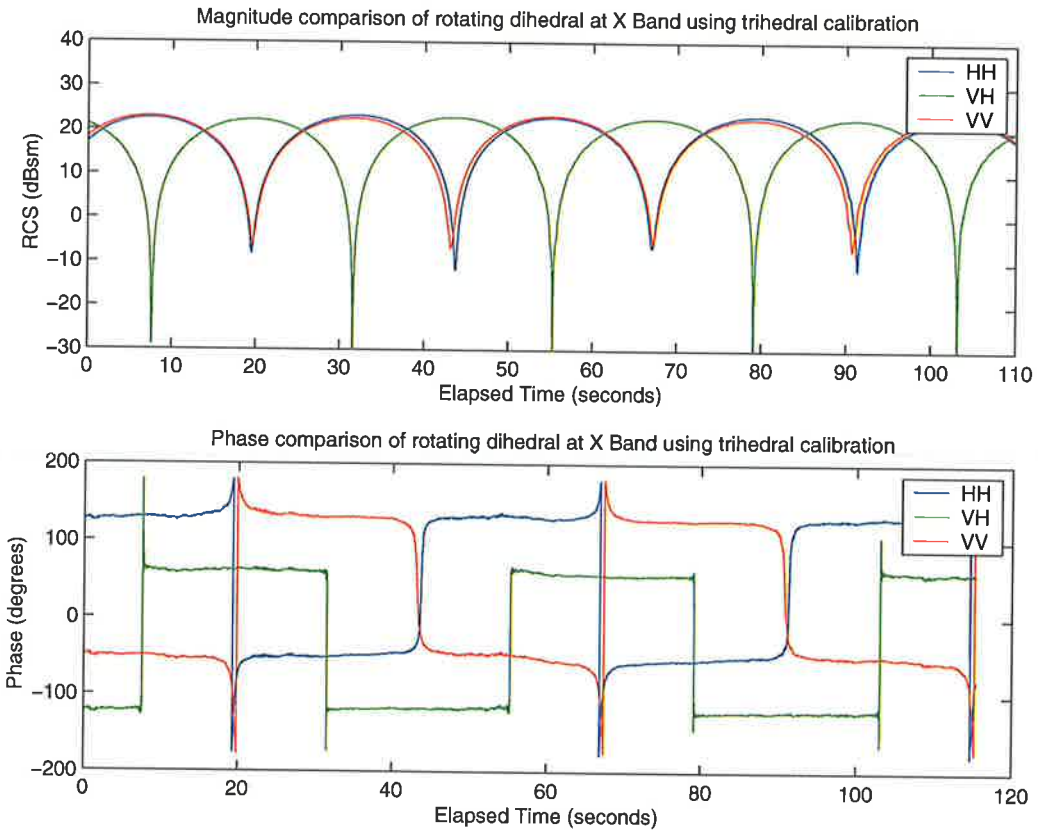

Figure 3-34 Calibration using only the trihedral information

The effect of the phase errors is illustrated by analysing the 3 × 3 coherency matrix described in Section 2.14.1. The 3 × 3 polarimetric coherency matrices $[T_3]$ were formed from the outer product of the Pauli scattering vector $\vec{k}_{3P}$ averaged over a 3×9 window. Eigenvalue analysis on the resulting $[T_3]$ matrices was performed and plots of polarimetric entropy (H), anisotropy (A) and scattering alpha ($\bar{\alpha}$) were produced. These are shown in Figure 3-35.

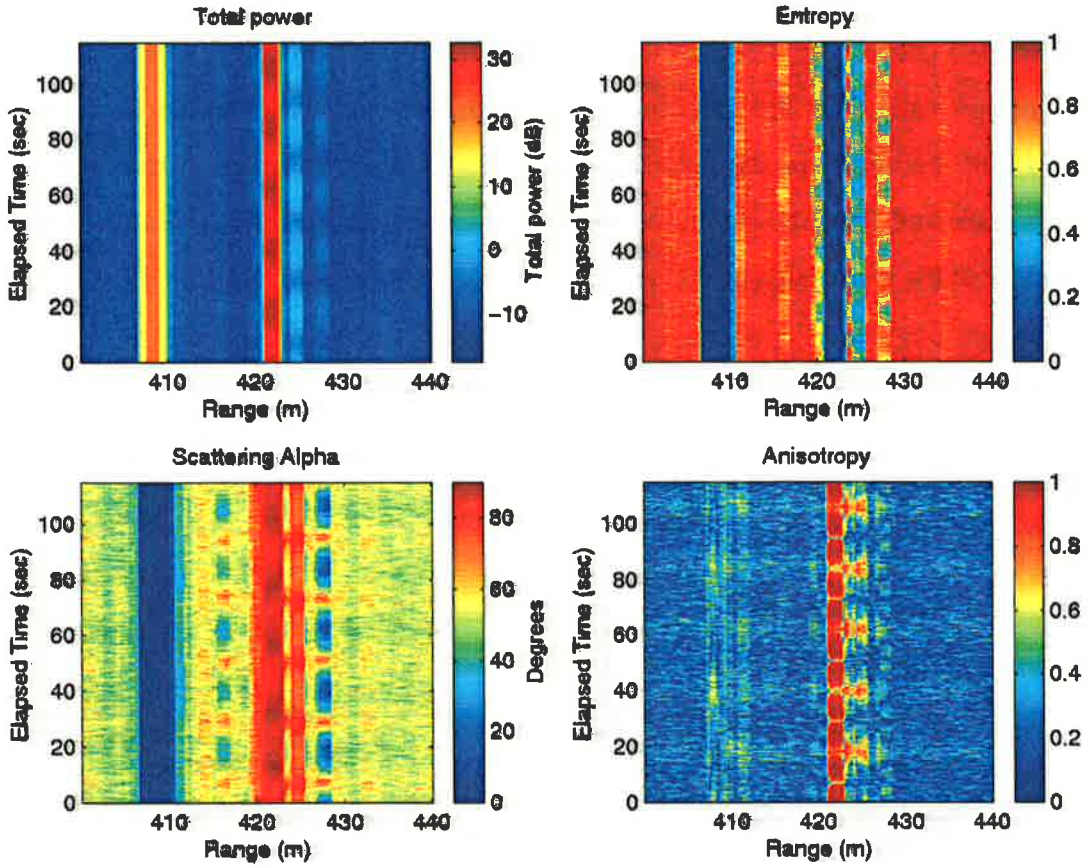

Figure 3-35 Calibration using only trihedral results

Figure 2-14 in Section 2.20 shows that the value of $\bar{\alpha}$ for a dihedral should be 90°, while the value from the trihedral should be 0°. Low entropy values would be expected in the cells corresponding to the trihedral array and the dihedral. As a result, λ_1 should be close to one while λ_2 and λ_3 two should be close to zero. Since only the HH/VV phase distortion has been accounted for, one would expect good results from the trihedral, since the off diagonal values of the [S] matrix will be small and thus the phase error between the co-polar and the cross-polar channels will have only a small influence on parameters derived in the polarimetric decomposition. In the case of the rotating dihedral, the influence of the HH/HV errors will become apparent when the co- and cross-polar returns are similar in magnitude and have less of an effect when. the co-polar return is significantly larger than the cross-polar return or vice-versa. As the dihedral is rotated about the LOS, the ratio between the co- and cross-polar values continually changes. At an orientation of 22.5° the co- and cross-polar returns should be equal, while at 0° and 45° the return in one of the channels is dominant.

Consequently one would expect a cyclical error pattern to be observed in some of polarimetric parameters. This is clearly evident in Figure 3-35 and Figure 3-36 where the entropy values for the dihedral varies almost sinusodially between 0 and 0.35. Significant variations in the anisotropy are also evident while the variation in $\bar{\alpha}$, which is derived from the eigenvectors rather than the eigenvalues, is relatively small and close to the ideal value of 90°.

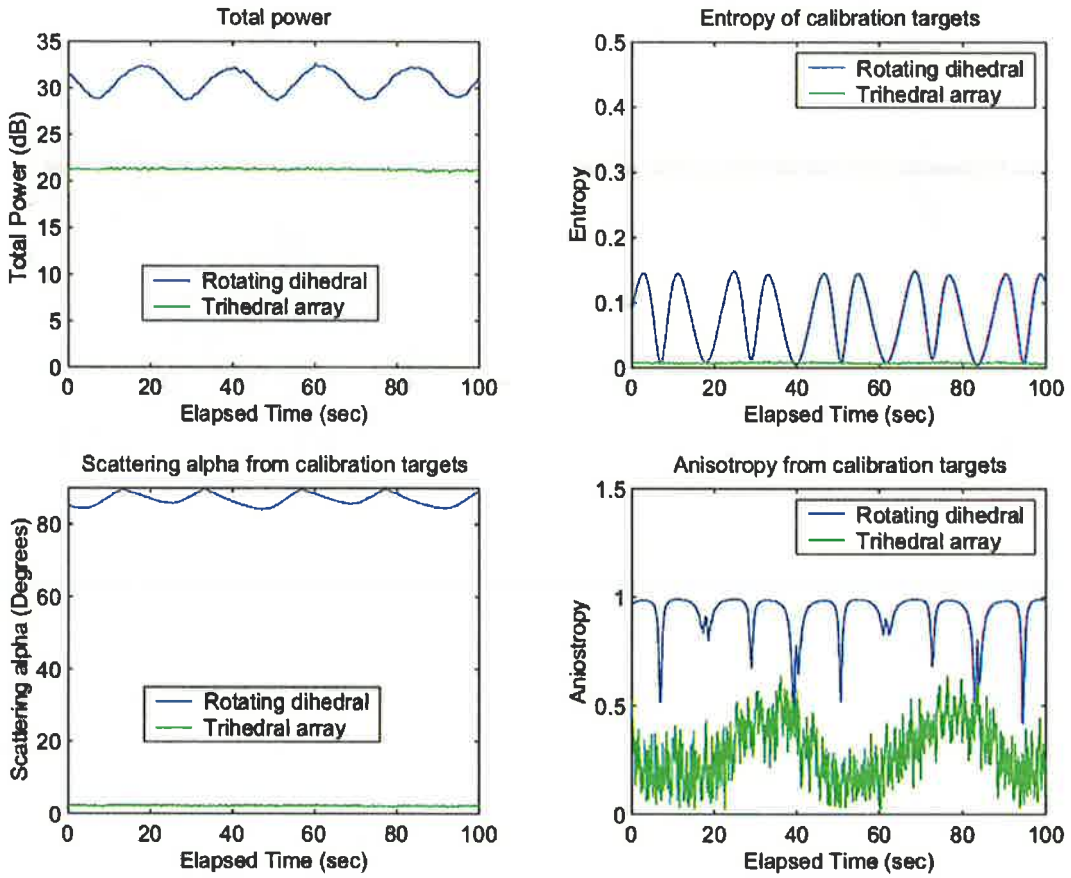

Figure 3-36 Comparison of the polarimetric parameters for the trihedral and dihedral

3.9.3 Dihedral calibration

The trihedral calibration results can be improved by incorporating measurements of a dihedral. Measurements of a dihedral rotated by 45° about the LOS enables an estimate of the difference in the phase errors ($\delta_1 - \delta_2$) to be obtained while the results from the trihedral provide an estimate for the sum of the phase errors ($\delta_1 + \delta_2$). The individual phase errors can be determined directly or via a least squares approach. Having determined the phase errors, the data can be symmetrised using Equation (3.16) and the VV channel can be calibrated using Equation (3.17).

Initially measurements of a dihedral at fixed orientations of 45° and 22.5° were used to determine the phase error terms. When rotated through 45° about the LOS an ideal dihedral has a scattering matrix of the form

$$[S_{45^\circ}] = \begin{bmatrix} 0 & 1 \\ 1 & 0 \end{bmatrix} \tag{3.29}$$

In this orientation the ideal dihedral yields a strong return in the cross-polar channels and zero return in the co-polar channels, however due to cross-talk, edge effects and alignment errors, the co-polar return will generally be non zero. When the dihedral is rotated about the LOS by 22.5° one would expect equally strong returns from all four channels and the scattering matrix will be of the form

$$[S_{22.5^\circ}] = \begin{bmatrix} 1 & 1 \\ 1 & 1 \end{bmatrix} \tag{3.30}$$

In this configuration the amplitude imbalances can be determined. The results of these measurements found that the δ_1 phase error value was 34° and the δ_2 phase error value was 135°. Applying the calibration correction factors to the measurements of the rotating dihedral described in the previous section gives the result shown in Figure 3-37. Comparison with the theoretical phase curves shown in Figure 3-32 shows that there is now good agreement between the two results. The coherency matrices were regenerated using the amplitude and phase corrections derived from the trihedral and dihedral measurements. The eigenvalue decomposition was recalculated and the new plots were produced showing the variations in the entropy, alpha and anisotropy for the cells containing the dihedral and trihedral targets. These results are shown in Figure 3-38. The effect of correcting for the helicity error between the HH and HV channels is evident in the entropy and anisotropy plots, which now yields superior estimates for both the dihedral and corner reflectors. Correcting for the helicity errors has only almost no effect on the $\bar{\alpha}$ values, which still vary from 85° to 90°. The best estimates are achieved when the co-polar return is largest and the entropy is lowest.

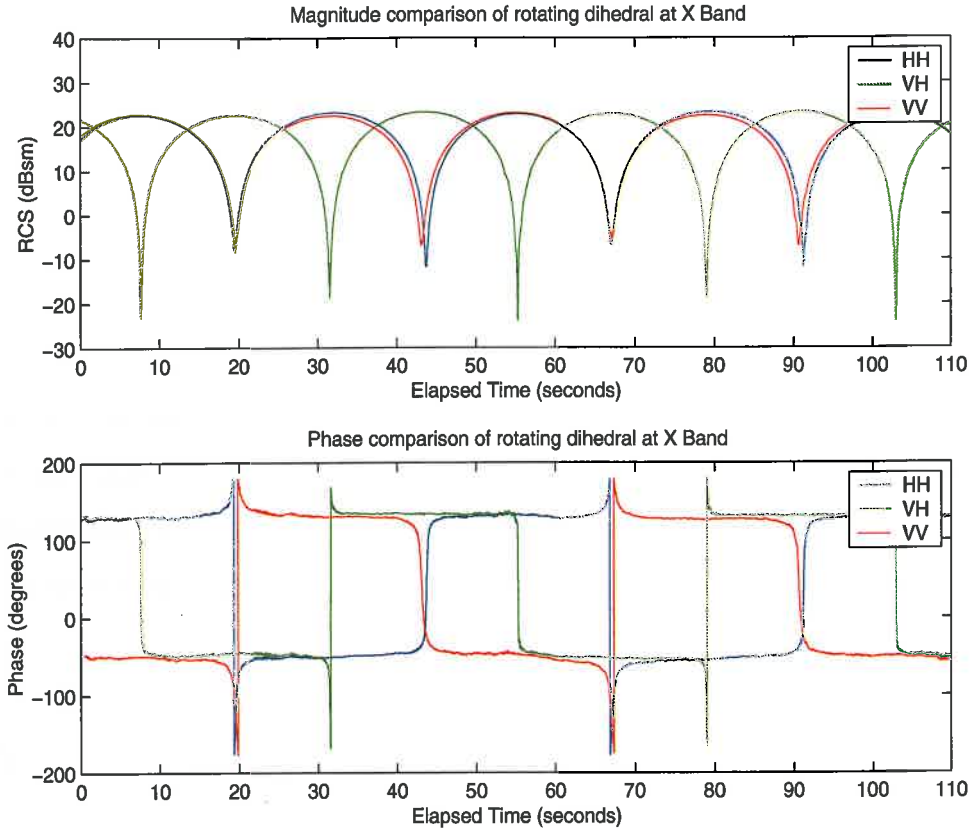

Figure 3-37 Calibrated rotating dihedral

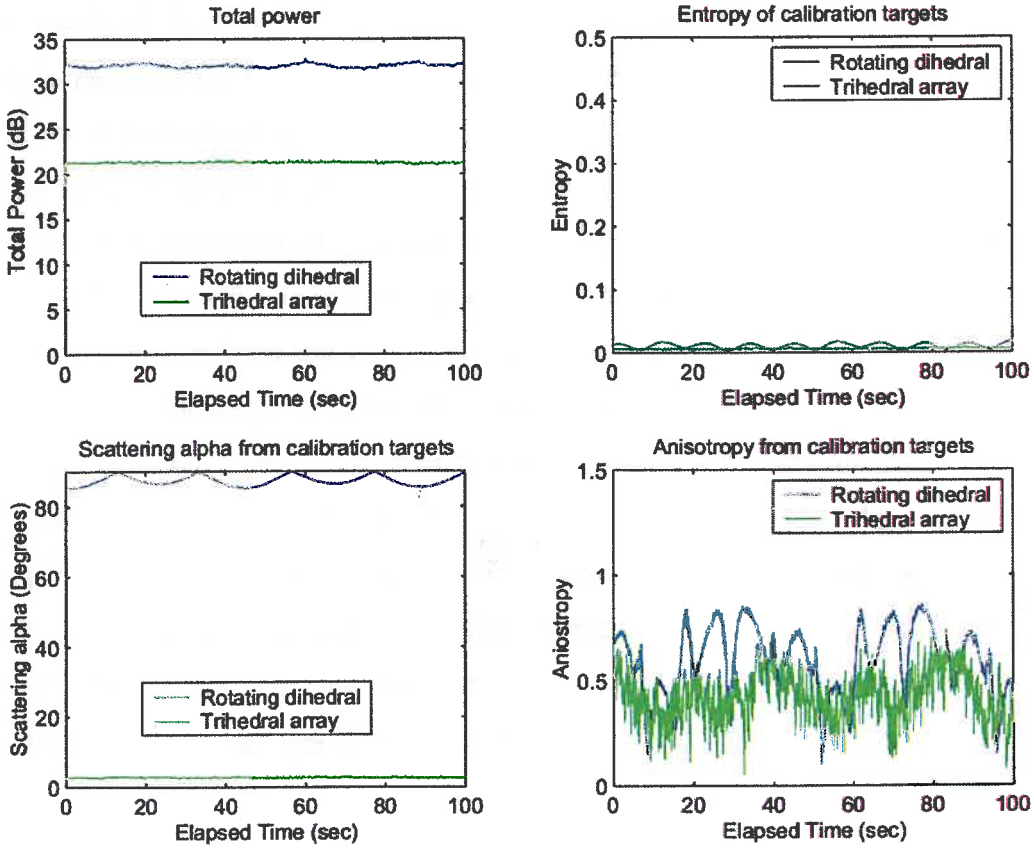

Figure 3-38 Comparison of the polarimetric parameters for the trihedral and dihedral

While the results obtained using the dihedral in the two fixed alignment orientations are good, there are practical issues that make such a calibration process difficult to implement in the field. The technique requires that the dihedral be accurately aligned and positioned for two measurements, which is relatively easy to accomplish with the desired accuracy in an anechoic chamber using positioning lasers, but in a field environment this more difficult.

The alignment problem was solved using a continuously rotating dihedral with measurements being accumulated over the full 360° as in the technique proposed by Muth [237]. The [*S*] matrix from the range cells containing the dihedral were extracted and histograms for the phase differences for the four channels were generated using HH channel as the reference phase. These histograms are shown in Figure 3-39.

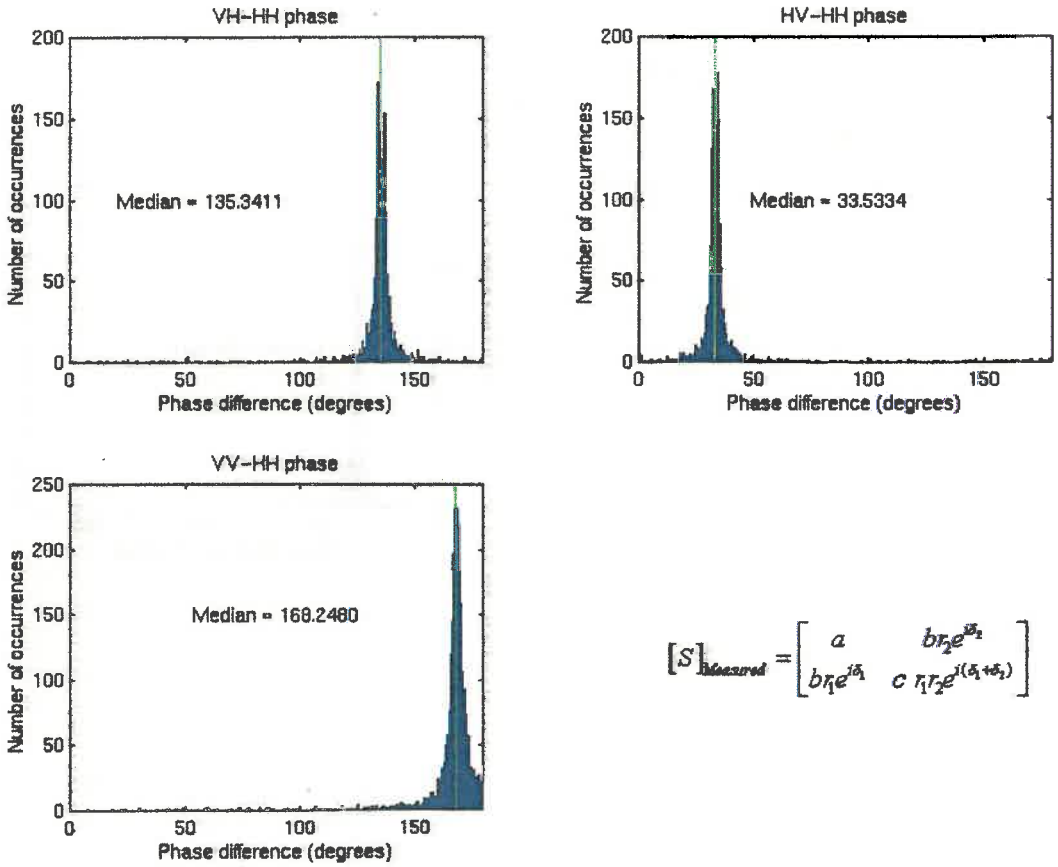

Figure 3-39 Rotating dihedral phase histograms

The median values for each histogram were calculated and provide direct estimates for the phase error terms. The results from the VH – HH and HV – HH phase histograms give estimates of the δ_1 and δ_2 phase errors while HH – VV phase histogram yields an estimate of the sum of the phase errors ($\delta_1 + \delta_2$). Using this technique the δ_1 error was found to be 33.5° while the δ_2 error was 135.3°, both of which agree with the static dihedral measurements. The ($\delta_1 + \delta_2$) phase error was estimated to be 168.2°, once again in good agreement with the value determined in the trihedral measurements. The histograms illustrate that there is a large spread of values, although the peak in the distribution is well defined. This can be attributed to poor phase estimates that result when the return in one of the receiver channels becomes very small. In these situations the estimate of the target phase becomes corrupted by system noise and other sources such as the return from the supporting structure. Accordingly, the results were filtered removing situations where the return in either channel was 30 dB below the peak values. This significantly reduced the spread of values with only a minor influence on the estimates of δ_1 and δ_2. The filtered results are shown in Figure 3-40.

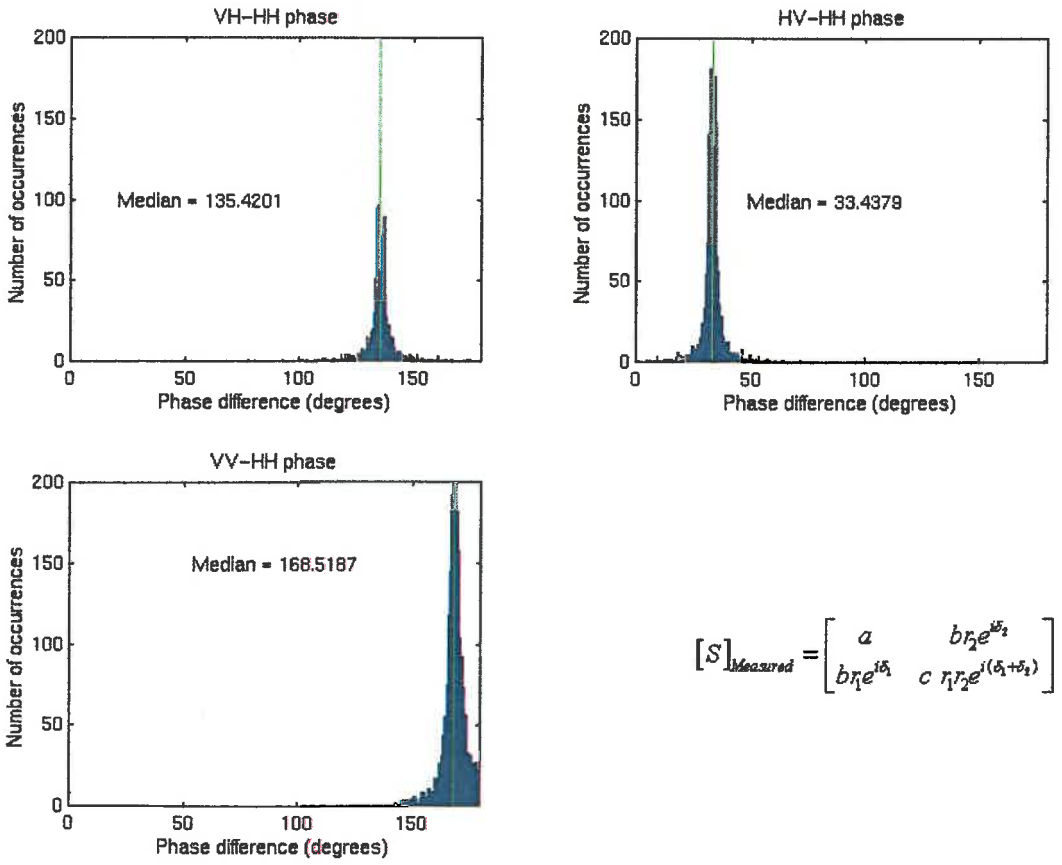

Figure 3-40 Filtered phase histograms

The revised estimates for the δ_1 and δ_2 errors were found to be 33.4° and 135.4°. Measurements with different frequency step sizes and numbers of steps showed that the phase errors were highly dependent upon the parameters used. Excellent repeatability of results was achieved between measurements across extended time periods indicating that the system has very good temporal stability. Nevertheless, phase calibration is performed prior to each measurement campaign to ensure that an accurate measure of the phase distortions introduced by the systems is maintained.

3.10 Delay line calibrator measurements

The results using the trihedral and the dihedral measurements confirm that good phase calibration can be achieved. Nevertheless, there is still the question regarding the effect that multipath interference has on the results. This issue was addressed using measurements from a dual delay line calibrator described in Section 3.2.11 deployed in a helicopter. Measurements were performed at a range of 1000 m and an altitude of 600 m ensuring that multipath effects did not influence the measurements.

Two alignment configurations were measured, the first with the H and V axes aligned with the radar and the second with the calibrator rotated around the LOS by 45°. In the first configuration the scattering matrices for the two delay lines are as follows.

$$S_{line1}^{0^0} = \begin{bmatrix} 1 & 0 \\ 0 & 0 \end{bmatrix} \quad S_{line2}^{0^0} = \begin{bmatrix} 0 & 0 \\ 0 & 1 \end{bmatrix} \tag{3.31}$$

The front line produces only a HH return while the second line yields only a VV return. This configuration facilitates radiometric calibration of the HH and VV channels (r_2/r_1) using the general calibration formulation defined in Equation (3.15), and gives a direct estimate for the cross-talk isolation of the system, but cannot provide HH/VV phase calibration. The ratio of the amplitude distortions was found to be around 0.6 dB (indicating good amplitude balance), while the channel isolation was observed to be better than 25 dB and at times exceeded 30 dB. A typical profile, illustrating the observed differences between the HH and HV range profiles in this configuration is shown in Figure 3-41.

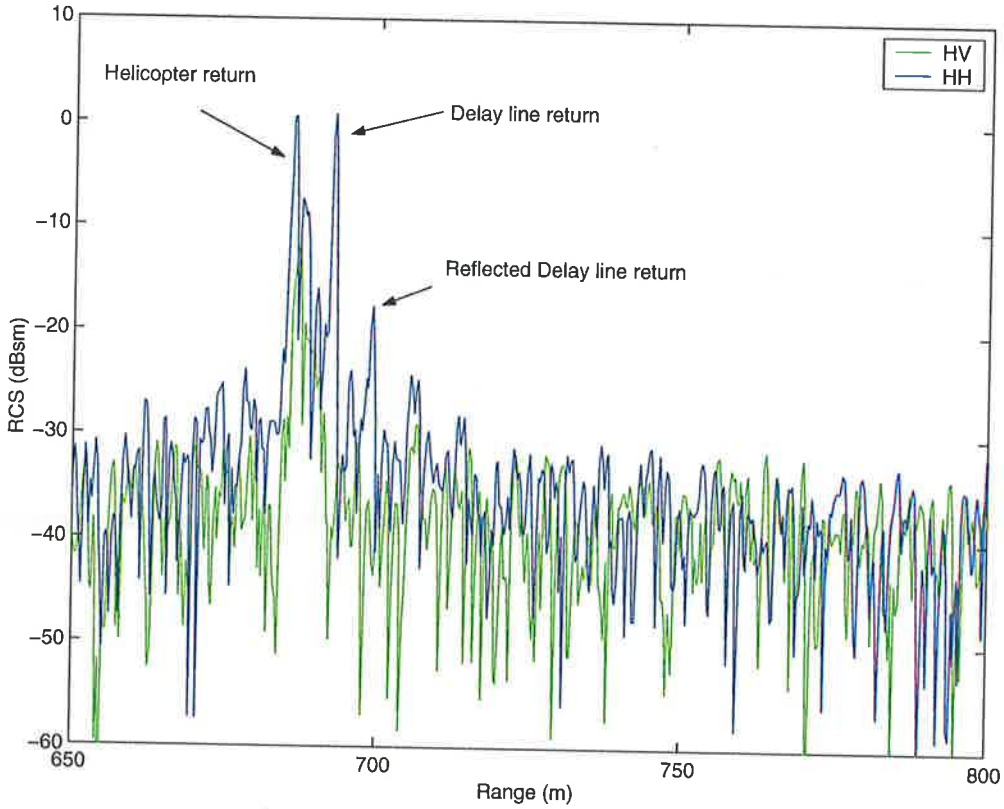

Figure 3-41 A typical range profile obtained with delay line calibrator

The return from the delay line is clearly separated from the helicopter return while the difference between the co-polar and cross-polar in the range cell corresponding to the calibrator illustrates the low cross-talk. A peak corresponding to a reflection in the delay line calibrator is also clearly evident and is delayed in range by twice the normal amount and is significantly attenuated.

In the second measurement configuration the calibrator is rotated by 45° degrees giving scattering matrices of the form

$$S_{line1}^{0^0} = \begin{bmatrix} 1 & 1 \\ 1 & 1 \end{bmatrix} \quad S_{line2}^{0^0} = \begin{bmatrix} 1 & -1 \\ -1 & 1 \end{bmatrix} \tag{3.32}$$

In this configuration the return from all four channels is strong enabling good amplitude and phase calibration. A typical range profile is shown in Figure 3-42.

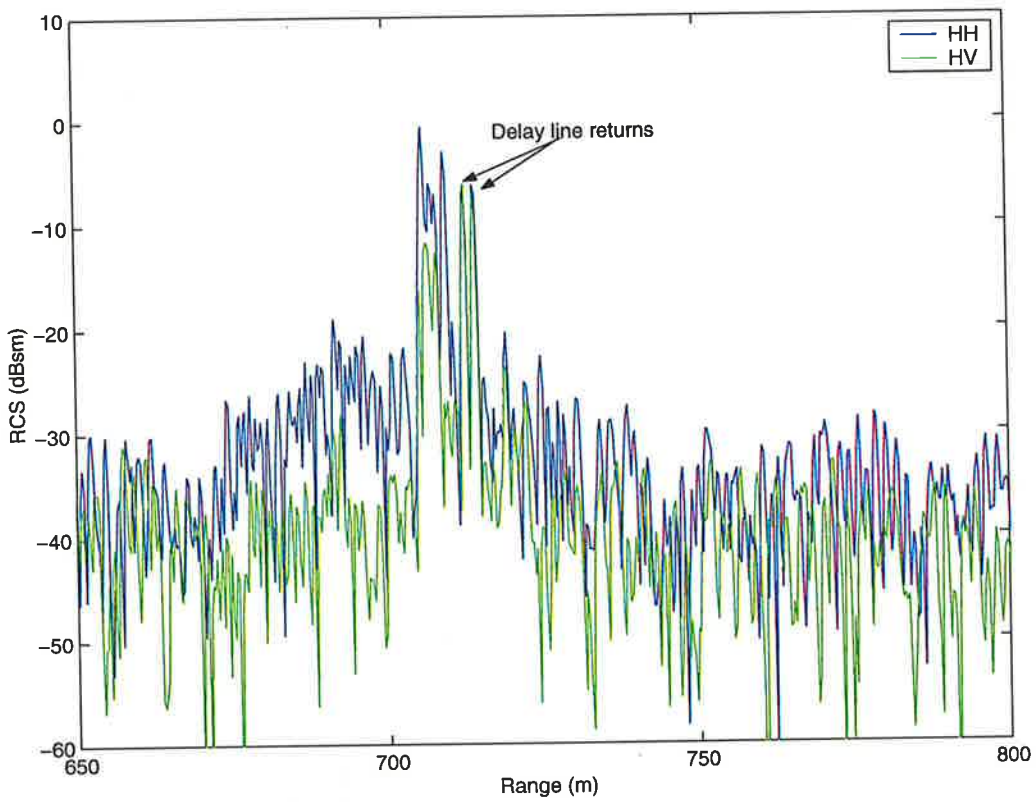

Figure 3-42 A typical range profile obtained with delay line calibrator held at 45°

The delay line calibrator has been measured in the DSTO anechoic chamber in both configurations and accurate values for the RCS values across the 8 – 18 GHz operating range have been obtained. The advantage of performing the radiometric calibration with the delay line calibrator is that the results are free from both interference caused by multipath and from interactions with the supporting structure since the return is well separated from the helicopter return. To determine the appropriate amplitude calibration factors, measurements of the delay line calibrator were collected for a period of 60 seconds. The return from the calibrator was then extracted from the recorded range profiles and the appropriate calibration factors for the four channels were determined in order to yield the same RCS values measured in the anechoic chamber.

When the delay line calibrator was designed it was hoped that both the radiometric and phase calibration could be achieved with one device. When phase calibration was attempted using the delay line calibrator a number of inconsistencies were observed. The sum of the phase errors $(\delta_1 + \delta_2)$ was found to be 155° for the front delay line

and 160° on the rear delay line. The phase difference $(\delta_1 - \delta_2)$, however was determined to be 140° for both the front and rear lines, which yields values of 7.5° (front) and 10° (rear) for δ_1 and 147.5° (front) and 150° (rear) for δ_2. Comparing these results with the previous measurements obtained from the dihedral and trihedral measurements where $(\delta_1 + \delta_2)$ was 168° and $(\delta_1 - \delta_2)$ was found to be 102°, it is clear that there is a significant discrepancy between the two results. The cause of this inconsistency was discovered when further tests were performed.

Ground based measurements of the delay line calibrator rotating through 360° were collected with the device mounted on the stepped motor used in the dihedral measurements as shown in Figure 3-43.

Figure 3-43 Rotating delay line calibrator

Range profiles were obtained using a stepped frequency waveform consisting of 256 frequencies, separated by 3.75 MHz, with a centre frequency of 9.5 GHz giving a range window of 40 m and a range resolution of 0.15 m. A typical range profile collected during the measurement is shown in Figure 3-44.

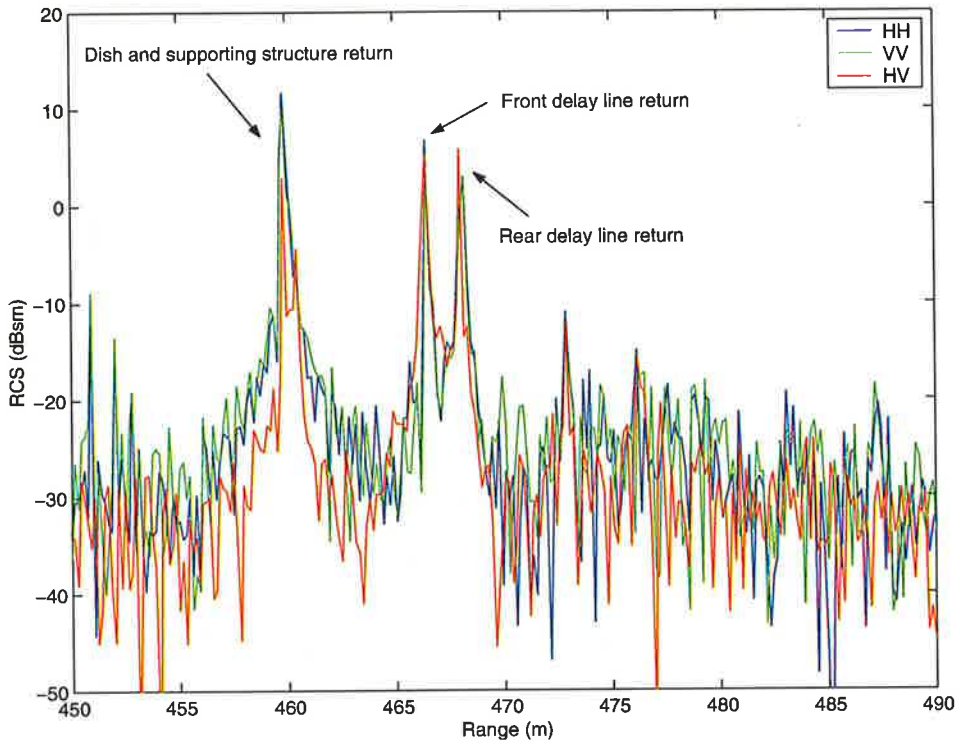

Figure 3-44 Range profiles obtained with the rotating delay line calibrator

The returns from the two delay lines were extracted from the range profiles and the scattering matrices were formed. Calibrated magnitude and phase plots were then generated using the phase correction estimates obtained from the rotating dihedral measurements and amplitude correction values derived from the delay line measurements with the calibrator deployed in the helicopter. These plots are shown in Figure 3-45 and Figure 3-46. The orientation dependence in the phase plots is clearly evident, especially in the case of the return from the second delay line where a significant offset exists between the HH and the VV phases for some orientations. Theoretically the HH and the VV phase returns should be the same, however, this behaviour is not observed. Experimental plots of the HH/VV phase of a rotating delay line calibrator show it to be a widely varying signal with 2π jumps at points where HH = VV = 0. This causes a rotation dependence of phase that makes calibration with such a device difficult. Results consistent with the trihedral and dihedral measurements can be obtained with careful selection of orientations of the calibrator. For example, if the orientation of the calibrator at an elapsed time of 65 seconds is selected, then the values of the δ_1 and δ_2 errors would be 32.5° and 134.2° respectively. Using measurements at an elapsed time of 40 seconds yields very similar

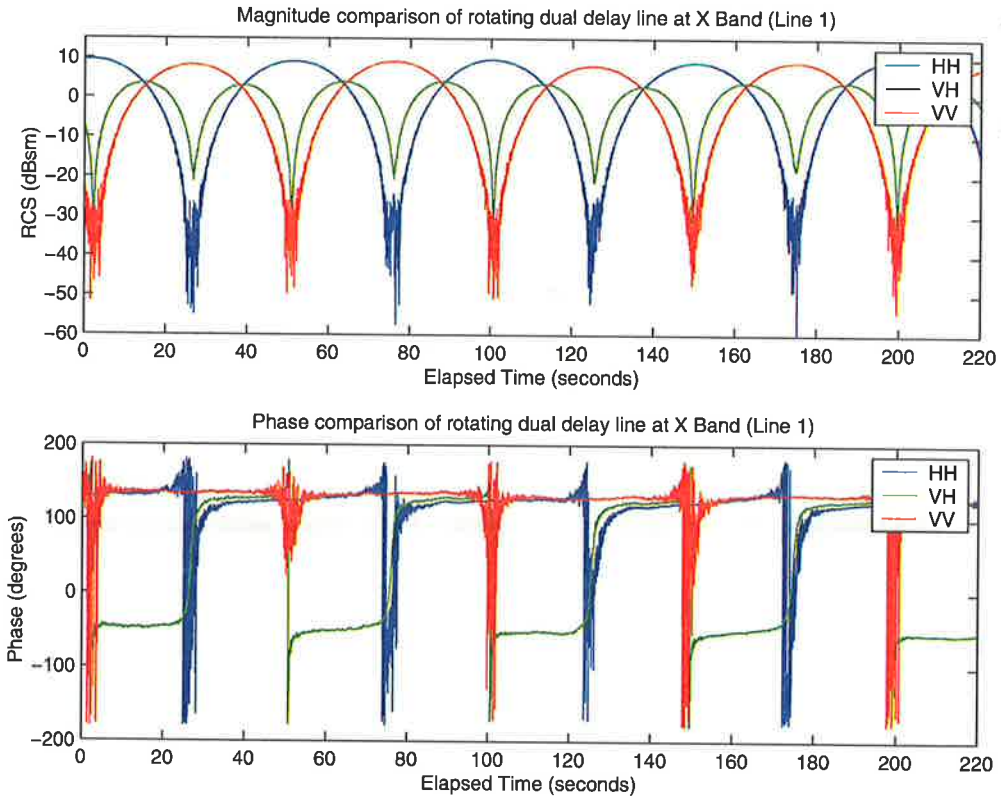

Figure 3-45 Magnitude and phase variation from line 1 on the dual delay line calibrator

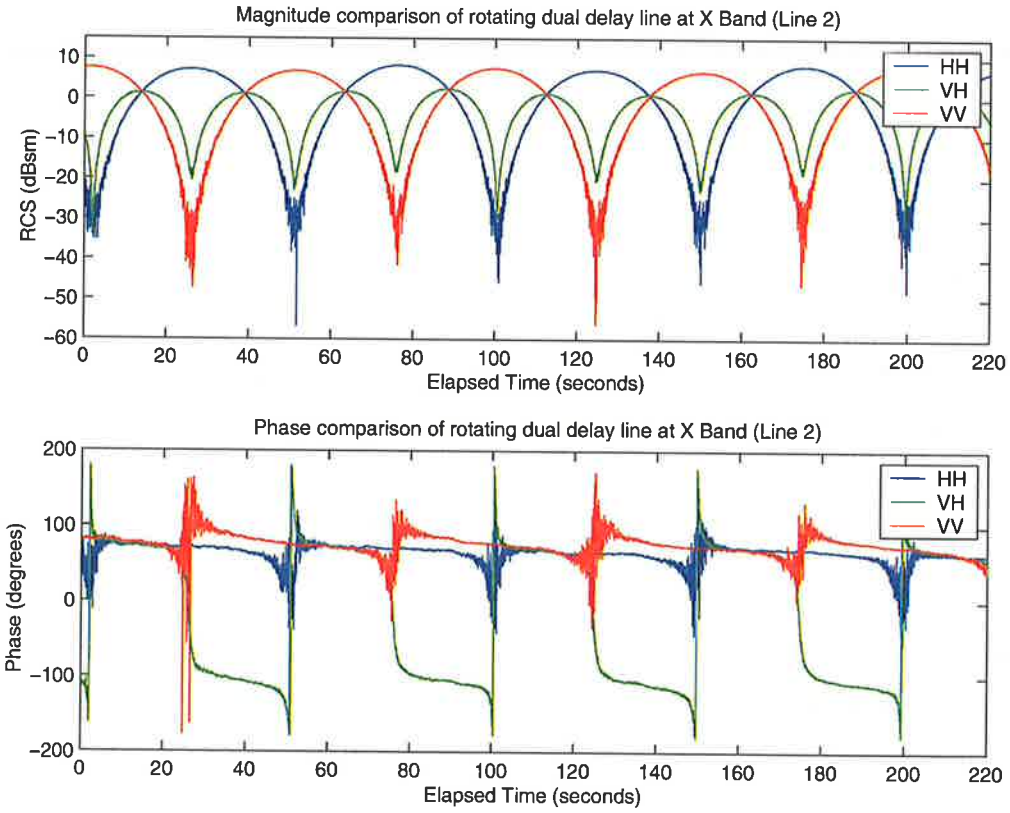

Figure 3-46 Magnitude and phase variation from line 2 on the dual delay line calibrator

results to those observed in the helicopter measurements and would result in helicity errors being introduced in the calibrated data. With careful selection of the orientation of the dual delay line calibrator good phase calibration can be achieved, however, the potential for introducing significant helicity errors is fairly high. Given the importance of accurate phase calibration, it was decided that measurements of the rotating dihedral measurements should be used instead. The median values found from the filtered histograms as shown in Figure 3-40 is the preferred approach.

3.11 Validation experiments

A number of validation measurements were performed to determine the accuracy of the calibration technique described in the previous section. Initially, additional analysis of the rotating dihedral measurements was performed. Comparisons of the calibrated and uncalibrated polarisation signatures were produced for dihedrals at a variety of orientations. The ideal polarisation signatures were generated from the [S] matrices obtained using the expression in Equation (3.28) for a variety of rotations about the LOS. An example plot is shown in Figure 3-47.

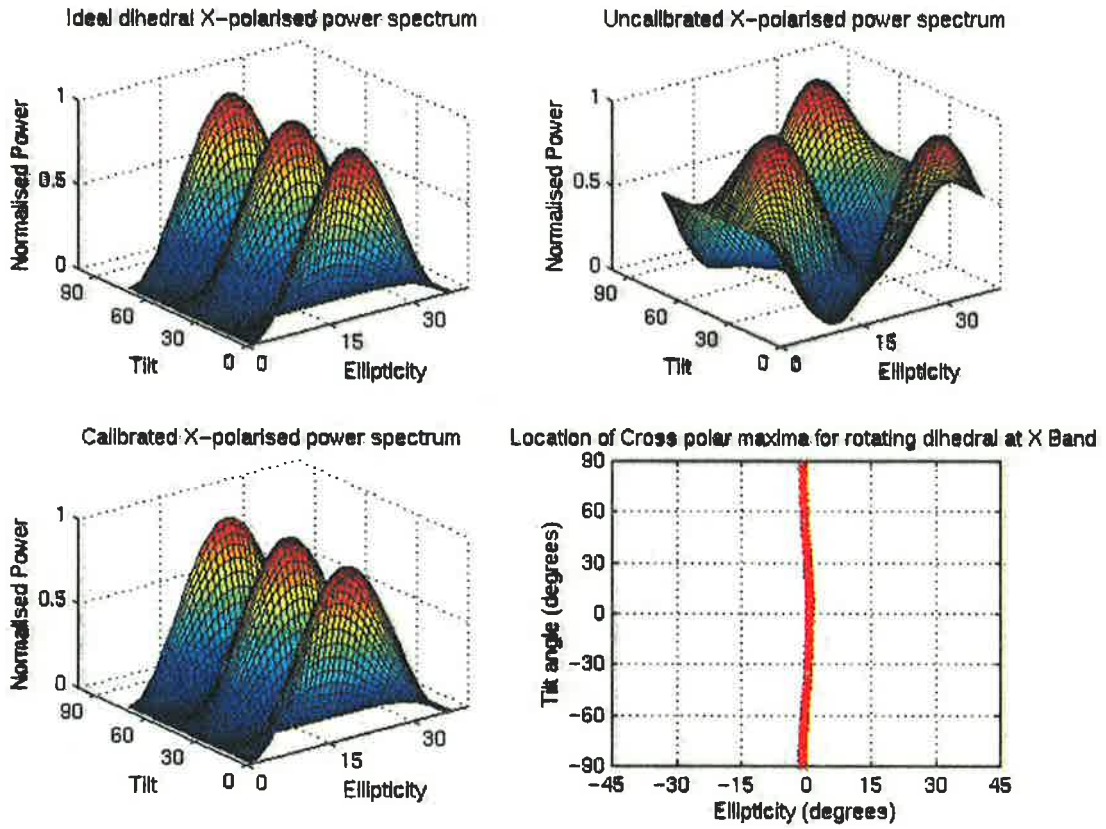

Figure 3-47 Comparison of dihedral polarisation signatures

Excellent agreement between the ideal and the calibrated signatures is achieved. To further illustrate the quality of the calibration, the locations of the cross-polar maxima were calculated for a complete 360° rotation of the dihedral at 1° intervals. Theoretically the location of the cross-polar maxima should lie on the line with ellipticity 0° and with a tilt angle corresponding the rotation of the dihedral about the LOS. From Figure 3-47 it is clear that the experiment and theoretical results were very similar with the ellipticity values for the cross-polar maxima ranging from –2.4° to 2.7°.

Additional tests were also performed using a trihedral and the delay line calibrator deployed in the helicopter. The received signals were range-processed and combined to form an estimate for the three-dimensional Pauli scattering vector for each range-time cell. The 3×3 polarimetric coherency matrices were then formed from the outer product of the Pauli scattering vector averaged over a 9×9 cell. The plots of the total power, polarimetric entropy (H) and scattering alpha ($\bar{\alpha}$) were then generated. The results of this analysis for the $400 \times 400 \times 400$ mm square corner reflector (shown in Figure 3-29) deployed in a small helicopter at a height of 300 m and a range of 2100 m are given in Figure 3-48.

The total power plot shows a single dominant return from the trihedral. The RCS of the trihedral is significantly larger than the helicopter and dominates the return. Low entropy values were observed in the range cells corresponding to the trihedral while high entropy values (close to one) were observed outside the target region. From Figure 2-14 and 2-15 it is clear that the value of $\bar{\alpha}$ for the trihedral should be close to 0° while in the high entropy regions a value close to 60° should be observed. The range cells containing the trihedral were extracted and the corresponding alpha values were plotted as a function of time. The values of $\bar{\alpha}$ varied between 1.9° and 5.1° during the measurement period. Ideally these values should be zero, although since the trihedral and helicopter are in the same range cell the helicopter return will have a small influence on the $\bar{\alpha}$ and entropy values.

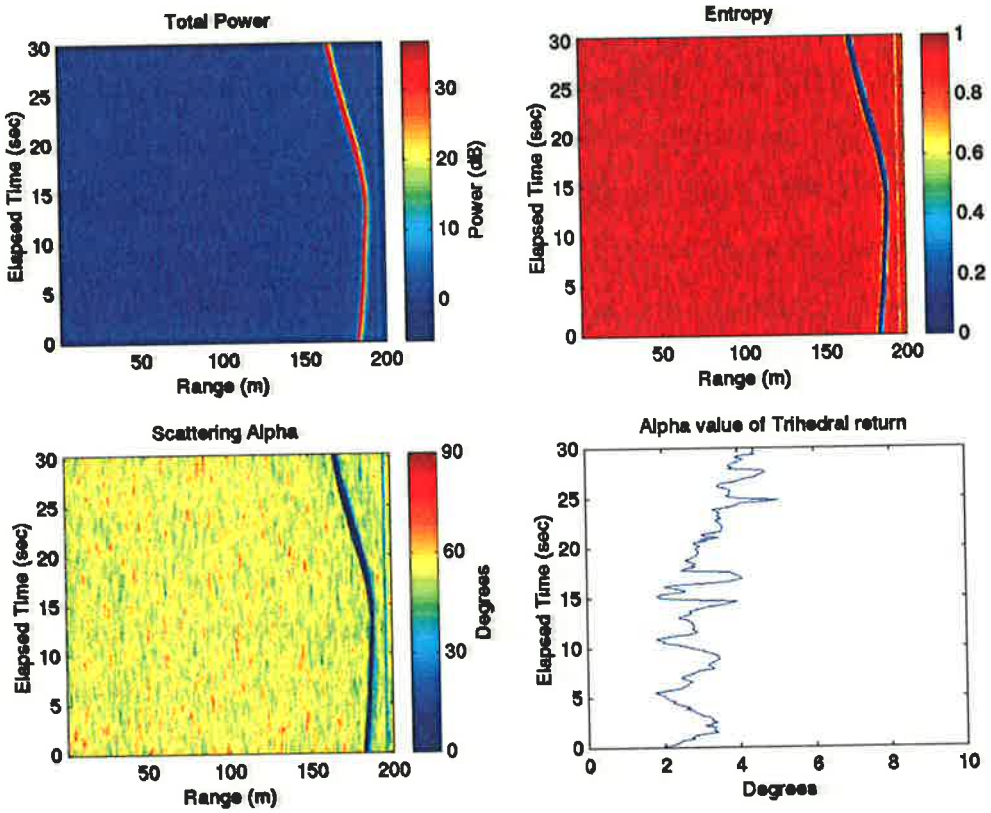

Figure 3-48 Polarimetric decomposition of a trihedral deployed in a helicopter

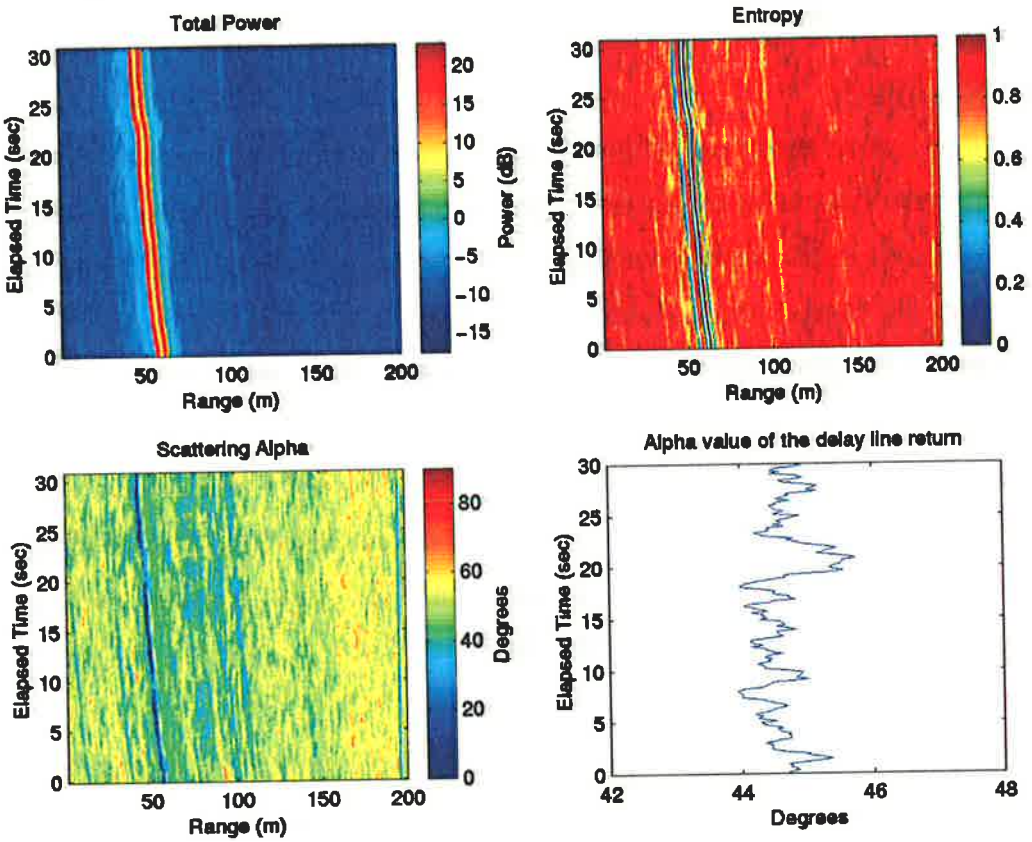

Figure 3-49 Polarimetric decomposition of the delay line calibrator deployed in a helicopter

To minimise the effect of errors introduced by the helicopter, additional measurements were also performed with the dual delay line calibrator, which separates the calibrator return in range from the helicopter return. Once again the received signals were range-processed and combined to form an estimate for the three-dimensional Pauli scattering vector from which the 3×3 polarimetric coherency matrices were then formed and averaged over a 9×9 cell. The results from this analysis are illustrated in Figure 3-49.

Two peaks are observed in the power plots, corresponding to the returns from the helicopter and the delay line calibrator. The range cells with the delay line return were extracted and the polarimetric parameters were plotted as a function of time. Low entropy values were observed in the range cells corresponding to the helicopter and the calibrator returns while high entropy values were found in the clutter regions. Theoretically, the value of $\bar{\alpha}$ for the delay line should be 45° due to its dipole like scattering behaviour (a strong return in only one element of the $[S]$ matrix). Alpha values ranging from 43.3° to 46.1° were observed confirming the quality of calibration process.

3.12 Synopsis

Calibration is an essential part of polarimetric measurements. A detailed examination of polarimetric calibration techniques based on the Barnes distortion model has been presented using matrix representations of the system distortions and the vectorised form of the $[S]$ matrix. An alternative formulation based on the Kronecker distortion matrix model has also been discussed. Methods for solving this system using active and passive point targets have been described while techniques using symmetrisation and the exploitation of the statistical properties of distributed clutter targets have also been presented. A range of common calibration targets have been discussed and the polarimetric properties have been illustrated with particular attention given to the suitability of these targets for field calibrations.

The steps taken in developing a robust, repeatable field calibration technique for the DSTO high resolution polarimetric radar system have been presented. The ratio of the amplitude distortions r_1/r_2 was found to be around 0.6 dB (indicating good amplitude balance) while the cross-talk was assessed using the delay line calibrator

and found to be around –27 dB. This inherently good system performance considerably simplifies the field calibration requirements and means that the only remaining parameters required for full polarimetric calibration are the transmit and receive phase imbalances δ_1 and δ_2. These were estimated from the rotating dihedral measurements and used to correct the data, assuming good temporal stability of the system. The outcome is that a novel calibration technique has been produced using a dual delay line calibrator and a rotating dihedral corner reflector. This formulation, based on a least squares matrix technique, permits the adoption of average calibration and symmetrisation procedures for quadpol single-look complex data sets. The results from field measurements demonstrate that phase errors of less than 4° have been achieved with channel isolation of 27 dB.

Chapter 4 DSTO high resolution polarimetric radar

The DSTO high resolution polarimetric radar system was developed in the late 1980's and has been progressively upgraded over the last fifteen years. In 1998, in order to support the research described in this thesis, the system was upgraded to enable collection of fully polarimetric data while maintaining sweep- to-sweep coherence. This chapter describes the current radar system, the hardware modifications that have occurred to support the work presented in this thesis and the software packages developed to implement the analysis and calibration techniques described in Chapters 2 and 3.

4.1 System specifications

The radar system is controlled by an Intel Pentium based personal computer. The new polarimetric mode increased the demands on both the data storage and processing requirements of the system and meant that a number of hardware upgrades were required. The original computer consisted of a dual Pentium motherboard fitted with Pentium 166 MHz processors and 64 MB of RAM. Data was written to 2 GB removable hard disks and processed offline. This has now been updated to a 1 GHz Pentium III processor with 512 MB of RAM and 60 GB of storage space. Data is written to recordable DVD-R or CD-R providing a flexible means of transferring results. Recently the video system has been updated from an analogue to a digital system allowing more accurate synchronisation between the radar sweeps and recorded video frames.

The radar system is mounted in a commercial van and can be powered by a petrol driven 240V 50 Hz single-phase generator. This enables testing to be performed in remote locations. Figure 4-1 shows the radar deployed on an RCS measurement trial. An overview of the main radar subsystems is shown in Figure 4-2.

Figure 4-1 The DSTO mobile high resolution polarimetric radar system

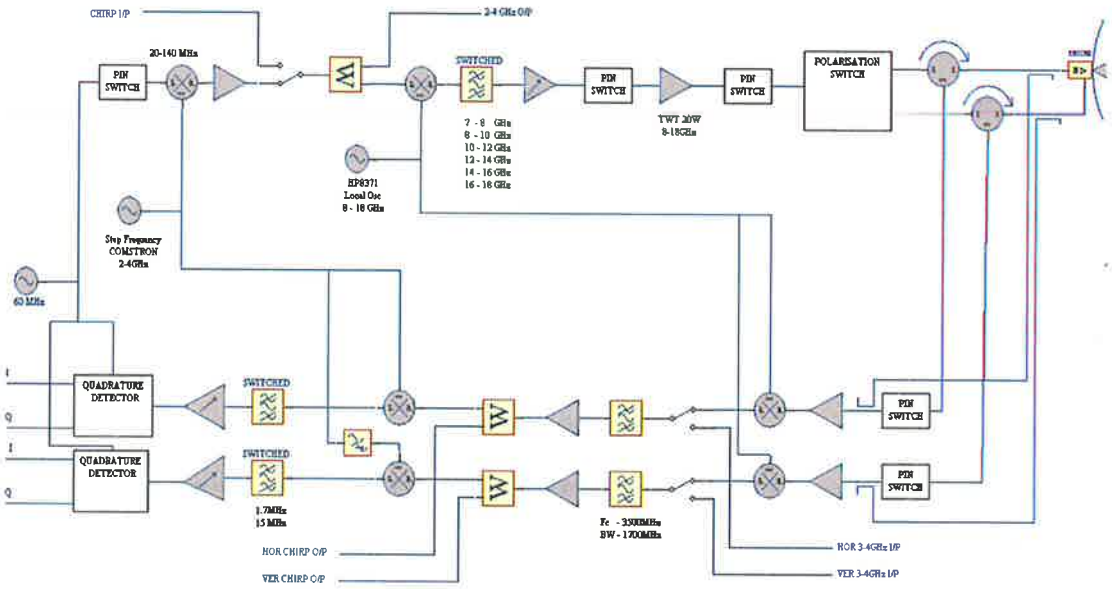

Figure 4-2 Overview of main radar systems

4.2 Transmitter

A programmable oscillator generates the local oscillator signal and provides a 10 MHz common phase and frequency reference signal that is used for the timing and data acquisition sampling signals within the radar. The local oscillator frequencies and the corresponding output frequencies are listed in Table 4-1.

Table 4-1 Relationship between the output frequency and the local oscillator frequency

Output Frequency (GHz)	Local Oscillator Frequency (GHz)	Filter Band
8 – 9	12	2
9 – 10	13	2
10 – 11	14	3
11 – 12	15	3
12 – 13	9	4
13 – 14	10	4
14 – 15	11	5
15 – 16	12	5
16 – 17	13	6
17 – 18	14	6

A Comstron frequency synthesiser is used to generate a CW signal in the range of 3.0 to 4.0 GHz. The radar computer digitally controls the Comstron through a dedicated parallel interface. The start frequency, frequency increment and number of frequency steps are used to generate a binary coded decimal (BCD) frequency array, which is written to the Comstron controller card. The elements of this array are generated using the following formula

$$Frequency(N) = \left| F_{Start} + (F_{Increment} \times N) - F_{Local} \right| - 60 \text{ MHz} \tag{4.1}$$

The number of frequency steps can be varied from 0 to 4096 and frequency increments of 0 to 100 MHz can be produced, subject to the restriction that the frequency range cannot exceed the filter bandwidth.

The output from the Comstron is fed to the up/down converter shown in Figure 4-3, where it is pulse-modulated by gating a 60 MHz signal applied to a single side band mixer. The signal is up-converted to the desired microwave frequency by mixing the signal with the local oscillator signal. The resulting signal passes through the microwave output conditioning circuit where is filtered and amplified to a suitable level to drive the travelling wave tube amplifier (TWTA). A single pole single throw (SPST) pin diode switch provides additional isolation between the TWTA and the up/down converter.

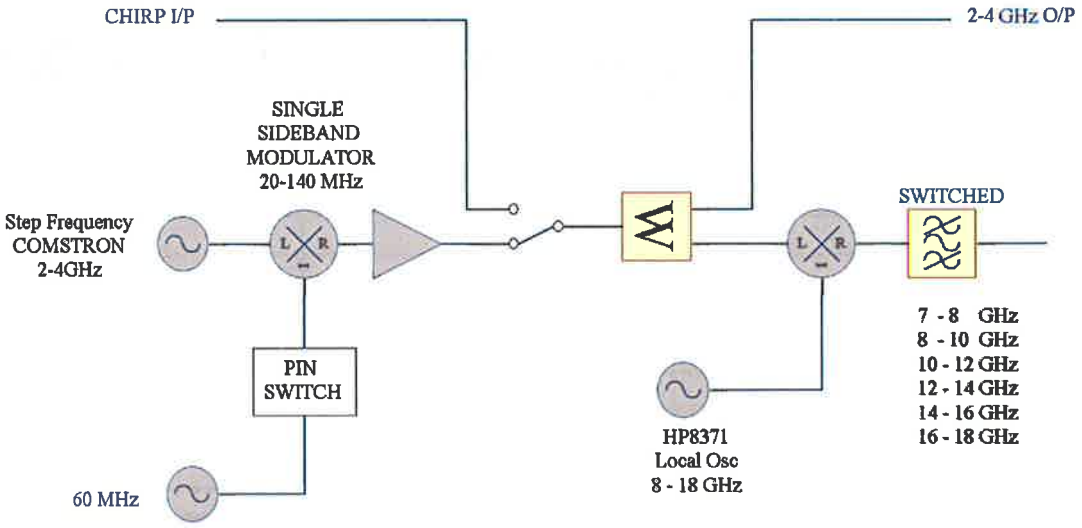

Figure 4-3 Up converter circuit

The signal is amplified in the TWTA giving 20 W peak pulses that are fed to the microwave head. The TWTA provides 55 dB of gain and has a noise figure of approximately 40 dB. The first stage of the microwave head consists of SPST pin diode switches that are used to isolate the transmitter during reception. The polarisation network (shown in Figure 4-4) follows and determines the polarisation of the transmitted pulse.

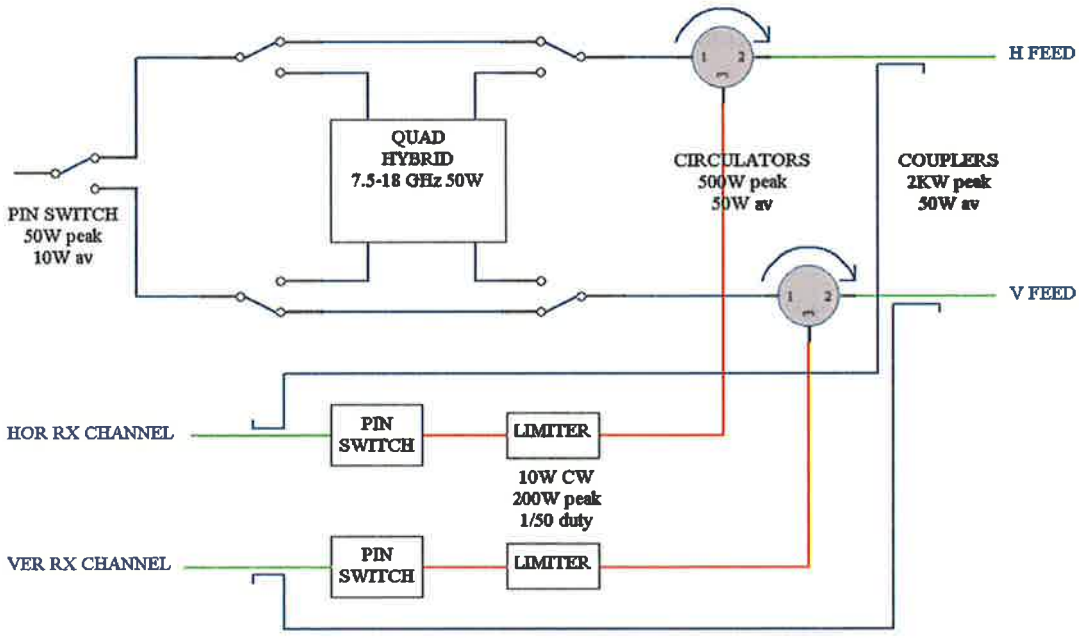

Figure 4-4 Polarisation network

Currently linear horizontal, linear vertical, left and right circular polarisations can be generated. The signal is then radiated from the antenna system via a circulator and a directional coupler. The output from the microwave head is connected to the input feeds of the antenna system using two flexible waveguides.

4.3 Antenna

The antenna is mounted on a tripod mast (shown in Figure 4-5) that allows height adjustments and manual steering of the antenna in azimuth and elevation. A TECOM dual polarised parabolic dish antenna is used that can be operated from 8 – 18 GHz and has an effective aperture of 24 inches. The antenna beamwidth and gain varies from 4.2° and 31 dB at 8 GHz to 2° and 36 dB at 18 GHz. A dual polarised, quad-ridged horn enables the antenna to simultaneously receive vertical and horizontal polarisations while providing greater than 20 dB of isolation between the channels with low phase and amplitude imbalance.

Figure 4-5 Antenna and tripod mount

The antenna elevation and azimuth is measured using a shaft encoder that has an angular resolution of 0.1°. These values are encoded as a BCD word and recorded for

each sweep. Tracking of targets is accomplished visually by sighting the target through a scope mounted on the side of the antenna. Provisions for mounting a digital video camera also exist and a variety of antenna mounting options can be implemented.

Recently the ability to operate the antenna remotely from a scissor lift has been added by increasing the cable lengths. Polarimetric measurements have yet to be performed in this new configuration but this will allow the possibility of investigating the polarimetric behaviour of scatterers over a much larger range of look down angles. However, it does introduce some new problems such as increased cable loss and greater susceptibility to phase changes caused by cable movements.

4.4 Receiver

The signals received by the antenna are fed via directional couplers and circulators into two identical receiver channels that measure the vertically and horizontally polarised components of the backscattered wave. The signals pass through a pin switch, directional coupler and microwave pre-amplifier before being mixed with the local oscillator signal yielding a 3 – 4 GHz signal. This signal is bandpass filtered and amplified before being fed to image rejection mixers located in the up/down converter shown in Figure 4-6. These mixers down-convert the signal to 60 MHz by mixing it with the signal from the Comstron oscillator. A digital phase shift can be added to the signal in the horizontal channel to account for phase imbalances in the receiver channels.

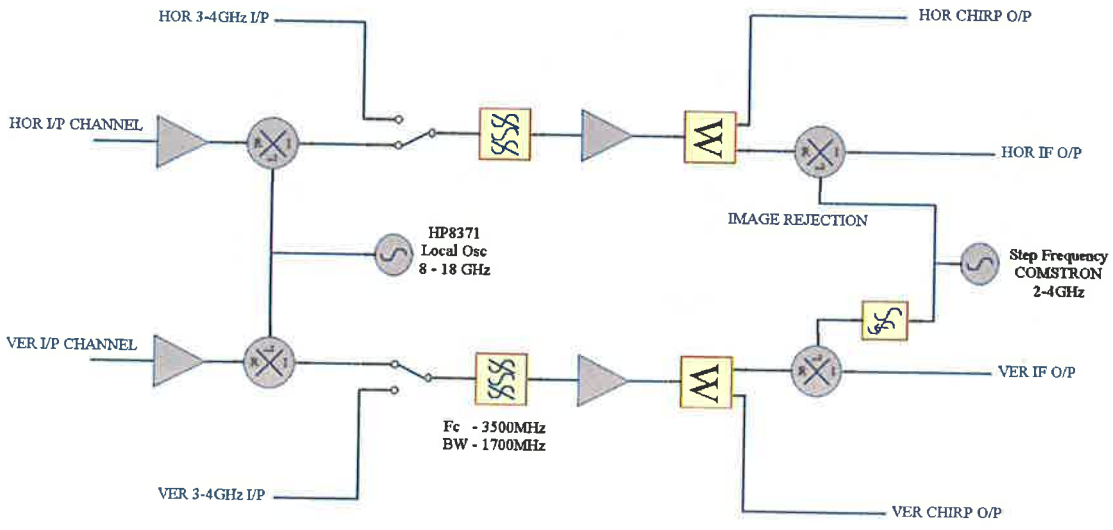

Figure 4-6 Down converter

The signals in the horizontal and vertical channels are fed into two identical 60 MHz IF strips (shown in Figure 4-7) where the signals are bandpass filtered and amplified to a suitable level for detection in 60 MHz quadrature detectors. These detectors produce I and Q outputs that represent the in-phase and quadrature components of the detected signals.

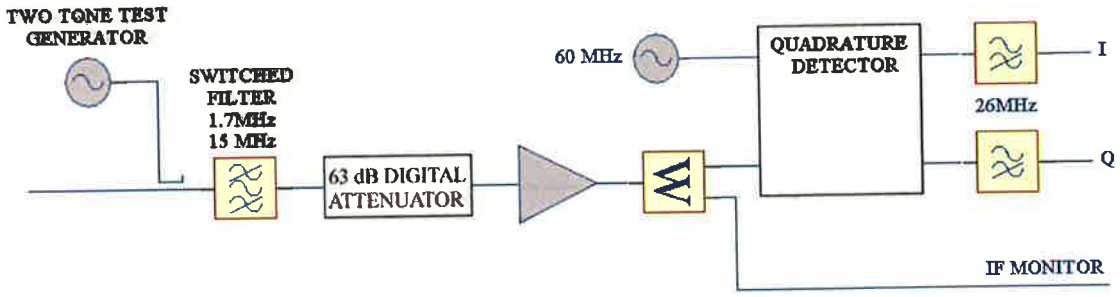

Figure 4-7 IF strip

During the radar transmit interval the receiver inputs are isolated from the circulator with pin switches. Samples of the transmitted pulses on the horizontal and vertical channels are fed into the microwave pre-amplifiers in the receiver channels via directional couplers. These signals travel through the receiver channels and are subsequently detected in the quadrature detectors. During the receive interval the pin switches connect the receiver input to the antenna circulator while the pin switches in the transmitter arm isolate the TWTA output.

4.5 Data acquisition and control system

The backscattered wave is recorded by simultaneously sampling the in-phase and quadrature outputs from the quadrature detectors on the two receiver channels. This is achieved using four 12-bit A/D converters. Pulses derived in the radar timing and control circuits determine the conversion instant, while the radar computer controls the rate at which the data is saved. The data rate is specified in sweeps per second and timing calculations are performed assuming that all the sweeps are saved regardless of whether the data is saturated. An option exists to discard saturated data but may result in the achieved data rate being lower than the specified rate. The data rate has no effect on the rate at which sweeps are transmitted. The radar always transmits and receives sweeps at the maximum sweep rate which is given by

$$\text{Sweep Rate} = \frac{1}{\text{PRI} \times \text{Number of Steps}} \tag{4.2}$$

where PRI is the pulse repetition interval. The radar timing circuits use a 100 ns resolution and the transmitter sample (TX) and receiver sample (RX) positions can be fine trimmed using a tapped delay line arrangement that has taps at 7 to 91 ns in 12 ns steps. The relationship between the timing parameters for the transmitted and received pulses is illustrated in Figure 4-8 and the parameter ranges are shown in Table 4-2.

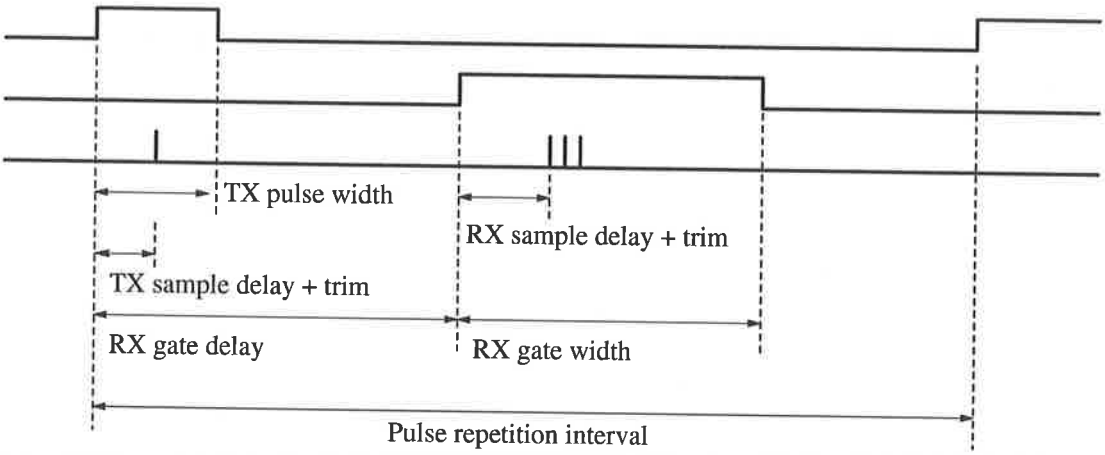

Figure 4-8 The relationship between the radar timing parameters

Table 4-2 Radar system timing parameters

Radar Input Parameter	Range
TX output power	–10 to +50 dBm
TX pulse width	0.1 – 25.5 μs
TX sample delay	0.1 – 25.5 μs
RX gate width	0.1 – 409.5 μs
RX sample delay	0.1 – 25.5 μs
Range	150 – 37000 m
Number of RX samples	0 – 255
TX sample fine trim	7,19,31,43,55,67,79,91 ns
RX sample fine trim	7,19,31,43,55,67,79,91 ns

Data acquisition, storing and processing can be broken into four major tasks that are listed below in order of priority:

Data capturing and pre-processing:

Read the data from the A/D boards and perform saturation and AGC analysis.

Data storage:

Write captured data to disk, inserting header and file breaks as appropriate.

Data processing and display:

Perform real time processing of captured data and display results.

User interface:

Update user interfaces and parameter displays to match the actual hardware settings and monitor control elements and respond appropriately.

Each of these tasks is an autonomous operation and is performed by separate threads in the radar van software. Data is passed between threads using a pipe mechanism and is read from the A/D converters at the end of each sweep. Results are written to the storage and processing threads in the form of a complete sweep. This allows each thread to easily determine where each sweep begins and ends. A sustained data recording rate of 650K/second can be achieved by the current system and for short periods of time, data rates of up to 850K/second can be accommodated. If the system is unable to keep up with the rate at which data is being captured, the data capturing thread will be blocked from sending data to the storage thread and sweeps will be discarded. Data is only written to the processing thread if there is sufficient room on the pipe for the whole sweep to be written.

Captured data is stored in binary data files. A maximum of 10,000 sweep records can be stored before the file is closed and another one is created. The files are numbered with the record number of the first sweep and an extension of either HOR (horizontal channel) or VER (vertical channel). Each data file starts with a file header that records information about the stepped frequency waveform such as the start frequency, frequency increment and number of steps. The sampling positions, transmitter and TWTA attenuation, polarisation settings and time and date information are also recorded in the file header. Each sweep record has its own separate sweep header that consists of the sweep number, time, range, receiver attenuation and the azimuth and elevation of the antenna.

4.6 Doppler mode

One of the problems associated with using stepped frequency waveforms with a large number of frequency steps is that it limits the radar's ability to perform Doppler

processing since the time between samples with the same frequency becomes large and results in aliasing problems. To address this problem a new waveform was proposed which consisted of a stepped frequency waveform interleaved with a constant frequency waveform thus allowing both Doppler and range profiles to be collected in the same radar sweep. Tests were performed with a person walking towards the radar carrying a corner reflector as shown in Figure 4-9.

Figure 4-9 Doppler mode testing

The waveform generated consisted of 256 frequency steps with a step size of 3.75 MHz interleaved with a constant frequency signal at the centre frequency of the first signal. The results were range and Doppler processed and the variations in the observed signals are shown in Figure 4-10. The strong return from the calibrator and the shift in the Doppler spectrum is clearly seen in both the HH and the VV images. The plot of the radial velocity versus time is shown in Figure 4-11. Initially the Doppler peak is seen at 0 m/s when the calibrator was still stationary. The peak return increases to 2.5 m/s after 5 seconds, reducing to 1.5 m/s after 15 seconds, before returning to 0 m/s at 30 seconds.

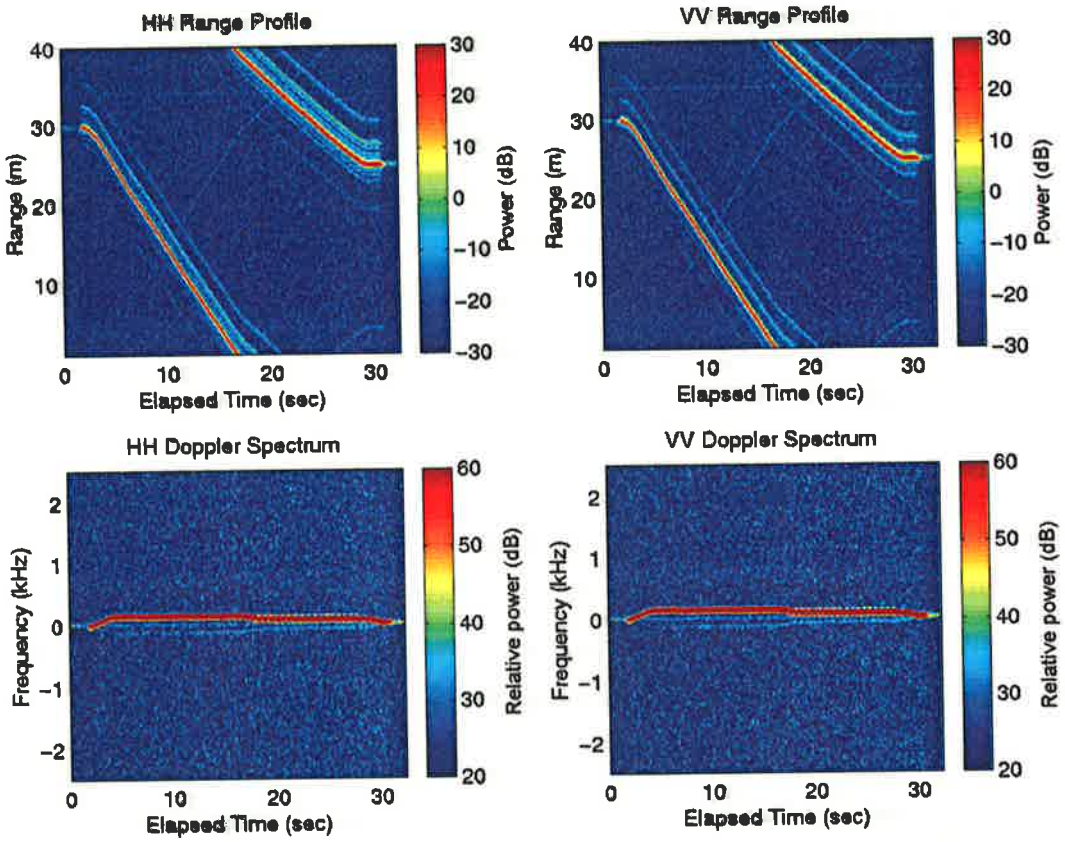

Figure 4-10 Range profiles and Doppler spectra

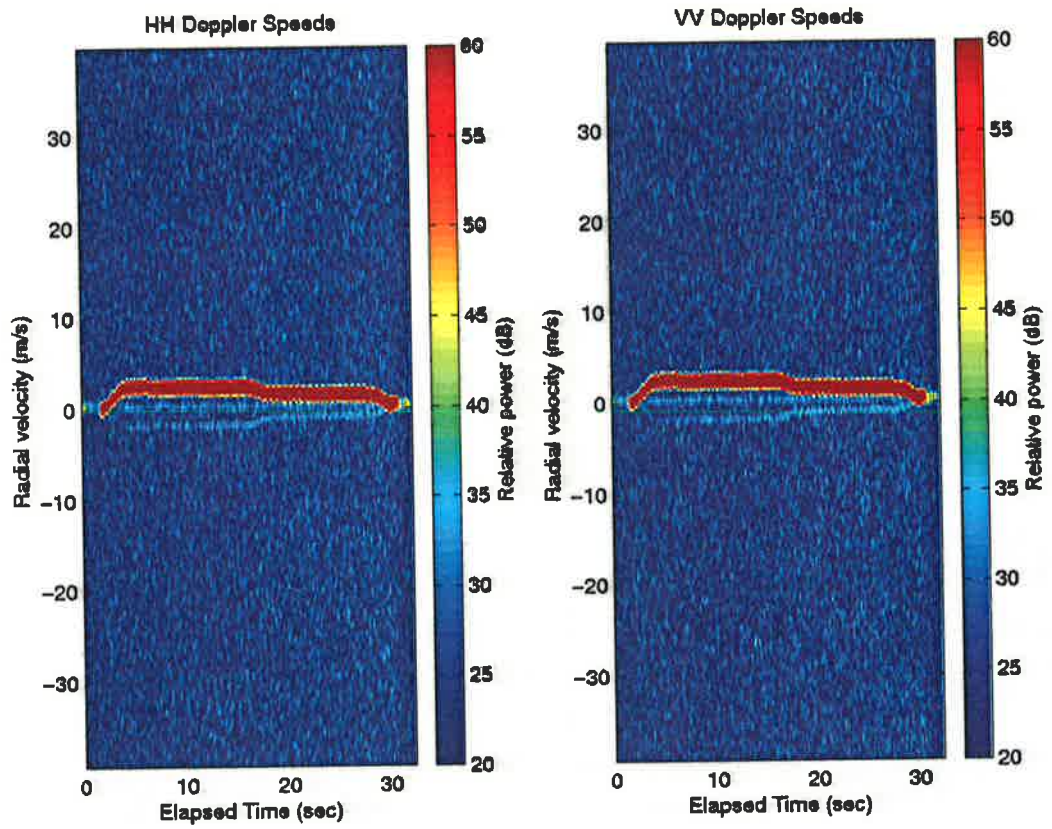

Figure 4-11 Radial velocity versus time for the Doppler mode experiment

4.7 Software tools

An extensive suite of software routines has been produced to support the new polarimetric mode. The software routines include code for reading, calibrating and processing the collected data and tools for analysing the processed data using the decomposition and analysis techniques discussed in Chapter 2. A tool for visualising the distribution of the characteristic polarisation states on the Poincaré sphere was also created. The following sections describe some of these tools and illustrate a number of example outputs that can be generated.

4.7.1 Data processing tools

To support the polarimetric data collection mode, software for reading the new radar data format was required. This was implemented as a Matlab subroutine that was integrated into RCSLAB. RCSLAB is a Matlab package that has been developed at DSTO for the analysis of fixed polarisation RCS measurements. It contains tools for calibrating, processing and analysing the data collected by the DSTO high resolution polarimetric radar system. The calibration package was modified to include the polarimetric calibration technique described in Chapter 3 using the dual delay line calibrator and rotating dihedral. A screenshot of the calibration software is shown in Figure 4-12.

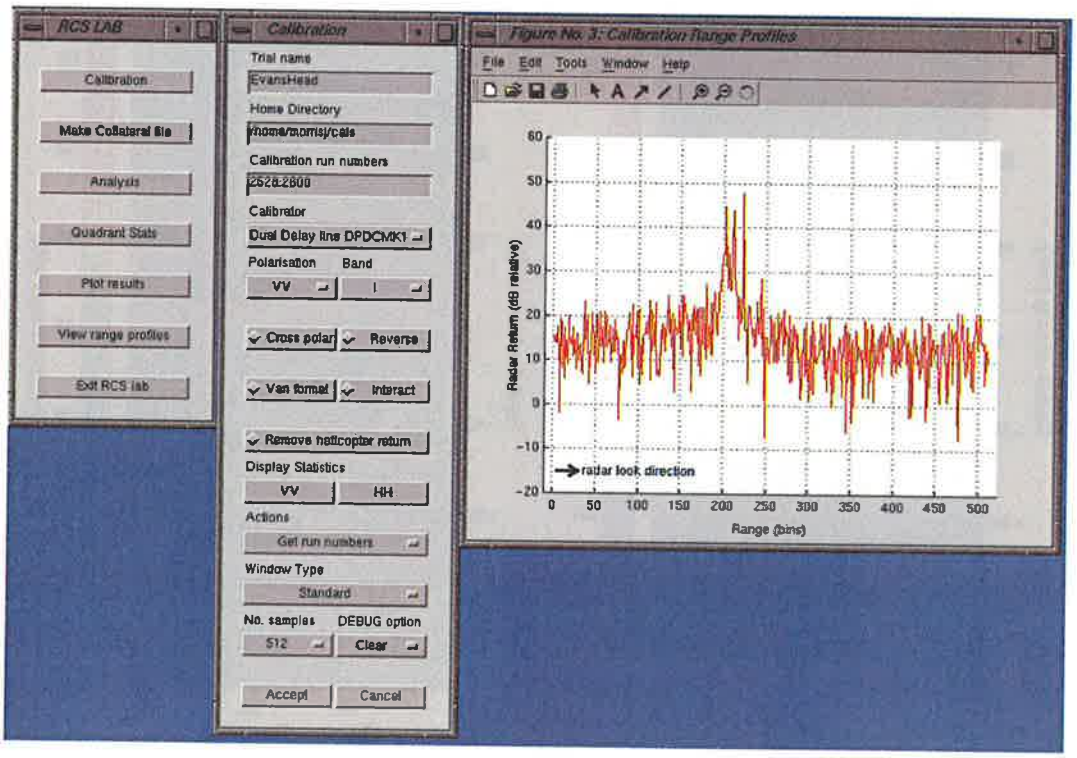

Figure 4-12 RCSLAB polarimetric calibration routine

A new module was added to RCSLAB for performing the polarimetric analysis. While a graphical user interface has not been implemented, command line based Matlab routines have been produced for processing the radar data files, generating range profiles and forming the coherency or covariance matrices for variable sized averaging windows. Eigenvalue decomposition routines supplied by Dr Shane Cloude have been integrated into the software package and a variety of output routines have been developed, including software for plotting the time variation of the polarimetric entropy H, anisotropy A, scattering alpha $\bar{\alpha}$ and the distribution of points in the $H-\bar{\alpha}$ and $H-A$ spaces. Routines for generating the image formed from the products of $[H][A]$, $[H][1-A]$, $[1-H][A]$ and $[1-H][1-A]$ and the distribution of points in the $H-A-\bar{\alpha}$ classification space have also been produced. These images have been used by Pottier [39] to interpret the scattering mechanism present in polarimetric measurements. Many of the low grazing angle sea measurements exhibited large clutter regions, which biased the distribution of points in the $H-\bar{\alpha}$ and $H-A$ spaces. The option of filtering out regions of high entropy and low backscattered power (corresponding to clutter) has been implemented so that the distribution of the returns of interest can be examined more closely. Examples of the filtering results are shown on Figure 4-13.

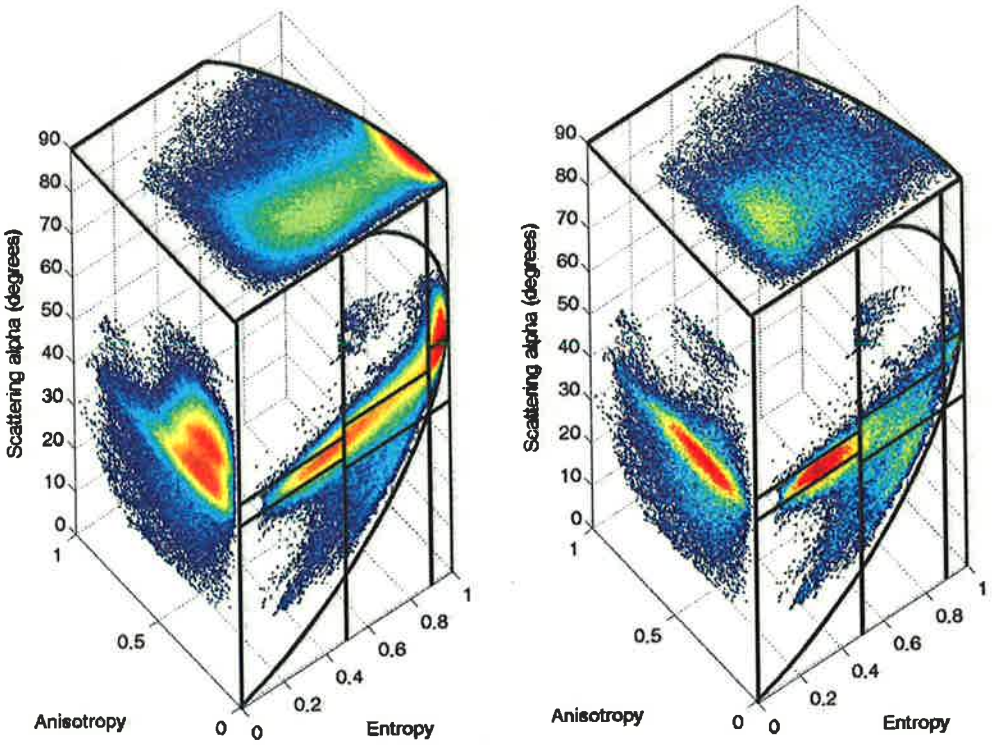

Figure 4-13 Comparison of distribution in $H-A-\bar{\alpha}$ space with and without clutter present

4.7.2 Theoretical tools

A number of tools have also been developed for studying the properties of elementary scatterers with idealised scattering matrices. Matlab code has been written for generating the polarisation signature plots for the co-polarised, cross-polarised and matched antenna cases and the co-polar and cross-polar relative phase-correlation plots. A number of examples of these plots for elementary scatterers are given in Section 3.2. Routines for calculating the elements of the [*S*] matrix in an arbitrary polarisation basis using the unitary transformation expressions given in Section 2.12 have been implemented along with software for obtaining a rotated scattering matrix, scattering vector or coherency matrix using the expressions given in Sections 2.15.1 and 2.15.2. This code has been used for predicting the scattering behaviour of the rotating dihedral used in the calibration procedure described in Chapter 3.

4.7.3 Visualisation of optimal polarisation states

While Matlab is good for generating simple 2D plots, it has only a basic interactive 3D visualisation capability. A significant amount of time and effort was spent developing a package for calculating and visualising the location and distribution of the optimal polarisation states on the Poincaré sphere. Initially the optimal polarisation states were found using the technique developed by Boerner and Xi [17], however, recently the approach proposed by Yang *et al.* [155] has been implemented due to numerical simplicity and the ability to correctly handle all the degenerate cases that can potentially lead to numerical problems in the other commonly used methods. The software was written in C++ and uses the Visualisation Toolkit (VTK)[2] for the 3D visualisation [238], while the graphical user interface (GUI) was produced using FLTK, the Fast Light Toolkit[3] (FLTK is pronounced 'fulltick'). The software developed has been named XPOL_VIS and has currently been compiled and tested on both SGI workstations and Linux platforms and in the future it will be ported to the windows environment. The main display is shown below in Figure 4-14.

[2] VTK is an open source project that can be downloaded from ***http://public.kitware.com/VTK/***

[3] FLTK is provided under the terms of the GNU Library Public License, Version 2 and is available for download from ***http://www.fltk.org/***

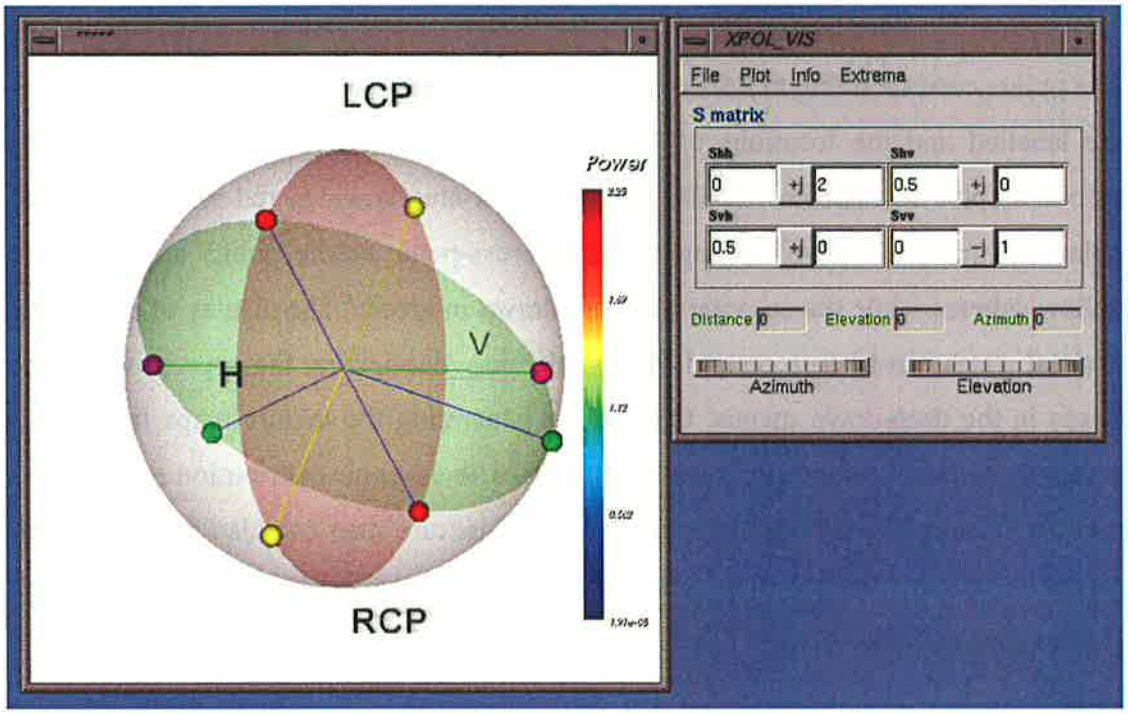

Figure 4-14 The main display window in XPOL_VIS showing the optimal polarisation state locations and the Huynen polarisation fork

The elements of the [*S*] matrix are entered as complex numbers on the main display window. The default option generates a texture map showing the cross-polar power distribution on the Poincaré sphere.

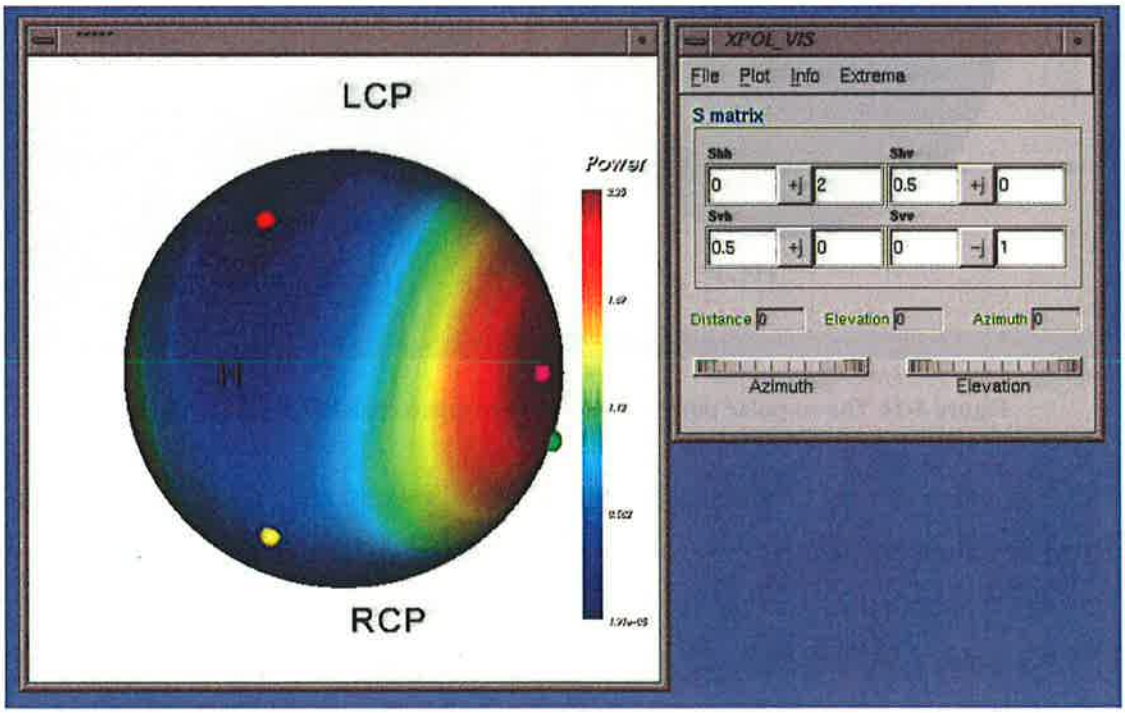

Figure 4-15 The cross-polar power distribution mapped onto the Poincaré sphere

The points corresponding to horizontal, vertical and left and right circular polarisation are labelled and the locations of the optimal polarisation points are indicated by coloured spheres. The cross-polar null locations are shown in red while the cross-polar maxima are shown in magenta. The cross-polar saddle points are drawn as yellow spheres while the co-polar nulls are drawn in green. The display of any of the optimal states can be turn on and off by selecting /deselecting the appropriate check boxes in the drop-down menus. Options for generating the texture maps for the co-polar or the matched antenna cases also exist. The co-polar distribution map for the previous example is shown in Figure 4-16. The texture map can also be removed to reveal the Huynen polarisation fork and the target characteristic plane of Kennaugh [12] as seen in Figure 4-14.

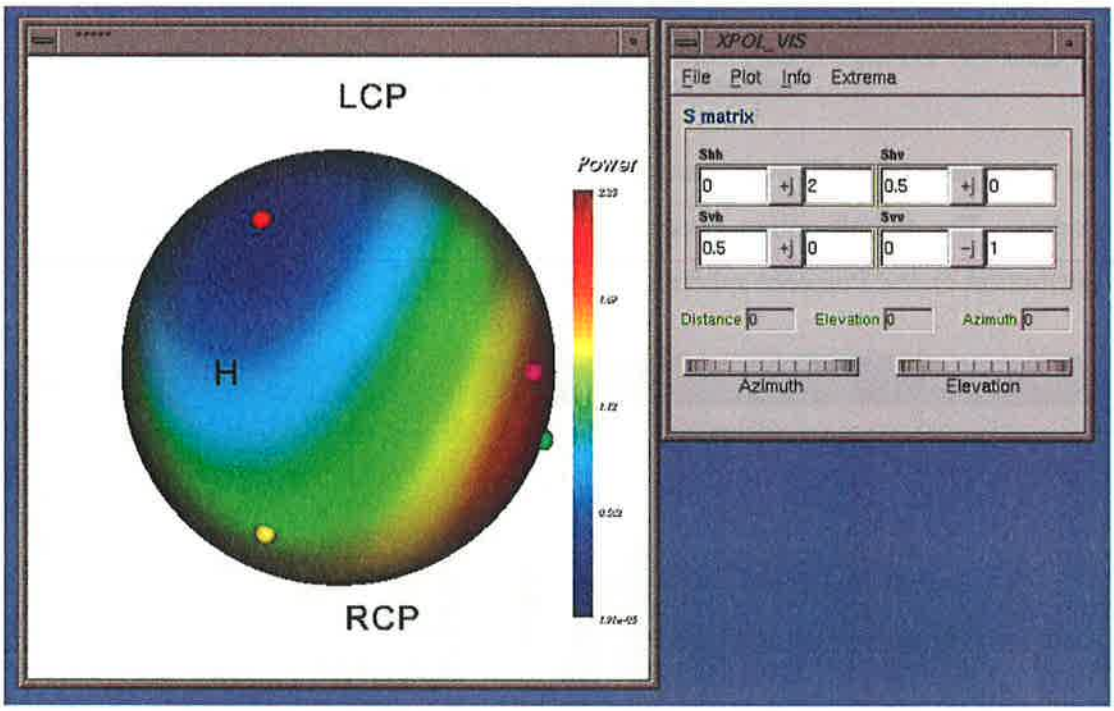

Figure 4-16 The co-polar power distribution mapped onto the Poincaré sphere

The orientation of the Poincaré sphere can be varied interactively using mouse inputs. These functions include rotating, zooming and panning. Generating images from a range of camera positions can be used to produce animated sequences. The default option produces 36 images at 10° steps although finer steps can be specified. Example images showing six frames are shown in Figure 4-17 and Figure 4-18.

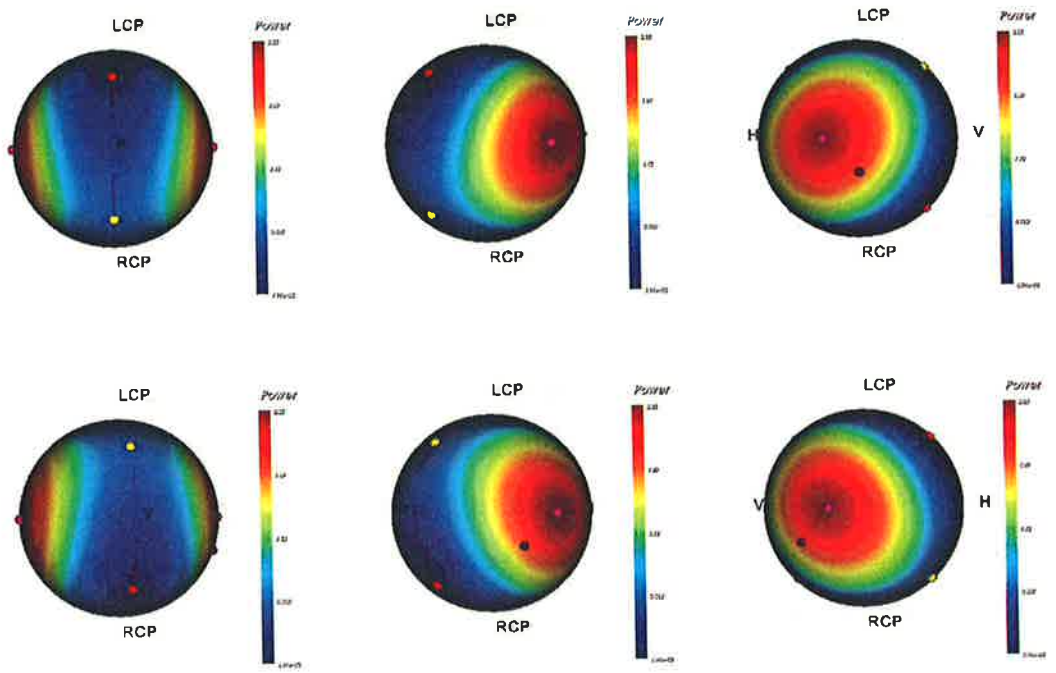

Figure 4-17 A sequence of cross-polar power images produced for varying camera positions

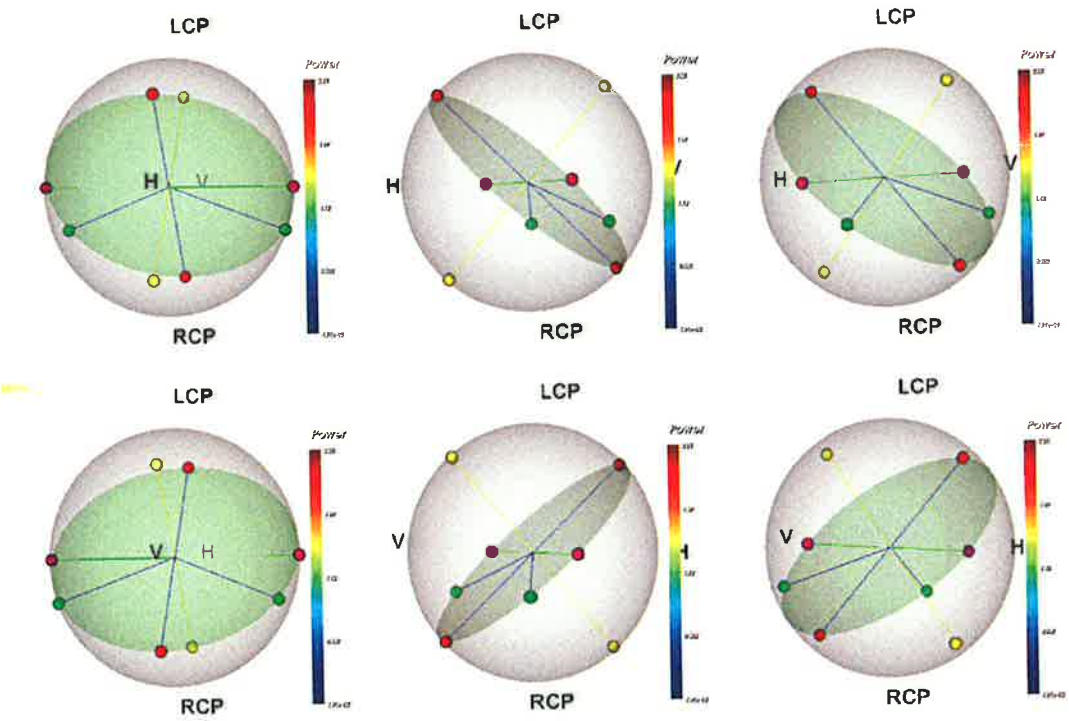

Figure 4-18 A sequence of polarisation fork images produced for varying camera positions

A number of other features have also been implemented, including the ability to import measured data and display the distribution of the optimal states within an image. The effect of LOS rotations and the effect of introducing various forms of

distortions into the [S] matrix can also be visualised using the software. Once again the animation feature is particularly useful in these cases.

4.8 Synopsis

The main features and measurement capabilities of the DSTO high resolution polarimetric radar system have been described and the hardware modifications that have been made in support of the work performed in this thesis have been presented. A brief description has been given of the software tools that have been developed to process, analyse and interpret the data collected. An interactive software package for visualising power distribution and location of the optimal polarisation states on the Poincaré sphere has also been discussed and a variety of outputs that can be produced by this program have been illustrated.

Chapter 5 Sea surface scattering

This chapter examines the models adopted to describe radar scattering from the ocean surface that provide a basis for the prediction and interpretation of polarimetric signatures. Two distinct physical *processes* need to be modelled:

- the geometry of the sea surface, in terms of (a) its natural structure as a random process associated with some distribution of wind-generated waves and (b) possible quasi-deterministic features such as ship wakes
- electromagnetic scattering from the surface, which in practice means finding a suitable approximate solution to Maxwell's equations

These processes are coupled in the sense that the domain of validity of the electromagnetic scattering model must include the class of surfaces that are consistent with the sea surface of interest and it must yield meaningful results for the illumination geometries of practical importance. For this reason, scattering at low grazing angles is of particular interest, since it exhibits some characteristics that cannot be explained by the standard two-scale or composite surface scattering models that are often applied at high grazing angles (20° – 70°). While numerous radar studies have been performed at grazing angles, few investigations have been performed with polarimetric radar, hence the polarisation dependence of the sea surface properties in this regime is still not well understood.

Initially the hydrodynamic aspects of the problems are discussed. Mathematical representations of the sea surface in terms of statistical processes describing the macrostructure and the superimposed microstructure are presented. Linear hydrodynamic models using parametric wave models are described, along with nonlinear models that provide a description of weakly interacting wind waves. The accuracy of these models and the requirements for wave-resolving radar measurements are also considered. Modelling of quasi-deterministic features arising from ship wakes is discussed, using numerical models capable of generating the surface elevations and velocity fields produced by steadily moving bodies, either submerged or on the surface. These results highlight the potential for exploiting the

Kelvin wake generated by a moving ship for validating ocean surface polarimetric measurements.

The electromagnetic aspects of scattering from features on the ocean surface are then discussed. An overview of the scattering techniques from rough surfaces is provided and includes a description of the small perturbation methods, techniques based on the Kirchhoff approximation, two-scale models and analytical scattering theories. The justification for adopting the two-scale model based on the extended Bragg models is given. This model is formulated using a covariance matrix approach so that depolarisation can be introduced, thus enabling predictions of the variations in the polarimetric parameters for progressive and breaking waves to be obtained.

Finally, the hydrodynamic and electromagnetic models are combined to illustrate the modelling of the polarimetric variations of breaking waves. The validation of scattering models using the surface elevations, slope and velocity fields predicted by the computational model *SWPE* combined with a two-scale model is presented and the potential for using this technique to validate the Doppler measurements performed with the DSTO radar system is discussed. Finally an example illustrating the differences arising from the linear and nonlinear wake models is given which highlights the importance of modelling the nonlinear components of gravity waves.

5.1 Hydrodynamic models of the sea surface

While the sea is governed by the laws of hydrodynamics, and is well modelled as an incompressible, inviscid, irrotational flow for which the fluid equations have a *relatively* simple form, its dynamic nature and essential nonlinearity make it exceptionally difficult to observe and characterise.

The irregular shape of the surface results from the presence and interactions of various waves, over a wide range of spatial and temporal scales, subject to the local wind stress and atmospheric turbulence, so the properties of these component waves are of central importance.

The vertical accelerations of surface oscillations are the result of two restoring forces, namely gravity and surface tension. These disturbances can be described

mathematically using potential theory by solving Laplace's equation with the appropriate (nonlinear) boundary conditions [239]. If the amplitude of the wave is assumed to be small relative to the wavelength and water depth, the equation can be linearised yielding the dispersion equation relating angular frequency to wave number, of the form

$$\omega^2 = \left(gk + \frac{\sigma k^3}{\rho} \right) \tanh(kd) \tag{5.1}$$

where g is the gravitational acceleration, σ is the surface tension of water, ρ is its density and d is the water depth. In this context, dispersion refers to the fact that the *celerity* C or phase speed of a wave depends on its wavenumber

$$C = \frac{\omega}{k} = \sqrt{\left(\frac{g}{k} + \frac{\sigma k}{\rho} \right) \tanh(kd)} \tag{5.2}$$

Ocean waves are often categorised as deepwater, intermediate or shallow. The water depth is considered *deep* when $\frac{d}{\lambda} > \frac{1}{2}$ or $kd > \pi$ [240], meaning that the same depth of water can be deep for short waves yet shallow for waves of long wavelength. Intermediate waves occur where the water column depth is in the range of $\frac{\lambda}{2}$ to $\frac{\lambda}{20}$ while shallow water waves occur when the depth is less than $\frac{\lambda}{20}$ of the wavelength.

In the case of deepwater waves, $\tanh(kd)$ tends to one and the celerity is independent of depth. For small wavelengths, surface tension is the predominant restoring force and the waves are termed *capillary* waves. At larger wavelengths, the first term under the square root sign in Equation (5.2) dominates and the resulting disturbance is called a *gravity* wave whose celerity increases as $\sqrt{\lambda}$.

In shallow water, $\tanh(kd)$ can be approximated by the first term in the Taylor expansion kd and the expression for the celerity becomes

$$C = \frac{\omega}{k} = \sqrt{\left(g + \frac{\sigma k^2}{\rho}\right) d} \tag{5.3}$$

The second term in Equation (5.3) decreases rapidly with increasing wavelength, thus for gravity waves in this regime, the phase speed can be closely approximated by $\sqrt{gd}$ and hence is independent of wavenumber. This allows the possibility of non-dispersive waves.

5.1.1 Statistical description of the sea surface

The general representation of the sea surface as a statistical process is conveniently described in terms of two components – a macrostructure corresponding to a superposition of a continuous spectrum of roughly periodic waves, whose mean direction and directional spreading behavior vary with wavelength, together with a superimposed microstructure consisting of ripples, foam and spray [80]. The former, the directional wave spectrum $S(\vec{k})$, may include discrete low frequency components in the form of swell, which has been generated by distant storms rather than local winds and is hence highly directional and in the short term relatively monochromatic. Ripples result from turbulent gusts of wind near the sea surface while foam and spray are produced by the interference of various wind and swell waves and atmospheric turbulence.

In most studies the 'oceanographic' model of the sea surface is adopted, that is, superposition of weakly-interacting primary waves, whose directional power density $S(\vec{k})$ is governed by an appropriate radiative transport equation,

$$\frac{\partial S(\vec{k})}{\partial t} = S_{in} + S_{nl} + S_{dis} + ... \tag{5.4}$$

where S_{in} is the source term for wave generation by wind or other causes, S_{nl} is the source term for nonlinear wave-wave interactions, and S_{dis} represents dissipation processes. The waves represented in $S(\vec{k})$ are then taken to be those satisfying the dispersion relation given in Equation (5.1) with the nonlinearity relegated to its role in Equation (5.4). Accordingly, when the sea is not too rough the resultant surface has

approximately Gaussian statistics. For higher sea states, when the nonlinear contributions are more significant the Gram-Charlier expansion [241] provides a better description, though it is far less convenient mathematically. Various non-Gaussian models [242-247] have been proposed which provide more realistic descriptions of the probability distribution of the surface elevations in such conditions.

Standard models for $S(\vec{k})$ have been developed by oceanographers, with the Pierson-Moskowitz [248] and Joint North Sea Wave Project (JONSWAP) models developed by Hasselmann *et al.* [249] being perhaps the most widely used.

The Pierson-Moskowitz spectrum describes the wave energy density as a function of wave frequency as

$$S_{pm}(f) = \frac{\alpha g^2}{(2\pi)^4 f^5} \exp\left[-\frac{5}{4}\left(\frac{f}{f_p}\right)^{-4}\right] \tag{5.5}$$

where α is a constant depending on wind velocity, g the gravitational acceleration, f is wave frequency in terms of *Hz* and f_p the frequency where the spectral peak is located. In the JONSWAP spectrum,

$$S_{JONSWAP}(f) = \frac{\alpha g^2}{(2\pi)^4 f^5} \exp\left[-\frac{5}{4}\left(\frac{f}{f_p}\right)^{-4}\right] \gamma^d \tag{5.6}$$

where,

$$d = \exp\left[-\frac{(f-f_p)^2}{2\sigma^2 f_p^2}\right] \quad \text{and} \quad \sigma = \begin{cases} 0.07 & \text{for } f \le f_p \\ 0.09 & \text{for } f > f_p \end{cases} \tag{5.7}$$

γ is known as the *peak-shape parameter* and represents the ratio of the maximum spectral energy density to the maximum of the corresponding Pierson-Moskowitz spectrum. The term, γ^d is commonly referred to as the *peak enhancement factor* and Equation (5.6) illustrates that the JONSWAP spectrum is the product of the

corresponding Pierson-Moskowitz spectrum and the peak enhancement factor. Based on ocean wave measurements, γ is assumed to be a random variable of a normal distribution with a mean 3.30 and the variance 0.62 [250].

In addition to these two well-known frequency spectra, other parametric models for $S(\vec{k})$ have been proposed, based on the numerous theoretical and empirical studies detailing candidate equilibrium wind wave spectra [249, 251-254]. While the long-wave JONSWAP spectrum is generally accepted as a reasonable representation of fetch-limited wind-wave development, in the high frequency regime the models are weak in both theory and observation and remain unreconciled across the full range of wavenumbers [255], despite numerous studies [252, 254].

For remote sensing studies, precise knowledge of the short-scale wave roughness is of great importance. As a first-order approximation, studies often present a spectrum for high wavenumbers as an independent contribution to the sea surface geometry, but. it is now recognised that the short waves are intimately coupled with intermediate and long-scale waves necessitating the need for full wavenumber models such as those developed by Donelan and Pierson [256], Apel [257] and Elfouhaily *et al.* [258]. Elfouhaily *et al.* [258] notes that a *good* wave spectrum should be capable of reproducing certain observations. In particular, in the high frequency regime the integration of the slope spectrum should provide the wind-dependent mean square slopes results of Cox and Munk [259], while also representing the dynamics of gravity-capillary wave curvature seen in laboratory measurements made by Jahne and Riemer [260] and Hara *et al.* [261]. The two dimensional wavenumber spectrum proposed by Elfouhaily *et al.* [258] was developed to meet these criteria and is valid over all wavenumbers, is relatively simple in its analytic form and is quite well suited to electromagnetic models.

Of course, the adoption of a spectral representation implies that the surface is weakly stationary or slowly varying in its statistical characterisation. Further, for high resolution (wave-resolving) radar, where the range cell dimensions may be as small as 0.15 m, while the dominant sea wavelength may be 15 m, say, it is obvious that the

spectral representation of the gravity waves is not appropriate for the local scattering calculations.

One of the key advantages of polarimetric radar is the ability to estimate the large-scale surface slopes when the characteristic length scale l of large-scale slope variability satisfies $l >> \lambda$ and when small scale roughness is present so as to provide a Bragg scattering surface texture with its distinctive scattering matrix [262]. Schuler and Lee [65] showed that long wave tilts in the azimuthal direction could be measured directly from their influence on the polarimetric signature and applied this result to measure terrain slopes on land [66]. This technique can also be applied to measurements of the sea surface to extract information on the directional wave spectrum $S(\vec{k})$.

5.2 Quasi-deterministic surface features

In addition to the stochastic surface arising from wind-generated waves, scenarios occur in which the sea surface exhibits quasi-deterministic features. The Kelvin wake produced by a moving ship is one such example. Two computationally efficient codes, named *SWPE* ("Sea Wave Pattern Evaluation") and *NFSFS* ("Nonlinear Free-Surface Flow Solver"), developed by Scullen and Tuck [263, 264] were used to examine the surface elevations, slope and velocity fields produced by a moving vessel.

5.2.1 Sea Wave Pattern Evaluation (SWPE)

SWPE has its origins in the wave resistance prediction programs, MITCHELL and POLYMICH described by Tuck [265] and Lazauskas and Tuck [266] respectively. It computes the surface elevations and velocity fields produced by steadily moving bodies either submerged or on the surface using the Michell-Kelvin "thin ship" approximation [267]. It models the disturbance of the body by a (known) continuous distribution of singularities along the center-plane of the body, while assuming that the kinematic and dynamic free surface boundary conditions can be approximated by a linearised condition on the plane equilibrium surface. Calculations of the wave elevation and velocity potentials behind surface piercing and fully submerged monohull or general multihull vessels can be produced, while the near-field wave

elevations are determined using a special polynomial representation of the Green's function of the local field.

5.2.2 Nonlinear Free-Surface Flow Solver

NFSFS solves for the wave pattern produced by a fully submerged object travelling at constant velocity within an inviscid incompressible fluid, beneath a free surface under gravity. The solution method enforces the Neumann boundary condition on the vessel body boundary (i.e. the normal component of velocity is zero over the body), while the kinematic and dynamic exact (Stokes) boundary conditions are satisfied at the free surface. An additional constraint (the radiation condition) ensures that the disturbance in flow generated by the body tends to zero in the upstream direction. NFSFS differs from SWPE in that the surface boundary conditions are applied in full, nonlinear form, as opposed to SWPE's linear approach. This nonlinear approach allows for greater accuracy of results, but is computationally more complex since the free-surface location is unknown a priori. Accordingly, a Newton-like iterative procedure is adopted in which an approximation to the surface wave pattern is gradually refined from an initial guess until convergence is achieved at a quadratic rate. A detailed description of the problem and the solution procedure is given in [268].

5.2.3 Exploitation of quasi-deterministic surface features

One of the problems encountered in the validation of ocean surface polarimetric measurements using computer models is that there are generally two unknowns present; the scattering model being assessed and the stochastic surface geometry that provides the test environment. One possible solution for solving the ambiguity inherent in this scenario is to replace the stochastic surface with a quasi-deterministic surface, such as the Kelvin wake generated by a moving ship. This approach is illustrated in Section 5.6.3 where the surface displacements and surface flows predicted by SWPE are combined with the electromagnetic scattering codes described in the Section 5.4 to yield predictions of the polarimetric signatures. These predictions are compared with experimental polarimetric measurements of wakes in Chapter 6.

5.3 Nonlinear hydrodynamics

An exact scattering theory for the ocean is useless unless the proper kinematics and dynamics of the ocean wind waves is used. In particular the properties of short

gravity-capillary waves, which are Bragg scatterers at microwave frequencies, and their interaction with other waves is required. Since the 1960's there have been numerous papers examining the perturbation theories of the nonlinear hydrodynamic equations at a free boundary. Hasselman [269-271] was the first to provide a reasonably complete description of a perturbation approach about a mean equilibrium level expanded up to fifth order in slope and experimental results have shown that this approach provides an adequate description of weakly interacting wind waves for most situations [272-274]. In this technique the wave-wave interactions were classified as either resonant or non-resonant interactions. Hasselman's approach was extended by Valenzuela and Laing [275] to incorporate the effects of surface tension. Second-order resonance was shown to be possible among capillary waves, while resonance among gravity waves only starts from the third order. Only gravity waves are supported in Hasselmann's approach, but combining Hasselman's formulation and Valenzuela and Laing's derivation, capillary waves can also be investigated under the same terms as wave-wave interactions.

In parallel with these developments, Zakharov [276] proposed another approach in which the boundary conditions were rewritten at the surface itself, rather than expanding the variables with respect to a mean reference at equilibrium. In this approach the canonical properties of the velocity potential and the surface elevation are established in terms of a well defined Hamiltonian and makes fewer simplifying assumptions about the original hydrodynamic properties. In essence it involves evaluating the boundary conditions at the free surface itself and then truncating them in orders of the surface elevation.

These developments lead to controversy as whether Hasselman's and Zakharov's approach were equivalent, with papers by Watson and West [277], Hammack and Henderson [278], Dias and Kharif [279] making conflicting claims. Recently Elfouhaily *et al.* [280] illustrated the similarities and differences between the two approaches and showed that either the velocity potential or the elevation can be equivalent, but not both variables simultaneously. Elfouhaily *et al.* [280] showed that the resonant condition determines which canonical variable will be the same.

5.3.1 Weak wave-wave interactions

The ability to model nonlinear processes is of specific interest for the interpretation of polarimetric measurements performed using the DSTO radar system. In particular, the role of processes that cause the surface to evolve through states not consistent with simple linearised hydrodynamics is of special significance. Much of the previous research in the context of microwave radar has focussed on the highly nonlinear extreme case of wave breaking [85, 87, 90, 102, 281, 282]. The integrated effect of the weak interactions engendered by the free surface hydrodynamic boundary conditions has also been studied and used in the estimation of altimeter bias [283-286].

Weak wave-wave interactions modify the instantaneous surface geometry resulting in sharpened crests and flattened troughs. Accurate measurement of surface slope or the statistical distribution of surface slope provides a window onto this aspect of nonlinearity. Another consequence is the temporal decoherence associated with exchange of energy between normal modes. In field theoretic notation, we can write the Hamiltonian of the wave field as a sum over orders of wave interaction,

$$H = \sum_k \omega_k a_k^+ a_k + \sum_{k,j} V_{k,j} a_k^+ a_j a_{k-j} + \sum_{j,k,l} \Gamma_{j,k,l} a_k^+ a_l^+ a_j a_{k+l-j} + ... \equiv H_2 + H_3 + H_4 + ... \qquad (5.8)$$

where a_k^+ and a_k are the creation and annihilation operators for the normal modes $\psi_k = e^{i(kx-\omega_k t)}$. The time evolution of the surface, represented here by a state vector $\Psi(t)$, is then given by

$$\Psi(t) = e^{iH(t-t_0)}\Psi(t_0) \qquad (5.9)$$

If we make the approximation that H=H$_0$ then the surface is predicted to evolve as

$$\Psi_{lin}(t) = e^{iH_0(t-t_0)}\Psi(t_0) = e^{iH_0(t-t_0)}\sum_k c_k \psi_k(t_0) = \sum_k c_k e^{iH_0(t-t_0)} e^{i(kx-\omega_k t_0)} \qquad (5.10)$$

which becomes

$$\Psi_{lin}(t) = \sum_k c_k e^{-i\omega_k(t-t_0)} e^{i(kx-\omega_k t_0)} = \sum_k c_k e^{i(kx-\omega_k t)} = \sum_k c_k \psi_k(t) \qquad (5.11)$$

Equation (5.11) is the state resulting from independent propagation of the normal modes, as expected. This raises some interesting questions such as for a given initial state $\Psi(t_0)$, how does the actual surface observed at a later time, $\Psi_{obs}(t)$, differ from $\Psi_{lin}(t)$? This is obviously a vitally important issue when the radar observation process involves coherent integration. How this difference manifests itself in a given radar signature will influence the choice of radar parameters, while the higher order terms in the Hamiltonian provide a means for further examining the underlying physics of the nonlinearities.

Given that polarimetric radar is well suited to the measurement of large-scale surface slopes when small-scale roughness is present, the potential exists to measure the spatial slope pattern with a precision sufficient to identify the presence of nonlinear contributions and to determine their spatial properties. For X band radar, where $\lambda\sim$ 0.03 m, this corresponds to a minimum length scale of ~ 1 m, which is adequate for resolving surface gravity waves in the frequency band above ~ 0.5 Hz.

While the continuing development of improved representations of the sea surface is vital, the need to achieve commensurate fidelity in the electromagnetic scattering techniques is equally important. A brief overview of the models commonly used to model scattering from the sea surface is given in the following section.

5.4 Electromagnetic surface scattering models

The ocean surface becomes visible to radar systems due to the air-sea interactions. Bragg scattering is widely recognised as the dominant mechanism contributing to the microwave backscatter from the ocean surface away from the specular direction. More specifically, the scattering is from the ocean waves of wavenumber $k = 2k_0 \sin\theta$ travelling along the LOS, where θ is the angle of incidence of the propagation vector in relation to the local surface normal, and k_0 is the wavenumber of the electromagnetic radiation in free space. To first-order, for capillary waves and second-order for gravity waves, the intensity of the Bragg scatter is proportional to the spectral density of the *Bragg resonant wave* and the Doppler shift induced is equal to the frequency of the Bragg resonant wave. If both advancing and receding waves are present then the two spectral lines appear either side of zero Doppler frequency.

The fact that the ocean surface acts like a diffraction grating with the principal returns contributed by the Bragg resonant water waves was first recognised by Crombie [287] in 1955 during his observations at HF frequencies of the Doppler spectrum of radar sea echoes. This is illustrated in Figure 5-1.

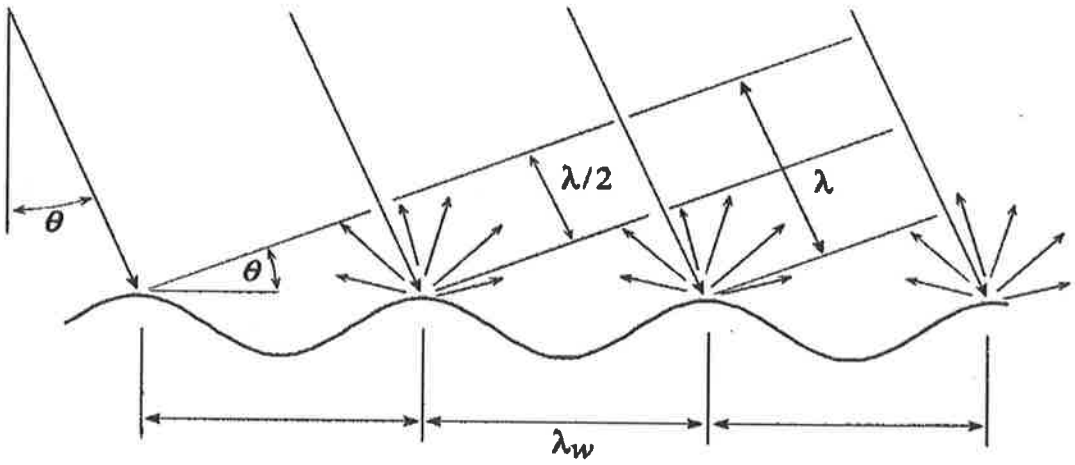

Figure 5-1 Representation of Bragg scattering from the ocean surface

Crombie correctly determined that radio waves were backscattered by ocean waves corresponding to half the radio wavelength (for near grazing incidence) travelling in the radial direction. He also observed that the scattering ocean waves travelled in *trains* superimposed on the crests of longer waves, and thus recognised the presence of *parasitic waves* usually present in water waves. Crombie suggested the possibility of higher order contributions and predicted a continuous spectrum for higher frequencies where the resonant water waves are much shorter than the dominant waves of the sea. Most of these pioneering observations were later verified and quantified by Wright [288-290] and Bass *et al.* [291, 292] for microwave frequencies and led to the present understanding of the scattering physics of electromagnetic waves for the ocean surface.

5.4.1 Electromagnetic scattering from rough surfaces

A great deal of attention has been focused on the scattering of electromagnetic waves from surfaces with different scales of roughness. Scattering from the sea is a special case of scattering from a rough surface. All available closed-form models for electromagnetic scattering from random surfaces are asymptotic solutions of the exact

Maxwell equations. Scattering from a rough surface is often formulated as a *global boundary value problem* (GBVP) in electromagnetics whose solution, in practice, invariably relies on introducing a number of assumptions and approximations. Typically examples of such simplifications of the electromagnetic aspects of the problem are:

(i) Adopting the Rayleigh hypothesis.
(ii) Replacing the vector wave equation with the Helmholtz equation and solving for temporal variability via the quasi-stationary approximation.
(iii) Modelling the seawater as a perfectly electrically conducting fluid.

Formulations based on the exact GBVP, though elegant, are often of little practical value [293]. Two approaches are commonly pursued that are asymptotic solutions to the exact Maxwell equations based on: (a) the small perturbation method (SPM) originally developed by Rice [294], (b) the Kirchhoff approximation [127] which uses integral techniques based on Green's theorem.

5.4.2 The small perturbation method

Perturbation theory was first applied by Lord Rayleigh [295] to obtain a low frequency asymptotic solution of a monochromatic plane wave incident onto a sinusoidal surface separating two different media. Rice [294] later used this approach to obtain a first-order small perturbation method for scattering of electromagnetic waves from a two-dimensional, randomly rough, perfectly or finitely conducting surface. This approach yields a grating theory where the randomly rough surface profile is decomposed in a set of sinusoidal gratings by means of the Fourier transform [296].

The small perturbation method starts with a rigorous integral equation (either surface or volume integral) satisfied by the electromagnetic fields. This equation is obtained from the harmonic Maxwell differential equations using a technique such as the extinction theorem. Building an expansion in powers of a small parameter, and equating the terms of the same order provides a solution with a domain of validity that is directly linked to the radius of convergence of the expansion series.

The SPM relies on two simplifying approximations. The first assumes that the wave heights are much smaller than the radar wavelength and the second is a boundary condition (Rayleigh's hypothesis) that matches the spectrum of outgoing plane waves to the incident field. Essentially, it exploits the smallness of the roughness slope to generate an expansion for the boundary condition and the smallness of the roughness amplitude to generate an expansion for the scattered field. The SPM carries the polarisation factors but does not properly account for longer scale features on the scattering surface and therefore fails to reproduce the near specular scattering.

In many cases, scattering problems of interest have progressed beyond the limits of accuracy of first-order SPM. Consequently many researchers have investigated ways of extending these theories using different series expansions with better convergence and larger domains of validity. Examples include the phase perturbation method (PPM) [297-299], the unified perturbation method (UPM) [300] and higher order SPM techniques such as second order perturbation methods developed by Valenzuela [301], the third-order SPM by Johnson [302] fourth-order SPM by Demir and Johnson [303] and the fully polarimetric extension of SPM by van Zyl *et al.* [136] which retains the scattered fields up to second order accuracy. Barrick [304, 305] also developed a second order perturbation theory, which has been used almost exclusively for modelling Doppler spectra of signals backscattered from the ocean, particularly at HF. This approach is formulated to include second-order scattering and hydrodynamic effects; it has been generalised to describe bistatic polarimetric scattering by Anderson *et al.* [306]. The validity of these techniques remains a topic of great interest and numerous papers have been published on the regions of validity of the SPM [307-310], PPM [311] and UPM [300, 312, 313].

5.4.3 The Kirchhoff approximation

The Kirchhoff method was developed by Antokolskii, Brekhovskikh, Isakovich, Davis, Beckmann and others but is referred to as the Kirchhoff approximation (KA) since it is based on the Kirchhoff formulation of diffraction theory. References to the original work are given in Beckmann and Spizzichino [127] and Bass and Fuks [314]. The KA is generally used with integral formulations based on Green's second vector theorem. This theorem states that the scattered field at any point within a source free region bounded by a closed surface can be expressed in terms of the tangential fields

on the surface. Mathematically, this can be expressed as the Stratton-Chu integral although the assumption on the scattering mechanisms is purely heuristic.

The Kirchhoff approximation requires that the incident wavelength be smaller than the radius of curvature of the surface, so that in the neighbourhood of any point on the surface the field may be represented by the sum of the incident field and a reflected field evaluated by assuming that the surface is locally *planar*. It is valid for gently undulating surfaces with a large radius of curvature and incidence angle close to the normal to the surface. The regions of validity of this technique have been extensively studied [315-319] and a plot showing the regions of validity for the KA, SPM and small slope approximation is shown in Figure 5-2

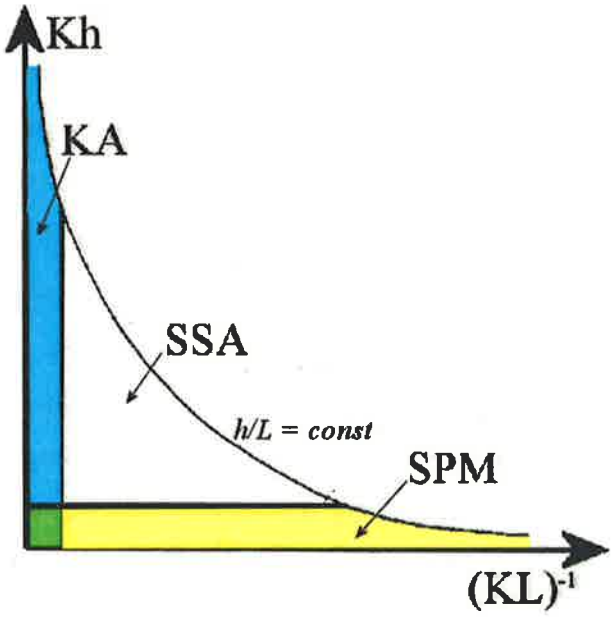

Figure 5-2 Regions of validity of classical SPM and KA approach (based in Fig 1.1 in [320])

Shadowing functions and iterations [321-326] have also been proposed to improve the accuracy and domain of validity of the KA methods. The term physical optics is sometimes used synonymously with the KA, but should more precisely be reserved for the combination of KA with shadowing corrections for the unlit regions of the surface.

The KA accurately models the quasi-specular problem but lacks the polarisation sensitivity of the SPM. Holiday [327] published an approach that combines the two

limits by including the second iteration of the surface-current integral equations, thus extending the Kirchhoff approach to include the polarisation sensitivity of the SPM for the backscattering case. Other authors have also investigated this problem including Rodrigez and Kim [300], Tatarski [328] and Voronovich [329]. While these techniques have a larger domain of applicability and provide the polarisation sensitivity lacking in the original Kirchhoff formulation, they are difficult to utilise. Voronovich [329, 330] proposed another technique referred to as the first-order *small slope approximation* SSA(1) which relies, in particular, on discerning and utilising the symmetry and transformation properties that the solution must possess. The results are expressed as a systematic series and more accurate results can be obtained by evaluation of higher order terms, but this becomes numerical cumbersome.

Recently Elfouhaily [331] developed the extended Kirchhoff approach (EKA) for bistatic scattering from gently sloping, perfectly conducting surfaces. Analytical iterations of the surface current integral equation are performed in the EKA using the approach originally adopted by Holliday *et al.*[332]. Both the EKA and SSA have similar analytic forms and have attractive features including relative simplicity and the absence of an artificial surface scale separation. West [333] found that the backscattered cross sections by the EKA model to be quite accurate for small and intermediate incidence angles and under certain conditions even at low grazing angles. Toporkov *et al.* [334] reported anomalous nulls occurring at large scattering angles for horizontal polarisation using the EKA technique, which were not present with the SSA, but obtained identical results to the SSA using a refined 2-D version of the EKA [335]. Toporkov *et al.* [334] also investigated the Doppler spectra predicted using the EKA and SSA using linear and nonlinear surface models and found generally good agreement for vertical polarisation but significant discrepancies in horizontal polarisation results. Better prediction of the spectral separation at LGA has been obtained using the second order SSA [336].

5.4.4 Bragg / Composite surface models

The two-scale model (TSM) is a heuristic concept that was originally conceived by Kur'yanov [337] for determining the scattering of acoustic waves from rough surfaces. This approach was later applied to electromagnetic waves by Fuks [338] and Valenzuela [64] and now is widely used for the theoretical interpretation of radar

scattering data, due to its relative simplicity and more importantly, its transparent physical background [339]. Other two-scale models [340-343] have been developed with wider ranges of validity and a simplistic representation of the composite model is shown in Figure 5-3.

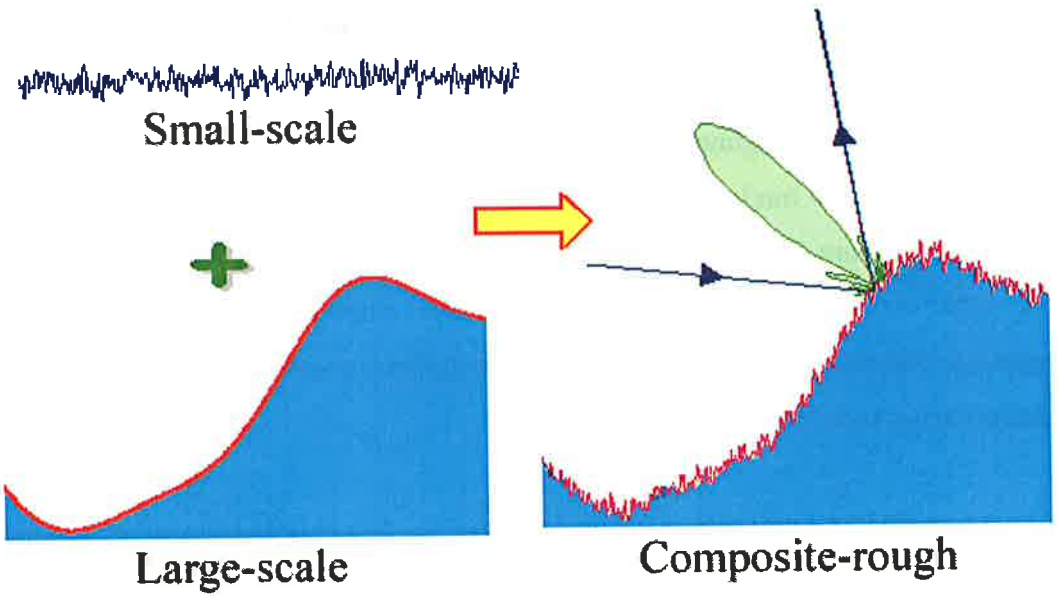

Figure 5-3 Composite surface model

In the TSM, the whole spectrum of roughness is separated into two classes corresponding to the large and small-scale components. The TSM postulates that the rough water surface is slightly rough over small scales and that the large-scale waves may be treated by a tangent plane approximation in which they tilt and advect the Bragg scattering waves, but at moderate incidence angles do not themselves contribute to the scattering. Three different mechanisms contribute to the modulation of the Bragg scattering produced by the large-scale tilts:

1. The surface tilt changes angle of incidence and hence changes the wavenumber responsible for the resonant Bragg scattering.
2. The surface tilt modifies the direction of the local surface normal for each facet and changes the local incident and scattering angles, which modifies the RCS values.
3. For vector waves, local tilts modify the polarisation states producing induced cross-polarisation terms due to the LOS rotation.

Although the TSM provides a physically correct description of the process of scattering it suffers from two inherent drawbacks. The parameter separating the large and small-scale roughness is chosen arbitrarily (within certain limits) since the power spectra encountered in most applications do not suggest a natural division of scales [339]. This complicates the calculation of corrections since it is impossible to determine if differences between experimental data and theoretical measurements should be attributed to inaccuracies in the scattering calculations or to an inadequate model of the surface roughness. Fuks [338] showed that the ambiguity in separating the roughness scales hinders the solution of the inverse problem of determining the roughness spectrum by characterisation of the scattered field. Nevertheless, TSM work rather well for the case of the ocean surface, since the separation between the large-scale component and the small-scale component is somehow related to gravity and capillary waves [344].

Generally the TSM treats the small-scale waves as free propagating wind generated waves. Problems are encountered at low grazing angles when the vertical component of the wavenumber of the incident radiation is no longer small compared with the surface displacement. Plant [345] recently showed that this limitation could be overcome with a slightly expanded version of the theory using the full Kirchhoff integral, to which Bragg scattering is an approximation.

The fact that σ^0_{HH} values are occasionally found to be larger than or equal to σ^0_{VV} for short integration times for incident angles between 20° and 80° is often quoted as evidence for non-Bragg scattering [79, 109, 346]. These results have led to attempts to add non-Bragg scattering from the sea surface to the theory [70, 109, 256, 347]. Plant [96] demonstrated that there is no evidence for non-Bragg scattering and that for incidence angles up to about 50° and that the discrepancies in the RCS values are caused by fading. He showed that the standard TSM scattering theory yields probabilities of finding $\sigma^0_{HH} > \sigma^0_{VV}$ that are only slightly smaller than those found experimentally. Plant [112] also showed that for higher incident angles, Bragg scattering from bound, tilted waves could be used to account for anomalies in the Doppler spectra and for part of the under-prediction of the σ^0_{HH} values. At very high angles of incidence (LGA) this theory still does not account for the differences in the

RCS values, but the addition of a non-Bragg component that is independent of the incidence angle and polarisation brings the simulated cross sections and probability distributions into good agreement with the experimental data. Plant proposed that the physical interpretation of the non-Bragg component is return for the sea spray just above the air/sea surface.

5.4.5 Analytical scattering theories

In the search for more effective formulations, as number of approximate analytic theories have been developed, including the integral equation model [348], the quasi-slope expansion [328], tilt invariant scattering theory [349], the distorted Born approximation [350], the heuristic scattering mode [351], local spectral expansion [352-354], Green's functions refinement [355] and mean-field theories [356, 357]. These approaches are based on approximations for the scattered fields of a single deterministic surface. Averaging is applied to these approximations to yield statistical moments of the scattered fields. Stochastic theories have also been developed which assume the field quantities to be random variables before the application of integral scattering operators. Examples include the smoothing method [358, 359] and operator-based approaches [360, 361]

Analytical scattering theories are of great importance since they provide physical insights, which cannot be obtained from the scattering properties alone and thus can be used to explore how variations in the surface parameters will affect the scattering behaviour. However, for most cases it is difficult to obtain a precise characterisation of the domain of validity [362] and some techniques require unacceptably long computation times for evaluation of the higher-order expansion terms [363, 364].

5.4.6 Surface scattering feature models

An alternative method to the GBVP approach assumes that the surface is made up of various scattering features or obstacles present on or near the sea surface. These models are referred to as *scattering feature models*. One of the first models was developed by Goldstein [365] to explain the polarisation dependence of sea return at low grazing angles. He proposed that spray droplets thrown upwards from the waves caused destructive interference between the direct and reflected waves, producing the observed differences in the HH and VV returns. Unfortunately, this model failed to

explain why a difference in the HH and VV returns remained when no spray was present. Goldstein's model was at least based on an observable feature of the sea environment. Other models have been conceived with scattering shapes that were unrelated to observable sea features. In many cases these shapes were selected simply because convenient solutions existed. Examples included techniques using smooth circular metallic disks [366], arrays of semi-infinite planes [367] and hemispherical bosses [368].

Other models have been proposed that are more closely related to the structure of the sea. Stokes waves [369] are commonly observed on natural water surfaces and have a quasi-trochoidal structure whose crest resembles a wedge. This property has been used in a number of scattering feature models [70, 72, 101]. These models usually incorporate the geometrical theory of diffraction (GTD) to explain the scattering. However, these models are only strictly applicable when the edge of the wedge is normal to the plane of incidence unless generalised via the uniform theory of diffraction (UTD). Nevertheless, these models give results that are as good as and in some case better than the predictions from the first-order Bragg or composite-surface models [293].

Other models have been developed that model the return based on scattering from plume water masses generated at breaking wave crests. Wetzel [370] modelled the plume as a conducting half cylinder sitting on an inclined flat plane. He assumed that the incident electromagnetic field consisted of the direct field reflected from the cylindrical surface, plus an indirect field associated with the multipath contribution produced by the reflected electromagnetic waves from the smooth water surface ahead of the cylinder. This model is highly sensitive to changes in the local grazing angle, plume diameter and position and polarisation changes. This is due to the substantial difference in the LGA Fresnel reflection coefficients for seawater at horizontal and vertical polarisations. Wetzel's plume model was combined with a Bragg scattering model [371] and produced improved predictions of the polarisation signatures at LGA than models based on the Bragg model alone or composite Bragg and wedge scattering models.

A major problem with all of the scattering feature models is that assumptions must be made about the shapes, size, orientation, speed and lifetime of the features themselves. While scattering feature models are mainly used to model LGA sea clutter, there is evidence that feature scattering occurs at all grazing angles [293].

5.4.7 Clutter statistics

In target detection problems, statistical distributions are commonly used to describe the electromagnetic scattering characteristics of the ocean surface. Radar engineers have empirically compared radar data with Gaussian, log-normal, Weibull and K-distributions [372, 373]. For depression angles of five degrees or more and for large cell areas, these statistics are usually reported as Rayleigh. For smaller angles and cell sizes the temporal statistics have distributions with shapes that fall between Rayleigh and the log-normal [80]. Conditions that cause spatial sea echo variations with large standard deviations will also cause temporal sea echo variations with large standard deviations. Therefore, depending on the sea surface details, spatial sea echo distributions are usually expected to lie between Rayleigh and log-normal [374]. At LGA the probability distributions assume a different form due to sea spikes [375]. Hansen and Cavaleri [77] performed measurements at LGA and plotted their results as cumulative distribution functions on Rayleigh probability paper. They found that the VV data could be fitted by a straight line, while the HH data started linear but curved sharply for larger radar cross sections. Olin [75] found that this data could be fitted by a single Weibull distribution for the VV data, while the HH distributions required two independent Weibull fits suggesting the presence of multiple scattering mechanisms. Sayama *et al.* [376] recently reported that sea clutter amplitudes obeyed the log-Weibull distribution using millimetre wave radar at low grazing angles and for high sea states found that the sea-clutter amplitudes obeyed the log-normal, log-Weibull and K-distributions in terms of the temporal and small scale fluctuations at X band [377, 378]. In this case the Akaike Information Criteria (AIC) [379] was used to determine the clutter statistics since it produces a more rigorous fit to the distribution of data than the least squares method.

5.5 Covariance matrix formulation of Bragg models

A model for the covariance matrix of rough surface scattering is required in order to interpret the entropy data for sea clutter in terms of wave processes on the ocean

surface. The Bragg and the extended Bragg model can be formulated using the covariance matrix approach, allowing the depolarisation processes that occur in sea surface scattering to be studied using the decomposition techniques discussed in Chapter 2.

5.5.1 First-order two-scale Bragg scattering model

The development of the two-scale first-order Bragg scattering model begins with the first-order SPM described in Section 5.4.2. The interaction between the electromagnetic waves and surface is manifest through a coupling of the electromagnetic fields to a component of the surface roughness spectrum, which is in resonance with the radar wavelength and local geometry. To first-order, the scattering matrix [S] for the Bragg surface can be written as

$$[S]=\begin{bmatrix} S_{HH} & S_{HV} \\ S_{VH} & S_{VV} \end{bmatrix}=m_S\begin{bmatrix} B_{\perp}(\theta,\varepsilon_r) & 0 \\ 0 & B_{\parallel}(\theta,\varepsilon_r) \end{bmatrix} \tag{5.12}$$

where m_S is the backscatter amplitude containing the information about the roughness conditions of the surface and $B_{\perp}$ and $B_{\parallel}$ are the Bragg coefficients perpendicular and parallel to the incidence plane. These are both functions of the complex permittivity ε_r and the local angle of incidence θ and are defined as

$$B_{\perp}(\theta,\varepsilon_r)=\frac{\cos\theta-\sqrt{\varepsilon_r-\sin^2\theta}}{\cos\theta+\sqrt{\varepsilon_r-\sin^2\theta}} \qquad B_{\parallel}(\theta,\varepsilon_r)=\frac{(\varepsilon_r-1)(\sin^2\theta-\varepsilon_r(1+\sin^2\theta))}{\left(\varepsilon_r\cos\theta+\sqrt{\varepsilon_r-\sin^2\theta}\right)^2} \tag{5.13}$$

From Equation (5.12) it is clear that the co-polarised ratio $B_{\perp}/B_{\parallel}$ depends only on the complex permittivity and the local angle of incidence and is independent of the surface roughness. The Bragg model predicts different scattering amplitudes for coefficients perpendicular and parallel to the incidence plane with $B_{\parallel}>B_{\perp}$. It is convenient to characterise the ratio of scattering amplitudes using the scattering alpha parameter α_B since it is independent of surface roughness and depends only on the dielectric constant and the angle of incidence. In Equation (2.123), the normalised Pauli scattering vector (for the backscattering case) is defined as

$$\vec{e}_{3P} = \frac{1}{\left|\vec{k}_{3P}\right|}\vec{k}_{3P} = \frac{1}{\left|\vec{k}_{3P}\right|}\begin{bmatrix} \cos\alpha e^{i\phi} \\ \sin\alpha\cos\beta e^{i\delta} \\ \sin\alpha\sin\beta e^{i\gamma} \end{bmatrix} = \frac{1}{\sqrt{2}\left|\vec{k}_{3P}\right|}\begin{bmatrix} S_{HH}+S_{VV} \\ S_{HH}-S_{VV} \\ 2S_{XY} \end{bmatrix} \tag{5.14}$$

Substituting the Bragg coefficients gives

$$\vec{e}_{3P}(\theta,\varepsilon_r) = \frac{1}{\sqrt{2}\left|\vec{k}_{3P}(\theta,\varepsilon_r)\right|}\begin{bmatrix} S_{HH}+S_{VV} \\ S_{HH}-S_{VV} \\ 2S_{XY} \end{bmatrix} = \frac{1}{\sqrt{2}\sqrt{\left|B_\perp\right|^2+\left|B_\parallel\right|^2}}\begin{bmatrix} B_\perp+B_\parallel \\ B_\perp-B_\parallel \\ 0 \end{bmatrix} \tag{5.15}$$

Three element unitary complex vectors have five degrees of freedom and can be parameterised in terms of five angles using Equation (2.122)

$$\vec{e}_{3P}(\theta,\varepsilon_r) = \frac{1}{\left|\vec{k}_{3P}\right|}\begin{bmatrix} \cos\alpha e^{i\phi} \\ \sin\alpha\cos\beta e^{i\delta} \\ \sin\alpha\sin\beta e^{i\gamma} \end{bmatrix} = \frac{1}{\sqrt{2}\sqrt{\left|B_\perp\right|^2+\left|B_\parallel\right|^2}}\begin{bmatrix} B_\perp+B_\parallel \\ B_\perp-B_\parallel \\ 0 \end{bmatrix} \tag{5.16}$$

Thus the alpha parameter for the Bragg model α_B can be defined as

$$\alpha_B = \cos^{-1}\left(\frac{\left|B_\perp+B_\parallel\right|}{\sqrt{2}\sqrt{\left|B_\perp\right|^2+\left|B_\parallel\right|^2}}\right) \tag{5.17}$$

In the case of scattering from the sea surface we assume that the dielectric constant ε_r is constant hence variations in α_B are a result of changes in the angle of incidence θ. The first-order Bragg model predicts that, for grazing angles $\left(\theta \simeq 90^\circ\right)$, the Bragg coefficient parallel to the incidence plane will be much larger than the coefficient perpendicular to the plane $\left(B_\parallel \gg B_\perp\right)$. Examining the expression in Equation (5.17) it is clear that in this case the value of α_B tends to 45°. On the other hand, in the case of normal incidence $\left(\theta \simeq 0^\circ\right)$, the scattering coefficients become equal, and the value of alpha tends to zero. Consequently, as the angle of incidence decreases, one would expect to observe a corresponding decrease in the alpha parameter. This behaviour is illustrated in Figure 5-4.

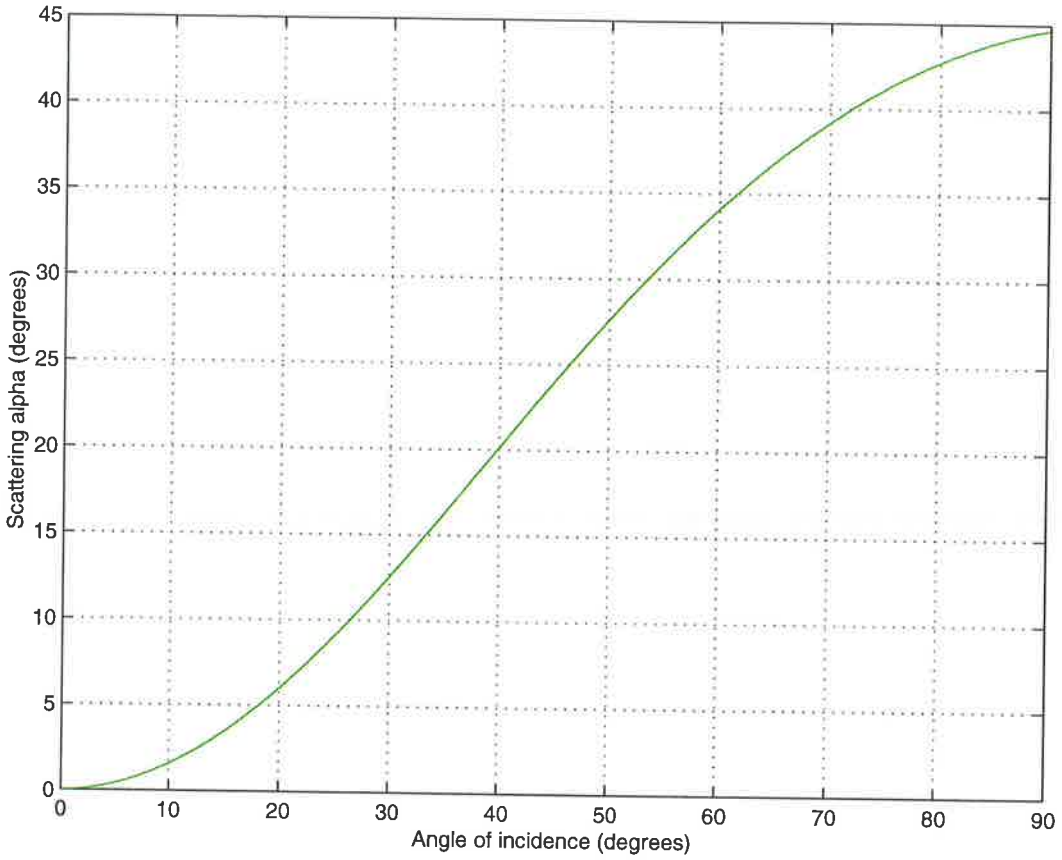

Figure 5-4 Variation of Bragg alpha angle with angle of incidence for sea water

From Equation (2.62) we know that the polarimetric coherency matrix is defined as

$$[T_3(\theta,\varepsilon_r)] = \left\langle \vec{k}_{3P}(\theta,\varepsilon_r)\cdot\vec{k}_{3P}^{\dagger}(\theta,\varepsilon_r)\right\rangle \tag{5.18}$$

From Equation (5.12) it is clear that the first-order Bragg model always predicts zero cross-polarisation and no depolarisation. Consequently, the coherency matrix $[T_3(\theta,\varepsilon_r)]$ predicted by this model will be of rank 1, hence the entropy and anisotropy values are always zero. It is clear that such a model is too simplistic for microwave polarimetric studies of sea clutter, where depolarisation is observed in measured data [74, 82, 90, 281].

The widely used two-scale model, described in Section 5.4.4 combines a small scale roughness superimposed on a larger-scale that tilts the Bragg facets and modulates the return. The tilting of the surface means that the tilted scattering matrix can have a non-zero cross-polarised component induced by the effective rotation about the LOS

(see Section 2.15.1). However, the induced cross-polarised returns in such a model are completely correlated with the co-polarised components. Consequently the entropy and anisotropy values are still zero and the model does not permit depolarisation to take place. In order to proceed, a modified approach is required to yield predictions of a depolarising covariance matrix. This can be achieved using the extended or X-Bragg model [380].

5.5.2 The extended Bragg model

The extended Bragg model was developed by Hajnsek [142] for the inversion of surface parameters from polarimetric SAR image data sets. This model enables predictions of a depolarising covariance matrix by the addition of a reflection symmetric depolarising component to the Bragg model. The assumption of azimuthal symmetry is too severe, but reflection symmetry with respect to the local surface normal provides a means for modelling the depolarisation in the presence of large-scale tilts and hence extends the model to a two-scale roughness profile.

The expression for the scattered electric field generated by the Bragg facet shown Figure 5-5, which can be written as

$$E_{pq}^{s} = i\ 2k\cos\theta\ B_{pq}\ \hat{Z}\left(2k\sin\theta\right) \tag{5.19}$$

The scattered field amplitude depends on the Fourier transform of the surface profile $\hat{Z}$, thus the average scattered power depends on the component of the power spectrum of the surface roughness that matches the incident wavelength. The polarisation dependence is only a function of the *local* angle of incidence θ and the dielectric constant ε_r though the set of Bragg coefficients B_{HH}, B_{VV} and B_{VH}. These are averaged over a statistical distribution $P(\beta)$ to obtain a surface that depolarises incident radiation and generates cross-polarisation while maintaining reflection symmetry about the local normal to the Bragg facet. In the case where the surface is sloped, additional cross-polarisation terms are induced due to the LOS rotation.

In order to proceed, a right-handed co-ordinate system must be established, centred on a Bragg facet as shown in Figure 5-5.

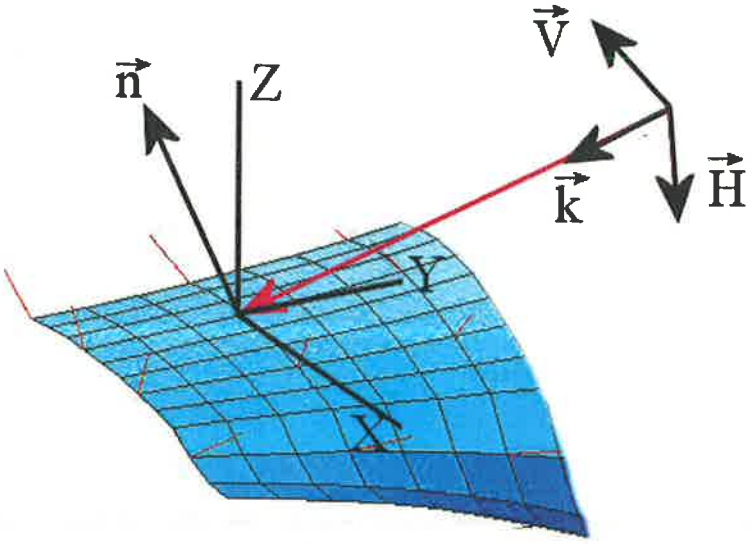

Figure 5-5 Scattering geometry for an arbitrary surface

The expression for the local surface normal can be written as

$$\vec{n} = n_x\vec{x} + n_y\vec{y} + n_z\vec{z} \tag{5.20}$$

Two principal slope components can also be defined from this normal. The first is the *range slope* defined as the rotation about the x-axis and the second is the *azimuth slope* defined as the rotation about the y-axis. The range slope is defined by the angle γ and can be written in terms of the local surface normal components as

$$\tan\gamma = \frac{\partial n_y}{\partial n_z} = -\frac{n_y}{n_z} \tag{5.21}$$

Similarly the azimuth slope is defined by the angle ω which is given by

$$\tan\omega = \frac{\partial n_x}{\partial n_z} = -\frac{n_x}{n_z} \tag{5.22}$$

The local tangent to the surface $\vec{t}$ can then be found by calculating the cross product between the incident wave propagation vector $\vec{k}$ and the normal to the surface $\vec{n}$. This can be written as

$$\vec{t} = \frac{\vec{n} \times \vec{k}}{\left| \vec{n} \times \vec{k} \right|} \tag{5.23}$$

Having defined the new local co-ordinate system it is now possible to modify the local scattering matrix in two ways.

- The local angle of incidence θ used for evaluation of the Bragg coefficients is no longer simply the angle of incidence ϕ but is now defined from the inner product between the surface normal and incident wave vector as shown in Equation (5.24) [175]

$$\cos\theta = \vec{n} \bullet \vec{k} = -n_y \sin\phi + n_z \cos\phi = \frac{\tan\gamma \sin\phi + \cos\phi}{\sqrt{1 + \tan^2\gamma + \tan^2\omega}} \tag{5.24}$$

- The combined effect of range and azimuth slopes causes an effective rotation of the surface in the plane of polarisation through an angle β defined as [175]

$$\begin{aligned} \cos\beta &= \vec{h} \bullet \vec{t} \\ \sin\beta &= -\left| \vec{h} \times \vec{t} \right| \end{aligned} \Rightarrow \tan\beta = \frac{-n_x}{n_y \cos\phi + n_z \sin\phi} = \frac{\tan\omega}{\sin\phi - \cos\phi \tan\gamma} \tag{5.25}$$

Thus the combined effect of the azimuth and range slope angles is to modify the scattering matrix of the Bragg facet to

$$[S(\beta,\theta,\varepsilon_r)] = \begin{bmatrix} \cos\beta & \sin\beta \\ -\sin\beta & \cos\beta \end{bmatrix} \begin{bmatrix} B_\perp(\theta,\varepsilon_r) & 0 \\ 0 & B_\parallel(\theta,\varepsilon_r) \end{bmatrix} \begin{bmatrix} \cos\beta & -\sin\beta \\ \sin\beta & \cos\beta \end{bmatrix} \tag{5.26}$$

This can be re-written in the Pauli scattering vector form as

$$\vec{k}_{3P}(\beta,\theta,\varepsilon_r) = \begin{bmatrix} 1 & 0 & 0 \\ 0 & \cos 2\beta & \sin 2\beta \\ 0 & -\sin 2\beta & \cos 2\beta \end{bmatrix} \begin{bmatrix} B_\perp(\theta,\varepsilon_r) + B_\parallel(\theta,\varepsilon_r) \\ B_\perp(\theta,\varepsilon_r) - B_\parallel(\theta,\varepsilon_r) \\ 0 \end{bmatrix} = [R_{3P}(\beta)] \vec{k}_{3P}(\theta,\varepsilon_r) \tag{5.27}$$

From Equation (2.62) we know that the polarimetric coherency matrix is defined as

$$[T_3(\theta,\varepsilon_r)] = \left\langle \vec{k}_{3P}(\theta,\varepsilon_r)\cdot\vec{k}_{3P}^{\dagger}(\theta,\varepsilon_r)\right\rangle \tag{5.28}$$

In Section 2.16.1, the general form of the coherency matrix $[T_3]$ representing the backscattering case under reflection symmetry was shown to be

$$[T_3] = \begin{bmatrix} t_{11} & t_{12} & 0 \\ t_{12}^{*} & t_{22} & 0 \\ 0 & 0 & t_{33} \end{bmatrix} \tag{5.29}$$

Using the effective rotation angle β defined in Equation (5.25), which represents any mismatch between the radar polarisation axes and the projection of the axis of symmetry of the medium into the plane of polarisation, the expression of the rotated coherency matrix $[T_3(\beta)]$ can be written as follows using Equation (2.81)

$$[T_3(\beta)] = [R_{3P}(\beta)]\begin{bmatrix} t_{11} & t_{12} & 0 \\ t_{12}^{*} & t_{22} & 0 \\ 0 & 0 & t_{33} \end{bmatrix}[R_{3P}(\beta)]^{-1} \tag{5.30}$$

where $R_{3P}(\beta)$ is the rotation matrix defined in Equation (2.80) as

$$[R_{3P}(\beta)] = \begin{bmatrix} 1 & 0 & 0 \\ 0 & \cos 2\beta & \sin 2\beta \\ 0 & -\sin 2\beta & \cos 2\beta \end{bmatrix} \tag{5.31}$$

Thus the coherency matrix for the tilted depolarising surface facet is given by

$$[T_{3S}(\beta,\theta,\varepsilon_r)] = m_S[R_{3P}(\beta)]\left\langle \vec{k}_{3P}(\theta,\varepsilon_r)\cdot\vec{k}_{3P}^{\dagger}(\theta,\varepsilon_r)\right\rangle[R_{3P}(\beta)]^{-1} \tag{5.32}$$

Substituting the expression for $\vec{k}_{3P}(\theta,\varepsilon_r)$ into Equation (5.32) yields

$$[T_{3S}(\beta,\theta,\varepsilon_r)] = m_S[R_{3P}(\beta)]\begin{bmatrix} a(\theta,\varepsilon_r) & b(\theta,\varepsilon_r) & 0 \\ b^{*}(\theta,\varepsilon_r) & c(\theta,\varepsilon_r) & 0 \\ 0 & 0 & 0 \end{bmatrix}[R_{3P}(\beta)]^{-1} \tag{5.33}$$

where

$$
\begin{aligned}
a(\theta,\varepsilon_r) &= \left\langle \left| B_{\perp}(\theta,\varepsilon_r) + B_{\parallel}(\theta,\varepsilon_r) \right|^2 \right\rangle \\
b(\theta,\varepsilon_r) &= \left\langle \left(B_{\perp}(\theta,\varepsilon_r) + B_{\parallel}(\theta,\varepsilon_r) \right) \left(B_{\perp}(\theta,\varepsilon_r) - B_{\parallel}(\theta,\varepsilon_r) \right)^* \right\rangle \\
c(\theta,\varepsilon_r) &= \left\langle \left| B_{\perp}(\theta,\varepsilon_r) - B_{\parallel}(\theta,\varepsilon_r) \right|^2 \right\rangle
\end{aligned}
\tag{5.34}
$$

Expanding Equation (5.33) and using the properties of reflection symmetric media given in Equation (2.87) yields

$$
\left[T_{3S}(\beta,\theta,\varepsilon_r)\right] = m_S \begin{bmatrix} a(\theta,\varepsilon_r) & b(\theta,\varepsilon_r)\cos(2\beta) & 0 \\ b^*(\theta,\varepsilon_r)\cos(2\beta) & c(\theta,\varepsilon_r)\cos^2(2\beta) & 0 \\ 0 & 0 & c(\theta,\varepsilon_r)\sin^2(2\beta) \end{bmatrix} \tag{5.35}
$$

Finally, configurational averaging over a statistical distribution $P(\beta)$, which represents the distribution of surface slopes, is performed and the coherency matrix for the Bragg facet becomes

$$
\left[T_{3S}(\theta,\varepsilon_r)\right] = \int_{-\pi}^{\pi} P(\beta) \cdot \left[T_{3S}(\beta,\theta,\varepsilon_r)\right] d\beta \tag{5.36}
$$

Substituting Equation (5.35) into Equation (5.36) gives

$$
\left[T_{3S}(\theta,\varepsilon_r)\right] = m_S \begin{bmatrix} a(\theta,\varepsilon_r) & b(\theta,\varepsilon_r)\tau & 0 \\ b^*(\theta,\varepsilon_r)\tau & c(\theta,\varepsilon_r)\delta & 0 \\ 0 & 0 & c(\theta,\varepsilon_r)(1-\delta) \end{bmatrix} \tag{5.37}
$$

where

$$
\begin{aligned}
\tau &= \int_{-\pi}^{\pi} P(\beta)\cos(2\beta)\, d\beta \\
\delta &= \int_{-\pi}^{\pi} P(\beta)\cos^2(2\beta)\, d\beta
\end{aligned}
\tag{5.38}
$$

A summary of the small-scale scattering from each Bragg facet predicted by the extended Bragg model is given in Equation (5.39).

$$E_{pq}^{s} = i\ 2k\cos\theta\ B_{pq}\ \hat{Z}\left(2k\sin\theta\right)$$

$$\Rightarrow \begin{cases} B_{HH} = B_{\perp} = & \dfrac{\cos\theta - \sqrt{\varepsilon_r - \sin^2\theta}}{\cos\theta + \sqrt{\varepsilon_r - \sin^2\theta}} \\ B_{VV} = B_{\parallel} = & \dfrac{(\varepsilon_r - 1)\left[\sin^2\theta - \varepsilon_r(1+\sin^2\theta)\right]}{\left(\varepsilon_r\cos\theta + \sqrt{\varepsilon_r - \sin^2\theta}\right)^2} \\ B_{HV} = B_{VH} = & 0 \end{cases} \tag{5.39}$$

$$\Rightarrow \begin{cases} a = & \left|B_{HH} + B_{VV}\right|^2 \\ b = & \left(B_{HH} + B_{VV}\right)\left(B_{HH} - B_{VV}\right)^* \\ c = & \left|B_{HH} - B_{VV}\right|^2 \end{cases}$$

$$\Rightarrow \left[T_S(\theta,\varepsilon_r)\right] = m_S \begin{bmatrix} a & b\tau & 0 \\ b^*\tau & c\delta & 0 \\ 0 & 0 & c(1-\delta) \end{bmatrix} \quad \begin{aligned} \delta &= \int_{-\pi}^{\pi} P(\beta)\cos^2(2\beta)\ d\beta \\ \tau &= \int_{-\pi}^{\pi} P(\beta)\cos(2\beta)\ d\beta \end{aligned}$$

In the two-scale model each Bragg facet is subject to a large-scale tilt. To incorporate this into the extended Bragg model, the combined effect of any azimuth or range tilts needs to be accounted for. Using the same analysis that was applied to the individual Bragg facets the modified coherence matrix becomes

$$\left[T_s(\beta',\theta,\varepsilon_r)\right] = \left[R_{3P}(\beta')\right]\left[T_s(\theta,\varepsilon_r)\right]\left[R_{3P}(\beta')\right]^{-1} \tag{5.40}$$

where the combined effect of range and azimuth slopes causes an effective rotation of the facet in the plane of polarisation through an angle β' as defined by Equation (5.25). On expansion the $\left\langle HV.(HH-VV)^*\right\rangle$ is no longer zero since the tilt generates correlation between the *HV* and the *HH–VV*, although due to the symmetry assumption the phase of $\left\langle HV.(HH-VV)^*\right\rangle$ remains zero meaning there is no helicity in the surface scattering [381].

5.6 Modelling radar returns from sea models

At the beginning of this chapter it was noted that in order to describe radar scattering from the ocean surface an understanding of the physical processes that influence the geometry and electromagnetic scattering from the sea surface is required. The previous sections have considered these two problems separately. The following section illustrates a number of examples in which the two-scale Bragg models are combined with the surface descriptions produced using SWPE and NFSFS to generate predictions of the polarimetric signatures.

5.6.1 Justification for adopting the two-scale Bragg models

The two-scale models based on the Bragg and extended Bragg models were used to predict the scattering from surfaces predicted using the SWPE and NFSFS codes described in Section 5.2 and for modelling the changes in the polarimetric parameters (entropy / anisotropy / scattering alpha) that occur during wave breaking. While there are some problems with TSM, particularly at LGA (as noted in Section 5.4.4) there are sufficient reasons to justify the selection of this approach. These reasons include the fact the TSM provides a physically correct description of the process of scattering, which can be evaluated efficiently while providing a simple means for modelling the depolarisation processes that occur in sea surface scattering.

The SWPE simulation results are generally evaluated on a fine grid which typically ranges from 301×301 up to 1001×1001 points. A computationally efficient model was required particularly when multiple antenna elevations were considered. The fact that the two-scale Bragg models can be adapted to run on a multi-processor environment using a parallel algorithm, since the scattering from individual grid points can be determined independently, was seen as a significant advantage.

While problems are often encountered at LGA angles using TSM, only situations in which the Bragg scattering assumptions remain valid have been considered. Thus the numerical simulations have been restricted to scenarios with low sea states, or small surface displacements (in the case of ship wakes) with low surface roughness. A simple shadowing routine was also incorporated into the TSM, removing some of the problems areas commonly encountered at LGA, but multipath effects and the contribution from bounded waves and non-Bragg scatterers was not addressed. The

importance of these effects at LGA has been noted and attempts to incorporate these features into the scattering models will be made in the future.

5.6.2 Analysis of the entropy of breaking ocean waves

While the case of non-breaking waves is of great interest, the extreme case of breaking waves has been studied extensively both experimentally and using numerical techniques [85, 89, 90, 102, 382-387]. In particular West has performed extensive studies on the electromagnetic scattering behaviour from breaking waves at LGA [86, 88, 108, 388-391].

The extended Bragg model was used to derive a simple description of the polarimetric behaviour of a breaking ocean wave. Initially the surface is modelled as a flat X-Bragg surface. As the wave propagates towards the radar the model increases the wave slope causing a local decreasing the angle of incidence. As the local wave slope increases, there is a temporal increase in surface roughness due to the breaking wave processes. From Equation (5.33), it is clear that the eigenvalue decomposition of $[T]$ will be *invariant* to any azimuthal surface tilts (β). Thus the eigenvalues of $[T]$ and the polarimetric parameters derived from them, such as the entropy and anisotropy, will depend only on the local angle of incidence θ (i.e. range tilts), the dielectric constant ε_r and the surface roughness, which is governed by the width (β_1) of distribution of surface slopes $P(\beta)$.

For simplicity we assume that $P(\beta)$ is uniform about zero with width $2\beta_1$ as shown in Figure 5-6.

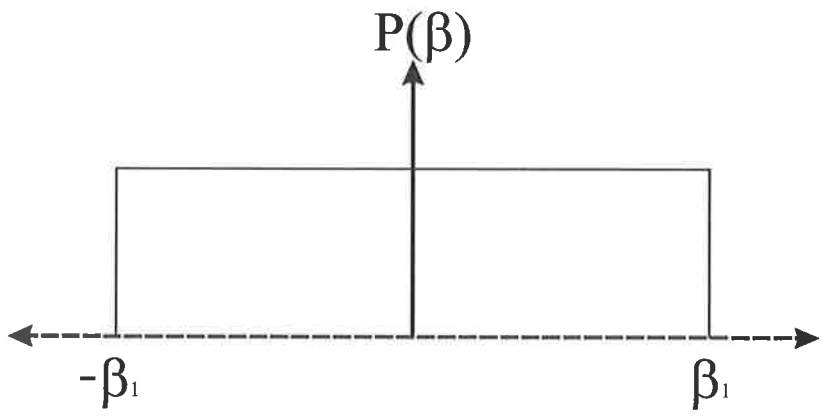

Figure 5-6 Uniform distribution of surface slope

Thus the distribution $P(\beta)$ can be defined as

$$P(\beta)=\begin{cases}\dfrac{1}{2\beta_1} & |\beta|\le\beta_1 \\ 0 & \text{Otherwise}\end{cases} \qquad 0\le\beta_1\le\frac{\pi}{2} \tag{5.41}$$

Thus substituting Equation (5.41) in Equation (5.38) gives

$$\begin{aligned}\tau &= \int_{-\pi}^{\pi} P(\beta)\cos(2\beta)\ d\beta = \int_{-\beta_1}^{\beta_1}\frac{1}{2\beta_1}\cos(2\beta)\ d\beta = \sin c(2\beta_1) \\ \delta &= \int_{-\pi}^{\pi} P(\beta)\cos^2(2\beta)\ d\beta = \int_{-\beta_1}^{\beta_1}\frac{1}{2\beta_1}\cos^2(2\beta)\ d\beta = \frac{1}{2}(1+\sin c(4\beta_1))\end{aligned} \tag{5.42}$$

where $\sin c(x)=\dfrac{\sin(x)}{x}$. Substituting Equation (5.42) into Equation (5.37) the coherency matrix for the extended Bragg model becomes

$$[T_{3S}(\theta,\varepsilon_r)]=m_S\begin{bmatrix} a(\theta,\varepsilon_r) & b(\theta,\varepsilon_r)\sin c(2\beta_1) & 0 \\ b^*(\theta,\varepsilon_r)\sin c(2\beta_1) & c(\theta,\varepsilon_r)\dfrac{(1+\sin c(4\beta_1))}{2} & 0 \\ 0 & 0 & c(\theta,\varepsilon_r)\dfrac{(1-\sin c(4\beta_1))}{2}\end{bmatrix} \tag{5.43}$$

The width of the distribution of slopes determines the roughness component and controls both the polarimetric coherence and the level cross-polarisation power. When $\beta_1=0$, the coherency matrix reduces to the simple first-order Bragg model discussed in Section 5.5.1 and the polarimetric coherence becomes unity and the cross-polar power is zero. As the value of β_1 increases, the coherence reduces while the cross-polar power increases. When β_1 = 90° the surface becomes azimuthally symmetric. The increase in the cross-polar power is faster than the fall in coherency and thus for small β_1 values the polarimetric anisotropy will be close to unity as shown in Figure 5-7. As the value of β_1 increases the anisotropy will fall monotonically to zero. These properties are discussed in more detail in [392].

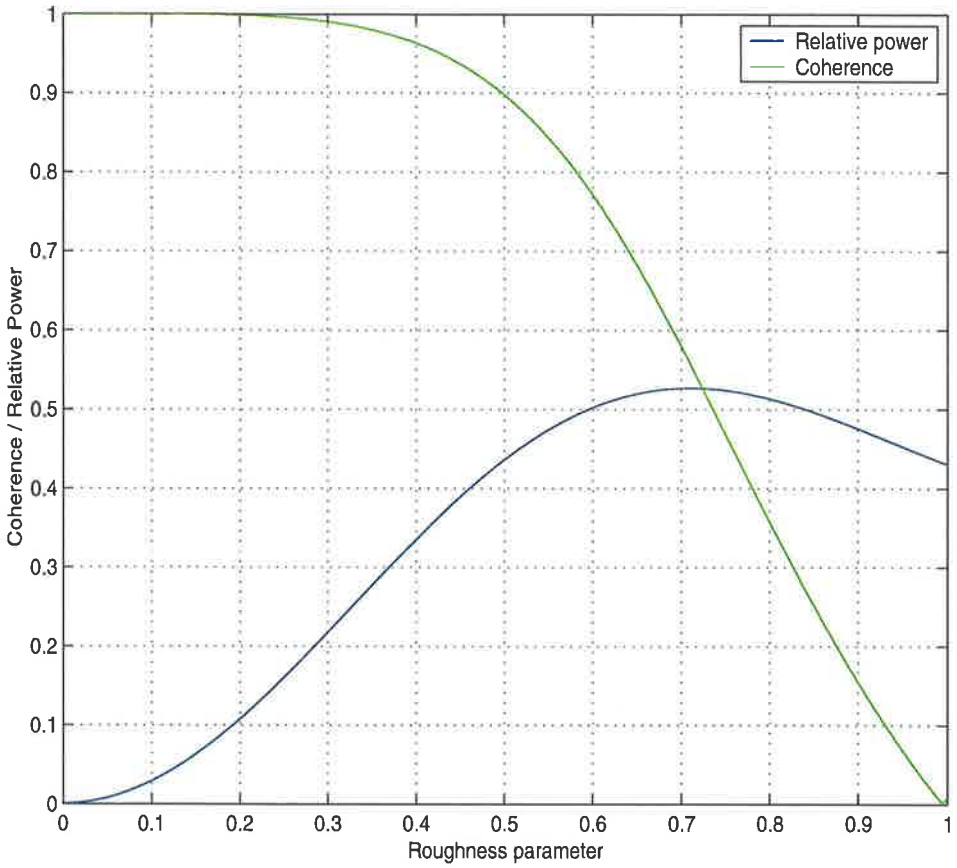

Figure 5-7 The variation in relative power and coherence with surface roughness

The polarimetric coherence between the left-left and the right-right circular polarisation, γ_{LLRR}, can be shown to be related to the elements of the coherency matrix via the following expression [392]

$$\gamma_{LLRR} = \frac{T_{22} - T_{33}}{T_{22} + T_{33}} = \sin c\left(4\beta_1\right) \tag{5.44}$$

This highlights the fact that the γ_{LLRR} depends only on the surface roughness β_1. Since the anisotropy can be interpreted as a generalised rotation invariant expression for γ_{LLRR} [392] it is evident that the anisotropy is independent of the dielectric properties of the surface and that for smooth surfaces (low β_1) the anisotropy will be close to unity. Increases in the surface roughness will result in a reduction in the anisotropy.

Figure 5-8 shows the variations in entropy that occur for changes in the surface roughness and angle of incidence. This plot illustrates that the entropy increases with higher roughness and with larger angles of incidence. As a wave forms one would expect an increase in the range tilt and hence a decrease in the local angle of incidence. If the surface roughness remains constant then it is clear from Figure 5-8 and the X-Bragg model would predict that the entropy should decrease. However, if there is an increase in the surface roughness (as a result of wave entering the breaking state) combined with an increase in the range tilt, then the X-Bragg model suggests that the entropy can remain unchanged.

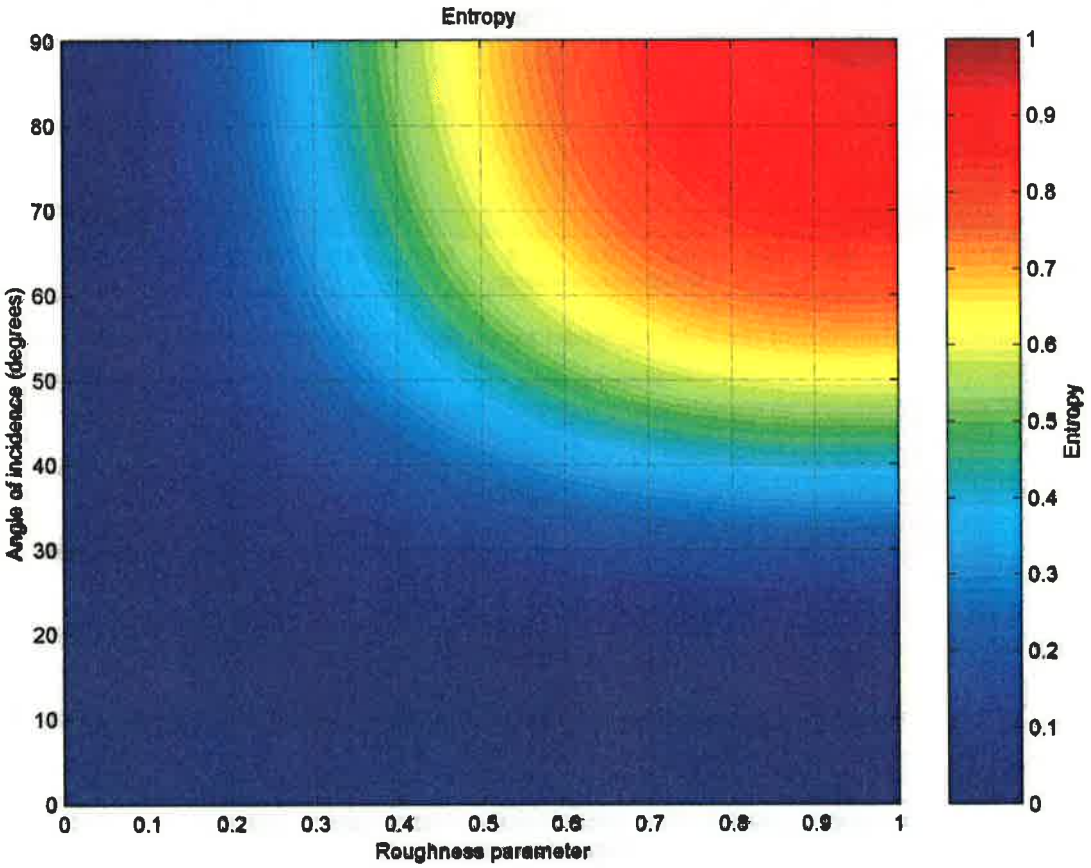

Figure 5-8 Entropy of the X-Bragg model vs. surface roughness and angle of incidence

On the other hand, we see that the anisotropy value, shown in Figure 5-9, depends mainly on the roughness and is largely insensitive to wave tilting. Hence, if we have an increase in surface roughness there should be a decrease in anisotropy coupled with unchanging entropy.

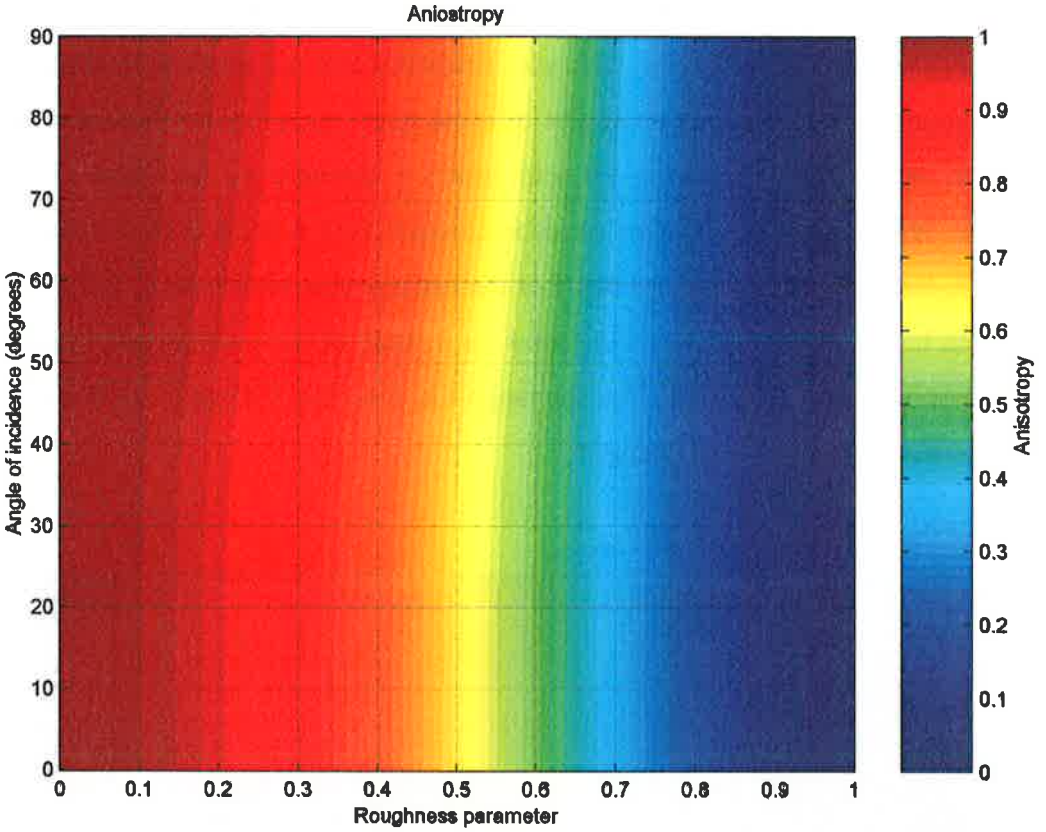

Figure 5-9 Anisotropy of the X-Bragg model vs. surface roughness and angle of incidence

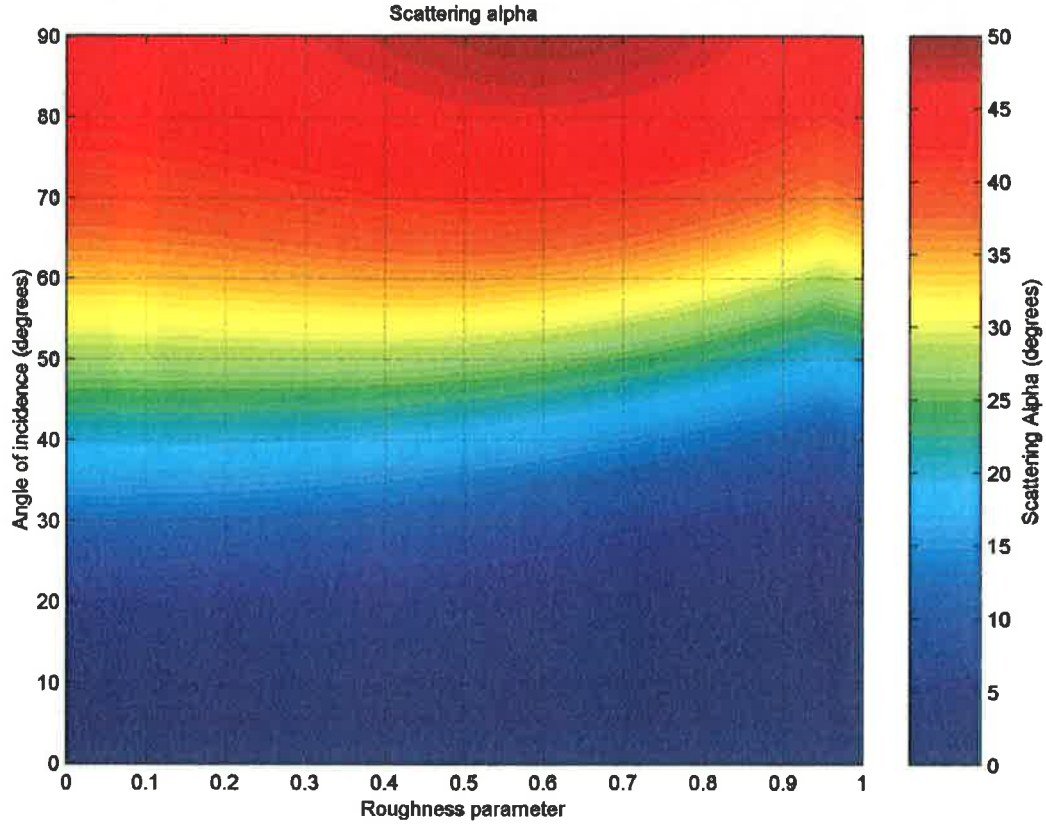

Figure 5-10 Alpha Parameter of the X-Bragg model vs. surface roughness and angle of incidence

The variation in scattering alpha parameter $\bar{\alpha}$, shown in Figure 5-10, illustrates that increasing the surface roughness produces only a slight increase in $\bar{\alpha}$ values, while changes to the angle of incidence, caused by wave tilting which changes the local range slope, have a much stronger effect. Thus, in the case of a breaking wave, where an increase in range tilt correlated with increasing roughness is expected, at least for upwind viewing geometry, the X-Bragg model predicts that the alpha parameter should fall.

In summary, the X-Bragg model predicts that for a breaking ocean wave the entropy will remain relatively unchanged while there will be a combined drop in the anisotropy and alpha angle. To examine how well this model agrees with observations of breaking ocean waves, measurements in the littoral zone were performed at Evans Head in New South Wales and Yallingup in Western Australia. Good agreement was observed and a detailed comparison is given in Chapter 6.

5.6.3 Validation of ocean surface measurements

Validation of ocean surface polarimetric measurements using computer models is difficult because there are generally two unknowns present; the scattering model being assessed and the stochastic surface geometry that provides the test environment. One possible solution for solving the ambiguity is to replace the stochastic surface with a quasi-deterministic one. The approach proposed in this work replaces the stochastic surface with a Kelvin wake generated by a moving ship. At the moment, certain limitations of the DSTO radar prevent this technique from being fully exploited, but we present some preliminary results obtained using the surface elevation, slope and velocity fields predicted by SWPE combined with the two-scale Bragg scattering model described in Section 5.5.1

To illustrate some of the capabilities of the SWPE code, a simple hull model was created for a pilot boat, similar to the one measured in the Queenscliff experiment described in Chapter 6. The model dimensions were matched to the length, beam and draft of the pilot boat, so that a good estimate of the surface wake pattern could be obtained. The model consisted of 1340 flat patches and a 3D representation of the hull is illustrated in Figure 5-11.

Figure 5-11 Pilot boat model

The wake produced by the pilot boat model was calculated using SWPE assuming a constant speed of 6.4 ms^{-1} (the estimated speed of the pilot boat in the Queenscliff measurements) travelling in the negative $\vec{x}$ direction. The surface displacements were calculated on a regularly spaced grid with a 410 m extent in the $\vec{x}$ direction and 300 m extent in the $\vec{y}$ direction and a spatial resolution of 1 m in both directions. The resulting wake pattern is shown in Figure 5-12.

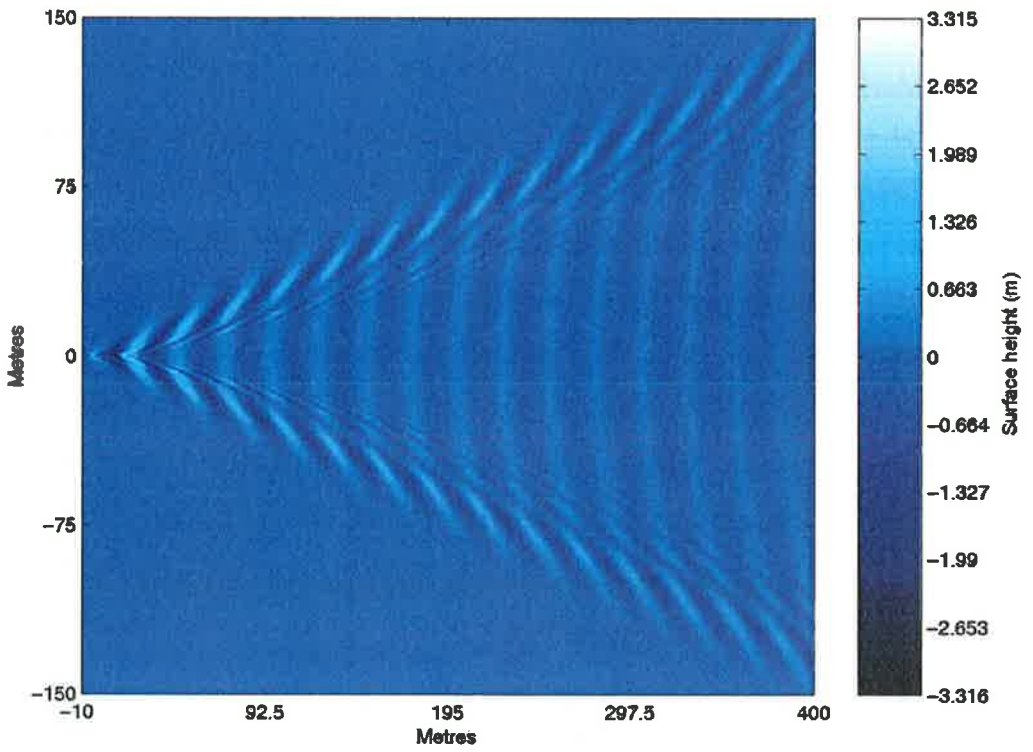

Figure 5-12 Pilot boat wake elevation pattern

SWPE assumes that the ambient sea conditions are perfectly calm, thus the surface displacements outside of the wake regions are zero. To generate more realistic predictions, an additional routine for generating ambient sea conditions based Pierson-

Moskowitz directional wave spectrum [248] has also been developed. These results can be easily combined with the SWPE output results to give more realistic predictions.

The surface displacement produced by SWPE was then used with the two-scale Bragg model to calculate the polarimetric response from the resulting surface. First a bicubic surface is fitted to the surface displacements. The local surface normals $\vec{n}_i$ and the angle of incidence ϕ_i from the specified radar position are calculated at each grid point. These parameters are then used to determine the local angle of incidence θ_i to the surface and the effective rotation of the surface β_i in the plane of polarisation using the analysis presented in Section 5.5.2. These values are then used in the Bragg model given in Equation (5.26) to determine the elements of $[S]$. Images of the simulated polarimetric response in the HH, VV and cross-polar channels are shown in Figure 5-13.

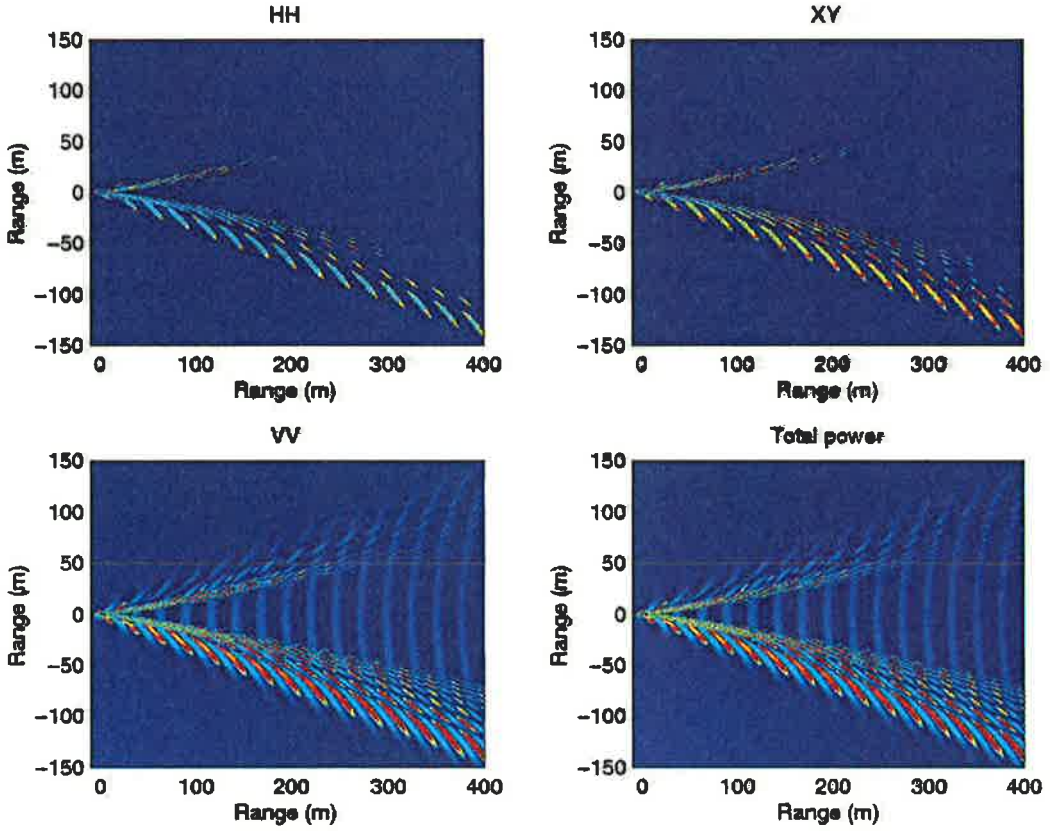

Figure 5-13 Simulated polarimetric response from the pilot boat wake pattern

The simulation was run using a look down angle of 1.5° to match the measurement conditions during the Queenscliff measurement. A number of radar look directions were also considered to determine how the polarimetric signature varied with look direction. Due to the low angle of incidence, the VV return is significantly stronger than the other channels as seen in Figure 5-13. Shadowed regions were identified using a physical optics approach and the return from these regions was set at the background clutter level. While the simple Bragg model predicts that the cross-polar response should be zero, Figure 5-13 illustrates that the range tilts produce an induced cross-polar response due to the effective rotation about the LOS (see Section 2.15.1).

The scattering code for calculating the polarimetric response from the wake surfaces produced by SWPE has a high degree of flexibility in terms of illumination and viewing geometry. To illustrate this the polarimetric response was generated for a range of antenna aspects and elevation angles. A wake pattern produced by the pilot boat was recalculated using a smaller 80 m × 80 m grid (to reduce computation time). Once again, 1 m grid spacings were used in both directions. The polarimetric response for aspects of 0° (looking in the positive $\vec{x}$ direction), 90° (looking in the positive $\vec{y}$ direction) and 180° (looking in the negative $\vec{x}$ direction) were calculated at elevation angles of 1°, 5°, 10°, 15° and 20°. The results of these simulations are shown in Figure 5-14 to Figure 5-17 and illustrate that the cross-polar response in the linear polarisation basis provides far greater sensitivity and ability to map the wake slope pattern than the co-polar responses.

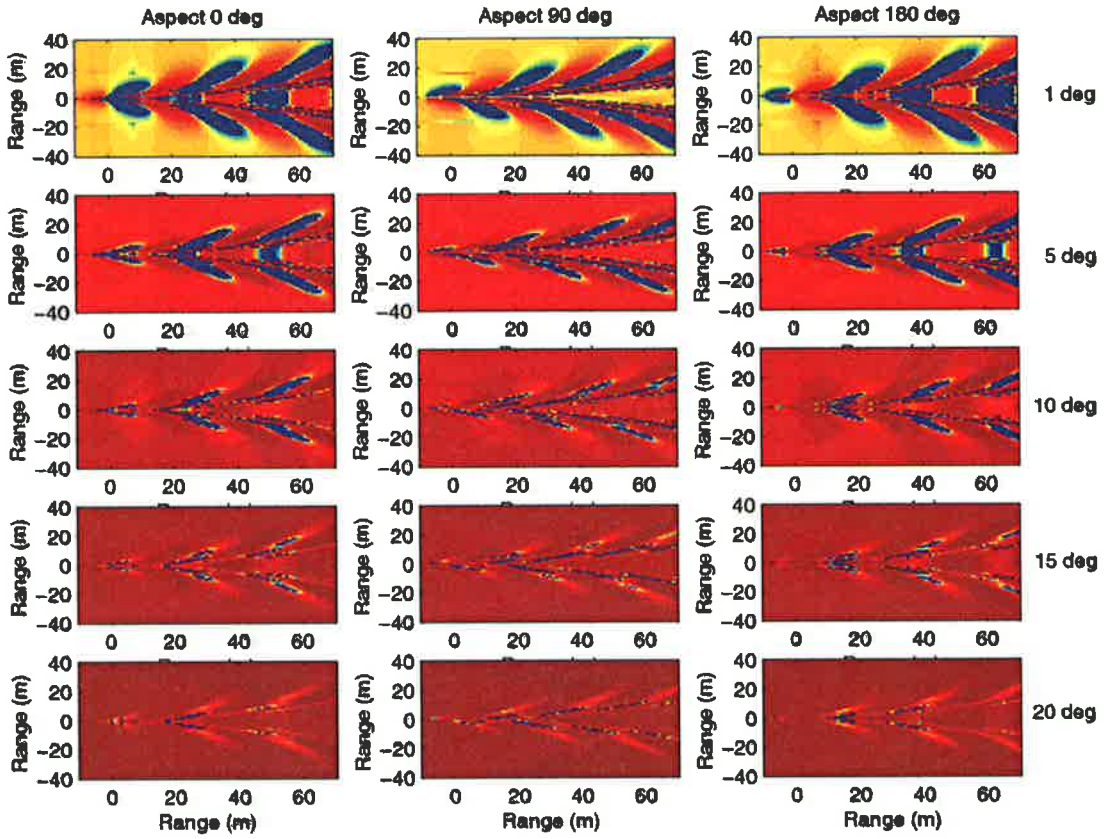

Figure 5-14 The effect of varying aspect and elevations angles on the VV response

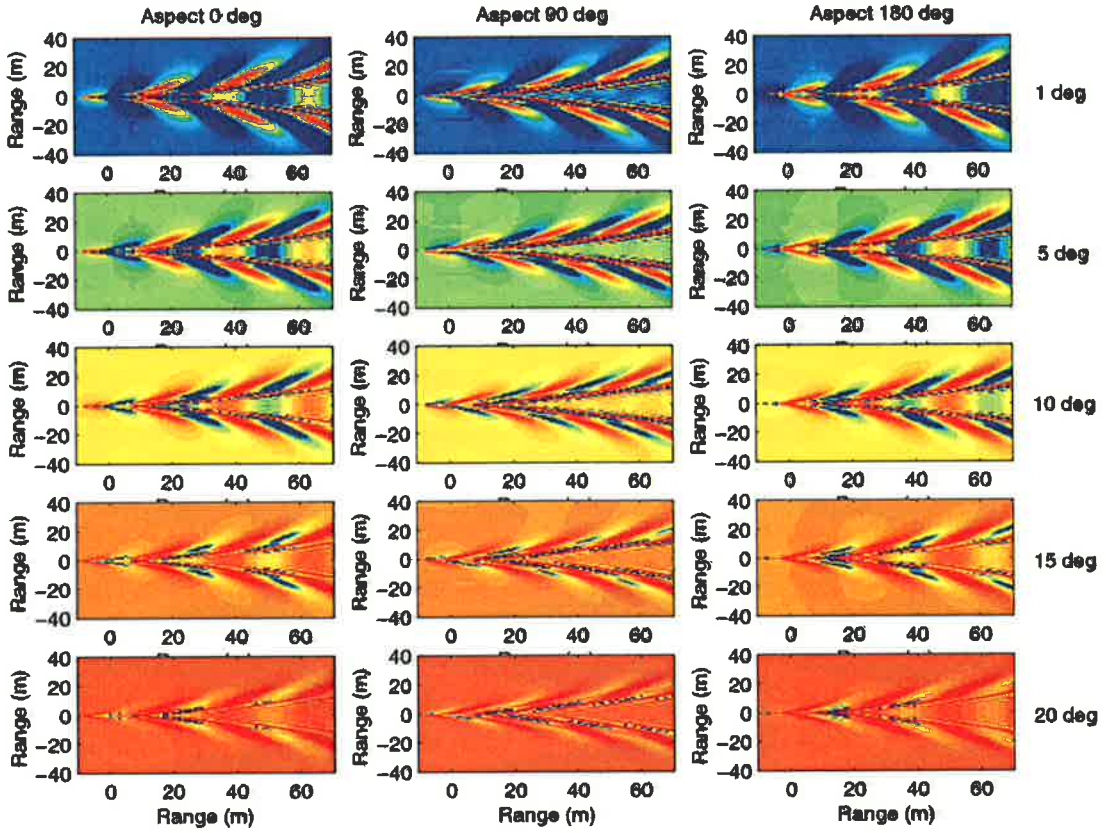

Figure 5-15 The effect of varying aspect and elevations angles on the HH response

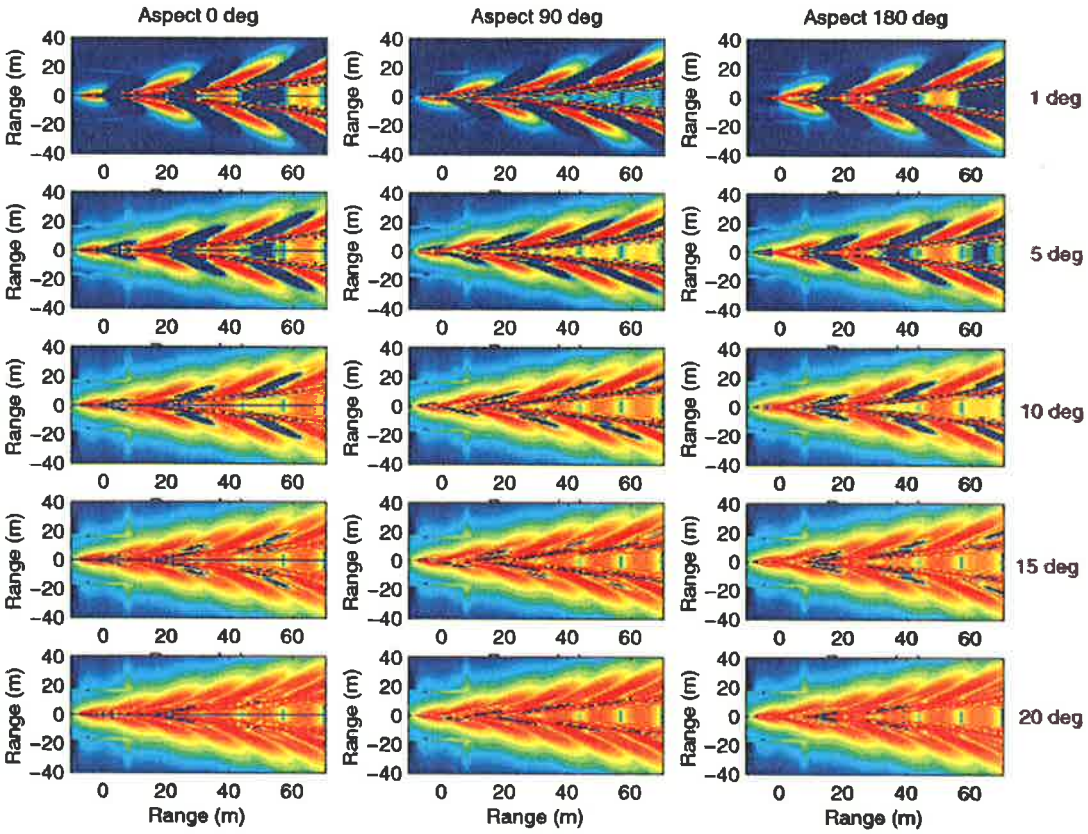

Figure 5-16 The effect of varying aspect and elevations angles on the cross-pol response

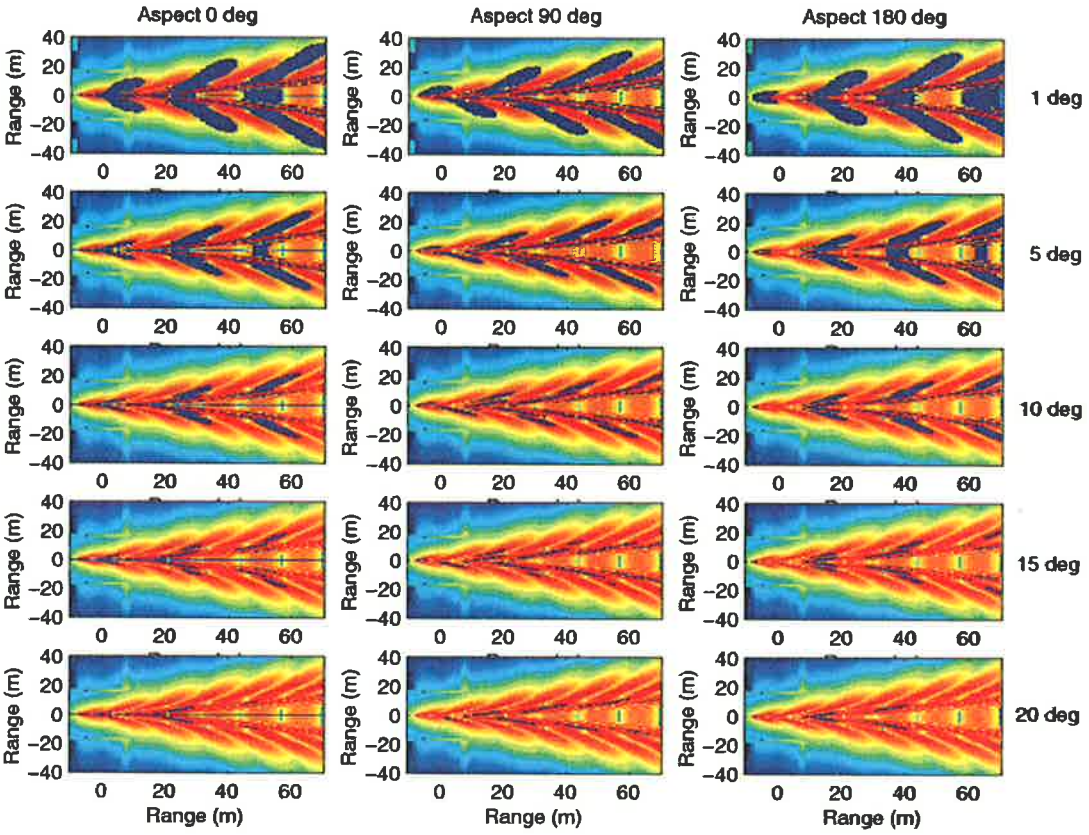

Figure 5-17 The effect of varying aspect and elevations angles on the Ratio of VV/XY power

SWPE is also capable of producing the surface slopes and velocities of the resulting wake patterns. One key advantage of polarimetric radar, identified earlier in this chapter, is the ability to estimate the large-scale surface slopes. In theory, polarimetric measurements with the DSTO radar could to be used to validate the slope predictions produced by SWPE, while measurements of the polarimetric Doppler signatures provide, in principle a means for validating the surface flows. At present there are certain hardware limitations that prevent this technique from being fully exploited. Details of the problems encountered in the Doppler processing of high resolution results are discussed in Chapter 6.

To illustrate the ability to generate the slope and velocity fields, a simulation using the pilot boat model was run. The vessel was assumed to be travelling at a speed of 6.4 ms^{-1} using a 30 m × 30 m grid with 0.5 m resolution in both directions, assuming a water eddy viscosity ν_e of 5×10^{-3} m^2s^{-1}, which is typical for ship wakes [393, 394]. The plot of the surface slopes is shown in Figure 5-18 while the surface velocity plot is shown in Figure 5-19.

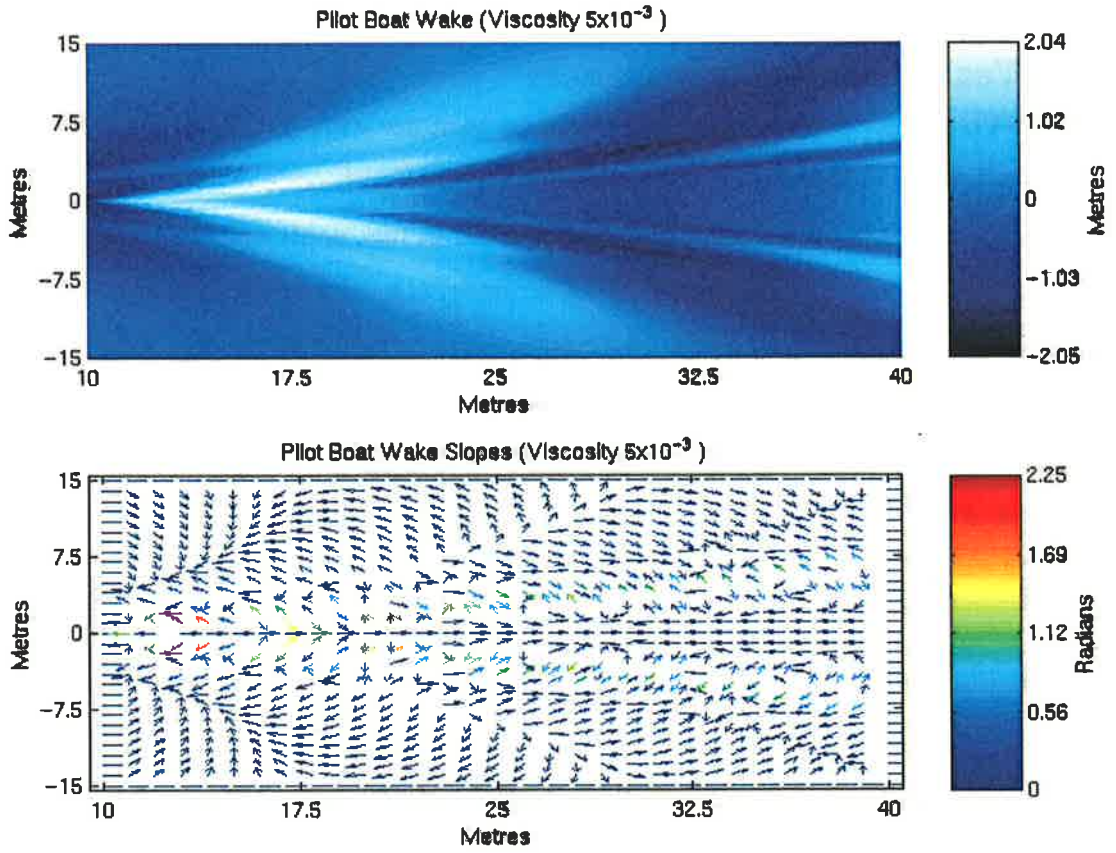

Figure 5-18 Pilot boat surface displacements and wake slopes

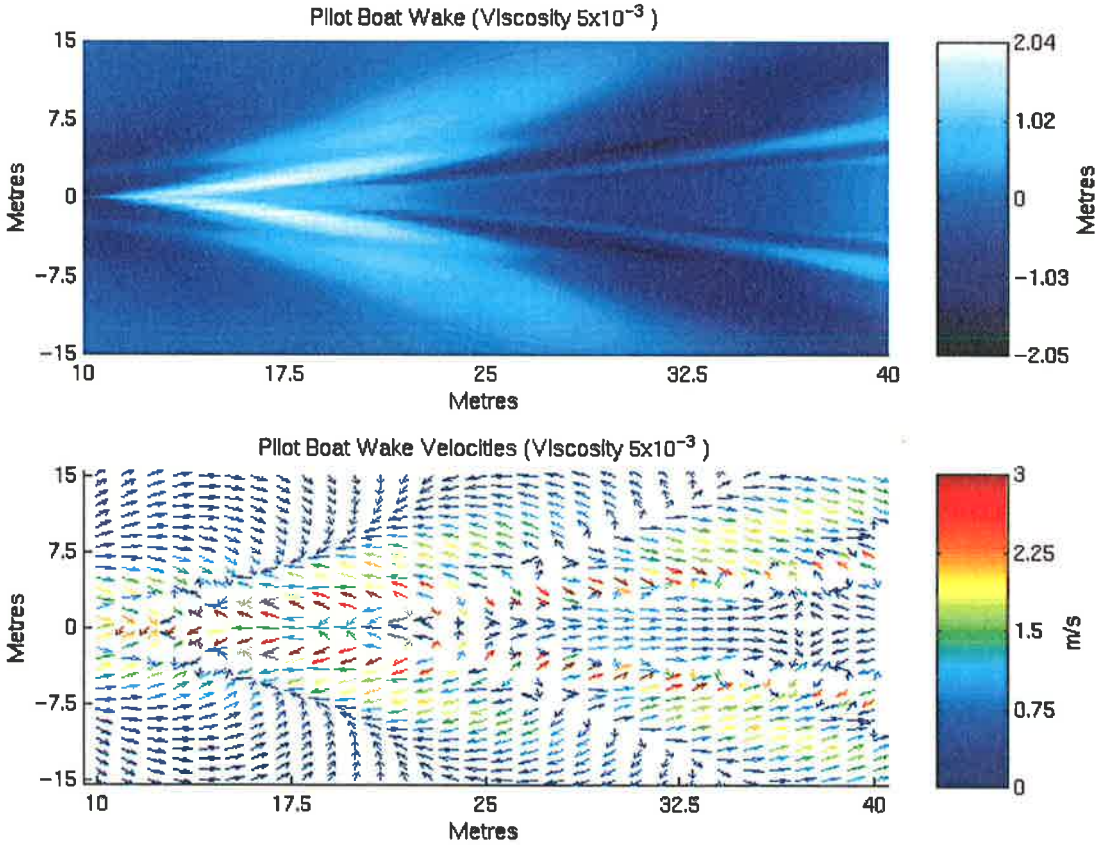

Figure 5-19 Pilot boat surface displacements and surface velocities

5.7 Weakly nonlinear processes

The SWPE results presented in the previous sections were produced using linear solutions for the surface boundary conditions. The NFSFS code differs from SWPE in that the surface boundary conditions are applied in full, nonlinear form. While the continuing development of improved electromagnetic scattering techniques is of crucial importance, the need to achieve commensurate fidelity in the representation of the sea surface is vital. The nonlinear approach adopted in NFSFS allows for greater accuracy of results and enables comparisons to be made between the linear and nonlinear solutions to assess the effect the nonlinear contributions have on the resulting surface elevation patterns.

Polarimetric radar is well-suited to the measurement of large-scale surface slopes when the characteristic length scale l of large-scale slope variability satisfies $l >> \lambda$. For X band radar, where $\lambda \sim 0.03$ m, this corresponds to a minimum length scale of ~ 1 m, which is adequate for resolving surface gravity waves in the frequency band

above ~ 0.5 Hz. Thus we are motivated to assess the potential of polarimetric radar for measuring the spatial slope pattern with a precision sufficient to identify the presence of nonlinear contributions and to determine their spatial properties.

To highlight the nonlinear contributions, a comparison between the wakes as computed using SWPE and NFSFS was performed. The nonlinearity arises both at the free surface, where the kinematic and dynamic boundary conditions apply, and in the approximations used to model the rigid body condition. The predicted surface elevations produced by SWPE and NFSFS for a uniformly-translating submerged spheroid are shown in Figure 5-20 and Figure 5-21 respectively. The results were determined using a 200 m × 80 m regularly spaced grid with the object travelling at 10 ms^{-1} at a depth of 5 m.

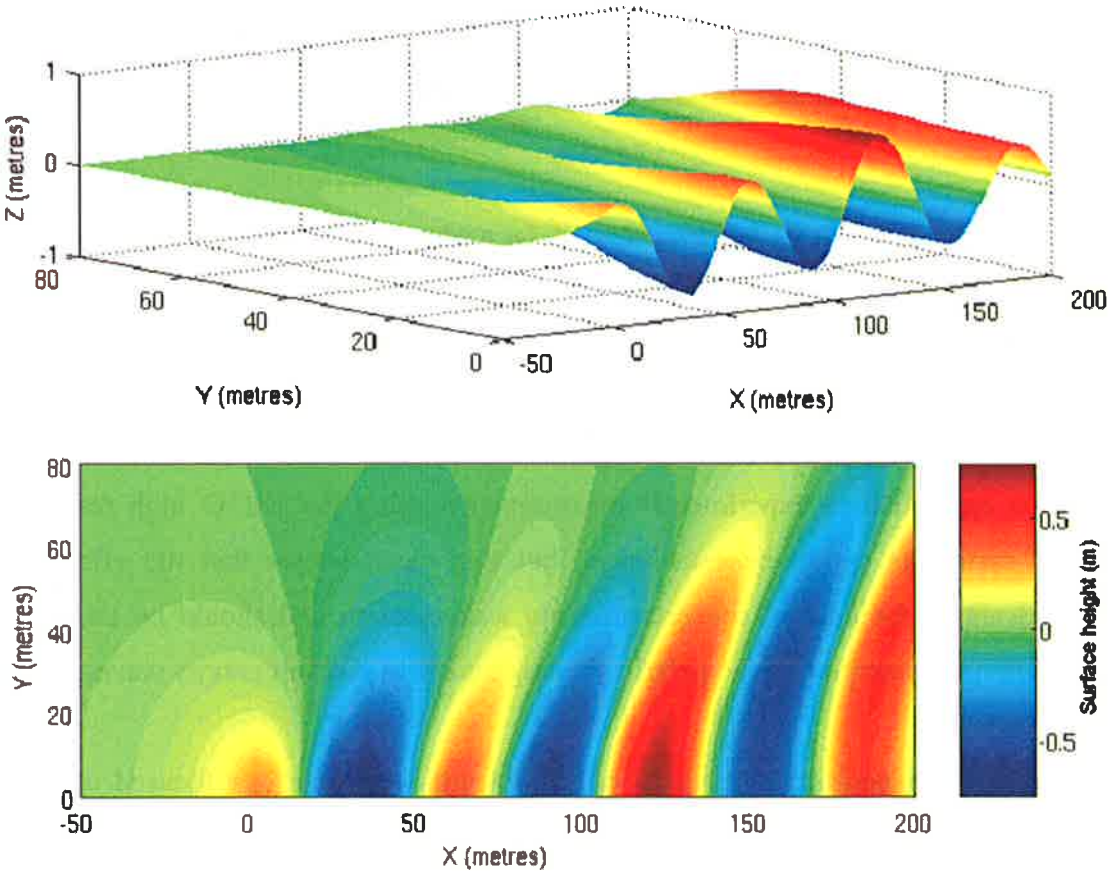

Figure 5-20 SWPE results for a submerged spheroid

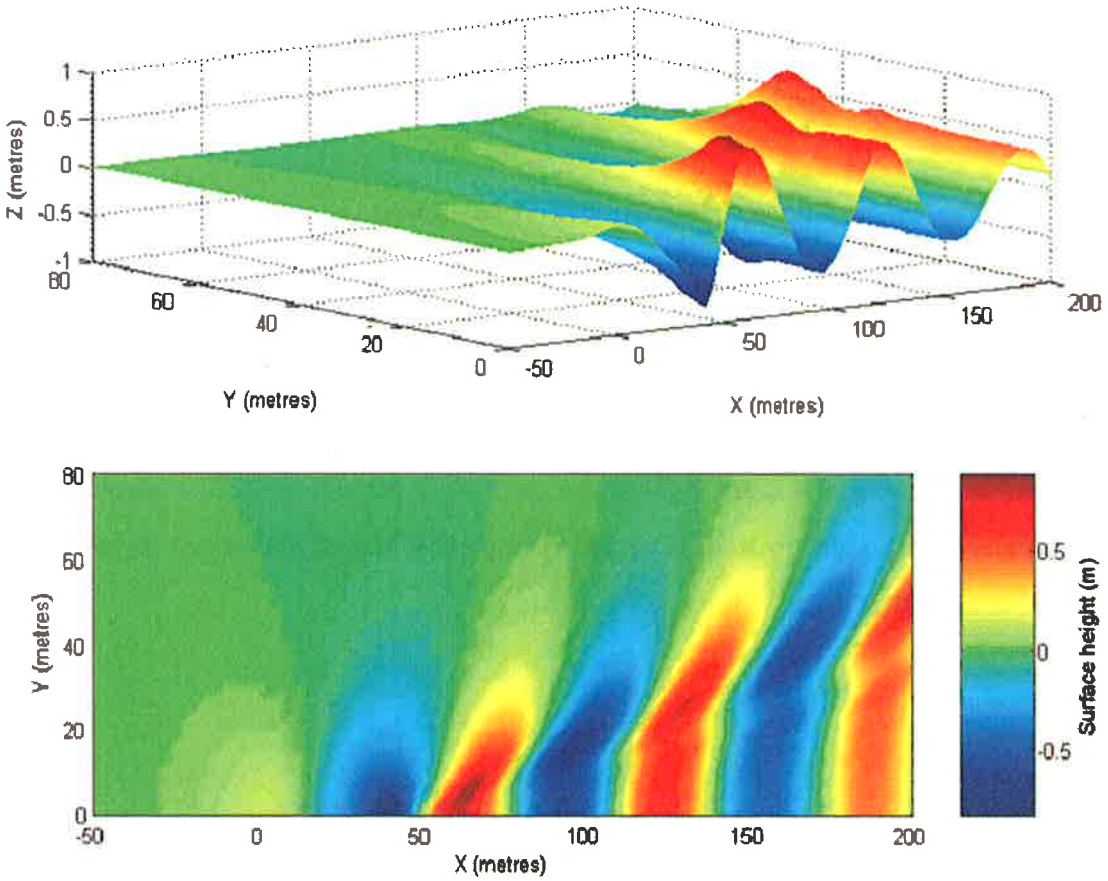

Figure 5-21 NFSFS results for a submerged spheroid

The SWPE and NFSFS results demonstrate that while the surface elevations predicted by imposing linear and the full nonlinear boundary conditions are similar in magnitude, the surface features are noticeable different. Whether such nonlinearities can be quantified in experimental measurements using the DSTO high resolution radar system is yet to be established, but this result shows that the effects are significant in the case of the deterministic wake pattern and should be taken into account when interpreting the polarimetric signatures of random gravity waves.

Most of the experimental research on nonlinearities to date has focused on wave breaking initiated by the interaction between the wake and the ambient sea waves. One of the problems with shallow grazing angle radar measurements of breaking waves is that it is difficult to predict when and where wave breaking events are going to occur. While radar measurements can interrogate a range of locations simultaneously, the concept of initiating wave breaking events using a ship wake was

conceived, thus enabling some control over when and where the wave breaking events would occur. This idea has been demonstrated using the wake produced by a ship [395]. Modelling of this process has not been attempted, but the experimental findings are discussed in Chapter 6.

5.8 Synopsis

A review of the hydrodynamic models and electromagnetic scattering techniques adopted to describe radar scattering from the ocean surface has been presented. Linear hydrodynamic models using parametric wave models have been described, along with nonlinear models that provide a description of weakly interacting wind waves. The modelling of quasi-deterministic features arising from ship wakes using the SWPE and NFSFS code has also been discussed and the potential for exploiting the Kelvin wake generated by a moving ship for validating ocean surface polarimetric measurements has been highlighted. An overview of the scattering techniques from rough surfaces has been given, including a description of the small perturbation methods, techniques based on the Kirchhoff approximation, two-scale models and analytical scattering theories. The formulation of the Bragg and extended Bragg two-scale models using a covariance matrix approach has been outlined, illustrating how depolarisation can be introduced into the models, enabling predictions of the variations in the polarimetric parameters for progressive and breaking waves to be obtained.

The justification for adopting the two-scale model based on the extended Bragg models has been explained and the limitations of these models at LGA have been acknowledged. Examples in which the surface elevation, slope and velocity fields predicted by SWPE are combined with a two-scale Bragg model have also been presented to yield predictions of the polarimetric scattering from the resulting surfaces. The potential for using these results to obtain information of the directional wave spectrum and to assist in the interpretation of Doppler measurements has also been discussed. Finally, an example illustrating the differences arising from the linear and nonlinear wake models has been shown which highlights the importance of modelling the nonlinear components of gravity waves.

Chapter 6 Observed polarimetric signatures of features on the ocean surface

This chapter describes polarimetric measurements of features on the sea surface acquired using the DSTO mobile high resolution polarimetric radar system, their processing and interpretation using the models proposed in Chapter 5. Data was collected at a range of locations around Australia as illustrated in Figure 6-1.

Figure 6-1 Locations where polarimetric data was obtained

Low grazing angle measurements of the ocean, performed at Evans Head in New South Wales and Yallingup in Western Australia are presented. These results provide a good comparison between the polarimetric characteristics of the near shore wave field for two instances; one when the wave field is almost monochromatic and the other when a broader spectrum of waves is present. A comparison with the values predicted with the X-Bragg model discussed in Chapter 5 is given and shows good agreement in both cases. The potential for exploiting wakes as a tool for testing scattering theories and nonlinear contributions such as induced wave breaking is then considered. Wake measurements performed in Darwin Harbour are described that demonstrate the ability to measure wake structures using the DSTO radar system at

low grazing angles. A more detailed investigation of the polarimetric properties of a pilot boat wake acquired at Queenscliff, Victoria is then reported. These results are studied using eigenvalue analysis of the coherency matrix using the techniques described in Chapter 2 and a scalar method derived from the location of the cross-polar null locations. The results produced by SWPE using the model of the pilot boat hull, for the same scattering geometry and estimated boat speed, are compared with the experimental measurements and show similar trends. Finally, the potential for using ship wakes as a tool for studying nonlinear scattering processes is demonstrated using the wake produced by a boat to initiate wake breaking events with some control over where and when the scattering events take place.

6.1 Evans Head measurements

In October 2002 the DSTO mobile high resolution polarimetric radar facility was deployed at Evans Head, NSW to collect polarimetric data of breaking ocean waves in the littoral or surf zone. The measurements performed at Evans Head represented a scenario in which a broad spectrum of waves was present. The resulting sea surface exhibited a range of surface geometries and different degrees of nonlinear wave interactions. In such complex conditions, it is difficult to relate the physical scattering processes to the observed polarimetric behaviour. Measurements were collected in three different look directions, as indicated in Figure 6-2 to determine the differences in the polarimetric entropy, anisotropy and scattering alpha based on the radar look direction. The variation in these parameters is of particular interest as it can be shed light on the physical scattering processes, variations in the surface roughness and the degree of surface tilting using the analysis techniques described in Chapter 2. The measurements also provided an opportunity to collect experimental data to compare with the theoretical predictions of the X-Bragg model described in Chapter 5.

6.1.1 Experimental setup

The radar van was deployed at Postman's Hill, approximately 500 m from the beach at an elevation of 50 m above sea level. This site offered a good, clear, unobstructed view of the breaking waves from an elevated position. A look down angle of approximately 5° was achieved in these measurements. An elevated view of the sea conditions taken from a helicopter during the calibration measurements is shown in Figure 6-3.

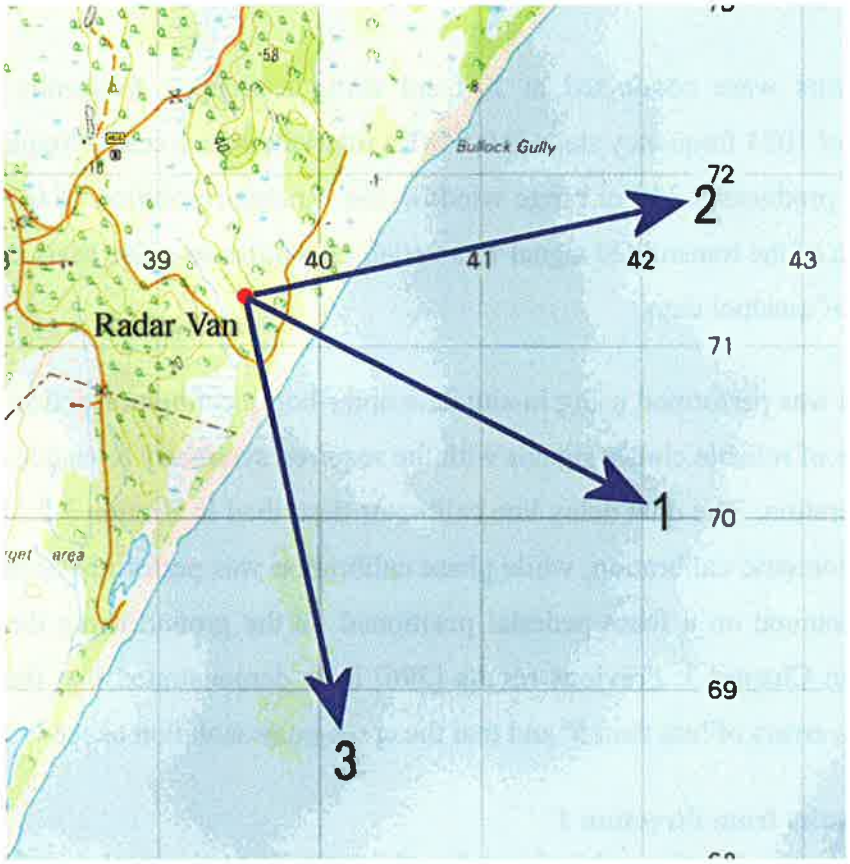

Figure 6-2 Evans Head measurement site

Figure 6-3 Aerial view of the Evans Head site

Measurements were conducted at X band using a stepped frequency waveform consisting of 1024 frequency steps at 0.5 MHz intervals with a centre frequency of 9.4 GHz. This produces a 300 m range window and a range resolution of 0.293 m. The polarisation of the transmitted signal was varied on a pulse-to-pulse basis enabling the collection of quadpol data.

Calibration was performed using in-situ helicopter-borne calibration reflectors, due to the absence of reliable clutter signals with the required symmetry to enable distributed target calibration. The dual delay line calibrator described in Section 3.2.11 was used for the radiometric calibration, while phase calibration was performed with a rotating dihedral mounted on a foam pedestal positioned on the ground using the technique described in Chapter 3. Previous results [396] have demonstrated that this approach gives phase errors of less than 5° and that the cross-polar isolation exceeds 27 dB.

6.1.2 Results from direction 1

The measurements performed looking directly out to sea were analysed first. In this case (direction 1 shown in Figure 6-2) the direction of propagation $\vec{k}$ was approximately orthogonal to the incoming swell. Measurements were accumulated over a range of 500 to 800 m for a period of 600 seconds. The received signals were then range-processed and combined to form an estimate of the scattering matrix for each range-time cell. The variation in the magnitude of the elements of the scattering matrix over a 200 second segment of the data is shown in Figure 6-4.

The received signals were combined to form an estimate for the 3 dimensional Pauli scattering vector $\vec{k}_{3P}$ for each range-time cell. The 3×3 polarimetric coherency matrices were then calculated from the outer product of $\vec{k}_{3P}$ averaged over a 9×9 cell. The eigenvalue decomposition was performed and the polarimetric entropy, anisotropy and scattering alpha values were determined for each cell. Images illustrating the variation in these parameters over a 70 second section of the data are shown in Figure 6-5.

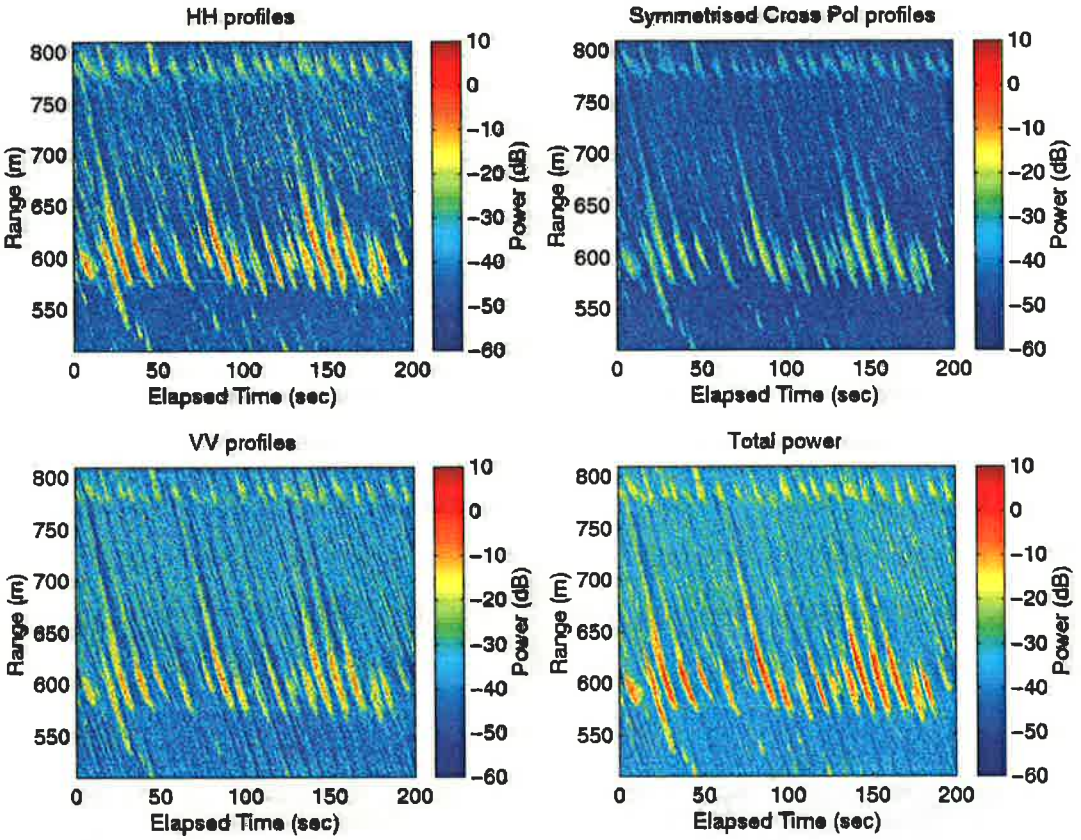

Figure 6-4 The variation in magnitude of the [*S*] matrix elements observed in direction 1

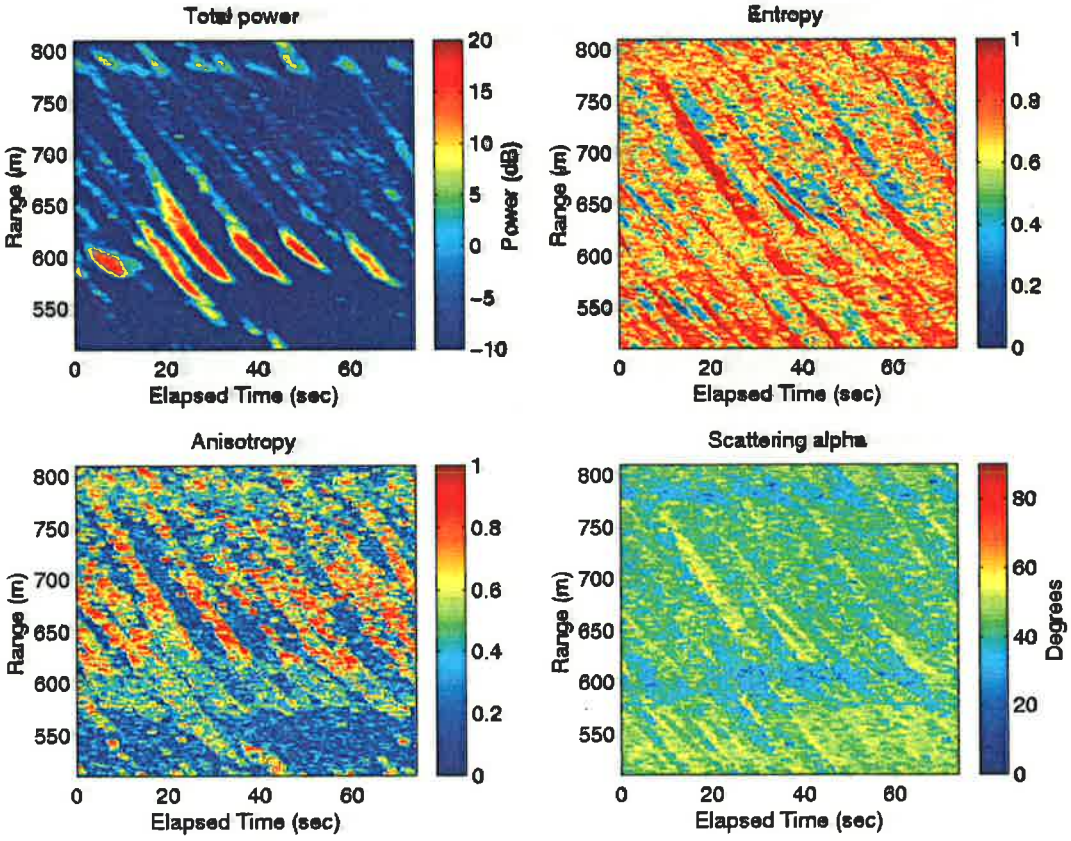

Figure 6-5 The variation in the polarimetric quantities in direction 1

Two wave breaking regions are evident in the results shown in Figure 6-4. The main breaking occurs close to the shoreline at ranges between 600 and 650 m, while there is also evidence of wave breaking at a range of 780 m. On further inspection of the local bathymetry, a sandbar was discovered at this range. In Figure 6-5 it is clear that there are a large number of cells that contain high entropy values combined with low power returns due to a combination of shadowing from the incoming waves, the scattering geometry and surface conditions. The regions of maximum interest are the lower entropy / high power regions corresponding to returns from the incoming waves as they form and break. To aid in the interpretation of the data, the results were filtered, removing regions with high entropy and low power so that the variation in the polarimetric parameters could be more readily observed. The filtered plots of entropy, anisotropy and scattering alpha values are shown in Figure 6-6.

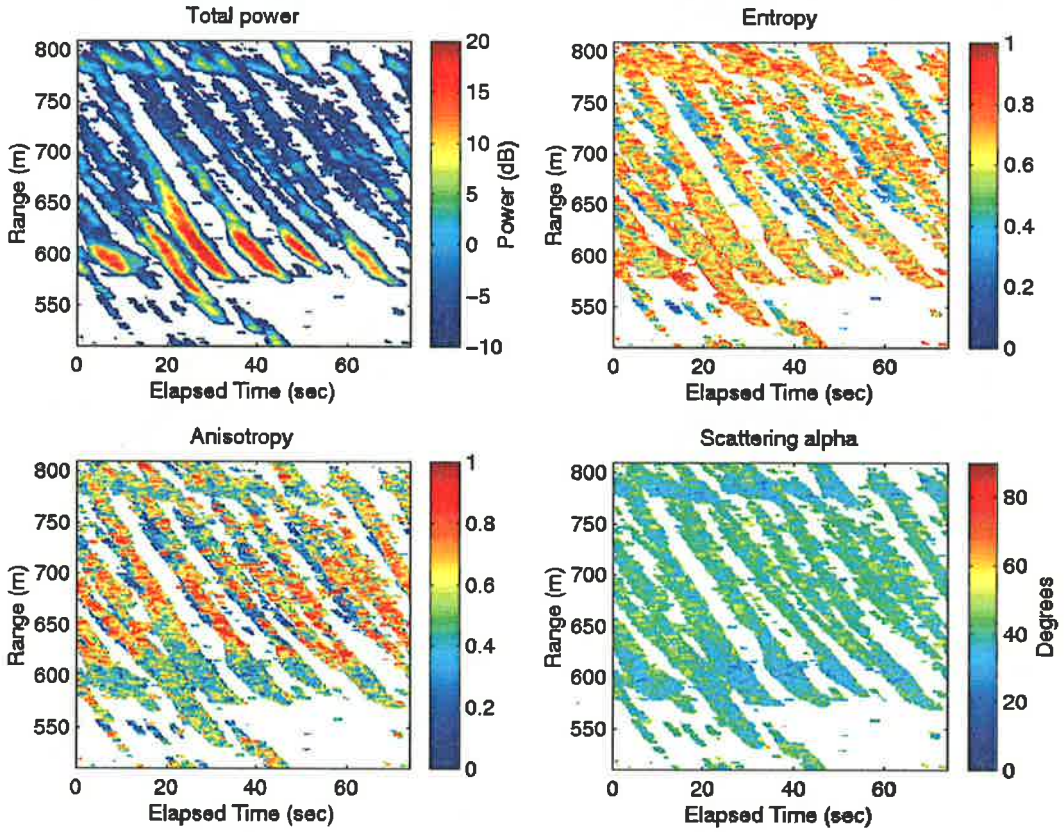

Figure 6-6 Filtered results looking in direction 1

The distribution of the points in the $H-A-\bar{\alpha}$ space was determined using the complete data set and is shown in Figure 6-7, and the distribution of points after the data has been filtered is shown in Figure 6-8.

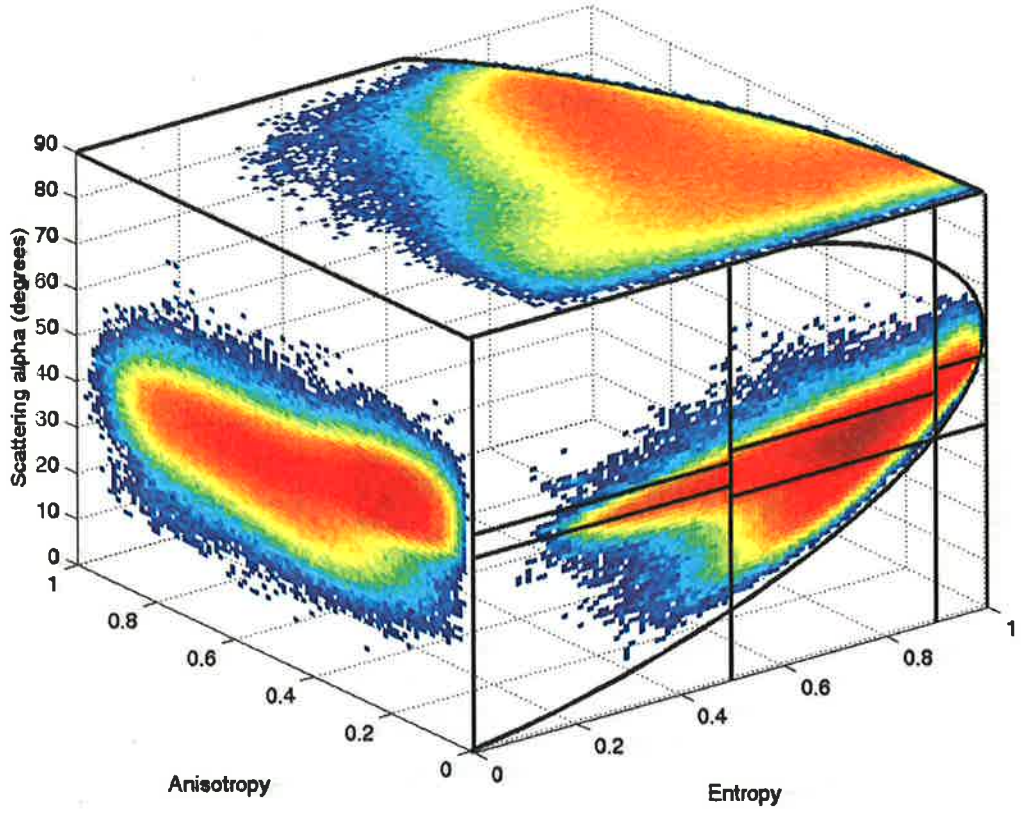

Figure 6-7 The distribution of points in the $H-A-\overline{\alpha}$ space observed in direction 1

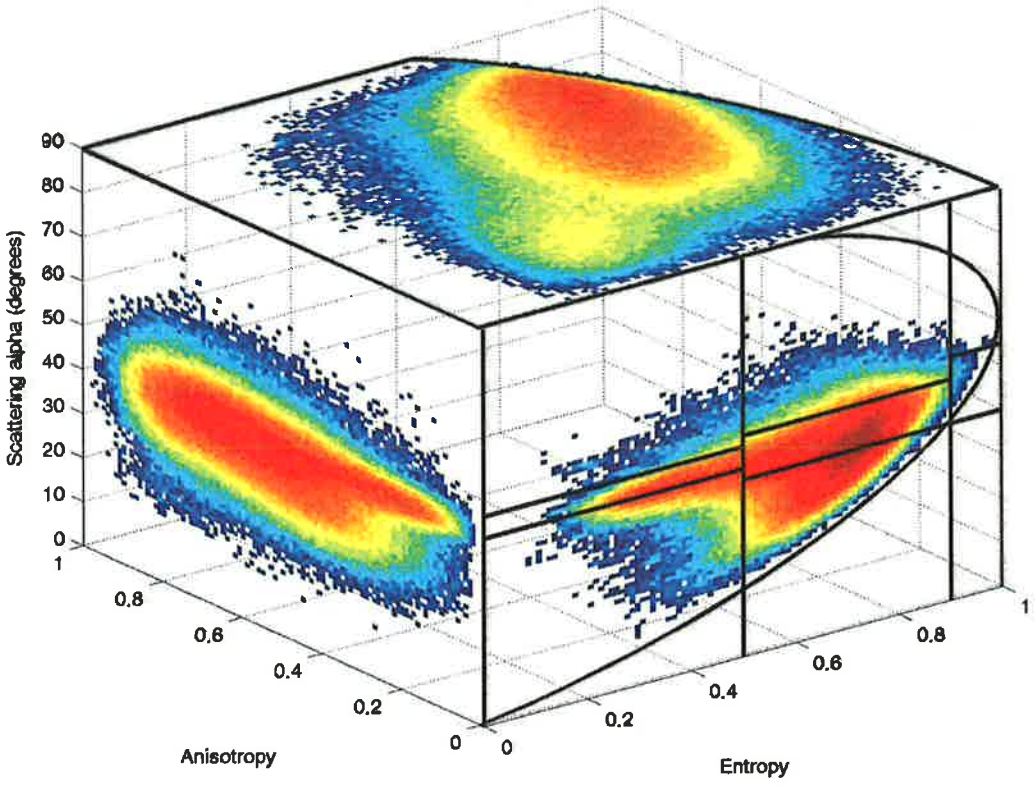

Figure 6-8 Filtered distribution of points in the $H-A-\overline{\alpha}$ space observed in direction 1

The distribution of the points in the $H-A-\bar{\alpha}$ space shows that the main concentration of points occurs for entropy values ranging from 0.6 to 0.8 with $\bar{\alpha}$ values ranging between 30° and 45° and anisotropy values ranging from 0.4 to 0.8.

The images formed from the matrix products corresponding to $[H][A]$, $[1-H][A]$, $[H][1-A]$ and $[1-H][1-A]$ were also created and are shown in Figure 6-9.

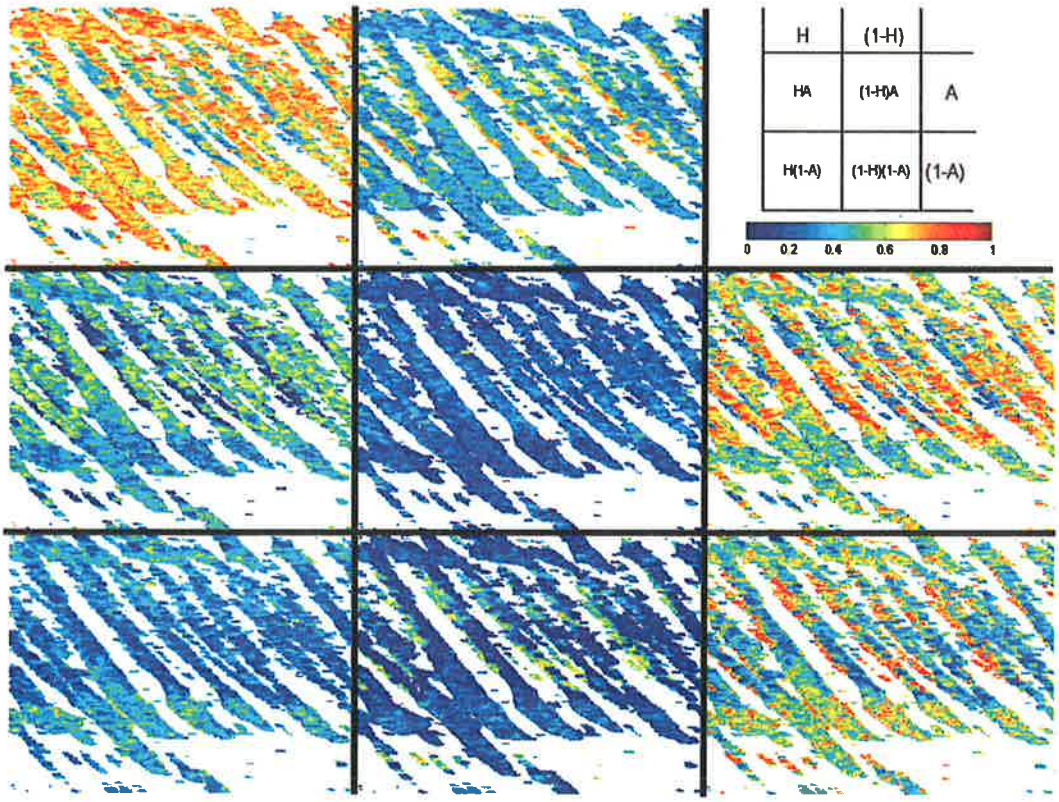

Figure 6-9 Image products formed between $[H]$, $[1-H]$,$[A]$ and $[1-A]$ for direction 1

In Chapter 2 it was shown that the $[H][A]$ image highlights situations in which there are two dominant scattering processes with similar probability values, the $[H][1-A]$ image highlights the clutter regions, $[1-H][1-A]$ highlights the presence of a single dominant scattering process and the $[1-H][A]$ images highlights regions in which there are two scattering mechanisms present with the secondary process having a medium probability.

The results in the $[H][A]$ image in Figure 6-9 suggest that as the wave forms and begins to break there are two dominant scattering processes present with similar

probability values. As the waves come closer to shore and begin to break, the $[H][1-A]$ image indicates that the scattering appears more random, suggesting that the surface acts as a depolariser. The $[1-H][1-A]$ also suggests that there is some evidence of a single dominant scattering mechanism located at the wave front. This is possibly due to specular scattering from the wave front prior to breaking

These results are consistent with the wavetank measurements and simulations from spilling breakers performed by Sletten and Wu [85] and West and Sletten [94] which suggest that there are multiple scattering mechanisms present and that the scattering is dominated by multipath effects. In studies of mechanically generated breaking waves at low grazing angles, Lee *et al.* [281, 397, 398] showed that enhanced scattering compared with Bragg scattering levels occurs throughout the evolutionary process of wave-breaking and that the breaking wave surface is an efficient depolariser. They also demonstrated [109] that at small grazing angles non-Bragg scattering was due to fast scatterers generated by the wave breaking and that with increasing wave steepness and surface roughness, mechanisms of multiple scattering and multipath interference become increasingly important.

Attempts were made to study the polarimetric Doppler signatures of the Evans Head results so that a comparison could be made with the previous studies [101, 281, 398, 399]. However, the large sweep size used in the measurements meant that aliasing problems were encountered during the Doppler processing. These problems are discussed in more detail in Section 6.2.3.

6.1.3 Results from direction 2

Next, the measurements taken looking in direction 2 (in Figure 6-2), approximately 45° to the incoming waves, were processed. Measurements were collected for ranges varying from 650 to 950 m over a period of roughly 600 seconds. Once again the received signals were range-processed and combined to form an estimate of the scattering matrix for each range-time cell. The variation in the magnitudes of the elements of the scattering matrix over a 200 second period that was representative of the scattering characteristics observed over the ten minute measurement period is shown in Figure 6-10.

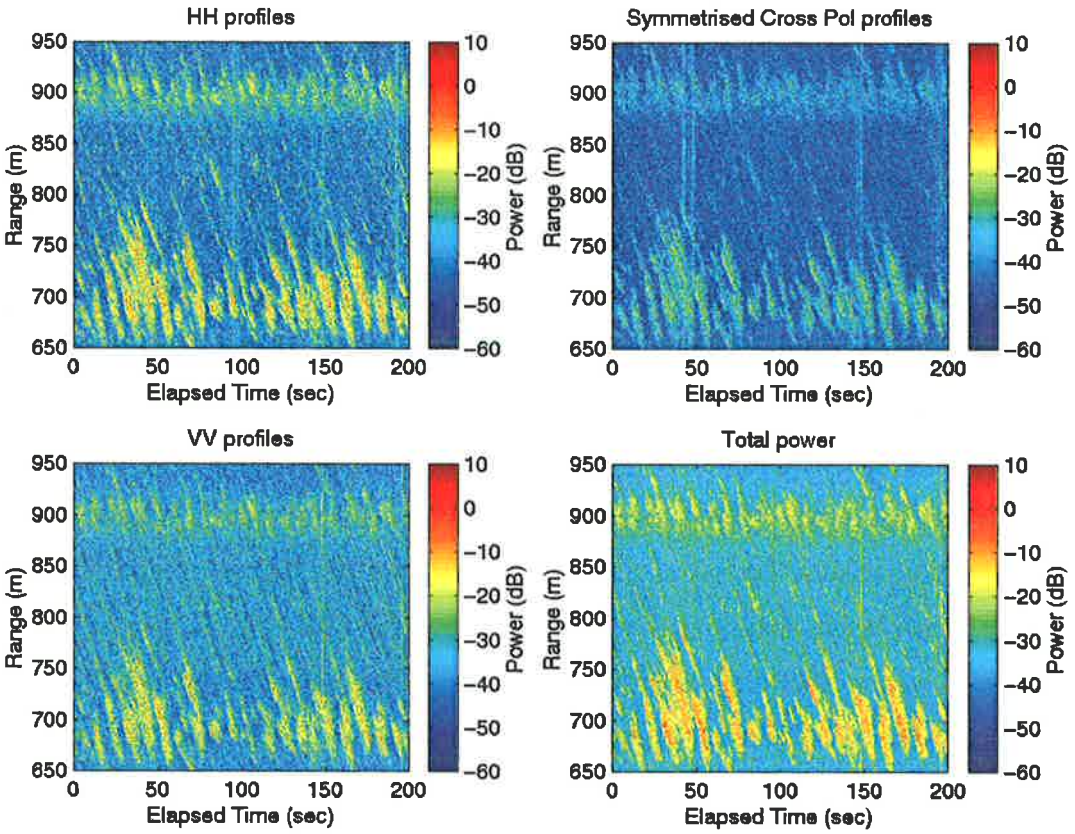

Figure 6-10 Variation in the magnitudes of the elements of [*S*] observed in direction 2

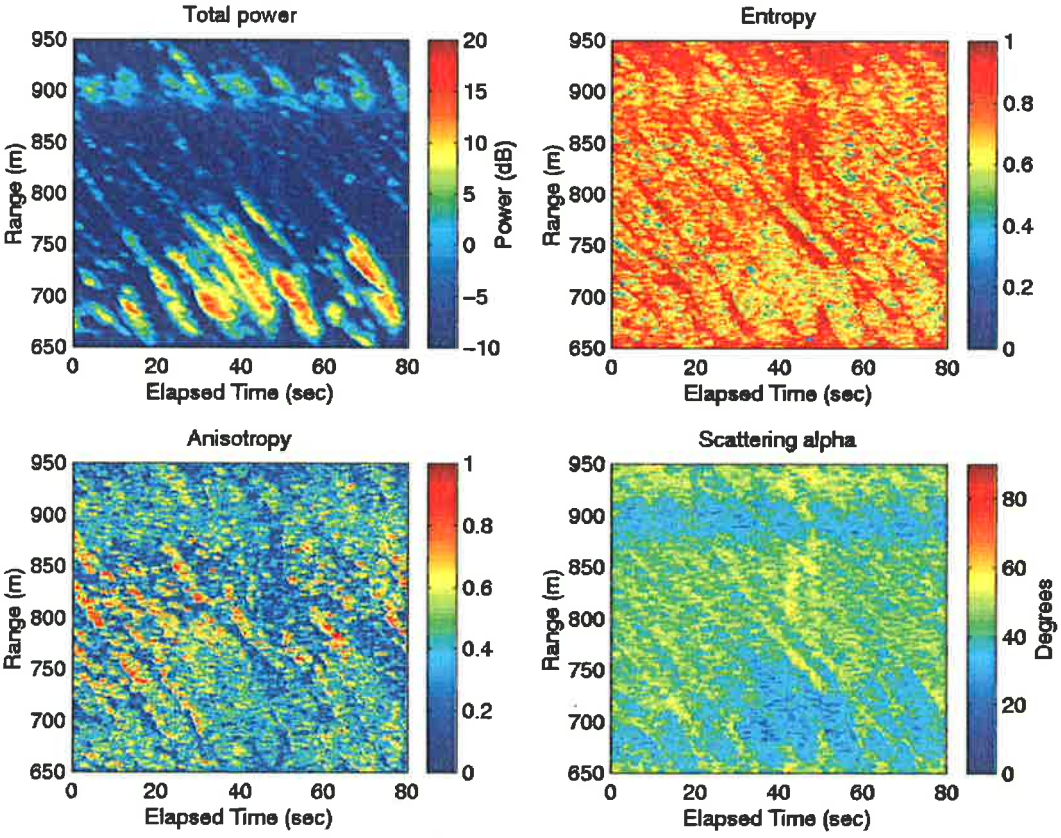

Figure 6-11 The variations in H, $\overline{\alpha}$, A and total power observed in direction 2

The coherency matrices were calculated, averaging over a 9 × 9 window. The eigenvalue decomposition was performed and the polarimetric entropy, anisotropy and scattering alpha values were determined for each cell. Images illustrating the variation in these parameters over an 80 second section of the data are shown in Figure 6-11. The results were filtered to remove the regions with low power and high entropy producing the images shown in Figure 6-12.

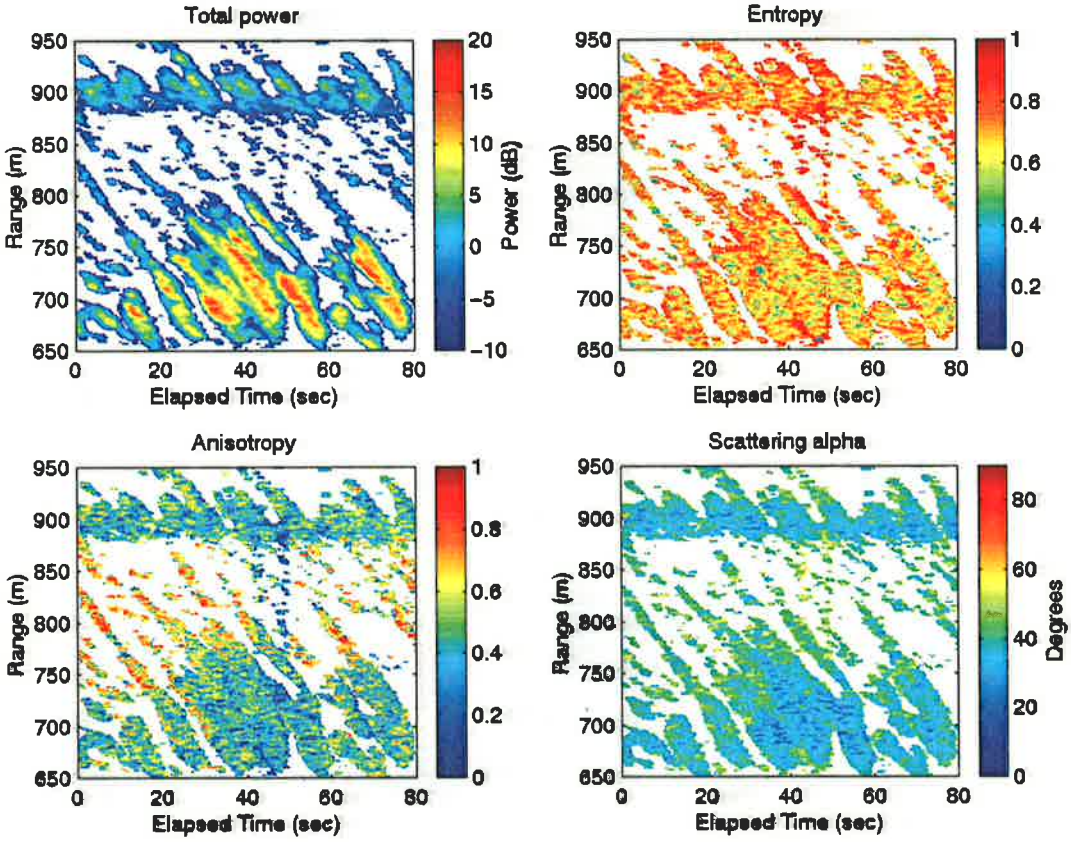

Figure 6-12 Filtered results looking in direction 2

The results looking in direction 2 appear similar to those obtained in the first direction. Evidence of wave breaking both near the shore and in the sandbar region is again apparent. The entropy values range between 0.6 to 0.8 while the scattering alpha values are around 35° in the wave breaking regions and between 40° and 45° in the regions where the waves begin to form prior to breaking. The anisotropy values are slightly lower in direction 2 while the total power values are also reduced.

The distribution of points in the $H-A-\bar{\alpha}$ space is shown in Figure 6-13 and the filtered results are shown in Figure 6-14.

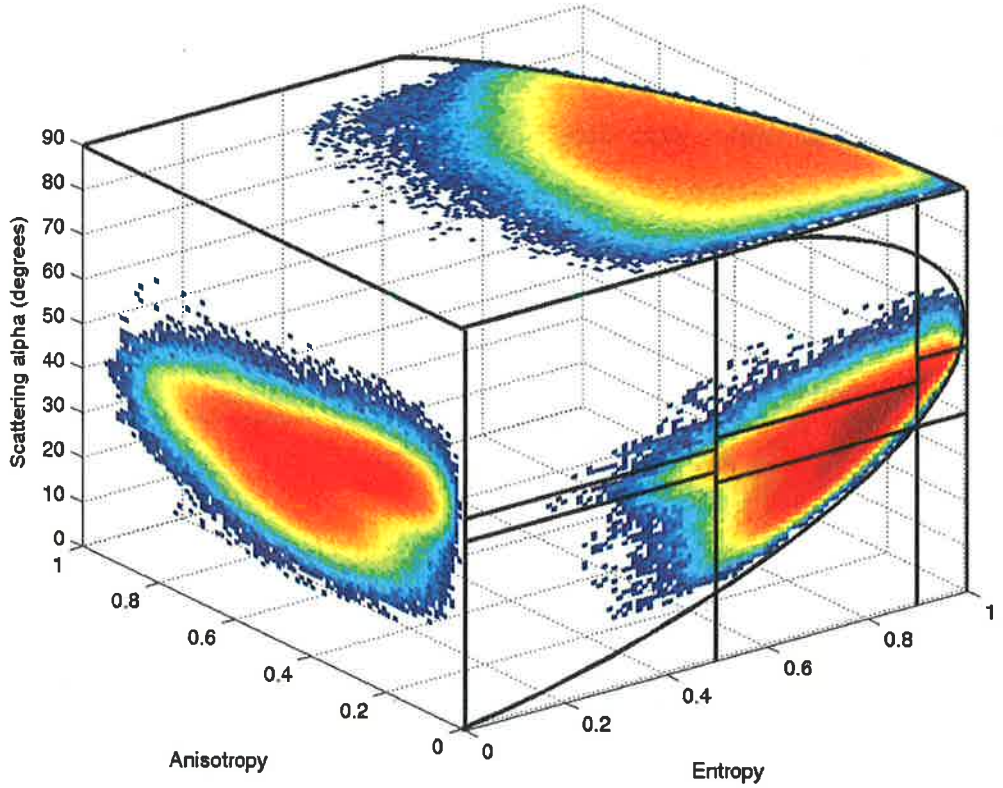

Figure 6-13 The distribution of points in the $H-A-\overline{\alpha}$ space in direction 2

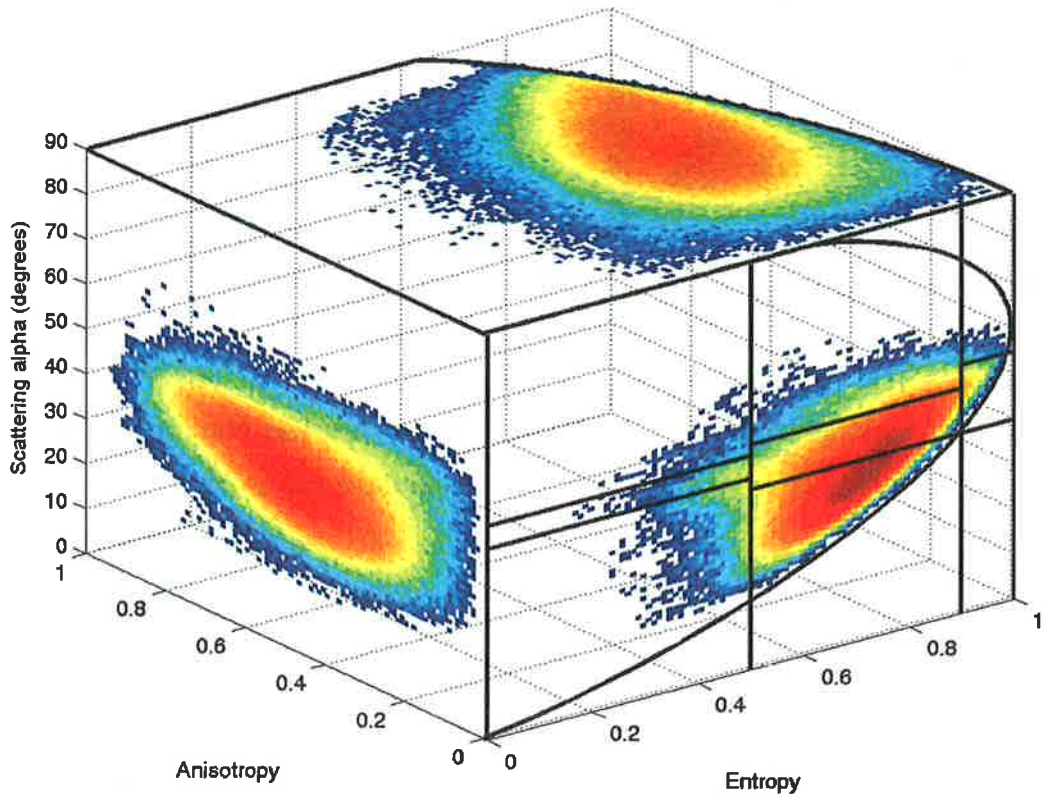

Figure 6-14 Filtered distribution of points in the $H-A-\overline{\alpha}$ space in direction 2

The main difference between these results in Figure 6-14 and those for direction 1 is the absence of points in the region corresponding to entropy values ranging from 0.25 to 0.5 with scattering alpha values ranging from 35° to 45°. These values are possibly due to the lack of specular scattering from the wave front due to the change in the look direction. To confirm this hypothesis the images formed from the matrix products corresponding to $[H][A]$, $[1-H][A]$, $[H][1-A]$ and $[1-H][1-A]$ were also created and are shown in Figure 6-15.

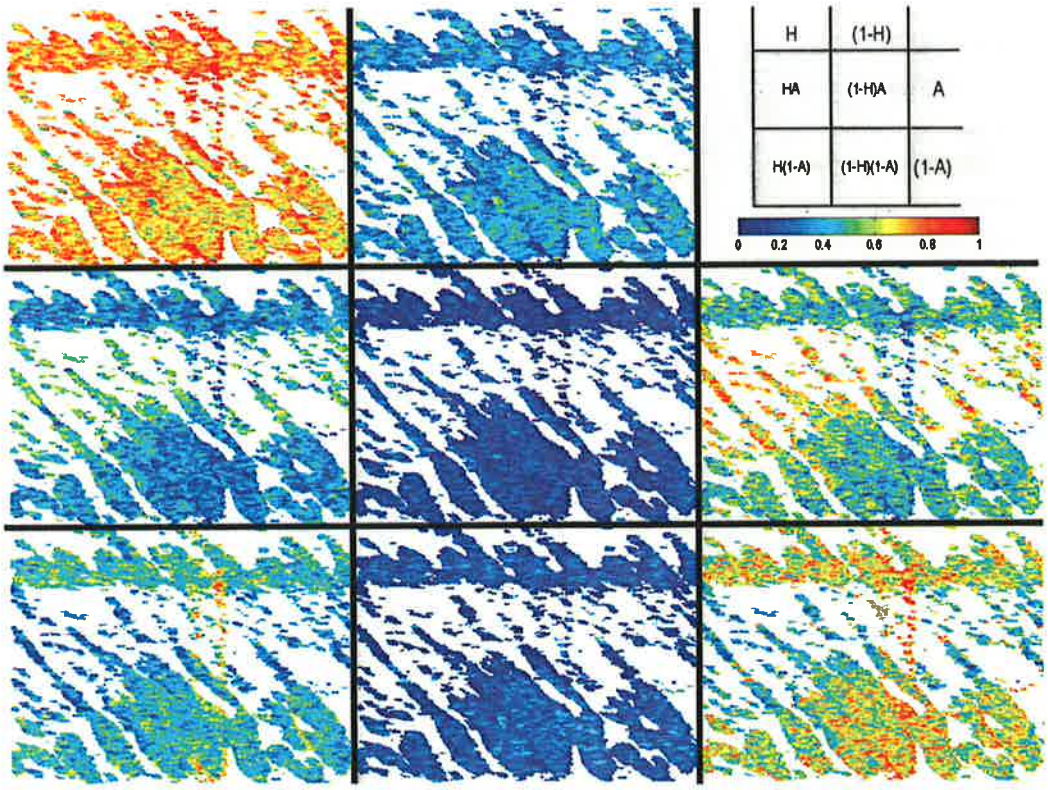

Figure 6-15 Image products formed between $[H]$, $[1-H]$,$[A]$ and $[1-A]$ for direction 2

There are a number of conclusions that can be made from the results shown in Figure 6-15. The $[H][A]$ image product indicates the presence of multiple scattering processes, while the $[H][1-A]$ values are slightly higher than the results for direction 1, suggesting that the scattering is more random (more depolarisation) looking in this direction. The values in the $[1-H][1-A]$ image are much lower than those observed for direction 1. This is consistent with the previous analysis that suggested that the high values observed in this image product in direction 1 were caused by specular scattering from the front of the wave.

6.1.4 Results from direction 3

The measurements performed looking in the final direction (direction 3 in Figure 6-2), approximately 45° to the right of the incoming waves, were then processed. Once again the measurements were collected for approximately 600 seconds at a similar range. Plots illustrating the variation in the magnitudes of the elements of the scattering matrix over a 200 second period were produced and are shown in Figure 6-16.

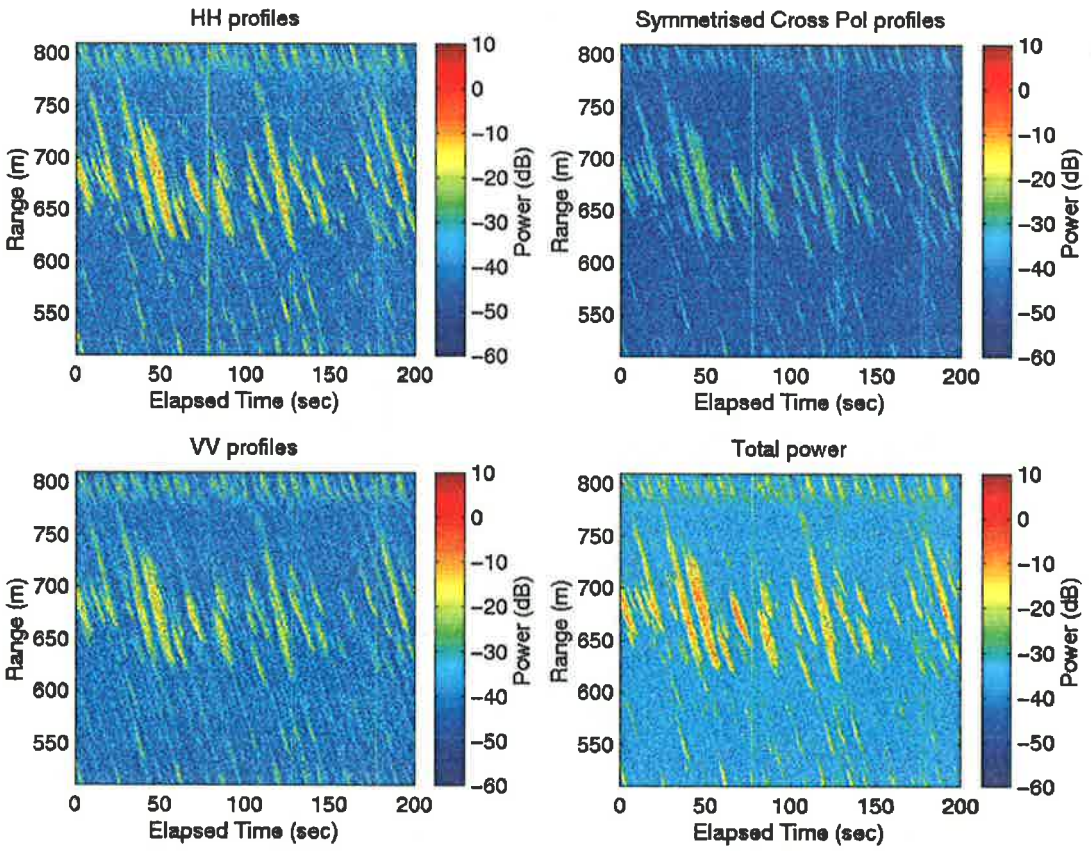

Figure 6-16 Variation in the magnitudes of the elements of [*S*] observed in direction 3

Once again wave breaking cause by the presence of the sandbar at a range of 800 m from the radar is visible in the results shown in Figure 6-16, while much stronger returns are observed from the breaking waves closer to the shoreline. Plots illustrating the variation in the polarimetric parameters over a 75 second section of the data are shown in Figure 6-17 while the filtered results are shown in Figure 6-18.

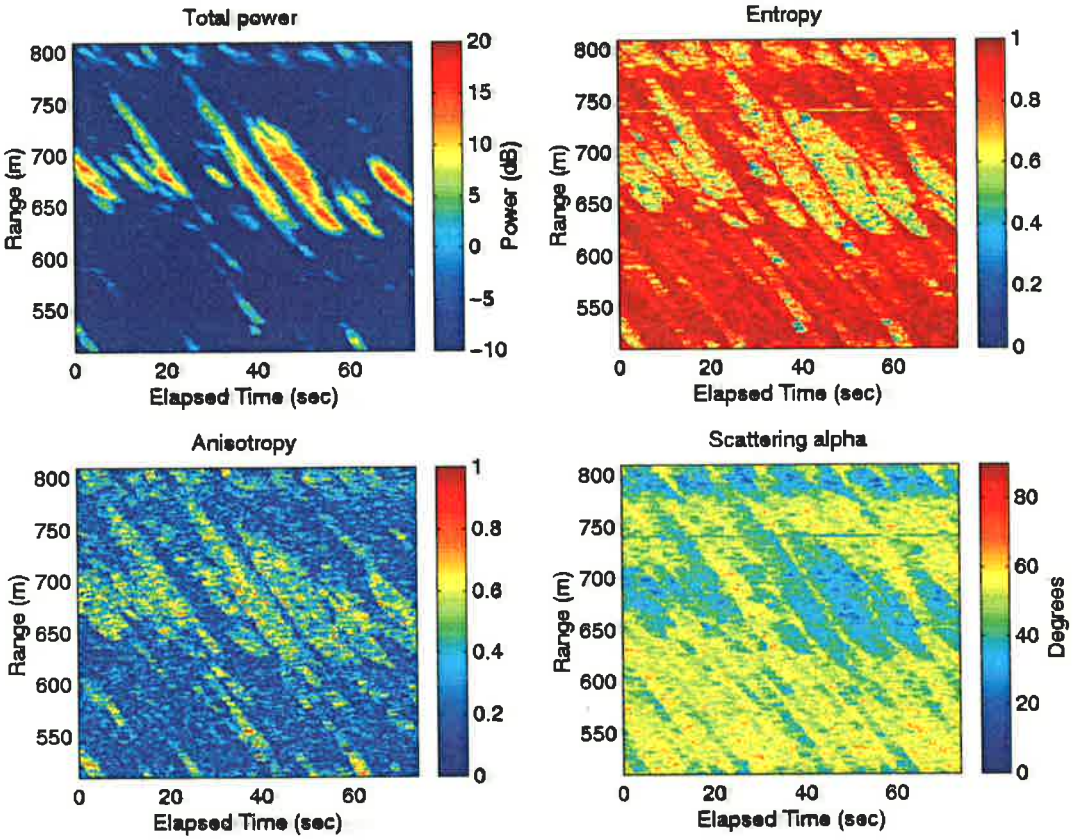

Figure 6-17 The variations in H, $\overline{\alpha}$, A and total power observed in direction 3

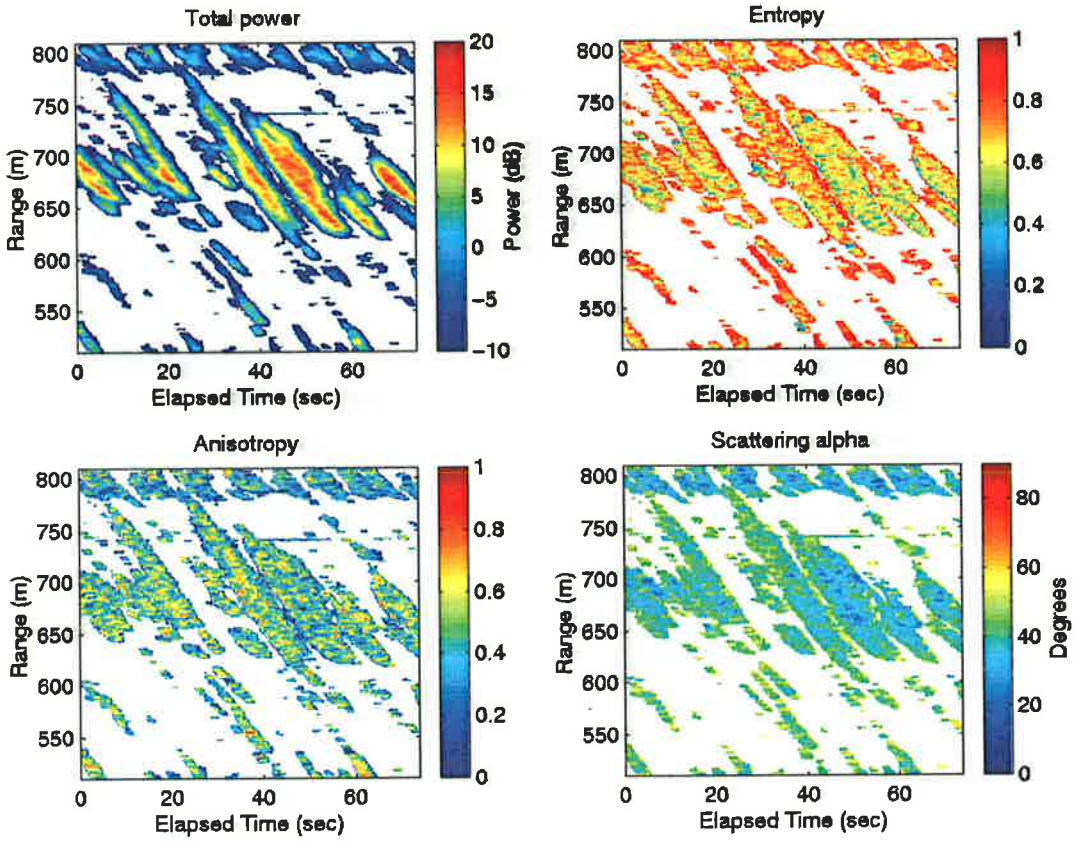

Figure 6-18 Filtered results looking in direction 3

The results in Figure 6-17 illustrate that there are much larger clutter regions in direction 3 and that the total power values are smaller than the results for direction 1 but similar to direction 2, as expected. The entropy values in the filtered regions are still in the range of 0.6 to 0.8 while there are more regions with low (around 30°-35°) scattering alpha values suggesting that there are more frequent wave breaking events observed in this direction. The anisotropy values are similar to the values observed in direction 2 and generally lower than the values from direction 1.

The distribution of points in the $H-A-\bar{\alpha}$ space in Figure 6-19 clearly shows that the majority of the points lie in the high entropy clutter regions. Once again the results were filtered so that the regions of interest, corresponding to the incoming waves, could be separated from the clutter regions. The filtered distribution of points in the $H-A-\bar{\alpha}$ space is consistent with the results for direction 2 with slightly more points in high entropy regions. The image products corresponding to [H][A], [1–H][A], [H][1–A] and [1–H][1–A] were also calculated and are shown in Figure 6-21.

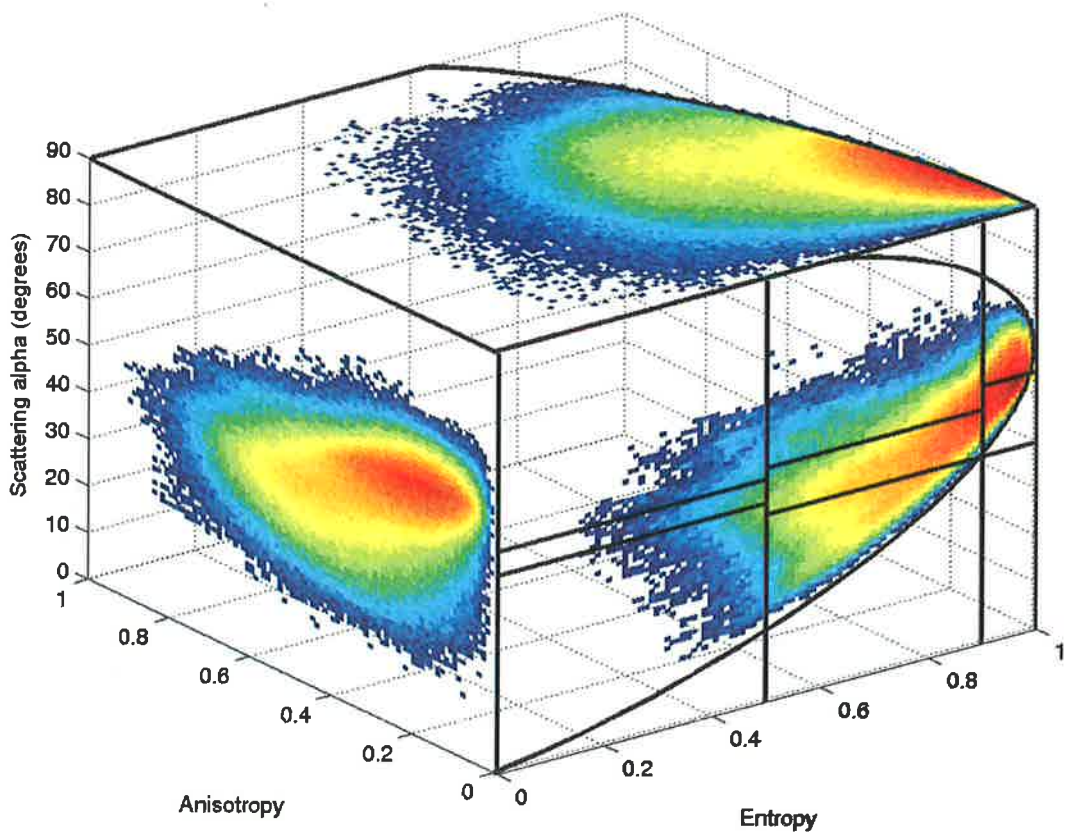

Figure 6-19 The distribution of points in the $H-A-\bar{\alpha}$ space observed in direction 3

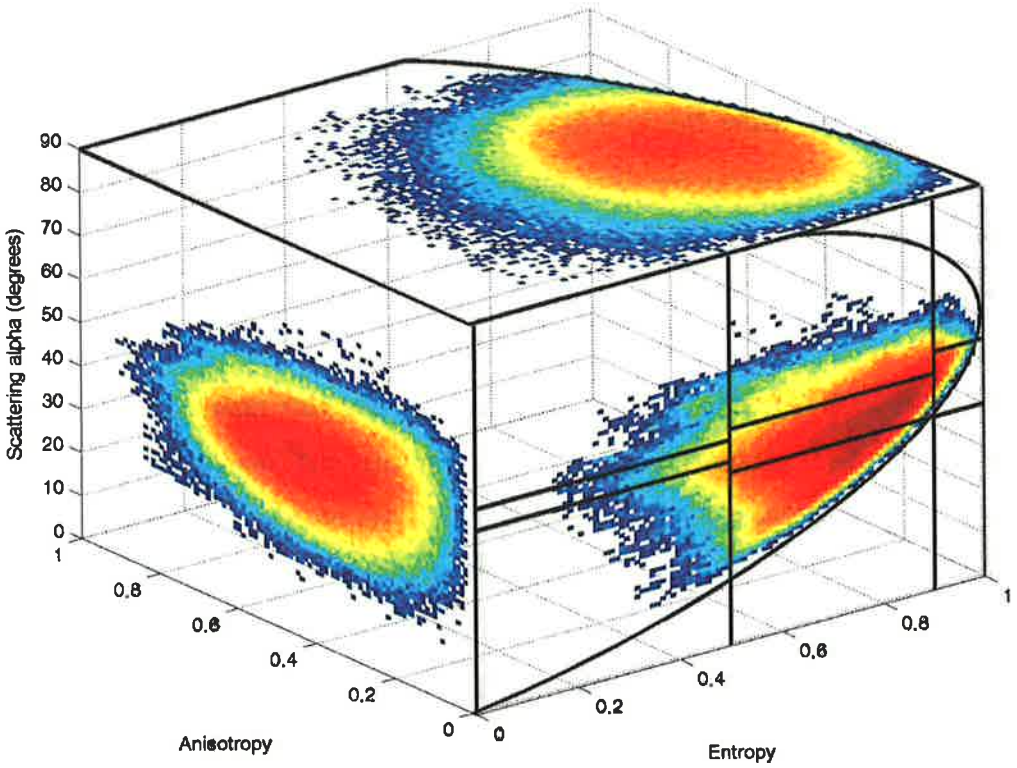

Figure 6-20 Filtered distribution of points in the $H-A-\overline{\alpha}$ space in direction 3

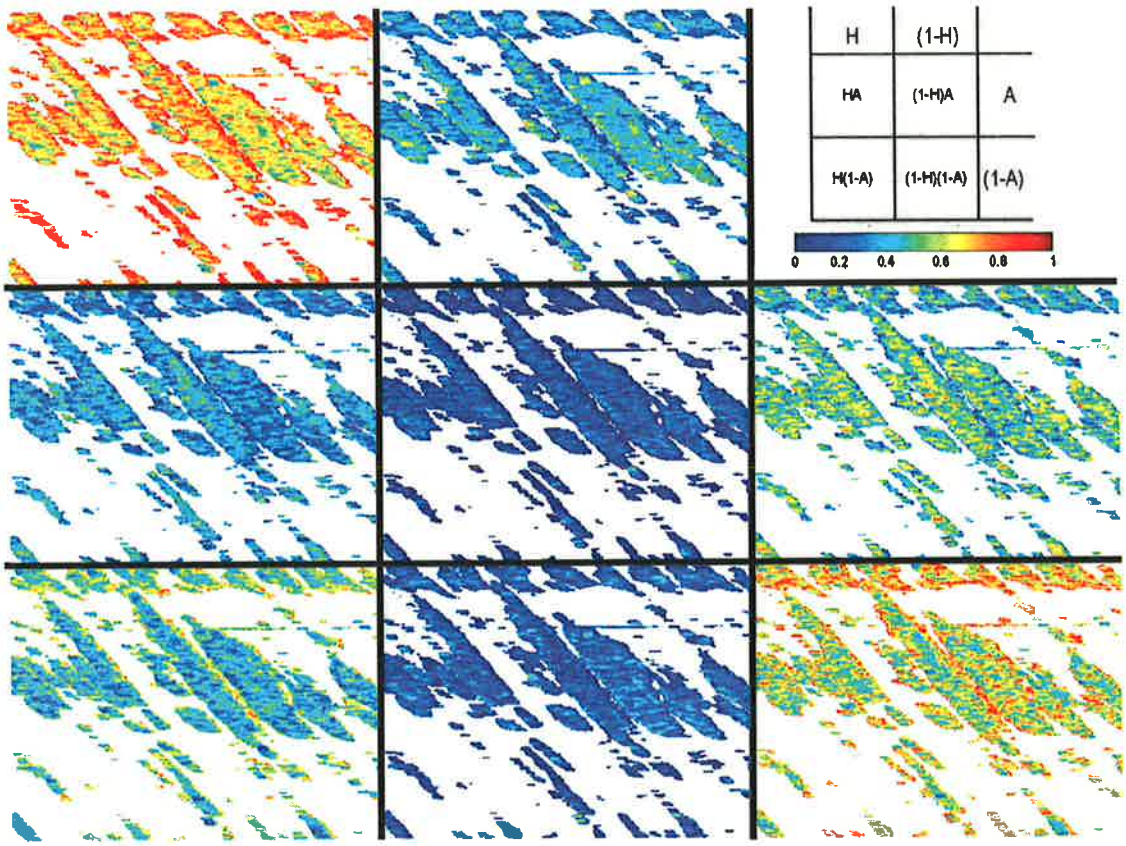

Figure 6-21 Image products formed between [*H*], [1–*H*],[*A*] and [1–*A*] for direction 3

The image products for direction 3 are very similar to the results obtained looking in direction 2. The $[H][A]$ image product again suggests the presence of multiple scattering processes while the $[1-H][1-A]$ shows very little evidence of specular scattering, as was observed for direction 1. The values in the $[H][1-A]$ image are slightly higher than in direction 2, suggesting that the scattering is more random in this look direction caused by more frequent wave breaking events.

In each of the look directions there is evidence that there are characteristic variations in the polarimetric parameters as the wave forms and begins to break. The measurements in direction 1 looking orthogonal to the incoming waves were studied in more detail. The variations in the entropy, anisotropy and $\bar{\alpha}$ values were compared with the results predicted by the X-Bragg model described in Chapter 5 using the numerical simulation described in the following section.

6.1.5 Simulated breaking wave using the X-Bragg model

In Chapter 5 it was shown that the X-Bragg model predicts that the entropy of a breaking wave should remain fairly constant as the wave forms with a slight increase during the breaking process. The X-Bragg model also predicts that the anisotropy and $\bar{\alpha}$ values should drop once the wave begins to break. To demonstrate this, a simulation based on the X-Bragg model was run to illustrate a typical example of the expected range (time) variation of $H/A/\bar{\alpha}$ for a breaking wave process. The results of this simulation are shown in Figure 6-22.

The Evans Head measurements were performed at a low grazing angle of around 5°, corresponding to an angle of incidence of 85°. Thus, in the far range (>128 units in Figure 6-22), where the wave is not yet formed, the behaviour is described by a flat Bragg scattering surface observed at an angle of incidence of 85°. At a range of 128, the wave starts to break. In the simulation this is modelled as a progressive tilting of the wave front (increase in θ) combined with an increase in the surface roughness (increase the β_1). At range of 64 units, the wave is in a steady breaking state as it progresses towards the radar.

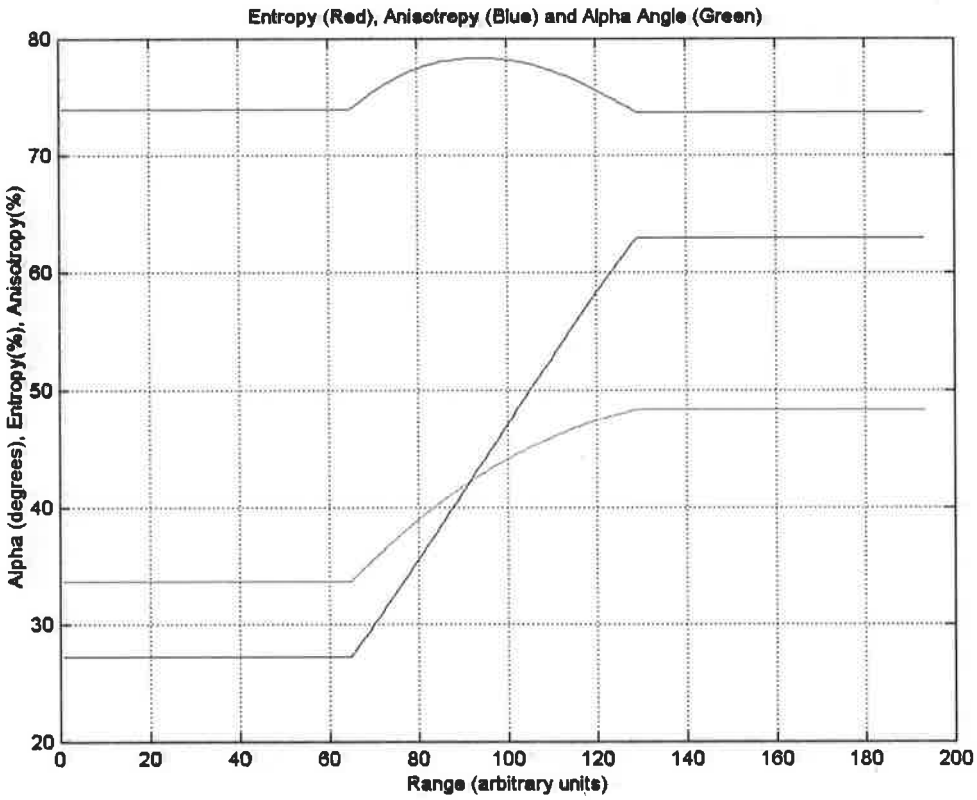

Figure 6-22 X-Bragg prediction of entropy variation for a breaking wave

Figure 6-22 illustrates that the simulation predicts that the entropy, before and after breaking, remains relatively unchanged while there is a small increase during the formation of the wave itself. The anisotropy shows a much larger change, falling steeply from a high value before breaking to a low one after breaking. This is accompanied by a reduction in the alpha parameter.

In order to obtain a comparison with the X-Bragg simulation results, the results shown in Figure 6-6 were studied in more detail. Regions corresponding to individual waves are identified and a "wave-track" was selected as shown by the highlighted region in Figure 6-23.

The mean statistics for each range bin within the highlighted region were extracted and plotted as a function of range and are shown in Figure 6-24. The behaviour is similar to that predicted by the X-Bragg model in that the entropy remains fairly constant along the track while both the anisotropy and the scattering alpha drop as predicted.

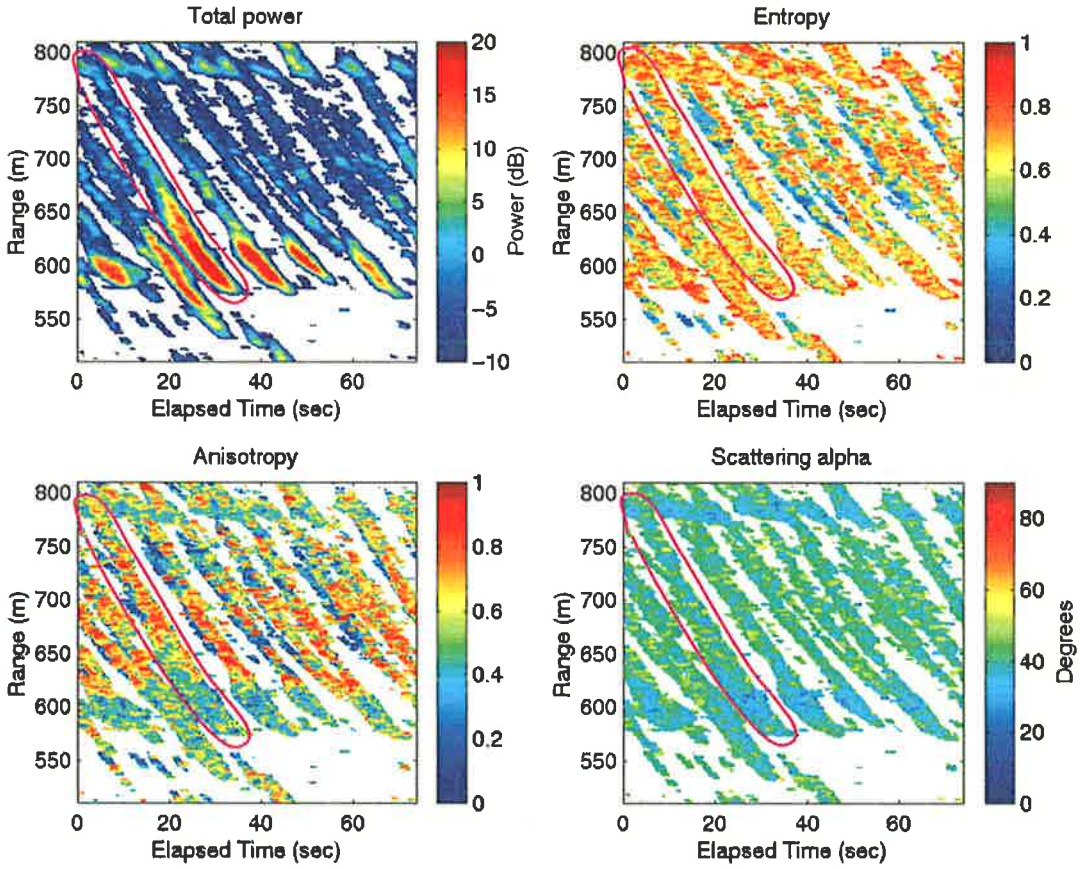

Figure 6-23 Selected wave track from the data obtained in direction 1

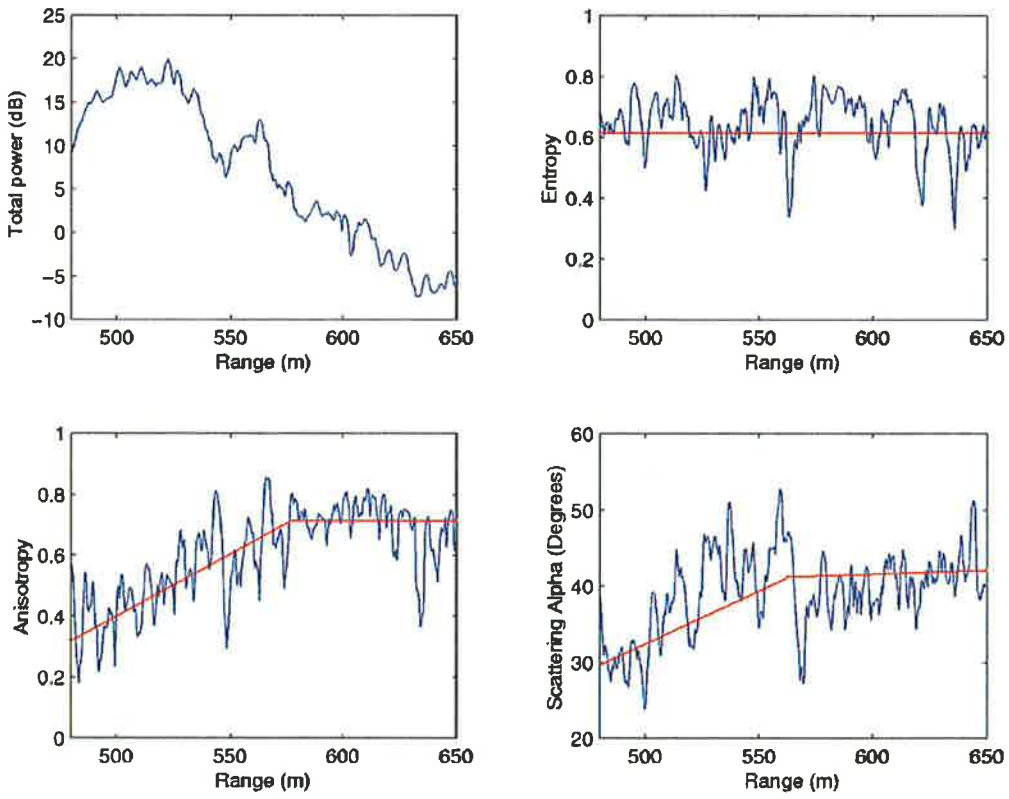

Figure 6-24 The variation in total power, entropy, $\overline{\alpha}$ and anisotropy for a breaking wave

6.2 Yallingup measurements

In February 2003, a series of polarimetric measurements of sea clutter were performed at Yallingup in Western Australia (see Figure 6-25). Additional sea clutter data was collected from an elevated position of around 5°, the possibility of exploiting the polarisation-Doppler domain with the DSTO radar system was explored. Previous attempts at performing Doppler processing of the measured results had suggested that the sampling rate of the radar might be too low for sweep sizes in excess of 256 steps when using the fully polarimetric mode. To reduce the time between frequency measurements, a smaller step size was selected and the polarisation of the transmitted pulse was fixed throughout the measurements. Consequently, the time between measurements at the same frequency was reduced by a factor of four.

Figure 6-25 Yallingup measurement location

6.2.1 Experimental setup

The DSTO highresolution radar van was deployed on the Yallingup beach road giving a clear, unobstructed view of the incoming ocean waves. Measurements were conducted using the two waveforms shown in Table 6-1.

Table 6-1 Radar waveforms used during the Yallingup measurements

Parameter	Waveform 1	Waveform 2
Start frequency	9324 MHz	9324 MHz
Frequency step	0.5 MHz	0.5 MHz
Number of steps	256	128
Pulse width	2 ms	2 ms
PRI	40 µs	40 µs
Range Window	300 m	300 m
Range Resolution	1.17 m	2.34 m
Switching	Pulse to pulse	Fixed VV pol

In the Evans Head measurements described in Section 6.1, the lack of a reference marker in the range profiles meant that at times it was difficult to compare results taken at different look angles. In the Yallingup measurements a fishing boat, fitted with a cluster corner reflector (shown in Figure 6-26), was deployed to provide a reference point for all of the measurements. The omni-directional scattering characteristics of the reflector ensured that a strong signal was obtained regardless of the orientation of the boat.

Figure 6-26 Cluster corner reflector

The antenna system was set up on top of the radar van to yield the highest possible look-down angle. The experimental set-up and the region of sea observed during the measurements are shown in Figure 6-27. The images show that the sea consisted of a regularly spaced, almost monochromatic swell. The radar range window was positioned so that the observed patch of sea represented the region in which the waves begin to form with the possibility of wave-breaking occurring at the close ranges.

Figure 6-27 Experimental set-up and ocean view from the Yallingup site

6.2.2 Waveform 1 results

The data collected using the first stepped frequency waveform (in Table 6-1) was analysed first and consisted of 256 frequency steps at 0.5 MHz intervals. Records were collected over a range of 420 to 720 m for a period of 600 seconds. A number of data sets were collected during the day with consistent sea conditions throughout the measurement period. Consequently there was little variation in the scattering behaviour observed between data sets. The received signals were range-processed and then combined to form an estimate for the scattering matrix for each range-time cell. The variation in the magnitude of the elements of the scattering matrix over a period of 150 seconds is shown in Figure 6-28.

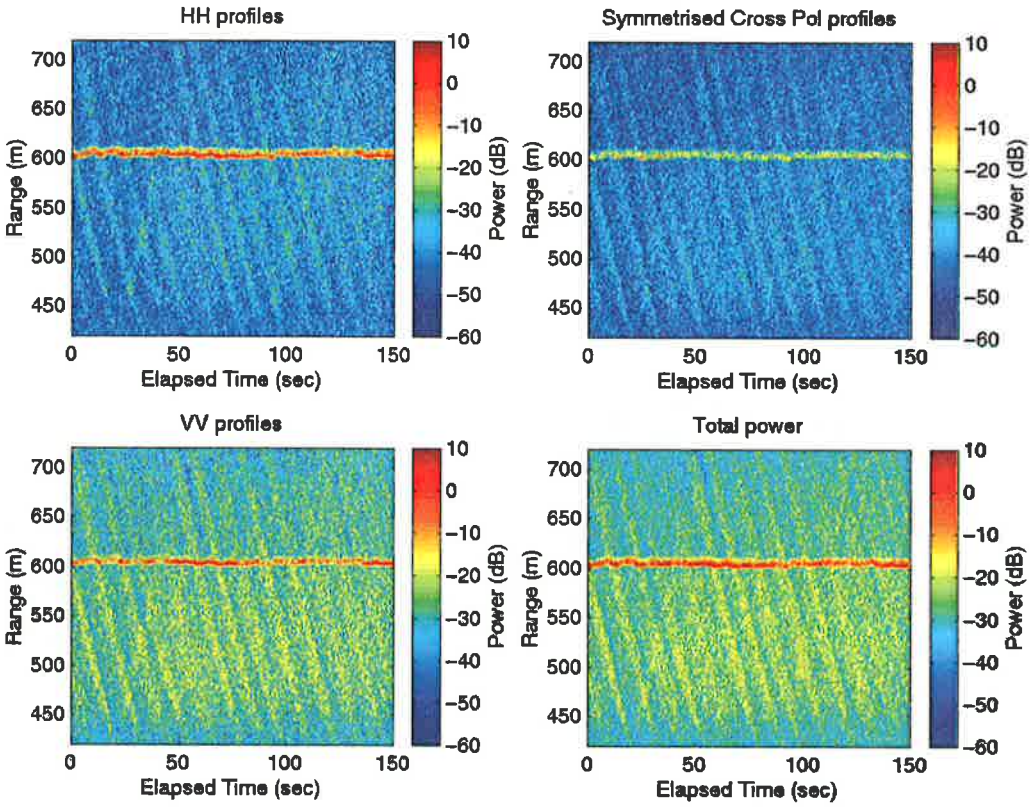

Figure 6-28 The variations in the magnitude of [*S*] elements for waveform 1

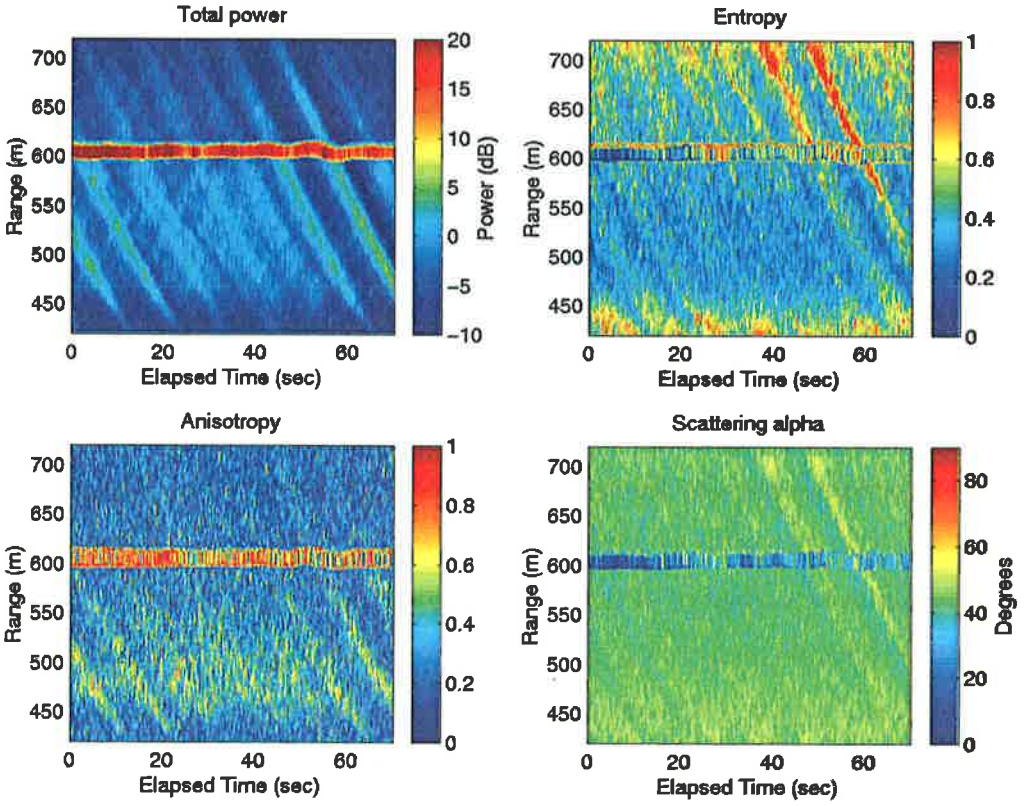

Figure 6-29 The variation in the polarimetric parameters observed for waveform 1

The processed results were combined to form an estimate of $\vec{k}_{3P}$ for each range-time cell. Averaging the outer product of the Pauli scattering vectors over a 9×9 cell produced the 3×3 polarimetric coherency matrices. An eigenvalue decomposition of the coherency matrix was performed and the H, A and $\bar{\alpha}$ values were determined. The variations observed in these parameters in a 70 second section of the data are illustrated in Figure 6-29.

The total power plot shows a strong return from the fishing boat and cluster corner reflector, located at a range of 600 m while the returns from the incoming waves are easily identified. To assist in the interpretation of the results, the data sets was filtered using a similar technique to that applied in the Evans Head processing. The regions of low power and the returns from the boat and cluster corner reflector were removed and the filtered results are shown in Figure 6-30.

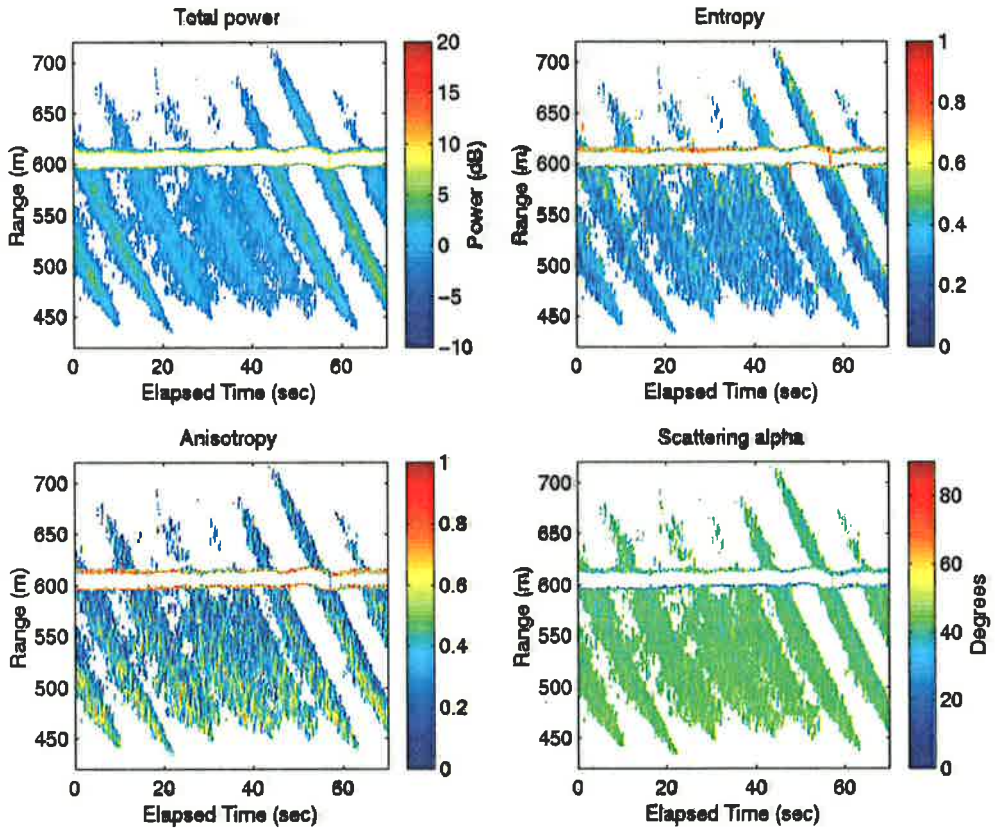

Figure 6-30 Filtered results for waveform 1

A number of observations can be made from the filtered results. The entropy values are significantly lower than the results obtained during the Evans Head measurements

where the typical values observed were in the range of 0.6 to 0.8. In the Yallingup measurements the entropy values range between 0.2 and 0.4. The fact that a broad spectrum of waves was presented in the Evans Head data coupled with the frequent wave breaking events explains the higher entropy values. The general characteristics are more readily seen in the plots of the distribution of points in the $H-A-\bar{\alpha}$ space shown in Figure 6-31.

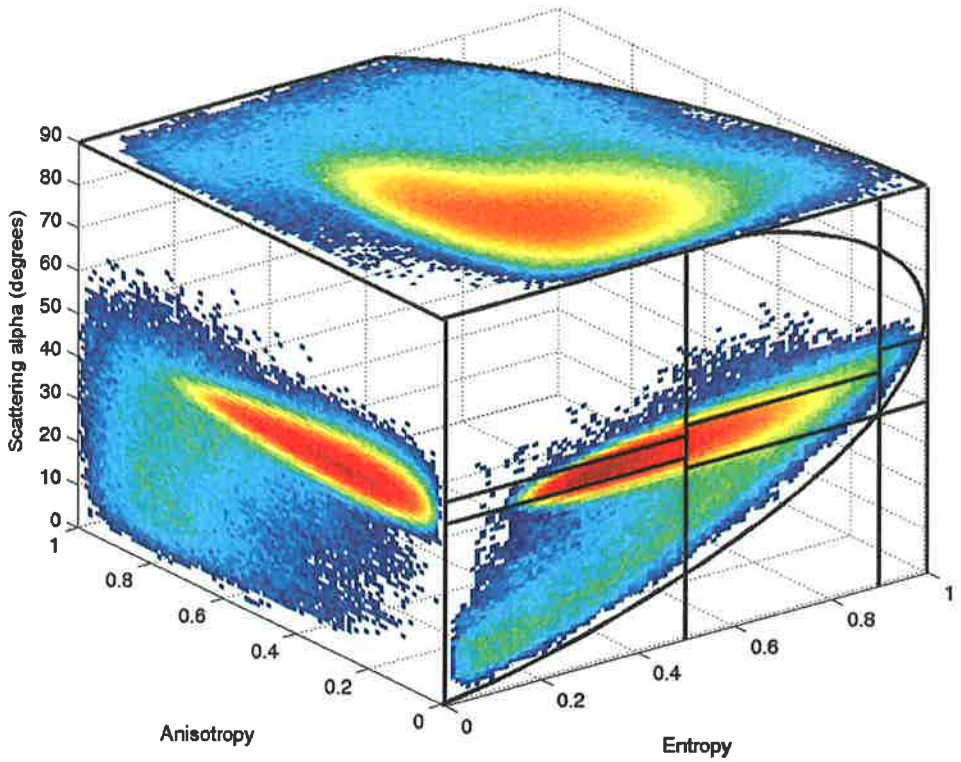

Figure 6-31 The distribution of points in the $H-A-\bar{\alpha}$ space for waveform 1

The return from the boat fitted with the cluster corner reflector causes a spread in the distribution of points in the $H-A-\bar{\alpha}$ space, particularly in the low entropy and low $\bar{\alpha}$ regions. The data was filtered to remove the influence of the boat and the clutter regions, producing the distribution of points in the $H-A-\bar{\alpha}$ space shown in Figure 6-32. The filtered distribution of points in the $H-A-\bar{\alpha}$ space show that the majority of points lie in a narrow band in the $H-\bar{\alpha}$ plane, corresponding to entropy values ranging from 0.2 to 0.4 and $\bar{\alpha}$ values in the range of 40° – 45°. In the Evans Head results this region was associated with specular scattering from the wave front. Giving the simple structure of the waves and the lack of wave breaking observed it is not surprising that the majority of points lie in this region of the $H-A-\bar{\alpha}$ space.

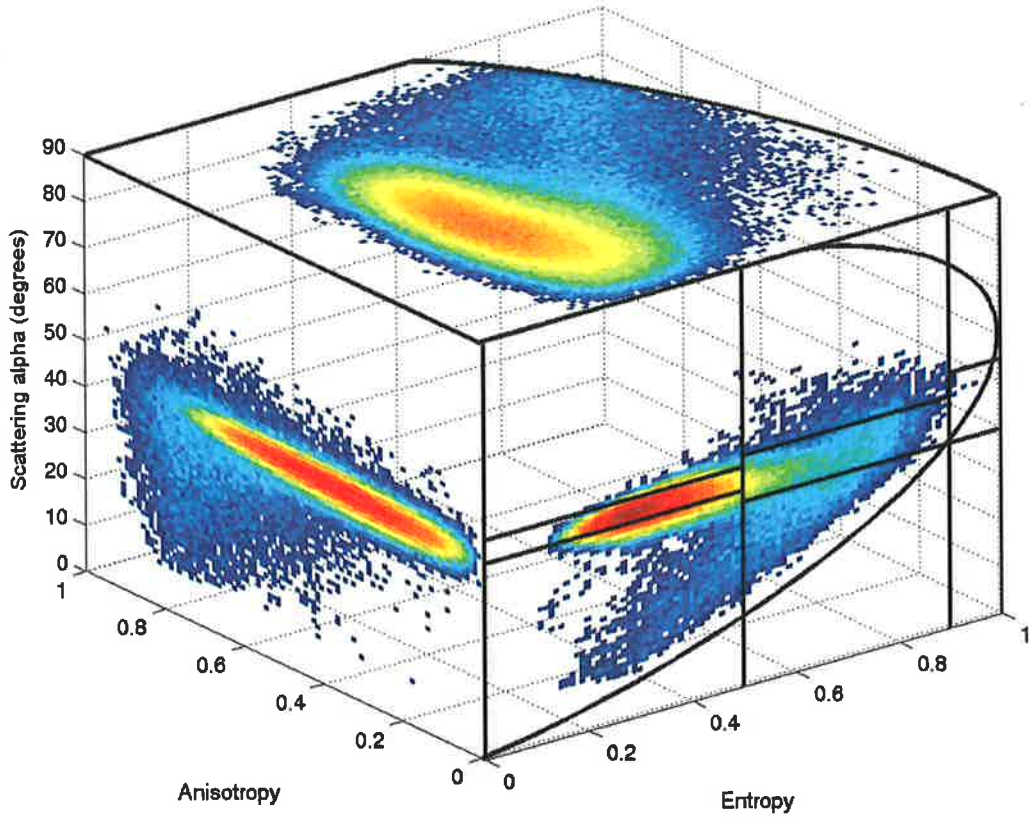

Figure 6-32 Filtered distribution of points in the $H-A-\bar{\alpha}$ space for waveform 1

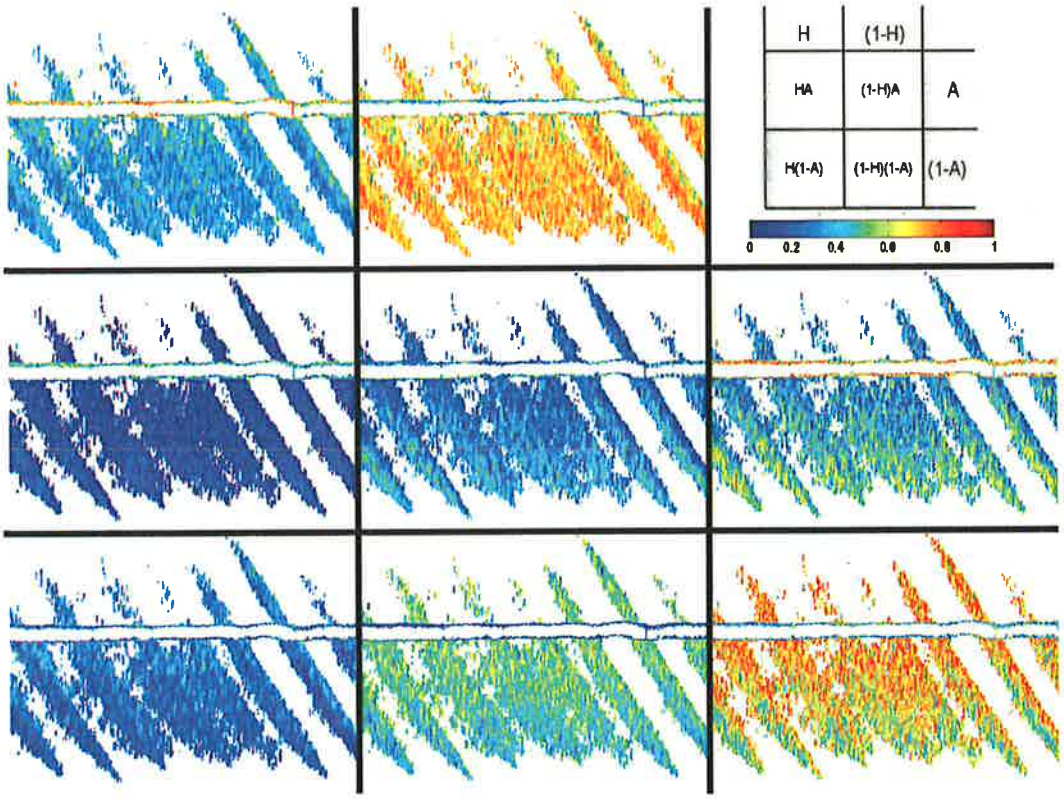

Figure 6-33 Image products formed between [*H*], [1–*H*],[*A*] and [1–*A*] for waveform 1

The image products formed from the combinations of the entropy and anisotropy images and their complementary images are shown in Figure 6-33. These results confirm that in most regions there is a single dominant scattering mechanism present while at close ranges there are slightly higher values in the $[1-H][A]$ image, suggesting two scattering mechanisms are present as the wave begins to enter a breaking state.

A single wave track was isolated so that variation in the polarimetric parameters could be studied in more detail. The wave track selected is shown in Figure 6-34.

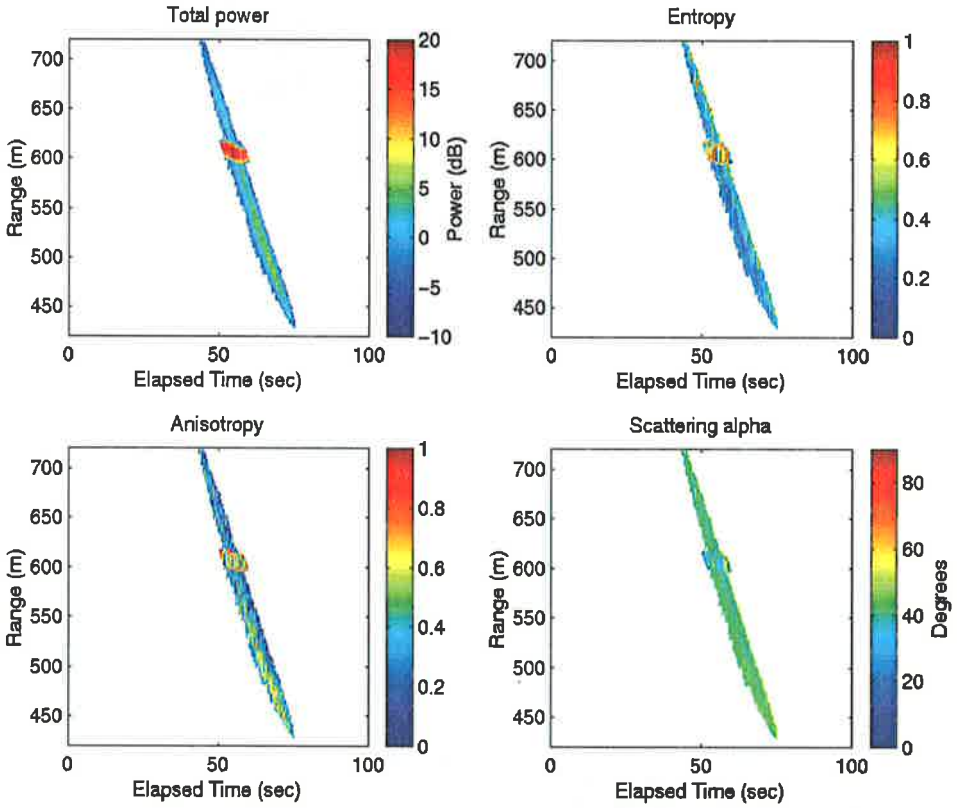

Figure 6-34 The variation in the polarimetric parameters along a wave track

The total power plot shows a steady increase as the wave comes closer in range, while the strong return from the fishing boat and cluster corner reflector is clearly seen at a range of 600 m. The entropy values remain relatively constant along the wave track with slightly lower values observed from the front of the wave. The anisotropy plot shows that there is an increase in values in the low entropy regions indicating a reduction in the surface roughness and the $\bar{\alpha}$ values remain relatively constant along the track. The values from the center of the wave track were extracted and the returns

from the boat and corner reflector removed. These values were plotted as a function of range and are shown in Figure 6-35.

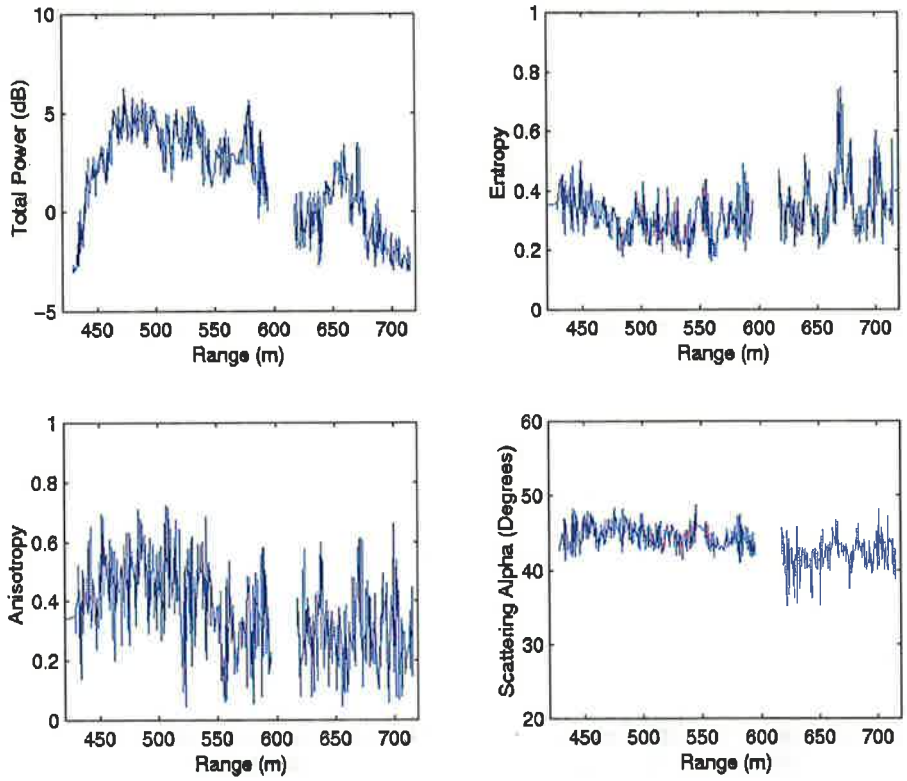

Figure 6-35 The variation in the polarimetric parameters from the center of the wave track

The variations observed in Figure 6-35 can be explained using the results from the X-Bragg model discussed in Chapter 5. Figure 5-7 illustrates that the X-Bragg model predicts that the $\bar{\alpha}$ values are relatively insensitive to changes in the surface roughness. The fact that the $\bar{\alpha}$ values do not change significantly as the wave travels towards the radar suggests that the angle of incidence (the local range slope) remains relatively constant along the wave track. The fact that the $\bar{\alpha}$ values are in the range of 40° to 45° is consistent with values predicted by the Bragg model (See Figure 5-1) for low grazing angles. Figure 5-6 illustrates the variation in the anisotropy predicted by the X-Bragg model. This indicates that the anisotropy is largely insensitive to wave tilts but is strongly influenced by the degree of surface roughness. The observed increase in anisotropy at close ranges suggests that there is a decrease in the surface roughness. From Figure 5-5 it is clear that a decrease in roughness coupled with a constant angle on incidence should mean that the entropy remains largely unchanged. This prediction is consistent with the experimental findings shown in Figure 6-35.

6.2.3 Doppler processing

The data collected using the second waveform (in Table 6-1) was analysed next. This waveform differed from the previous waveform in that a fixed polarisation was used during the measurements and consequently, polarimetric processing could not be performed. The motivation for collecting this data was to explore the possibility of exploiting the Doppler domain. Previous attempts at performing Doppler processing, while using the polarimetric mode, indicated the sampling rate was too low. Aliasing problems were evident in the Doppler domain for waveforms with large numbers of frequency steps. In an attempt to overcome this problem, the number of frequency steps was reduced to 128 and the polarisation of the transmitted pulse was fixed for the duration of the measurement. VV polarisation was selected as the previous results indicated that the strongest returns were observed in this channel. Data was collected over a range of 420 to 720 m for a period of 600 seconds. The results were range-processed and the variations in magnitude of VV and HV returns are shown in Figure 6-36.

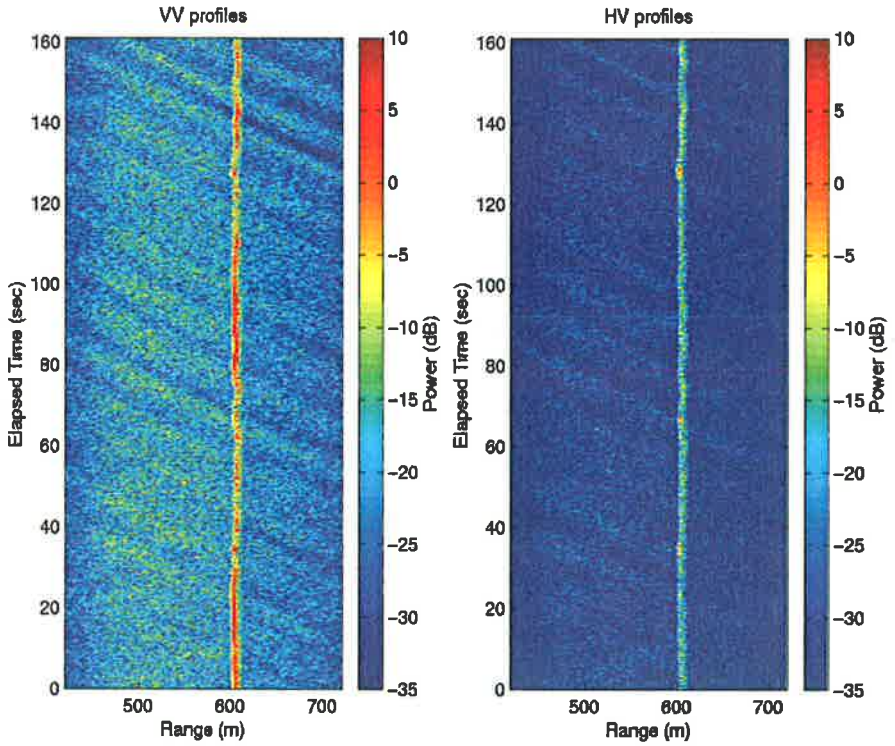

Figure 6-36 Variation in the VV and HV returns using waveform 2

The Doppler spectrum was calculated using 256 points with a 64 point overlap and is shown in Figure 6-37. The occurrence of wave groups is particularly clear in this

representation, since the orbital velocity (and hence the Doppler shift) is proportional to wave amplitude.

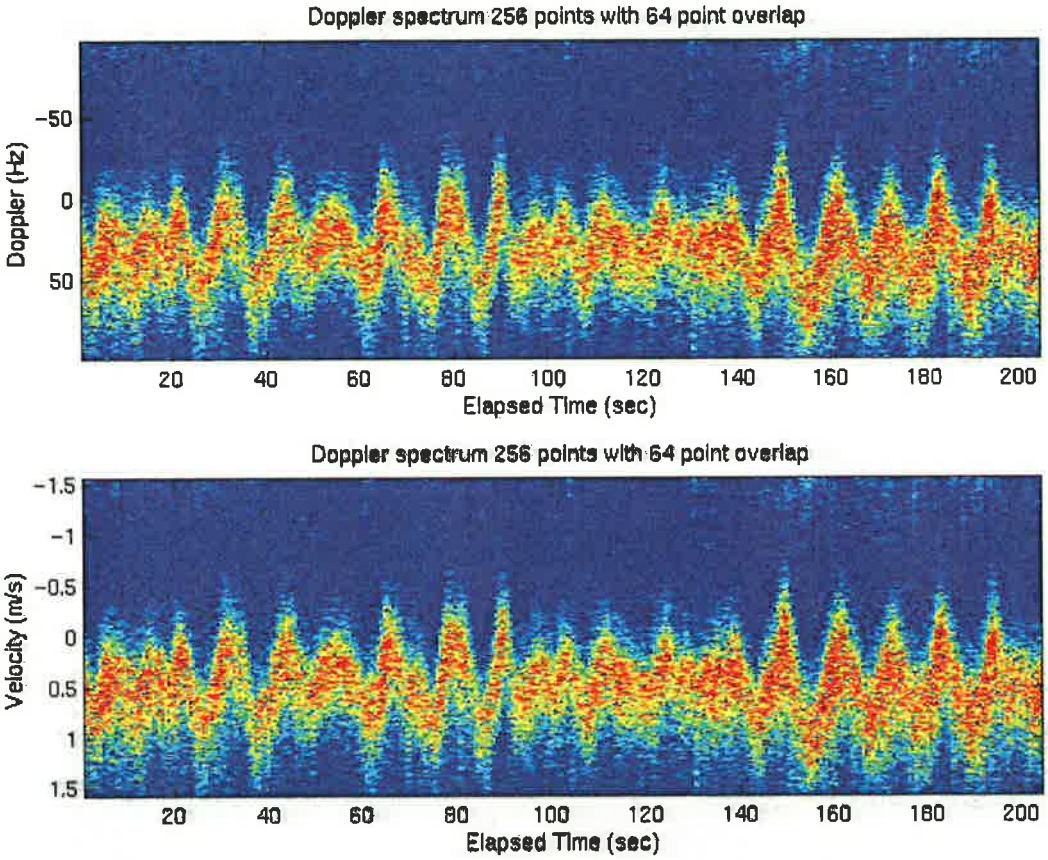

Figure 6-37 Doppler spectrum using waveform 2

6.3 Polarimetric measurements of wakes

In addition to the low angle measurements of sea clutter and breaking waves, a number of wake measurements were conducted. Initially, the motivation for these measurements was to demonstrate the ability to measure the polarimetric characteristics of wakes at low grazing angles and to provide comparison data for the modelled results produced by the SWPE and NFSFS codes discussed in Chapter 5. However, as noted in Chapter 5, there is the potential for using ship wakes as a tool for studying nonlinear scattering processes such as wave breaking. Section 5.7 suggested that wave breaking events could be initiated using the interaction between the wake and the incoming swell crests. This hypothesis is demonstrated in Section 6.5, with some control over where and when the scattering events take place, using the wake produced by a boat.

6.3.1 Darwin Harbour measurements

In November 2000 measurements were conducted in Darwin Harbour involving a wave-piercing catamaran to demonstrate that polarimetric wake images could be obtained at low grazing angles using the DSTO radar system. Details of the catamaran are shown in Table 6-1 and a picture of the vessel is shown in Figure 6-38.

Table 6-2 Wave piercing catamaran specifications

Overall length	86.6 m
Waterline length	76.4 m
Beam	26.0 m
Beam of hulls	4.33 m
Draft	3.50 m
Deadweight	415 tonnes
Service speed	40 knots
Lightship speed	48 knots

Figure 6-38 Wave piercing catamaran

The DSTO high resolution radar van was positioned at Emery point in Darwin Harbour, and the cooperating vessel was instructed to perform a number of straight line runs at 30 knots along a bearing of 154° True at a range of 1.5 km. The radar antenna was set at a bearing of 263° True to align the radar look direction with the perpendicular to the classical diverging wake arm, so that the wake echoes could be accumulated effectively in spite of the high speed of the boat, as shown in Figure 6-39.

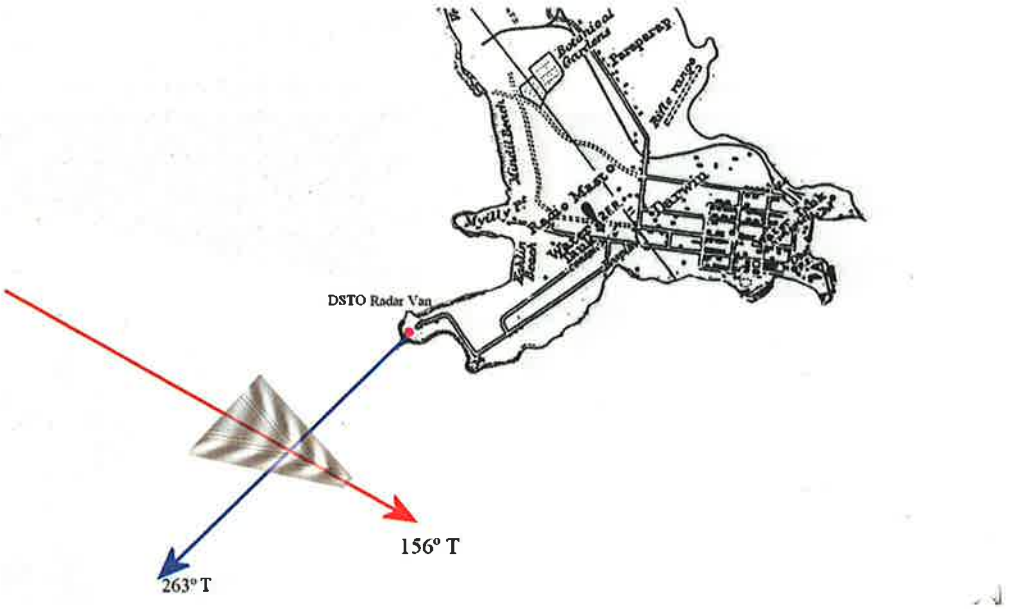

Figure 6-39 Darwin Harbour wake measurement geometry

High resolution range profiles were recorded using a stepped frequency waveform consisting of 1024 frequency steps at 0.5 MHz intervals giving a 300 m radar window, a signal bandwidth of 512 MHz and a range resolution of 0.293 metres. The range window was positioned at a range of 1.5 km so that the ship would pass through in the more distant half of the processed range footprint so as to maximize the observation period of the wake as it propagated through the range window towards the radar. Data was collected over a period of 90 seconds and the variation in the magnitudes of the [*S*] matrix elements is shown in Figure 6-40.

The results clearly show the strong return from the boat as it passed through the range window followed by regularly spaced returns from the wake structure as it moves toward the radar. The speed of the wake was estimated using the slope of the returns in the radar images and was found to be 14.2 m/s.

Examination of the structure of the regions of enhanced backscatter suggests that there is little convincing evidence of scattering from discrete breaking events. This is consistent with the visual observation that the sea state was extremely low, so that echoes resulted primarily from the microscale capillary wave structure being tilted, advected and modulated by the wake components. This hypothesis could be tested by coherent Doppler processing of the radar returns, but would require some modifications to the existing radar data acquisition system.

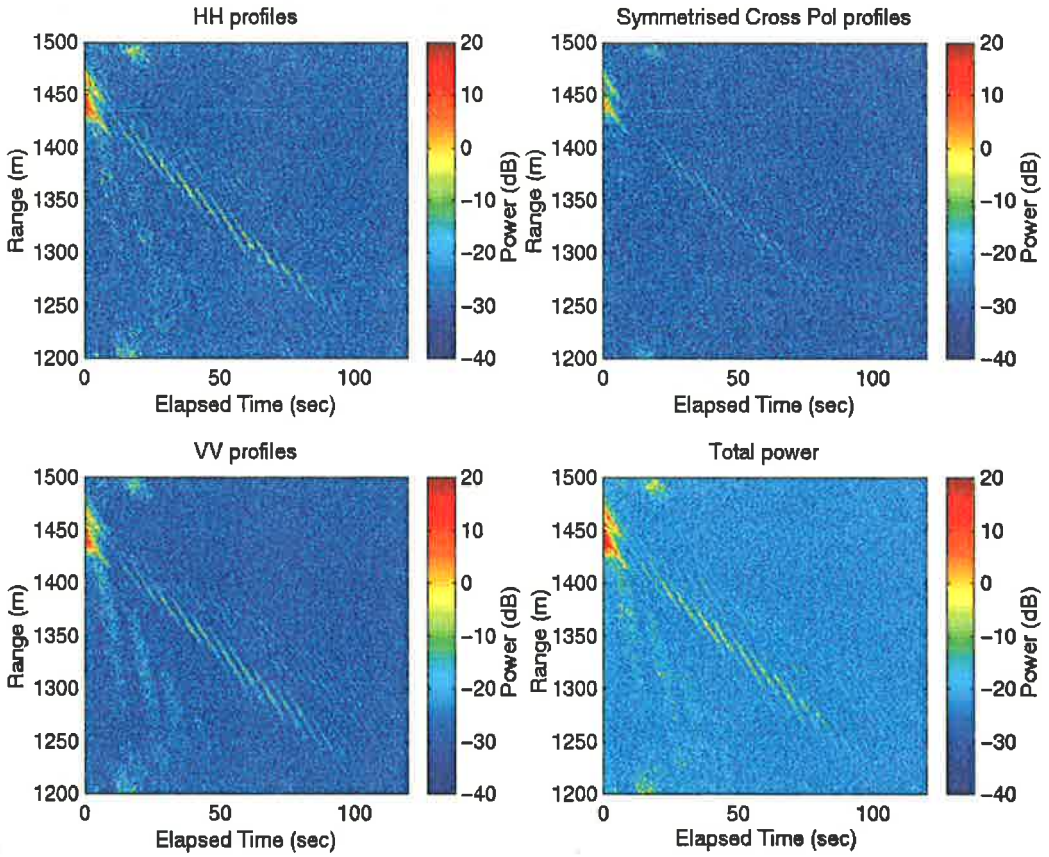

Figure 6-40 Results from Darwin harbour wake measurement

During the measurements, the polarisation of the transmitted pulse was varied at the end of every frequency sweep rather than on a pulse-to-pulse basis. This meant that some of the elements of the [S] matrix were separated by the sweep period rather than a pulse interval. Consequently a detailed polarimetric analysis of these results could not be performed, but the variation in the polarimetric parameters observed in measurements of a wake produced by a pilot boat observed at Queenscliff, Victoria is described in Section 6.4.

6.3.2 Comparison with modelled results

The SWPE code described in Section 5.2.1 was used to generate a prediction of the wake produced by the catamaran. An accurate CAD model of the catamaran hull was obtained and is shown highlighted in Figure 6-41. This model was converted to provide a suitable input file for SWPE. The simulated wake pattern was produced using a 1000 × 1000 m grid with a grid spacing of 1 m in both directions, assuming that the catamaran was travelling at a speed of 15 ms^{-1} in the negative $\vec{x}$ direction. An

image of the predicted surface elevations for the catamaran model is shown in Figure 6-42.

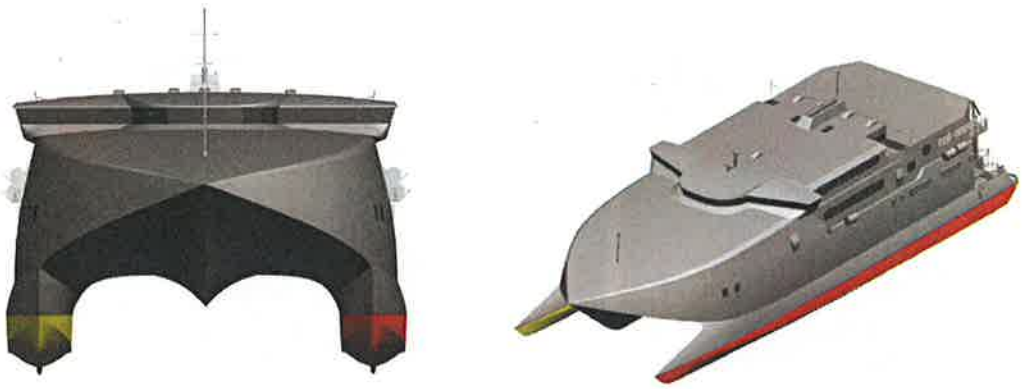

Figure 6-41 CAD model of wave-piercing catamaran

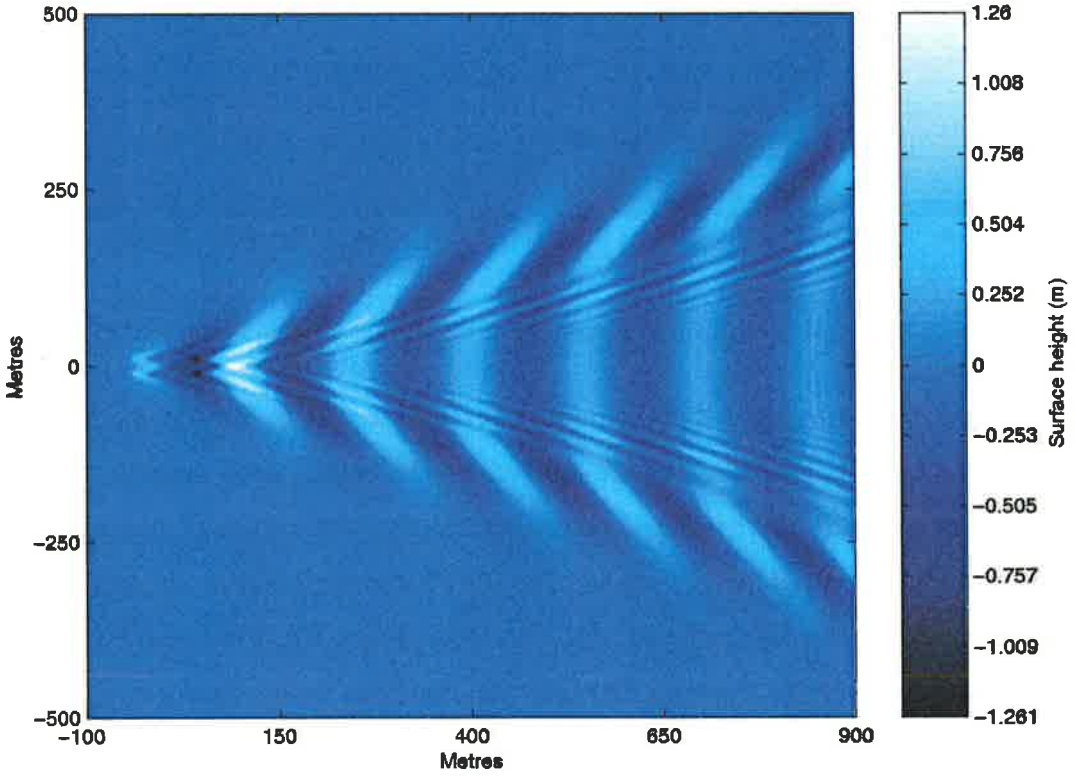

Figure 6-42 The surface elevation pattern generated by the wave piercing catamaran

The surface predicted by SWPE was used to generate the polarimetric response using the two-scale Bragg model described in Chapter 5. The radar was positioned at a distance of 2 km with a look down angle of 0.5° at an aspect such that the direction of propagation vector $\vec{k}$ was orthogonal to the diverging wake, to match the

measurement conditions specified in Darwin. The results from the simulation are shown in Figure 6-43.

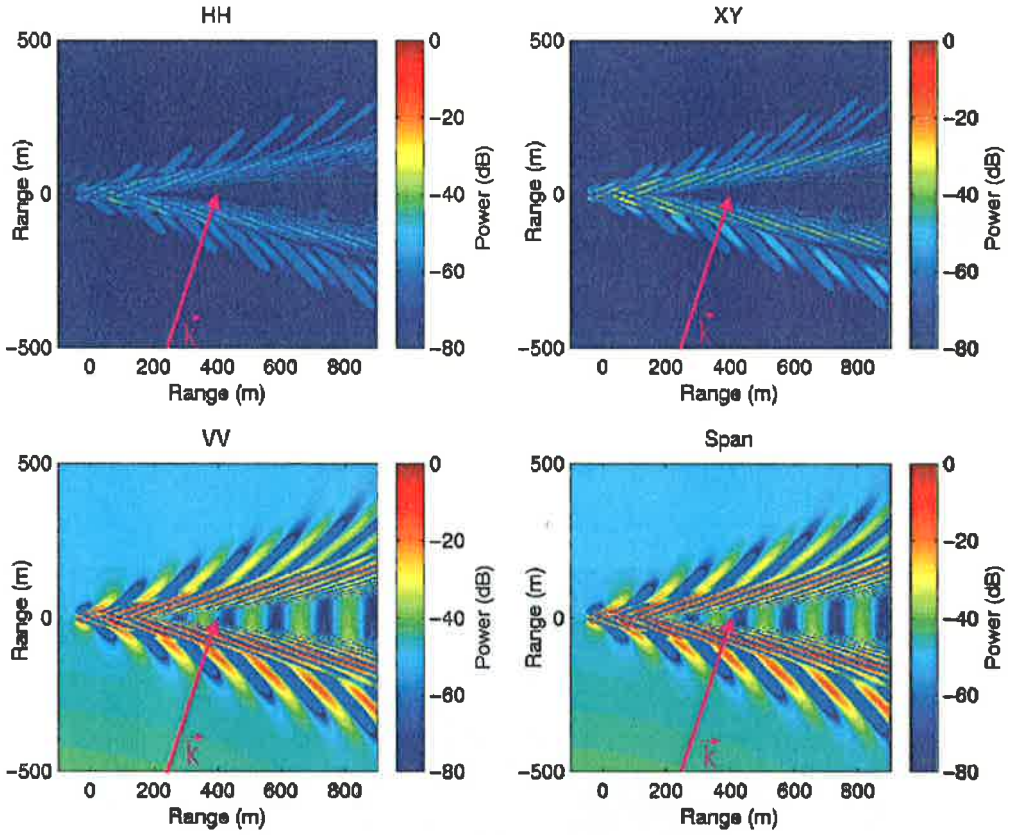

Figure 6-43 Predicted polarimetric response from the surface elevation produced by SWPE

The simulation results show that the dominant return occurs in the VV channel while the HH and cross-polar responses are predicted to be significantly smaller. These trends are evident in the measured results in Figure 6-40, although the cross-polar return is not as strong as the HH values. The SWPE simulation also suggests that both sides of the diverging wake should be visible, though not equal in intensity, however the experimental results illustrate that only returns from wake structures on the side closest to the radar were observed. This is attributable to the very low radiated power and hence poor SNR.

6.4 Queenscliff pilot boat wake measurements

In November 2001, wake measurements of a pilot boat were collected at Queenscliff in Port Phillip Bay near Melbourne, Australia. The results from the measurements in Darwin Harbour demonstrated that wake structures were evident in the radar images

at low grazing angles. The polarisation of the transmitted pulse was switched only at the end of each sweep, so a detailed polarimetric analysis of the results could not be carried out. At Queenscliff, the polarisation of the transmitted pulse was varied on a pulse-to-pulse basis ensuring that a more detailed polarimetric analysis of the data could be performed. Measurements were collected from a site adjacent to the Queenscliff lighthouse, as this location was easily accessible by road and offered elevated, unobstructed views of the main shipping channel. On the day that the measurements were performed, the sea state was extremely low and very little backscatter was observed from the sea surface, resulting in extremely high entropy values. Measurements of a number of small fishing vessels and oil tankers were obtained during the day, but the most interesting set of results was obtained from a pilot boat operated by the Queenscliff sea pilots. This vessel measured 16.5 m in length and 5.25 m in beam, with a draught of 2.0 m and was capable of speeds of up to 25 knots. High resolution polarimetric range profiles were recorded at X band while the vessel was travelling between its base at Queenscliff and pilot boarding grounds located 4 miles south-west from the Point Lonsdale Lighthouse. A vessel similar to the ship observed in the measurements is shown in Figure 6-44.

Figure 6-44 Pilot boat

6.4.1 Generation of range profiles

To obtain high resolution range profiles, the pulsed mode of the radar was used with a stepped frequency waveform. During the measurements, the radar sweep parameters were configured to produce a 300 m range window that did not exhibit any range fold-over effects. This was achieved by matching the range window to the pulse width of the transmitter using a 2 μs pulse and a pulse repetition interval of 40 μs. High

resolution range profiles were recorded using a stepped frequency waveform consisting of 1024 frequency steps at 0.5 MHz intervals giving a signal bandwidth of 512 MHz and a range resolution of 0.293 m. The polarisation of the transmitted pulses was varied on a pulse-to-pulse basis to yield range profiles for the HH, HV, VH and VV polarisation states.

6.4.2 Wake measurements

Data was collected while the pilot boat conducted a high speed pass during a return journey between the pilot boarding grounds and its base located at Queenscliff. The radar antenna was placed on top of the radar van to achieve the maximum possible look-down angle as shown in Figure 6-45.

Figure 6-45 DSTO radar van deployed at Queenscliff

In this configuration, the radar antenna was approximately 10 m above sea level, giving a look-down angle of 1.5°. During the data collection the radar operator visually tracked the pilot boat and positioned the range window to span the wake

sector behind the ship. Measurements were accumulated at a fixed bearing and range so that the same patch of sea could be observed during the measurement time. The pilot boat continued on its course, disappearing from the radar footprint approximately 10 seconds after the measurements commenced. The radar continued to make measurements of the same region of sea so that the diverging wake arms could be observed as they propagated towards and away from the radar. Measurements were conducted over a period of 50 seconds resulting in 518 range profiles.

6.4.3 Wake analysis

The received signals were range-processed and combined to form an estimate for the scattering matrix for each range-time cell. The variation in the magnitude of the elements of the scattering matrix is shown in Figure 6-46.

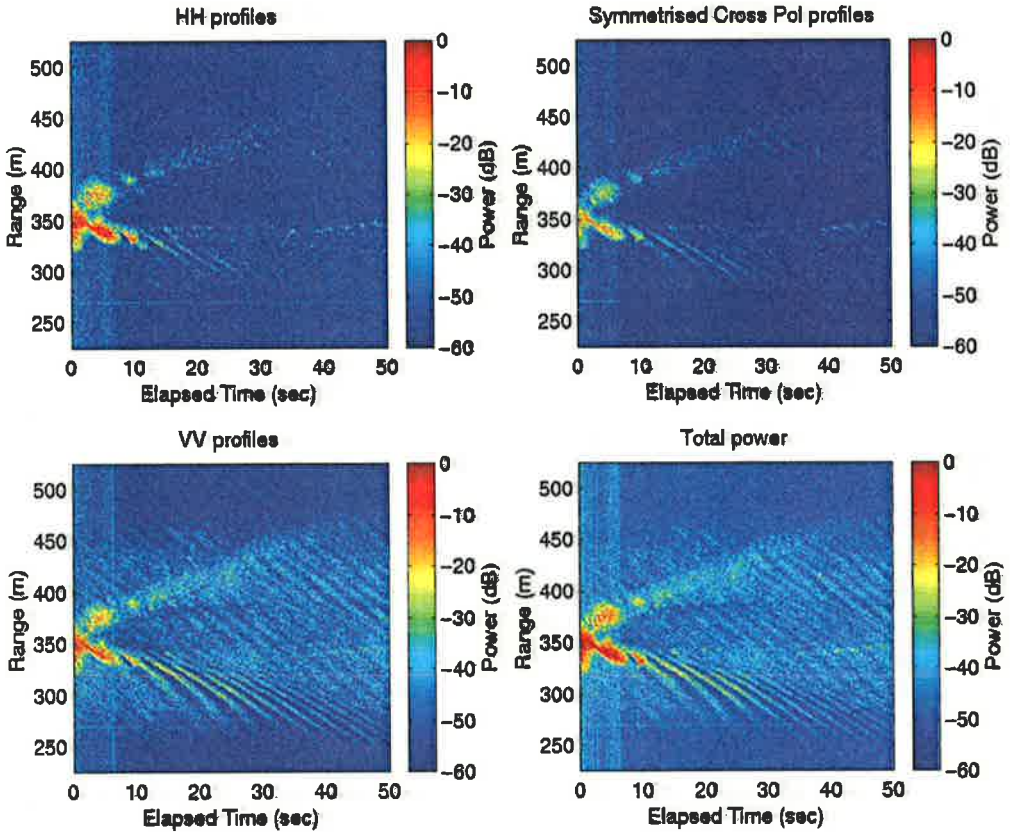

Figure 6-46 Range profile images of the pilot boat wake

The diverging wake structure is clearly evident, particularly in the VV image. This is consistent with the Bragg scattering model, which predicts that the dominant scattering mechanism at low grazing angles will be the VV return. The results were

then analysed using a technique that derived a scalar quantity based on the location of the characteristic polarisation states for each range cell and using the eigenvalue analysis of the coherency / covariance matrix described previously.

6.4.3.1 Scalar technique

The characteristic polarisation states for the [*S*] matrices in each range-time cell in the wake image were determined using the technique developed by Yang *et al* [155]. Inspection of the locations of these characteristic states on the Poincaré sphere revealed that the polarisation signatures were highly non-uniformly distributed in the spatial domain. The location of the cross-polar nulls showed that the corresponding eigenvector distribution made a strong transition in moving from the diverging wake region to the ambient clutter regions. This is illustrated in Figure 6-47.

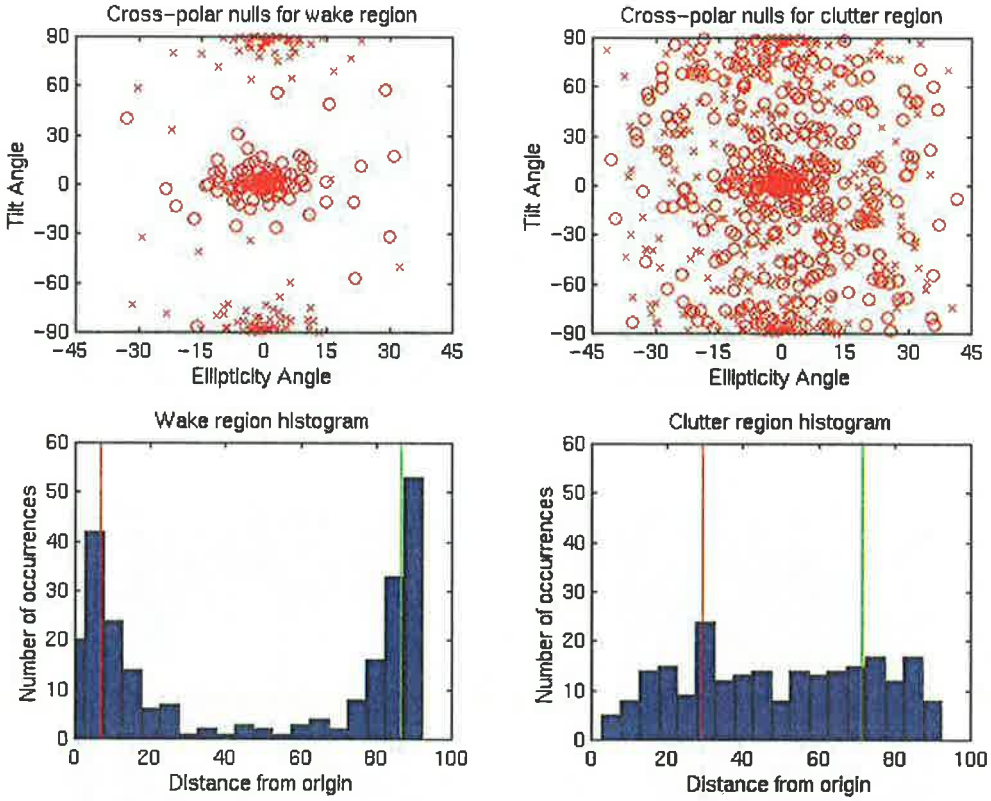

Figure 6-47 Cross-polar null distributions for wake and clutter regions

The distances from the origin to each cross-polar null in the selected wake and clutter regions shown in Figure 6-47 were then calculated and plotted as a histogram. The diverging wake region exhibited a bimodal distribution while the clutter regions were more uniformly distributed as shown in Figure 6-47. The histograms were split into two halves and the mean values of the points present in each region were calculated.

The red and green lines in Figure 6-47 indicate these values. These scalar values were then used to define features that could be used to classify spatial regions of interest as either wake or clutter. In essence this scheme tests a given sample against the prior distributions shown in Figure 6-47 and assigns the sample accordingly.

The range profile images were then divided into 5 × 5 cells. The cross-polar null locations were calculated for each [S] matrix in the cell and the distances of the nulls from the origin were determined. Histograms of these values were produced and the mean values of the points in the two halves were calculated. This defined two scalar values that were used to create the images shown in Figure 6-48.

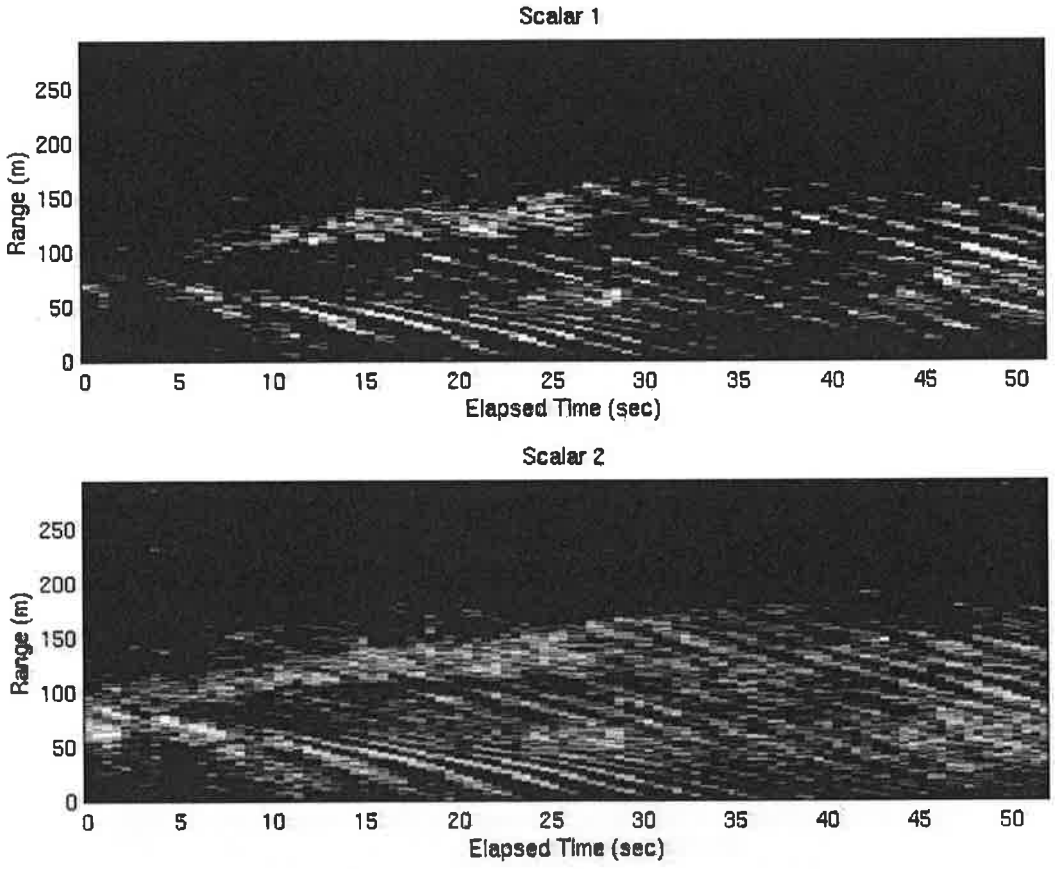

Figure 6-48 Wake images in the polarisation domain

The top image in Figure 6-48 represents the mean value of the points in the left half of the cross-polar null histograms. Bright areas correspond to small mean values and are identified as wake crest regions. Dark regions correspond to larger mean values, suggesting that the points in these regions correspond to clutter. Similarly, in the bottom image in Figure 6-48 represents the mean value of the points in the right half

of the cross-polar null histograms. Bright areas (wake regions) correspond to large mean values while dark regions (clutter) correspond to smaller mean values. The wake features are clearly evident in both images even though the resolution has been reduced as a result of the cell averaging process.

In addition to the diverging wake contributions, additional structure can be seen within the wake region corresponding to ambient sea waves propagating obliquely relative to the line of advance of the pilot boat. The physical mechanism for the enhancement of these contributions is not clear but it may be related to interactions between the long ambient sea waves and vorticity within the turbulent wake region.

The scalar values can also be used to generate *polarimetric maps* of the wake regions as illustrated in Figure 6-49. This figure shows a small section of the total power image taken from Figure 6-46. Markers have been superimposed on top of the image are defined by the scalar values. In this case the red markers represent regions where the scalar values are small and map onto the wake crest regions. The green markers correspond to large scalar values and map into the clutter regions. The blue markers indicate intermediate values. One possible interpretation for these values is that they indicate regions where wave breaking is occurring.

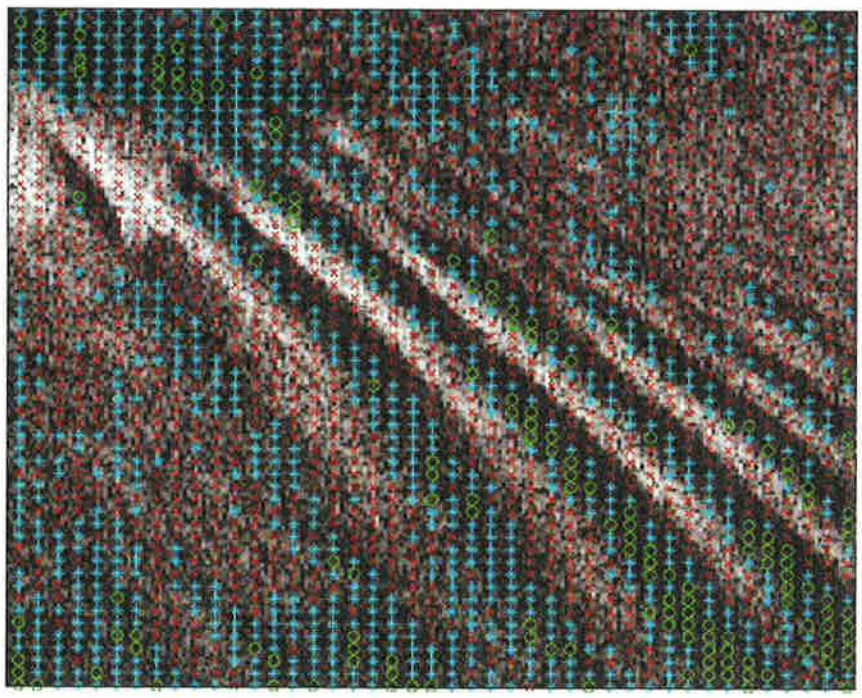

Figure 6-49 Identification of wake regions using the scalar parameter

6.4.3.2 Eigenvalue analysis

Additional polarimetric analysis of the pilot boat wake was performed with the eigenvalue decomposition technique (See Section 2.17.2) used in the Evans Head and Yallingup measurements. This analysis was performed to see how the results compared with the results obtained using the scalar method. First the Pauli scattering vector for each range-time cell was determined and the coherency matrices were then formed, averaging the outer product of the Pauli scattering vector over a 9×9 window. The eigenvalues of the coherency matrices were calculated and images of the variation in the polarimetric scattering entropy H, anisotropy A and the average scattering alpha $\bar{\alpha}$ were generated and are shown in Figure 6-50.

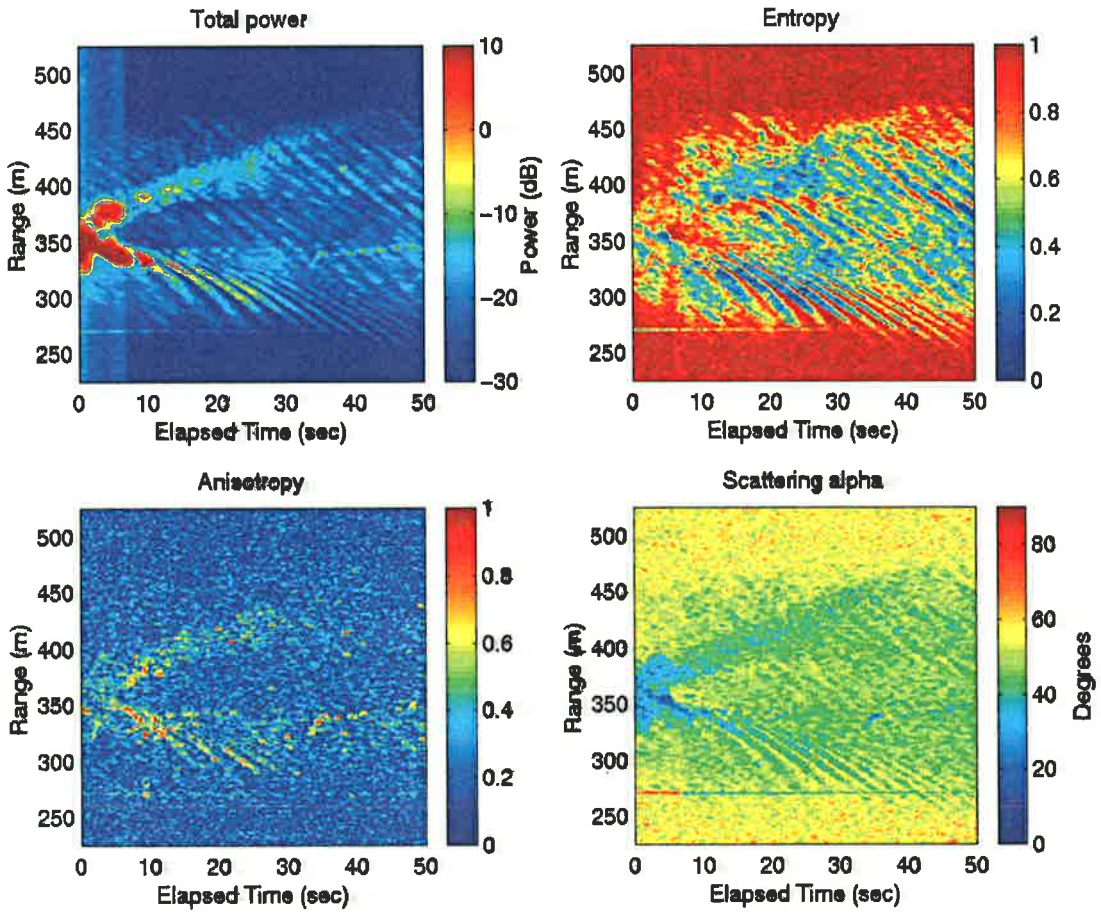

Figure 6-50 The variation in the polarimetric parameters observed for the pilot boat wake

To assist in the interpretation of the results, the data was filtered to remove the clutter regions. The filtered entropy, anisotropy and $\bar{\alpha}$ images are shown in Figure 6-51.

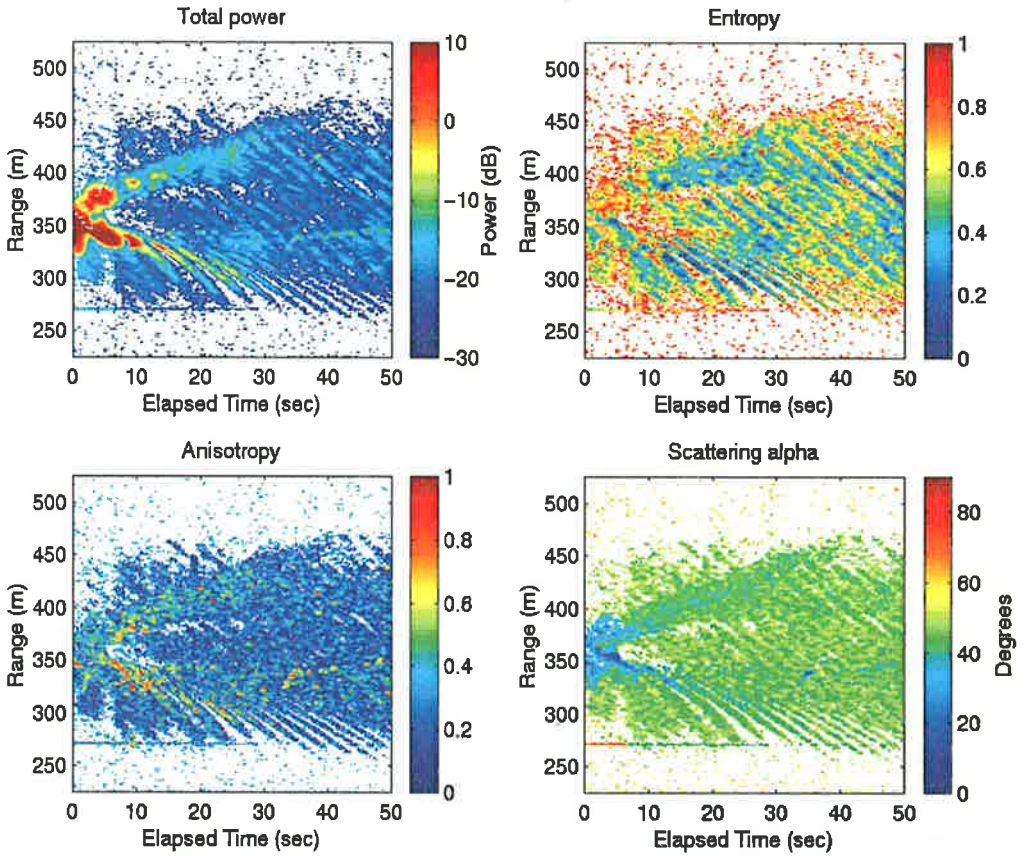

Figure 6-51 Filtered results for the pilot boat wake

There are a number of conclusions that can be made from the images shown in Figure 6-50. It is clear that the entropy provides and a good means for distinguishing between the wake and clutter regions. The clutter regions appear as high entropy regions, corresponding to areas with low backscatter and random scattering behaviour. The wake regions emerge as low entropy regions suggesting the presence of a single dominant scattering mechanism. In most cases this is surface scattering from the face of the diverging wake as it travels towards the radar. This conclusion is supported by the results in the anisotropy image that illustrates that in the low entropy regions there are higher anisotropy values suggesting low surface roughness. The $\bar{\alpha}$ image indicates high values in the clutter regions with typical values of around 55°. In the regions close to the vessel there are a number of regions with low $\bar{\alpha}$ values. These values are typically around 35° and are similar to the values observed in the Evans Head measurements for breaking waves. The $\bar{\alpha}$ values further from the boat on the diverging wake arms and in the region corresponding to ambient sea waves propagating obliquely relative to the line of advance of the ship, exhibit values in the

range of 40° to 45°. These values are consistent with the Bragg model predictions for of tilted surfaces observed at low grazing angles. The distribution of points in the $H-A-\bar{\alpha}$ space in Figure 6-52 clearly shows that the majority of the points lie in the high entropy clutter regions. The results were filtered so that the distribution of the points in the wake regions could be studied. These results are shown in Figure 6-53.

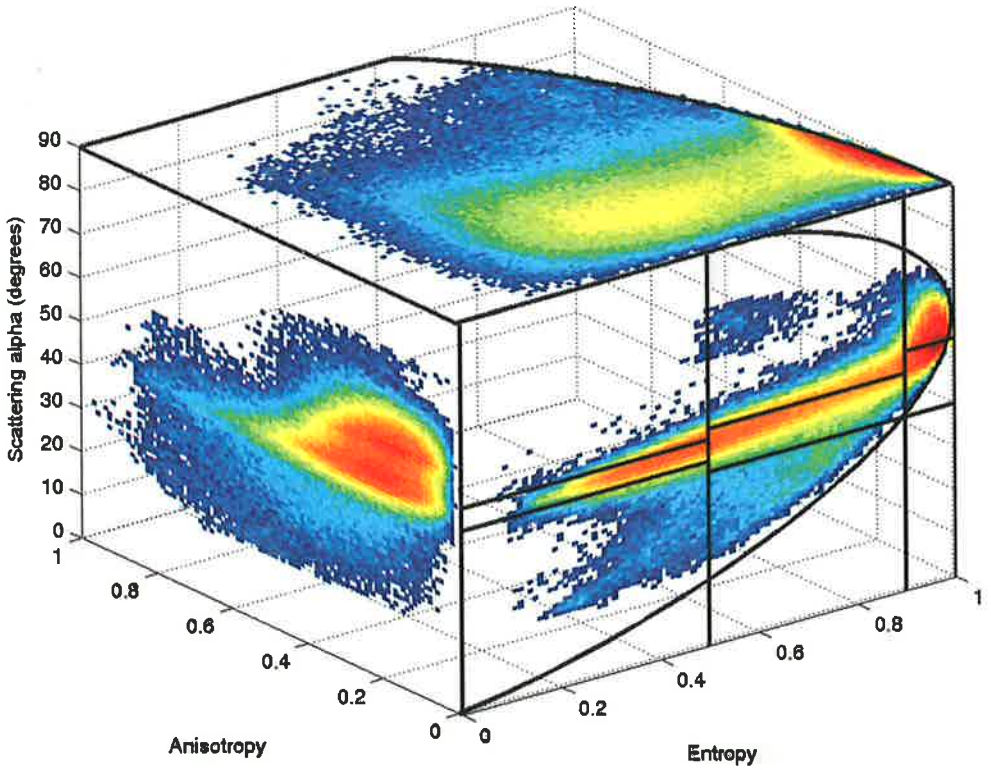

Figure 6-52 The distribution of points in the $H-A-\bar{\alpha}$ space for the pilot boat wake

The filtered distribution of points in the $H-A-\bar{\alpha}$ space indicates that the majority of points exhibit $\bar{\alpha}$ values in the range of 40° to 45° distributed fairly evenly across entropy values ranging from 0.2 to 0.8. The image products corresponding to [H][A], [1–H][A], [H][1–A] and [1–H][1–A] were also calculated using the filtered entropy and anisotropy images. These results are shown in Figure 6-54. The [1–H][1–A] indicates that in the wake regions there is a single dominant scattering mechanism present. There is some evidence of multiple scattering mechanism in the [H][A] and [1–H][A] images in the regions where low $\bar{\alpha}$ values were observed. This adds further support to the notion that these regions correspond to areas where wave breaking events taking place.

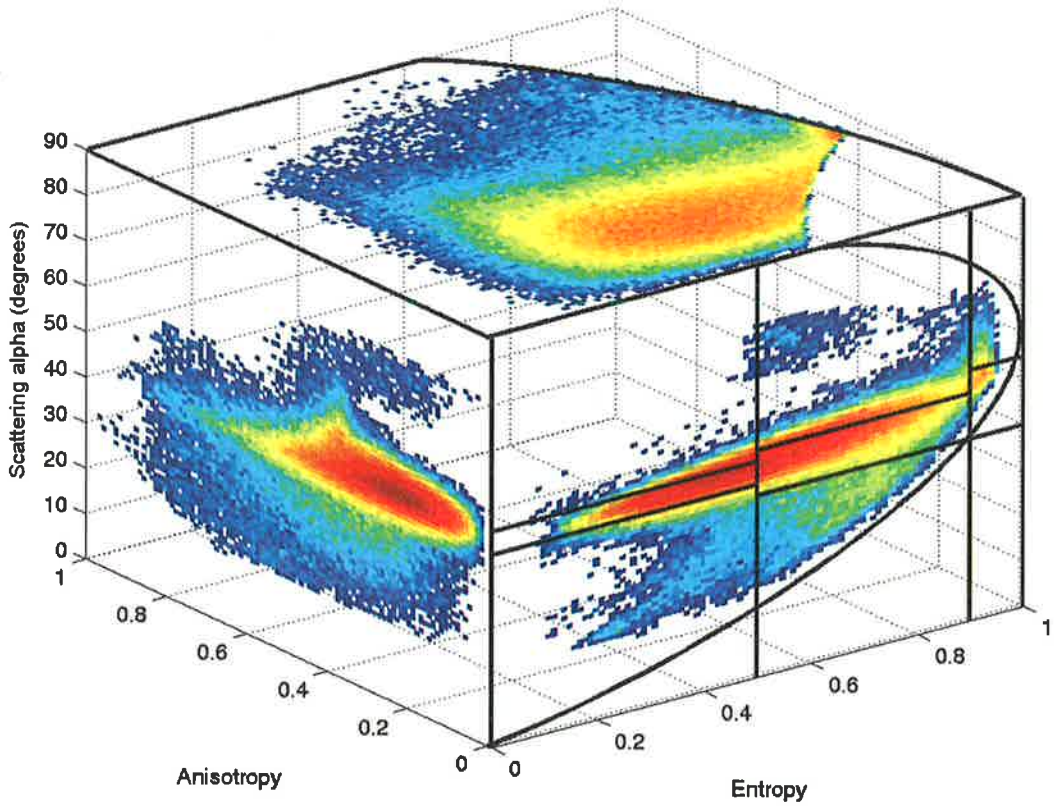

Figure 6-53 Filtered distribution of points in the $H-A-\bar{\alpha}$ space for the pilot boat wake

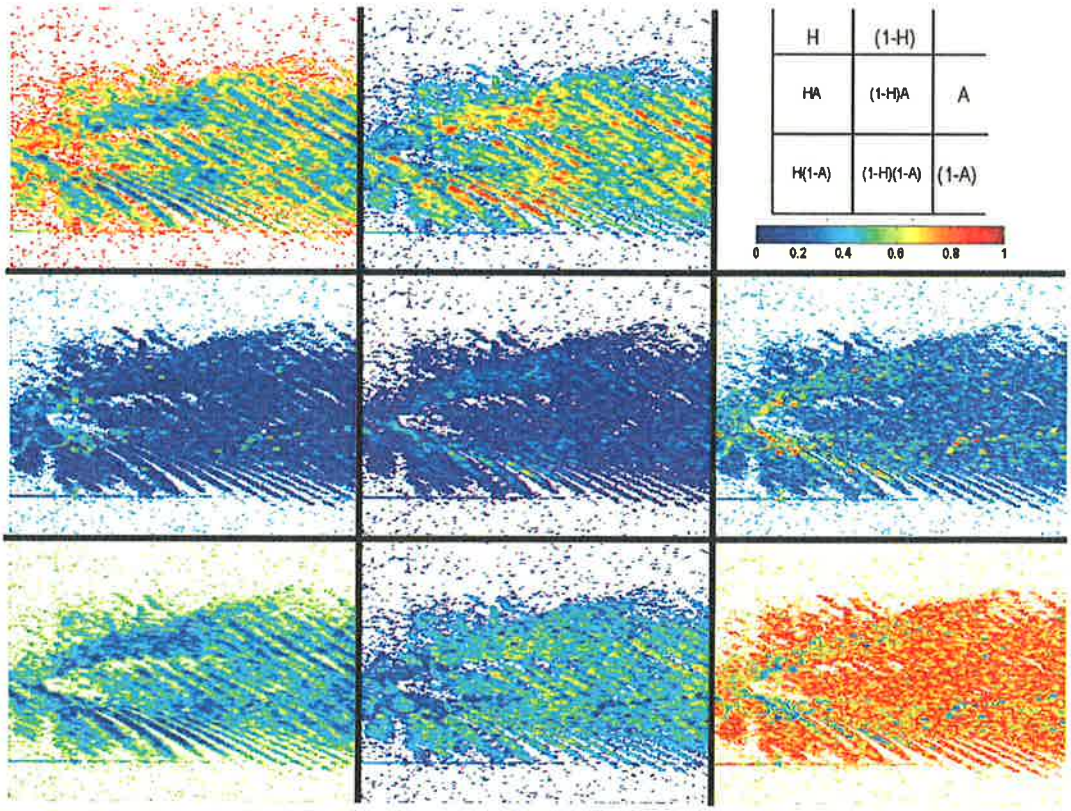

Figure 6-54 Image products formed between [*H*], [1–*H*],[*A*] and [1–*A*] for the pilot boat wake

6.4.4 Comparison of techniques

A comparison between the results obtained used the eigenvalue analysis of the coherency matrix and the scalar technique based on the distribution of the cross-polar null states is shown in Figure 6-55. It is clear that both techniques yield very similar results and provide an effective means of discriminating between the clutter and wake regions.

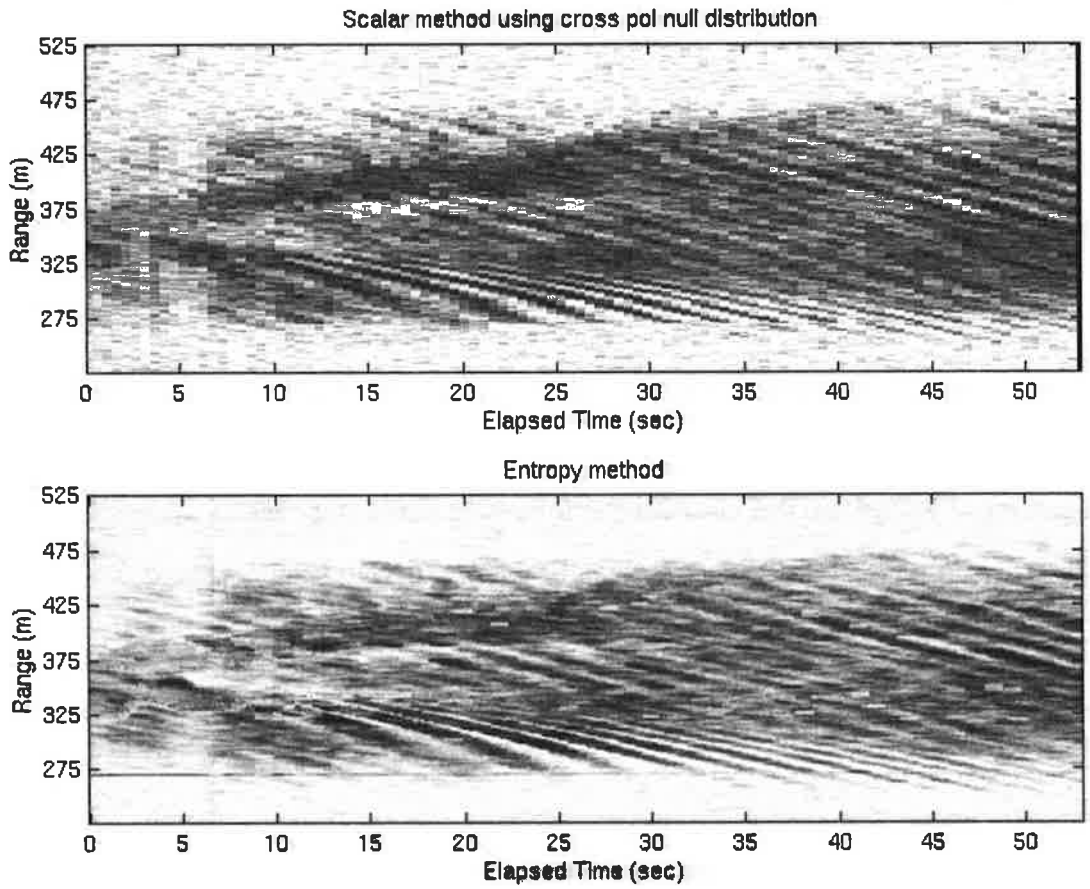

Figure 6-55 Comparison between the entropy and scalar techniques

The fact that the two results are very similar is not surprising when one considers the manner in which the images were constructed. In regions of low entropy, there is a single dominant scattering mechanism present. Consequently one would expect the distribution of the cross-polar nulls to be spatially distributed in a similar region on the Poincaré sphere. According to the definition of the scalar quantity proposed in Section 6.4.3, one would expect a small value for the scalar quantity representing the mean value in the left half of the histogram. In regions with high entropy, one expects to observe random noise-like scattering, hence the spatial distribution of the cross-

polar null states on the Poincaré sphere should be random, leading to high scalar values. One of the differences observed between the plots arises in the wave breaking areas. In the entropy plots these regions exhibit values similar to the clutter regions, whereas in the scalar method the values are in the intermediate range.

6.4.5 Enhanced wake detection

Given the increased cost and complexity of polarimetric systems, it is important to assess whether polarimetry can enhance wake detection at low grazing angles. There have been several papers [113, 114, 400] that have shown at it is possible to improve the detection of wakes in SAR imagery using polarimetric processing. However, at low grazing angles, the task is complicated by the fact that the entropy values from the sea clutter are generally high.

Although the absolute values of the eigenvalues are important to assess the total scattered power by the target, it is the distribution of this power across the eigenvalue spectrum that is important in assessing the processing gains to be had in polarimetric processing. To illustrate this consider the following scattering vectors $\vec{k}_1$ and $\vec{k}_2$. The vectors are orthogonal if the inner product of their scattering vectors is zero

$$\left.\begin{aligned} \vec{k}_1 &= \left|\vec{k}_1\right| \underline{w}_1 = \left[S_{HH} \quad S_{HV} \quad S_{VV}\right]_1^T \\ \vec{k}_2 &= \left|\vec{k}_2\right| \underline{w}_2 = \left[S_{HH} \quad S_{HV} \quad S_{VV}\right]_2^T \end{aligned}\right\} \Rightarrow \underline{w}_1^{*T} \underline{w}_2 = 0 \tag{6.1}$$

For target detection in the presence of depolarising clutter, the receiver threshold is set according a quadratic form as follows

$$Q = \vec{k}^{*T} [C]^{-1} \vec{k} > Threshold \tag{6.2}$$

If Q is greater than some threshold then a target is detected. In this instance $\vec{k}$ corresponds to an instantaneous measurement of the scattering matrix and [C] is the covariance matrix of the background clutter. The receiver threshold is usually set to obtain a constant false alarm rate through knowledge of the statistics of Q (commonly assumed multi-variate Gaussian). Equation (6.2) can be rewritten in the form

$$Q = \left|\vec{k}\right|^2 \vec{w}^{\dagger}\left(\frac{1}{\lambda_1}\vec{e}_1\vec{e}_1^{\dagger} + \frac{1}{\lambda_2}\vec{e}_2\vec{e}_2^{\dagger} + \frac{1}{\lambda_3}\vec{e}_3\vec{e}_3^{\dagger}\right)\vec{w} = \frac{\left|\vec{k}\right|^2}{\lambda_1}\left|\vec{w}^{\dagger}.\vec{e}_1\right|^2 + \frac{\left|\vec{k}\right|^2}{\lambda_2}\left|\vec{w}^{\dagger}.\vec{e}_2\right|^2 + \frac{\left|\vec{k}\right|^2}{\lambda_3}\left|\vec{w}^{\dagger}.\vec{e}_3\right|^2 \quad (6.3)$$

In this form it is clear that the best target-to-clutter ratio is obtained when the observed normalised scattering vector $\vec{w}$ is orthogonal to the first two eigenvectors of [C] and lies parallel to the minimum eigenvector. Thus, an upper bound on the processing gain is then given by the ratio of the maximum and minimum eigenvalues of $[C]$. In the event that the entropy is zero, the minimum eigenvalue will be zero and the max processing gain will be infinite. At the other extreme, if the entropy is one then all three eigenvalues are equal and the maximum processing gain is 0 dB. In this case polarimetry provides no advantage over single channel intensity based detection. If the anisotropy is high then the processing gain is obtained for a specific scattering mechanism but if it is close to zero then the processing gain can be obtained for a subspace of target scattering mechanisms. Clearly, for good detection performance we require low entropy combined with low anisotropy.

The image of the ratio between the maximum and minimum eigenvalues was generated for pilot boat wake and is shown in Figure 6-56. The maximum theoretical gains occur in the regions where a single dominant scattering, particularly on the diverging wake arms. In the clutter regions, where the entropy is high, the processing gains are close to zero. In general the processing gain illustrated in Figure 6-56 will not be achieved as the observed scattering vector will not satisfy the optimal conditions. Additional studies to identify the probability of the target scattering vector lying in the subspace spanned by the two smaller eigenvectors would be required to determine the practical processing gains that can be achieved at low grazing angles.

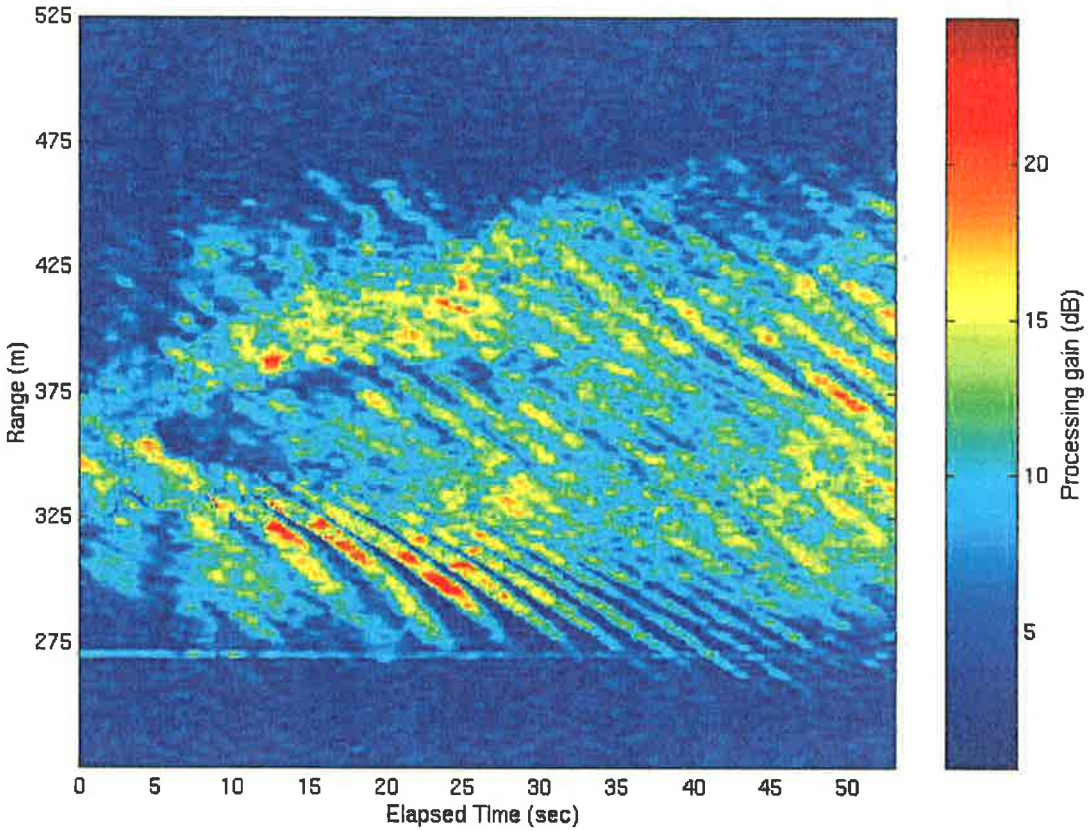

Figure 6-56 Maximum processing gain using the polarisation domain

6.4.6 SWPE modelling

SWPE was used to generate the predicted wake using the pilot boat hull model assuming a constant speed of 6.4 ms^{-1} (the estimated speed of the pilot boat in the Queenscliff measurements) travelling in the negative $\vec{x}$ direction. The surface displacements were calculated on a regularly spaced grid with a 410 m extent in the $\vec{x}$ direction and 300 m extent in the $\vec{y}$ direction and a spatial resolution of 1 m in both directions. The surface displacement produced by SWPE was used to calculate the polarimetric response from the surface using a look down angle of 1.5° and at an aspect that ensured that the direction of propagation $\vec{k}$ was approximately orthogonal to the diverging wake arms. Additional details of the SWPE parameters and the method used to generate the polarimetric response is given in Section 5.7.3. The predicted polarimetric response is shown in Figure 6-57.

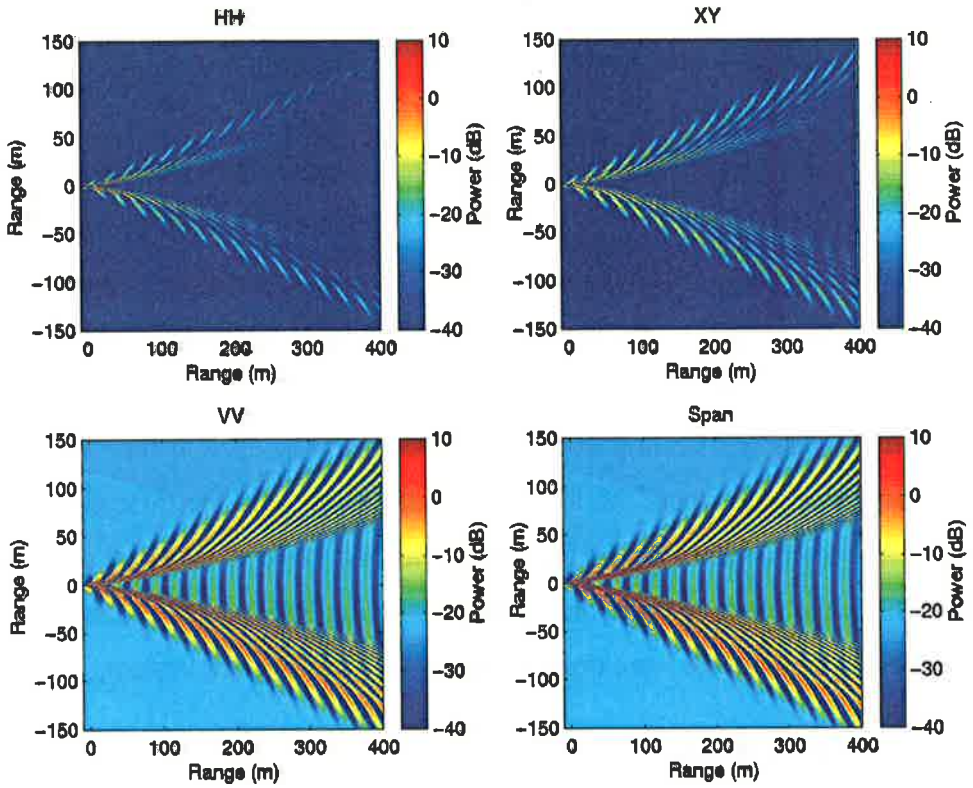

Figure 6-57 Predicted polarimetric response from the pilot boat wake

The simulation results illustrate that the strongest return will appear in the VV channel and that a strong response is produced from the diverging wake arms. In general there is good agreement between the modelled results and the experiment values.

6.5 Induced wave breaking measurements

Ocean wave modelling and the quantitative parameterisation of the air-sea exchange requires a good understanding of both wave breaking and the subsequent dissipation of energy in the ocean [401]. Understanding the mechanics of these processes is essential but is complicated by the fact that in general wave breaking does not occur periodically at the same location but rather, periodically at different locations, as is observed in wave-group related breaking [402]. Shallow grazing angle radar measurements can contribute significantly to the observational basis for ocean wave modelling since they can interrogate a range of locations simultaneously, however the problem of knowing when and where the wave breaking events are going to occur still remains. The solution is to study mechanically-generated breaking waves in a laboratory environment where the wave breaking events can be localised to suit

cameras, radars and other measurement devices. The complaint about such studies is that the tank boundary conditions are generally not very realistic.

The importance of identifying the role of nonlinear contributions in radar returns from the sea has been highlighted in Section 5.8. The idea of initiating wave breaking events using a ship wake was suggested to enable some control over when and where the wave breaking events would occur. In November 1999, a series of wake measurements were conducted at a site near Newcastle off the New South Wales coast involving a mechanized landing craft (LCM 8 class). It is often the case that such vessels steam at speeds where the transverse wake dominates the diverging wake. In order to observe this phenomenon, the vessel was instructed to steam directly towards and away from the radar, along a line of the prevailing ESE winds. Measurements at X and Ku band frequencies were obtained using the DSTO radar system.

6.5.1 Target Description

The vessel used in the wake measurements was a mechanized landing craft (LCM class) used by amphibious forces to transport equipment and troops. A picture of a vessel, similar to the one used in the measurements is shown in Figure 6-58 and the dimensions and capabilities of the vessel are given in Table 6-3.

Figure 6-58 Mechanised Landing Craft (LCM class)

Table 6-3 Mechanised landing craft dimensions

Length	22.4 m
Beam	6.4 m
Draught	1.6 m
Top speed	11 knots

Measurements were performed at X and KU band frequencies using a stepped frequency waveform. High resolution range profiles were recorded using a waveform consisting of 1024 frequency steps at 0.5 MHz intervals producing a 300 m range window. This produced a signal bandwidth of 512 MHz and a range resolution of 0.293 metres. A 2 μs pulse width and a 40 μs pulse repetition rate were used to eliminate the possibility of range fold over effects.

6.5.2 X band in-bound measurements

The first set of measurements were performed at X band. The vessel was instructed to execute and in-bound run at 10 knots heading directly towards the radar. The starting range for the first run was 1935 m and the final range of 1590 m. The radar van was positioned on Fort Drive directly below Fort Scratchley, at a height of approximately 12 metres above sea level, giving a look down angle of 0.36°. Pictures of the trial site and an aerial view of the sea conditions are shown in Figure 6-59 and Figure 6-60.

Figure 6-59 Radar Van deployed at Newcastle site

Figure 6-60 An aerial view of the Newcastle measurement site

During the measurement the seastate was estimated to be between 1 and 2. The polarisation of the transmitted signals was varied on a sweep-to-sweep basis enabling the horizontal and vertical responses to be obtained in a single run, but this meant that some of the elements of the [*S*] matrix were separated by the sweep period and consequently a detailed polarimetric analysis of these results could not be performed. Nevertheless, the ratio between the co-polar and cross-polar values for the wave breaking events was determined and compared with wave-tank results. Approximately 90 seconds of data was recorded for the inbound run giving a total of 1000 records. The raw range profiles recorded are shown below in Figure 6-61.

During the measurements the target moved through the radar range window. To assist in the interpretation of the results, the range profiles were aligned so that the target remained in a constant set of range bins for the duration of the measurement. Initially the slope of the target track was estimated and a coarse linear correction was applied to the data. A fine correction procedure was then used to align the data using a matching criterion based on the correlation between adjacent range bins. In some cases manual alignment of adjacent profiles was required to achieve the desired results. The results of the alignments are shown in Figure 6-62.

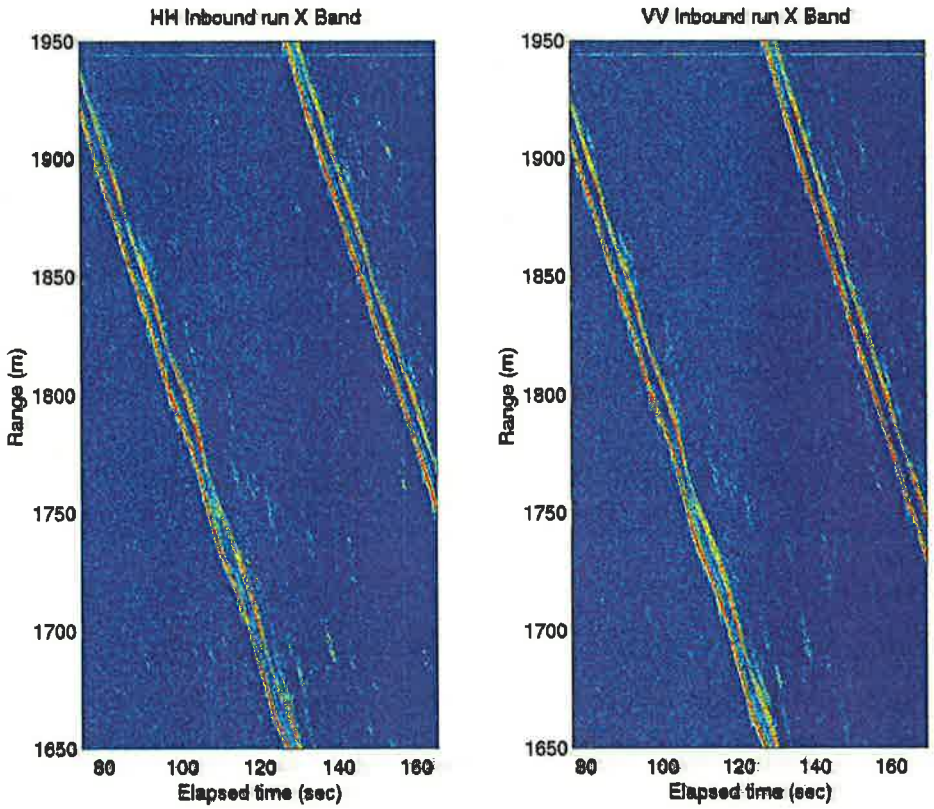

Figure 6-61 Raw range profiles results from the inward run at X band

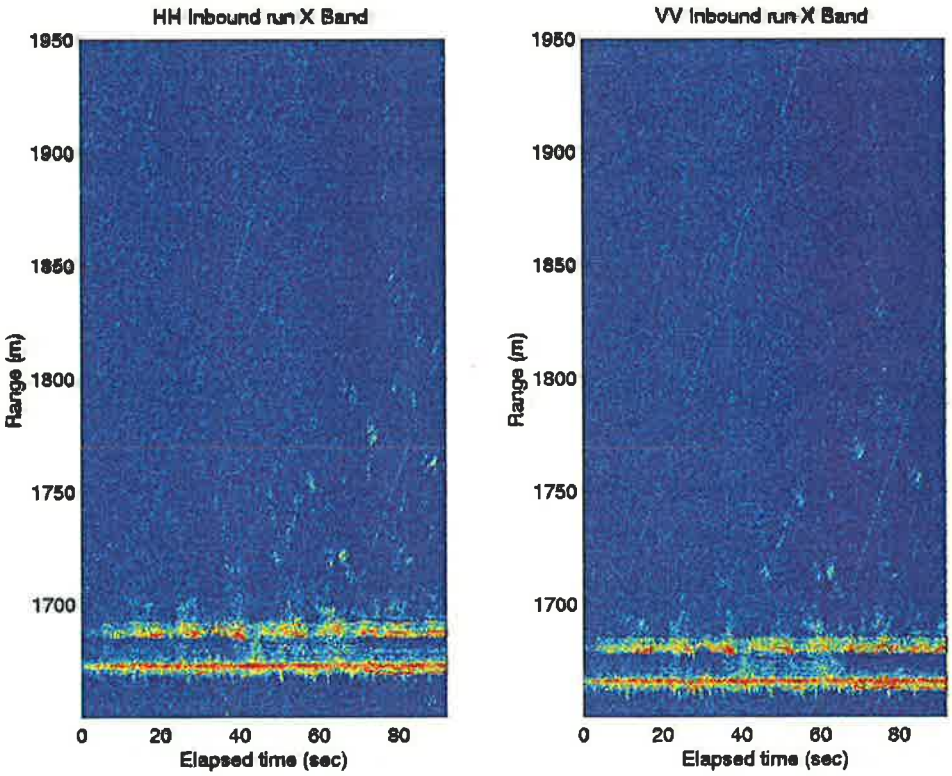

Figure 6-62 Aligned results from the inward run at X band

The aligned data indicates some interesting periodic transient enhancements during the inbound runs. These events were hypothesised to be produced by wave breaking events precipitated by the superposition of the dominant wake components with the crests of the incoming swell. On this hypothesis, one would expect to observe the same transients on the out-bound run but at a much higher frequency. In the out-bound case the relative velocity corresponds to the sum of the boat and wave speeds, whereas the in-bound leg would yield interceptions at the frequency associated with the difference of the two speeds.

Using the speed of the vessel, the theoretical interception rate can be determined. An aerial photograph of the area taken during the calibration measurements was used to estimate the swell wavelength L. The group velocity and period of the incoming swell was determined from the swell wavelength and the known bathymetry. Combining this estimate with the known velocity of the ship enables the time interval t_{wb} between induced wave breaking events to be calculated using the following expression

$$\tau_{wb} = \frac{2\pi}{k}.\left[u \pm \frac{1}{2}\sqrt{\frac{g.\tanh(kd)}{k}}\right]^{-1} \tag{6.4}$$

where $k = 2\pi/L$, u is the ship speed perpendicular to the wave crests, d is the water depth and g is the gravitational acceleration $\equiv 9.8$ ms^{-2}. The solution for the inbound ship corresponds to the minus sign in Equation (6.4) and substituting the estimated values yields $t_{wb} \approx 12.2$ seconds. Analysis of the recorded data found that the time between events varied from 10.8 to 13.2 seconds with a mean value of around 12.1 seconds while the duration of enhancements ranged from 4.7 to 6.8 seconds.

6.5.3 X band out-bound measurements

The second set of measurements was also performed at X band and the vessel was instructed to execute an out-bound run heading directly away from the radar. Data was collected at ranges varying from 1575 to 2160 m using the same sweep parameters in the in-bound run. Measurements were recorded over a 70 second period giving a total of 760 records. The raw range profiles collected during this run are shown in Figure 6-63. Once again the range profiles were aligned so that the target

remained in the same set of range bins throughout the measurement. The aligned results for the out-bound run are shown below in Figure 6-64.

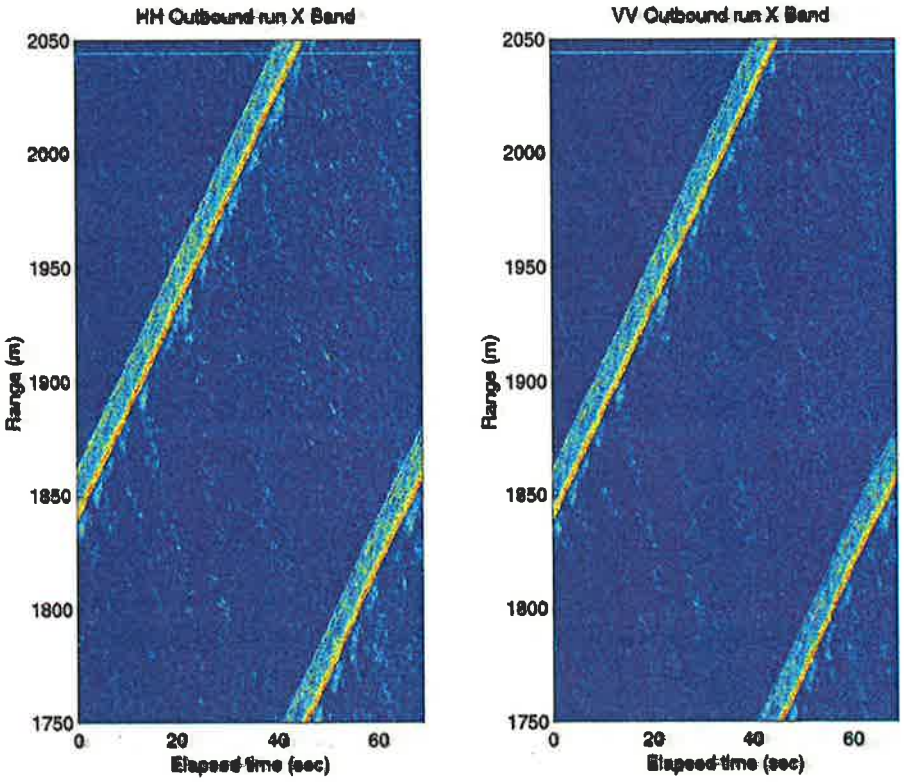

Figure 6-63 Raw range profiles recorded from the out-bound run at X band

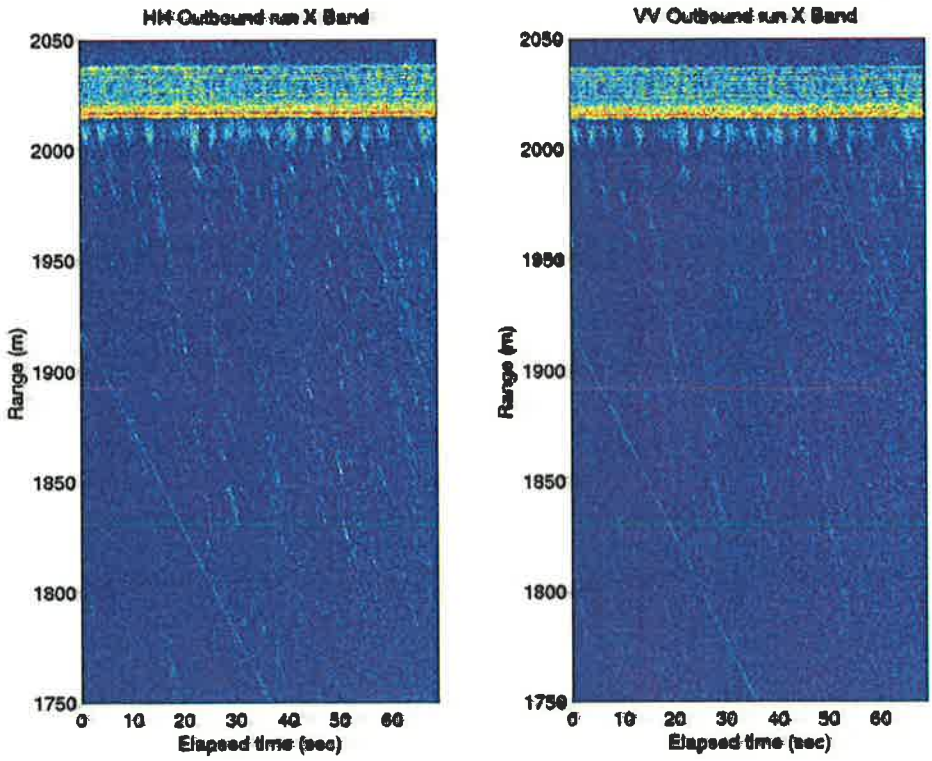

Figure 6-64 Aligned results from the out-bound run at X band

The periodic transient enhancements are also clearly evident in the out-bound run. Once again these events were attributed to the interaction between the dominant wake components and the incoming swell crests. The frequency of these events increased significantly in accordance with the fact that the relative velocity corresponds to the sum of the boat and wave speeds whereas during the in-bound run the interceptions occurred at the frequency associated with the difference of the two speeds. Using the knowledge for the wave period and the estimate of the boat speed of 9.6 knots, the theoretical intercept rate was determined using Equation (6.4). Substituting the estimated values gives $t_{wb} \approx 3.1$ seconds. Analysis of the recorded data found that the time between wave breaking events varied from 2.8 to 3.7 and the duration of enhancement ranged from 1.7 to 3.3 seconds.

The results obtained in the in-bound and out-bound runs are significant as the complaint about laboratory wave tank measurements is that the generated waves and the tank boundary conditions are very unrealistic. At-sea measurements, while realistic, lack the control over where and when the wave breaking events take place. Using a vessel to create the wave breaking events provides a means of achieving the best of both worlds, with some obvious but acceptable limitations.

6.5.4 Ku band in-bound measurements

The final set of measurements performed involved an in-bound run at Ku band. The vessel was instructed to make an in-bound run at 10 knots from a starting range of 2160 metres finishing at a range of 1440 metres. Data records were recorded using a stepped frequency waveform consisting of 512 steps of 1 MHz centred about 16.5 GHz. This produced a signal bandwidth of 512 MHz and a range resolution of 0.293 metres. Data records were recorded for 110 seconds giving a total of 1300 records. The raw range profiles recorded in this run are shown in Figure 6-65. The range profiles were again aligned so that the target remained in the same set of range bins for the duration of the measurement and the results are shown in Figure 6-66.

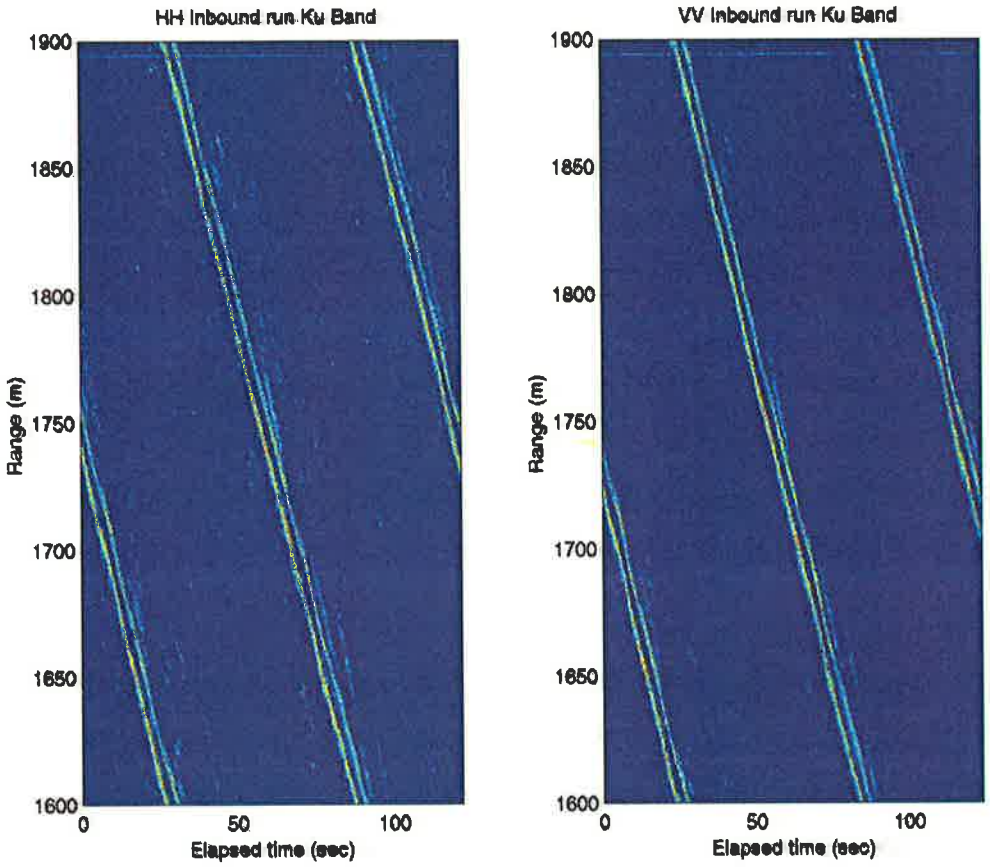

Figure 6-65 Raw range profiles from the in-bound run at Ku band

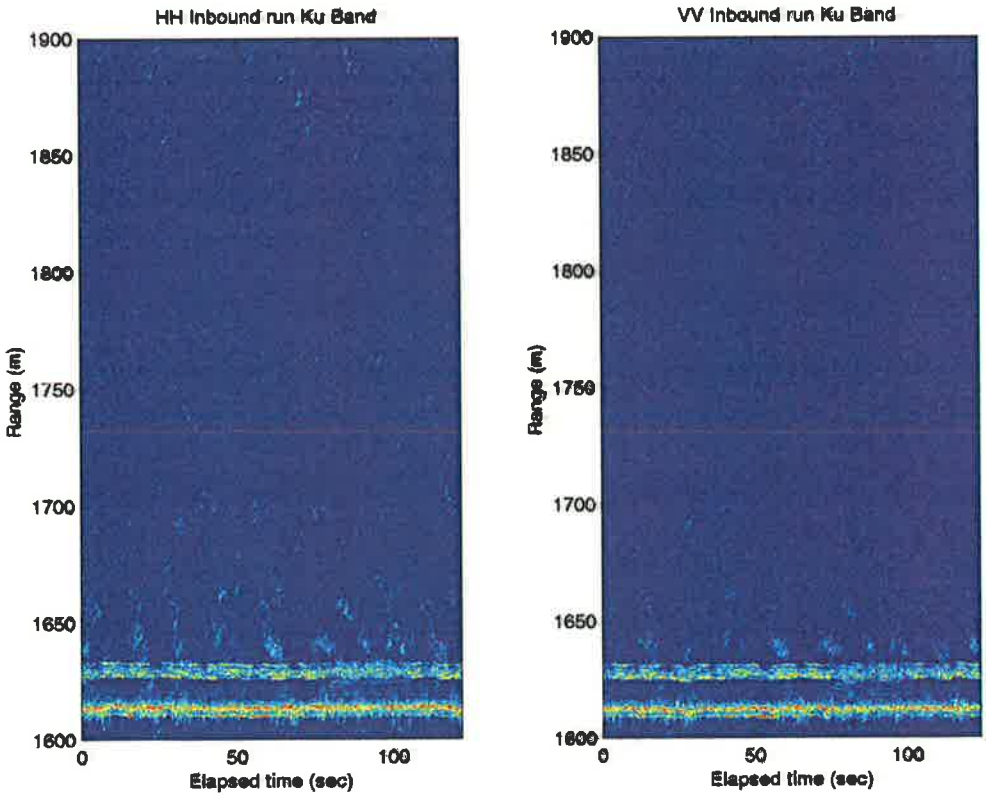

Figure 6-66 Aligned results from the in-bound run at Ku band

The results of the Ku band experiment clearly show the interaction between the dominant wake components and the swell crests. The return from these events is stronger than the results observed in the X band measurements. The higher frequency means that small scale scattering phenomenon are observable which accounts for the increased structure that can be seen in the range profile images.

Due to time restrictions, an out-bound Ku band measurement was not performed. This is unfortunate since there is evidence in the in-bound run to suggest that the interaction between the wave and incoming swell would be even more pronounced than in the X band case.

6.5.5 Wave breaking events

The wave breaking events observed in the in-bound and out-bound runs were studied in more detail. The ratio between the co-polar and cross-polar powers was calculated for one of the periods of enhancement observed during the in-bound and outbound runs. The raw results (green) and the results obtained using a moving average filter (blue) are shown in Figure 6-67 and Figure 6-68.

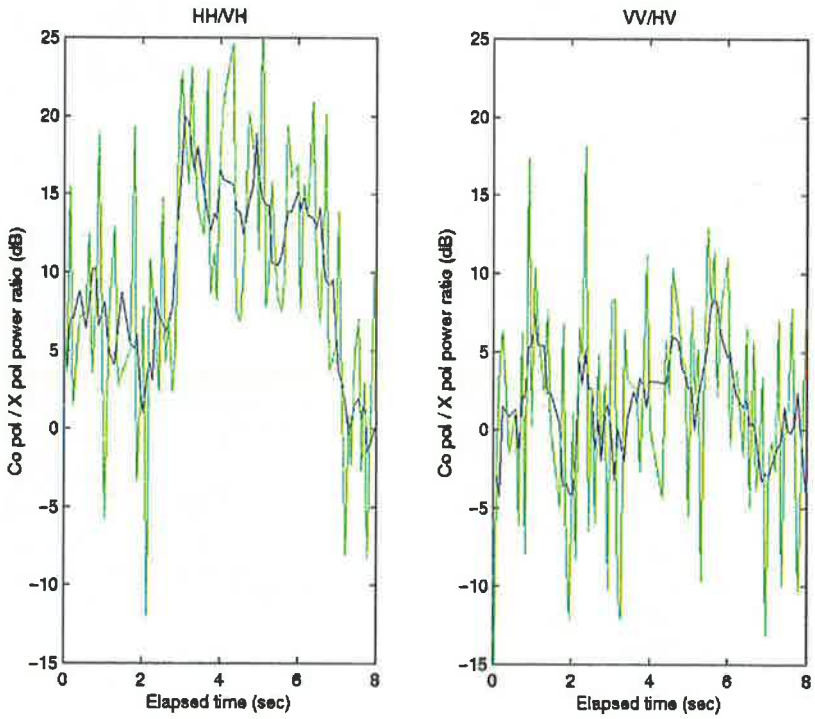

Figure 6-67 Ratio of the co- and cross-polar power rations during breaking (in-bound run)

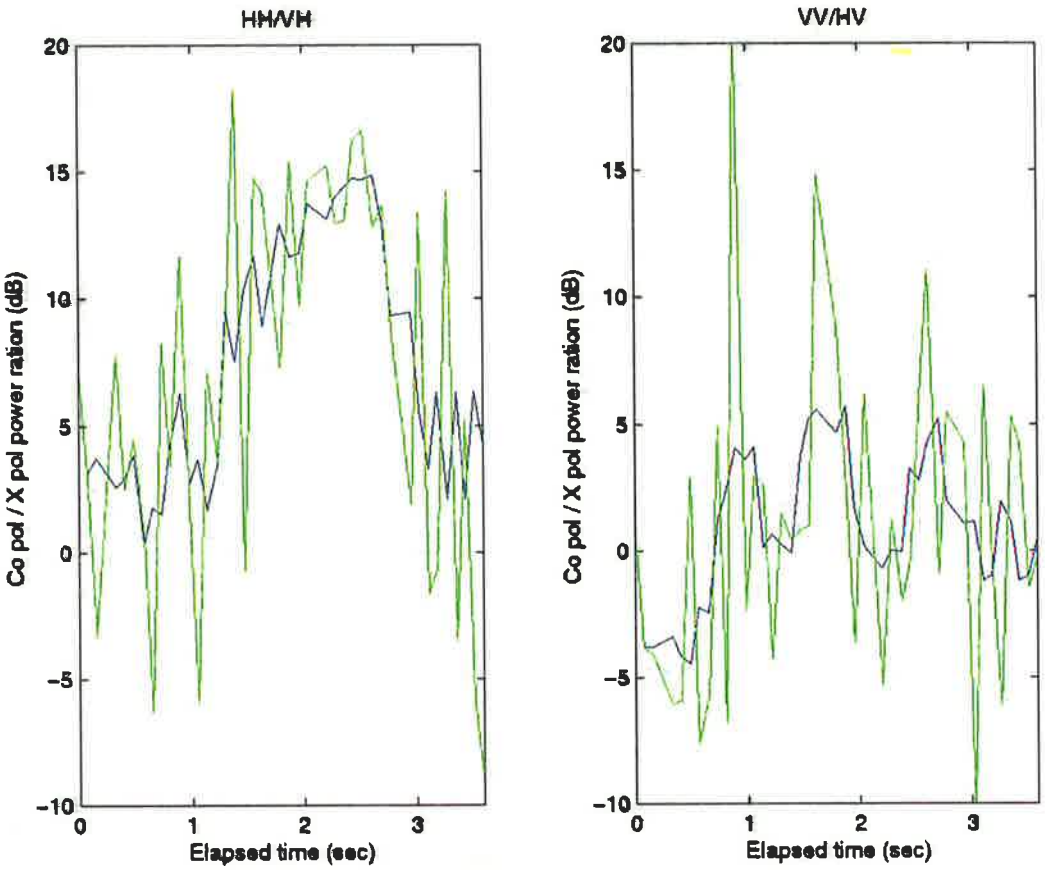

Figure 6-68 Ratio of the co- and cross-polar power rations during breaking (out-bound run)

The enhanced HH return is clearly evident in both cases. The results were compared with the experimental wavetank results obtained by Fuchs *et al.* [90] shown in Figure 6-69 which illustrates the variation in the HH, VV and the ratio of HH/VV during the four phases of the wave breaking process. This figure illustrates that during the *steepening-cresting phase* the HH/VV ratio rises quickly to about 0 dB. In the *plunging jet phase* the peak HH and HH/VV ratios are observed, while in the splashing-ploughing phase the HH returns drop and the HH and VV returns seem to decorrelate. In the final *decaying scar phase* the HH returns drop back to the background levels while the HH/VV ratio returns to values between 0 and –10 dB. Fuchs *et al.* [90] also discusses the variations in the Doppler spectra that occur during the stages of breaking. Once again due to the aliasing problems encountered in the Doppler processing with large frequency steps, a comparison of the observed changes in the Doppler speeds during the wave breaking events in the inbound and outbound runs could not be performed. Details of the variations observed in the wavetank measurements are described in [90]. Nevertheless the results in both the inbound and

outbound measures exhibit many of the characteristics observed in the wavetank measurements and give support for the hypothesis that the periodic returns observed in the inbound and outbound run are indeed a results of induced wave breaking events.

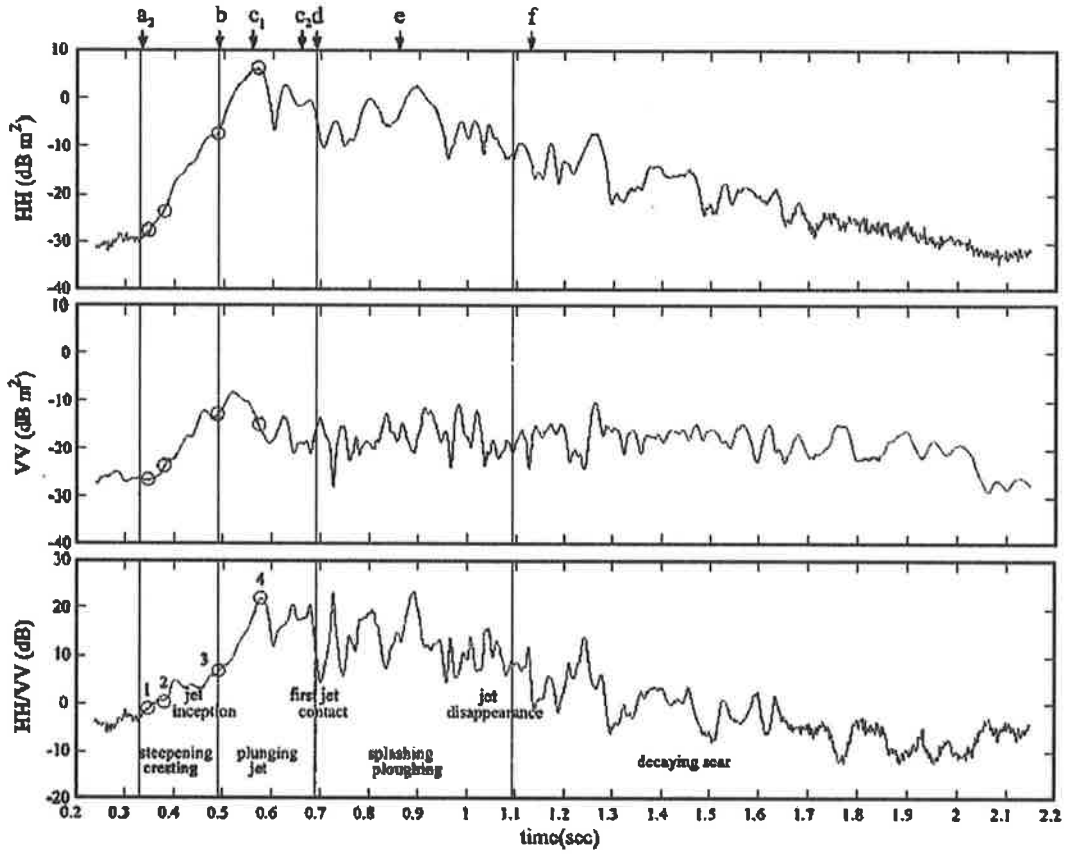

Figure 6-69 Wavetank results from Fuchs *et al.* [90] (Fig 9) showing the variations that occur during the four phases of wave breaking

6.6 Synopsis

This chapter has described the polarimetric analysis of the experimental data collected during this study with the DSTO high resolution radar system. It has shown the differences between polarimetric characteristics of the near shore wave field for an almost monochromatic scenario and the case where a broad spectrum of waves is present. The results illustrate that the distribution of points in the $H-A-\overline{\alpha}$ is influenced by the radar look direction and the degree of wave breaking present. There are indications to suggest that multiple scattering mechanisms are present during breaking and that the level of depolarisation increases as the wave forms and enters the breaking state. Characteristic decreases in the anisotropy and scattering alpha values were also observed for breaking waves while the entropy values appeared to

remain relatively constant. A comparison with the values predicted with the X-Bragg model showed that good agreement with the experimental findings and suggested that the drops in A and $\bar{\alpha}$ are a result of the increased tilting of the wave front combined with an increase in the surface roughness.

The potential for exploiting wakes as a tool for testing scattering theories and investigating nonlinear contributions has been demonstrated. Wake measurements performed in Darwin Harbour confirmed the ability to measure wake structures using the DSTO radar system at low grazing angles. A detailed investigation of the polarimetric properties of a pilot boat wake acquired at Queenscliff has been given using eigenvalue analysis of the coherency matrix and a scalar method derived from the location of the cross-polar null locations. The use of ship wakes as a laboratory for studying nonlinear scattering processes has been demonstrated using the interaction between the wake produced by a boat and incoming swell crests. Using the vessel to create the wave breaking events provides a means of achieving some control over where and when the wave breaking events are going to take place (with some acceptable limitations) while maintaining realistic boundary conditions.

Chapter 7 Conclusion and summary of contributions

This dissertation presents the findings from polarimetric investigations of radar echoes from features on the sea surface, including freely-propagating gravity and capillary waves, breaking waves and ship wakes, with special emphasis on using the Cloude-Pottier $H/A/\bar{\alpha}$ decomposition of the coherence/covariance matrix. While previous radar studies at low grazing angles have mainly been concerned with the RCS statistics, frequency responses, the dependence of clutter power on co- versus cross- polarisation and the form of the Doppler spectra, the work presented in this thesis focuses on the variations in the polarimetric parameters ($H/A/\bar{\alpha}$) while using the $H-\bar{\alpha}$, $H-A$ and $H-A-\bar{\alpha}$ spaces to examine and characterise the scattering mechanisms present.

A vital precursor issue addressed in this work is the polarimetric calibration of high resolution radar systems, focussing on the need to be able to calibrate in the field as opposed to the ideal laboratory environment. After reviewing existing techniques, constructing and testing several, a hybrid approach was devised, based on the use of a dual delay line calibrator together with a rotating dihedral reflector. The calibration trials have shown that the resultant distortion of the amplitude ratio r_1/r_2 in the DSTO radar system is less than 0.6 dB while the cross-talk was assessed to be around –27 dB using the dual delay line calibrator. This inherently good system performance simplifies the field calibration requirements and means that the only remaining parameters required for full polarimetric calibration are the transmit and receive phase imbalances δ_1 and δ_2. These values were obtained from measurements of a rotating dihedral and extensive field measurements demonstrated that the residual phase errors are less than 4° at X band. The outcome is a novel calibration technique that permits the adoption of average calibration and symmetrisation procedures for polarimetric single-look complex data sets. This result is significant since accurate calibration ensures that meaningful information about the scattering characteristics of targets can be obtained from the polarimetric decomposition of the coherency matrix and from the location of the optimal polarisation states on the Poincaré sphere. It also offers the

possibility of improved target classification and identification from polarimetric measurements.

A number of contributions have been made to the understanding of the polarimetric variations of progressive and breaking waves observed at low grazing angles. While numerous studies of radar scattering from waves have been performed at low grazing angles in the field, in wave tank measurements and using numerical simulations, the polarisation dependence of scattering in this regime is poorly understood. The measurements performed at Evans Head in New South Wales and Yallingup in Western Australia add to this area of knowledge by providing a comparison between the polarimetric characteristics of the near shore wave field for two instances: one when the wave field is almost monochromatic and the other when a broader spectrum of waves is present. The results illustrate that the distribution of points in the $H-A-\bar{\alpha}$ is influenced by the radar look direction and the degree of wave breaking present. Analysis of the image products formed between the entropy and anisotropy images and their complementary images indicates that multiple scattering mechanisms are present during breaking and that the depolarisation increases as the wave forms and enters the breaking state. These findings are consistent with observations from wave tank experiments. Characteristic decreases in the anisotropy and scattering alpha values have also been observed for the breaking waves while the entropy values appear to remain relatively constant. A comparison with the values predicted with the extended Bragg scattering model shows good agreement with the experimental findings and suggests that the decrease in A and $\bar{\alpha}$ are a result of the increased tilting of the wave front combined with an increase in the surface roughness.

Contributions have been made to the numerical modelling of the polarimetric properties of ship wakes. While previous studies have been carried out that demonstrated the advantages of polarimetric processing of simulated SAR data for the detection of ship wakes at low to medium angles of incidence, the benefits of polarimetry for wake detection closer to grazing has hitherto received far less attention. Efforts to gain a better understanding of the polarimetric variations that occur in wake returns were undertaken using computer models of wakes produced by a wave piercing catamaran and a pilot boat models. The computational model *SWPE*

has been used to generate predictions of the surface elevation, slope and velocity fields produced by steadily moving bodies either submerged or on the surface. The question of the importance of nonlinear hydrodynamic effects was addressed by comparing predictions from *SWPE* with those from a fully nonlinear code, *NFSFS*. This investigation concluded that the effects of nonlinearity were significant in the case of the deterministic wake pattern, from which the important conclusion can be drawn that they should be taken into account when interpreting the polarimetric signatures of random gravity waves. The surfaces elevations predicted by *SWPE* and *NFSFS* have been used as input to the electromagnetic scattering models based on the two-scale extended Bragg model, which enables a depolarising covariance matrix to be defined. This model was selected since it provides a physically meaningful description of the scattering process that can be evaluated efficiently while providing a direct basis for modelling the depolarisation processes that occur in sea surface scattering. Predictions of the polarimetric scattering from the predicted wake surfaces have been produced and exhibit many of the features observed in the experimental measurements establishing the validity of the scattering model in a qualitative terms and perhaps providing a basis for a quantitative assessment. These results are significant since they highlight the potential for exploiting wakes as a 'laboratory' for validating ocean surface polarimetric measurements. One of the problems encountered in these kinds of measurements is that there are generally two unknowns present: the scattering model being assessed and the stochastic surface geometry that provides the test environment. The solution proposed in this work, to remove this ambiguity, is to replace the stochastic surface with a quasi-deterministic surface in the form of a Kelvin wake produced by a moving ship, but this technique has not been fully exploited experimentally due to hardware limitations of the DSTO radar.

The results from the experimental measurements of ship wakes have also produced some notable contributions. The ability to measure the polarimetric properties of ship wakes at low grazing angles has been demonstrated and the comparison with the computational results shows good agreement. Polarimetric analysis of the results from the pilot boat measurements performed at Queenscliff using the Cloude-Pottier $H/A/\bar{\alpha}$ decomposition of the coherence/covariance matrix has been presented and has demonstrated that the entropy parameter provides a good means for distinguishing between the wake and clutter regions. An alternative approach using a novel

technique based on the location of the cross-polar null states has been presented. The equivalence of these approaches has been highlighted and the ability to generate polarimetric maps of the wake regions established. The application of wakes as a tool for studying highly nonlinear hydrodynamic processes has also been demonstrated using the interaction between the wake produced by a boat and ambient swell crests. This result is significant as a common complaint about laboratory wave tank measurements is that the generated waves and the tank boundary conditions are not representative of real ocean conditions. At-sea measurements, while realistic, lack the control over where and when the wave breaking events take place. Using a vessel to create the wave breaking events provides a means of achieving the best of both worlds, with some obvious but acceptable limitations.

Looking to the future there are a number of extensions to this work that could be considered. Proper exploitation of the Doppler domain is seen as one of the key areas for future work. Modification to the current radar hardware is required to achieve this goal as outlined in Chapter 6 which described the problems encountered while trying to perform Doppler processing with the waveforms needed for high range resolution. Eliminating this limitation would add an extra dimension to the processing by enabling analysis in the range-Doppler-polarisation domain. Doppler information would also enable comparisons with the velocity fields predicted by SWPE to be obtained and would enable information on the directional wave spectrum to be extracted.

Another extension to the current work would be to look at more general, bistatic scattering geometries. In recent years there has been significant interest in bistatic measurements, particularly with airborne and spaceborne polarimetric SAR. The bistatic case introduces a completely new set of problems with one of the major challenges being bistatic field calibration and finding a suitable set of calibration targets. Plans are currently in place to add a bistatic polarimetric capability to the DSTO radar system.

Chapter 8 Bibliography

[1] W.-M. Boerner, "Historical development of radar polarimetry, incentives for this workshop, and overview of contributions to these proceedings", in *Direct and Inverse Methods in Radar Polarimetry*, C-350 Part 1, *NATO-ASI Series C, Mathematical & Physical Sciences*, W.-M. Boerner, *et al.*, Eds, Kluwer Academic Publishers. Dordrecht, Netherlands: pp. 1-32, 1992.

[2] W. Swindell, *Polarized Light*, Stroudsburg, Pennsylvania, USA: Halsted Press, 1975.

[3] M. Born and E. Wolf, *Principles of Optics*, 7th ed., Cambridge, UK: Cambridge University Press, 1999.

[4] D. Pritchard, *The Radar War: Germany's Pioneering Achievement, 1904-1945*, Wellingborough, North Hampshire, England: Patrick Stephens, 1989.

[5] H. E. Guerlac, "Radar in World War II", Volume 8, *The History of Modern Physics 1800-1950*, Springer-Verlag. New York, 1987.

[6] R. W. Burns, *Radar Development to 1945 (IEE Radar, Sonar, Navigation and Avionics Series 2)*, London, UK: Institute of Electrical & Electronics Engineers, 1988.

[7] M. I. Skolnik, *Introduction to Radar Systems*, 2nd ed., New York: McGraw-Hill, 1980.

[8] G. Sinclair, "The transmission and reception of elliptically polarized radar waves", *Proceedings Institute of Radio Engineers*, vol. 38, no. 2, pp. 148-151, 1950.

[9] E. M. Kennaugh, "Polarization Properties of Radar Reflections", Master's Thesis, Ohio State University, Columbus, Ohio, USA, March 1952.

[10] G. A. Deschamps, "Part 2: Geometrical representation of the polarization state of a plane electromagnetic wave", *Proceedings of Institute of Radio Engineers*, vol. 39, no. 5, pp. 540-544, 1951.

[11] H. Gent, "Elliptically polarized waves and their reflections from radar targets: A theoretical analysis", TRE-MEMO 584, Telecommunications Research Establishment, Cheltenham, England, UK, March 1954.

[12] E. M. Kennaugh, "Effects of the Type of Polarisation on Echo Characteristics", Reports 381-1 to 394-24, Antenna Laboratory, The Ohio State University Research Foundation, Columbus, Ohio, 1949-1954.

[13] J. R. Huynen, "Phenomenological Theory of Radar Targets", Ph.D. Thesis, Technical University Delft, Bronder-Offset, Rotterdam, The Netherlands, December 1970.

[14] S. R. Cloude, "Uniqueness of target decomposition theorems in radar polarimetry", in *Direct and Inverse Methods in Radar Polarimetry*, Part 1, *NATO-ASI Series C, Mathematical & Physical Sciences*, W.-M. Boerner, *et al.*, Eds, Kluwer Academic Publishers. Dordrecht, The Netherlands: pp. 267-296, 1992.

[15] S. R. Cloude, "Polarimetry: The Characterisation of Polarimetric Effects in EM Scattering", Ph.D. Thesis, Faculty of Engineering, University of Birmingham, Birmingham, UK, October 1986.

[16] E. Krogager, "Decomposition of the Sinclair matrix into fundamental components with application to high resolution radar target imaging", in

Direct and Inverse Methods in Radar Polarimetry, Part 2, *NATO-ASI Series C, Mathematical & Physical Sciences*, W.-M. Boerner, *et al.*, Eds, Kluwer Academic Publishers. Dordrecht, The Netherlands: pp. 1459-1478, 1992.

[17] W.-M. Boerner and A.-Q. Xi, "The characteristic radar target polarization state theory for the coherent monostatic and reciprocal case using the generalized polarization transformation ratio formulation", *Archiv Der Elektrischen Ubertragung, AEU*, vol. 44, no. 4, pp. 273-281, 1990.

[18] J. D. Copeland, "Radar target classification by polarization properties", *Proceedings of Institute of Radio Engineers*, vol. 48, no. 7, pp. 1290-1296, 1960.

[19] J. L. Eaves and E. K. Reedy, *Principles of Modern Radar*, New York: Van Nostrand Reinhold, 1987.

[20] A. J. Poelman and J. R. F. Guy, "Polarization information utilization in primary radar: an introduction and up-date to activities at SHAPE Technical Centre", in *Inverse Methods in Electromagnetic Imaging*, W.-M. Boerner, *et al.*, Eds, Kluwer Academic Publishers. Dordrecht, Netherlands: pp. 521-572, 1985.

[21] A. I. Kozlov, A. I. Logvin, and L. A. Zhivotovsky, "Review of past and current research in the USSR on the fundamentals and basics of radar polarimetry and high resolution radar imaging", in *Direct and Inverse Methods in Radar Polarimetry*, C-350 Part 1, *NATO-ASI Series C, Mathematical & Physical Sciences*, W.-M. Boerner, *et al.*, Eds, Kluwer Academic Publishers. Dordrecht, The Netherlands: pp. 45-59, 1992.

[22] W.-M. Boerner, "Polarization utilization in microwave imaging, radar target mapping, and electromagnetic inverse scattering", Comm. Lab. Rept. No. 78-3, UIC-EECS/CSL, Chicago, October 1978.

[23] M. Davidovitz and W.-M. Boerner, "Extension of Kennaugh's optimal polarization concept to the asymmetric scattering matrix case", *IEEE Transactions on Antennas & Propagation*, vol. AP-34, no. 4, pp. 569-574, 1986.

[24] A. B. Kostinski and W.-M. Boerner, "On foundations of radar polarimetry", *IEEE Transactions on Antennas & Propagation*, vol. AP-34, no. 12, pp. 1395-1404, 1986.

[25] S. K. Chaudhuri and W.-M. Boerner, "A polarimetric model for the recovery of high frequency scattering centers from bistatic / monostatic scattering matrix data", *IEEE Transactions on Antennas & Propagation*, vol. AP-35, no. 1, pp. 87-93, 1987.

[26] Z. H. Czyz, "Bistatic radar target classification by polarisation properties", *Proceedings of Fifth International Conference on Antennas and Propagation (ICAP'87)*, York, U.K., 30 March - 2 April, 1987, pp. 545-548.

[27] Z. H. Czyz, "On theoretical foundations of coherent bistatic radar polarimetry", *Proceedings of SPIE'97, vol. 3120, Wideband Interferometric Sensing and Imaging Polarimetry*, San Diego, CA, USA, July 28-29, 1997, pp. 69-105.

[28] A. L. Germond, E. Pottier, and J. Saillard, "Nine polarimetric bistatic target equations", *Electronics Letters*, vol. 33, no. 17, pp. 1494-1495, 1997.

[29] A.-L. Germond, E. Pottier, and J. Saillard, "First approach on polarimetric bistatic radar target", *Proceedings of PIERS 1996*, Innsbruck, Austria, 8 July, 1996, pp. 630.

[30] A.-L. Germond, E. Pottier, and J. Saillard, "Foundations of bistatic radar polarimetry theory", *Proceedings of IEE International Radar Conference, Radar'97*, Edinburgh, U.K., October 14 -16, 1997, pp. 833-837.

[31] E. Lüneburg and S. R. Cloude, "Bistatic scattering", *Proceedings of SPIE'97, vol. 3120, Wideband Interferometric Sensing and Imaging Polarimetry*, San Diego, CA, USA, July 28-29, 1997, pp. 56-68.

[32] K. Tragl, "Polarimetric radar backscattering from reciprocal random targets", *IEEE Transactions on Geoscience & Remote Sensing*, vol. 28, no. 5, pp. 856-864, 1990.

[33] L. M. Novak, M. C. Burl, and W. W. Irving, "Optimal polarimetric processing for enhanced target detection", *IEEE Transactions on Aerospace & Electronic Systems*, vol. 29, no. 1, pp. 234-244, 1993.

[34] E. Lüneburg, "Radar polarimetry: A revision of basic concepts", in *Direct and Inverse Electromagnetic Scattering*, A. H. Serbest and S. R. Cloude, Eds, Addison Wesley Longman Ltd. Harlow, UK: pp. 257-275, 1996.

[35] S. R. Cloude and E. Pottier, "A review of target decomposition theorems in radar polarimetry", *IEEE Transactions on Geoscience & Remote Sensing*, vol. 34, no. 2, pp. 498-518, 1996.

[36] S. R. Cloude and E. Pottier, "An entropy-based classification scheme for land applications of polarimetric SAR", *IEEE Transactions on Geoscience & Remote Sensing*, vol. 35, no. 1, pp. 68-78, 1997.

[37] E. Krogager, S. R. Cloude, J.-S. Lee, T. L. Ainsworth, and W.-M. Boerner, "Interpretation of high resolution polarimetric SAR data", *Proceedings of 4th International Workshop on Radar Polarimetry (JIPR '98)*, IRESTE, University of Nantes, France, July 13-17, 1998, pp. 165-170.

[38] A. I. Kozlov, "Radar contrast between two objects", *Radioelectronika*, vol. 22, no. 7, pp. 63-67, 1979.

[39] E. Pottier and J.-S. Lee, "Application of the H/A/Alpha polarimetric decomposition theorem for unsupervised classification of fully polarimetric SAR data based on the Wishart distribution", *Proceedings of CEOS SAR workshop*, Toulouse, France, October 26-29, 1999, pp. 80/1-80/6.

[40] E. Pottier and S. R. Cloude, "Application of the H/A/alpha polarimetric decomposition theorem for land classification", *Proceedings of SPIE'97, vol. 3120, Wideband Interferometric Sensing and Imaging Polarimetry*, San Diego, CA, USA, July 28-29, 1997, pp. 132-143.

[41] E. Pottier, "The H/A/alpha polarimetric decomposition approach applied to POLSAR data processing", *Proceedings of the PIERS Workshop on Advances in Radar Methods*, Baveno, Italy, July 20-22, 1998, pp. 120-122.

[42] W.-M. Boerner, H. Mott, E. Lüneburg, B. Brisco, R. Brown, and J. S. Paterson, "Polarimetry in Remote Sensing: Basic and Applied Concepts", in *Chapter 5 in The Manual of Remote Sensing*, R. A. Reyerson, Ed., 3rd Edition ed, John Wiley & Sons. New York: pp. 271-357, 1998.

[43] J. J. van Zyl, "Unsupervised classification of scattering behaviour using radar polarimetry data", *IEEE Transactions on Geoscience & Remote Sensing*, vol. 27, no. 1, pp. 36-45, 1989.

[44] E. Pottier, "Unsupervised classification scheme of POLSAR images based on the complex Wishart distribution and the H/A/alpha polarimetric decomposition theorem", *Proceedings of 4th International Workshop on Radar Polarimetry (JIPR '98)*, IRESTE, University of Nantes, France, July 13-17, 1998, pp. 535-548.

[45] J.-S. Lee, M. R. Grunes, T. L. Ainsworth, L. Du, D. L. Schuler, and S. R. Cloude, "Unsupervised classification using polarimetric decomposition and complex Wishart classifier", *Proceedings of IGARSS 1998*, Seattle, Washington, USA, July 6-10, 1998, pp. 2178-2180.

[46] A. Freeman and S. Durden, "A three-component scattering model to describe polarimetric SAR data", *Proceedings of SPIE '92, vol. 1748, Radar Polarimetry*, San Diego, CA, USA, July 23-24, 1992, pp. 213-224.

[47] J.-S. Lee, M. R. Grunes, and S. A. Mango, "Speckle reduction in multipolarization, multifrequency SAR imagery", *IEEE Transactions on Geoscience & Remote Sensing*, vol. 29, no. 4, pp. 535-544, 1991.

[48] J.-S. Lee, I. Jurkevich, P. Dewale, P. Wambacq, and A. Oosterlinch, "Speckle filtering of synthetic aperture radar images : A review", *Remote Sensing Reviews*, vol. 8, pp. 313-340, 1994.

[49] J.-S. Lee, M. R. Grunes, and W.-M. Boerner, "Polarimetric property preservation in SAR speckle filtering", *Proceedings of SPIE'97, vol. 3120, Wideband Interferometric Sensing and Imaging Polarimetry*, San Diego, CA, USA, July 28-29, 1997, pp. 236-242.

[50] J.-S. Lee, M. R. Grunes, T. L. Ainsworth, L.-J. Du, D. L. Schuler, and S. R. Cloude, "Unsupervised classification using polarimetric decomposition and the complex Wishart classifier", *IEEE Transactions on Geoscience and Remote Sensing*, vol. 37, no. 5, pp. 2249-2258, 1999.

[51] S. J. Anderson, I. Abramovich Yu, and W. M. Boerner, "On the solvability of some inverse problems in radar polarimetry", *Proceedings of SPIE'97, vol. 3120, Wideband Interferometric Sensing and Imaging Polarimetry*, San Diego, CA, USA, July 28-29, 1997, pp. 28-36.

[52] S. J. Anderson, "S-matrix eigenvector dynamics on the Poincaré sphere", *Proceedings of the Workshop on Wideband Imaging and Sensing Polarimetry*, Adelaide, South Australia, August, 1992, pp. 5.

[53] S. J. Anderson, "Ionospheric Faraday rotation signatures in the space-time-frequency domain", *Proceedings of the 5th International Conference on HF Radio Systems and Techniques*, Edinburgh, Scotland, UK, 22-25 July, 1991, pp. 167-172.

[54] S. J. Anderson and Y. I. Abramovich, "Recent developments in HF skywave radar polarimetry", *Proceedings of IGARSS 2000*, Honolulu, HI, USA, 24-28 July, 2000, pp. 1319-1322.

[55] S. J. Anderson, Y. I. Abramovich, and W.-M. Boerner, "Measuring polarisation dynamics of the generalised HF skywave channel transfer function", *Proceedings of the International Symposium on Antennas and Propagation, ISAP 2000*, Fukuoka, Japan, 21-25 August, 2000, pp.

[56] S. R. Cloude and K. P. Papathanassiou, "Polarimetric optimisation in radar interferometry", *Electronics Letters*, vol. 33, no. 13, pp. 1176-1178, 1997.

[57] S. R. Cloude and K. P. Papathanassiou, "Polarimetric SAR interferometry", *IEEE Transactions on Geoscience & Remote Sensing*, vol. 36, no. 5, pp. 1551-1565, 1998.

[58] S. R. Cloude and K. P. Papathanassiou, "Coherence optimisation in polarimetric SAR interferometry", *Proceedings of IGARSS 1997*, Singapore, August 3-8, 1997, pp. 1932-1934.

[59] K. Papathanassiou, "Polarimetric SAR Interferometry", Ph.D. Thesis, Department of Physics, Technical University Graz, Graz, Austria, January 1999.

[60] A. Reigber, "Polarimetric SAR Tomography", Ph.D. Thesis, Faculty of Civil Engineering, University of Stuttgart, Stuttgart, Germany, 2001.
[61] A. Reigber and A. Moreira, "First demonstration of SAR tomography using polarimetric airborne SAR data", *IEEE Transactions Geoscience and Remote Sensing*, vol. 38, no. 5, pp. 2142-2152, 2000.
[62] W.-M. Boerner, "Recent advances in extra-wide-band polarimetry, interferometry and polarimetric interferometry in synthetic aperture remote sensing and its applications", *IEE Proceedings: Radar, Sonar & Navigation*, vol. 150, no. 3, pp. 113-124, 2003.
[63] D. L. Schuler, J.-S. Lee, and K. W. Hoppel, "Polarimetric SAR image signatures of the ocean and Gulf stream features", *IEEE Transactions Geoscience and Remote Sensing*, vol. 31, no. 6, pp. 1210-1221, 1993.
[64] G. R. Valenzuela, "Scattering of electromagnetic waves from a tilted, slightly rough surface", *Radio Science*, vol. 22, no. 4, pp. 1057-1066, 1968.
[65] D. L. Schuler and J.-S. Lee, "A microwave technique to improve the measurement of directional ocean wave spectra", *International Journal of Remote Sensing*, vol. 16, no. 2, pp. 199-215, 1995.
[66] D. L. Schuler, J.-S. Lee, and G. DeGrande, "Measurement of topography using polarimetric SAR images", *IEEE Transactions Geoscience and Remote Sensing*, vol. 34, no. 5, pp. 1266-1277, 1996.
[67] G. Valenzuela, "Theories for the interaction of electromagnetic and ocean waves - A review", *Boundary Layer Meteorology*, vol. 13, no. 1, pp. 61-85, 1978.
[68] A. I. Kalmykov and V. V. Pustovoytenko, "On polarization features of radio signals scattered from the sea surface at small grazing angles", *Journal of Geophysical Research*, vol. 81, no. 12, pp. 1960-1964, 1976.
[69] B. L. Lewis and I. D. Olin, "Experimental and theoretical model of high-resolution radar backscatter from the sea", *Radio Science*, vol. 15, no. 4, pp. 815-828, 1980.
[70] D. R. Lyzenga, A. L. Maffett, and R. A. Schuchman, "The contribution of wedge scattering to the radar cross section of the ocean surface", *IEEE Transactions on Geoscience & Remote Sensing*, vol. GE-21, no. 4, pp. 502-505, 1983.
[71] D. S. W. Kwoh and B. M. Lake, "A deterministic, coherent, and dual-polarized laboratory study of microwave backscattering from water waves. Short gravity waves without wind", *IEEE Journal of Oceanic Engineering*, vol. 5, no. OE-9, pp. 291-308, 1984.
[72] G. P. Kulemin, "Polarization and spectral features of spiky sea backscattering", *Proceedings of SPIE'98, vol. 3395, Radar Sensor Technology III*, Orlando, Florida, April 16, 1998, pp. 162-171.
[73] G. P. Kulemin, M. G. Balan, and J. A. Pedenko, "Polarization characteristics of microwave backscattering by sea wave nonstationarities", *Proceedings of IEE International Radar Conference Radar'97*, Edinburgh, U.K., October 14-16, 1997, pp. 90-94.
[74] D. J. McLaughlin, N. Allan, E. M. Twarog, and D. B. Trizna, "High resolution polarimetric radar scattering measurements of low grazing angle sea clutter", *IEEE Journal of Oceanic Engineering*, vol. 20, no. 3, pp. 166-178, 1995.
[75] I. D. Olin, "Amplitude and temporal statistics of sea spike clutter", *Proceedings of IEE International Radar Conference RADAR'82*, London, U.K., October 18-20, 1982, pp. 198-202.

[76] D. B. Trizna, J. P. Hansen, P. Hwang, and J. Wu, "Laboratory studies of radar sea spikes at low grazing angles", *Journal of Geophysical Research*, vol. 96, no. C7, pp. 12,529-12,537, 1991.

[77] J. P. Hansen and V. F. Cavaleri, "High Resolution Radar Sea Scatter, Experimental Observations and Discriminants", Report No. 8557, Naval Research Laboratory, Washington, D. C., 1982.

[78] E. G. Eckert, C. L. Rino, A. Siegel, and T. Webster, "Ocean microwave backscatter from the LOGAN experiment", *Proceedings of IGARSS 1994*, Pasadena, CA, USA, August 8 -12, 1994, pp. 815-817.

[79] P. H. Y. Lee, J. D. Barter, K. L. Beach, C. L. Hindman, B. M. Lake, H. Rungaldier, J. C. Shelton, A. B. Williams, R. Yee, and H. C. Yuen, "X band microwave backscattering from ocean waves", *Journal of Geophysical Research*, vol. 100, no. C2, pp. 2591-2611, 1995.

[80] M. W. Long, *Radar Reflectivity of Land and Sea*, 2nd ed., Dedham, Massachusetts, USA: Artech House, 1983.

[81] A. Khenchaf, "The Brewster angle effect on sea surface scattering for near-grazing incidence", *Proceedings of IGARSS'99*, Hamburg, Germany, 28 June-2 July, 1999, pp. 2622-2624.

[82] M. Sletten and D. B. Trizna, "An ultrawideband polarimetric radar for the study of sea scatter", *IEEE Transactions on Antennas & Propagation*, vol. AP-42, no. 11, pp. 1461-1466, 1994.

[83] M. A. Sletten, D. B. Trizna, and J. P. Hansen, "Ultrawide-band radar observations of multipath propagation over the sea surface", *IEEE Transactions on Antennas and Propagation*, vol. 44, no. 5, pp. 646-651, 1996.

[84] M. A. Sletten, "Multipath scattering in ultrawide-band radar sea spikes", *IEEE Transactions on Antennas & Propagation*, vol. 46, no. 1, pp. 45-56, 1998.

[85] M. A. Sletten and J. Wu, "Ultrawideband, polarimetric radar studies of breaking waves at low grazing angles", *Radio Science*, vol. 31, no. 1, pp. 181-192, 1996.

[86] J. C. West, "Ray analysis of low-grazing scattering from a breaking water wave", *IEEE Transactions on Geoscience and Remote Sensing*, vol. 37, no. 6, pp. 2725-2727, 1999.

[87] D. B. Trizna, "A model for Brewster angle damping and multipath effects on the microwave radar sea echo at low grazing angles", *IEEE Transactions on Geoscience and Remote Sensing*, vol. 35, no. 5, pp. 1232-1244, 1997.

[88] J. C. West, J. M. Sturm, and M. Sletten, "Small grazing angle radar scattering from a breaking water wave: Demonstration of Brewster angle damping", *Proceedings of IGARSS 1996*, Lincoln, NE, USA, May 27-31, 1996, pp. 2207-2209.

[89] J. Fuchs, T. Lamont-Smith, and M. P. Tulin, "Laboratory measurements of LGA Doppler spectral components and their physical sources unveiled", *Proceedings of IGARSS 1998*, Seattle, Washington, USA, July 6-10, 1998, pp. 2276-2278.

[90] J. Fuchs, D. Regas, T. Waseda, S. Welch, and M. P. Tulin, "Correlation of hydrodynamic features with LGA radar backscatter from breaking waves", *IEEE Transactions on Geoscience and Remote Sensing*, vol. 37, no. 5, pp. 2442-2460, 1999.

[91] J. Fuchs and M. P. Tulin, "Laboratory measurements of the joint dependence of radar frequency and water wavelength on sea-spike returns", *Proceedings of IGARSS'98*, Seattle, WA, USA, 6-10 July, 1998, pp. 2101-2103.

[92] J. Fuchs, S. Welch, T. Waseda, D. Regas, and M. P. Tulin, "Inside the sea-spike: low grazing angle radar imaging of laboratory waves repeatedly breaking in wave groups", *Proceedings of IGARSS'97*, Singapore, 3-8 August, 1997, pp. 714-18 vol.

[93] N. Ebuchi, H. Kawamura, and Y. Toba, "Physical processes of microwave backscattering from laboratory wind wave surfaces", *Journal of Geophysical Research*, vol. 98, no. C8, pp. 14669-14681, 1993.

[94] J. C. West and M. A. Sletten, "Multipath EM scattering from breaking ocean waves at grazing incidence", *Radio Science*, vol. 32, no. 4, pp. 1455-1467, 1997.

[95] P. Wang, Y. Yao, and M. P. Tulin, "An efficient numerical tank for non-linear water waves, based on the multi-subdomain approach with BEM", *International Journal for Numerical Methods in Fluids*, vol. 20, no. 12, pp. 1315-1336, 1995.

[96] W. J. Plant, "Microwave sea return at moderate to high incidence angles", *Waves in Random Media*, vol. 13, no. 4, pp. 339-354, 2003.

[97] A. D. Rozenberg, I. E. Ostrovskii, and A. I. Kalmykov, "Frequency shift of radiation scattered from a rough sea surface", *Izv. Vyssh. Uchebn. Zaved Radiofiz*, vol. 8, pp. 234-240, 1966.

[98] V. W. Pidgeon, "Doppler dependence of radar sea return", *Journal of Geophysical Research*, vol. 73, no. 4, pp. 1333-1341, 1968.

[99] G. R. Valenzuela and M. B. Laing, "Study of Doppler spectra of radar sea echo", *Journal of Geophysical Research*, vol. 75, pp. 551-563, 1970.

[100] E. M. Poulter, M. J. Smith, and J. A. McGregor, "Microwave backscatter from the sea surface: Bragg scattering by short gravity waves", *Journal of Geophysical Research*, vol. 99, no. C4, pp. 7929-7943, 1994.

[101] D. B. Trizna, "A model for Doppler peak spectral shift for low grazing angle sea scatter", *IEEE Journal of Oceanic Engineering*, vol. 10, no. 4, pp. 368-375, 1985.

[102] M. J. Smith, E. M. Poulter, and J. A. McGregor, "Doppler radar measurements of wave groups and breaking waves", *Journal of Geophysical Research*, vol. 101, no. C6, pp. 14269-14282, 1996.

[103] N. Allan, "Remote Sensing the Ocean Surface at Low Grazing Angles Using an X-band Polarimetric Radar", Ph.D. Thesis, The Department of Electrical and Computer Engineering, Northeastern University, Boston, Massachusetts, November 1994.

[104] N. Allan, C. L. Trump, D. B. Trizna, and D. J. McLaughlin, "Dual-polarised Doppler radar measurements of ocean fronts", *IEEE Transactions Geoscience and Remote Sensing*, vol. 37, no. 1, pp. 395-417, 1999.

[105] D. E. Hasselmann and M. Schieler, "Radar backscatter from the sea surface", *Proceedings of the 8th symposium on Naval Hydrodynamics*, Arlington,VA,1970, pp. 361-388.

[106] A. D. Rozenberg, D. C. Quigley, and W. K. Melville, "Laboratory study of polarized scattering by surface waves at grazing incidence. I. Wind waves", *IEEE Transactions on Geoscience and Remote Sensing*, vol. 33, no. 4, pp. 1037-1046, 1995.

[107] A. D. Rozenberg, D. C. Quigley, and W. Kendall Melville, "Laboratory study of polarized microwave scattering by surface waves at grazing incidence: the influence of long waves", *IEEE Transactions on Geoscience and Remote Sensing*, vol. 34, no. 6, pp. 1331-1342, 1996.

[108] J. C. West, J. Shiouj-Jhy, J. H. Duncan, and Q. Haibing, "LGA scattering from breaking water waves-further results", *Proceedings of IGARSS 1999*, Hamburg, Germany, 28 June-2 July, 1999, pp. 2625-2627.
[109] P. H. Y. Lee, J. D. Barter, K. L. Beach, B. M. Lake, H. Rungaldier, H. R. Thompson, Jr., L. Wang, and R. Yee, "What are the mechanisms for non-Bragg scattering from water wave surfaces?" *Radio Science*, vol. 34, no. 1, pp. 123-138, 1999.
[110] H. H. Helmken and M. J. Vanderhill, "Very low grazing angle radar backscatter from the ocean surface", *Proceedings of IEEE International Radar Conference*, Arlington, VA , USA, 7-10 May, 1990, pp. 181-188.
[111] H. F. Helmken, "Low-grazing-angle radar backscatter from the ocean surface", *IEE Proceedings Radar and Signal Processing*, vol. 137, no. 2, pp. 113, 1990.
[112] W. J. Plant, "A model for microwave Doppler sea return at high incidence angles: Bragg scattering from bound, tilted waves", *Journal of Geophysical Research*, vol. 102, no. C9, pp. 21131-21146, 1997.
[113] E. Pottier, W.-M. Boerner, and D. L. Schuler, "Polarimetric detection and estimation of ship wakes", *Proceedings of IGARSS 1999*, Hamburg, Germany, 28 June - 2 July, 1999, pp. 2458-2460.
[114] P. Imbo, J.-C. Souyris, and M. Yeremy, "Wake detection in polarimetric SAR images", *Proceedings of IGARSS 2001*, Sydney, NSW, Australia, July 9-13, 2001, pp. 2819-2821.
[115] J. A. Stratton, *Electromagnetic Theory*, New York: McGraw-Hill Book Company, 1941.
[116] IEEE Standard 145-1983, *IEEE Standard Definitions of Terms for Antennas*: IEEE Publications, 1983.
[117] H. Mott, *Antennas for Radar and Communications: A Polarimetric Approach*, New York: John Wiley & Sons, 1992.
[118] J. D. Kraus, *Electromagnetics*, 5th ed., New York: McGraw-Hill Education, 1999.
[119] R. Schmeider, "Stokes algebra formalism", *Journal of the Optical Society of America*, vol. 59, no. 3, pp. 297-302, 1969.
[120] D. H. O. Bebbington, "Geometrical concepts in optimal polarimetry: Stokes formalism in a Minkowski space", *Proceedings of SPIE '92, vol. 1748, Radar Polarimetry*, San Diego, CA, USA, July 23-24, 1992, pp. 132-143.
[121] W.-L. Yan and W.-M. Boerner, "Optimal polarization states determination of the Stokes reflection matrices (M_p) for the coherent case, and of the Mueller matrix (M) for the partially polarized case", *Journal of Electromagnetic Waves & Applications*, vol. 5, no. 10, pp. 1123-1149, 1991.
[122] E. Lüneburg and S. R. Cloude, "Radar versus optical polarimetry", *Proceedings of SPIE'97, vol. 3120, Wideband Interferometric Sensing and Imaging Polarimetry*, San Diego, CA, USA, July 28-29, 1997, pp. 361-372.
[123] G. A. Deschamps and P. E. Mast, "Poincaré sphere representation of partially polarized fields", *IEEE Transactions on Antennas & Propagation*, vol. AP-21, no. 4, pp. 474-478, 1973.
[124] C. D. Graves, "Radar polarization power scattering matrix", *Proceedings of Institute of Radio Engineers*, vol. 44, no. 2, pp. 248-252, 1956.
[125] R. C. Jones, "A new calculus for the treatment of optical systems II: Proof of the three general eqivalence theorems", *Journal of the Optical Society of America*, vol. 31, no. 7, pp. 493-499, 1941.

[126] R. C. Jones, "A new calculus for the treatment of optical systems III: The Stokes theory of optical activity", *Journal of the Optical Society of America*, vol. 31, no. 7, pp. 500-503, 1941.
[127] P. Beckmann and A. Spizzichino, *The Scattering of Electromagnetic Waves From Rough Surfaces*, Norwood, Massachusetts, USA: Artech House, 1987.
[128] E. Lüneburg, "Principles in radar polarimetry : The consimilarity transformation of radar polarimetry versus the similarity transformation in optical polarimetry", *IEICE Transactions on Electronics, Special Issue on Electromagnetic Theory*, vol. E-78C, no. 10, pp. 1339-1345, 1995.
[129] E. Lüneburg and W.-M. Boerner, "Optimal procedures in radar polarimetry", *Proceedings of Progress in Electromagnetic Research Symposium (PIERS'94)*, Noordwijk, Netherlands, July 11-15, 1994, pp. 1813-1816.
[130] F. T. Ulaby and C. Elachi, *Radar Polarimetry For Geoscience Applications*, Norwood, Massachussetts, USA: Artech House, 1990.
[131] K. Gottfried, *Quantum Mechanics, Volume I: Fundamentals*, Reading, Massachusetts, USA: Addison-Wesley, 1966.
[132] D. H. Bebbington, "Target vectors - spinorial concepts", *Proceedings of 2nd International Workshop on Radar Polarimetry*, University of Nantes, France, September 9 - 10, 1992, pp. 26-36.
[133] R. M. Azzam and N. M. Bashara, *Ellipsometry and Polarized Light*, Third Edition ed., Amsterdam, The Netherlands: North Holland Press, 1989.
[134] J. J. van Zyl, "On the Importance of Polarization in Radar Scattering Problems", Ph.D. Thesis, California Institute of Technology, Pasadena, California, USA, December 1985.
[135] H. A. Zebker, J. J. van Zyl, and D. N. Held, "Imaging radar polarimetry from wave synthesis", *Journal of Geophysical Research*, vol. 92, no. B1, pp. 683-701, 1987.
[136] J. J. van Zyl, H. A. Zebker, and C. Elachi, "Imaging radar polarization signatures: Theory and observation", *Radio Science*, vol. 22, no. 4, pp. 529-543, 1987.
[137] A. P. Agrawal and W.-M. Boerner, "Redevelopment of Kennaugh's target characteristic polarization state theory using the polarization transformation ratio formalism for the coherent case", *IEEE Transactions on Geoscience & Remote Sensing*, vol. 27, no. 1, pp. 2-14, 1989.
[138] L. Ferro-Famil, "Multi-Temporal and Multi-Frequency Remote Sensing of Natural Media Using Polarimetric SAR Data", Ph.D. Thesis, University of Nantes, France, December 2000.
[139] E. Lüneburg and W.-M. Boerner, "Homogeneous and inhomogeneous Sinclair and Jones matrices", *Proceedings of SPIE'97, vol. 3120, Wideband Interferometric Sensing and Imaging Polarimetry*, San Diego, CA, USA, July 28-29, 1997, pp. 45-54.
[140] H. A. Zebker and J. J. Van Zyl, "Imaging radar polarimetry: A review", *Proceedings of the IEEE*, vol. 79, no. 11, pp. 1583-1606, 1991.
[141] J. J. van Zyl, H. A. Zebker, and C. Elachi, "Polarimetric SAR Applications", in *Radar Polarimetric For Geoscience Applications*, F. Ulaby and C. Elachi, Eds, Artech House. Norwood, Massachussetts, USA: pp. 315-360, 1990.
[142] I. Hajnsek, "Inversion of Surface Parameters Using Polarimetric SAR", Ph.D. Thesis, University Jena, Institute of Geography, Department of Geoinformatik, Jena,Germany, September 2001.

[143] W.-M. Boerner, W.-L. Yan, A.-Q. Xi, and Y. Yamaguchi, "On the basic principles of radar polarimetry: The target characteristic polarization state theory of Kennaugh, Huynen's polarization fork concept, and its extension to the partially polarized case", *Proceedings of the IEEE*, vol. 79, no. 10, pp. 1538-1550, 1991.

[144] J. J. van Zyl, "Application of Cloude's target decomposition theorem to polarimetric imaging radar data", *Proceedings of SPIE '92, vol. 1748, Radar Polarimetry*, San Diego, CA, USA, July 23-24, 1992, pp. 184-191.

[145] S. R. Cloude, "Group theory and polarisation algebra", *Optik*, vol. 75, no. 1, pp. 26-36, 1986.

[146] M. Borgeaud, R. T. Shin, and J. A. Kong, "Theoretical models for polarimetric radar clutter", *Journal of Electromagnetic Waves & Applications*, vol. 1, no. 1, pp. 73-91, 1987.

[147] W.-M. Boerner, W. L. Yan, A.-Q. Xi, and Y. Yamaguchi, "Comparison of optimization procedures for the 2*2 Sinclair and the 4*4 radar polarimetry and its application to radar target versus background", *Proceedings of the International Conference on Electromagnetics in Aerospace Applications (ICEAA'91)*, Torino, Italy, September 17-20, 1991, pp. 299-307.

[148] J. J. van Zyl, C. H. Papas, and C. Elachi, "On the optimum polarization of incoherently reflected waves", *IEEE Transactions on Antennas & Propagation*, vol. AP-35, no. 7, pp. 818-825, 1987.

[149] Y. Yamaguchi, W.-M. Boerner, H.-J. Eom, M. Sengoku, S. Motooka, and T. Abe, "On characteristic polarization states in the cross-polarized radar channel", *IEEE Transactions on Geoscience & Remote Sensing*, vol. 30, no. 5, pp. 1078-1080, 1992.

[150] A.-Q. Xi and W.-M. Boerner, "Determination of the characteristic polarization states of the radar target scattering matrix (S(AB)) for the coherent, monostatic and reciprocal propagation space using the polarization ratio rho transformation formulation", in *Direct and Inverse Methods in Radar Polarimetry*, C-350 Part 1, *NATO-ASI Series C, Mathematical & Physical Sciences*, W.-M. Boerner, *et al.*, Eds, Kluwer Academic Publishers. Dordrecht, The Netherlands: pp. 297-348, 1992.

[151] R. A. Horn and C. R. Johnson, *Matrix Analysis*, Cambridge, England: Cambridge University Press, 1985.

[152] J. C. Hubbert, "A comparison of radar, optic, and specular null polarization theories", *IEEE Transactions on Geoscience & Remote Sensing*, vol. 32, no. 3, pp. 658-671, 1994.

[153] T. Takagi, "On an algebraic problem related to an analytical theorem of Caratheodory and Fejer and on allied theorem of Landau", *Japanese J. Math*, vol. 1, pp. 83-93, 1927.

[154] C.-L. Liu, X. Zhang, Y. Yamaguchi, H.-J. Eom, and W.-M. Boerner, "Comparison of optimization procedures for 2x2 Sinclair, 2x2 Graves, 3x3 covariance, and 4x4 Mueller (symmetric) matrices in coherent radar polarimetry and its application to target versus background discrimination in microwave remote sensing and imaging", *Proceedings of SPIE '92, vol. 1748, Radar Polarimetry*, San Diego, CA, USA, July 23-24, 1992, pp. 144-173.

[155] J. Yang, Y. Yamaguchi, H. Yamada, Z. H. Czyz, W.-M. Boerner, H. Mott, E. Lüneburg, and Y. Peng, "The characteristic polarization states and the equi-power curves", *IEEE Transactions on Geoscience & Remote Sensing*, vol. 40, no. 2, pp. 305-313, 2002.

[156] S. R. Cloude, "Polarimetric optimisation based on the target covariance matrix", *Electronics Letters*, vol. 26, no. 20, pp. 1670-1671, 1990.
[157] E. Lüneburg, V. Ziegler, A. Schroth, and K. Tragl, "Polarimetric covariance matrix analysis of random radar targets", *Proceedings of AGARD Symposium on Target and Clutter Scattering and their Effects on Military Radar Performance (AGARD-CP-501)*, Ottowa, Canada, May 6-9, 1991, pp. 27.1-27.12.
[158] A. B. Kostinski, B. D. James, and W.-M. Boerner, "Optimal reception of partially polarized waves", *Journal of the Optical Society of America A Optics & Image Science*, vol. 5, no. 1, pp. 58-64, 1988.
[159] W.-M. Boerner and W.-L. Yan, "Basic principles of radar polarimetry and its applications to target recognition problems with assessments of the historical development and of the current state-of-the art", *Proceedings of Electromagnetic Modelling and Measurements for Analysis and Synthesis Problems*, Lucca, Italy, August 10-21, 1991, pp. 311-363.
[160] J. Yang, Y. Yamaguchi, H. Yamada, and S. Lin, "The formulae of the characteristic polarization states in the CO-POL channel and the optimal polarization state for contrast enhancement", *IEICE Transactions on Communications*, vol. E80-B, no. 10, pp. 1570-1575, 1997.
[161] K. Tragl, E. Lueneburg, A. Schroth, and V. Ziegler, "A polarimetric covariance matrix concept for random radar targets", *Proceedings of Seventh International Conference on Antennas and Propagation ICAP '91*, York, UK, April 15-18, 1991, pp. 396-399.
[162] W.-M. Boerner, M. B. El-Arini, C. Y. Chan, and P. M. Mastoris, "Polarization dependence in electromagnetic inverse problems", *IEEE Transactions on Antennas & Propagation*, vol. 29, no. 2, pp. 262-271, 1981.
[163] H. Mueller, "The foundations of optics", *Journal Optical Society of America*, vol. 38, pp. 661, 1948.
[164] A. Graham, *Kronecker Products and Matrix Calculus With Applications*, New York: Halsted Press, John Wiley & Sons, 1981.
[165] H. C. Van de Hulst, *Light Scattering By Small Particles*, 2nd ed., New York: Dover Publications, 1982.
[166] D. Deirmendjian, *Electromagnetic Scattering on Spherical Polydispersions*, New York: American Elsevier Publishing Company, 1969.
[167] S. Chandrasekhar, *Radiation Transfer*, New York: Dover Publications, 1960.
[168] E. Pottier, "On Dr J.R. Huynen's main contributions in the development of polarimetric radar techniques and how the 'radar targets phenomenological concept' becomes a theory", *Proceedings of SPIE '92, vol. 1748, Radar Polarimetry*, San Diego, CA, USA, July 23-24, 1992, pp. 72-85.
[169] G. A. Ioannidis and D. E. Hammers, "Optimum antenna polarizations for target discrimination in clutter", *IEEE Transactions on Antennas & Propagation*, vol. AP-27, no. 3, pp. 357-363, 1979.
[170] E. Pottier and J. Saillard, "Fondement mathématiques de la polarimétrie et son application au domaine du radar", *Annales des Télécommunications*, vol. 47, no. 7, pp. 314-336, 1992.
[171] A. Guissard, "The Mueller matrix in radar polarimetric measurements", *Proceedings of IGARSS 1993*, Tokyo, Japan, August 18-21, 1993, pp. 371-373.

[172] A. Guissard, "Mueller and Kennaugh matrices in radar polarimetry", *IEEE Transactions on Geoscience & Remote Sensing*, vol. 32, no. 3, pp. 590-597, 1994.

[173] F. Le Roy-Brehonnet, B. Le Jeune, P. Y. Gerligand, J. Cariou, and J. Lotrian, "Analysis of depolarizing optical targets by Mueller matrix formalism", *Pure & Applied Optics*, vol. 6, no. 3, pp. 385-404, 1997.

[174] D. L. Schuler, J.-S. Lee, and T. L. Ainsworth, "Compensation of terrain azimuthal slope effects in geophysical parameter studies using polarimetric SAR data", *Remote Sensing of Environment*, vol. 69, no. 2, pp. 139-155, 1999.

[175] J.-S. Lee, D. L. Schuler, and T. L. Ainsworth, "Polarimetric SAR data compensation for terrain azimuth slope variation", *IEEE Transactions on Geoscience & Remote Sensing*, vol. 38, no. 5, pp. 2153-2163, 2000.

[176] S. R. Cloude, "Target decomposition theorems in radar scattering", *Electronics Letters*, vol. 21, no. 1, pp. 22-24, 1985.

[177] J. R. Huynen, "Comment on target decomposition theorem", in *Direct and Inverse Methods in Radar Polarimetry*, C-350 Part 1, *NATO-ASI Series C, Mathematical & Physical Sciences*, W.-M. Boerner, *et al.*, Eds, Kluwer Academic Publishers. Dordrecht, The Netherlands: pp. 387-399, 1992.

[178] J. R. Huynen, "Measurement of the target scattering matrix", *Proceedings of the Institute of Electrical Engineers*, vol. 53, pp. 936-946, 1965.

[179] E. Krogager, "New decomposition of the radar target scattering matrix", *Electronics Letters*, vol. 26, no. 18, pp. 1525-1527, 1990.

[180] W. L. Cameron, N. N. Youssef, and L. K. Leung, "Simulated polarimetric signatures of primitive geometric shapes", *IEEE Transactions on Geoscience & Remote Sensing*, vol. 34, no. 3, pp. 793-803, 1996.

[181] W. L. Cameron and L. K. Leung, "Feature motivated polarization scattering matrix decomposition", *Proceedings of the International Radar Conference, RADAR'90*, Arlington,VA, USA, May 7-10, 1990, pp. 549-557.

[182] M. Yeremy, J. W. M. Campbell, K. Mattar, and T. Potter, "Ocean surveilllance with polarimetric SAR", *Canadian Journal of Remote Sensing*, vol. 27, no. 4, pp. 328-344, 2001.

[183] H. Rais and A. W. Mansfield, "L-Band/P-Band SAR comparison for search and rescue : Recent results", *Proceedings of SPIE'99, vol. 3371, Automatic Target Recognition VIII*, Orlando, FL, USA, April 5 - 9,1999, 1999, pp. 194-201.

[184] R. Touzi and F. Charbonneau, "Characterization of target symmetric scattering using polarimetric SARs", *IEEE Transactions on Geoscience & Remote Sensing*, vol. 40, no. 11, pp. 2507-2516, 2002.

[185] E. Krogager and Z. H. Czyz, "Properties of the sphere, diplane, helix decomposition", *Proceedings of 3rd International Workshop on Radar Polarimetry (JIPR '95)*, IRESTE, University of Nantes, France, March 23-25, 1995, pp. 106-114.

[186] J. R. Huynen, "Theory and measurement of surface torsion (polarimetric phyllotaxis)", in *Direct and Inverse Methods in Radar Polarimetry*, C-350 Part 1, *NATO-ASI Series C, Mathematical & Physical Sciences*, W.-M. Boerner, *et al.*, Eds, Kluwer Academic Publishers. Dordrecht, The Netherlands: pp. 581-623, 1992.

[187] S. R. Cloude and E. Pottier, "Concept of Polarisation Entropy in Optical Scattering", *Optical Engineering*, vol. 34, no. 6, pp. 1599-1610, 1995.

[188] S. R. Cloude, "An entropy based classification scheme for polarimetric SAR data", *Proceedings of IGARSS 1995*, Florence, Italy, July 10 - 14, 1995, pp. 2000-2002.
[189] W.-M. Boerner, W.-L. Yan, A.-Q. Xi, and Y. Yamaguchi, "Basic concepts of radar polarimetry", in *Direct and Inverse Methods in Radar Polarimetry*, C-350 Part 1, *NATO-ASI Series C, Mathematical & Physical Sciences*, W.-M. Boerner, *et al.*, Eds, Kluwer Academic Publishers. Dordrecht, Netherlands: pp. 155-245, 1992.
[190] E. Pottier, "Contribution of Polarimetry in the Discrimination of Radar Targets. Application to High Resolution ISAR Imaging", Ph.D. Thesis, IRESTE, Nantes, France, December 1990.
[191] E. Krogager, "Aspects of Polarimetric Radar Imaging", Ph.D. Thesis, Technical University of Denmark, Lyngby, Denmark, March 1993.
[192] J. Yang, "On Theoretical Problems in Radar Polarimetry", Ph.D. Thesis, Niigata University, Japan, September 1999.
[193] G. T. Ruck, D. E. Barrick, W. D. Stuart, and C. K. Krichbaum, *Radar Cross Section Handbook*, London, UK: Plenum Press, 1970.
[194] T. B. A. Senior, "Scattering by a sphere", *Proceedings of the Institute of Electrical Engineers*, vol. 111, no. 5, pp. 907-916, 1964.
[195] W. Wiesbeck and D. Kahny, "Single reference, three target calibration and error correction for monostatic, polarimetric free space measurements", *Proceedings of the IEEE*, vol. 79, no. 10, pp. 1551-1558, 1991.
[196] D. G. Michelson and E. V. Jull, "Depolarizing trihedral corner reflectors for radar navigation and remote sensing", *IEEE Transactions on Antennas & Propagation*, vol. 43, no. 5, pp. 513-518, 1995.
[197] G. Nesti and M. Hohmann, "An efficient calibration procedure for polarimetric radar system", *Proceedings of IGARSS 1990*, Washington, D.C, May 20-24, 1990, pp. 1099-1103.
[198] J. C. Souyris, P. Borderies, P. F. Combes, and H. J. Mametsa, "Evaluation of several shaped dihedrals useful for polarimetric calibration", *IEEE Transactions on Geoscience & Remote Sensing*, vol. 33, no. 4, pp. 1026-1036, 1995.
[199] "Bruderhedral data sheet", Trimillenium Corporation, Grand Junction, Colorado, http://www.gosti.com/FTP/bh.pdf, 2001.
[200] D. R. Sheen, E. L. Johansen, L. P. Elenbogen, and E. S. Kasischke, "The gridded trihedral : A new polarimetric SAR calibration reflector", *IEEE Transactions on Geoscience and Remote Sensing*, vol. 30, no. 6, pp. 1149-1153, 1992.
[201] J. J. van Zyl, "Calibration of polarimetric radar images using only image parameters and trihedral corner reflector responses", *IEEE Transactions on Geoscience & Remote Sensing*, vol. 28, no. 3, pp. 337-348, 1990.
[202] J. D. Klein and A. Freeman, "Quadpolarization SAR calibration using target reciprocity", *Journal of Electromagnetic Waves & Applications*, vol. 5, no. 7, pp. 735-751, 1991.
[203] T.-S. Cecile, "The polarimetric calibration best trade-offs", *Proceedings of RTO SCI Symposium on Non-Cooperative Air Target Identification Using Radar*, Mannheim, Germany, April 22-24, 1998, pp. 11.1-11.7.
[204] R. M. Barnes, "Polarimetric Calibration Using In-scene Reflectors", Lincoln Lab Techical Report TT-65, MIT Lincoln Laboratory, Lexington, Massachusetts, USA, September 1986.

[205] A. J. Blanchard and B. R. Jean, "Antenna effects in depolarisation measurements", *IEEE Transactions on Geoscience & Remote Sensing*, vol. 21, no. 1, pp. 113-117, 1983.
[206] M. A. Woods, "A Calibration Procedure for a Coherent Scattering Matrix Radar", RSRE memo 3889, Royal Signals and Radar Establishment, Great Malvern, Worcestershire, UK, 1986.
[207] R. Touzi, C. E. Livingstone, J. R. C. Lafontaine, and T. I. Lukowski, "Consideration of antenna gain and phase patterns for calibration of polarimetric SAR data", *IEEE Transactions on Geoscience & Remote Sensing*, vol. 31, no. 6, pp. 1132-1145, 1993.
[208] M. W. Whitt, F. T. Ulaby, P. Polatin, and V. V. Liepa, "A general polarimetric radar calibration technique", *IEEE Transactions on Antennas & Propagation*, vol. 39, no. 1, pp. 62-67, 1991.
[209] K. Sarabandi and F. T. Ulaby, "A convenient technique for polarimetric calibration of single-antenna radar systems", *IEEE Transactions on Geoscience & Remote Sensing*, vol. 28, no. 6, pp. 1022-1033, 1990.
[210] A. Freeman and C. Werner, "Calibration of multipolarisation imaging radar", *Proceedings of IGARSS 1988*, Edinburgh, Scotland, September 13-16, 1988, pp. 335-339.
[211] S. Riegger, W. Wiesbeck, and A. J. Sieber, "On the origin of cross-polarization in remote sensing", *Proceedings of IGARSS '87*, Ann Arbor, MI, USA, May 18-21, 1987, pp. 677-680.
[212] W. Wiesbeck and S. Riegger, "A complete error model for free space polarimetric measurements", *IEEE Transactions on Antennas and Propagation*, vol. 39, no. 8, pp. 1105-1111, 1991.
[213] A. Freeman, "SAR calibration: An overview", *IEEE Transactions on Geoscience & Remote Sensing*, vol. 30, no. 6, pp. 1107-1121, 1992.
[214] E. Krogager, "Absolute phase of the radar target scattering matrix", *Electronics Letters*, vol. 26, no. 22, pp. 1834-1835, 1990.
[215] K. Sarabandi, F. T. Ulaby, and M. A. Tassoudji, "Calibration of polarimetric radar systems with good polarization isolation", *IEEE Transactions on Geoscience & Remote Sensing*, vol. 28, no. 1, pp. 70-75, 1990.
[216] K. Sarabandi, L. E. Pierce, and F. T. Ulaby, "Calibration of a polarimetric imaging SAR", *IEEE Transactions on Geoscience & Remote Sensing*, vol. 30, no. 3, pp. 540-549, 1992.
[217] S. H. Yueh, J. A. Kong, R. M. Barnes, and R. T. Shin, "Calibration of polarimetric radars using in-scene reflectors", *Journal of Electromagnetic Waves & Applications*, vol. 4, no. 1, pp. 27-48, 1990.
[218] K. Sarabandi, Y. Oh, and F. T. Ulaby, "Performance characterization of polarimetric active radar calibrators and a new single antenna design", *IEEE Transactions on Antennas & Propagation*, vol. 40, no. 10, pp. 1147-1154, 1992.
[219] R. K. Hawkins, R. Touzi, and C. E. Livingstone, "Polarimetric calibration results and error budget for SAR-580 system", *Proceedings of CEOS SAR workshop*, Toulouse, France, October 26-29, 1999, pp. 1-6.
[220] M. Fujita, "Development of a retrodirective PARC for ALOS/PALSAR calibration", *IEEE Transactions on Geoscience and Remote Sensing*, vol. 41, no. 10, pp. 2177-2186, 2003.

[221] A. Freeman, Y. Shen, and C. L. Werner, "Polarimetric SAR calibration experiment using active radar calibrators", *IEEE Transactions on Geoscience & Remote Sensing*, vol. 28, no. 2, pp. 224-240, 1990.

[222] A. Freeman, "A new system model for radar polarimeters", *IEEE Transactions on Geoscience & Remote Sensing*, vol. 29, no. 5, pp. 761-767, 1991.

[223] S. H. Yueh, S. V. Nghiem, and R. Kwok, "Symmetrization of cross-polarized responses in polarimetric radar images using reciprocity", *IEEE Transactions on Geoscience & Remote Sensing*, vol. 31, no. 6, pp. 1180-1185, 1993.

[224] S. Quegan, "A unified algorithm for phase and cross-talk calibration of polarimetric data-theory and observations", *IEEE Transactions on Geoscience & Remote Sensing*, vol. 32, no. 1, pp. 89-99, 1994.

[225] S. V. Nghiem, S. H. Yueh, R. Kwok, and F. K. Li, "Symmetry properties in polarimetric remote sensing", *Radio Science*, vol. 27, no. 5, pp. 693-711, 1992.

[226] B. D. Jersak, "Bistatic, Fully Polarimetric Radar Cross-Section Calibration Techniques and Measurement Error Analysis", Ph.D. Thesis, University of Texas, Arlington, December 1993.

[227] A. Freeman, J. J. van Zyl, J. D. Klein, H. A. Zebker, and Y. Shen, "Calibration of Stokes and scattering matrix format polarimetric SAR data", *IEEE Transactions on Geoscience & Remote Sensing*, vol. 30, no. 3, pp. 531-539, 1992.

[228] D. Kahny, K. Schmitt, and W. Wiesbeck, "Calibration of bistatic polarimetric radar systems", *IEEE Transactions on Geoscience & Remote Sensing*, vol. 30, no. 5, pp. 847-852, 1992.

[229] J. R. Gau and W. D. Burnside, "New polarimetric calibration technique using a single calibration dihedral", *IEE Proceedings Microwaves Antennas & Propagation*, vol. 142, no. 1, pp. 19-25, 1995.

[230] L. A. Muth, "Calibration standards and uncertainties in radar cross section measurements", *Proceedings of the 1999 IEEE Radar Confererence (Radar '99)*, Breste, France, May 17-21, 1999, pp. 326-331.

[231] L. A. Muth, P. A. Domich, M. W. Byron, and A. L. Buterbaugh, "Polarimetric calibration standards for monostatic radar systems", *Proceedings of NCSL Workshop & Symposium 1998*, Albuquerque,New Mexico, July 19-23, 1998, pp. 699-715.

[232] P. Brouard, S. Attia, and R. Guern, "MERIC recent developments", *Proceedings of RTO SCI Symposium on Non-Cooperative Air Target Identification Using Radar*, Mannheim, Germany, April 22-24, 1998, pp. 9.1-9.7.

[233] B. C. Brock, "A simple polarimetric calibration method which utilizes a reference target", *Proceedings of IEEE Antennas and Propagation Society International Symposium*, Chicago, Illinois, USA, July 20-24, 1992, pp. 565-568.

[234] T.-J. Chen, T.-H. Chu, and F.-C. Chen, "A new calibration algorithm of wide-band polarimetric measurement system", *IEEE Transactions on Antennas & Propagation*, vol. 39, no. 8, pp. 1188-1192, 1990.

[235] T.-J. Chen and T.-H. Chu, "Calibration of polarimetic radar system using three perfectly polarization-isolated calibrators", *Proceedings of IEEE Antennas and Propagation Society International Symposium*, Chicago, Illinois, USA, July 20-24, 1992, pp. 569-572.

[236] K. Kitayama, Y. Takayanagi, Y. Yamaguchi, and H. Yamada, "Polarimetric calibration target using a corrugated parallel plate target", *Electronics and Communications in Japan*, vol. 83, no. 10, pp. 914-921, 2000.

[237] L. A. Muth and R. C. Wittmann, "Calibration of polarimetric radar systems", *IEEE Antennas and Propagation Society International Symposium*,1997, pp. 830-833.

[238] W. Schroeder, K. Martin, and B. Lorensen, *The Visualization Toolkit An Object-Oriented Approach To 3D Graphics*, 3rd Edition ed.: Kitware, Inc, 2003.

[239] R. A. Dalrymple and R. G. Dean, *Water Wave Mechanics for Engineers and Scientists*, 2nd ed., Singapore: World Scientific Pub Co Inc, 1993.

[240] I. A. Svendsen and I. G. Jonsson, *Hydrodynamics of Coastal Regions*: Technical University of Denmark, 1980.

[241] C. V. Charlier, "Uber Die Darstellung Willkurlicher Funktionen", *Arkiv fur Matematik, Astronomioch Fysik*, vol. 9, no. 20, 1905.

[242] V. I. Tatarskii and V. V. Tatarskii, "Statistical non-Gaussian model of sea surface with anisotropic spectrum for wave scattering theory .II", *Journal of Electromagnetic Waves & Applications*, vol. 13, no. 7, pp. 901-902, 1999.

[243] V. I. Tatarskii and V. V. Tatarskii, "Statistical non-Gaussian model of sea surface with anisotropic spectrum for wave scattering theory .I", *Journal of Electromagnetic Waves & Applications*, vol. 13, no. 7, pp. 899-900, 1999.

[244] V. V. Tatarskii and V. I. Tatarskii, "Non-Gaussian statistical model of the ocean surface for wave-scattering theories", *Waves in Random Media*, vol. 6, no. 4, pp. 419-435, 1996.

[245] D. B. Creamer, F. Henyey, R. Schult, and J. Wright, "Improved linear representation of ocean surface waves", *Journal of Fluid Mechanics*, vol. 205, pp. 135-161, 1989.

[246] F. S. Henyey, D. B. Creamer, K. B. Dysthe, R. L. Schult, and J. A. Wright, "The energy and action of small waves riding on large waves", *Journal of Fluid Mechanics*, vol. 189, pp. 443-462, 1988.

[247] F. S. Henyey, "Hamiltonian description of stratified fluid dynamics", *Physics of Fluids*, vol. 26, no. 1, pp. 40-47, 1983.

[248] W. J. Pierson and L. Moskowitz, "A proposed spectral form for fully developed wind seas based on the similarity theory of S.A. Kitaigorodskii", *Journal of Geophysical Research*, vol. 69, pp. 5181-5190, 1964.

[249] K. Hasselmann, T.P. , T. P. Barnett, E. Bouws, H. Carlson, D. E. Cartwright, K. Enke, J. A. Ewing, H. Gienapp, D. E. Hasselmann, P. Kruseman, A. Meerburg, P. Müller, D. J. Olbers, K. Richter, W. Sell, and H. Walden, "Measurements of wind-wave growth and swell decay during the Joint North Sea Wave Project (JONSWAP)", *Dtsch. Hydrogr. Z.*, vol. 8, no. 12, pp. 95, 1973.

[250] M. K. Ochi, "A Series of JONSWAP wave Spectra for Offshore Structure Design", *Proceedings of 2nd International Conference on Behaviour of Offshore Structures*, London, UK, August, 1979, pp. 75-86.

[251] H. Mitsuyasu, F. Tasai, T. Suhara, S. Mizuno, M. Ohkusu, T. Honda, and K. Rikiishi, "Observations of the directional spectrum of ocean waves using a cloverleaf buoy", *Journal of Physical Oceanography*, vol. 5, no. 4, pp. 750-760, 1975.

[252] S. A. Kitaigordskii, V. P. Krasitskii, and M. M. Zaslavskii, "On Phillips' theory of equilibrium range in the spectra of wind-generated gravity waves", *Journal of Physical Oceanography*, vol. 5, no. 3, pp. 410-420, 1975.
[253] K. K. Kahma, "A study of the growth of the wave spectrum with fetch", *Journal of Physical Oceanography*, vol. 11, no. 11, pp. 1503-1515, 1981.
[254] O. M. Phillips, "Spectral and statistical properties of the equilibrium range in wind-generated gravity waves", *Journal of Fluid Mechanics*, vol. 156, no. 7, pp. 505-531, 1985.
[255] M. L. Banner, "Equilibrium spectra of wind waves", *Journal of Physical Oceanography*, vol. 20, no. 7, pp. 966-984, 1990.
[256] M. A. Donelan and W. J. Pierson, Jr., "Radar scattering and equilibrium ranges in wind-generated waves with application to scatterometry", *Journal of Geophysical Research*, vol. 92, no. C5, pp. 4971-5029, 1987.
[257] J. R. Apel, "An improved model of the ocean surface wave vector spectrum and its effects on radar backscatter", *Journal of Geophysical Research*, vol. 99, no. C8, pp. 16269-16291, 1994.
[258] T. Elfouhaily, B. Chapron, K. Katsaros, and D. Vandemark, "A unified directional spectrum for long and short wind-driven waves", *Journal of Geophysical Research*, vol. 102, no. C7, pp. 15781-15796, 1997.
[259] C. S. Cox and W. H. Munk, "Statistics of the sea surface derived from sun glitter", *Journal of Marine Research*, vol. 13, pp. 198-227, 1954.
[260] B. Jahne and K. S. Riemer, "Two-dimensional wave number spectra of small-scale water surface waves", *Journal of Geophysical Research*, vol. 95, no. C7, pp. 11531-11546, 1990.
[261] T. Hara, E. J. Bock, and D. Lyzenga, "In situ measurements of capillary-gravity wave spectra using a scanning laser slope gauge and microwave radars", *Journal of Geophysical Research*, vol. 99, no. C6, pp. 12593-12602, 1994.
[262] J.-S. Lee, D. L. Schuler, T. L. Ainsworth, E. Krogager, D. Kasilingam, and W.-M. Boerner, "On the estimation of radar polarization orientation shifts induced by terrain slopes", *IEEE Transactions on Geoscience & Remote Sensing*, vol. 40, no. 1, pp. 30-41, 2002.
[263] E. O. Tuck, D. C. Scullen, and L. Lazauskas, "Sea Wave Pattern Evaluation : SWPE 5.0 User's Manual", The University of Adelaide, Adelaide, SA, 30th March 2001.
[264] D. C. Scullen and E. O. Tuck, "Nonlinear free-surface flow solver: Users' guide", The University of Adelaide, Adelaide, SA, May 1 2002.
[265] E. O. Tuck, "Wave Resistance of Thin Ships and Catamarans", Report #T8701, Department of Applied Mathematics, The University of Adelaide, Adelaide, South Australia, 1987.
[266] L. Lazauskas and E. O. Tuck, "Low drag multihulls for sporting, commerical and military applications", *Proceedings of 4th International Conference on Fast Sea Transport - FAST97*, Sydney, Australia, 21 - 23 July, 1997, pp. 647-652.
[267] J. H. Michell, "The resistance of a ship", *Phil. Mag.*, vol. 45, no. 5, pp. 106-123, 1898.
[268] D. C. Scullen, "Accurate Computation of Steady Nonlinear Free-Surface Flows", Ph.D. Thesis, Department of Applied Mathematics, The University of Adelaide, Adelaide, South Australia, February 1998.

[269] K. Hasselmann, "On the non-linear energy transfer in a gravity wave spectrum, 1, General theory", *Journal of Fluid Mechanics*, vol. 12, pp. 481-500, 1961.
[270] K. Hasselmann, "On the non-linear energy transfer in a gravity wave spectrum, 2, Conservation theorems; wave particle analogy; irreversibility", *Journal of Fluid Mechanics*, vol. 15, pp. 273-281, 1962.
[271] K. Hasselmann, "On the non-linear energy transfer in a gravity wave spectrum, 3, Evaluation of the energy flux and swell-sea interaction for Neumann spectrum", *Journal of Fluid Mechanics*, vol. 15, pp. 385-398, 1962.
[272] W. J. Plant and D. L. Schuler, "Remote sensing of the sea surface using one- and two-frequency microwave techniques", *Radio Science*, vol. 15, no. 3, pp. 605-615, 1980.
[273] W. J. Plant and J. W. Wright, "Spectral decomposition of short gravity wave systems", *Journal of Physical Oceanography*, vol. 9, no. 3, pp. 621-624, 1979.
[274] W. J. Plant and J. W. Wright, "Growth and equilibrium of short gravity waves in a wind-wave tank", *Journal of Fluid Mechanics*, vol. 82, pp. 767-793, 1977.
[275] G. R. Valenzuela and M. B. Laing, "Nonlinear energy transfer in gravity-capillary wave spectra, with applications", *Journal of Fluid Mechanics*, vol. 54, pp. 507-520, 1972.
[276] V. Zakharov, "Stability of periodic waves of finite amplitude on the surface of a deep fluid", *Journal of Applied Mech. Tech. Physics*, vol. 2, pp. 190-194, 1968.
[277] K. M. Watson and B. J. West, "A transport-equation description of nonlinear ocean surface wave interactions", *Journal of Fluid Mechanics*, vol. 70, pp. 815-826, 1975.
[278] J. L. Hammack and D. M. Henderson, "Resonant interactions among surface water waves", *Annual Review of Fluid Mechanics*, vol. 25, pp. 55-97, 1993.
[279] F. Dias and C. Kharif, "Nonlinear gravity and capillary-gravity waves", *Annual Review of Fluid Mechanics*, vol. 31, pp. 301-346, 1999.
[280] T. Elfouhaily, D. R. Thompson, D. Vandemark, and B. Chapron, "Truncated Hamiltonian versus surface perturbation in nonlinear wave theories", *Waves in Random Media*, vol. 10, no. 1, pp. 103-116, 2000.
[281] P. H. Y. Lee, J. D. Barter, K. L. Beach, B. M. Lake, H. Rungaldier, H. R. Thompson, Jr., and R. Yee, "Scattering from breaking gravity waves without wind", *IEEE Transactions on Antennas & Propagation*, vol. 46, no. 1, pp. 14-26, 1998.
[282] T. Lamont-Smith, "An empirical model of EM scattering from steepening wave profiles derived from numerical computations", *IEEE Transactions on Geoscience and Remote Sensing*, vol. 41, no. 6, pp. 1447-1454, 2003.
[283] T. Elfouhaily, D. Thompson, D. Vandemark, and B. Chapron, "Short waves in the electromagnetic bias theories", *Proceedings of IGARSS 1999*, Hamburg, Germany, 28 June-2 July, 1999, pp. 989-991.
[284] T. Elfouhaily, D. R. Thompson, B. Chapron, and D. Vandemark, "Improved electromagnetic bias theory", *Journal of Geophysical Research*, vol. 105, no. C1, pp. 1299-1310, 2000.
[285] T. Elfouhaily, D. Thompson, D. Vandemark, and B. Chapron, "Inclusion of hydrodynamic modulations to the improved electromagnetic bias theory", *Proceedings of IGARSS 2000*, Honolulu, HI, USA, July 24-28, 2000, pp. 3181-3183.

[286] T. Elfouhaily, D. R. Thompson, B. Chapron, and D. Vandemark, "Improved electromagnetic bias theory: inclusion of hydrodynamic modulations", *Journal of Geophysical Research*, vol. 106, no. C3, pp. 4655-4664, 2001.
[287] D. D. Crombie, "Doppler spectrum of the sea echo at 13.56 Mc/s", *Nature*, vol. 175, pp. 681-682, 1955.
[288] J. W. Wright, "Detection of ocean waves by microwave radar; modulation of short gravity-capillary waves", *Boundary-Layer meterology*, vol. 13, pp. 87-105, 1978.
[289] J. W. Wright, "Backscattering from capillary waves with application to sea clutter", *IEEE Transactions on Antennas and Propagation*, vol. AP-14, no. 6, pp. 749-754, 1966.
[290] J. W. Wright, "A new model for sea clutter", *IEEE Transactions on Antennas and Propagation*, vol. AP-16, no. 2, pp. 217-223, 1968.
[291] F. Bass, I. Fuks, A. Kalmykov, I. Ostrovsky, and A. Rosenberg, "Very high frequency radiowave scattering by a disturbed sea surface Part I: Scattering from a slightly disturbed boundary", *IEEE Transactions on Antennas and Propagation*, vol. 16, no. 5, pp. 554-559, 1968.
[292] F. Bass, I. Fuks, A. Kalmykov, I. Ostrovsky, and A. Rosenberg, "Very high frequency radiowave scattering by a disturbed sea surface Part II: Scattering from an actual sea surface", *IEEE Transactions on Antennas and Propagation*, vol. 16, no. 5, pp. 560-568, 1968.
[293] M. I. Skolnik, *Radar Handbook*, 2nd ed., New York: McGraw-Hill, 1990.
[294] S. O. Rice, "Reflection of electromagnetic waves from slightly rough surfaces", *Communication on Pure and Applied Mathematics*, vol. 4, no. 3, pp. 351-378, 1951.
[295] J. W. S. Rayleigh, *The Theory of Sound*, vol. 2, 2nd ed., London: Macmillan, 1896.
[296] J. Ingers and M. Breidne, "Surface roughness scattering theories - a numerical comparison", *Proceeding of SPIE'88, vol 1029, Scattering and Diffraction*, Hamburg, Germany, 19-21 September, 1988, pp. 111-118.
[297] D. P. Winebrenner and A. Ishimaru, "Application of the phase-perturbation technique to randomly rough surfaces", *Journal of the Optical Society of America A-Optics & Image Science*, vol. 2, no. 12, pp. 2285-2294, 1985.
[298] D. Winebrenner and A. Ishimaru, "Investigation of a surface field phase perturbation technique for scattering from rough surfaces", *Radio Science*, vol. 20, no. 2, pp. 161-170, 1985.
[299] R. M. Fitzgerald and A. A. Maradudin, "A reciprocal phase-perturbation theory for rough-surface scattering", *Waves in Random Media*, vol. 4, no. 3, pp. 275-296, 1994.
[300] E. Rodriguez and Y. Kim, "A unified perturbation expansion for surface scattering", *Radio Science*, vol. 27, no. 1, pp. 79-93, 1992.
[301] G. R. Valenzuela, "Depolarization of EM waves by slightly rough surfaces", *IEEE Transactions on Antennas and Propagation*, vol. AP-15, no. 4, pp. 552-557, 1967.
[302] J. T. Johnson, "Third-order small-perturbation method for scattering from dielectric rough surfaces", *Journal of the Optical Society of America A-Optics & Image Science*, vol. 16, no. 11, pp. 2720-3276, 1999.
[303] M. A. Demir and J. T. Johnson, "Fourth- and higher-order small-perturbation solution for scattering from dielectric rough surfaces", *Journal of the Optical*

Society of America A-Optics & Image Science, vol. 20, no. 12, pp. 2330-2337, 2003.

[304] D. E. Barrick, "The ocean waveheight nondirectional spectrum from inversion of the HF sea-echo Doppler spectrum", *Remote Sensing of Environment*, vol. 6, no. 3, pp. 201-227, 1977.

[305] D. E. Barrick, J. M. Headrick, R. W. Bogle, and D. D. Crombie, "Sea backscatter at HF: interpretation and utilization of the echo", *Proceedings of the IEEE*, vol. 62, no. 6, pp. 673-680, 1974.

[306] S. J. Anderson and W. C. Anderson, "Bistatic HF scattering from the ocean surface and its application to remote sensing of seastate'", *Proceedings of the 1987 IEEE APS International Symposium*, Blacksburg, VA, USA, June, 1987, pp. 205.

[307] E. I. Thorsos and D. R. Jackson, "The validity of the perturbation approximation for rough surface scattering using a Gaussian roughness spectrum", *Journal of the Acoustical Society of America*, vol. 86, no. 1, pp. 261-277, 1989.

[308] M. J. Kim, H. M. Berenyi, R. E. Burge, and S. Tajbakhsh, "Region of validity of perturbation theory for dielectrics and finite conductors", *Waves in Random Media*, vol. 5, no. 3, pp. 305-327, 1995.

[309] J. M. Soto-Crespo, M. Nieto-Vesperinas, and A. T. Friberg, "Scattering from slightly rough random surfaces: a detailed study on the validity of the small perturbation method", *Journal of the Optical Society of America A-Optics & Image Science*, vol. 7, no. 7, pp. 1185-1201, 1990.

[310] M. J. Kim and A. J. Stoddart, "The region of validity of perturbation theory", *Waves in Random Media*, vol. 3, no. 4, pp. 325-342, 1993.

[311] S. L. Broschat, E. I. Thorsos, and A. Ishimaru, "The phase perturbation technique vs. an exact numerical method for random rough surface scattering", *Journal of Electromagnetic Waves & Applications*, vol. 3, no. 3, pp. 237-256, 1989.

[312] K. Yunjin, E. Rodriguez, and S. L. Durden, "A numerical assessment of rough surface scattering theories: vertical polarization", *Radio Science*, vol. 27, no. 4, pp. 515-527, 1992.

[313] Y. Kim and E. Rodriguez, "Comparison of the unified perturbation method with the two-scale expansion", *IEEE Transactions on Geoscience & Remote Sensing*, vol. 30, no. 3, pp. 510-515, 1992.

[314] F. G. Bass and I. M. Fuks, *Wave Scattering By Statistically Rough Surfaces*, New York: Pergamon Press, 1979.

[315] E. I. Thorsos, "The validity of the Kirchhoff approximation for rough surface scattering using a Gaussian roughness spectrum", *Journal of the Acoustical Society of America*, vol. 82, no. 1, pp. 79-92, 1988.

[316] E. I. Thorsos, "Studies of scattering theory using numerical methods", *Waves in Random Media*, vol. 1, no. 3, pp. 165-190, 1991.

[317] R. R. Lentz, "A numerical study of electromagnetic scattering from ocean-like surface", *Radio Science*, vol. 9, no. 12, pp. 1139-1146, 1974.

[318] M. F. Chen and A. K. Fung, "A numerical study of the regions of validity of the Kirchhoff and small-perturbation rough surface scattering models", *Radio Science*, vol. 23, no. 2, pp. 163-170, 1988.

[319] A. Khenchaf, F. Daout, and J. S. Saillard, "Polarization degradation in the sea surface environment", *Proceedings of OCEANS'95*, San Diego, California, USA, October 9-12, 1995, pp. 1517-1522.

[320] A. Voronovich, *Wave Scattering from Rough Surfaces*, London, UK: Springer-Verlag, 1994.
[321] C. Bourlier and G. Berginc, "Shadowing function with single reflection from anisotropic Gaussian rough surface. Application to Gaussian, Lorentzian and sea correlations", *Waves in Random Media*, vol. 13, no. 1, pp. 27-58, 2003.
[322] N. C. Bruce, "On the validity of the inclusion of geometrical shadowing functions in the multiple-scatter Kirchhoff approximation", *Waves in Random Media*, vol. 14, no. 1, pp. 1-12, 2004.
[323] C. Bourlier, G. Berginc, and J. Saillard, "Monostatic and bistatic statistical shadowing functions from a one-dimensional stationary randomly rough surface. II. Multiple scattering", *Waves in Random Media*, vol. 12, no. 2, pp. 175-200, 2002.
[324] D. A. Kapp and G. S. Brown, "Effect of correlation between shadowing and shadowed points in rough surface scattering", *IEEE Transactions on Antennas & Propagation*, vol. 42, no. 8, pp. 1154-60, 1994.
[325] G. S. Brown, "The validity of shadowing corrections in rough surface scattering", *Radio Science*, vol. 19, no. 6, pp. 1461-1468, 1984.
[326] I. M. Fuks, "Effective probability density function of rough surface slopes when strong shadowing is present", *Waves in Random Media*, vol. 12, no. 4, pp. 401-416, 2002.
[327] D. Holliday, "Resolution of a controversy surronding the Kirchhoff approach and the small perturbation method in rough surface scattering theory", *IEEE Transactions on Antennas & Propagation*, vol. 35, no. 1, pp. 120-127, 1987.
[328] V. I. Tatarskii, "The expansion of the solution of the rough-surface scattering problem in powers of quasi-slopes", *Waves in Random Media*, vol. 3, no. 2, pp. 127-146, 1993.
[329] A. Voronovich, "Small-slope approximation for electromagnetic wave scattering at a rough interface of two dielectric half-spaces", *Waves in Random Media*, vol. 4, no. 3, pp. 337-367, 1994.
[330] A. G. Voronovich, "Small-slope approximation in wave scattering by rough surfaces", *Zhurnal Eksperimentalnoi i Teoreticheskoi Fiziki*, vol. 89, no. 1, pp. 116-125, 1985.
[331] T. Elfouhaily, D. R. Thompson, D. Vandemark, and B. Chapron, "A new bistatic model for electromagnetic scattering from perfectly conducting random surfaces", *Waves in Random Media*, vol. 9, no. 3, pp. 281-294, 1999.
[332] D. Holliday, G. St-Cyr, and N. E. Woods, "A radar ocean imaging model for small to moderate incidence angles", *International Journal of Remote Sensing*, vol. 7, no. 12, pp. 1809-1834, 1986.
[333] J. C. West, "Analysis of the iterative Kirchhoff approximation for rough surface scattering", *Proceedings of IGARSS 1999*, Hamburg, Germany, 28 June-2 July, 1999, pp. 2410-2412.
[334] J. V. Toporkov and G. S. Brown, "Numerical study of the extended Kirchhoff approach and the lowest order small slope approximation for scattering from ocean-like surfaces: Doppler analysis", *IEEE Transactions on Antennas & Propagation*, vol. 50, no. 4, pp. 417-425, 2002.
[335] T. Elfouhaily, D. R. Thompson, D. E. Freund, D. Vandemark, and B. Chapron, "A new bistatic model for electromagnetic scattering from perfectly conducting random surfaces: numerical evaluation and comparison with SPM", *Waves in Random Media*, vol. 11, no. 1, pp. 33-43, 2001.

[336] J. T. Johnson, J. V. Toporkov, and G. S. Brown, "A numerical study of backscattering from time-evolving sea surfaces: comparison of hydrodynamic models", *IEEE Transactions on Geoscience & Remote Sensing*, vol. 39, no. 11, pp. 2411-2420, 2001.
[337] B. F. Kur'yanov, "The scattering of sound at a rough surface with two types of roughness", *Soviet Physics-Acoustics*, vol. 8, pp. 252-257, 1963.
[338] I. M. Fuks, "Variance equations and the inverse scattering problem for a weakly rough surface", *Izvestiya Vysshikh Uchebnykh Zavedenii Radiofizika*, vol. 28, no. 2, pp. 177-83, 1985.
[339] A. G. Voronovich, "The effect of the modulation of Bragg scattering in small-slope approximation", *Waves in Random Media*, vol. 12, no. 3, pp. 341-349, 2002.
[340] G. R. Brown, "Simplification in the stochastic Fourier transform approach to random surface scattering", *IEEE Transaction on Antennas and Propagation*, vol. AP-33, no. 1, pp. 48-55, 1985.
[341] W. J. Plant, "A two scale model of short wind-generated waves and scatterometry", *Journal of Geophysical Research*, vol. 91, no. C9, pp. 735-749, 1986.
[342] A. K. Fung and K. S. Chen, "Dependence of the surface backscattering coefficients on roughness, frequency and polarization states", *International Journal of Remote Sensing*, vol. 13, no. 9, pp. 1663-1680, 1992.
[343] A. Guissard and P. Sobieski, "An approximate model for the microwave brightness temperature of the sea", *International Journal of Remote Sensing*, vol. 8, no. 11, pp. 1607-1627, 1987.
[344] D. Lemaire, P. Sobieski, C. Craeye, and A. Guissard, "Two-scale models for rough surface scattering: Comparison between the boundary perturbation method and the integral equation method", *Radio Science*, vol. 37, no. 1, pp. 1-16, 2002.
[345] W. J. Plant, "A stochastic, multiscale model of microwave backscatter from the ocean", *Journal of Geophysical Research*, vol. 107, no. C9, pp. 1-21, 2002.
[346] D. S. W. Kwoh, B. M. Lake, and H. Rungaldier, "Microwave scattering from internal wave modulated surface waves: a shipboard real aperture coherent radar study in the Georgia Strait Experiment", *Journal of Geophysical Research*, vol. 93, no. C10, pp. 235-248, 1988.
[347] D. Walker, "Experimentally motivated model for low grazing angle radar Doppler spectra of the sea surface", *IEE Proceedings: Radar, Sonar & Navigation*, vol. 147, no. 3, pp. 114-120, 2000.
[348] K. S. Chen, A. K. Fung, and D. A. Weissman, "A backscattering model for ocean surface", *IEEE Transactions on Geoscience & Remote Sensing*, vol. 30, no. 4, pp. 811-817, 1992.
[349] M. I. Charnotskii and V. I. Tatarskii, "Tilt-invariant theory of rough-surface scattering. I", *Waves in Random Media*, vol. 5, no. 4, pp. 361-380, 1995.
[350] G. Ljungdahl and S. W. Lovesey, "Surface scattering near grazing angles: the distorted wave Born approximation for rough surfaces", *Physica Scripta*, vol. 53, no. 6, pp. 734-748, 1996.
[351] A. Garcia-Valenzuela, "A heuristic model approximation for scattering from perfectly conducting one-dimensional random rough surfaces", *Waves in Random Media*, vol. 6, no. 3, pp. 213-228, 1996.

[352] A. Garcia-Valenzuela, "The local spectral expansion method for the scattering of light from two-dimensional perfectly conducting surfaces", *Revista Mexicana de Fisica*, vol. 43, no. 6, pp. 906-915, 1997.

[353] A. Garcia-Valenzuela, "The local spectral expansion method for scattering from one-dimensional dielectric-dielectric rough interfaces", *Journal of Electromagnetic Waves & Applications*, vol. 11, no. 6, pp. 775-805, 1997.

[354] A. Garcia-Valenzuela and R. E. Collin, "The local spectral expansion method for scattering from perfectly conducting surfaces rough in one dimension", *Journal of Electromagnetic Waves & Applications*, vol. 11, no. 1, pp. 37-63, 1997.

[355] W. T. Shaw and A. J. Dougan, "Green's function refinement as an approach to radar backscatter: general theory and applications to LGA scattering from the ocean", *IEEE Transactions on Antennas & Propagation*, vol. 46, no. 1, pp. 57-66, 1998.

[356] O. Calvo-Perez, A. Sentenac, and J. J. Greffet, "Light scattering by a two-dimensional, rough penetrable medium: a mean-field theory", *Radio Science*, vol. 34, no. 2, pp. 311-335, 1999.

[357] A. Sentenac, G. Toso, and M. Saillard, "Study of coherent scattering from one-dimensional rough surfaces with a mean-field theory", *Journal of the Optical Society of America A-Optics & Image Science*, vol. 15, no. 4, pp. 924-931, 1998.

[358] J. G. Watson and J. B. Keller, "Rough surface scattering via the smoothing method", *Journal of the Acoustical Society of America*, vol. 75, no. 6, pp. 1705-1708, 1984.

[359] G. S. Brown, "A new approach to the analysis of rough surface scattering", *IEEE Transactions on Antennas & Propagation*, vol. 39, no. 7, pp. 943-948, 1991.

[360] J. A. DeSanto, "Exact spectral formalism for rough-surface scattering", *Journal of the Optical Society of America A-Optics & Image Science*, vol. 2, no. 12, pp. 2202-2207, 1985.

[361] G. S. Brown, "Simplifications in the stochastic Fourier transform approach to random surface scattering", *IEEE Transactions on Antennas & Propagation*, vol. AP-33, no. 1, pp. 48-55, 1985.

[362] K. F. Warnick and W. C. Chew, "Numerical simulation methods for rough surface scattering", *Waves in Random Media*, vol. 11, no. 1, pp. 1-30, 2001.

[363] E. Rodriguez, K. Yunjin, and S. L. Durden, "A numerical assessment of rough surface scattering theories: horizontal polarization", *Radio Science*, vol. 27, no. 4, pp. 497-513, 1992.

[364] T. Yang and S. L. Broschat, "A comparison of scattering model results for two-dimensional randomly rough surfaces", *IEEE Transactions on Antennas & Propagation*, vol. 40, no. 12, pp. 1505-1512, 1992.

[365] H. Goldstein, "Frequency dependence of the properties of sea echo", *Physical Review*, vol. 70, pp. 938-946, 1946.

[366] M. Katzin, "On mechanisms of radar sea clutter", *Proceedings of Institute of Radio Engineers*, vol. 45, no. 1, pp. 44-54, 1957.

[367] W. S. Ament, "Forward and backscattering by certain rough surfaces", *IRE Transactions on Antennas and Propagation*, vol. 5, no. 1, pp. 363-373, 1956.

[368] V. Twersky, "On the scattering and reflection of electromagnetic waves by rough surfaces", *IEEE Transactions on Antennas & Propagation*, vol. AP-5, no. 1, pp. 81-90, 1957.

[369] B. Kinsman, *Wind Waves*, Englewood Cliffs, New Jersey, USA: Prentice-Hall, 1965.
[370] L. B. Wetzel, "Models For Electromagnetic Scattering From The Sea At Extremely Low Grazing Angles", Memorandum, Report No. 6098, Naval Research Laboratory, Washington D.C, December 1987.
[371] E. M. Twarog, D. J. McLaughlin, and N. Allan, "High resolution polarimetric radar scattering measurements of low grazing angle sea clutter", *Proceedings of IGARSS 1996*, Lincoln, NE, USA, May 27-31, 1996, pp. 905-907.
[372] F. A. Fay, J. Clarke, and R. S. Peter, "Weibull distribution applied to sea clutter", *Proceedings of IEE International Radar Conference RADAR'77*, London, U.K., October 25-28, 1977, pp. 101-104.
[373] D. C. Schleher, "Radar detection in Weibull clutter", *IEEE Transactions on Aerospace Electronic Systems*, vol. AES-12, no. 6, pp. 736-743, 1976.
[374] G. R. Valenzuela and M. B. Laing, "On the Statistics of Sea Clutter", Report No. 7349, Naval Research Laboratory, Washington, D.C., December 30 1971.
[375] D. Trizna, "Measurement and Interpretation of North Atlantic Ocean Marine Radar Sea Scatter", Report No. 9099, Naval Research Laboratory, Washington, D.C., May 1988.
[376] S. Sayama and M. Sekine, "Detection of radar target embedded in sea clutter using a millimeter wave radar", *Proceedings of the 2000 International Symposium on Antennas and Propagation*, Fukuoka, Japan, 21-25 August, 2000, pp. 963-966.
[377] S. Sayama and M. Sekine, "Weibull distribution and K-distribution of sea clutter observed by X-band radar and analyzed by AIC", *IEICE Transactions on Communications*, vol. E83-B, no. 9, pp. 1978-1982, 2000.
[378] S. Sayama and M. Sekine, "Log-normal, log-Weibull and K-distributed sea clutter", *IEICE Transactions on Communications*, vol. E85-B, no. 7, pp. 1375-1381, 2002.
[379] H. Akaike, "Information theory and an extension of the maximum likelihood principle", *Proceedings of the 2nd International Symposium of Information Theory*, Akademiai Kiado, Budapest,1973, pp. 267-281.
[380] S. R. Cloude and D. G. Corr, "A new parameter for soil moisture estimation", *Proceedings of IGARSS 2002*, Toronto, Canada, June 24-28, 2002, pp. 641-643.
[381] S. R. Cloude, "Radar Polarimetry in Sea Clutter Studies", Report AELc/02/14, AEL Consultants, Fife, Scotland, UK, November 2002.
[382] M. L. Banner, A. V. Babanin, and I. R. Young, "Breaking probability for dominant waves on the sea surface", *Journal of Physical Oceanography*, vol. 30, no. 12, pp. 3145-3160, 2000.
[383] D. B. Coakley, P. M. Haldeman, D. G. Morgan, K. R. Nicolas, D. R. Penndorf, L. B. Wetzel, and C. S. Weller, "Electromagnetic scattering from large steady breaking waves", *Experiments in Fluids*, vol. 30, no. 5, pp. 479-487, 2001.
[384] E. B. Dano, D. R. Lyzenga, G. Meadows, L. Meadows, H. Van Sumeren, and R. Onstott, "Radar backscatter from mechanically generated transient breaking waves. II. Azimuthal and grazing angle dependence", *IEEE Journal of Oceanic Engineering*, vol. 26, no. 2, pp. 201-215, 2001.
[385] M. C. Haller and D. R. Lyzenga, "Comparison of radar and video observations of shallow water breaking waves", *IEEE Transactions on Geoscience & Remote Sensing*, vol. 41, no. 4, pp. 832-844, 2003.

[386] K. Hyunjun and J. T. Johnson, "Radar image study of simulated breaking waves", *IEEE Transactions on Geoscience & Remote Sensing*, vol. 40, no. 10, pp. 2143-2150, 2002.

[387] L. B. Wetzel, "On microwave scattering by breaking waves", in *Wave Dynamics and Radio Probing of the Ocean Surface*, O. M. Phillips and K. Hasselmann, Eds, Plenum. New York: pp. 273-284, 1986.

[388] J. C. West, "Low-grazing-angle (LGA) sea-spike backscattering from plunging breaker crests", *IEEE Transactions on Geoscience & Remote Sensing*, vol. 40, no. 2, pp. 523-526, 2002.

[389] J. C. West and Z. Zhiqin, "Electromagnetic modeling of multipath scattering from breaking water waves with rough faces", *IEEE Transactions on Geoscience & Remote Sensing*, vol. 40, no. 3, pp. 583-592, 2002.

[390] J. C. West and J. Shiou-Jyh, "Two-scale treatment of low-grazing-angle scattering from spilling breaker water waves", *Radio Science*, vol. 37, no. 4, pp. 1-12, 2002.

[391] J. C. West, "Small slope approximation modeling of scattering from a spilling breaker wave crest", *Proceedings of IGARSS 2003*, Toulouse, France, 21-25 July, 2003, pp. 139-141.

[392] S. R. Cloude, "Eigenvalue parameters for surface roughness studies", *Proceeding of SPIE'99, vol. 3754, Polarisation : Measurement, Analysis and Remote Sensing II*, Denver, Colorado, USA, 19-21 July, 1999, pp. 2-13.

[393] E. O. Tuck, D. C. Scullen, and L. Lazauskas, "Sea Wave Pattern Evaluation Part 6 report : Viscosity Factors", The University of Adelaide, Adelaide, SA, 2002.

[394] W. T. Lindemuth, T. J. Ratcliffe, and A. M. Reed, "Comparitive Accuracy of Numerical Kelvin Wake Code Predictions - "Wake Off"", Department of The Navy, Bethesda, MD USA, 1991.

[395] J. Morris, S. Anderson, and A. Parfitt, "Polarimetric observations of wave breaking induced by ship wakes", *Proceedings of IGARSS 2001*, Sydney, NSW, Australia., 9-13 July, 2001, pp. 2958-2960.

[396] J. T. Morris, S. J. Anderson, and S. R. Cloude, "A novel technique for calibrating polarimetric radars", *Proceedings of Eighth Australian Symposium on Antennas*, Sydney, NSW, Australia, February 12-13, 2003, pp. 43.

[397] P. H. Y. Lee, J. D. Barter, K. L. Beach, B. M. Lake, H. Rungaldier, J. C. Shelton, H. R. Thompson, Jr., and R. Yee, "Depolarization in microwave scatterometry", *Proceedings of IGARSS 1996*, Lincoln, NE, USA, May 27-31, 1996, pp. 2213-2215.

[398] P. H. Y. Lee, J. D. Barter, K. L. Beach, B. M. Lake, H. Rungaldier, J. C. Shelton, H. R. Thompson, Jr., and R. Yee, "Dependence of polarimetric Doppler spectra on breaking-wave energy", *Proceedings of IGARSS 1996*, Lincoln, NE, USA, May 27-31, 1996, pp. 2201-2203.

[399] V. U. Zavorotny and A. G. Voronovich, "Two-scale model and ocean radar Doppler spectra at moderate- and low-grazing angles", *IEEE Transactions on Antennas and Propagation*, vol. 46, no. 1, pp. 84-92, 1998.

[400] D. Kasilingam, D. Schuler, J.-S. Lee, and S. Malhotra, "Modulation of polarimetric coherence by ocean features", *Proceedings of IGARSS 2002*, Toronto, Canada, June 24-28, 2002, pp. 432-434.

[401] C. L. Stevens, E. M. Poulter, M. J. Smith, and J. A. McGregor, "Nonlinear features in wave-resolving microwave radar observations of ocean waves", *IEEE Journal of Oceanic Engineering*, vol. 24, no. 4, pp. 470-480, 1999.

[402] M. A. Donelan, M. S. Longuet-Higgins, and J. S. Turner, "Periodicity in whitecaps", *Nature*, vol. 239, pp. 449-451, 1972.